

# PROPERTIES OF **Crystalline Silicon**

**Edited by**  
**ROBERT HULL**  
**University of Virginia, USA**

Published by: INSPEC, The Institution of Electrical Engineers,  
London, United Kingdom

© 1999: The Institution of Electrical Engineers

This publication is copyright under the Berne Convention and the Universal Copyright Convention. All rights reserved. Apart from any fair dealing for the purposes of research or private study, or criticism or review, as permitted under the Copyright, Designs and Patents Act, 1988, this publication may be reproduced, stored or transmitted, in any forms or by any means, only with the prior permission in writing of the publishers, or in the case of reprographic reproduction in accordance with the terms of licences issued by the Copyright Licensing Agency. Inquiries concerning reproduction outside those terms should be sent to the publishers at the undermentioned address:

The Institution of Electrical Engineers,  
Michael Faraday House,  
Six Hills Way, Stevenage,  
Herts. SG1 2AY, United Kingdom

While the author and the publishers believe that the information and guidance given in this work are correct, all parties must rely upon their own skill and judgment when making use of them. Neither the author nor the publishers assume any liability to anyone for any loss or damage caused by any error or omission in the work, whether such error or omission is the result of negligence or any other cause. Any and all such liability is disclaimed.

The moral right of the author to be identified as author of this work has been asserted by him/her in accordance with the Copyright, Designs and Patents Act 1988.

#### **British Library Cataloguing in Publication Data**

A CIP catalogue record for this book  
is available from the British Library

**ISBN 0 85296 933 3**

Printed in England by Short Run Press Ltd., Exeter

## Foreword

Information technology is one of the key drivers of progress into the 21<sup>st</sup> century, transforming the way in which we communicate, learn, work, live. It will be essential for the growth of our economy as well as for the solutions of some of the most critical problems facing society. The electronic systems industry needed to support this vision has now overtaken the automotive industry in terms of contribution to the global economy. Micro- and optoelectronic sensors and transducers are the basis of a rapidly growing business segment. But to a very large extent electronic systems are based upon the technology for producing integrated circuits. And this technology - that just celebrated its 40<sup>th</sup> anniversary - is synonymous with *silicon* technology: its material properties combined with its abundance in nature have given silicon a unique position in the fabrication of miniaturized devices that is not likely to be challenged soon.

The business based upon this silicon integrated circuit itself is unique and particularly challenging. It is unique because over more than 3 decades it has sustained a market growth of 15% per year. It is at the same time extremely challenging, because this growth is based on an exponential technology development, resulting in electronic functions with continuously improved performance and reliability, reduced power consumption and a 25-30% per-year cost reduction.

Supporting this productivity increase is the growth of circuit complexity by a factor of approximately 2 every year as predicted by Gordon Moore in 1975 and resulting from feature scaling, die size increase and circuit cleverness. Some of the historical contributions to increased productivity – such as manufacturing yield improvement – are no longer available, and device scaling still remains the largest contributor to productivity growth. The Semiconductor Industry Association has coordinated the consensus building on the future technology requirements for maintaining the historical rate of advancement. The resulting vision is documented in the “National Technology Roadmap for Semiconductors” – the next update of which is likely to become known as the “International Technology Roadmap for Semiconductors” – predicting 50-nm features by 2012.

The challenges faced by the semiconductor community as it moves into production of metal-oxide-semiconductor (MOS) transistor devices with dimensions below 100 nm are enormous. As technology scales and materials are improved, they are stressed to their intrinsic limits and a thorough understanding of the fundamental properties is needed. At the same time new materials, new patterning techniques and new device structures will be required: new gate dielectrics and gate electrode materials and processes, as well as new interconnect materials and processes to replace the familiar metals, dielectrics and contact materials used in device interconnect structures. Also when removing ‘bottlenecks’ process technologists will require insight into the fundamentals.

In early stages of technology development modelling and simulation are extensively used in order to obtain insight into the directions of technology. It is clear that when devices are further scaled, tools will be needed to model physical and chemical processes at an atomic

level and to simulate carrier transport under non-equilibrium conditions. The development of such tools will require advanced understanding of the fundamental processes.

Competitiveness of the IC industry has always been linked to advances in material preparation and process technology. But the IC industry has grown up in recent years. Among others things, this means that the costs together with the risks have risen. This has resulted in much more fragmentation and specialization as illustrated by the current successful business model based on the collaboration of “fab-less” design companies with “foundries” specializing in cost-effective and state-of-the-art manufacturing. The trend towards the “system-on-a-chip” has led to a growing need for truly multidisciplinary teams of experts with a deep technical insight in specific areas such as process modules or integration combined with a good understanding of system and electronic circuit design, or vice versa. Communication among the members of such teams has created an increased need for up-to-date and in-depth reviews of materials properties and technology.

The 18 chapters of this new book from the EMIS Datareviews series are the result of an ambitious project bringing together contributions from a worldwide group of experts covering a broad spectrum from silicon physics and material properties to device technology. The balance of coverage and presentation should make this volume a valuable working information resource for academics, semiconductor process developers and electronic device simulation engineers needing meaningful, usable data as they seek to advance their understanding and exploitation of silicon.

Inspired by the increased use of the Internet the editors will hopefully revive their plan to launch an online system. We believe such a service allowing regular additions and revisions would be of value to the thousands of materials and technology specialists who need instant access to a growing amount of data and knowledge. But for now and in the years to come, the present book will serve the needs of the “silicon community” more than adequately.

Roger de Keersmaecker  
IMEC, Leuven, Belgium

May 1999

## **Introduction**

This volume collects fundamental physical and materials data for crystalline silicon into a single, authoritative source. The scope of the volume ranges from fundamental electronic and optical properties of silicon, through mechanical, thermal and defect properties, to crystal growth, doping and interfaces with other technologically important materials (note that silicon-based heterostructures, silicon carbide and metal silicides are covered in other EMIS volumes from INSPEC, while volumes on silicon oxides are planned).

The material is organized into individual "Datareviews", each authored by an expert in that particular field. Sets of Datareviews are then collected into chapters, each edited by an internationally recognized authority. The previous EMIS book, *Properties of silicon* (INSPEC, 1988) is widely used in academic and engineering laboratories and it is our hope that this volume will serve as a substantially enhanced and updated reference source for scientists, engineers and technical managers doing research into silicon-based materials and structures, or working with silicon technology.

The volume editor would like to thank the 100 authors and 18 chapter editors who have contributed their time and expertise to this project. In addition, he would like to recognize the outstanding support provided by John Sears, the managing editor of the EMIS Datareviews series. Acknowledgement should also be given to the careful, detailed MS preparation and indexing work of Pamela Sears and to Dr Peter Capper for copy editing and typesetting such a diversity of MSS to achieve the structural integrity and homogeneity needed for a reference work of this kind.

Robert Hull

University of Virginia  
May 1999

## Contributors

<b>T. Abe</b> editor, chapter 1	Shin-Etsu Handotai Co, Ltd. 2-13-1 Isobe, Annaka, Gunma 379-01, Japan
<b>C.A.J. Ammerlaan</b> 11.3-11.5	University of Amsterdam, Van der Waals-Zeeman Institut Valckenierstraat 65, NL-1019 Amsterdam, Holland
<b>M.J. Anc</b> 18.9	Ibis Technology Corporation 32 Cherry Hill Drive, Danvers, Ma 01923, USA
<b>D.E. Aspnes</b> editor, chapter 12	North Carolina State University, Dept. of Physics Box 8202, Raleigh, NC 27695-8202, USA
<b>J.C. Bean</b> editor, chapter 2	University of Virginia, Dept. of Electrical Engineering Thornton Hall, Charlottesville, VA 22903-2442, USA
<b>H.S. Bennett</b> 7.5	University of Newcastle upon Tyne, Solid State Physics Group Dept. of Physics, Newcastle upon Tyne, NE1 7RU, UK
<b>P.R. Briddon</b> 6.9	University of Newcastle upon Tyne, Physics Dept. Newcastle upon Tyne, NE1 7RU, UK
<b>R.E. Brindos</b> 14.1, 14.5	University of Florida, SWAMP Center Dept. of Materials Science and Engineering 525 Engineering Bldg., PO Box 116130 FL 32611-6130, USA
<b>P. D. Bristowe</b> 6.6	University of Cambridge, Dept. of Materials Science and Metallurgy, Pembroke Street, Cambridge CB2 3QZ, UK
<b>M.R.Brozel</b> editor, chapter 4	UMIST, Centre for Electronic Materials PO Box 88, Manchester M60 1QD, UK
<b>R.J. Carter</b> 5.7, 5.8	North Carolina State University, Dept.of Physics Box 8202, Raleigh, NC 27695-88202, USA
<b>M.-J. Caturla</b> 14.2	Lawrence Livermore National Laboratory, Chemistry and Materials Science L-268, 7000 East Avenue, Livermore, CA 94550, USA
<b>Y.J. Chabal</b> 5.5, 18.3, 18.6	Lucent Technologies, Bell Laboratories 600 Mountain View, Murray Hill, NJ 07974, USA
<b>S. Coffa</b> 9.14, 14.3	CNR-IMETEM, Stadale Primosole 50 I-95121 Catania, Italy
<b>S.R. Crowder</b> 18.7	IBM Corporation, Microelectronics Division Semiconductor R&D Center, 1580 Route 52 Hopewell Junction, NY 12533, USA

<b>P. Deak</b> 6.1	Physical Institute of the Technical University of Budapest H-1521 Budapest, Hungary
<b>P.R. de la Houssaye</b> 18.2	NRad, NCCOSc RDT Division, D805, Rm. 22953475 Strothe Road San Diego, Ca 92152-6341, USA
<b>T. D. de la Rubia</b> 14.2	Lawrence Livermore National Laboratory, Chemistry and Materials Science L-268, 7000 East Avenue, Livermore, CA 94550, USA
<b>E. Dornberger</b> 1.6	Wacker Siltronic AG Postfach 1140, D-84479 Burghausen, Germany
<b>D.J. Dunstan</b> 7.8	Queen Mary and Westfield College, Dept.of Physics Mile End Road, London, E1 4NS, USA
<b>R. Elliman</b> editor, chapter 14	Australian National University, Electronic Materials Engineering Dept., GPO Box 4, Canberra, ACT 0200, Australia
<b>C.P. Ewels</b> 6.3	University of Sussex, School of Chemistry, Physics and Environmental Sciences, Falmer, Brighton, BN1 9QJ, UK
<b>A. George</b> editor, chapter 3	Ecole des Mines de Nancy, Laboratoire de Physique des Materiaux CNRS UMR 7556, Parc de Saurupt, F-54042 Nancy, France
<b>M.D. Giles</b> 10.3	Intel Corporation MS: RN2-40, 2200 Mission College Blvd., Santa Clara, Ca 95052, USA
<b>D.W. Greve</b> 2.2, 2.3	Carnegie Mellon University, Dept. of Electrical and Computer Engineering, Hamerschlag Hall, Pittsburgh PA 15213, USA
<b>H. Grimmelis</b> editor, chapter 11	Lund Institute of Technology, Dept.of Solid State Physics Box 118, S-22100 Lund, Sweden
<b>V. Grivickas</b> 13.1, 13.4-13.8	Chalmers University of Technology, Physical Electronics and Photonics, Dept. of Microelectronics and Photonics 4-412 96 Goteborg, Sweden
<b>M. Heggie</b> editor, chapter 6	University of Sussex, School of Chemistry, Physics and Environmental Sciences, Falmer, Brighton, BN1 9QJ, UK
<b>M.M. Heyns</b> 5.6	North Carolina State University, Dept. of Physics Box 8202, Raleigh, NC 27695-88202, USA
<b>H. Hieslmair</b> 15.1-15.5	University of California at Berkeley, Dept. of Materials Science 587 Evans Hall, 1 Cyclotron Road, 272 Hearst Bldg. CA 94720, USA
<b>K. Hoshikawa</b> 1.4	Shin-Shyu University, Education Facility Nishi-Nagano, Nagano 380, Japan

<b>X. Huang</b> 1.4	Shin-Shyu University, Education Facility Nishi-Nagano, Nagano 380, Japan
<b>R. Hull</b> volume editor	University of Virginia, Dept. of Materials Science & Engineering Charlottesville, VA 22903, USA
<b>A.A. Istratov</b> 15.1-15.5	University of California at Berkeley, Dept. of Materials Science 587 Evans Hall, 1 Cyclotron Road, 272 Hearst Bldg. CA 94720, USA
<b>S. S. Iyer</b> editor, chapter 18	IBM Corporation, Microelectronics Division Bldg. 630 ZIP E40, 1580 Route 52, Hopewell Junction NY 12533, USA
<b>S.H. Jones</b> editor, chapter 8	Virginia Semiconductor, Inc. 1501 Powhatan Street, Fredericksburg, Virginia 22401, USA
<b>K.S. Jones</b> editor, chapter 10 14.1, 14.4, 14.5	University of Florida, SWAMP Center Dept. of Materials Science and Engineering 525 Engineering Bldg., PO Box 116130 FL 32611-6130, USA
<b>R. Jones</b> 6.3	University of Exeter, Dept. of Physics Exeter, EX4 4QJ, UK
<b>G. Jungnickel</b> 6.2	TU Chemnitz-Zwickau 09107 Chemnitz, Germany
<b>K. Kakimoto</b> 1.2	Kyushu University, Institute of Advanced Materials Study 6-1, Kasuga-koen, Kasuga 816, Japan
<b>P.H. Keys</b> 14.1, 14.5	University of Florida, SWAMP Center Dept. of Materials Sci. and Eng., 525 Engineering Bldg. PO Box 116130, FL 32611-6130, USA
<b>S. Kobayashi</b> 1.3	Sumitomo Metal Industries Ltd, Corporate R&D Laboratories 1-8 Fuso-cho, Amagasaki Hyogo, 660, Japan
<b>M. Lagally</b> <b>5.1, 5.2</b>	University of Wisconsin-Madison, Dept. of Materials Science, Engineering and Physics, 1509 University Avenue, Madison WI 53706, USA
<b>I. Lagnado</b> 18.2	NRad, NCCOSc RDT Division, D805, Rm. 229, 53475 Strothe Road San Diego, Ca 92152-6341, USA
<b>N. Lehto</b> 6.10	University of Sussex, School of Chemistry, Physics and Environmental Sciences, Falmer, Brighton, BN1 9QJ, UK
<b>J.L. Lindstrom</b> 13.3	Chalmers University of Technology, Physical Electronics and Photonics, Dept. of Microelectronics and Photonics 4-412 96 Goteborg, Sweden

<b>F. Liu</b> 5.1, 5.2	University of Wisconsin-Madison, Dept. of Materials Science, Engineering and Physics, 1509 University Avenue, Madison WI 53706, USA
<b>K. Maex</b> 17.1	IMEC VZW, ASE/VMT Kapeldreef 75, B-3001 Leuven, Belgium
<b>A. Mainwood</b> 6.4	King's College, London., Dept. of Physics Strand, London WC2R 2LS, UK
<b>S.A. McHugo</b> 15.1-15.5	Lawrence Berkeley National Laboratory,Bldg. 2-400 1 Cyclotron Road, CA 94720, USA
<b>M.A. Mendicino</b> 18.10	Motorola APRDL, Networking and Computing Systems Group 3501 Ed Bluestein Blvd, Mail Drop K-10, Austin TX 78721, USA
<b>K. Mitani</b> 18.4	Shin Etsu Handotai Co. Ltd., SEH Isobe R&D Center 2-13-1 Isobe Annaka-Shi, Guma Prefecture, 379-01 Japan
<b>J.-L. Mozos</b> 6.8	Helsinki University of Technology, Laboratory of Physics PO Box 1100, FIN-02015 HUT, Finland
<b>R.J. Nemanich</b> editor, chapter 5	North Carolina State University, Dept. of Physics Box 8202, Raleigh, NC 27695-88202, USA
<b>R.C. Newman</b> 9.7	Imperial College, Blackett Laboratory IRC Semiconductor Materials, London, SW17 2BZ, UK
<b>R.M Nieminen</b> 6.7, 6.8	Helsinki University of Technology, Laboratory of Physics PO Box 1100, FIN-02015 HUT, Finland
<b>Y. Okada</b> 3.1	Electrotechnical Laboratory, Physical Science Division 1-1-4, Umezono, Tsukuba, Ibaraki 305, Japan
<b>B. Pajot</b> 9.1-9.4	Universite Denis Diderot, Group de Physique des Solides 2, Place Jussieu - Tour 23, F-75251 Paris Cedex 05, France
<b>S.J. Pearson</b> editor, chapter 9	University of Florida, Dept. of Materials Science Rhines Hall, PO Box 116400, Gainesville, FL 32611, USA
<b>G. Pfeiffer</b> 18.5	MEMC Electronic Materials Inc., MZ 33 501 Pearl Drive, St. Peters, MO63376, USA
<b>A. Polman</b> 9.14	FOM Institute of Atomic and Molecular Physics Kruislaan 407, Amsterdam SJ 1098, Holland
<b>F. Priolo</b> 14.3	University di Catania, Dipartimento di Fisica Corso Italia 57, Catania I 95129, Italy
<b>M.J. Puska</b> 6.7	Helsinki University of Technology Laboratory of Physics, PO Box 1100, FIN-02015 HUT, Finland

<b>G.B.Rayner</b> 5.8	North Carolina State University, Dept. of Physics Raleigh, NC 27695-8202, USA
<b>S.G. Roberts</b> 3.8	University of Oxford, Dept. of Materials Parks Road, Oxford OX1 3PH, UK
<b>P. Roman</b> 5.4	Pennsylvania State University, Dept. of Electrical Engineering 214 Electrical Engineering West, University Park PA 16802, USA
<b>J. Ruzylo</b> 5.4	Pennsylvania State University, Dept. of Electrical Engineering 214 Electrical Engineering West, University Park PA 16802, USA
<b>K. Sadana</b> 18.9	IBM Corp., Thomas J.Watson Research Center PO Box 218, Yorktown Heights, NY 10598-0218, USA
<b>B. Schmiedeskamp</b> 7.3	Universitaet Bielefeld, Fakultat fur Physik D-33501 Bielefeld, Germany
<b>L.J. Schowalter</b> editor, chapter 17	Rensselaer Polytechnical Institute, Physics Dept. CIEEM 110 8th Street, Troy, NY 12180-3590, USA
<b>W. Schroter</b> 9.11, 9.12	Universitaet Goettingen, IV Physikalisches Institut der Georg-August Bunsenstrasse 13-15, D-37073 Goettingen, Germany
<b>M. Seibt</b> 9.11, 9.12	Universitaet Goettingen, IV Physikalisches Institut der Georg-August Bunsenstrasse 13-15, D-37073 Goettingen, Germany
<b>H. Siethoff</b> 3.6	Physikalisches Institut der, Universitaet Wuerzburg Am Hubland, D-97074 Wuerzburg, Germany
<b>G. P. Srivastava</b> 6.5	University of Exeter, Dept. of Physics Stocker Road, Exeter, EX4 4QL, UK
<b>M. Stavola</b> 9.8, 9.9	Lehigh University, 16 Memorial Drive East Bethlehem, PA 18015, USA
<b>E.Steinman</b> 11.2	Moscow State University, ISSP Institututski prospekt 15, 142432 Chernogolovka Moscow Region, Russia
<b>A. Strachan</b> 8.6	SILVACO International, Inc., 4701 Patrick Henry Drive #1 Santa Clara, CA 95054, USA
<b>M. Suezawa</b> 9.10	Tohoku University, Institute of Materials Research Katahira 2-1-1, Sendai 980, Japan
<b>K. Sumino</b> 3.5	Nippon Steel Corporation 20-1 Shintomi Futtsu, Chiba 293-8511, Japan
<b>B.G. Svensson</b> 13.2	Royal Institute of Technology, Solid State Electronics PO Box E-229 Kista, Stockholm S-164-40, Sweden

<b>K. Terashima</b> 1.1	Shounan Engineering University, Materials Engineering Dept. Nishi-Kaigan 1-1-25, Tsujido, Fujisawa-shi, Kanagawa 251, Japan
<b>G. Theodorou</b> 7.7	Aristotle University of Thessaloniki, Dept. of Physics 540 06 Thessaloniki, Greece
<b>R. Tung</b> 17.2	Lucent Technologies, Bell Labs Room 1t-102 700 Mountain Avenue, Murray Hill, NJ, USA
<b>R. Turton</b> editor, chapter 7	University of Newcastle upon Tyne, Solid State Physics Group Dept. of Physics, Newcastle upon Tyne, NE1 7RU, UK
<b>R.I.G. Uhrberg</b> 5.3	Linköping University, Dept. of Physics and Measurement Technology, Linkoping 581 83, Sweden
<b>G. Vanderschaeve</b> 3.7	CEMES/CNRS, 29 rue Jeanne Marvig BP 4347, F-31055 Toulouse, France
<b>W. von Ammon</b> 1.6	Wacker Siltronic AG, Postfach 1140 D-84479 Burghausen, Germany
<b>K. Wada</b> 1.5	NTT System Electronics Labs. 3-1, Morinosato, Wakamiya Atsugi-shi Kanagawa 243-01, Japan
<b>P. Wagner</b> 9.13	Wacker Siltronic AG, Postfach 1140 D-84479 Burghausen, Germany
<b>G.D. Watkins</b> 11.1	Lehigh University, Dept. of Physics 16 Memorial Drive East, Bethlehem, PA 18105, USA
<b>E.R. Weber</b> editor, chapter 15	University of California at Berkeley, Dept. of Materials Science 587 Evans Hall, CA 94720, USA
<b>J. Weber</b> 7.4	Max Planck Institut fuer Festkorperforschung Heisenbergstrasse, 70569 Stuttgart, Germany
<b>M.K. Weldon</b> 18.3, 18.6	Lucent Technologies, Bell Laboratories 600 Mountain View, Murray Hill, NJ 07974, USA
<b>M. Willander</b> editor, chapter 13	Chalmers University of Technology, Physical Electronics and Photonics, Dept. of Microelectronics and Photonics 4-412 96 Goteborg, Sweden
<b>K.R. Williams</b> editor, chapter 16	Lucas NovaSensor 1055 Mission Ct., Fremont, CA 94539-8203, USA
<b>E.B. Yakimov</b> 11.2	Moscow State University, ISSP Institututski Prospekt 15, 142432 Chernogolovka, Moscow Region, Russia
<b>H. Ying</b> 5.8	North Carolina State University, Dept. of Physics Box 8202, Raleigh, NC 27695-88202, USA

<b>T Yonehara</b> 18.8	Canon Inc. 6770 Tamura, Hiratsuka, Kangawa Prefecture, Japan
<b>I. Yonenaga</b> 3.5	Tohoku University, Institute for Materials Research Katahira 2-1-1, Sendai 980-8511, Japan
<b>V. Zielasek</b> 5.1, 5.2	University of Wisconsin-Madison, Dept. of Materials Science, Engineering and Physics, 1509 University Avenue, Madison WI 53706, USA

*Author address correction added in press:*

The entry for M.M.Heyns should read

<b>M.M.Heyns</b> 5.6	IMEC, VLSI Materials Technology Kapeldreef 75, Leuven B-3001, Belgium
-------------------------	--

In producing the present volume Datareviews by the following authors of *Properties of silicon* (INSPEC, 1988) were reproduced, adapted or merged:

**J.A. de Alamo, K.G. Barraclough, J.C. Brice, A.A. Brown, M.V. Chaparala,  
D. de Cogan, J.P.R. David, D.J. Godfrey, Y.M. Haddara, S.C. Hardy, H.-M. Kagaya,  
P.J. Mole, P.B. Moynagh, K.H. Nicholas, D. Nobili, M. Pawlik, P.J. Rosser,  
D. Schechter, B.S. Shivaram, T. Soma, M.N. Wybourne and J. Vaitkus.**

## Abbreviations

AAS	atomic absorption spectroscopy
AB	antibonding
AC	alternating current
AFM	atomic force microscopy
AM	Austin model
APCVD	atmospheric pressure chemical vapour deposition
APD	antiphase defect
APD	antiphase domain (boundary)
APW	augmented plane wave
ARPES	angle resolved photoemission spectroscopy
ASED	atom superposition and electron delocalisation
BC	bond centred
BCA	binary collision approximation
BDT	brittle-to-ductile transition
BESOI	bond and etchback silicon-on-insulator
BHS	Bachelet-Hamann-Schlüter
BOX	buried oxide
BP	Becke-Perdew
BPS	Burton Prim Slichter
BSD	backside damage
BSF	back surface field
BSOI	bonded silicon-on-insulator
BTE	Boltzmann transport
BZ	Brillouin zone
CB	conduction band
CCD	charge coupled device
CCM	cyclic cluster model
CI	configuration interaction
CITS	current-imaging-tunnelling spectroscopy
CMOS	complementary metal oxide semiconductor
CMP	chemical mechanical polishing
CNDO	complete neglect of differential overlap
CNDO/S	CNDO/spectroscopic
COP	crystal originated particle
COS	corona oxide semiconductor
CPAA	charged particle activation analysis
CPMD	Car-Parrinello molecular dynamics
CPU	central processing unit
C-V	capacitance-voltage
CVD	chemical vapour deposition
CW	continuous wave
CZ	Czochralski
Cz	Czochralski
CZN	cerium zinc nitrate
DAS	dimer adatom stacking fault
DC	direct current
DE-AAS	drop etching atomic absorption spectroscopy

DFT	density functional theory
DF-TB	density functional based tight binding
DHL	dislocation half-loop
DI	de-ionised
2DLFM	two-dimensional low-frequency motion
DLTS	deep level transient spectroscopy
DMC	diffusion Monte Carlo
2DNG	two-dimensional nucleation and growth
DO	differential overlap
DQMC	diffusion quantum Monte Carlo
DRAM	dynamic random access memory
DRIE	deep reactive ion etching
DSPE	double solid phase epitaxy
DZ	denuded zone
EBIC	electron-beam-induced current
ECR	electron cyclotron resonance
EELS	electron energy loss spectroscopy
ELID	electrolytic in-process dressing
ELTRAN R™	epitaxial layer transfer
EMA	effective mass approximation
EMT	effective mass theory
ENDOR	electron nuclear double resonance
EOR	end of range
EPM	empirical pseudopotential model
EPR	electron paramagnetic resonance
ESF	extrinsic stacking fault
ESR	electron spin resonance
ETB	empirical tight binding
FCC	face centred cubic
FD	fully-depleted
FEOL	front end of line
FET	field effect transistor
FFT	fast Fourier transform
FPD	flow pattern defect
FRS	forward recoil scattering
FTIR	Fourier transform infrared
FWHM	full width at half maximum
FWHP	full width at half peak
FZ	floating zone
GEA	gradient expansion approximation
GFA	gas fusion analysis
GGA	generalised gradient approximation
GOI	gate oxide integrity
GSMBE	gas-source molecular beam epitaxy
GTO	Gaussian-type orbital
GW	approximation to the self energy based on the one-electron Green's function G and screened Coulomb interaction W (Hedlin & Lundquist, 1969)
HBT	heterojunction bipolar transistor

HC	high carbon (content)
HEMT	high electron mobility transistor
HF	Hartree-Fock
HFR	Hartree-Fock-Roothaan
HL	high level
HNA	hydrofluoric-nitric-acetic
HREELS	high resolution electron energy loss spectroscopy
HREM	high resolution electron microscopy
HRTEM	high resolution transmission electron microscopy
HSC	Hamann-Schlüter-Chiang
HTEM	high resolution transmission electron microscopy
HTS	high temperature sputtering
HTS	high temperature superconducting
I	self-interstitial
IBAS	ion beam assisted sputtering
IBZ	irreducible Brillouin zone
IC	integrated circuit
IP3	input-referred third order intercept point
INDO	intermediate neglect of differential overlap
IPA	isopropyl alcohol
IR	infrared
IRAS	infrared absorption spectroscopy
ISF	intrinsic stacking fault
ITOX	internal thermal oxide/oxidation
I-V	current-voltage
JFET	junction field effect transistor
KB	Kleinman-Bylander
K-K	Kramers-Kronig
kMC	kinetic Monte Carlo
KS	Kohn-Sham
L	longitudinal
LA	longitudinal acoustic
LATID	large-angle-tilt implanted drain
LBIC	laser beam induced current
LC	low carbon (content)
LCAO	linear combination of atomic orbitals
LCGO	linear combination of Gaussian orbitals
LD	low dose
LDA	local density approximation
LDA-PP	local density approximation using pseudopotentials
LDI	lightly doped drain
LDF	local density functional
LED	light emitting diode
LEED	low energy electron diffraction
LEEM	low energy electron microscopy
LET	linear energy transfer
LHeT	liquid helium temperature
LL	low level
LMTO	linear muffin tin orbital

LNA	low noise amplifier
LO	local oscillator
LO	longitudinal optical
LPCVD	low pressure chemical vapour deposition
LPVPE	low pressure vapour phase epitaxy
LRP	limited reaction processing
LSD	local spin density
LSDA	local spin density approximation
LSI	large scale integration
LST	light scattering tomography
LTO	low temperature oxide
LVM	local vibrational mode
MBA	molecular beam allotaxy
MBE	molecular beam epitaxy
MC	Monte Carlo
MCM	molecular cluster model
MCZ	magnetic field-applied Czochralski
MD	molecular dynamics
MEMS	micro electromechanical systems
MESFET	metal-semiconductor field effect transistor
MFD	multiple stacking fault defect
MIM	metal insulator metal
MINDO	modified INDO
MIR	multiple internal reflection
MIT	multiple internal transmission
MIT-IR	multiple internal transmission infrared
ML	monolayer
MLDA	modified local density approximation
MNDO	modified NDDO
MODFET	modulation doped field effect transistor
MOS	metal oxide semiconductor
MOSFET	metal oxide semiconductor field effect transistor
MP	Monkhorst and Pack
M-S	metal-semiconductor
MS	molecular statics
MSPE	monolayer solid phase epitaxy
NAA	neutron activation analysis
ND	new thermal donor
NDDO	neglect of diatomic differential overlap
NDM	negative differential mobility
NDO	neglect of differential overlap
NF	noise figure
NFET	n channel field effect transistor
NI	not indicated
NMOS	n channel metal oxide semiconductor
NMOSFET	n channel MOSFET
NN	nearest neighbour
NNN	next nearest neighbour
ODE	orientation-dependent etch
ODMR	optically detected magnetic resonance

OED	oxidation enhanced diffusion
OIP3	output-referred third order intercept point
OISF	oxidation induced stacking fault
OME	oxide mediated epitaxy
OPW	orthogonalised plane wave
OSF	oxidation induced stacking fault
OV	oxygen-vacancy (centre)
PACE	plasma assisted chemical etching
PBS	poly-backside seal
PC	photoconductivity
PCD	photoconductivity decay
PDG	phosphorus diffusion gettering
PID	planar interstitial defect
PIMC	path integral Monte Carlo
PL	photoluminescence
PLE	photoluminescence excitation
PM	parametrised model
PMOS	p channel metal oxide semiconductor
PP	pseudopotential
PPPW	pseudopotential plane-wave
PR	piezoresistive
PRDDO	partial retention of diatomic differential overlap
PSG	phosphosilicate glass
PTIS	photothermal ionisation spectroscopy
PV	photovoltaic
PW	Perdew-Wang
PZ	Perdew-Zunger
QP	quasiparticle
RBE	reactive beam epitaxy
RBS	Rutherford backscattering
RE	rare earth
RF	radio frequency
RGA	residual gas analysis
RHEED	reflection high-energy electron diffraction
RIE	reactive ion etching
RMS	root mean square
RPCVD	reduced pressure chemical vapour deposition
RSCE	reverse short-channel effects
RT	room temperature
RTA	rapid thermal anneal
RTCVD	rapid thermal chemical vapour deposition
RTP	rapid thermal processing
RW	Rayleigh wave
SAD	selected area diffraction
SADS	silicide as the doping source
SANS	small angle neutron scattering
SB	Schottky barrier
SBH	Schottky barrier height
SBZ	surface Brillouin zone

SCF	self-consistent field
SCI	surface charge imaging
SCP	surface charge profiling
SDL	stable defect layer
SE	spectroscopic ellipsometry
SEM	scanning electron microscopy
SETB	semi-empirical tight-binding
SEU	single event upset
SF	stacking fault
SFT	stacking fault tetrahedra
SGS	SiGe on sapphire
SIMOX	separation by implantation of oxygen
SIMS	secondary ion mass spectrometry
SOI	silicon-on-insulator
SOS	silicon-on-sapphire
SPE	solid phase epitaxy
SPER	solid phase epitaxial regrowth
SPV	surface photovoltage
SQUID	superconducting quantum interference device
SR	spreading resistance
SRAM	static random access memory
SRH	Shockley-Read-Hall
SRP	spreading resistance profile
STD	shallow thermal donor
STIR	site total indicator reading
STM	scanning tunnelling microscopy
STO	Slater-type orbital
SX-LDA	screened-exchange local density approximation

T	tetrahedral
T	transverse
TA	transverse acoustical
TB	tight binding
TBMD	tight binding molecular dynamics
TBTE	tight-binding total-energy
TCAD	technology computer aided design
TCP	temperature coefficient of piezoresistance
TCR	temperature coefficient of resistance
TD	thermal donor
TD	threading dislocation
TDD	thermal double donor
TED	transient enhanced diffusion
TEM	transmission electron microscopy
TFSOS	thin film silicon on sapphire
TIME	Ti interlayer mediated epitaxy
TO	transverse optical
TR	transmit/receive
TTV	total thickness variation
TXRF	total reflectance X-ray fluorescence
UHV	ultra high vacuum
UHV/CVD	ultra high vacuum chemical vapour deposition
ULSI	ultra large scale integration

USTD	ultra-shallow thermal donor
UV	ultraviolet
V	vacancy
VFF	valence force field
VLPCVD	very low pressure chemical vapour deposition
VLSI	very large scale integration
VMC	variational Monte Carlo
VO	vacancy-oxygen
VPD-AAS	vapour phase decomposition atomic absorption spectroscopy
VPE	vapour phase epitaxy
VWN	Vosko-Wilk-Nusair
WLF	Wannier-like function
XPS	X-ray photoelectron spectroscopy
XRD	X-ray diffraction
XROI	X-ray and optical interferometry
XTEM	cross-sectional transmission electron microscopy
ZDO	zero differential overlap

# PROPERTIES OF **Crystalline Silicon**

**Edited by**  
**ROBERT HULL**  
**University of Virginia, USA**

Published by: INSPEC, The Institution of Electrical Engineers,  
London, United Kingdom

© 1999: The Institution of Electrical Engineers

This publication is copyright under the Berne Convention and the Universal Copyright Convention. All rights reserved. Apart from any fair dealing for the purposes of research or private study, or criticism or review, as permitted under the Copyright, Designs and Patents Act, 1988, this publication may be reproduced, stored or transmitted, in any forms or by any means, only with the prior permission in writing of the publishers, or in the case of reprographic reproduction in accordance with the terms of licences issued by the Copyright Licensing Agency. Inquiries concerning reproduction outside those terms should be sent to the publishers at the undermentioned address:

The Institution of Electrical Engineers,  
Michael Faraday House,  
Six Hills Way, Stevenage,  
Herts. SG1 2AY, United Kingdom

While the author and the publishers believe that the information and guidance given in this work are correct, all parties must rely upon their own skill and judgment when making use of them. Neither the author nor the publishers assume any liability to anyone for any loss or damage caused by any error or omission in the work, whether such error or omission is the result of negligence or any other cause. Any and all such liability is disclaimed.

The moral right of the author to be identified as author of this work has been asserted by him/her in accordance with the Copyright, Designs and Patents Act 1988.

#### **British Library Cataloguing in Publication Data**

A CIP catalogue record for this book  
is available from the British Library

**ISBN 0 85296 933 3**

Printed in England by Short Run Press Ltd., Exeter

## Foreword

Information technology is one of the key drivers of progress into the 21<sup>st</sup> century, transforming the way in which we communicate, learn, work, live. It will be essential for the growth of our economy as well as for the solutions of some of the most critical problems facing society. The electronic systems industry needed to support this vision has now overtaken the automotive industry in terms of contribution to the global economy. Micro- and optoelectronic sensors and transducers are the basis of a rapidly growing business segment. But to a very large extent electronic systems are based upon the technology for producing integrated circuits. And this technology - that just celebrated its 40<sup>th</sup> anniversary - is synonymous with *silicon* technology: its material properties combined with its abundance in nature have given silicon a unique position in the fabrication of miniaturized devices that is not likely to be challenged soon.

The business based upon this silicon integrated circuit itself is unique and particularly challenging. It is unique because over more than 3 decades it has sustained a market growth of 15% per year. It is at the same time extremely challenging, because this growth is based on an exponential technology development, resulting in electronic functions with continuously improved performance and reliability, reduced power consumption and a 25-30% per-year cost reduction.

Supporting this productivity increase is the growth of circuit complexity by a factor of approximately 2 every year as predicted by Gordon Moore in 1975 and resulting from feature scaling, die size increase and circuit cleverness. Some of the historical contributions to increased productivity – such as manufacturing yield improvement – are no longer available, and device scaling still remains the largest contributor to productivity growth. The Semiconductor Industry Association has coordinated the consensus building on the future technology requirements for maintaining the historical rate of advancement. The resulting vision is documented in the “National Technology Roadmap for Semiconductors” – the next update of which is likely to become known as the “International Technology Roadmap for Semiconductors” – predicting 50-nm features by 2012.

The challenges faced by the semiconductor community as it moves into production of metal-oxide-semiconductor (MOS) transistor devices with dimensions below 100 nm are enormous. As technology scales and materials are improved, they are stressed to their intrinsic limits and a thorough understanding of the fundamental properties is needed. At the same time new materials, new patterning techniques and new device structures will be required: new gate dielectrics and gate electrode materials and processes, as well as new interconnect materials and processes to replace the familiar metals, dielectrics and contact materials used in device interconnect structures. Also when removing ‘bottlenecks’ process technologists will require insight into the fundamentals.

In early stages of technology development modelling and simulation are extensively used in order to obtain insight into the directions of technology. It is clear that when devices are further scaled, tools will be needed to model physical and chemical processes at an atomic

level and to simulate carrier transport under non-equilibrium conditions. The development of such tools will require advanced understanding of the fundamental processes.

Competitiveness of the IC industry has always been linked to advances in material preparation and process technology. But the IC industry has grown up in recent years. Among others things, this means that the costs together with the risks have risen. This has resulted in much more fragmentation and specialization as illustrated by the current successful business model based on the collaboration of “fab-less” design companies with “foundries” specializing in cost-effective and state-of-the-art manufacturing. The trend towards the “system-on-a-chip” has led to a growing need for truly multidisciplinary teams of experts with a deep technical insight in specific areas such as process modules or integration combined with a good understanding of system and electronic circuit design, or vice versa. Communication among the members of such teams has created an increased need for up-to-date and in-depth reviews of materials properties and technology.

The 18 chapters of this new book from the EMIS Datareviews series are the result of an ambitious project bringing together contributions from a worldwide group of experts covering a broad spectrum from silicon physics and material properties to device technology. The balance of coverage and presentation should make this volume a valuable working information resource for academics, semiconductor process developers and electronic device simulation engineers needing meaningful, usable data as they seek to advance their understanding and exploitation of silicon.

Inspired by the increased use of the Internet the editors will hopefully revive their plan to launch an online system. We believe such a service allowing regular additions and revisions would be of value to the thousands of materials and technology specialists who need instant access to a growing amount of data and knowledge. But for now and in the years to come, the present book will serve the needs of the “silicon community” more than adequately.

Roger de Keersmaecker  
IMEC, Leuven, Belgium

May 1999

## **Introduction**

This volume collects fundamental physical and materials data for crystalline silicon into a single, authoritative source. The scope of the volume ranges from fundamental electronic and optical properties of silicon, through mechanical, thermal and defect properties, to crystal growth, doping and interfaces with other technologically important materials (note that silicon-based heterostructures, silicon carbide and metal silicides are covered in other EMIS volumes from INSPEC, while volumes on silicon oxides are planned).

The material is organized into individual "Datareviews", each authored by an expert in that particular field. Sets of Datareviews are then collected into chapters, each edited by an internationally recognized authority. The previous EMIS book, *Properties of silicon* (INSPEC, 1988) is widely used in academic and engineering laboratories and it is our hope that this volume will serve as a substantially enhanced and updated reference source for scientists, engineers and technical managers doing research into silicon-based materials and structures, or working with silicon technology.

The volume editor would like to thank the 100 authors and 18 chapter editors who have contributed their time and expertise to this project. In addition, he would like to recognize the outstanding support provided by John Sears, the managing editor of the EMIS Datareviews series. Acknowledgement should also be given to the careful, detailed MS preparation and indexing work of Pamela Sears and to Dr Peter Capper for copy editing and typesetting such a diversity of MSS to achieve the structural integrity and homogeneity needed for a reference work of this kind.

Robert Hull

University of Virginia  
May 1999

## Contributors

<b>T. Abe</b> editor, chapter 1	Shin-Etsu Handotai Co, Ltd. 2-13-1 Isobe, Annaka, Gunma 379-01, Japan
<b>C.A.J. Ammerlaan</b> 11.3-11.5	University of Amsterdam, Van der Waals-Zeeman Institut Valckenierstraat 65, NL-1019 Amsterdam, Holland
<b>M.J. Anc</b> 18.9	Ibis Technology Corporation 32 Cherry Hill Drive, Danvers, Ma 01923, USA
<b>D.E. Aspnes</b> editor, chapter 12	North Carolina State University, Dept. of Physics Box 8202, Raleigh, NC 27695-8202, USA
<b>J.C. Bean</b> editor, chapter 2	University of Virginia, Dept. of Electrical Engineering Thornton Hall, Charlottesville, VA 22903-2442, USA
<b>H.S. Bennett</b> 7.5	University of Newcastle upon Tyne, Solid State Physics Group Dept. of Physics, Newcastle upon Tyne, NE1 7RU, UK
<b>P.R. Briddon</b> 6.9	University of Newcastle upon Tyne, Physics Dept. Newcastle upon Tyne, NE1 7RU, UK
<b>R.E. Brindos</b> 14.1, 14.5	University of Florida, SWAMP Center Dept. of Materials Science and Engineering 525 Engineering Bldg., PO Box 116130 FL 32611-6130, USA
<b>P. D. Bristowe</b> 6.6	University of Cambridge, Dept. of Materials Science and Metallurgy, Pembroke Street, Cambridge CB2 3QZ, UK
<b>M.R.Brozel</b> editor, chapter 4	UMIST, Centre for Electronic Materials PO Box 88, Manchester M60 1QD, UK
<b>R.J. Carter</b> 5.7, 5.8	North Carolina State University, Dept.of Physics Box 8202, Raleigh, NC 27695-88202, USA
<b>M.-J. Caturla</b> 14.2	Lawrence Livermore National Laboratory, Chemistry and Materials Science L-268, 7000 East Avenue, Livermore, CA 94550, USA
<b>Y.J. Chabal</b> 5.5, 18.3, 18.6	Lucent Technologies, Bell Laboratories 600 Mountain View, Murray Hill, NJ 07974, USA
<b>S. Coffa</b> 9.14, 14.3	CNR-IMETEM, Stadale Primosole 50 I-95121 Catania, Italy
<b>S.R. Crowder</b> 18.7	IBM Corporation, Microelectronics Division Semiconductor R&D Center, 1580 Route 52 Hopewell Junction, NY 12533, USA

<b>P. Deak</b> 6.1	Physical Institute of the Technical University of Budapest H-1521 Budapest, Hungary
<b>P.R. de la Houssaye</b> 18.2	NRad, NCCOSc RDT Division, D805, Rm. 22953475 Strothe Road San Diego, Ca 92152-6341, USA
<b>T. D. de la Rubia</b> 14.2	Lawrence Livermore National Laboratory, Chemistry and Materials Science L-268, 7000 East Avenue, Livermore, CA 94550, USA
<b>E. Dornberger</b> 1.6	Wacker Siltronic AG Postfach 1140, D-84479 Burghausen, Germany
<b>D.J. Dunstan</b> 7.8	Queen Mary and Westfield College, Dept.of Physics Mile End Road, London, E1 4NS, USA
<b>R. Elliman</b> editor, chapter 14	Australian National University, Electronic Materials Engineering Dept., GPO Box 4, Canberra, ACT 0200, Australia
<b>C.P. Ewels</b> 6.3	University of Sussex, School of Chemistry, Physics and Environmental Sciences, Falmer, Brighton, BN1 9QJ, UK
<b>A. George</b> editor, chapter 3	Ecole des Mines de Nancy, Laboratoire de Physique des Materiaux CNRS UMR 7556, Parc de Saurupt, F-54042 Nancy, France
<b>M.D. Giles</b> 10.3	Intel Corporation MS: RN2-40, 2200 Mission College Blvd., Santa Clara, Ca 95052, USA
<b>D.W. Greve</b> 2.2, 2.3	Carnegie Mellon University, Dept. of Electrical and Computer Engineering, Hamerschlag Hall, Pittsburgh PA 15213, USA
<b>H. Grimmelis</b> editor, chapter 11	Lund Institute of Technology, Dept.of Solid State Physics Box 118, S-22100 Lund, Sweden
<b>V. Grivickas</b> 13.1, 13.4-13.8	Chalmers University of Technology, Physical Electronics and Photonics, Dept. of Microelectronics and Photonics 4-412 96 Goteborg, Sweden
<b>M. Heggie</b> editor, chapter 6	University of Sussex, School of Chemistry, Physics and Environmental Sciences, Falmer, Brighton, BN1 9QJ, UK
<b>M.M. Heyns</b> 5.6	North Carolina State University, Dept. of Physics Box 8202, Raleigh, NC 27695-88202, USA
<b>H. Hieslmair</b> 15.1-15.5	University of California at Berkeley, Dept. of Materials Science 587 Evans Hall, 1 Cyclotron Road, 272 Hearst Bldg. CA 94720, USA
<b>K. Hoshikawa</b> 1.4	Shin-Shyu University, Education Facility Nishi-Nagano, Nagano 380, Japan

<b>X. Huang</b> 1.4	Shin-Shyu University, Education Facility Nishi-Nagano, Nagano 380, Japan
<b>R. Hull</b> volume editor	University of Virginia, Dept. of Materials Science & Engineering Charlottesville, VA 22903, USA
<b>A.A. Istratov</b> 15.1-15.5	University of California at Berkeley, Dept. of Materials Science 587 Evans Hall, 1 Cyclotron Road, 272 Hearst Bldg. CA 94720, USA
<b>S. S. Iyer</b> editor, chapter 18	IBM Corporation, Microelectronics Division Bldg. 630 ZIP E40, 1580 Route 52, Hopewell Junction NY 12533, USA
<b>S.H. Jones</b> editor, chapter 8	Virginia Semiconductor, Inc. 1501 Powhatan Street, Fredericksburg, Virginia 22401, USA
<b>K.S. Jones</b> editor, chapter 10 14.1, 14.4, 14.5	University of Florida, SWAMP Center Dept. of Materials Science and Engineering 525 Engineering Bldg., PO Box 116130 FL 32611-6130, USA
<b>R. Jones</b> 6.3	University of Exeter, Dept. of Physics Exeter, EX4 4QJ, UK
<b>G. Jungnickel</b> 6.2	TU Chemnitz-Zwickau 09107 Chemnitz, Germany
<b>K. Kakimoto</b> 1.2	Kyushu University, Institute of Advanced Materials Study 6-1, Kasuga-koen, Kasuga 816, Japan
<b>P.H. Keys</b> 14.1, 14.5	University of Florida, SWAMP Center Dept. of Materials Sci. and Eng., 525 Engineering Bldg. PO Box 116130, FL 32611-6130, USA
<b>S. Kobayashi</b> 1.3	Sumitomo Metal Industries Ltd, Corporate R&D Laboratories 1-8 Fuso-cho, Amagasaki Hyogo, 660, Japan
<b>M. Lagally</b> <b>5.1, 5.2</b>	University of Wisconsin-Madison, Dept. of Materials Science, Engineering and Physics, 1509 University Avenue, Madison WI 53706, USA
<b>I. Lagnado</b> 18.2	NRad, NCCOSc RDT Division, D805, Rm. 229, 53475 Strothe Road San Diego, Ca 92152-6341, USA
<b>N. Lehto</b> 6.10	University of Sussex, School of Chemistry, Physics and Environmental Sciences, Falmer, Brighton, BN1 9QJ, UK
<b>J.L. Lindstrom</b> 13.3	Chalmers University of Technology, Physical Electronics and Photonics, Dept. of Microelectronics and Photonics 4-412 96 Goteborg, Sweden

<b>F. Liu</b> 5.1, 5.2	University of Wisconsin-Madison, Dept. of Materials Science, Engineering and Physics, 1509 University Avenue, Madison WI 53706, USA
<b>K. Maex</b> 17.1	IMEC VZW, ASE/VMT Kapeldreef 75, B-3001 Leuven, Belgium
<b>A. Mainwood</b> 6.4	King's College, London., Dept. of Physics Strand, London WC2R 2LS, UK
<b>S.A. McHugo</b> 15.1-15.5	Lawrence Berkeley National Laboratory,Bldg. 2-400 1 Cyclotron Road, CA 94720, USA
<b>M.A. Mendicino</b> 18.10	Motorola APRDL, Networking and Computing Systems Group 3501 Ed Bluestein Blvd, Mail Drop K-10, Austin TX 78721, USA
<b>K. Mitani</b> 18.4	Shin Etsu Handotai Co. Ltd., SEH Isobe R&D Center 2-13-1 Isobe Annaka-Shi, Guma Prefecture, 379-01 Japan
<b>J.-L. Mozos</b> 6.8	Helsinki University of Technology, Laboratory of Physics PO Box 1100, FIN-02015 HUT, Finland
<b>R.J. Nemanich</b> editor, chapter 5	North Carolina State University, Dept. of Physics Box 8202, Raleigh, NC 27695-88202, USA
<b>R.C. Newman</b> 9.7	Imperial College, Blackett Laboratory IRC Semiconductor Materials, London, SW17 2BZ, UK
<b>R.M Nieminen</b> 6.7, 6.8	Helsinki University of Technology, Laboratory of Physics PO Box 1100, FIN-02015 HUT, Finland
<b>Y. Okada</b> 3.1	Electrotechnical Laboratory, Physical Science Division 1-1-4, Umezono, Tsukuba, Ibaraki 305, Japan
<b>B. Pajot</b> 9.1-9.4	Universite Denis Diderot, Group de Physique des Solides 2, Place Jussieu - Tour 23, F-75251 Paris Cedex 05, France
<b>S.J. Pearson</b> editor, chapter 9	University of Florida, Dept. of Materials Science Rhines Hall, PO Box 116400, Gainesville, FL 32611, USA
<b>G. Pfeiffer</b> 18.5	MEMC Electronic Materials Inc., MZ 33 501 Pearl Drive, St. Peters, MO63376, USA
<b>A. Polman</b> 9.14	FOM Institute of Atomic and Molecular Physics Kruislaan 407, Amsterdam SJ 1098, Holland
<b>F. Priolo</b> 14.3	University di Catania, Dipartimento di Fisica Corso Italia 57, Catania I 95129, Italy
<b>M.J. Puska</b> 6.7	Helsinki University of Technology Laboratory of Physics, PO Box 1100, FIN-02015 HUT, Finland

<b>G.B.Rayner</b> 5.8	North Carolina State University, Dept. of Physics Raleigh, NC 27695-8202, USA
<b>S.G. Roberts</b> 3.8	University of Oxford, Dept. of Materials Parks Road, Oxford OX1 3PH, UK
<b>P. Roman</b> 5.4	Pennsylvania State University, Dept. of Electrical Engineering 214 Electrical Engineering West, University Park PA 16802, USA
<b>J. Ruzylo</b> 5.4	Pennsylvania State University, Dept. of Electrical Engineering 214 Electrical Engineering West, University Park PA 16802, USA
<b>K. Sadana</b> 18.9	IBM Corp., Thomas J.Watson Research Center PO Box 218, Yorktown Heights, NY 10598-0218, USA
<b>B. Schmiedeskamp</b> 7.3	Universitaet Bielefeld, Fakultat fur Physik D-33501 Bielefeld, Germany
<b>L.J. Schowalter</b> editor, chapter 17	Rensselaer Polytechnical Institute, Physics Dept. CIEEM 110 8th Street, Troy, NY 12180-3590, USA
<b>W. Schroter</b> 9.11, 9.12	Universitaet Goettingen, IV Physikalisches Institut der Georg-August Bunsenstrasse 13-15, D-37073 Goettingen, Germany
<b>M. Seibt</b> 9.11, 9.12	Universitaet Goettingen, IV Physikalisches Institut der Georg-August Bunsenstrasse 13-15, D-37073 Goettingen, Germany
<b>H. Siethoff</b> 3.6	Physikalisches Institut der, Universitaet Wuerzburg Am Hubland, D-97074 Wuerzburg, Germany
<b>G. P. Srivastava</b> 6.5	University of Exeter, Dept. of Physics Stocker Road, Exeter, EX4 4QL, UK
<b>M. Stavola</b> 9.8, 9.9	Lehigh University, 16 Memorial Drive East Bethlehem, PA 18015, USA
<b>E.Steinman</b> 11.2	Moscow State University, ISSP Institututski prospekt 15, 142432 Chernogolovka Moscow Region, Russia
<b>A. Strachan</b> 8.6	SILVACO International, Inc., 4701 Patrick Henry Drive #1 Santa Clara, CA 95054, USA
<b>M. Suezawa</b> 9.10	Tohoku University, Institute of Materials Research Katahira 2-1-1, Sendai 980, Japan
<b>K. Sumino</b> 3.5	Nippon Steel Corporation 20-1 Shintomi Futtsu, Chiba 293-8511, Japan
<b>B.G. Svensson</b> 13.2	Royal Institute of Technology, Solid State Electronics PO Box E-229 Kista, Stockholm S-164-40, Sweden

<b>K. Terashima</b> 1.1	Shounan Engineering University, Materials Engineering Dept. Nishi-Kaigan 1-1-25, Tsujido, Fujisawa-shi, Kanagawa 251, Japan
<b>G. Theodorou</b> 7.7	Aristotle University of Thessaloniki, Dept. of Physics 540 06 Thessaloniki, Greece
<b>R. Tung</b> 17.2	Lucent Technologies, Bell Labs Room 1t-102 700 Mountain Avenue, Murray Hill, NJ, USA
<b>R. Turton</b> editor, chapter 7	University of Newcastle upon Tyne, Solid State Physics Group Dept. of Physics, Newcastle upon Tyne, NE1 7RU, UK
<b>R.I.G. Uhrberg</b> 5.3	Linköping University, Dept. of Physics and Measurement Technology, Linkoping 581 83, Sweden
<b>G. Vanderschaeve</b> 3.7	CEMES/CNRS, 29 rue Jeanne Marvig BP 4347, F-31055 Toulouse, France
<b>W. von Ammon</b> 1.6	Wacker Siltronic AG, Postfach 1140 D-84479 Burghausen, Germany
<b>K. Wada</b> 1.5	NTT System Electronics Labs. 3-1, Morinosato, Wakamiya Atsugi-shi Kanagawa 243-01, Japan
<b>P. Wagner</b> 9.13	Wacker Siltronic AG, Postfach 1140 D-84479 Burghausen, Germany
<b>G.D. Watkins</b> 11.1	Lehigh University, Dept. of Physics 16 Memorial Drive East, Bethlehem, PA 18105, USA
<b>E.R. Weber</b> editor, chapter 15	University of California at Berkeley, Dept. of Materials Science 587 Evans Hall, CA 94720, USA
<b>J. Weber</b> 7.4	Max Planck Institut fuer Festkorperforschung Heisenbergstrasse, 70569 Stuttgart, Germany
<b>M.K. Weldon</b> 18.3, 18.6	Lucent Technologies, Bell Laboratories 600 Mountain View, Murray Hill, NJ 07974, USA
<b>M. Willander</b> editor, chapter 13	Chalmers University of Technology, Physical Electronics and Photonics, Dept. of Microelectronics and Photonics 4-412 96 Goteborg, Sweden
<b>K.R. Williams</b> editor, chapter 16	Lucas NovaSensor 1055 Mission Ct., Fremont, CA 94539-8203, USA
<b>E.B. Yakimov</b> 11.2	Moscow State University, ISSP Institututski Prospekt 15, 142432 Chernogolovka, Moscow Region, Russia
<b>H. Ying</b> 5.8	North Carolina State University, Dept. of Physics Box 8202, Raleigh, NC 27695-88202, USA

<b>T Yonehara</b> 18.8	Canon Inc. 6770 Tamura, Hiratsuka, Kangawa Prefecture, Japan
<b>I. Yonenaga</b> 3.5	Tohoku University, Institute for Materials Research Katahira 2-1-1, Sendai 980-8511, Japan
<b>V. Zielasek</b> 5.1, 5.2	University of Wisconsin-Madison, Dept. of Materials Science, Engineering and Physics, 1509 University Avenue, Madison WI 53706, USA

*Author address correction added in press:*

The entry for M.M.Heyns should read

<b>M.M.Heyns</b> 5.6	IMEC, VLSI Materials Technology Kapeldreef 75, Leuven B-3001, Belgium
-------------------------	--

In producing the present volume Datareviews by the following authors of *Properties of silicon* (INSPEC, 1988) were reproduced, adapted or merged:

**J.A. de Alamo, K.G. Barraclough, J.C. Brice, A.A. Brown, M.V. Chaparala,  
D. de Cogan, J.P.R. David, D.J. Godfrey, Y.M. Haddara, S.C. Hardy, H.-M. Kagaya,  
P.J. Mole, P.B. Moynagh, K.H. Nicholas, D. Nobili, M. Pawlik, P.J. Rosser,  
D. Schechter, B.S. Shivaram, T. Soma, M.N. Wybourne and J. Vaitkus.**

## Abbreviations

AAS	atomic absorption spectroscopy
AB	antibonding
AC	alternating current
AFM	atomic force microscopy
AM	Austin model
APCVD	atmospheric pressure chemical vapour deposition
APD	antiphase defect
APD	antiphase domain (boundary)
APW	augmented plane wave
ARPES	angle resolved photoemission spectroscopy
ASED	atom superposition and electron delocalisation
BC	bond centred
BCA	binary collision approximation
BDT	brittle-to-ductile transition
BESOI	bond and etchback silicon-on-insulator
BHS	Bachelet-Hamann-Schlüter
BOX	buried oxide
BP	Becke-Perdew
BPS	Burton Prim Slichter
BSD	backside damage
BSF	back surface field
BSOI	bonded silicon-on-insulator
BTE	Boltzmann transport
BZ	Brillouin zone
CB	conduction band
CCD	charge coupled device
CCM	cyclic cluster model
CI	configuration interaction
CITS	current-imaging-tunnelling spectroscopy
CMOS	complementary metal oxide semiconductor
CMP	chemical mechanical polishing
CNDO	complete neglect of differential overlap
CNDO/S	CNDO/spectroscopic
COP	crystal originated particle
COS	corona oxide semiconductor
CPAA	charged particle activation analysis
CPMD	Car-Parrinello molecular dynamics
CPU	central processing unit
C-V	capacitance-voltage
CVD	chemical vapour deposition
CW	continuous wave
CZ	Czochralski
Cz	Czochralski
CZN	cerium zinc nitrate
DAS	dimer adatom stacking fault
DC	direct current
DE-AAS	drop etching atomic absorption spectroscopy

DFT	density functional theory
DF-TB	density functional based tight binding
DHL	dislocation half-loop
DI	de-ionised
2DLFM	two-dimensional low-frequency motion
DLTS	deep level transient spectroscopy
DMC	diffusion Monte Carlo
2DNG	two-dimensional nucleation and growth
DO	differential overlap
DQMC	diffusion quantum Monte Carlo
DRAM	dynamic random access memory
DRIE	deep reactive ion etching
DSPE	double solid phase epitaxy
DZ	denuded zone
EBIC	electron-beam-induced current
ECR	electron cyclotron resonance
EELS	electron energy loss spectroscopy
ELID	electrolytic in-process dressing
ELTRAN R™	epitaxial layer transfer
EMA	effective mass approximation
EMT	effective mass theory
ENDOR	electron nuclear double resonance
EOR	end of range
EPM	empirical pseudopotential model
EPR	electron paramagnetic resonance
ESF	extrinsic stacking fault
ESR	electron spin resonance
ETB	empirical tight binding
FCC	face centred cubic
FD	fully-depleted
FEOL	front end of line
FET	field effect transistor
FFT	fast Fourier transform
FPD	flow pattern defect
FRS	forward recoil scattering
FTIR	Fourier transform infrared
FWHM	full width at half maximum
FWHP	full width at half peak
FZ	floating zone
GEA	gradient expansion approximation
GFA	gas fusion analysis
GGA	generalised gradient approximation
GOI	gate oxide integrity
GSMBE	gas-source molecular beam epitaxy
GTO	Gaussian-type orbital
GW	approximation to the self energy based on the one-electron Green's function G and screened Coulomb interaction W (Hedlin & Lundquist, 1969)
HBT	heterojunction bipolar transistor

HC	high carbon (content)
HEMT	high electron mobility transistor
HF	Hartree-Fock
HFR	Hartree-Fock-Roothaan
HL	high level
HNA	hydrofluoric-nitric-acetic
HREELS	high resolution electron energy loss spectroscopy
HREM	high resolution electron microscopy
HRTEM	high resolution transmission electron microscopy
HSC	Hamann-Schlüter-Chiang
HTEM	high resolution transmission electron microscopy
HTS	high temperature sputtering
HTS	high temperature superconducting
I	self-interstitial
IBAS	ion beam assisted sputtering
IBZ	irreducible Brillouin zone
IC	integrated circuit
IP3	input-referred third order intercept point
INDO	intermediate neglect of differential overlap
IPA	isopropyl alcohol
IR	infrared
IRAS	infrared absorption spectroscopy
ISF	intrinsic stacking fault
ITOX	internal thermal oxide/oxidation
I-V	current-voltage
JFET	junction field effect transistor
KB	Kleinman-Bylander
K-K	Kramers-Kronig
kMC	kinetic Monte Carlo
KS	Kohn-Sham
L	longitudinal
LA	longitudinal acoustic
LATID	large-angle-tilt implanted drain
LBIC	laser beam induced current
LC	low carbon (content)
LCAO	linear combination of atomic orbitals
LCGO	linear combination of Gaussian orbitals
LD	low dose
LDA	local density approximation
LDA-PP	local density approximation using pseudopotentials
LDI	lightly doped drain
LDF	local density functional
LED	light emitting diode
LEED	low energy electron diffraction
LEEM	low energy electron microscopy
LET	linear energy transfer
LHeT	liquid helium temperature
LL	low level
LMTO	linear muffin tin orbital

LNA	low noise amplifier
LO	local oscillator
LO	longitudinal optical
LPCVD	low pressure chemical vapour deposition
LPVPE	low pressure vapour phase epitaxy
LRP	limited reaction processing
LSD	local spin density
LSDA	local spin density approximation
LSI	large scale integration
LST	light scattering tomography
LTO	low temperature oxide
LVM	local vibrational mode
MBA	molecular beam allotaxy
MBE	molecular beam epitaxy
MC	Monte Carlo
MCM	molecular cluster model
MCZ	magnetic field-applied Czochralski
MD	molecular dynamics
MEMS	micro electromechanical systems
MESFET	metal-semiconductor field effect transistor
MFD	multiple stacking fault defect
MIM	metal insulator metal
MINDO	modified INDO
MIR	multiple internal reflection
MIT	multiple internal transmission
MIT-IR	multiple internal transmission infrared
ML	monolayer
MLDA	modified local density approximation
MNDO	modified NDDO
MODFET	modulation doped field effect transistor
MOS	metal oxide semiconductor
MOSFET	metal oxide semiconductor field effect transistor
MP	Monkhorst and Pack
M-S	metal-semiconductor
MS	molecular statics
MSPE	monolayer solid phase epitaxy
NAA	neutron activation analysis
ND	new thermal donor
NDDO	neglect of diatomic differential overlap
NDM	negative differential mobility
NDO	neglect of differential overlap
NF	noise figure
NFET	n channel field effect transistor
NI	not indicated
NMOS	n channel metal oxide semiconductor
NMOSFET	n channel MOSFET
NN	nearest neighbour
NNN	next nearest neighbour
ODE	orientation-dependent etch
ODMR	optically detected magnetic resonance

OED	oxidation enhanced diffusion
OIP3	output-referred third order intercept point
OISF	oxidation induced stacking fault
OME	oxide mediated epitaxy
OPW	orthogonalised plane wave
OSF	oxidation induced stacking fault
OV	oxygen-vacancy (centre)
PACE	plasma assisted chemical etching
PBS	poly-backside seal
PC	photoconductivity
PCD	photoconductivity decay
PDG	phosphorus diffusion gettering
PID	planar interstitial defect
PIMC	path integral Monte Carlo
PL	photoluminescence
PLE	photoluminescence excitation
PM	parametrised model
PMOS	p channel metal oxide semiconductor
PP	pseudopotential
PPPW	pseudopotential plane-wave
PR	piezoresistive
PRDDO	partial retention of diatomic differential overlap
PSG	phosphosilicate glass
PTIS	photothermal ionisation spectroscopy
PV	photovoltaic
PW	Perdew-Wang
PZ	Perdew-Zunger
QP	quasiparticle
RBE	reactive beam epitaxy
RBS	Rutherford backscattering
RE	rare earth
RF	radio frequency
RGA	residual gas analysis
RHEED	reflection high-energy electron diffraction
RIE	reactive ion etching
RMS	root mean square
RPCVD	reduced pressure chemical vapour deposition
RSCE	reverse short-channel effects
RT	room temperature
RTA	rapid thermal anneal
RTCVD	rapid thermal chemical vapour deposition
RTP	rapid thermal processing
RW	Rayleigh wave
SAD	selected area diffraction
SADS	silicide as the doping source
SANS	small angle neutron scattering
SB	Schottky barrier
SBH	Schottky barrier height
SBZ	surface Brillouin zone

SCF	self-consistent field
SCI	surface charge imaging
SCP	surface charge profiling
SDL	stable defect layer
SE	spectroscopic ellipsometry
SEM	scanning electron microscopy
SETB	semi-empirical tight-binding
SEU	single event upset
SF	stacking fault
SFT	stacking fault tetrahedra
SGS	SiGe on sapphire
SIMOX	separation by implantation of oxygen
SIMS	secondary ion mass spectrometry
SOI	silicon-on-insulator
SOS	silicon-on-sapphire
SPE	solid phase epitaxy
SPER	solid phase epitaxial regrowth
SPV	surface photovoltage
SQUID	superconducting quantum interference device
SR	spreading resistance
SRAM	static random access memory
SRH	Shockley-Read-Hall
SRP	spreading resistance profile
STD	shallow thermal donor
STIR	site total indicator reading
STM	scanning tunnelling microscopy
STO	Slater-type orbital
SX-LDA	screened-exchange local density approximation

T	tetrahedral
T	transverse
TA	transverse acoustical
TB	tight binding
TBMD	tight binding molecular dynamics
TBTE	tight-binding total-energy
TCAD	technology computer aided design
TCP	temperature coefficient of piezoresistance
TCR	temperature coefficient of resistance
TD	thermal donor
TD	threading dislocation
TDD	thermal double donor
TED	transient enhanced diffusion
TEM	transmission electron microscopy
TFSOS	thin film silicon on sapphire
TIME	Ti interlayer mediated epitaxy
TO	transverse optical
TR	transmit/receive
TTV	total thickness variation
TXRF	total reflectance X-ray fluorescence
UHV	ultra high vacuum
UHV/CVD	ultra high vacuum chemical vapour deposition
ULSI	ultra large scale integration

USTD	ultra-shallow thermal donor
UV	ultraviolet
V	vacancy
VFF	valence force field
VLPCVD	very low pressure chemical vapour deposition
VLSI	very large scale integration
VMC	variational Monte Carlo
VO	vacancy-oxygen
VPD-AAS	vapour phase decomposition atomic absorption spectroscopy
VPE	vapour phase epitaxy
VWN	Vosko-Wilk-Nusair
WLF	Wannier-like function
XPS	X-ray photoelectron spectroscopy
XRD	X-ray diffraction
XROI	X-ray and optical interferometry
XTEM	cross-sectional transmission electron microscopy
ZDO	zero differential overlap

## Contents

<i>Foreword</i> .....	x
<i>Introduction</i> .....	xii
<i>Contributors</i> .....	xiii
<i>Abbreviations</i> .....	xx
<b>1. Melt Growth</b> .....	<b>1</b>
1.1 Si Melt: Density, Surface Tension and Viscosity .....	3
1.2 Si Melt Convection in a Crucible .....	8
1.3 Si Melt Growth: Segregation of Light Elements, Dopants and Heavy Metals .....	16
1.4 Si Melt Growth: Oxygen Transportation during Czochralski Growth .....	23
1.5 Si Melt Growth: Concentration and Diffusivities of Vacancies and Interstitials .....	33
1.6 Si Melt Growth: Grown-In Defects and Simulation of Their Formation .....	39
<b>2. Epitaxial Growth</b> .....	<b>53</b>
2.1 c-Si MBE: Sources, Doping, Growth Rates, Uniformity .....	55
2.2 Gas-Source MBE of c-Si and Related Materials .....	69
2.3 UHV/CVD and Related Growth Techniques for Si and Other Materials .....	77
<b>3. Structural and Mechanical Properties</b> .....	<b>89</b>
<i>Crystalline Structure and Elastic Properties</i>	
3.1 Diamond Cubic Si: Structure, Lattice Parameter and Density .....	91
3.2 Elastic Constants and Moduli of Diamond Cubic Si .....	98
3.3 High Pressure Phases of c-Si .....	104
<i>Dislocations and Mechanical Properties</i>	
3.4 Core Structures and Energies of Dislocations in Si .....	108
3.5 Dislocation Mobilities in c-Si .....	113
3.6 Macroscopic Mechanical Behaviour of Si at High Temperature .....	122
3.7 Mechanical Behaviour of Si at Low Temperature .....	136
3.8 Fracture and the Brittle-Ductile Transition in Si .....	144

<b>4. Thermal Properties .....</b>	<b>149</b>
4.1 Specific Heats of c-Si and Molten Si .....	151
4.2 Thermal Expansion Coefficients of c-Si .....	153
4.3 Melting Points of Si .....	155
4.4 Phonon Spectrum of c-Si .....	159
4.5 Thermal Conductivity of c-Si .....	165
4.6 Thermal Diffusivity of c-Si .....	168
4.7 Surface Tension of Liquid Si .....	170
4.8 Heat of Fusion of Si .....	171
<b>5. Surface Properties and Cleaning .....</b>	<b>173</b>
5.1 Reconstruction of Si (001), (111) and (110) Surfaces .....	175
5.2 Structure of Clean Silicon Surfaces: Vicinal Si (001) and Si (111) Surfaces .....	183
5.3 Electronic Structure of c-Si Surfaces .....	189
5.4 Electrical Characterization of c-Si Surfaces .....	202
5.5 Passivation of c-Si Surfaces .....	211
5.6 Wet Chemical Cleaning and Surface Preparation of Si .....	219
5.7 HF Vapour Cleaning of Oxide on c-Si .....	226
5.8 Plasma and Other <i>In Situ</i> Cleaning Approaches to Cleaning of c-Si Surfaces .....	235
<b>6. Structural Modeling .....</b>	<b>243</b>
6.1 Approximate and Parametrised Quantum Chemical Methods for Structural Modeling of c-Si .....	245
6.2 Approximate and Parametrised Quantum Mechanical Methods for Structural Modeling of c-Si: the Tight Binding Approximation .....	257
6.3 Electronic Structure Calculations of Oxygen Point Defects in c-Si .....	267
6.4 Theoretical Modeling of Minor Impurities in c-Si .....	277
6.5 c-Si Surfaces - Review of Theoretical Studies .....	288
6.6 Microscopic Modeling of Grain Boundaries and Stacking Faults in c-Si .....	299
6.7 Vacancy Defects in c-Si: Electronic and Ionic Structures .....	309
6.8 Self Interstitials in c-Si: Structure and Migration Mechanisms .....	319
6.9 Ab Initio Modeling Techniques Applied to c-Si .....	330
6.10 Modeling of Dislocations in c-Si .....	357
<b>7. Band Structure .....</b>	<b>379</b>
7.1 Band Structure of c-Si: Overview .....	381
7.2 Calculational Methods for Determining the Band Structure of Bulk c-Si .....	383
7.3 Spin Orbit Splitting in Bulk c-Si .....	390

7.4	Variation of Bandgap with Temperature in c-Si .....	391
7.5	Variation of Bandgap with Doping in c-Si .....	394
7.6	Variation of Bandgap with Pressure in Bulk c-Si .....	399
7.7	Band Structure and Bandgaps in Strained Bulk c-Si .....	402
7.8	Effective Masses of Electrons and Holes in c-Si .....	408
<b>8.</b>	<b>Electrical Properties .....</b>	<b>411</b>
8.1	Resistivity and Carrier Concentrations of Doped c-Si, and Sheet Resistance of Ion-Implanted Bulk Si .....	413
8.2	Piezoresistance of c-Si .....	421
8.3	Electron Mobility, Diffusion and Lifetime in c-Si .....	430
8.4	Hole Mobility, Diffusion and Lifetime in c-Si .....	443
8.5	Carrier Ionization: Field, Temperature and Orientation Dependence .....	450
8.6	Modeling Equations and Parameters for Numerical Simulation .....	457
<b>9.</b>	<b>Impurities in Silicon .....</b>	<b>477</b>
9.1	Diffusion of O in c-Si .....	479
9.2	Segregation Coefficient of O in c-Si .....	484
9.3	Solubility of O in c-Si .....	488
9.4	O-related IR Absorption in c-Si .....	492
9.5	Precipitation, Segregation and IR Absorption of O in c-Si .....	499
9.6	Segregation Coefficient, Solubility and IR Absorption of C in c-Si .....	503
9.7	Diffusion of C in c-Si .....	506
9.8	Hydrogen Diffusion and Solubility in c-Si .....	511
9.9	Hydrogen Containing Point Defects in c-Si .....	522
9.10	Nitrogen in c-Si .....	538
9.11	Solubility and Diffusion of Transition Metal Impurities in c-Si .....	543
9.12	Deep Levels of Transition Metal Impurities in c-Si .....	561
9.13	Electronic States of Chalcogen-Related Donors in c-Si .....	573
9.14	Properties of Rare-Earth Doped c-Si .....	583
9.15	Alkali Impurities (Na, K, Li) in c-Si .....	593
<b>10.</b>	<b>Dopants In Silicon .....</b>	<b>597</b>
10.1	Diffusion of Al, Ga, In and Tl in c-Si .....	599
10.2	Diffusion of P, As and Sb in c-Si .....	607
10.3	Boron-Interstitial Clustering in c-Si .....	617
10.4	Solubility of B, Al, Ga, In, Tl, P, As and Sb in c-Si .....	620
10.5	Ion Implantation of B and P in c-Si .....	636

<b>11. Defect Levels in Silicon .....</b>	<b>641</b>
11.1 Vacancies and Interstitials and Their Interactions with Impurities in c-Si .....	643
11.2 Electrical and Optical Properties of Dislocations in c-Si .....	653
11.3 Shallow Thermal Donors in c-Si .....	659
11.4 Thermal Double Donors in c-Si .....	663
11.5 Double Donors and Acceptors in c-Si .....	669
<b>12. Optical Properties .....</b>	<b>677</b>
12.1 Optical Properties of c-Si: General Aspects .....	679
12.2 Optical Functions of Intrinsic c-Si for Photon Energies up to 7.5eV: Table .....	683
12.3 Optical Functions of Intrinsic c-Si for Selected Photon Energies: Table .....	691
12.4 Optical Functions of Liquid Si .....	696
<b>13. Photoconductivity and Photogenerated Carriers .....</b>	<b>697</b>
13.1 Photoconductivity of c-Si: General Remarks .....	699
13.2 Photoconductivity Spectra of Ion Implanted c-Si .....	702
13.3 Photoconductivity Spectra of Electron Irradiated c-Si .....	705
13.4 Bulk Lifetimes of Photogenerated Carriers in Intrinsic c-Si .....	708
13.5 Bulk Lifetimes of Photogenerated Carriers in Doped and Treated c-Si .....	712
13.6 Surface Recombination Velocity for c-Si .....	718
13.7 Mobility and Diffusion of Photogenerated Carriers in Intrinsic c-Si .....	722
13.8 Mobility and Diffusion of Photogenerated Carriers in Doped and Treated c-Si .....	726
<b>14. Implantation/Irradiation of Silicon .....</b>	<b>731</b>
14.1 Ion Implantation Range Theory .....	733
14.2 Ion Implantation into c-Si: Basic Mechanisms and Modeling .....	739
14.3 Electrical Properties of Ion Implanted and Electron Irradiated c-Si .....	746
14.4 Structure of Ion Implantation Induced Defects in c-Si .....	755
14.5 Energy Levels, Structure and Properties of Point Defects Induced by Ion Implantation and Electron Irradiation of c-Si .....	763
14.6 Dopant Ionization Energies in c-Si .....	773
<b>15. Gettering .....</b>	<b>775</b>
15.1 Gettering of Transition Metals in c-Si: Gettering in Silicon Technology .....	777
15.2 Gettering of Transition Metals in c-Si: Gettering Mechanisms .....	781
15.3 Gettering of Transition Metals in c-Si: Gettering Techniques .....	783
15.4 Gettering of Transition Metals in c-Si: Summary of Current State of Understanding .....	793
15.5 Gettering of Transition Metals in c-Si: Future Trends .....	794

<b>16. Etching .....</b>	<b>809</b>
16.1 Silicon Wet Isotropic Etch Rates .....	811
16.2 Silicon Wet Orientation Dependent (Anisotropic) Etch Rates .....	815
16.3 Silicon Preferential (Defect Delineation) Etch Rates .....	822
16.4 Silicon Plasmaless Gas-Phase Etch Rates .....	825
16.5 Silicon Sputtering and Ion Milling Etch Rates .....	828
16.6 Silicon Chemical Plasma and Reactive Ion Etch (RIE) Rates .....	832
16.7 Silicon Reactive Ion Beam and Ion Beam Assisted Etch Rates .....	842
16.8 Silicon Laser-Assisted Etch Rates .....	845
<b>17. Metal-Silicon Contacts .....</b>	<b>849</b>
17.1 Recent Advances in Silicide Technologies .....	851
17.2 Epitaxial Silicide Contacts .....	863
<b>18. Silicon on Insulator Technology .....</b>	<b>885</b>
18.1 Overview of SOI .....	887
18.2 Silicon on Sapphire .....	889
18.3 Physics and Chemistry of Silicon Wafer Bonding .....	905
18.4 Bond, Grindback and Polish SOI .....	923
18.5 Bond and Etch Back SOI .....	938
18.6 Hydrogen Induced Exfoliation of c-Si .....	942
18.7 Diffusion in SOI Material .....	957
18.8 SOI with Porous Si .....	976
18.9 Technology and Properties of SIMOX .....	979
18.10 Comparison of Properties of Available SOI Materials .....	992
<b>Index .....</b>	<b>1003</b>

## CHAPTER 2

### EPITAXIAL GROWTH (*Edited by J.C. Bean*)

- 2.1 c-Si MBE: sources, doping, growth rates, uniformity
- 2.2 Gas-source MBE of c-Si and related materials
- 2.3 UHV/CVD and related growth techniques for Si and other materials

## 2.1 c-Si MBE: sources, doping, growth rates, uniformity

J.C. Bean

July 1998

### A INTRODUCTION

Molecular beam epitaxy (MBE) consists of growth by evaporation and condensation of elemental species. These species generally evaporate as either single atoms or as molecules of 2–4 atoms. For Si, Mella and Brodsky [1] have determined that evaporation is primarily as single atoms, making the name MBE, strictly, a misnomer. The ideal species is one with a vapour pressure high enough that it can be evaporated from thermal sources, but low enough that it will condense on all other surfaces within the MBE system. If that atom is evaporated in a vacuum free of scattering, deposition will then be a line-of-sight process from the source to the first cool surface. Fluxes can then be tuned by simple geometrical considerations and stopped, instantly, by interposing deposition ‘shutters’. These attributes make MBE the most conceptually simple of the epitaxial growth techniques and provide control of composition, doping and layer thickness down to a scale of single atomic layers [2–4].

These considerations can be used to define generalized MBE operating conditions. To be free of scattering, deposition must occur over dimensions small compared to the vacuum mean free path [5]

$$\text{mean free path (cm)} = 5 \times 10^{-3}/P \text{ (torr)} \quad (1)$$

where P is the total pressure of the residual gas, which is assumed to be air-like in composition and at room temperature. The mean free path varies inversely as pressure and reaches 5 m at  $10^{-5}$  torr. Given typical MBE system dimensions of ~ 1 m, scattering is effectively absent in the MBE ultrahigh vacuum (UHV) ranges below  $10^{-7}$  torr.

Growth rates and doping levels are determined by the dispersal of atoms from a heated source. Relevant elemental partial pressures are given in FIGURE 1 [6]. These partial pressures can be converted to flux across a surface by the relationship [7]

$$\text{flux in a vapour (molecules/cm}^2 \text{ s}^{-1}) = 3.513 \times 10^{22} P \text{ (torr)} / (M(g) T(K))^{1/2} \quad (2)$$

where M is the molecular weight of the species and T is the absolute temperature. If the elemental charge and its vapour are confined in an isothermal volume, with only a small exit aperture, the flux of atoms at some distance outside that aperture can be approximated by multiplying EQN (2) by  $A \cos^2\theta/\pi L^2$ , where A is the area of the aperture, L is the distance from the aperture and θ is the angle between a normal to the aperture and the point in question. One thus arrives at the so called Knudsen relationship for flux from a thermal evaporation source:

$$\text{flux from a source (molecules/cm}^2 \text{ s}^{-1}) = 1.118 \times 10^{22} P(\text{torr}) A(\text{cm}^2) \cos^2\theta / L(\text{cm})^2 (M \text{ (mol. wt.)} T(K))^{1/2} \quad (3)$$

For sources with finite apertures, fluxes can be calculated by superimposing distributions of the above form. Flux from a freely evaporating solid or liquid surface (such as in the e-guns, below) can also be estimated in this manner if surface temperature can be evaluated. For MBE, source-to-substrate separations are generally on the order of 50 cm, with the substrate placed near the normal of the source.

## 2.1 *c-Si MBE: sources, doping, growth rates, uniformity*

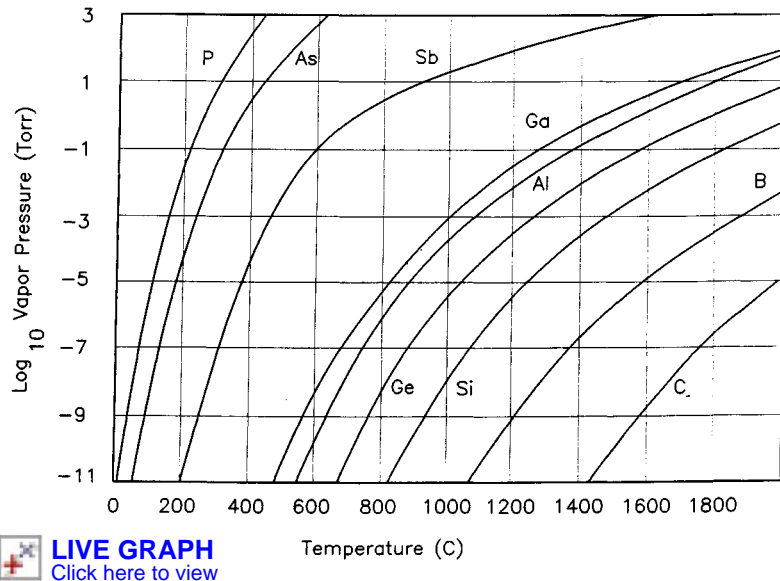


**FIGURE 1** Elemental vapour pressures of silicon, its electrical dopants, and elements (Ge and C) with which it may be combined as a compound semiconductor. Data from [6].

Desirable growth rates will be based, largely, on the degree of control required. Mechanical shutters can be inserted or withdrawn from the deposition path in a time somewhat less than 1 s. These shutters can then control the MBE flux on a monolayer or angstrom scale if growth rates are kept to values not much above 1 monolayer/s ( $\sim 1.3 \text{ \AA/s}$ ). As detailed below, at such rates, high quality crystal is generally grown on Si substrates at temperatures of 500–800°C. At these substrate temperatures, Si re-evaporation is essentially negligible (i.e. the sticking probability,  $s$ , is 1). Incident flux can thus be equated to areal incorporation rates. The Si data of FIGURE 1 and EQN (3) then predict typical Si source temperatures of  $\sim 1600^\circ\text{C}$ . Growth uniformity is controlled by the simple line-of-sight Si flux and can be geometrically trimmed to better than 5% across conventional wafers. However, growth (or deposition) occurs on both exposed and oxidised Si surfaces, in contrast to the selective epitaxial growth possible with halide based chemical vapour deposition (CVD).

One must take into account the possibility that the deposition shutters may not be ideally effective at blocking fluxes. Shutters generally have no direct cooling and will equilibrate at temperatures dictated by their relative exposure to thermal radiation from the source, the substrate and the chamber walls. For shutters modulating the very high temperature Si source, a separation of 10–15 cm is generally sufficient to assure that the shutter will settle at a temperature no higher than that of the substrate. Re-evaporation of Si from the shutter is thus also negligible and its shutter behaves in an ideal manner. However, the situation is not so straightforward for dopants where one is sensitive to fluxes of  $10^6$ – $10^9$  below that of Si. In particular, for high vapour pressure dopants, such as P and As, re-evaporation from inadvertently heated shutters or other surfaces has produced unintentional doping.

## B APPARATUS

A modern commercial Si MBE apparatus is shown in FIGURE 2 [8]. Growth occurs in the baked UHV chamber at the right. High temperature Si sources generally produce significant residual fluxes of hydrogen and other species requiring high capacity pumps. Both turbopumps and closed cycle He cryopumps are adequate but cryopumps have the pronounced advantage of being free of lubrication oils that can readily poison MBE through formation of compounds such as SiC. Cassettes of samples

## 2.1 *c-Si MBE: sources, doping, growth rates, uniformity*

are introduced via a vacuum interlock into a parking chamber at the left. For large, 100–300 mm diameter Si substrates, line-of-sight MBE growth is generally conducted by transferring wafers one-by-one through the growth chamber. For production applications, this single wafer processing is one of MBE's two principal shortcomings. The other is the tendency of material condensed on the chamber walls to disperse as fine particulates and be incorporated within the epitaxial layers [9]. With care [10,11], particulate induced epitaxial defects can be held below  $100/\text{cm}^2$  but values of greater than  $1000/\text{cm}^2$  have been measured in research systems.

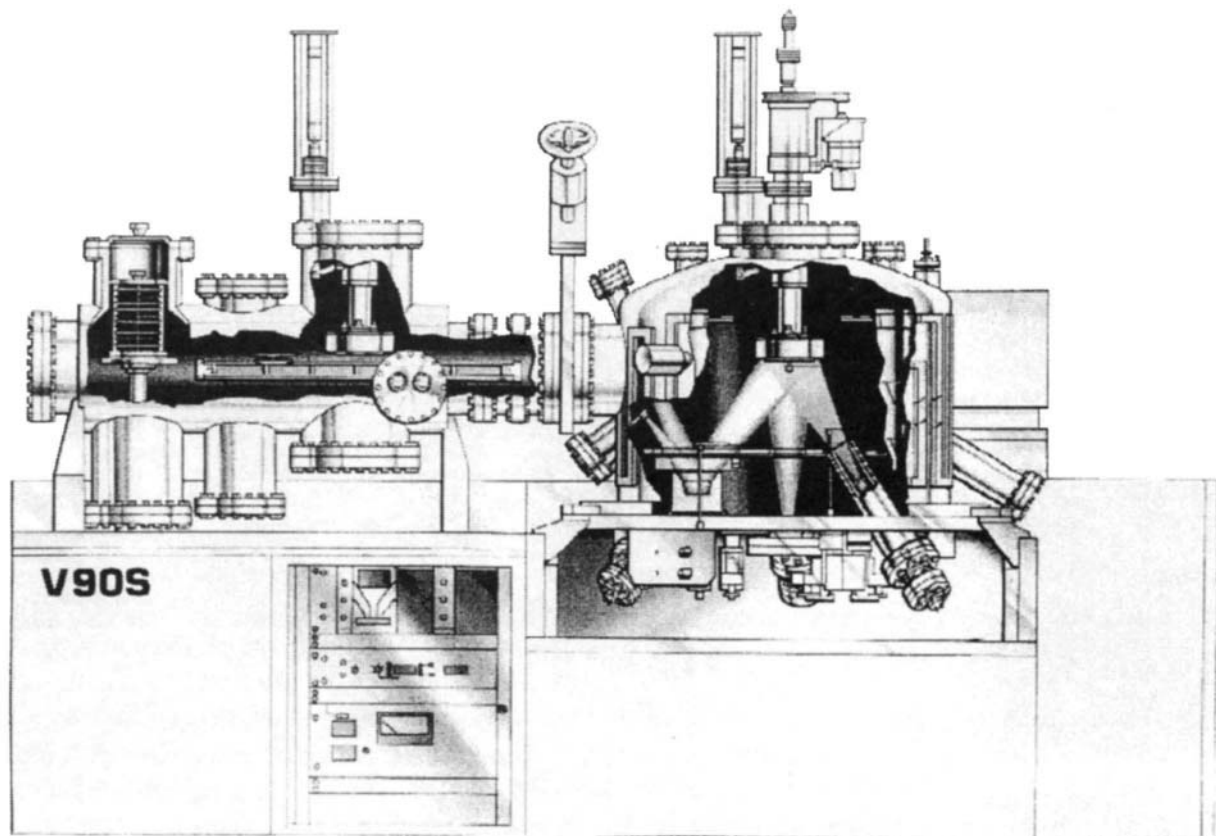


FIGURE 2 Modern commercial Si MBE system offered by VG Semicon Ltd. This model, V-90S, loads cassettes of ten wafers of up to 150 mm diameter. Deposition occurs in the right chamber one wafer at a time. Cutaway shows e-gun source at left with flux to both downward facing substrate and deposition meter. Doping Knudsen cell at right. Ion implantation doping system (FIGURE 9) is attached to downward inclined tube and flange at far right. (By permission of VG Semicon Ltd. [8].)

Materials are generally evaporated from simple resistively heated crucibles. Because thermal gradients across the crucible are small and the crucible opening limited, the Knudsen condition of EQN (3) is approximated and these sources are described as Knudsen cells (or K-cells). For these near isothermal crucibles, charge surface temperatures can be estimated and controlled based on thermocouple measurement of the crucible outside wall temperature. Heating is generally provided by resistive elements made from tungsten or tantalum, supported by alumina or boron nitride insulators. For crucible temperatures above  $\sim 1500^\circ\text{C}$ , these materials generally interact and outgas undesirable species providing an upper limit to their operating range. From FIGURE 1, it can be seen that this limit poses a problem only for Si, for the alternative crystalline components Ge and C, and for the lowest vapour pressure dopant, B. For these species, sources based on high-energy electron bombardment are substituted.

## 2.1 *c-Si MBE: sources, doping, growth rates, uniformity*

For the primary Si, Ge or C constituents, commercial ‘e-gun’ sources can be used, as depicted schematically in FIGURE 3. In these guns, a charge of the source material is fitted into a grounded, water-cooled, crucible and the upper surface bombarded by an electron beam. This beam is emitted from a filament biased at -10 kV and positioned below the crucible. From the filament, the 10 keV electrons are forced along a 270° arc by a perpendicular magnetic field. This geometry hides the high temperature filament from the deposition substrate and is essential to minimize contamination [12]. These sources can readily heat the source charge surface above 2000°C. However, the gradient in charge temperature means that evaporation rates cannot be estimated by measuring the backside temperature of the charge. Further, e-gun power has been shown to give only a poor indication of flux [13]. These sources must thus be used in conjunction with a separate flux sensor. For Si MBE, where UHV operation requires long sensor life, the preferred sensor is a commercial unit based on UV emission from the evaporants induced by electron bombardment within the sensor volume [14].

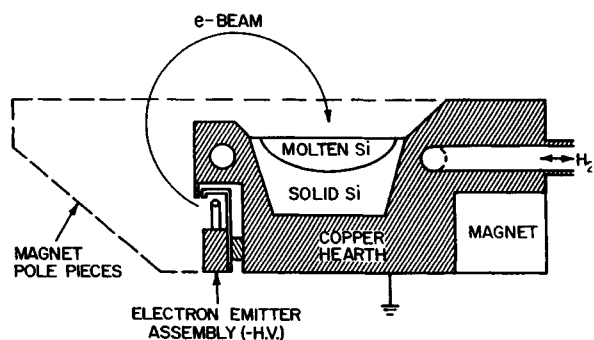


FIGURE 3 Schematic cross-section of commercial ‘e-gun’ evaporation source such as Temescal Inc.’s SF1H 270 models [12].

For lower level B evaporation, the need for a flux sensor has been circumvented by several experimental high temperature Knudsen cell designs, one of which is depicted in FIGURE 4 [15]. This cell retains the nominally isothermal crucible and thermocouple monitoring of a common Knudsen cell. However, in lieu of simple resistive heating, an electrically conductive crucible is bombarded by electrons emitted from smaller but hotter filaments. The primary challenge in such sources [16–18] is, again, to avoid low level contamination from these much hotter, but incompletely hidden, filaments.

## C GROWTH RATES AND TEMPERATURES

In contrast to CVD, Si MBE growth rates are not controlled by surface decomposition reactions. Si arrives at the substrate surface primarily as single atoms [1]. Dopants arrive as atoms, dimers or tetramers of a single species [6] that are readily decomposed. Instead, growth rate is controlled by two mechanisms: 1) the rate at which newly arrived atoms can migrate across the growing surface to find a highly coordinated site at which to be incorporated into the crystalline lattice; 2) competition with ambient contaminants for such sites.

Contamination limits minimum Si MBE growth rate and temperature. As growth rate is decreased, in the presence of a fixed vacuum contaminant flux, a higher percentage of surface sites will be taken by contaminants, and crystal quality will deteriorate. The temperature dependence of this minimum growth rate is more difficult to establish. At lower temperatures it may be harder to introduce contaminants at the Si surface because decomposition of H<sub>2</sub>O and CO<sub>2</sub> molecules may be suppressed.

## 2.1 *c-Si MBE: sources, doping, growth rates, uniformity*

However, lower temperatures may also increase the retention and build-up of contaminants by suppressing their removal through re-evaporation or diffusion into the crystal. Retention is highlighted by the data of FIGURE 5 showing the effect of H<sub>2</sub>O partial pressure on a static (growth rate = 0) Si surface [19,20]. From first principles, it is difficult to determine the temperature balance between contaminant introduction and removal on a growing Si surface. However, work on Si MBE spans 40 years and there has been a clear downward trend in minimum reported growth rate and temperature as vacuums improved from early 10<sup>-6</sup> torr to the current 10<sup>-10</sup> torr levels [21]. These data suggest that enhanced removal (decreased retention) at higher temperatures dominates. Under current UHV MBE conditions, it is generally believed that contaminants degrade growth only for rates below ~0.1 Å/s and temperatures well below 500°C. However, definitive data do not exist because of the difficulty of monitoring and controlling growth rates below 0.1 Å/s, given present day deposition flux monitors. Further, there is generally no practical incentive for growing at these glacial rates.

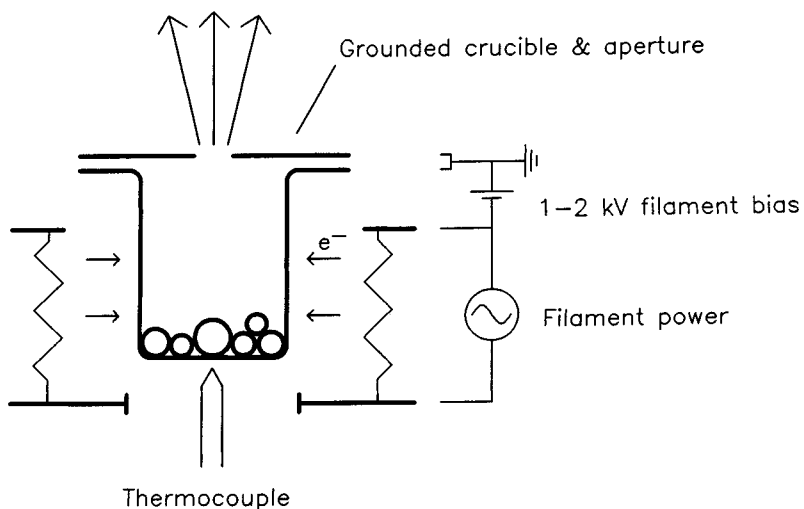


**FIGURE 4** Schematic cross-section of one of several experimental high temperature K-cell designs for use with the low vapour pressure dopant, boron. These high temperature cells differ from conventional units in that resistive filaments are biased and heated to the point where they emit high energy electrons which bombard a conducting crucible. (After [15].)

Maximum growth rate is limited by the intrinsic mechanism of surface migration. That is, a newly arrived atom must reach an attachment site before it is buried by other atoms. FIGURE 6 presents experimental data and modelling on surface migration limited growth [22,23]. The model assumes that, at lower temperatures, favoured attachment sites will be provided by random nucleation of surface dimer atom strings (i.e. elimination of dangling surface atomic bonds by pairing of adjacent Si atomic rows). The model was fit to data by adjusting parameters for surface vibrational frequency and thermal activation barrier.

FIGURE 6 defines a boundary between crystalline and amorphous material under sustained low temperature growth. However, even for conditions at the lower right of the figure, as growth begins, material does not instantaneously become amorphous. As material is deposited, only a small percentage of atoms may be buried before reaching crystalline attachment sites. Defects will be incorporated, but initial material will remain fundamentally crystalline. Only as growth continues and a critical number of flaws are incorporated will subsequent material assume a non-crystalline structure. Thus, at very low temperatures, one can define a maximum limit to epitaxial growth on a crystalline substrate. FIGURE 7 plots this calculated upper limit based on the parameters determined by the fitting in FIGURE 6. Subsequent experimental data, by another group [24], at a growth rate of

## 2.1 c-Si MBE: sources, doping, growth rates, uniformity

0.7 Å/s is in fundamental agreement, falling between predicted 0.3 and 1.0 Å/s curves. However, two points should be strongly noted. First, curves in FIGURES 6 and 7 assume dimer limited attachment sites. At more typical Si MBE temperatures above 500°C, surface migration is enhanced (relative to dimer nucleation) such that attachment occurs instead at propagating surface step edges. This transition invalidates the higher temperature extrapolation of FIGURE 7 which would otherwise contradict the known ability to sustain crystalline growth indefinitely at temperatures above ~400°C. Second, these models involve a concentration of defects below that necessary to amorphize layers. Thus, while nominally crystalline, these extreme low temperature layers may have defect concentrations hugely higher than those tolerable in electronic devices.

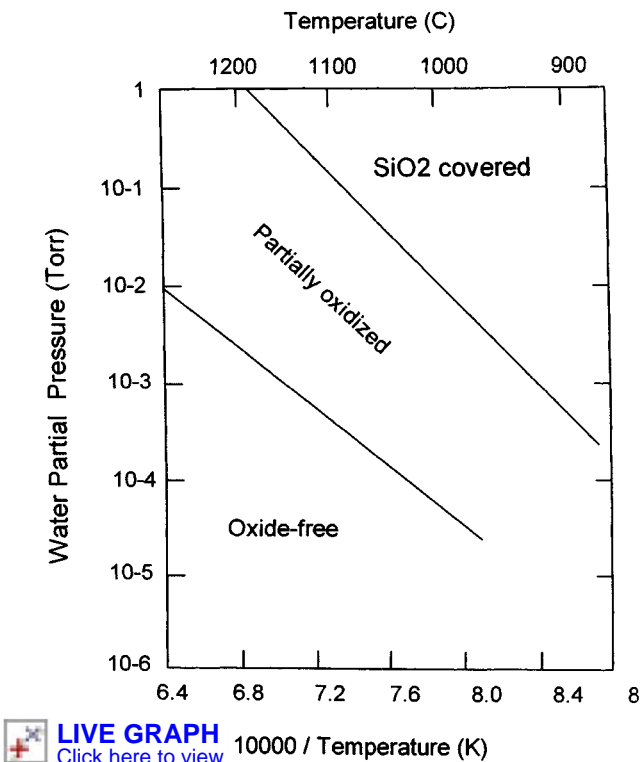


FIGURE 5 Effect of background water vapour on the surface state of a static Si surface. Maintenance of an atomically clean surface depends upon lower H<sub>2</sub>O partial pressures and higher growth temperatures. For MBE, where H<sub>2</sub>O pressure is 10<sup>-10</sup> torr, or lower, clean surfaces can be maintained at temperatures well below 500°C. (Data from [19,20].)

The upper temperature limit to Si MBE growth is determined by undesirable diffusion effects. The definition of ‘undesirable diffusion’ depends upon application of the material. For Si homoepitaxy directed at device applications, the goal is generally to take full advantage of MBE’s ability to control dopant introduction to atomic scales. In order to maintain this dopant control, diffusion lengths during growth should be small compared to the scales of carrier relaxation that will occur in the final device. This goal is met, for growth times on the order of 1 h, if growth occurs below 750–800°C. For SiGe strained layer heteroepitaxy, ‘undesirable diffusion’ instead takes the form of lateral SiGe surface diffusion to form strain reducing islands. For general SiGe devices, islanding is eliminated at growth temperatures at and below 550°C [25]. However, for SiGe devices dependent on smooth monolayer scale layers, it may be necessary to grow at below 450°C.

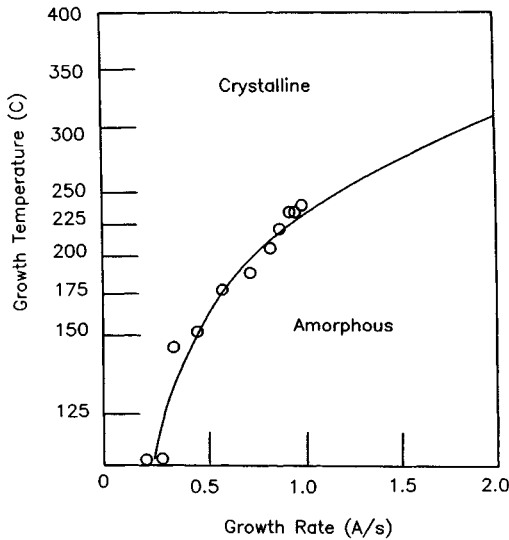


FIGURE 6 Limit on maximum growth rate, based on surface migration limited growth at low temperatures. Data fit by model assuming atomic attachment at dimer atom surface sites. This assumption, and the extrapolation to higher temperatures, breaks down above  $\sim 400^{\circ}\text{C}$ . (After [22].)

#### D CO-EVAPORATED ELEMENTAL DOPANTS

Dopants can be introduced by co-evaporation from separate elemental K-cells. For an idealized incorporation process, doping level is expressed as

$$\text{doping level (#/vol.)} = N_{\text{Si}} [s_{\text{dopant}}(T) n_{\text{dopant}} F_{\text{dopant}}]/F_{\text{Si}} \quad (4)$$

where  $N_{\text{Si}}$  is the number density of Si ( $5 \times 10^{22} \text{ cm}^{-3}$ ),  $s_{\text{dopant}}$  is the net probability that the dopant molecule will adhere to the Si surface,  $n_{\text{dopant}}$  is the number of atoms in the dopant molecule (typically 1–4), and  $F_{\text{dopant}}$  and  $F_{\text{Si}}$  are the dopant and Si molecular fluxes as evaluated from EQN (3). This expression includes the facts that for Si,  $s$  and  $n$  are 1 under MBE conditions.

The most common Si dopants are B, P and As. These dopants have shallow carrier binding energies and high solid solubilities readily compatible with concentrated doping (e.g.  $>1 \times 10^{18} \text{ cm}^{-3}$ ). From FIGURE 1 and early experiments, problems are identified in co-evaporating all three of these dopants. The vapour pressure of boron is so low that conventional K-cells produce insufficient flux and special electron bombardment cells [6,26,27] such as that shown if FIGURE 4 must be employed [28–31]. These cells are home-built and, for all but one design [15], there has been a notable lack of published data on growth of device-quality layers. For P and As, vapour pressures are so high that there is significant re-evaporation from unintentionally heated MBE surfaces. This produces uncontrolled low-level doping.

## 2.1 *c*-Si MBE: sources, doping, growth rates, uniformity

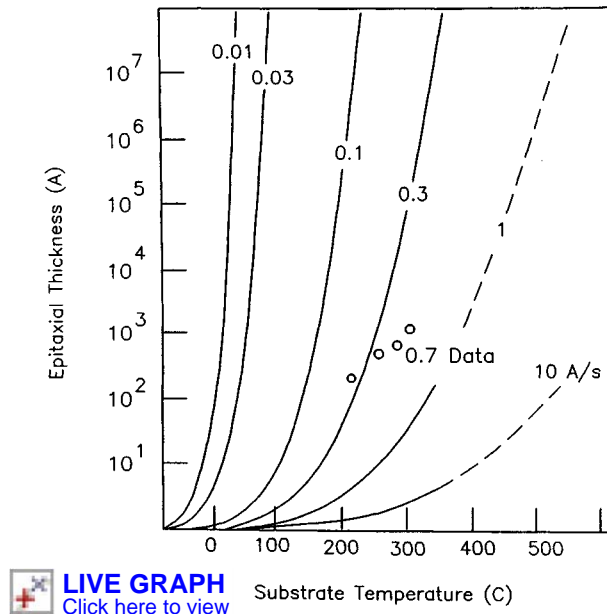


FIGURE 7 Limit on crystalline thickness for initial growth at very low temperature. As in FIGURE 6, model is again based on atomic attachment at dimer atom sites and thus breaks down above  $\sim 400^\circ\text{C}$  (model curves after [22], inset data from [24]).

The dopants Ga, Al and Sb offer the next best alternatives. Representative data from two experiments are combined in FIGURE 8 [32]. The top trace gives the K-cell temperature program during growth of the epitaxial layers. During four short periods, the K-cell temperature was raised by  $50^\circ\text{C}$  to produce an  $\sim 10$ -fold increase in dopant flux. The lower traces give C–V carrier profiles measured in the cooled layers. The Ga profile shows the expected four peaks with a sharpness consistent with the limitations of C–V profiling. However, the Al profile is distorted with the peaks strongly broadened and driven together. This distortion is due to the accumulation of a segregated layer of Al atoms on the Si surface during growth. Essentially, a dopant atom that has found a crystalline surface binding site is displaced by the subsequent arrival of a Si atom. Similar phenomena have been observed for Sn doping of GaAs MBE [33], but for compound semiconductor growth, dopant segregation is a rare exception to idealized incorporation described by EQN (4). Instead, for Si virtually all co-evaporated dopants exhibit segregation over at least some part of the growth range. This segregation is driven by the exceptional strength of the Si crystalline lattice and its unusually small lattice spacing.

Dopant segregation data [28–32,34–41] and models [42–45] are extremely complex. Segregation can be attributed to a size mismatch effect [44]. However, to account for detailed data, models must even invoke changes in the sign of the activation energies, dopant by dopant [42]. A complete description of these phenomena is beyond the scope of this Datareview. Instead TABLES 1 and 2 summarize conditions under which elemental dopants are usefully incorporated by co-evaporation.

TABLE 1 Net sticking probabilities for useful co-evaporated elemental dopants.

Dopant	$500^\circ\text{C}$	$600^\circ\text{C}$	$700^\circ\text{C}$	$800^\circ\text{C}$	Ref
B	$\sim 1$	$\sim 1$	$\sim 1$	$\sim 1$	[26]
Ga	0.15	0.007	$10^{-3}$	$10^{-4}$	[32]
Sb	0.1	0.005	$5 \times 10^{-4}$	$5 \times 10^{-5}$	[35]

## 2.1 c-Si MBE: sources, doping, growth rates, uniformity

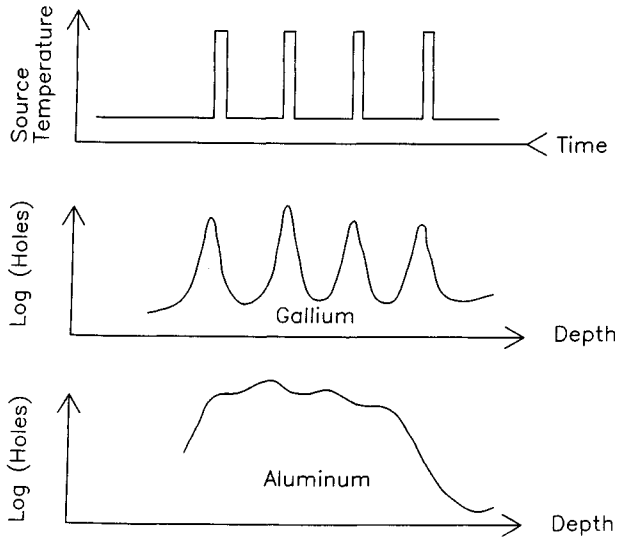


FIGURE 8 Data for co-evaporation doping experiments using Ga and Al. K-cell temperature program shown at top. Base temperature chosen to produce moderate doping level. Temperature increased by 50°C, four times during growth, to increase flux to epitaxial layer by ~10×. C-V doping profiles shown at middle and bottom from different samples. Ga profile shows expected four peaks with shape consistent with  $\log_{10}$  scale and room temperature carrier relaxation about dopant. Al profile is instead grossly distorted by segregation phenomena. Depth scales were converted from the temperature program and the known, constant, Si growth rates. (After [26].)

TABLE 2 Usable doping range/segregation behaviour.

Dopant	$T_{\text{growth}}$ (°C)	Dopant range ( $\text{cm}^{-3}$ )	Dopant behaviour	Ref
Al	500–800	All	Segregation	[32]
B	550–800	$10^{16}$ – $10^{19}$ $> 10^{20}$	~ Ideal Segregation	[29]
Ga	600–800	$\leq 10^{18}$ $> 10^{18}$	~ Ideal Segregation	[32]
	500	All	Segregation	
Sb	900 $\leq 800$	$\sim 10^{16}$ $\leq 10^{18}$ $> 10^{18}$	~ Ideal Segregation Segregation and degradation of crystallinity	[34,35]

Additional, more exotic, co-evaporation doping schemes have been explored. For certain dopants, incorporation behaviour has been somewhat improved by interrupting growth to either intentionally accumulate or attenuate surface dopant layers [35,46–48]. Others have sought to avoid home-built high temperature B sources or P re-evaporation effects by use of molecular species such as  $\text{B}_2\text{O}_3$  [49–53] or  $\text{Sn}_3\text{P}_4$  [54]. Due to various limitations, none of these exotic approaches have been widely accepted for growth of device quality layers.

## E CO-ION IMPLANTED DOPANTS

For Si MBE, the complexity and shortcomings of co-evaporation doping drove the development of alternatives based on simultaneous low energy ion implantation [13,55]. To overcome surface

## 2.1 c-Si MBE: sources, doping, growth rates, uniformity

segregation problems, dopants need be implanted only 10–20 Å below the growing epitaxial surface. At this depth, the dopant atom readily finds a fully co-ordinated lattice site from which it cannot be easily displaced. This penetration is sufficiently small that the atomic monolayer control of MBE is only marginally degraded.

At extremely low energies, the space charge in an ion beam counteracts the applied accelerating voltage imposing an upper limit on beam current density [56] which varies as  $V_{\text{appl}}^{3/2}$  (Child's law). To provide adequate co-implantation current densities, acceleration voltages of at least a kilovolt must be used. Ion penetration can then be minimized by use of molecular ions such as  $\text{BF}_2^+$  and  $\text{As}_2^+$ . These ions are readily produced in ion sources fed by source gases  $\text{BF}_3$  and  $\text{AsF}_5$ , such as those used in the dual 3 kV co-ion-implanter of FIGURE 9 [57]. Molecular ions tend to separate into individual atoms upon impact with the growing epitaxial surface. Penetration of the components can be estimated by low energy extrapolations of conventional ion implantation data and falls below 50 Å [58,59]. These estimates are confirmed by MBE experiments involving modulation doping for which setback of doped layers from SiGe quantum wells has a strong effect on the concentration of carriers falling into the wells. For the author's system, employing 3 keV molecular ions incident 60° off the substrate normal, such data indicated that ion penetration was much smaller than 100 Å [60]. Under the above conditions, layer doping follows a simple relationship of the form

$$\text{doping}_{\text{co-ion implantation}} (\# \text{ cm}^{-3}) = A' I(\text{nA})/R(\text{A/s}) \quad (5)$$

where  $I$  is the beam current,  $R$  is the Si growth rate and  $A'$  is a calibration constant which, for the author's system, has a value of about  $10^{15} \text{ cm}^{-3}$ . This relationship implies ~100% incorporation of implanted dopants on electrically active lattice sites. The strong advantage of co-ion implantation doping is that simple control is obtained for all dopants, independent of growth temperature or doping level. One is constrained only by the lower limit to current detection and upper limits of the source current. Together, these generally define an accessible doping range of at least  $10^{15} - 10^{19} \text{ cm}^{-3}$ . In the system of FIGURE 9, ion beam current to the sample is controlled by switching the magnet to the appropriate ion source and modulating the beam intensity by a downstream electrostatic attenuator and X-Y raster scanning plates. All of these functions are integrated into the PC based real-time control system of the V-90S based MBE system (FIGURE 2).

The principal shortcomings of co-ion implantation doping are the cost of the apparatus and the possibility of radiation damage to the material. Implantation systems adapted from high energy implant components have, indeed, been very expensive. However, smaller systems based on low-energy, largely off-the-shelf items such as FIGURE 9, have been built for less than 10% of the overall MBE system cost. Extensive radiation damage was reported in one of the earliest investigations of co-ion implantation doping [55]. However, this report is now contradicted by a large body of data on growth of demanding minority carrier [61] and high field electron devices [62], based on co-ion implanted material grown at 550–650°C. These device results are supported by studies of layer photoluminescence, which indicate bulk-like Si layer quality for growth temperatures above 600–650°C [63,64]. It is apparent that the proximity of the growing epitaxial surface hugely accelerates annealing of any point defects induced by implantation.

A final doping scheme of 'knock-on' implantation is depicted in FIGURE 10. Knock-on is based on the partial ionization of Si that occurs in e-gun evaporation sources (FIGURE 3) when the incoming electron beam crosses the path of the evaporating Si atoms. As a result, a few per cent of the Si atoms may be singly ionized. These ions are at ground potential but they may be accelerated into the growing epitaxial layer by application of a modest negative voltage to the substrate. If the epitaxial layer is covered by a segregated layer of a co-evaporated dopant, such as Sb, some fraction of these dopant atoms may be knocked into the substrate by the energetic Si ions. This knock-on can radically

## 2.1 c-Si MBE: sources, doping, growth rates, uniformity

increase the otherwise low incorporation of the segregated dopant as has been demonstrated both experimentally [65–68] and theoretically [58,67–69]. Further, this is accomplished with essentially no increase in system complexity using only conventional e-gun and Knudsen sources. The shortcomings are in control and damage. The process is dependent on the complex and the ill-controlled processes of surface segregation and accidental ionization. Further, unlike conventional co-implantation, which employs only low dopant ion currents, massive Si ion fluxes may be necessary to achieve the final, also accidental, knock-on of a fraction of the surface dopant.

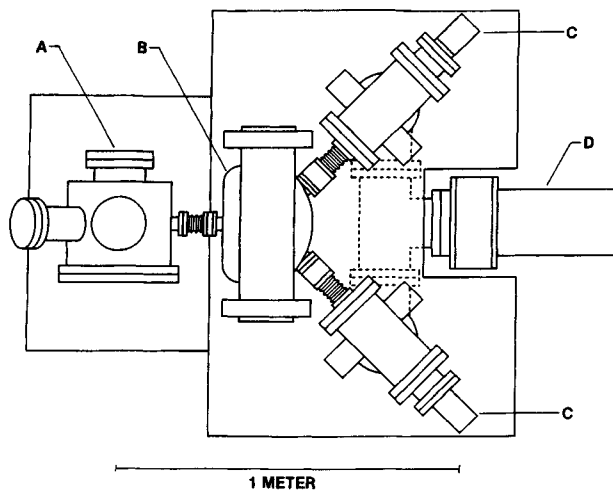


**FIGURE 9** Dual low energy co-ion implantation system. Two low energy, hot cathode, ion sources (C) produce steady  $\text{BF}_2^+$  and  $\text{As}_2^+$  beams from  $\text{BF}_3$  and  $\text{AsF}_5$  source gases. Magnet (B) selects the beam which is then variably attenuated and X-Y swept in a downstream chamber (A) to control doping level. Modulated beam is then directed into the MBE growth chamber. Both sources are pumped by a shared cryopump (D). All components, except for the magnet and modulators, are off-the-shelf ([57]).

## F CONCLUSION

Molecular beam epitaxy produces low temperature (500–800°C) growth of device quality Si on single wafers. Layer thickness and dopant placement can be controlled, easily, down to scales of 1–10 Å. The basic deposition process is conceptually simple but depends on the absence of contaminants produced only by ultrahigh vacuum environments. Dopant incorporation is more complex but can be achieved by careful selection of co-evaporated dopants or by use of co-ion implantation.

## REFERENCES

- [1] H. Mella, M.H. Brodsky [ *Thin Solid Films (Switzerland)* vol.46 (1977) p.299 ]
- [2] J.C. Bean [ in *Impurity Doping Processes in Silicon* Ed. F.F.Y. Wang (North Holland, 1981) ch.4 ]
- [3] E.H.C. Parker (Ed.) [ *The Technology and Physics of Molecular Beam Epitaxy* (Plenum Press, 1985) ]
- [4] J.C. Bean [ in *Germanium Silicon: Physics and Materials* Eds. J.C. Bean, R. Hull *Semicond. Semimet.* (Academic Press, 1998) ch.1 ]
- [5] A. Roth [ in *Vacuum Technology* (North Holland, 1979) p.36 ]
- [6] R.E. Honig [ *RCA Rev. (USA)* vol.23 (1962) p.567 ]
- [7] A. Roth [ in *Vacuum Technology* (North Holland, 1979) p.35 ]

## 2.1 c-Si MBE: sources, doping, growth rates, uniformity

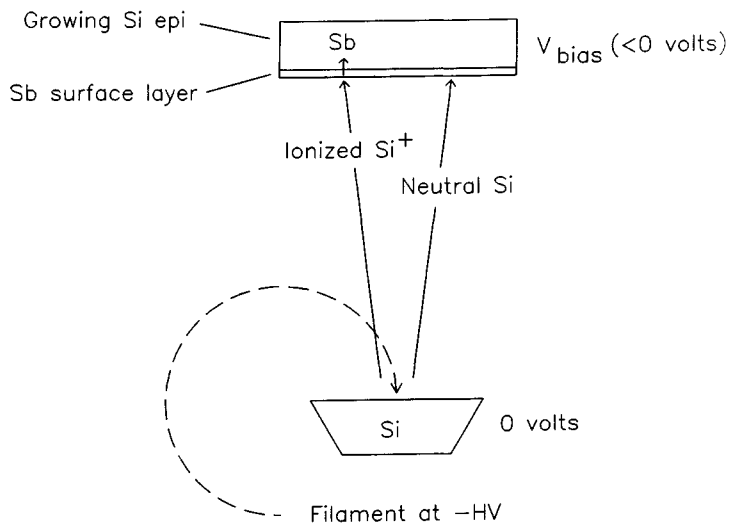


FIGURE 10 Schematic of the knock-on implantation process. From an e-gun evaporation source, a fraction of the evaporating Si atoms are ionized as they cross the path of the incoming electron beam.

The Si substrate is then biased negatively to attract these positive ions. Epitaxial growth is intentionally conducted using a co-evaporated dopant under conditions producing extensive surface segregation. Dopant atoms in the segregated surface layers can then be knocked into the epitaxial layer by the Si ions to a depth where they can no longer segregate, thereby enhancing otherwise low incorporation.

- [8] Model V-90S, VG Semicon Ltd., East Grinstead, Sussex, UK
- [9] S. Matteson, R.A. Bowling [ *J. Vac. Sci. Technol. A (USA)* vol.6 (1988) p.2504 ]
- [10] In early use of a V-90S MBE system, the author grew epitaxial layers with undetectable dislocation etch pits. From the area examined, this detection limit was estimated at 10–100 cm<sup>-2</sup>.
- [11] H. Tatsumi, H. Hirayama, A. Aizaki [ *Appl. Phys. Lett. (USA)* vol.54 (1988) p.629 ]
- [12] E-gun contamination issues are elaborated in [4].
- [13] J.C. Bean, E.A. Sadowski [ *J. Vac. Sci. Technol. (USA)* vol.20 (1982) p.137 ]
- [14] ‘Sentinel’ model sensors, Inficon-Leybold Inc., E. Syracuse, NY, USA
- [15] H. Kibbel, E. Kasper, P. Narozny, H.-U. Schreiber [ *Thin Solid Films (Switzerland)* vol.184 (1990) p.163 ]
- [16] R.A.A. Kubiak, W.Y. Leong, E.H.C. Parker [ *Appl. Phys. Lett. (USA)* vol.44 (1984) p.878 ]
- [17] S. Andrieu, J.A. Chrovoczek, Y. Campidelli, E. Andre, F.F. d’Avitaya [ *J. Vac. Sci. Technol. B (USA)* vol.6 (1988) p.835 ]
- [18] M.W. Denhoff [ *J. Vac. Sci. Technol. B (USA)* vol.8 (1990) p.1035 ]
- [19] F.W. Smith, G. Ghidini [ *J. Electrochem. Soc. (USA)* vol.129 (1982) p.1300 ]
- [20] G. Ghidini, F.W. Smith [ *J. Electrochem. Soc. (USA)* vol.131 (1984) p.2924 ]
- [21] J.C. Bean [ *Proc. 1981 Int. Electron Device Meeting* (IEEE Press, 1981) p.6 ]
- [22] H. Jorke, H.-J. Herzog, H. Kibbel [ *Phys. Rev. B (USA)* vol.40 (1989) p.2005 ]
- [23] H. Jorke, H. Kibbel, F. Schaffler, H.-J. Herzog, [ *Thin Solid Films (Switzerland)* vol.183 (1989) p.307 ]
- [24] D.J. Eaglesham, H.-J. Gossman, M. Cerullo [ *Phys. Rev. Lett. (USA)* vol.65 (1990) p.1227 ]
- [25] J.C. Bean, L.C. Feldman, A.T. Fiory, S. Nakahara, I.K. Robinson [ *J. Vac. Sci. Technol. A (USA)* vol.2 (1984) p.436 ]

## 2.1 c-Si MBE: sources, doping, growth rates, uniformity

- [26] S. Andrieu [ *J. Vac. Sci. Technol. B (USA)* vol.6 (1988) p.835 ]
- [27] M.W. Denhoff [ *J. Vac. Sci. Technol. B (USA)* vol.8 (1990) p.1035 ]
- [28] H. Jorke, H. Kibbel [ *Appl. Phys. Lett. (USA)* vol.57 (1990) p.1763 ]
- [29] C.P. Parry et al [ *Appl. Phys. Lett. (USA)* vol.58 (1991) p.481 ]
- [30] M.R. Sardela, W.-X. Ni, J.O. Ekberg, J.-E. Sundgren, G.V. Hansson [ *Mater. Res. Soc. Symp. Proc. (USA)* vol.220 (1991) p.109 ]
- [31] C.P. Parry, R.A.A. Kubiak, S.M. Newstead, E.H.C. Parker, T.E. Whall [ *Mater. Res. Soc. Symp. Proc. (USA)* vol.220 (1991) p.103 ]
- [32] G.E. Becker, J.C. Bean [ *J. Appl. Phys. (USA)* vol.48 (1974) p.3395 ]
- [33] A.Y. Cho [ *J. Appl. Phys. (USA)* vol.46 (1975) p.1733 ]
- [34] J.C. Bean [ *Appl. Phys. Lett. (USA)* vol.33 (1978) p.654 ]
- [35] S.S. Iyer, R.A. Metzger, F.G. Allen [ *Appl. Phys. Lett. (USA)* vol.52 (1981) p.5608 ]
- [36] U. Konig, H. Kibbel, E. Kasper [ *J. Vac. Sci. Technol. (USA)* vol.16 (1979) p.985 ]
- [37] J. Knall, J.-E. Sundgren, J.E. Greene, A. Rockett, S.A. Barnett [ *Appl. Phys. Lett. (USA)* vol.45 (1984) p.689 ]
- [38] R.A.A. Kubiak, G. Patel, W.Y. Leong, R. Houghton, E.H.C. Parker [ *Appl. Phys. A (Germany)* vol.41 (1986) p.233 ]
- [39] K. Nakagawa, M. Miyao, Y. Shiraki [ *Jpn. J. Appl. Phys. (Japan)* vol.11 (1988) p.L2013 ]
- [40] R.A.A. Kubiak, C.P. Parry [ *Mater. Res. Soc. Symp. Proc. (USA)* vol.220 (1991) p.63 ]
- [41] S. Fukatsu, S. Kubo, Y. Shiraki, R. Ito [ *Appl. Phys. Lett. (USA)* vol.58 (1991) p.1152 ]
- [42] S. Andrieu, F. Arnaud d'Avitaya, J.C. Pfister [ *J. Appl. Phys. (USA)* vol.65 (1989) p.2681 ]
- [43] J.-E. Sundgren, J. Knall, W.-X. Ni, M.-A. Hasan, L.C. Markert, J.E. Greene [ *Thin Solid Films (Switzerland)* vol.183 (1989) p.281 ]
- [44] G. Pindoria, R.A.A. Kubiak, S.M. Newstead, D.P. Woodruff [ *Surf. Sci. (Netherlands)* vol.234 (1990) p.17 ]
- [45] W.-X. Ni, G.V. Hansson, J.-E. Sundgren, L.C. Markert, J.E. Greene [ *Mater. Res. Soc. Symp. Proc. (USA)* vol.220 (1991) p.91 ]
- [46] W.F.J. Slijkerman, P.M. Zagwijn, J.F. van der Veen, A.A. van Gorkum, G.F.A. van de Walle [ *Appl. Phys. Lett. (USA)* vol.55 (1989) p.963 ]
- [47] H.-J. Gossmann, E.F. Schubert, D.J. Eaglesham, M. Cerullo [ *Appl. Phys. Lett. (USA)* vol.57 (1990) p.2440 ]
- [48] D.A. Grutzmacher, K. Ebert, A.R. Powell, B.A. Ek, T.O. Sedgewick, S.S. Iyer [ *Thin Solid Films (Switzerland)* vol.163 (1993) p.225 ]
- [49] R.M. Ostrom, F.G. Allen [ *Appl. Phys. Lett. (USA)* vol.48 (1986) p.221 ]
- [50] T.E. Jackman et al [ *Appl. Phys. Lett. (USA)* vol.53 (1988) p.877 ]
- [51] T.L. Lin, R.W. Fathauer, P.J. Grunthaner [ *Appl. Phys. Lett. (USA)* vol.55 (1989) p.795 ]
- [52] T. Tatsumi [ *Thin Solid Films (Switzerland)* vol.184 (1990) p.1 ]
- [53] T.L. Lin, R.W. Fathauer, P.J. Grunthaner [ *Thin Solid Films (Switzerland)* vol.184 (1990) p.31 ]
- [54] R.A.A. Kubiak, G. Patel, W.Y. Leong, R. Houghton, E.H.C. Parker [ *Appl. Phys. A (Germany)* vol.41 (1986) p.233 ]
- [55] Y. Ota [ *J. Appl. Phys. (USA)* vol.51 (1980) p.1102 ]
- [56] J.C. Bean, R. Dingle [ *Appl. Phys. Lett. (USA)* vol.35 (1979) p.925 ]
- [57] J.C. Bean, M. Cerullo, R. Leibenguth [ in *Silicon Molecular Beam Epitaxy II* Eds. J.C. Bean, L.J. Schowalter (Electrochemical Society, Pennington, NJ, 1988) p.574 ]
- [58] J.-E. Sundgren, J. Knall, W.-X. Ni, M.-A. Hasan, L.C. Markert, J.E. Greene [ *Thin Solid Films (Switzerland)* vol.183 (1989) p.281 ]
- [59] W.-X. Ni et al [ *Phys. Rev. B (USA)* vol.40 (1989) p.10449 ]
- [60] R. People, J.C. Bean, D.V. Lang [ *J. Vac. Sci. Technol. A (USA)* vol.3 (1985) p.846 ]
- [61] G.S. Higashi, J.C. Bean, R. Yadavish, H. Temkin [ *Appl. Phys. Lett. (USA)* vol.56 (1990) p.2560 ]

## 2.1 c-Si MBE: sources, doping, growth rates, uniformity

- [62] H. Temkin, J.C. Bean, T.P. Pearsall, N.A. Olsson, D.V. Lang [ *Appl. Phys. Lett. (USA)* vol.49 (1986) p.155 ]
- [63] J.-P. Noel, J.E. Greene, N.L. Rowell, D.C. Houghton [ *Appl. Phys. Lett. (USA)* vol.56 (1990) p.265 ]
- [64] N.L. Rowell, D.C. Houghton, J.-P. Noel, J.E. Greene [ *Thin Solid Films (Switzerland)* vol.184 (1990) p.69 ]
- [65] H. Jorke, H.-J. Herzog, H. Kibbel [ *Appl. Phys. Lett. (USA)* vol.47 (1985) p.511 ]
- [66] R.A.A. Kubiak, W.Y. Leong, E.H.C. Parker [ *Appl. Phys. Lett. (USA)* vol.46 (1985) p.565 ]
- [67] H. Jorke, H. Kibbel [ *J. Electrochem. Soc. (USA)* vol.133 (1986) p.774 ]
- [68] F. Schaffler, H. Jorke [ *Thin Solid Films (Switzerland)* vol.184 (1990) p.75 ]
- [69] B. Fritzsch, B. Wolf, A. Zehe [ *Solid State Commun. (USA)* vol.72 (1989) p.13 ]

## **2.2 Gas-source MBE of c-Si and related materials**

D.W. Greve

March 1999

### **A INTRODUCTION**

Gas-source molecular beam epitaxy (GSMBE) combines some of the important advantages of chemical vapour deposition and molecular beam epitaxy for the growth of silicon and related materials. In this Datareview the characteristics of the GSMBE technique are summarized, with specific emphasis on the role of surface hydrogen in determining the epitaxial layer growth rate and atomic segregation during growth.

### **B MOTIVATION FOR GSMBE**

Early work on gas-source molecular beam epitaxy (GSMBE) was motivated by some of the perceived limitations of conventional solid-source silicon MBE. Certain defects ('spitting' defects) were attributed to the use of electron-beam sources [1]. In addition, GSMBE may potentially lead to reduced metallic contamination through the elimination of source contamination by falling particles. A further advantage mentioned in early work is the elimination of regular venting for source loading. GSMBE also is capable of selective growth (that is, nucleation does not readily occur on  $\text{SiO}_2$  layers). Finally, when gas sources are used there is some hydrogen on surfaces during growth; this has beneficial effects, including improvement in the transition abruptness.

It is also appropriate to contrast GSMBE with other low-pressure gas phase epitaxial growth techniques such as UHV/CVD. These other techniques operate at reactant partial pressures which are only slightly higher (perhaps an order of magnitude higher) than those used for GSMBE. One major difference is that analysis tools (such as RHEED and other surface science tools) are readily used in GSMBE since the system geometry permits easy access to the wafer surface and since the total pressure is low. Another important difference with multiwafer UHV/CVD is the absence of heated surfaces near the wafer which can adsorb/desorb species such as phosphorus, leading to dopant persistence effects.

### **C GSMBE SYSTEMS**

Typically GSMBE systems have much in common with conventional MBE. However, the use of capture pumping (either cryoshrouds or cryopumps) is less desirable due to the potential for the release of large quantities of pyrophoric gas; often high-capacity turbopumps are used during growth. Controlled quantities of gas are introduced using either low-range mass flow controllers, UHV leak valves, or subchambers with part of the gas flow directed to the growth chamber. In contrast to III-V GSMBE, cracking injectors are not used. Unreacted gas is directed toward the substrate by the injector (which can be as simple as a stainless steel tube). Due to the directionality of the incident gas stream, the flux striking the surface is enhanced above that calculated from the chamber pressure.

Total chamber pressures during growth are typically in the range  $10^{-4}$ – $10^{-5}$  torr; at these pressures collisions between gas molecules are unlikely and consequently no gas phase reactions occur. Disilane ( $\text{Si}_2\text{H}_6$ ) is more commonly used as a source gas since it has a higher sticking coefficient than silane ( $\text{SiH}_4$ ), leading to reduced gas load on the pumping system for a given growth rate.  $\text{Ge}_x\text{Si}_{1-x}$

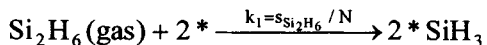
## 2.2 Gas-source MBE of c-Si and related materials

alloys are usually grown using either  $\text{GeH}_4$  or  $\text{Ge}_2\text{H}_6$  reactants, although one group has used a solid Ge source [2]. The most common dopant sources are diborane ( $\text{B}_2\text{H}_6$ ) and phosphine ( $\text{PH}_3$ ) or arsine ( $\text{AsH}_3$ ).

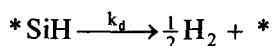
### D GROWTH RATES AND KINETICS

The growth of silicon and related materials from hydride reactants is limited by the desorption of hydrogen. As a result, useful growth temperatures in either CVD or GSMBE are limited to temperatures well above the minimum epitaxial growth temperature observed in solid-source MBE [3]. We focus here on the specific behaviour of disilane and digermane as source gases. UHV/CVD growth from silane and germane has been discussed in detail in another Datareview [4]; GSMBE growth from these species is similar since no gas-phase reactions occur in either growth technique.

Since gas-phase reactions are absent in GSMBE, the growth kinetics are determined by the reactions occurring on the wafer surface. Decomposition of disilane on Si(001) has been studied by Gates and Chang [5], who note that various initial reactions could occur in parallel. However, the two-site initial reaction



has been often used in modelling the growth rate from disilane [6–8] and careful measurements show that it accurately accounts for the growth rate. In this reaction  $k_1 (\text{cm}^2)$  is the reaction rate constant,  $*$  represents an empty surface site and  $*X$  represents the species X on a surface site. The rate constant  $k_1 = s_{\text{Si}_2\text{H}_6} / N$ , where  $s_{\text{Si}_2\text{H}_6}$  is the clean-surface sticking coefficient and N is the density of surface sites. The trihydride species rapidly decompose to the monohydride by multiple reaction pathways [9]. The desorption of hydrogen from the surface (and the consequent creation of new surface reaction sites) is limited by desorption from the monohydride



This reaction is often written as a single-site reaction as it is generally considered to be first-order in the hydrogen surface coverage on (100) silicon. The desorption rate constant is given by

$$k_d = k_{d0} e^{-E_d / kT}$$

A range of values have been reported for the prefactor  $k_{d0} (\text{s}^{-1})$  and the activation energy  $E_d$  [10], with  $E_d$  generally in the range 47–58 kcal/mol.

Depending upon the growth conditions, either the silane reactive adsorption or the hydrogen desorption step limits the growth rate. FIGURE 1 illustrates the measured growth rates from disilane on (001) substrates as a function of temperature [6]. At high temperatures the growth rate is nearly constant and is limited by the supply of reactant, while at low temperatures the growth rate is limited by the thermally activated desorption of hydrogen. It is in this low-temperature regime where there is appreciable surface coverage with hydrogen. The observed activation energy for growth of silicon at low temperatures is in reasonable agreement with that observed in hydrogen desorption studies.

Much of the interest in GSMBE concerns the growth of  $\text{Ge}_x\text{Si}_{1-x}$  heterostructures. When digermane is introduced in order to grow  $\text{Ge}_x\text{Si}_{1-x}$  alloys, there are a number of qualitative changes in the growth process:

## 2.2 Gas-source MBE of *c*-Si and related materials

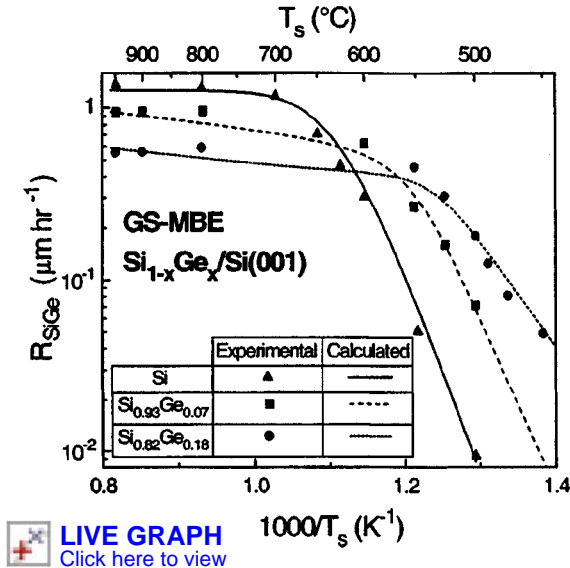


FIGURE 1 Growth rates from disilane and digermante on (001) substrates. (From [6].)

- The activation energy for hydrogen desorption decreases due to the lower strength of the Ge–H bond [6,11]. Consequently the hydrogen surface coverage decreases with increasing germanium fraction. At the same time, the desorption process becomes second order in hydrogen coverage [6].
- Germanium tends to segregate to the surface, leading to a higher germanium surface concentration than that in the bulk of the film. The degree of surface segregation decreases with increasing hydrogen coverage. The surface germanium concentration also depends on the growth temperature. At low temperatures surface segregation is limited by the kinetics of site interchange, while at high temperatures thermal equilibrium determines the relative occupancy of surface and subsurface sites.
- The clean-surface sticking coefficients of both disilane and digermante decrease with increasing germanium surface concentration, although their ratio remains approximately constant. The sticking coefficients of digermante and disilane on various (001) surfaces are presented in TABLE 1.

TABLE 1 Sticking coefficients of disilane and digermante on (001) Si and (001) Ge surfaces.  
(From [6]).

	Si	Ge
$\text{Si}_2\text{H}_6$	0.036	0.0068
$\text{Ge}_2\text{H}_6$	0.28	0.52

The consequences of these phenomena can be seen in FIGURE 1, where the disilane flux has been kept constant while increasing the digermante flux. In the high-temperature regime the growth rate decreases with increasing germanium fraction, since in this regime the sticking coefficients determine the growth rate. In contrast, the growth rates are increased at low temperatures due to the greater hydrogen desorption rates.

## E DOPING IN GSMBE

In principle, doping in GSMBE can be performed using the same solid sources used in conventional MBE. Indeed, in early work boron doping was reported using an  $\text{HBO}_2$  source [12]. However, there are significant advantages to an all-gas source system. As a result, the most commonly used doping sources in GSMBE are diborane ( $\text{B}_2\text{H}_6$ ) for p-type doping and phosphine ( $\text{PH}_3$ ) or arsine ( $\text{AsH}_3$ ) for n-type doping. In the following the characteristics of these two sources and the upper limits on attainable doping concentration will be discussed.

Diborane doping in GSMBE is straightforward because the boron concentration in the film is proportional to the diborane flow rate over a wide range of doping concentrations. This linearity has been demonstrated for growth of boron-doped (001) silicon over the range from  $10^{15}$  to  $10^{19} \text{ cm}^{-3}$  [13]. Careful studies over a wide range of growth temperatures show that the diborane reactive sticking coefficient has a small temperature dependence, ranging from  $6.4 \times 10^{-4}$  at  $600^\circ\text{C}$  to  $1.4 \times 10^{-3}$  at  $950^\circ\text{C}$  [14]. At high boron concentrations additional diffraction spots are observed in RHEED together with evidence of surface roughening at high growth temperatures [15]. The boron concentration corresponding to the onset of these changes is above  $5 \times 10^{19} \text{ cm}^{-3}$  at  $600^\circ\text{C}$ . Boron also influences the surface reactions, with a decrease in growth rate observed at high temperatures (indicating a reduction in reactive sticking coefficients) and an increase at low temperatures (consistent with an increased hydrogen desorption rate). Like germanium, boron has a tendency to segregate to the surface, although this does not prevent the growth of relatively abrupt profiles. Transition abruptness is discussed in more detail in the following section.

Doping is more difficult for n-type material. In early work, phosphine ( $\text{PH}_3$ ) was used for n-type doping [16]. Surface science studies have shown that the phosphine sticking coefficient is nearly unity and that phosphorus on the surface blocks surface sites [17,18]. In addition, phosphorus exhibits strong surface segregation. Consequently the introduction of phosphine leads to a decrease of growth rate along with poor incorporation of phosphorus. For growth at  $680^\circ\text{C}$ , the growth rate was observed to decrease by a factor of two for a phosphorus concentration of about  $2 \times 10^{18} \text{ cm}^{-3}$  [16]. Nevertheless, the phosphorus concentration was found to be proportional to the phosphine flux and it was possible to achieve doping as high as  $2 \times 10^{20} \text{ cm}^{-3}$ . In more recent work, arsine ( $\text{AsH}_3$ ) was used [19]. Active arsenic concentrations of  $6 \times 10^{18} \text{ cm}^{-3}$  were obtained in silicon and  $1.5 \times 10^{19} \text{ cm}^{-3}$  in 10% germanium-silicon. As in the case of phosphorus, there was strong segregation of arsenic to the surface during growth.

## F TRANSITION ABRUPTNESS

GSMBE is important because of its potential for the growth of structures with highly abrupt transitions in doping or layer composition. The achievement of abrupt layers is facilitated by the presence of some hydrogen on the surface during growth. There are two known mechanisms for this improvement in transition abruptness.

Hydrogen is known to reduce the tendency toward islanded (or Stranski-Krastanov) growth of strained epitaxial layers. Clear evidence for the role of hydrogen is found in work by Sakai and Tatsumi [20], where atomic hydrogen was supplied separately to the surface during solid-source MBE growth of germanium on (001) silicon. In this work uniform germanium layers were grown with hydrogen on the surface while undulated layers were formed at the same substrate temperature when no hydrogen was present. The formation of non-uniform or islanded layers is due to the reduction of total strain energy when islands are formed. The formation of islands is limited by the rate of surface diffusion of adatoms. It has been suggested [20] that hydrogen reduces the surface diffusivity of adatoms, thus reducing the rate at which islands form.

## 2.2 Gas-source MBE of c-Si and related materials

Hydrogen also improves the abruptness of transitions in germanium concentration. As noted earlier, both germanium and boron tend to segregate to the surface during growth. The segregation of germanium can be seen quite vividly in RHEED oscillations [21,22]. When silicon is grown on a germanium-silicon layer, the RHEED oscillations are initially more rapid due to segregation of germanium to the growth surface, where it increases the hydrogen desorption rate.

For high growth temperatures or low growth rates, interchange of atoms between surface and subsurface sites is relatively rapid. When this is the case, thermal equilibrium is established and the surface concentration  $\theta_i$  and the bulk concentration  $x_i$  are related by

$$\frac{\theta_i}{x_i} = \frac{1 - \theta_i}{1 - x_i} e^{-\Delta H_s / kT}$$

where  $\Delta H_s$  is the segregation enthalpy of species  $i$  [23]. The segregation enthalpy is negative for boron and germanium indicating that these species tend to segregate to the surface ( $\theta_i > x_i$ ). Studies of germanium segregation during GSMBE growth [6] have shown that  $\Delta H_s$  is reduced in magnitude from  $-0.28$  eV to  $-0.10$  eV when hydrogen is present on the surface. The beneficial effect of hydrogen has been directly demonstrated by Ohta et al [24] who showed substantially reduced germanium segregation when atomic hydrogen was supplied to the surface. In a related study [25], the abruptness of heterostructures grown by solid-source MBE, UHV/CVD, and APCVD were compared using secondary ion mass spectrometry (SIMS). Structures grown by solid-source MBE showed evidence of appreciable germanium segregation even for growth at  $450^\circ\text{C}$ . Segregation was reduced for UHV/CVD growth (which has hydrogen coverage roughly comparable to GSMBE) and was entirely absent for APCVD, which had the highest hydrogen coverage.

## G SELECTIVE GROWTH

Since GSMBE requires active sites for reaction with incoming molecules, nucleation on silicon dioxide layers is difficult and as a result a limited degree of selective growth is possible. This delayed nucleation on silicon dioxide was apparent in early studies of molecular beam deposition from silane [26]. Subsequently, selective growth from disilane [27] was reported and selectivity was also found in the growth of  $\text{Ge}_x\text{Si}_{1-x}$  layers [28]. Selective growth of  $\text{Ge}_x\text{Si}_{1-x}$  was subsequently applied to the fabrication of heterojunction bipolar transistors [29].

Unlike the situation for gas-phase selective epitaxy with chlorine-containing reactants, there are limitations on the thickness of material which can be grown selectively in GSMBE. Selective growth is best characterized by an incubation time which is dependent on disilane flux and substrate temperature. The observed incubation time is typically of the order of tens of minutes at  $600^\circ\text{C}$  and decreases with increasing disilane flux [30]. This is sufficient for the selective growth of layers 1000 Å in thickness, which have been applied in devices.

## H LAYER QUALITY AND DEVICES

Early GSMBE studies show that the material grown in this way is highly suitable for devices. Heterojunction diodes fabricated by GSMBE showed good ideality factors ( $n=1.12-1.22$  for layers with  $x=0.11-0.33$ ) [31]. GSMBE was also used in an early study of  $\text{Ge}_x\text{Si}_{1-x}/\text{Si}$  heterojunction bipolar transistors [32].

## 2.2 Gas-source MBE of *c*-Si and related materials

Important measures of the suitability of an epitaxial layer for devices include residual carrier concentration, carrier mobility, and the presence of recombination centres. In the following, some reported measurements of these various quantities in GSMBE material will be summarized.

Yoshinobu et al [33] reported that undoped layers were n-type with carrier concentrations in the  $10^{14}$  cm $^{-3}$  range. The electron mobility was 1500 cm $^2$ /V s at room temperature. Controllable doping over the range from  $10^{15}$  to  $10^{19}$  cm $^{-3}$  was also noted in an early report [13]. More recently, hole mobilities were measured and found to be equal to those in bulk material [34].

Photoluminescence studies provide an indication of the presence of defects as band-edge photoluminescence will not be observed if there are other parallel recombination paths. In a comparison of multiple quantum well structures grown by three different techniques, it was found that band-edge luminescence was observed in material grown by UHV/CVD and GSMBE but that broad emission bands were observed in unannealed material grown by solid-source MBE [35]. Photoluminescence also provides evidence that the transition abruptness is improved in GSMBE-grown quantum wells [36]. FIGURE 2 shows the photoluminescence peak position as a function of well width in MBE and GSMBE-grown quantum wells. The GSMBE-grown structures agree well with calculations based on a square-well potential, while the MBE-grown layers show a shift consistent with a graded top interface.

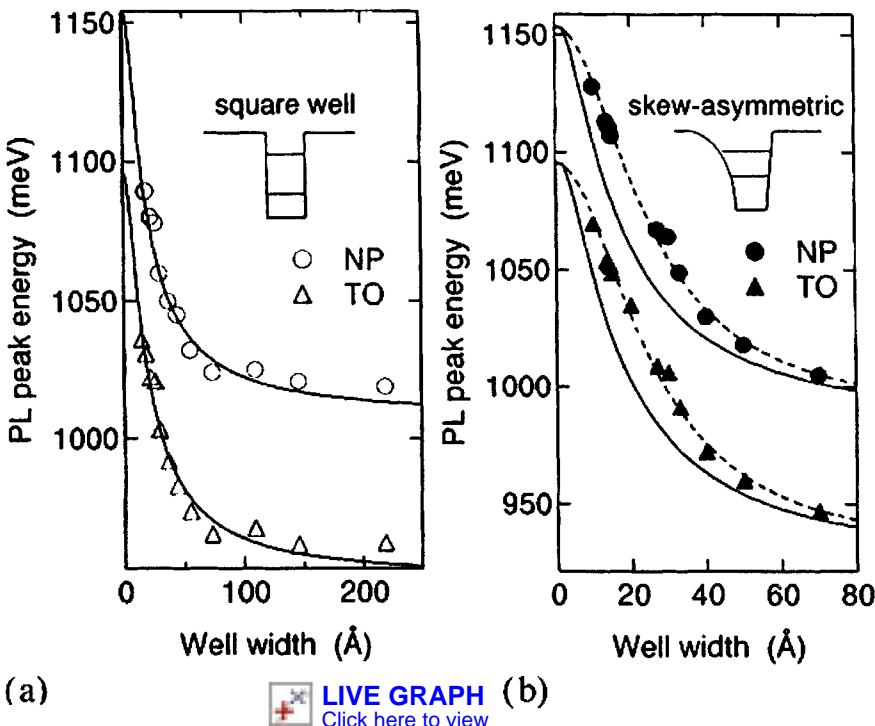


FIGURE 2 Photoluminescence peak position as a function of well width in (a) GSMBE-grown and (b) MBE-grown quantum wells. (From [36].)

More recently, some additional device structures have been fabricated by GSMBE. Single-quantum-well pin junction diodes have been reported which exhibit narrow (5.5 meV) electroluminescence lines [37]. Two-dimensional electron gas measurements have also been reported using GSMBE material [38]. In this work, a 100 Å silicon channel was formed on a Ge<sub>0.30</sub>Si<sub>0.70</sub> relaxed buffer. Electron mobilities of 1000 cm $^2$ /V s and 53 000 cm $^2$ /V s were measured at room temperature and 0.4 K, respectively.

## I CONCLUSION

Gas source molecular beam epitaxy combines the compatibility with in situ analysis characteristic of molecular beam epitaxy and the beneficial effects of surface hydrogen found in chemical vapour deposition. The hydrogen surface coverage depends upon the growth conditions, tending to decrease with increasing growth temperature and increasing germanium fraction. Hydrogen present on the surface has beneficial effects on segregation and surface morphology.

## REFERENCES

- [1] J.C. Bean [ *J. Electron. Mater. (USA)* vol.19 (1990) p.1055 ]
- [2] F.C. Zhang, J. Singh, P.K. Bhattacharya [ *Appl. Phys. Lett. (USA)* vol.67 (1995) p.85 ]
- [3] D.J. Eaglesham, H.-J. Gossman, M. Cerullo [ *Phys. Rev. Lett. (USA)* vol.65 (1990) p.1227-30 ]
- [4] D.W. Greve [ Datareview in this book: 2.3 UHV/CVD and related growth techniques for c-Si and other materials ]
- [5] S.M. Gates, C.M. Chang [ *Chem. Phys. Lett. (USA)* vol.184 (1991) p.448 ]
- [6] H. Kim, N. Taylor, T.R. Bramblett, J.E. Greene [ *J. Appl. Phys. (USA)* vol.84 (1998) p.6372 ]
- [7] X.F. Hu et al [ *Appl. Phys. Lett. (USA)* vol.71 (1997) p.376-8 ]
- [8] K. Werner, S. Butzke, S. Radelaar, P. Balk [ *J. Cryst. Growth (Netherlands)* vol.13 (1993) p.338 ]
- [9] S.M. Gates, C.M. Greenlief, D.B. Beach [ *J. Chem. Phys. (USA)* vol.93 (1990) p.7493-503 and references therein ]
- [10] D.J. Doren [ in *Advances in Chem. Phys.*, Vol. XCV, Eds. I. Prigogine, S.A. Rice (J. Wiley and Sons, 1996) ]
- [11] B.M.H. Ning, J.E. Crowell [ *Surf. Sci. (Netherlands)* vol.295 (1993) p.79-98 ]
- [12] H. Hirayama, K. Koyama, M. Hiroi, T. Tatsumi [ *Appl. Phys. Lett. (USA)* vol.57 (1990) p.780 ]
- [13] H. Hirayama, M. Hiroi, K. Koyama [ *Appl. Phys. Lett. (USA)* vol.58 (1991) p.1991 ]
- [14] Q. Lu, T.R. Bramblett, N.-E. Lee, M.-A. Hasan, T. Karasawa, J.E. Greene [ *J. Appl. Phys. (USA)* vol.77 (1995) p.3067 ]
- [15] H. Kim et al [ *J. Appl. Phys. (USA)* vol. 82 (1997) p.2288 ]
- [16] H. Hirayama, T. Tatsumi [ *Appl. Phys. Lett. (USA)* vol.55 (1989) p.131 ]
- [17] M.L. Yu, B.S. Meyerson [ *J. Vac. Sci. Technol. A (USA)* vol.2 (1984) p.446 ]
- [18] N. Maity, L.-Q. Xia, J.R. Engstrom [ *Appl. Phys. Lett. (USA)* vol.66 (1995) p.1909 ]
- [19] J.M. Fernandez, M.H. Xie, A. Matsumura, S.M. Mokler, J. Zhang, B.A. Joyce [ *Mater. Sci. Technol. (UK)* vol.11 (1995) p.396 ]
- [20] A. Sakai, T. Tatsumi [ *Appl. Phys. Lett. (USA)* vol.64 (1994) p.52 ]
- [21] N. Ohtani, S.M. Mokler, M.H. Xie, J. Zhang, B.A. Joyce [ *Appl. Phys. Lett. (USA)* vol.62 (1993) p.2042 ]
- [22] K. Werner et al [ in *Mechanisms of Heteroepitaxial Growth Symposium* (Materials Research Society, Pittsburgh, PA, 1992) p.261-6 ]
- [23] J.E. Greene, S.A. Barnett, A. Rockett [ *Appl. Surf. Sci. (Netherlands)* vol.22/23 (1985) p.520 ]
- [24] B. Ohta, S. Fukatsu, Y. Ebuchi, T. Hattori, N. Usami, Y. Shiraki [ *Appl. Phys. Lett. (USA)* vol.65 (1994) p.2975 ]
- [25] D.A. Grutzmacher et al [ *Appl. Phys. Lett. (USA)* vol.63 (1993) p.2531 ]
- [26] B.A. Joyce, R.R. Bradley, G.R. Booker [ *Philos. Mag. (UK)* vol.17 (1967) p.1167 ]
- [27] H. Hirayama, T. Tatsumi, N. Aizaki [ *Appl. Phys. Lett. (USA)* vol.52 (1988) p.2242 ]
- [28] H. Hirayama, M. Hiroi, K. Koyama, T. Tatsumi [ *Appl. Phys. Lett. (USA)* vol.56 (1990) p.1107 ]

- [29] H.Hirayama, M. Hiroi, K. Koyama, T. Tatsumi [ *Appl. Phys. Lett. (USA)* vol.56 (1990) p.2645 ]
- [30] K. Aketagawa, T. Tatsumi, J. Sakai [ *Appl. Phys. Lett. (USA)* vol.59 (1991) p.1735 ]
- [31] H. Hirayama, M. Hiroi, K. Koyama, T. Tatsumi [ *J. Cryst. Growth (Netherlands)* vol.105 (1990) p.46-51 ]
- [32] H. Hirayama, M. Hiroi, K. Koyama, T. Tatsumi [ *Appl. Phys. Lett. (USA)* vol.56 (1990) p.2645 ]
- [33] T. Yoshinobu, T. Fuyuki, H. Matsunami [ *Jpn. J. Appl. Phys 2, Lett. (Japan)* vol.31 (1992) p.L1213-15 ]
- [34] Q. Lu, T.R. Bramblett, N.-E. Lee, M.-A. Hasan, T. Karasawa, J.E. Greene [ *J. Appl. Phys. (USA)* vol.77 (1995) p.3067 ]
- [35] K. Terashima, M. Tajima, N. Ikarashi, T. Niino, M. Hiroi, T. Tatsumi [ *J. Electron. Mater. (USA)* vol.21 (1992) p.1081 ]
- [36] S. Fukatsu, H. Yoshida, A. Fujiwara, Y. Takhashi, Y. Shiraki, R. Ito [ *Thin Solid Films (Switzerland)* vol.222 (1992) p.1-4 ]
- [37] Y. Kato, S. Fukatsu, N. Usami, Y. Shiraki [ *J. Cryst. Growth (Netherlands)* vol.136 (1994) p.355-60 ]
- [38] J.M. Fernandez et al [ *J. Mater. Sci.: Mater. Electron. (UK)* vol.6 (1995) p.330-5 ]

## CHAPTER 3

### STRUCTURAL AND MECHANICAL PROPERTIES (Edited by A. George)

#### Crystalline structure and elastic properties

- 3.1 Diamond cubic Si: structure, lattice parameter and density
  - 3.2 Elastic constants and moduli of diamond cubic Si
  - 3.3 High pressure phases of c-Si
- #### Dislocations and mechanical properties
- 3.4 Core structures and energies of dislocations in Si
  - 3.5 Dislocation mobilities in c-Si
  - 3.6 Macroscopic mechanical behaviour of Si at high temperature
  - 3.7 Mechanical behaviour of Si at low temperature
  - 3.8 Fracture and brittle–ductile transition in Si

### **3.1 Diamond cubic Si: structure, lattice parameter and density**

Y. Okada

June 1998

#### **A INTRODUCTION**

The highly perfect crystalline structure of extremely pure silicon single crystals is the starting point for many metrological applications. The determination of Avogadro's number, or of the ratio of Planck constant and the neutron mass are typical experiments based on an exact knowledge of the lattice spacing of a reference crystal.

#### **B STRUCTURE OF SILICON**

At ordinary pressure, silicon crystallises in the diamond structure, with an fcc Bravais lattice and a two-atom basis. The chemical bond is purely covalent, each atom being tetrahedrally coordinated and its valence electrons occupying  $sp^3$  hybrid orbitals. Silicon transforms to several other phases at higher pressures as shown in Datareview 3.3.

#### **C THE LATTICE PARAMETER OF Si**

Of concern here are absolute methods for lattice parameter measurements of single crystals. The absolute methods allow us to measure the lattice parameters in the metric system or with respect to a fixed X-ray emission wavelength, taken as a secondary standard. Up to now only two such methods have reached an accuracy  $\Delta a/a$  in the order of  $10^{-7}$ : the Bond method [1] and simultaneous X-ray and optical interferometry (XROI) [2].

The accuracy of the Bond method is limited by that of the X-ray wavelength used. Top values are obtained with the best known  $CuK\alpha_1$  line, with  $\Delta\lambda/\lambda = 3 \times 10^{-7}$ . In XROI what is measured is the ratio of X-ray to optical periods and a greater accuracy ( $\Delta a/a = 3 \times 10^{-8}$ ) results, thanks to the highly stabilised optical wavelength delivered by the laser.

At such an accuracy, experimental values must be corrected for temperature, pressure and crystal defects including mainly unwanted impurities.

The first result using XROI was obtained by Deslattes and Henins [3] at the National Institute for Standards and Technology (NIST) but was later recognized to be wrong [4].

The values derived for ideally pure Si at 22.500°C under vacuum, from three sets of independent measurements by XROI, are given below :

$a = 543102.032 \pm 0.033$ fm	PTB (1990)
$a = 543102.044 \pm 0.017$ fm	IMGC (1994)
$a = 543101.99 \pm 0.09$ fm	NRLM (1995)

The first value was given in [5], based on measurements performed by Becker and co-workers [6,7] at the Physikalisch-Technische Bundesanstalt (PTB), Braunschweig (Germany); the second by Basile et al [8] at the Istituto di Metrologia 'G. Colonnetti' (IMGC), Torino (Italy); and the third by Fujimoto et al [9] at the National Research Laboratory of Metrology (NRLM), Tsukuba (Japan). They are

### 3.1 Diamond cubic Si: structure, lattice parameter and density

consistent within estimated errors and slightly higher than the value recommended by Cohen and Taylor [10], which was

$$a = 543101.96 \pm 0.11 \text{ fm} \quad \text{CODATA (1986)}$$

(This latter value was adjusted in order to minimise the inconsistency between two determinations of Avogadro's number.)

A new value from the NIST Group, closer to the PTB value but still given as 'preliminary', is cited in [11].

The potential and limitations of diffraction techniques based on the Bond method are demonstrated in FIGURE 1 where 15 values cited in the literature are displayed besides values obtained by XROI [1,12–20]. These data are given for 25.0°C under normal atmosphere pressure. Due to the larger uncertainties, diffraction data were not corrected for impurity content. Of special interest is the comparison of the lattice parameter as measured in one and the same almost perfect single crystal by six laboratories using three diffraction methods [20]. The achieved accuracy is about  $\Delta a/a = 3 \times 10^{-6}$ .

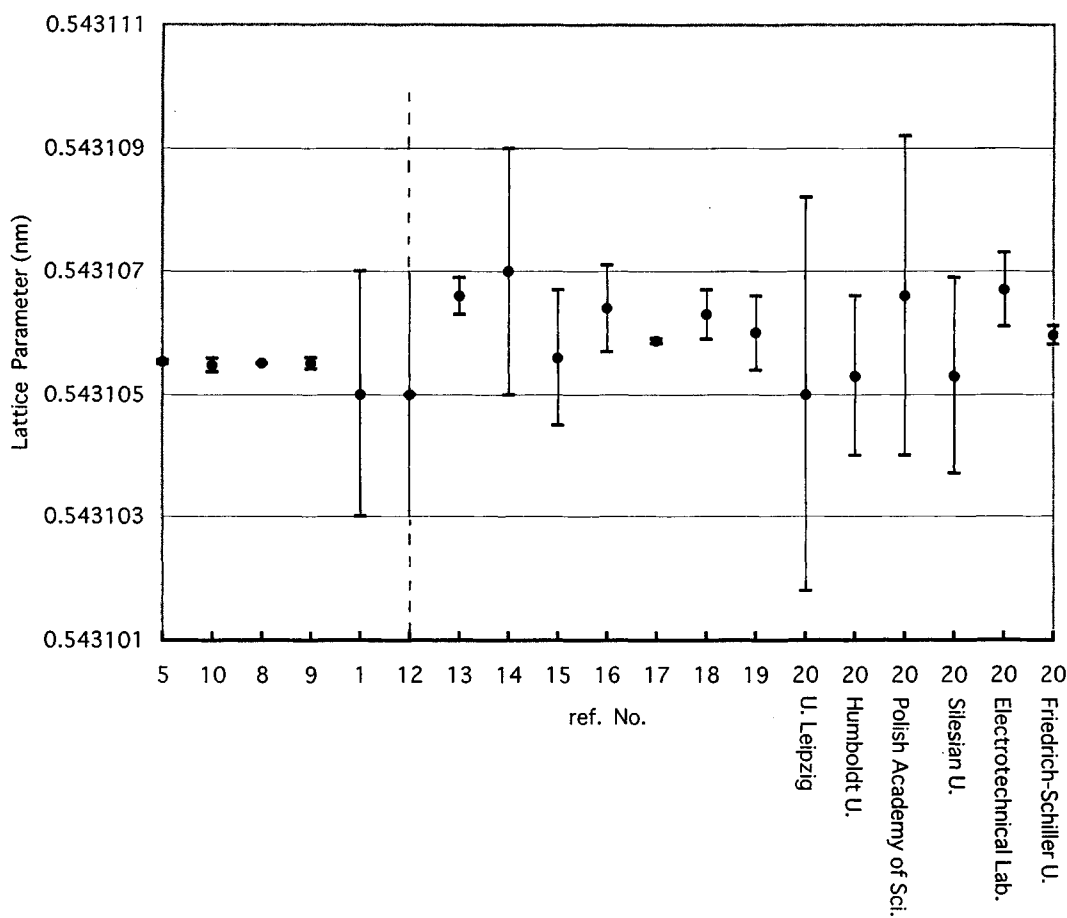


FIGURE 1 Lattice parameters of Si single crystals at 298.2 K. Except for XROI measurements, values were deduced using  $\alpha_{298.2} = 2.6 \times 10^{-6} \text{ K}^{-1}$  and  $\lambda (\text{CuK}\alpha_1) = 0.15405945 \text{ nm}$ .

### 3.1 Diamond cubic Si: structure, lattice parameter and density

#### D THE INFLUENCE OF TEMPERATURE

The temperature dependence of the lattice parameter of silicon was measured by Lyon et al [21] below 340 K and, between room temperature and 1500 K, by Okada and Tokumaru [19], who proposed the following phenomenological relation, valid between 120 K and 1500 K, for the linear thermal expansion coefficient,  $\alpha(T)$ :

$$\alpha(T) = (3.725 \{1 - \exp[-5.88 \times 10^{-3} (T-124)]\} + 5.548 \times 10^{-4} T) \times 10^{-6} \text{ K}^{-1} \quad (1)$$

where  $T$  is the absolute temperature expressed in Kelvin. The accuracy of this description is about  $2 \times 10^{-7} \text{ K}^{-1}$ .

At 25.0°C (298.2 K), the recommended value is

$$\alpha_{298.2} = (2.59 \pm 0.05) \times 10^{-6} \text{ K}^{-1}$$

$\alpha$  varies from about zero at 130 K to  $4.5 \times 10^{-6} \text{ K}^{-1}$  at 1400 K.

The lattice parameter at  $T$  K is given by

$$a(T) = a_0 \left[ \int_{295.7}^T \alpha(T) dT + 1 \right] \quad (2)$$

where  $a_0$  is the lattice parameter at 295.7 K.

The difference between the macroscopic linear thermal expansion and the lattice parameter thermal expansion allowed Okada to determine the concentration of the dominant point defects in a float-zone Si single crystal at high temperature [22]. It has been found that vacancies are predominant in concentration over self-interstitials. The fraction of point defects in thermal equilibrium at 1300 K is  $(6.8 \pm 2.3) \times 10^{-5}$ , corresponding to a concentration of vacancies of  $(3.4 \pm 1.2) \times 10^{18} \text{ cm}^{-3}$ .

#### E THE INFLUENCE OF PRESSURE

Changes in volume,  $\Delta V$ , due to hydrostatic compression (e.g. atmospheric pressure) of single crystal may be estimated in terms of elastic constants (Data review 3.2). The bulk modulus  $B$  is:

$$B = -\frac{P}{(\Delta V/V)} = \frac{1}{3} (C_{11} + 2C_{12}) \quad (3)$$

The lattice contraction of Si under hydrostatic pressure was measured by Yamamoto et al [23] up to 6.5 GPa.

#### F THE INFLUENCE OF IMPURITIES

According to Vegard's law, substitutional atoms having a smaller (larger) atomic radius than the parent lattice atom (Si) should result in a uniform contraction (expansion) of the crystal unit cell in proportion to their concentration. The modification of the lattice parameter  $\Delta a$  is expressed by

### 3.1 Diamond cubic Si: structure, lattice parameter and density

$$\frac{\Delta a}{a} = \beta N \quad (4)$$

where  $N$  is the concentration of the impurity in atoms per  $\text{cm}^3$ .

Coefficients  $\beta$  have been determined for oxygen and carbon, which are the most frequent unwanted impurities in Si, and also for usual dopant atoms. Such measurements may achieve a high accuracy of a few parts of  $10^{-8}$  for  $\Delta a/a$ , by comparison of the lattice spacings in crystals with different impurity concentrations. This can be accomplished with a double crystal X-ray diffractometer and does not necessitate XROI [5,11]. Care must be taken, however, because the spatial distribution of impurities is often inhomogeneous.

Recent and very accurate measurements by Windisch and Becker [5] confirmed that Vegard's law is valid for C and O (although not a substitutional atom).

Substitutional carbon decreases the lattice parameter in direct proportion to its concentration with

$$\beta_C = (-6.9 \pm 0.5) \times 10^{-24} \quad \text{cm}^3/\text{atom}$$

Oxygen increases the lattice spacing in direct proportion to the number of atoms per  $\text{cm}^3$  with

$$\beta_O = (4.4 \pm 0.2) \times 10^{-24} \quad \text{cm}^3/\text{atom}$$

(These coefficients were used to determine the lattice parameter of ideally pure Si given above, from XROI measurements in actual crystals.)

In contrast to oxygen and carbon, dopant impurities are usually added intentionally in silicon crystals and can be avoided, or reduced below a level at which their effect is not detectable when a standard crystal is grown for lattice parameter measurements. A fair approximation of the expansion or contraction due to a dopant, which may be important to estimate residual stresses in diffused wafers and devices, is given by Vegard's law with the coefficient  $\beta$  calculated from the tetrahedral covalent radii,  $r$ :

$$\beta = \left[ \frac{r_i - r_{\text{Si}}}{r_{\text{Si}}} \right] \frac{1}{N_{\text{Si}}} \quad (5)$$

where  $N_{\text{Si}}$  is the number of Si atoms per  $\text{cm}^3$ .

For boron, Okada has shown that the reduction due to substitutional B atoms in concentrations between  $2.5 \times 10^{17}$  and  $10^{20} \text{ cm}^{-3}$  follows Vegard's law using the covalent radii of Van Vechten and Philips [24] ( $r_{\text{Si}} = 0.1173 \text{ nm}$ ,  $r_B = 0.0853 \text{ nm}$ ) in CZ single crystals [25] with  $\beta_B = -5.46 \times 10^{-24} \text{ cm}^3/\text{atom}$ . This value is in fair agreement with those of Horn [26], Mc Quhae and Brown [27] and also Celotti et al [28], which range from  $-4.5$  to  $-5.6 \times 10^{-24} \text{ cm}^3/\text{atom}$ , but is definitely higher than that obtained by Cohen [29] ( $-2.3 \times 10^{-24} \text{ cm}^3/\text{atom}$ ) in diffused wafers.

For antimony, the only experimental value appears to be that of Bublik et al [30] who observed a fair agreement between the calculated value with  $r_{\text{Sb}} = 0.1405 \text{ nm}$  [24] and observations in Si doped with  $1 \times 10^{19} \text{ Sb atoms/cm}^3$ . The experimental expansion coefficient is  $\beta_{\text{Sb}} = 2.8 \times 10^{-24} \text{ cm}^3/\text{atom}$ .

### *3.1 Diamond cubic Si: structure, lattice parameter and density*

Phosphorus has been shown to contract the Si lattice, as expected from its smaller radius ( $r_p = 0.1128$  nm [24]). Measured values of  $\beta_p$  range from  $-0.72 \times 10^{-24}$  cm<sup>3</sup>/atom [29], very near the calculated value ( $-0.77 \times 10^{-24}$  cm<sup>3</sup>/atom), to significantly higher absolute values of  $-1.0 \times 10^{-24}$  [27], and even  $-1.8 \times 10^{-24}$  cm<sup>3</sup>/atom [28].

The tetrahedral radius of arsenic given by [24] ( $r_{As} = 0.1225$  nm) appears to be overestimated. Measured values show hardly detectable effects [30,31].

Expansion or contraction of the lattice parameters induces stresses in the near surface layer of diffused wafers. Dislocations are produced when impurity levels exceed some critical value. For P, B and Sn, this critical concentration is  $5 \times 10^{20}$  cm<sup>-3</sup>,  $3 \times 10^{19}$  cm<sup>-3</sup> and  $10^{19}$  cm<sup>-3</sup>, respectively, according to Yeh and Joshi [32].

## **G DENSITY OF SILICON**

Density of highly pure Si single crystals has been accurately measured for the purpose of obtaining a solid state density standard, which could replace water, the commonly used density standard [33]. Very accurate density measurements are also needed to determine the Avogadro constant [34,35]. Si standards were prepared and measured at NIST where they have been used since 1972. The measured density of silicon was [33–36]:

$$\rho_{Si} = 2.3290028 \text{ g/cm}^3 \quad \text{at } 25^\circ\text{C}$$

More recently, a comparison of solid density standards between NIST and IMGC has given consistent values within 1 ppm for the two crystals considered [37]. An obvious cause of minute difference in densities could be a small change of the atomic weight M, due to variations of isotope abundance ratios. A universality in the ratio M/ρ with a measurement uncertainty of 0.5 ppm was shown [34,35] but was recently questioned by new measurements [38]. The relative variation of the atomic weight of Si can be as high as  $\pm 40$  ppm [39]. In view of these uncertainties, a convenient value of single crystal silicon density, sufficient for most practical purposes, should be:

$$\rho_{Si} = 2.32900 \pm 0.00008 \text{ g/cm}^3$$

as proposed by Tatsumi and Ohsaki [40].

At not too high doping levels ( $\leq 10^{18}$  atoms/cm<sup>3</sup>), density changes are negligible since there is, to a first order, a compensation between the expansion (or contraction) of the lattice and addition (or withdrawal) of weight.

The effect of temperature on density can be evaluated from the thermal expansion coefficients given above.

## **H CONCLUSION**

Silicon crystallises in the diamond structure, at normal pressure, and is purely covalently bonded. Both X-ray and combined X-ray and optical interferometry techniques have been used to accurately measure the lattice parameter of silicon. The variations of lattice parameter with temperature, pressure and impurity content (O, C, B, Sb and P) have been summarised. The density of silicon has been detailed and the variation with doping below  $\sim 10^{18}$  cm<sup>-3</sup> is negligible.

### 3.1 Diamond cubic Si: structure, lattice parameter and density

## REFERENCES

- [1] W.L. Bond [ *Acta Crystallogr. (Denmark)* vol.13 (1960) p.814 ]
- [2] U. Bonse, M. Hart [ *Appl. Phys. Lett. (USA)* vol.6 (1965) p.155 ]
- [3] R.D. Deslattes, A. Henins [ *Phys. Rev. Lett. (USA)* vol.31 (1973) p.972 ]
- [4] R.D. Deslattes, M. Tanaka, G.L. Greene, A. Henins, E.G. Kessler Jr. [ *IEEE Trans. Instrum. Meas. (USA)* vol.IM-36 (1987) p.166 ]
- [5] D. Windisch, P. Becker [ *Phys. Status Solidi A (Germany)* vol.118 (1990) p.379 ]
- [6] P. Becker et al [ *Phys. Rev. Lett. (USA)* vol.46 (1981) p.1540 ]
- [7] P. Becker, P. Seyfried, H. Siegert [ *Z. Phys. B. Condens. Matter (Germany)* vol.48 (1982) p.17 ]
- [8] G. Basile, A. Bergamin, G. Cavagnero, G. Mana, E. Vittone, G. Zosi [ *Phys. Rev. Lett. (USA)* vol.72 (1994) p.3133 ]
- [9] H. Fujimoto, K. Nakayama, M. Tanaka, G. Misawa [ *Jpn. J. Appl. Phys. (Japan)* vol.34 (1995) p.5065 ]
- [10] E.R. Cohen, B.N. Taylor [ *Rev. Mod. Phys. (USA)* vol.59 (1987) p.1121 ]
- [11] E.C. Kessler, A. Henins, R.D. Deslattes, L. Nielsen, M. Arif [ *J. Res. Natl. Inst. Stand. Technol. (USA)* vol.99 (1994) p.1 ]
- [12] I. Henins, J.A. Bearden [ *Phys. Rev. (USA)* vol.135 (1964) p.A890 ]
- [13] R.L. Barns [ *Mater. Res. Bull. (USA)* vol.2 (1967) p.273 ]
- [14] A. Segmuller [ *Adv. X-ray Anal. (USA)* vol.12 (1970) p.455 ]
- [15] T. Hom, W. Kiszenick, B. Post [ *J. Appl. Crystallogr. (Denmark)* vol.8 (1975) p.457 ]
- [16] C.R. Hubbard, F.A. Mauer [ *J. Appl. Crystallogr. (Denmark)* vol.9 (1976) p.1 ]
- [17] T. Hori, H. Araki, H. Inoue, T. Ogawa [ *X-sen Bunsaki no Shinpo (Japan)* vol.9 (1977) p.35 (in Japanese) ]
- [18] K. Lukaszewicz, D. Kucharczyk, M. Malinowski, A. Pietraszko [ *Krist. Tech. (Germany)* vol.13 (1978) p.561 ]
- [19] Y. Okada, Y. Tokumaru [ *J. Appl. Phys. (USA)* vol. 56 (1984) p.314 ]
- [20] J. Härtwig et al [ *Phys. Status Solidi A (Germany)* vol.142 (1994) p.19 ]
- [21] K.G. Lyon, C.L. Salinger, C.A. Swenson, G.K. White [ *J. Appl. Phys. (USA)* vol.48 (1977) p.865 ]
- [22] Y. Okada [ *Phys. Rev. B (USA)* vol.41 (1990) p.10741 and vol.45 (1992) p.6352 ]
- [23] Y. Yamamoto, M. Nomura, H. Fujiwara [ *Jpn. J. Appl. Phys. (Japan)* vol.16 (1977) p.397 ]
- [24] J.A. Van Vechten, J.C. Phillips [ *Phys. Rev. B (USA)* vol.2 (1970) p.2160 ]
- [25] Y. Okada [ *Researches of the Electrotechnical Lab. (Japan)* vol.913 (1990) p.45 (in Japanese) ]
- [26] F.H. Horn [ *Phys. Rev. (USA)* vol.97 (1955) p.1521 ]
- [27] K.G. Mc Quhae, A.S. Brown [ *Solid-State Electron. (UK)* vol.15 (1972) p.259 ]
- [28] G. Celotti, D. Nobili, P. Ostaja [ *J. Mater. Sci. (UK)* vol.9 (1974) p.821 ]
- [29] B.G. Cohen [ *Solid-State Electron. (UK)* vol.10 (1967) p.33 ]
- [30] V.T. Bublik, S.S. Gorelik, A.N. Dubrovina [ *Sov. Phys.-Solid State (USA)* vol.10 (1969) p.2247 ]
- [31] I.N. Smirnov [ *Sov. Phys.-Dokl. (USA)* vol.20 (1975) p.224 ]
- [32] T.H. Yeh, M.L. Joshi [ *J. Electrochem. Soc. (USA)* vol.116 (1969) p.73 ]
- [33] H.A. Bowman, R.M. Schoonover, C.L. Carroll [ *J. Res. Natl. Bur. Stand. A (USA)* vol.78 (1974) p.13 ]
- [34] R.D. Deslattes et al [ *Phys. Rev. Lett. (USA)* vol.33 (1974) p.463 ]
- [35] R.D. Deslattes, A. Henins, R.M. Schoonover, C.L. Carroll, H.A. Bowman [ *Phys. Rev. Lett. (USA)* vol.36 (1976) p.898 ]
- [36] R.D. Deslattes [ *Annu. Rev. Phys. Chem. (USA)* vol.31 (1980) p.435 ]
- [37] A. Peuto, R.S. Davis [ *J. Res. Natl. Bur. Stand. (USA)* vol.90 (1985) p.217 ]

### *3.1 Diamond cubic Si: structure, lattice parameter and density*

- [38] K. Fujii, M. Tanaka, Y. Nezu, A. Sakuma, A. Leistner, W. Giardini [ *IEEE Trans. Instrum. Meas. (USA)* vol.44 (1995) p.542 ]
- [39] B.W. Petley [ *The Fundamental Physical Constants and the Frontier of Measurement* (Bristol, Hilger, 1985) sections 3.4.1 and 3.5 ]
- [40] Y. Tatsumi, H. Ohsaki [ in *Properties of Silicon* Ed. INSPEC (IEE, London, UK, 1988) ch.1 p.3-6 ]

## 3.2 Elastic constants and moduli of diamond cubic Si

A. George

July 1997

### A INTRODUCTION

This Datareview gives values for the second and third order elastic constants, Sections B and C, the compliances, Section D, the bulk modulus, Section E, and the average elastic moduli in the isotropic approximation, Section F. Finally, in Section G, the dependence of the elastic constants on doping level is summarised.

### B SECOND ORDER ELASTIC CONSTANTS

The second order elastic constants or stiffness, as defined by Kittel [1] or Hirth and Lothe [2] relate stresses  $\sigma$  to elastic strains  $\epsilon$ , according to Hooke's law. In cubic crystals, three constants  $C_{11}$ ,  $C_{12}$  and  $C_{44}$  are sufficient to determine all stress components whatever the state of strain:

$$\begin{aligned}\sigma_{ii} &= C_{11} \epsilon_{ii} + C_{12} (\epsilon_{jj} + \epsilon_{kk}) \\ \sigma_{ij} &= 2C_{44} \epsilon_{ij} \quad (i \neq j)\end{aligned}$$

The  $\epsilon_{ij}$  are usually measured by ultrasonic methods. A discussion of current techniques and of theoretical calculations in semiconductors was given by Chen et al [3].

Early data for pure Si were reported by McSkimin and co-workers [4–6]. At room temperature, and atmospheric pressure, the most accurate data seem to be those of Hall [7].

$$\begin{aligned}C_{11} &= 1.6564 \times 10^{11} \text{ Pa} \\ C_{12} &= 0.6394 \times 10^{11} \text{ Pa} \\ C_{44} &= 0.7951 \times 10^{11} \text{ Pa}\end{aligned}$$

The error in  $C_{ij}$  is 0.02%. The values of McSkimin are within 0.1% of Hall's values.

The temperature dependence of  $C_{ij}$  was investigated by McSkimin [4] in the range 77–300 K, by Hall [7] in the range 4.2–310 K and by Burenkov and Nikanorov [8] up to 1273 K, but apparently with a lesser accuracy. (Their  $C_{11}$  and  $C_{12}$  at 293 K are about 5% lower than Hall's values, while their  $C_{44}$  agrees with Hall's within 1%).

Below 100 K, the  $C_{ij}$  change very little and the extrapolated values at 0 K used in more recent textbooks [3,9] are:

$$\begin{aligned}C_{11} &= 1.6772 \times 10^{11} \text{ Pa} \\ C_{12} &= 0.6498 \times 10^{11} \text{ Pa} \\ C_{44} &= 0.8036 \times 10^{11} \text{ Pa}\end{aligned}$$

which are 0.1% higher than the data measured by Hall [7] at 4.2 K.

Between 150 and 1000 K the decrease of the  $C_{ij}$  with increasing temperature is fairly linear. The measured rates are:

### 3.2 Elastic constants and elastic moduli of diamond cubic Si

$$\left(\frac{1}{C_{11}}\right) \frac{dC_{11}}{dT} = -9.4 \times 10^{-5} \text{ K}^{-1} \quad [9]$$

$$= -9.3 \times 10^{-5} \text{ K}^{-1} \quad [8]$$

$$\left(\frac{1}{C_{12}}\right) \frac{dC_{12}}{dT} = -9.8 \times 10^{-5} \text{ K}^{-1} \quad [9]$$

$$\left(\frac{1}{C_{44}}\right) \frac{dC_{44}}{dT} = -8.3 \times 10^{-5} \text{ K}^{-1} \quad [9]$$

$$= -1.0 \times 10^{-4} \text{ K}^{-1} \quad [8]$$

$$= -7.3 \times 10^{-5} \text{ K}^{-1} \quad [8]$$

Rates given in [9] were extracted from the  $C_{ij}(T)$  data of Hall [7], which cover a limited temperature range compared to that of Burenkov and Nikanorov [8].

### C THIRD ORDER ELASTIC CONSTANTS

Measurements of the  $C_{ij}$  as functions of applied hydrostatic pressure up to 8 GPa [5,10] show that they are not constant beyond stresses of some hundreds of MPa. Non-linearity effects must be described in terms of higher order elastic constants. The conventional description is due to Thurston and Brugger [11] who used the Lagrangian form of elastic tensors. A summary of elastic theories was given by Nielsen [12].

Cubic crystals have six third-order elastic constants  $C_{ijk}$ , which are measured by monitoring the ultrasonic velocities as a function of external static pressure (hydrostatic or uniaxial). Such measurements were performed by McSkimin and Andreatch [6] and by Hall [7]. The data of Hall for pure Si at 298 K are:

$$C_{111} = -7.95 \times 10^{11} \text{ Pa} \pm 0.10 \times 10^{11} \text{ Pa}$$

$$C_{112} = -4.45 \times 10^{11} \text{ Pa} \pm 0.10 \times 10^{11} \text{ Pa}$$

$$C_{123} = -0.75 \times 10^{11} \text{ Pa} \pm 0.05 \times 10^{11} \text{ Pa}$$

$$C_{144} = 0.15 \times 10^{11} \text{ Pa} \pm 0.05 \times 10^{11} \text{ Pa}$$

$$C_{166} = -3.10 \times 10^{11} \text{ Pa} \pm 0.05 \times 10^{11} \text{ Pa}$$

$$C_{456} = -0.86 \times 10^{11} \text{ Pa} \pm 0.05 \times 10^{11} \text{ Pa}$$

The two sets of data [6,7] agree within the estimated error bars, except for  $|C_{111}|$  found to be 4% higher by McSkimin.

### D COMPLIANCES

The compliances express elastic strains as functions of stresses [1,2]. Using the notations of Hirth and Lothe [2], the compliances are noted  $S'_{ij}$  and are given by the relations:

### 3.2 Elastic constants and elastic moduli of diamond cubic Si

$$S'_{11} = \frac{C_{11} + C_{12}}{(C_{11} - C_{12})(C_{11} + 2C_{12})}$$

$$S'_{12} = \frac{-C_{12}}{(C_{11} - C_{12})(C_{11} + 2C_{12})}$$

$$S'_{44} = \frac{1}{C_{44}}$$

(These quantities are noted  $S_{ij}$  by Kittel [1].)

Using the  $C_{ij}$  of Hall [7] we obtain for pure Si:

$$S'_{11} = 0.7691 \times 10^{11} \text{ Pa}$$

$$S'_{12} = -0.2142 \times 10^{11} \text{ Pa}$$

$$S'_{44} = 1.2577 \times 10^{11} \text{ Pa}$$

at 298 K, and atmospheric pressure, with an error of 0.02%.

## E BULK MODULUS

The bulk modulus  $B$  is defined as  $B = -V(dP/dV)$  where  $V$  is the volume and  $P$  the hydrostatic pressure.

The compressibility  $K$  is defined as  $K = 1/B$ .

In cubic crystals,  $B$  is given by the following linear combination of elastic constants:

$$B = \frac{C_{11} + 2C_{12}}{3}$$

Using the  $C_{ij}$  measured by Hall [7] we obtain at 298 K and atmospheric pressure:

$$B = 0.9784 \times 10^{11} \text{ Pa}$$

$$K = 1.0221 \times 10^{-11} \text{ Pa}^{-1}$$

(The error in  $B, K$  is 0.02%).

When non-linear effects become noticeable, the bulk modulus changes with pressure as

$$B(P) = B(0) - B'P$$

where the dimensionless  $B' = -(dB/dP)$  is expressed in terms of third-order elastic constants as:

$$B' = -(C_{111} + 6C_{112} + 2C_{123}) / 9B$$

in the framework of Lagrangian elastic theory. With Hall's values for the  $C_{ijk}$ , we obtain:

### 3.2 Elastic constants and elastic moduli of diamond cubic Si

$$B' = 4.11$$

at 298 K, and atmospheric pressure. The error in  $B'$  is about 2%.

#### F AVERAGE ELASTIC MODULI IN THE ISOTROPIC APPROXIMATION

Silicon is not elastically isotropic. The anisotropy of cubic solids is conveniently characterised by the anisotropy ratio,  $A = 2 C_{44} / (C_{11} - C_{12})$  and the anisotropy factor,  $H = 2 C_{44} + C_{12} - C_{11}$ .

In pure Si, at ambient temperature and pressure:

$$A = 1.56$$

$$H = 5.74 \times 10^{11} \text{ Pa}$$

In view of the difficulties of exact calculations in anisotropic media, one is often satisfied with the isotropic approximation. In isotropic solids, two quantities are sufficient to relate stresses and strains. General use is made of the shear modulus  $\mu$ , such as  $\sigma_{ij} = 2 \mu \varepsilon_{ij}$ , and of the Poisson's ratio  $\nu$ , the ratio of transverse contraction to elongation in simple tension. Also commonly used is the Young's modulus,  $E$ , the ratio of simple tensile stress to strain.

There are two ways to define these average quantities in real solids. The Voigt average is over the elastic constants  $C_{ij}$  and is appropriate for a polycrystalline material in which the grains of different orientations have the same stress. The Voigt average is also better to deal with local strains around dislocations. In contrast, the Reuss average is over the compliances  $S'_{ij}$  and is better when the grains have the same state of strain or in cases involving long-range internal stress-fields.

In cubic crystals, average moduli are defined as follows:

**Voigt average**

$$\text{shear modulus} \quad \mu = C_{44} - \frac{1}{5} H$$

$$\text{Poisson's ratio} \quad \nu = \frac{C_{12} - H/5}{2(C_{12} + C_{44} - 2H/5)}$$

$$\text{Young's modulus} \quad E = 2\mu(1 + \nu)$$

**Reuss average**

$$\text{shear modulus} \quad \mu_R = \left( S'_{44} + \frac{4}{5} J \right)^{-1}$$

$$\text{Poisson's ratio} \quad \nu_R = \left( -S'_{12} - \frac{J}{5} \right) \left( S'_{11} - \frac{2J}{5} \right)^{-1}$$

$$\text{Young's modulus} \quad E_R = \left( S'_{11} - \frac{2}{5} J \right)^{-1}$$

### 3.2 Elastic constants and elastic moduli of diamond cubic Si

with  $J = S'_{11} - S'_{12} - \frac{S'_{44}}{2}$

Using the  $C_{ij}$  of Hall [7] we obtain, for pure Si at ambient temperature and pressure:

$$\mu = 6.80 \times 10^{11} \text{ Pa}$$

$$v = 0.218$$

$$E = 16.56 \times 10^{11} \text{ Pa}$$

$$\mu_R = 6.49 \times 10^{11} \text{ Pa}$$

$$v_R = 0.228$$

$$E_R = 15.94 \times 10^{11} \text{ Pa}$$

## G DOPING DEPENDENCE OF ELASTIC CONSTANTS

As explained by Keyes [13], the elastic properties of semiconductors depend on the carrier concentration, so that the elastic constants are expected to change significantly with electronic doping.

Second-order elastic constants were measured in heavily doped n-type Si by Hall [7], for a carrier concentration  $n = 2.0 \times 10^{19} \text{ cm}^{-3}$  (phosphorus) in the range 4.2–310 K, and by Beilin et al [14] for  $n = 4.8 \times 10^{19} \text{ cm}^{-3}$  (arsenic) at 78 and 295 K. Hall also measured the  $C_{ijk}$ . Heavily doped p-type Si was investigated by Mason and Bateman [15] for various concentrations from  $5 \times 10^{17}$  to  $3 \times 10^{19} \text{ cm}^{-3}$  (boron and gallium). Theoretical approaches were given by Keyes [13], Kim [16] and Khan and Allen [17] (see also [3]). The typical effect of heavy doping is to decrease the  $C_{ij}$  by 1–3% and to modify the temperature dependences. The  $C_{ijk}$  can be changed in much larger proportions.

## H CONCLUSION

Second order elastic constants, or stiffness, relate stresses to strains and this Datareview has summarised their values and variation with temperature. Third order elastic constants are required to describe the pressure dependence, above a few hundred MPa. Values are also given for the compliances, at ambient temperature and pressure, and the bulk modulus, at ambient temperature and pressure and at higher pressure. Silicon is not elastically isotropic and an approximation is needed, via the Voigt and Reuss averages, using the shear modulus, Poisson's ratio and Young's modulus. Elastic constants change markedly on doping with P, As, B and Ga.

## REFERENCES

- [1] C. Kittel [ *Introduction to Solid State Physics* 4th Edn (Wiley, 1971) ch.4 ]
- [2] J.P. Hirth, J. Lothe [ *Theory of Dislocations* 2nd Edn (Wiley, 1982) ch.2 ]
- [3] A.B. Chen, Arden Sher, W.T. Yost [ in *The Mechanical Properties of Semiconductors and Semimetals* vol.37 (Academic Press, 1992) ch.1 ]
- [4] H.J. McSkimin [ *J. Appl. Phys. (USA)* vol.24 (1953) p.988 ]
- [5] H.J. McSkimin, P. Andreatch [ *J. Appl. Phys. (USA)* vol.35 (1964) p.2161 ]
- [6] H.J. McSkimin, P. Andreatch [ *J. Appl. Phys. (USA)* vol.35 (1964) p.3312 ]
- [7] J.J. Hall [ *Phys. Rev. (USA)* vol.161 (1967) p.756 ]
- [8] Yu.A. Burenkov, S.P. Nikanorov [ *Sov. Phys.-Solid State (USA)* vol.16 (1974) p.963 ]

### 3.2 Elastic constants and elastic moduli of diamond cubic Si

- [9] [ *Landolt-Bornstein Numerical Data and Functional Relationships in Science and Technology*, New Series, Ed. K.H. Hellwidge (Springer Verlag, Germany, 1979) vol.17 and 22 ]
- [10] V.A. Goncharova, E.V. Chernysheva, F.F. Voronor [ *Sov. Phys.-Solid State (USA)* vol.25 (1983) p.2118 ]
- [11] R.N. Thurston, K. Brugger [ *Phys. Rev. (USA)* vol.133 (1964) p.A1604 ]
- [12] O.H. Nielsen [ *Phys. Rev. B (USA)* vol.34 (1986) p.5808 ]
- [13] R.W. Keyes [ *Solid State Physics* vol.20 Eds. H. Ehrenreich, F. Seitz, D. Turnbull (Academic Press, 1976) p.37 ]
- [14] V.M. Beilin, Yu.Kh. Vekilov, O.M. Krasil'nikov [ *Sov. Phys.-Solid State (USA)* vol.12 (1970) p.531 ]
- [15] W.P. Mason, T.B. Bateman [ *Phys. Rev. (USA)* vol.134 (1964) p.A1387 ]
- [16] C.K. Kim [ *J. Appl. Phys. (USA)* vol.52 (1981) p.3693 ]
- [17] F.S. Khan, P.B. Allen [ *Phys. Status Solidi B (Germany)* vol.128 (1985) p.31 ]

### 3.3 High pressure phases of c-Si

A. George

July 1997

#### A INTRODUCTION

Under atmospheric pressure, Si has the diamond cubic structure up to the melting temperature. At high pressures, no less than eleven other crystalline phases have been experimentally identified. Some of them are thermodynamically stable phases which appear when the pressure is increased above some level. Several others are metastable phases, which form from the former ones during pressure release. At least one phase—Si-IV in the list below—requires both high pressure and heating above room temperature. Except for the usual low-pressure and the Si-IV phase which are semiconducting, all phases of Si have metallic conductivity.

#### B EXPERIMENTAL RESULTS

TABLE 1 gives the structure and pressure region of each phase with the conventional labelling using capital roman numbers [1,2].

TABLE 1 Crystalline phases of Si.

Designation	Structure	Space group	Pressure region (GPa)	Refs
Si-I	diamond cubic	Fd3m	0–12.5	[1,2]
Si-II	body centred tetragonal ( $\beta$ -Sn)	I4 <sub>1</sub> /amd	8.8–16	[2–6,17]
Si-III (or BC8)	body centred cubic (basis of 8 atoms)	Ia $\bar{3}$	2.1–0	[2,3,6,7]
Si-IV	diamond hexagonal (lonsdaleite)	P6 <sub>3</sub> /mmc	—	[8–13]
Si-V	primitive hexagonal	P6/mmm	14–35	[2,4]
Si-VI	unidentified		34–40	[4,14]
Si-VII	hexagonal close packed	P6 <sub>3</sub> /mmc	40–78.3	[3,4,15]
Si-VIII	tetragonal (~30 atoms per unit cell)	P4 <sub>1</sub> 2 <sub>1</sub> 2	14.8–0	[16]
Si-IX	tetragonal (12 atoms per unit cell)	P4 <sub>2</sub> 22	12–0	[16]
Si-X	face centred cubic	Fm3m	78.3–230	[14,15]
Si-XI (or Imma)	body centred orthorhombic	Imma	13/15	[17]
Si-XII (or R8)	trigonal (8 atoms per unit cell)	R $\bar{3}$	12–2.0	[18–20]

The transformation sequence of stable phases at increasing hydrostatic pressure, as determined using diamond-anvil cells and X-ray diffraction with synchrotron sources, is:

I → II → XI → V → VI → VII → X

There is no sharp transition and two-phase regions exist over wide ranges of pressure [2].

### 3.3 High pressure phases of c-Si

Metastable phases observed on decompression depend on pressure release conditions. For stepwise slow decompression the sequence is:



Si-VIII was obtained from a mixture of II + V after a rapid release of P from 14.8 GPa. Si-IX was obtained from a mixture of I + II after a rapid release of P from 12 GPa [16].

Note: the recent discovery of new intermediate phases has resulted in some changes in the former classification. We follow here the recommendations in [17,18], but the reader must be aware that no general agreement seems to have been reached so far.

The Si-VI structure is still undetermined. It cannot be described simply by relayering of basal planes, such as occurs in the double-hcp structure, which was first proposed in [14,15].

Increasing the pressure results in a decrease of the atomic volume, consistently with an increase of the co-ordination number, at least for the simple structures where it can be defined, from 4 in Si-I to 12 in Si-X.

Diamond-hexagonal Si-IV has an identical atomic volume to that of diamond cubic Si-I. It can be obtained from the metastable Si-III phase by heating [8] or after plastic deformation at moderate temperatures (670–970 K) and under confining pressure, especially beneath micro-hardness indentation [11]. Si-IV appears as ribbons or platelets embedded in Si-I, with  $\{511\}_{\text{d.c.}}$  habit plane and the following orientation relationship:

$$\begin{aligned} & (0\bar{1}1)_{\text{d.c.}} \parallel (0001)_{\text{d.h.}} \\ & [011]_{\text{d.c.}} \parallel [\bar{1}2\bar{1}0]_{\text{d.h.}} \end{aligned}$$

The d.c.  $\rightarrow$  d.h. transformation is closely related to deformation twinning and was described as a martensitic transformation taking place at twin-twin intersections or after secondary twinning [11–13].

Lattice parameters of high pressure phases of Si are given in TABLE 2: see the references for the atomic positions within the cell and various bond lengths in complex structures.

There have been a number of theoretical studies of the high pressure phases of Si [21,27], using different first-principles techniques to calculate and compare total energies: ab-initio pseudo-potential within the local density functional formalism [21,22], linear muffin-tin-orbitals (LMTO) method [23] and generalised pseudo-potential theory [23]. Investigations of the full sequence of transformations can be found in [22,25,27]. A detailed study of Si-III was given in [24,25]. The recently discovered Si-XI phase was studied in [26]. Recently, Needs and Mujica [27] have compared eleven possible phases, including all actually observed ones, except for Si-VI, VIII, X and XI. They found good agreement with experiments. Among the few remaining discrepancies, the calculated pressure ( $\sim 86$  GPa) for the Si-I to Si-II transition is significantly lower than the experimental results.

### 3.3 High pressure phases of c-Si

TABLE 2 Lattice parameters of high pressure phases of Si.

Designation	Pressure (GPa)	Lattice parameters (nm)	Refs
Si-II	11.2 $\pm$ 0.2	a = 0.4690 $\pm$ 0.0006 c = 0.258 $\pm$ 0.0005	[2]
	12.5	a = 0.4686 c = 0.2585	[5]
	10.3	a = 0.4665 $\pm$ 0.0001 c = 0.2572 $\pm$ 0.0001	[17]
	16 atom bcc cell		
Si-III	0	a = 0.6620 $\pm$ 0.0011	[2,3]
	0	a = 0.6636 $\pm$ 0.0005 a = 0.6637 $\pm$ 0.0001	[7] [19]
	8 atom rhombohedral-cell		
	0	a = 0.5748 $\pm$ 0.0001 $\alpha$ = 109.47°	[19]
Si-IV	2	a = 0.5716 $\alpha$ = 109.47	[19]
		a= 0.38 c = 0.628	[8]
		a = 0.386 c = 0.631	[9,11]
Si-V	16	a = 0.2551 $\pm$ 0.0006 c = 0.2387 $\pm$ 0.0007	[2,3]
	16	a = 0.2527 c = 0.2373	[4]
	18	a = 0.2539 $\pm$ 0.0001 c = 0.2380 $\pm$ 0.0001	[17]
	36	a = 0.2463 c = 0.2320	[14]
Si-VII	41–42	a = 0.2524 $\pm$ 0.0009 c = 0.4142 $\pm$ 0.005	[3]
	43	a = 0.2444 c = 0.4152	[4]
Si-VIII		a = 0.8627 c = 0.7500	[16]
Si-IX		a = 0.77482 c = 0.3856	[16]
Si-X	87 $\pm$ 7	a = 0.3341 $\pm$ 0.0003	[14]
Si-XI	$\sim$ 13	a = 0.4737 $\pm$ 0.0001 b = 0.4502 $\pm$ 0.0001 c = 0.2550 $\pm$ 0.0001	[17]
Si-XII	8.2	a = 0.5620 $\pm$ 0.0003 $\alpha$ = 110.07 $\pm$ 0.03°	[19]
	2	a = 0.5712 $\alpha$ = 109.99°	[19]

(The zero pressure means atmospheric pressure here.)

### 3.3 High pressure phases of c-Si

## C CONCLUSION

As pressure increases, the diamond cubic structure of silicon changes to one of eleven other crystalline phases. Some of these are thermodynamically stable while others form on decompression. Most of these high pressure phases are metallic. Diamond-anvil cells and X-ray synchrotron diffraction are the experimental tools used. Lattice parameter values for all the phases are also tabulated.

## REFERENCES

- [1] J.F. Cannon [ *J. Phys. Chem. Ref. Data (USA)* vol.3 (1994) p.781 ]
- [2] J.Z. Hu, I.L. Spain [ *Solid State Commun. (USA)* vol.51 (1984) p.263 ]
- [3] J.Z. Hu, L.D. Merkle, C.S. Menoni, I.L. Spain [ *Phys. Rev. B (USA)* vol.34 (1986) p.4679 ]
- [4] H. Olijnyk, S.K. Sikka, W.B. Holzapfel [ *Phys. Lett. A (Netherlands)* vol.703 (1984) p.137 ]
- [5] J.C. Jamieson [ *Science (USA)* vol.139 (1963) p.762 ]
- [6] T.I. Dyuzhera, S.S. Kabalkina, V. Novichkov [ *Sov. Phys. JETP (USA)* vol.47 (1978) p.931 ]
- [7] J.S. Kasper, S.M. Richards [ *Acta Crystallogr. (Denmark)* vol.77 (1964) p.752 ]
- [8] R.H. Wentorf, J.S. Kasper [ *Science (USA)* vol.179 (1963) p.338 ]
- [9] V.G. Eremenko, V.I. Nikitenko [ *Phys. Status Solidi A (Germany)* vol.14 (1972) p.317 ]
- [10] T.Y. Tan, H. Föll, S.M. Hu [ *Philos. Mag. A (UK)* vol.44 (1981) p.127 ]
- [11] P. Pirouz, R. Chaim, V. Dahmen, K.H. Westmacott [ *Acta Metall. Mater. (USA)* vol.38 (1990) p.313 ]
- [12] V. Dahmen, K.H. Westmacott, P. Pirouz, R. Chaim [ *Acta Metall. Mater. (USA)* vol.38 (1990) p.323 ]
- [13] P. Pirouz, U. Dahmen, K.H. Westmacott, R. Chaim [ *Acta Metall. Mater. (USA)* vol.38 (1990) p.329 ]
- [14] S.J. Duclos, Y.K. Vohra, A.L. Ruoff [ *Phys. Rev. B (USA)* vol.41 (1990) p.12021 ]
- [15] S.J. Duclos, Y.K. Vohra, A.L. Ruoff [ *Phys. Rev. Lett. (USA)* vol. 58 (1987) p.775 ]
- [16] Y.X. Zhao, F. Buehler, J.R. Sites, I.L. Spain [ *Solid State Commun. (USA)* vol.59 (1986) p.679 ]
- [17] M.J. McMahon, R.J. Nelmes [ *Phys. Rev. B (USA)* vol.47 (1993) p.8337 ]
- [18] J. Crain, G.J. Ackland, J.R. Maclean, R.O. Piltz, P.D. Hatton, G.S. Pawley [ *Phys. Rev. B (USA)* vol.52 (1994) p.4072 ]
- [19] R.O. Piltz, J.R. Maclean, S.J. Clark, G.J. Ackland, P.D. Halton, J. Crain [ *Phys. Rev. B (USA)* vol.52 (1995) p.4072 ]
- [20] A. Kailer, Y.G. Gogotsi, K.G. Nickel [ *J. Appl. Phys. (USA)* vol.81 (1997) p.3057 ]
- [21] M.T. Yin, M.L. Cohen [ *Phys. Rev. Lett. (USA)* vol.45 (1980) p.1004 ]
- [22] M.T. Yin, M.L. Cohen [ *Phys. Rev. B (USA)* vol.26 (1982) p.5668 ]
- [23] A.K. McMahan, J.A. Noriorty [ *Phys. Rev. B (USA)* vol.27 (1983) p.3235 ]
- [24] R. Biswas, R.M. Martin, R.J. Needs, O.H. Nielsen [ *Phys. Rev. B (USA)* vol.30 (1984) p.3210 ]
- [25] R. Biswas, R.M. Martin, R.J. Needs, O.H. Nielsen [ *Phys. Rev. B (USA)* vol.35 (1987) p.9559 ]
- [26] S.P. Lewis, M.L. Cohen [ *Phys. Rev. B (USA)* vol.48 (1993) p.16144 ]
- [27] R.J. Needs, A. Mujica [ *Phys. Rev. B (USA)* vol.51 (1995) p.9652 ]

## 3.4 Core structures and energies of dislocations in Si

A. George

July 1997

### A INTRODUCTION

This Datareview discusses the important structural defects of stacking faults and dislocations in silicon. Stacking fault energies are discussed and found to be independent of doping levels. Dislocation motion is described and the formation and migration energies of both kinks and antiphase defects are estimated.

### B EXPERIMENTAL RESULTS

The diamond cubic structure is a face centred cubic (fcc) structure with a basis of two atoms distant by  $a/4[111]$  vector (i.e. two interpenetrating fcc sublattices displaced by the same vector). It can be viewed as a periodic stacking of three pairs of {111} layers ... aA bB cC aA ... [1–3].

The only low energy stacking faults respect the tetrahedral bonding of first-neighbour atoms and are of two types:

- a) Intrinsic stacking faults (ISF) correspond to the removal of one double layer  
... cC aA bB ; aA bB cC ...

Such a fault can also be created by a suitable shear of the upper half of the crystal by  $a/6<112>$ , which puts the cC layer into aA position (and shifts similarly the upper layers).

- b) Extrinsic stacking faults (ESF) correspond to the insertion of one extra double layer  
... cC aA bB ; aA ; cC aA bB cC ...

Such a fault can be created by annealing under oxidising atmosphere, the SF resulting from condensation of excess interstitials produced during oxide formation.

Stacking fault energies  $\gamma_{sf}$  are determined by measuring the width of appropriate dislocation configurations in which the stacking fault tension is equilibrated by the known repulsive force between enclosing dislocations. Recommended values for Si are [4]:

$$\begin{aligned}\gamma_{sf, \text{int}} &= 65 \pm 10 \text{ mJ m}^{-2} \\ \gamma_{sf, \text{ext}} &= 60 \pm 10 \text{ mJ m}^{-2}\end{aligned}$$

Electronic doping does not induce significant changes in  $\gamma_{sf}$ , but segregation of impurities in the plane of the fault can lead to apparently lower energies (wider dislocation dissociations).

Glissile dislocations involved in plastic deformation have Burgers vectors  $\bar{b}$  of the  $a/2<110>$  type ( $|\bar{b}| = 0.384 \text{ nm}$ ) and, in most circumstances, glide in {111} planes

As proved by weak beam TEM [5] and HRTEM [6–8], dislocations are dissociated in their slip plane into two Shockley partial dislocations, with  $\bar{b} = a/6<112>$  Burgers vector ( $|\bar{b}| = 0.222 \text{ nm}$ )

### 3.4 Core structures and energies of dislocations in Si

enclosing a ribbon of intrinsic stacking fault. For a full dislocation of given sign, the sequence of partial dislocations is determined according to the topological rules given by [1].

Because of the double-layer stacking of {111} planes, dislocations can be formed by shear between either the narrowly-spaced planes e.g.  $B\ddot{c}$  ('glide set dislocations') or the widely-spaced planes e.g.  $b\ddot{B}$  ('shuffle set dislocations') [1–3]. Narrowly-spaced planes are connected by three times more covalent bonds than widely-spaced planes. Yet, since a low-energy stacking fault can only be created between narrowly spaced planes, it is now well accepted that dislocations usually belong to the 'glide set', although it has been conjectured that local transformation to the 'shuffle set' could occur in some circumstances, for example when the dislocation absorbs or emits single point defects, vacancies or self-interstitials [9].

Isolated dislocations show a strong tendency to align along  $\langle 110 \rangle$  directions, thus forming hexagon loops, with segments at  $120^\circ$  angles. Thus, two types of dislocation segments are of special interest: screw dislocations with the line direction  $\vec{\ell}$ , parallel to the Burgers vector  $\vec{b}$ , and  $60^\circ$  dislocations, so-labelled by the angle of  $60^\circ$  between  $\vec{\ell}$  and  $\vec{b}$ . These preferred orientations correspond to lower core energies. It is said that dislocations feel a Peierls potential and lie in Peierls valleys, in reference to the Peierls–Nabarro model of dislocation core and of dislocation glide (see below and Datareview 3.5 in this volume).

Note: When the dislocation density,  $\rho$ , is large ( $\rho \geq 10^8 / \text{cm}^3$  in plastically deformed Si), dislocations exert long-range stresses on each other and the spatial fluctuations of the effective stress-field lead to the disappearance of the preferred  $\langle 110 \rangle$  orientations as soon as  $\tau \leq \mu b \sqrt{\rho}/2$ , where  $\tau$  is the applied stress and  $\mu$  the shear modulus [10,11].

FIGURE 1 represents a dislocation half-loop in its glide plane. The screw segment is dissociated into two  $30^\circ$  Shockley partials ( $(\vec{b}, \vec{\ell}) = 30^\circ$ ), while the  $60^\circ$  segments are dissociated into one  $30^\circ$  partial and one  $90^\circ$  partial ( $(\vec{b}, \vec{\ell}) = 90^\circ$ ). The sequence of partials (e.g.  $90^\circ$  leading,  $30^\circ$  trailing, with reference to the direction of expansion of the half-loop) is reversed on two adjacent  $60^\circ$  segments of the same loop.

Measurements of dissociation widths in the presence of large stresses [12–14] give evidence that mobilities of  $30^\circ$  and  $90^\circ$  partials are different and that the mobility of a given partial may be changed depending on its leading or trailing position.

Atomic bonding is modified in the dislocation core. If no reconstruction could occur, one dangling bond would be created per atom, as shown on the left segment in the figure. In Si, cores are reconstructed for both kinds of partials [15–17]. Reconstruction of the  $30^\circ$  partial takes place by pairing atoms, parallel to the dislocation line, which entails only a slight distortion and a doubling of the period along  $\vec{\ell}$ . On the  $90^\circ$  partial, bonds reform across the dislocation line. Obviously, both kinds of reconstruction should lead to antiphase defects (APDs).

Dislocations depart from  $\langle 110 \rangle$  Peierls valleys at kinks, which are of prime importance for dislocation motion, which proceeds by nucleation of kink pairs and sideways migration of kinks along the dislocation line. Kinks are very narrow, one atomic distance. The different kinds of kinks which can form on  $90^\circ$  and  $30^\circ$  partials have been listed by Hirsch [18]. Kinks may be formed with or without dangling bonds. On the  $30^\circ$  partial, a kink with a dangling bond is formally equivalent to a reconstructed kink associated with an APD. The two kinks of a kink-pair on a  $30^\circ$  partial have different structures (FIGURE 2). On the  $90^\circ$  partials, kinks have no dangling bond provided they are associated with an APD.

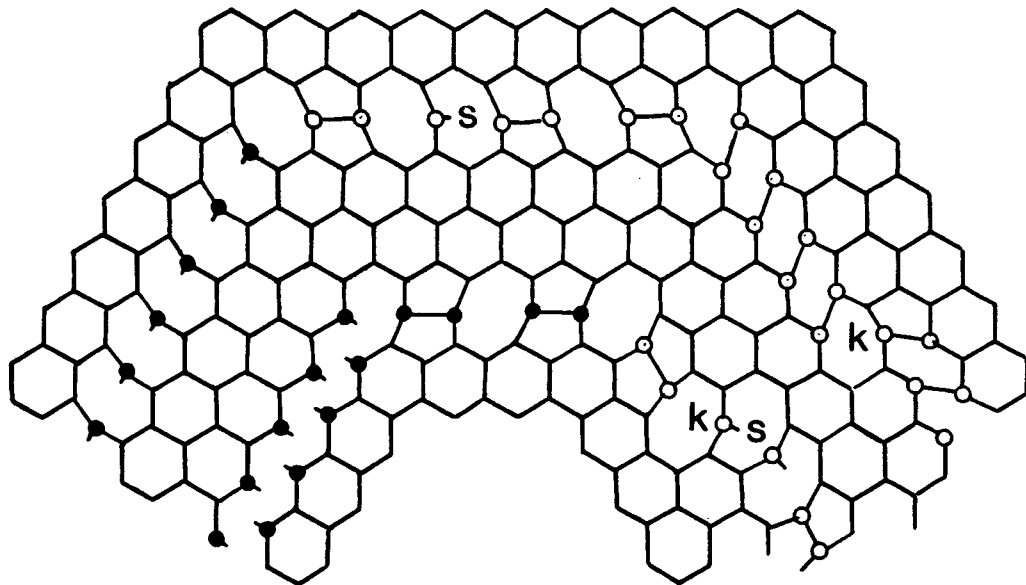


FIGURE 1 Plan view of a dissociated dislocation half-loop in diamond cubic silicon, showing unreconstructed (left) and reconstructed (top and right) Shockley partials, with antiphase defects (S) and one kink (k).

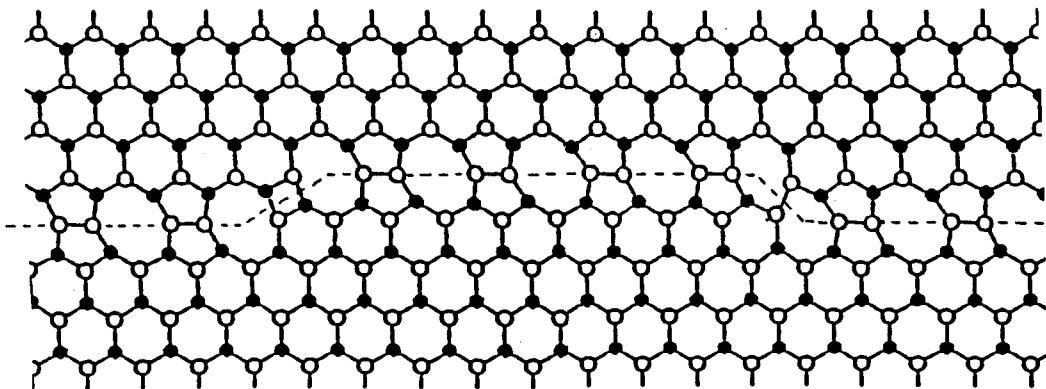


FIGURE 2 Plan view of a  $30^\circ$  Shockley partial with an expanding kink pair, showing the different atomic bondings at left and right kinks.

Important characteristics of kinks and APDs are their formation energy,  $F_k$ , which determines their concentration on dislocation lines, and their migration energy,  $W_m$ . Such energies are not known accurately. Estimates were obtained from indirect observation of dislocation motion [19,20] and, very recently, by direct imaging of moving kinks by HRTEM [21] or by theoretical calculations [22–25]. TABLES 1 and 2 gather presently available data.

All atomic mechanisms involved in dislocation motion can be classified into three distinct categories [22]:

- low energy barriers ( $< 0.2$  eV)

Such mechanisms are very fast and involve bond exchange between two atoms, one which is normally bonded and one which already has a dangling bond.

### 3.4 Core structures and energies of dislocations in Si

- medium energy barriers (0.6–1.3 eV)

These mechanisms are slower but very important since they comprise the lower-energy modes for the production and motion of all major defects. These bond-switching mechanisms involve bond breaking but are always accompanied by formation of another bond.

- high energy barriers ( $> 1.6$  eV)

Such mechanisms involve the breaking of a covalent bond with the creation of two dangling bonds. Being very slow, they are probably inoperative.

It appears that nucleation and migration of kinks occur more easily in the presence of existing APDs, which appear to be highly mobile.

A consistent picture of net dislocation motion based on a detailed sequence of atomistic events has not yet emerged, although the phenomenological description of dislocation velocities is rather simple (see Datareview 3.5).

TABLE 1 Formation and migration energies of core defects in the  $30^\circ$  Shockley partial in undoped silicon.

	Formation energy (eV)	Migration energy (eV)	Ref
<u>Theory</u>			
Right kink	—	$2.1 \pm 0.3$	[23]
Antiphase defect	0.81	0.17	[22]
Right kink	0.82–0.89	0.74	[22]
Left kink	0.82–1.22	0.82	[22]
Right complex (kink + APD)	0.79	1.04	[22]
Left complex	1.12	0.22	[22]
<u>Experiment</u>			
Kink	$0.80 \pm 0.15$	$1.24 \pm 0.07$	[21]

TABLE 2 Formation and migration energies of core defects in the  $90^\circ$  Shockley partial in undoped silicon.

	Formation energy (eV)	Migration energy (eV)	Ref
<u>Theory</u>			
Kink (without dangling bond)	0.1	1.8	[24]
Kink (with dangling bond)	1.75	—	[24]
Antiphase defect	1.31	0.04	[25]
<u>Experiment</u>			
Kink	$0.80 \pm 0.15$	$1.24 \pm 0.07$	[21]

## C CONCLUSION

Both intrinsic and extrinsic stacking faults occur in silicon and these have been detailed in this Datareview. The stacking fault energies are determined from measurement of the dislocation configuration width. Doping does not affect these energies but impurity segregation leads to an apparent lowering. Both screw and 60° dislocations occur in silicon. Kinks and antiphase defects are important in describing dislocation motion and the formation and migration energies are tabulated.

## REFERENCES

- [1] J.P. Hirth, J. Lothe [ *Theory of Dislocations* 2nd Edn (John Wiley & Sons, New York, USA, 1982) ]
- [2] S. Amelinckx [ in *Dislocations in Solids* Ed. F.R.N. Nabarro, vol.2 (North Holland, Amsterdam, 1979) p.67 ]
- [3] H. Alexander [ in *Dislocations in Solids* Ed. F.R.N. Nabarro, vol.7 (North Holland, Amsterdam, 1986) p.113 ]
- [4] C.B. Carter [ in *Dislocations 1984* Eds. P. Veyssiére, L. Kubin, J. Castaing (Editions du CNRS, Paris, 1984) p.227 ]
- [5] I.L.F. Ray, D.J.H. Cockayne [ *Proc. R. Soc. (UK)* vol.A325 (1971) p.543 ]
- [6] G.R. Anstis, P.B. Hirsch, C.J. Humphreys, J.L. Hutchison, A. Ourmazd [ *Inst. Phys. Conf. Ser. (UK)* vol.60 (1981) p.15 ]
- [7] A. Bourret, J. Thibault-Desseaux, C. d'Anterroches [ *Inst. Phys. Conf. Ser. (UK)* vol.60 (1981) p.9 ]
- [8] A. Olsen, J. Spence [ *Philos. Mag. A (UK)* vol.43 (1981) p.947 ]
- [9] F. Louchet, J. Thibault-Desseaux [ *Rev. Phys. Appl. (France)* vol.22 (1987) p.267 ]
- [10] A. Oueldennaoua, R. Allem, A. George, J.P. Michel [ *Philos. Mag. A (UK)* vol.57 (1988) p.51 ]
- [11] R. Allem, J.P. Michel, A. George [ *Philos. Mag. A (UK)* vol.59 (1989) p.273 ]
- [12] K. Wessel, H. Alexander [ *Philos. Mag. (UK)* vol.35 (1977) p.1523 ]
- [13] P. Grosbres, J.L. Demenet, H. Garem, J.C. Desoyer [ *Phys. Status Solidi A (Germany)* vol.84 (1984) p.481 ]
- [14] J.L. Demenet, P. Boivin, J. Rabier [ *Inst. Phys. Conf. Ser. (UK)* vol.104 (1989) p.415 ]
- [15] S. Marklund [ *Phys. Status Solidi B (Germany)* vol.85 (1978) p.673 ]
- [16] R. Jones [ *J. Phys. (France)* vol.40 (1979) p.C6-23 ]
- [17] R. Jones, A. Umerski, P. Sitch, M.J. Heggie, S. Öberg [ *Phys. Status Solidi A (Germany)* vol.137 (1993) p.389 ]
- [18] P.B. Hirsch [ *Mater. Sci. Technol. (UK)* vol.1 (1985) p.666 ]
- [19] F. Louchet [ *Philos. Mag. A (UK)* vol.43 (1981) p.1289 ]
- [20] H. Gottschalk, N. Miller, S. Sauerland, P. Specht, H. Alexander [ *Phys. Status Solidi A (Germany)* vol.138 (1993) p.547 ]
- [21] H.R. Kolar, J.C.H. Spence, H. Alexander [ *Phys. Rev. Lett. (USA)* vol.77 (1996) p.4031 ]
- [22] V.V. Bulatov, S. Yip, A.S. Argon [ *Philos. Mag. A (UK)* vol. 117 (1995) p.453 ]
- [23] Y.M. Huang, J.C.H. Spence, O.F. Sankey [ *Phys. Rev. Lett. (USA)* vol. 74 (1995) p.3392 ]
- [24] S. Öberg, P.K. Sitch, R. Jones, M.J. Heggie [ *Phys. Rev. B (USA)* vol.51 (1995) p.13138 ]
- [25] R.W. Nunes, J. Bennetto, D. Vanderbilt [ *Phys. Rev. Lett. (USA)* vol.77 (1996) p.1516 ]

## 3.5 Dislocation mobilities in c-Si

K. Sumino and I. Yonenaga

June 1998

### A INTRODUCTION

Si is the material in which the kinetic properties of dislocations and related phenomena are known most accurately at present. Such knowledge is indispensable for the understanding of a variety of phenomena which occur during crystal growth, device processing, and also device operation. On the bases of these kinds of knowledge important technologies such as the growth of dislocation-free crystals, and the suppression of the occurrence of wafer warping due to thermal stress, etc., have been developed successfully. From the scientific viewpoint, the motion of dislocations in any semiconductor crystal is interesting since the crystal is characterised by an extremely high Peierls potential. As a consequence, dislocations in such a crystal can move at appreciable rates only at high temperatures. They move in a viscous manner and their velocities depend very sensitively on the temperature, and weakly on the stress, in comparison with other kinds of materials such as metals and ionic crystals.

Many papers [1–8] have so far reported experimental results on the velocities of dislocations in Si measured as functions of stress and temperature. It should be noted that the reliability of the experimental data is related to the experimental technique adopted. In most studies dislocation velocities have been measured by means of an ‘intermittent technique’; namely, the positions of dislocations are determined at room temperature by the etch pit technique or by X-ray topography, while they are displaced by stress at elevated temperature. Such intermittent techniques have several origins for error in determining the accurate velocity of dislocations. The most important and unavoidable origin of the error is the immobilisation of dislocations caused by impurities.

In the following, the most reliable experimental data, i.e. the so called ‘top data’, of the mobilities of  $60^\circ$  and screw dislocations, which are the basic types of dislocations, in Si are given. Effects brought about by various kinds of impurities are also described. Both have been investigated by means of in situ X-ray topography. A brief review of the recombination enhanced motion of dislocations is then given. The elementary process of dislocation motion is discussed in a later part of the Datareview. In the final part, cross-slip and climb motion of dislocations are described. Readers may refer to comprehensive reviews [9–11] on the kinetic properties of dislocations in semiconductors for further details.

### B HIGH PURITY SILICON

Experimental data on the velocities of  $60^\circ$  and screw dislocations in a high purity Si crystal obtained by Imai and Sumino [8] by means of in situ X-ray topography are shown in FIGURE 1. The velocities of isolated  $60^\circ$  and screw dislocations at various temperatures are plotted against shear stress. The velocities of  $60^\circ$  and screw dislocations under various stresses are plotted against reciprocal temperature in FIGURE 2. The velocities of both types of dislocations in high purity Si are linear with respect to the shear stress in the stress range 1–40 MPa, and the activation energy  $Q$  is independent of the shear stress in the temperature range 600–800°C. The dislocation velocity  $v$  is expressed well by the following equation as a function of the stress  $\tau$  and the temperature  $T$ :

$$v = v_0 (\tau/\tau_0)^m \exp(-Q/kT), m = 1 \quad (1)$$

where  $k$  is the Boltzmann constant and  $\tau_0$  is 10 MPa. The magnitudes of  $v_0$  are  $1.0 \times 10^4$  and  $3.5 \times 10^4$  m/s, and those of  $Q$  are 2.20 and 2.35 eV for  $60^\circ$  and screw dislocations, respectively. Loops of dislocations in motion retain the shape of a regular hexagon or a half-hexagon when their velocities are described by EQN (1) [8].

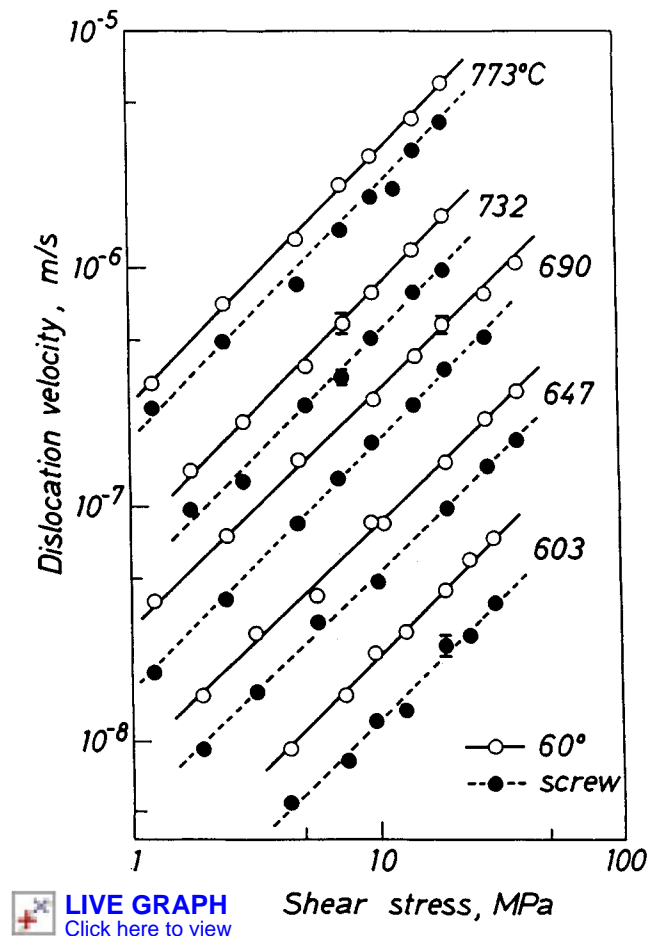


FIGURE 1 Dislocation velocity in high purity Si plotted against shear stress for various temperatures [8].

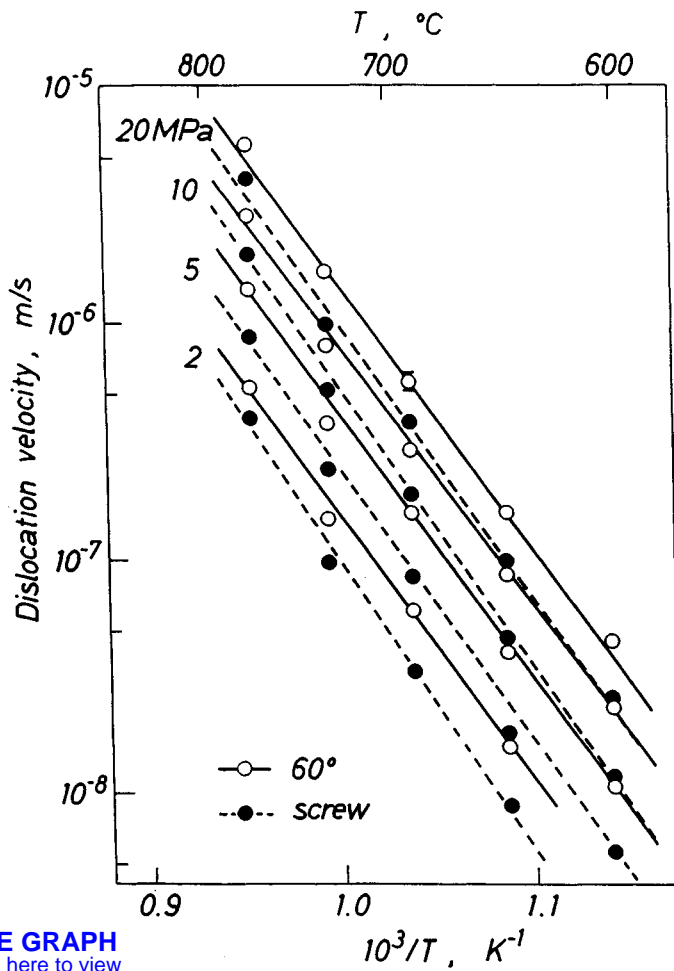
Data on dislocation mobilities at higher temperatures are limited. In the temperature range up to about 1050°C, the same magnitudes of  $Q$  as given above were obtained by Farber and Nikitenko [7] using an intermittent technique. However, the magnitude of  $Q$  was measured to be about 4 eV at temperatures higher than 1050°C. Although the exact reason for such deviation is not understood at present, it might imply that a high concentration of point defects at such high temperatures produced an effect on the dislocation motion when the velocities were measured using an intermittent technique.

### C SILICON DOPED WITH IMPURITIES

Light element impurities, e.g. C, N, O, dissolved in Si do not affect the velocities of  $60^\circ$  and screw dislocations when the dislocations are moving under high stress. Such impurities are electrically inactive when they are in the dissolved state. The dislocation velocities under such high stresses are measured to be the same as those moving in high purity Si under the same stresses, and the

### 3.5 Dislocation mobilities in c-Si

dislocations retain the shape of a regular hexagon or a half hexagon as in the case of high purity Si. However, these kinds of light element impurities do influence the kinetic behaviour of dislocations under low stresses, depending on their concentrations. FIGURE 3 shows the relationship between the velocity of a  $60^\circ$  dislocation and the shear stress at various temperatures in Si doped with C, O or N impurities at concentrations of  $1.0 \times 10^{17}$ ,  $7.4 \times 10^{17}$  or  $5.4 \times 10^{15}$  atoms  $\text{cm}^{-3}$ , respectively, together with that in high purity Si, measured by Imai and Sumino [8]. Dislocations originally in motion under a high stress cease to move when the stress is reduced below about 3 MPa in the O-doped Si and about 4 MPa in the N-doped Si. The velocity of dislocations in the O-doped Si decreases more rapidly than in the high purity Si as the stress is decreased toward the critical stress for the cessation of dislocation motion. In such a low stress range, dislocation loops lose their regular hexagon shape and assume an irregular shape. Both the deviation of the dislocation velocity from that in high purity Si with decreasing stress in the low stress range and the critical stress for the cessation of dislocation motion become remarkable as the concentration of dissolved O impurities increases.



 **LIVE GRAPH**  
Click here to view

FIGURE 2 Dislocation velocity in high purity Si plotted against reciprocal temperature for various shear stress [8].

Donor impurities such as P, As and Sb enhance the velocity of both  $60^\circ$  and screw dislocations. The increase in the dislocation velocity from that in high purity Si due to doping with donor impurities under any stress at any temperature is determined only by the concentration and is not influenced by the impurity species. FIGURE 4 shows the effect of electrically active impurities on the relation

### 3.5 Dislocation mobilities in c-Si

between the velocity and the reciprocal temperature for  $60^\circ$  and screw dislocations under a shear stress of 20 MPa [8]. Doping by donor impurities decreases the magnitudes of both  $Q$  and  $v_0$  as shown in TABLE 1 but does not affect the stress exponent  $m$  in EQN (1) when the stress is high. On the one hand, even the donor impurities that enhance the dislocation velocity lead to the rapid decrease in the dislocation velocity with decreasing stress in the low stress range, resulting in an apparently large stress exponent  $m$ , and also to the cessation of dislocation motion under low stresses [8]. Thus, the breakdown of the linear relationship between the dislocation velocity and the stress appears similar to that in Si doped with light element impurities.

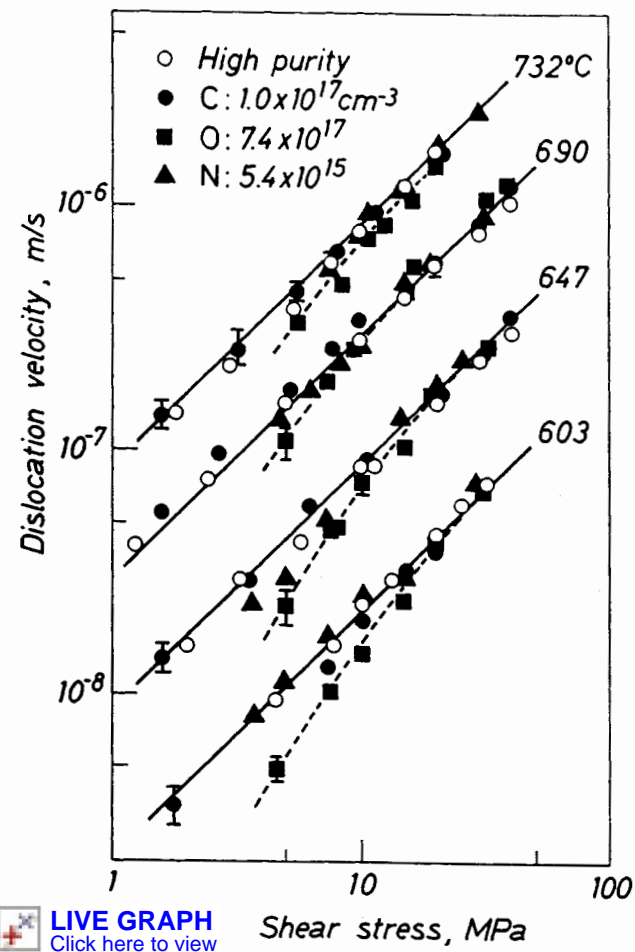


FIGURE 3 Velocity versus shear stress for  $60^\circ$  dislocations at various temperatures in Si doped with light impurities C, O or N (concentrations as shown in the figure). Open circles and solid lines are for high purity Si [8].

### 3.5 Dislocation mobilities in c-Si

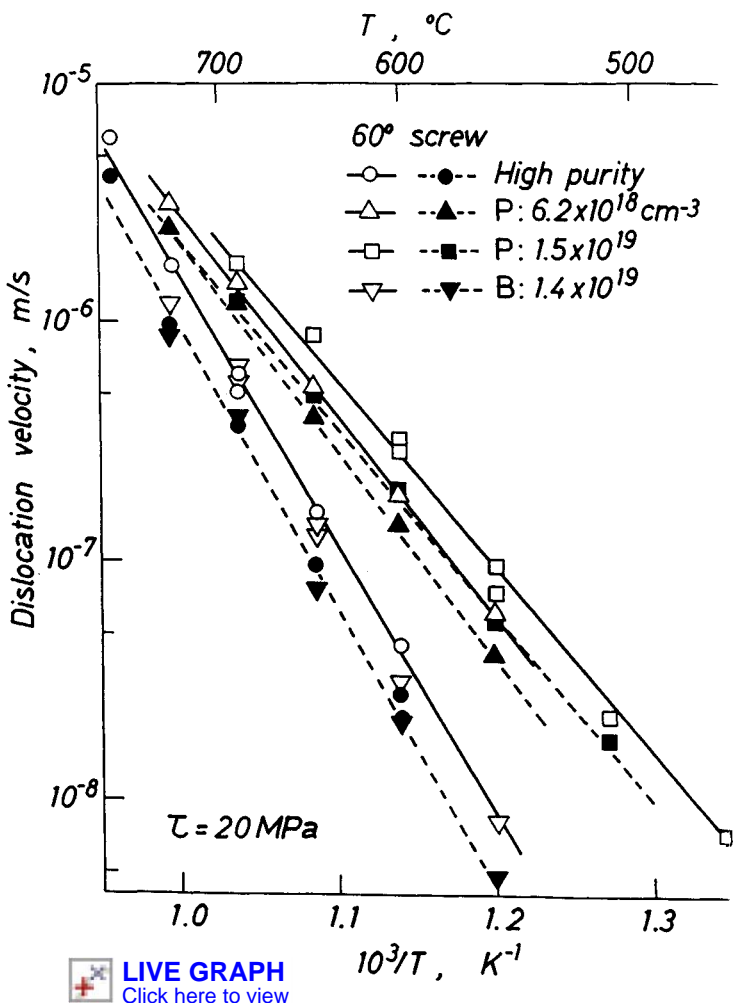


FIGURE 4 Velocities of  $60^\circ$  and screw dislocations under a shear stress of 20 MPa plotted against reciprocal temperature in Si doped with electrically active impurities P or B (concentrations as shown in the figure). Open and solid circles are for high purity Si [8].

TABLE 1 Magnitudes of  $v_0$  and Q of  $60^\circ$  and screw dislocations in high purity Si and Si doped with various impurities under a shear stress of 20 MPa [8].

	60° dislocations		Screw dislocations	
	$v_0$ ( $\text{m s}^{-1}$ )	Q (eV)	$v_0$ ( $\text{m s}^{-1}$ )	Q (eV)
High purity Si	$1.0 \times 10^4$	2.20	$3.5 \times 10^4$	2.35
P doped Si	$3.3 \times 10^1$	1.66	$7.0 \times 10^1$	1.74
[P] = $6.2 \times 10^{18} \text{ cm}^{-3}$	$1.7 \times 10^1$	1.58	9.5	1.57
[P] = $1.5 \times 10^{19} \text{ cm}^{-3}$	$6.0 \times 10^3$	2.18	$7.0 \times 10^3$	2.23
B doped Si				
[B] = $1.4 \times 10^{19} \text{ cm}^{-3}$				

Acceptor impurities such as B in Si affect the dislocation velocity very little, as also shown in FIGURE 4. The magnitude of Q in EQN (1) in B-doped Si is determined to be only slightly smaller than that in high purity Si up to a B concentration of  $1.4 \times 10^{19}$  atoms  $\text{cm}^{-3}$  [8], as shown in TABLE 1.

## D DISLOCATION IMMOBILISATION DUE TO REACTION WITH IMPURITIES

As shown in the previous section, dislocations originally moving under a high stress in a Si crystal doped with certain kinds of impurities cease to move when they are brought under a low stress after showing a perturbation in shape under intermediate stresses. Such cessation of motion is thought to be caused by segregation of impurities on the dislocations. This effect is called dislocation immobilisation due to impurity gettering. Once dislocations cease to move and are halted at a high temperature where diffusion of impurities is appreciable, an extra stress, termed the release stress, is needed to restart dislocation motion. The release stress increases with increasing duration of the halt.

FIGURE 5 shows the release stress at 647°C for 60° dislocations measured against the duration of ageing at the same temperature in Si doped with O impurities at concentrations of  $1.5 \times 10^{17}$  and  $7.5 \times 10^{17}$  atoms  $\text{cm}^{-3}$ , P impurities at a concentration of  $1.2 \times 10^{19}$  atoms  $\text{cm}^{-3}$  and N impurities at a concentration of  $5.5 \times 10^{15}$  atoms  $\text{cm}^{-3}$  [12]. The release stress was measured by means of in situ X-ray topography. The release stress increases with increasing duration of ageing, i.e. with increasing number of impurity atoms gettered by the dislocations. The number of impurity atoms accumulated on a unit length of the dislocation core can be estimated from the concentration and diffusion coefficient of the impurities as a function of the temperature and the duration of ageing. The strength of immobilisation of a dislocation per gettered atom increases in the order O, P and N. However, because of a high diffusion rate and a rather high solubility of O impurities in Si at high temperatures, immobilisation of dislocations due to impurity gettering proceeds most efficiently in O-doped Si.

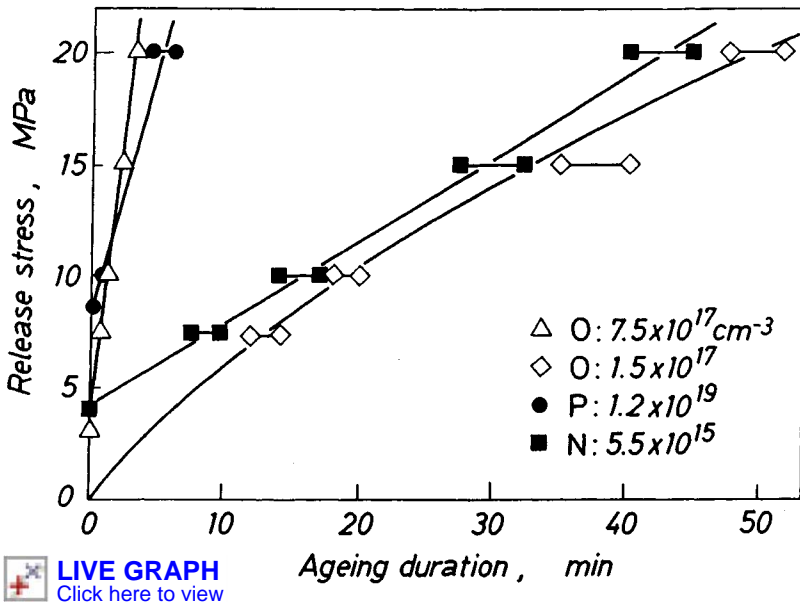


FIGURE 5 Variation of release stress at 647°C for initially fresh 60° dislocations against the duration of ageing at 647°C in Si doped with O, P or N [12] (concentrations as shown in the figure).

The stress needed to release a dislocation from the impurities gettered due to ageing has been measured for Czochralski Si as a function of the temperature at which the stress is applied [13]. The release stress after a fixed ageing decreases with an increase in the stressing temperature, showing that the release process of an aged dislocation from the gettered impurities is a thermally activated one. The energy of interaction of a pinning agent with a dislocation and the mean separation of the pinning agents along the dislocation line are deduced from the release stress versus temperature

relation experimentally measured by analysis based on a well accepted theoretical model. They have been determined to be of magnitudes around 3 eV and  $10^{-6}$  m, respectively, after ageing at 730°C for 5 to 20 min.

## E RECOMBINATION ENHANCED MOTION

Dislocation motion is enhanced during carrier injection into a crystal by forward biasing or by laser irradiation. The phenomenon is termed recombination enhanced motion of dislocations. FIGURE 6 shows how dislocation velocity in Si is enhanced by laser illumination at an energy of 1.17 eV [14] or by electron irradiation at an energy of 30 keV [15]. Velocities of 60° dislocations measured under fixed stresses in the dark and under the illumination/irradiation are plotted against reciprocal temperature. The enhancement of dislocation velocity is prominent at low temperatures but not at high temperatures. The enhancement takes place only during illumination/irradiation.

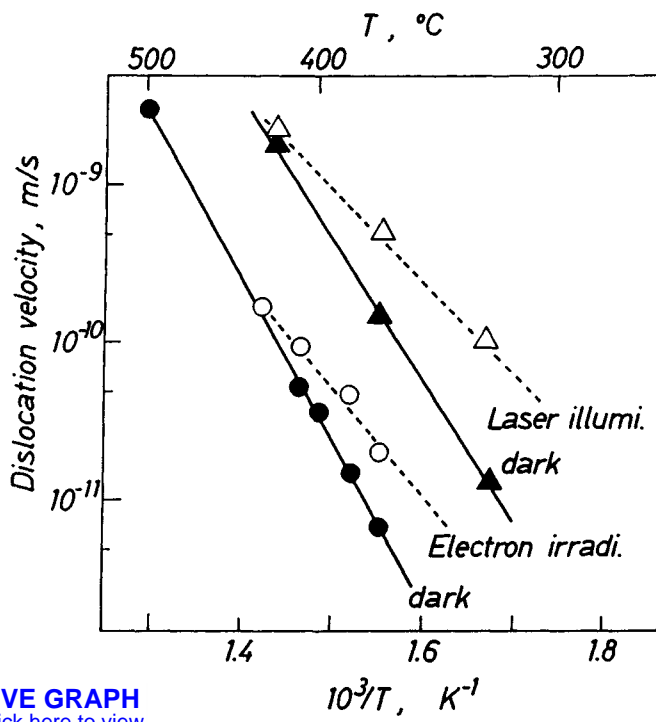


FIGURE 6 Enhanced dislocation motion in Si against reciprocal temperature which is induced by laser illumination at an energy of 1.17 eV [14] or by electron irradiation at an energy of 30 keV [15]. Solid symbols are data in the dark and open symbols are data under irradiation (triangles)/illumination (circles).

The recombination enhanced motion of a dislocation is interpreted to be caused by non-radiative electron-hole recombination at the dislocation. The energy released by the recombination is converted to a lattice vibration and can help either double kink nucleation or kink migration in the elementary process of dislocation motion as described in the following section. It is more likely that the recombination occurs at localised defects such as kinks, rather than on defect-free parts of the dislocation. The detailed discussion is given by Maeda and Takeuchi [16].

## F ELEMENTARY PROCESS OF DISLOCATION MOTION

It is commonly accepted that the elementary process of dislocation glide in a semiconductor consists of the thermally activated nucleation of a double kink on a straight dislocation line lying along the Peierls valley and the subsequent expansion of the generated kink pair along the dislocation line. Hirth and Lothe [17] derived the following equation for dislocation velocity on such a model:

$$v = (2b_p b h^2 v_D / kT) \tau \exp[-(E_k + W_m) / kT] \quad (2)$$

where  $b_p$  and  $b$  are the magnitudes of the Burgers vectors of a partial and a total dislocation, respectively,  $h$  is the period of the Peierls potential,  $v_D$  the Debye frequency,  $E_k$  the formation energy of a single kink, and  $W_m$  the activation energy of kink motion along the dislocation line. EQN (2) has a form similar to the experimental one given by EQN (1) with respect to the dependence of the dislocation velocity on the stress and the temperature.  $Q$  in EQN (1) may be interpreted to be the sum of  $E_k$  and  $W_m$ .

The enhancement of dislocation mobility with doping of donor impurities may be interpreted by the model that some acceptor level is associated with a kink on a dislocation and that the kink concentration or the kink mobility increases through the reduction of  $E_k$  or  $W_m$ , respectively, due to the occupation of such a level by electrons [18,19]. A similar mechanism may operate in the recombination enhanced motion of dislocations.

Some groups have tried to estimate the magnitudes of  $E_k$  and  $W_m$  separately using the pulse stress technique, internal friction, etc. Recently Kolar et al [20] determined the magnitudes of  $E_k$  and  $W_m$  to be 0.73 eV and 1.24 eV, respectively, by means of *in situ* high resolution electron microscopy of moving partial dislocations at 600°C in high purity FZ-Si. They suggested that the elementary process of dislocation motion is controlled by the process of kink migration. However, the complete microscopic picture which accounts for the exact dislocation velocity in Si seems not yet to have been established.

## G CROSS-SLIP AND CLIMB

Cross-slip and climb motion of dislocations play central roles in multiplication of dislocations and also in the recovery of plastically deformed crystals. Only qualitative observations are available for these processes in Si.

Multiplication centres for dislocations were observed to be formed through cross-slip of dislocations in Si by means of X-ray topography [21]. Möller et al [22] determined the activation energy for the cross-slip of isolated extended screw dislocations, by the intermittent technique, utilising the etch pit method and X-ray topography. However, it is not clear at present what is the rate determining process for cross-slip in Si.

Climb motion of dislocations is controlled by the supersaturation and diffusivity of point defects. Ourmazd et al [23] and Thibault-Desseaux et al [24] reported the climb of extended dislocations due to the absorption of the supersaturated interstitial atoms induced by electron irradiation and by plastic deformation, respectively, while Minowa et al [25] observed the climb process of extended dislocations absorbing interstitial atoms emitted from oxygen precipitates in Si. Observations by these groups were performed by means of transmission electron microscopy.

## H CONCLUSION

The most reliable data on the mobilities of 60° and screw dislocations in high purity Si and impurity-doped Si have been reviewed. Brief reviews have also been given of the recombination enhanced motion of dislocations, the elementary process of dislocation motion, and the cross-slip and climb of dislocations in Si.

## REFERENCES

- [1] A.R. Chaudhuri, J.R. Patel, L.G. Rubin [ *J. Appl. Phys. (USA)* vol.33 (1962) p.2736-46 ]
- [2] J.R. Patel, P.E. Freeland [ *Phys. Rev. Lett. (USA)* vol.18 (1967) p.833-5 ]
- [3] V.N. Erofeev, V.I. Nikitenko, V.B. Osvenskii [ *Phys. Status Solidi (Germany)* vol.35 (1969) p.79-88 ]
- [4] V.N. Erofeev, V.I. Nikitenko [ *Sov. Phys.-Solid State (USA)* vol.13 (1971) p.116-20 ]
- [5] A. George, C. Escavarage, G. Champier, W. Schröter [ *Phys. Status Solidi B (Germany)* vol.53 (1972) p.483-96 ]
- [6] A. George, G. Champier [ *Phys. Status Solidi A (Germany)* vol.53 (1979) p.529-40 ]
- [7] B.Ya. Farber, V.I. Nikitenko [ *Phys. Status Solidi B (Germany)* vol.73 (1982) p.K141-4 ]
- [8] M. Imai, K. Sumino [ *Philos. Mag. A (UK)* vol.47 (1983) p.599-621 ]
- [9] H. Alexander [ in *Dislocations in Solids* vol.7 Ed. F.R.N. Nabarro (North-Holland, Amsterdam, 1986) p.113-234 ]
- [10] K. Sumino [ in *Handbook on Semiconductors* vol.3 Ed. S. Mahajan (Elsevier Science B.V., Amsterdam, 1994) p.73-181 ]
- [11] K. Sumino, I. Yonenaga [ in *Semiconductors and Semimetals* vol.42 Ed. F. Shimura (Academic Press Inc., New York, 1994) p.449-511 ]
- [12] K. Sumino, M. Imai [ *Philos. Mag. A (UK)* vol.47 (1983) p.753-66 ]
- [13] M. Sato, K. Sumino [ Proc. IXth Yamada Conf. on Dislocations in Solids Tokyo, 27-31 Aug. 1984, Eds. H. Suzuki, T. Ninomiya, K. Sumino, S. Takeuchi (University of Tokyo Press, Tokyo, 1985) p.391-4 ]
- [14] K.H. Küster, H. Alexander [ *Physica B (Netherlands)* vol.116 (1983) p.594-9 ]
- [15] N. Maeda, K. Kimura, S. Takeuchi [ *Bull. Acad. Sci. USSR Phys. Ser. (USA)* vol.51 (1987) p.93-8 ]
- [16] K. Maeda, S. Takeuchi [ in *Dislocations in Solids* vol.10 Eds. F.R.N. Nabarro, M.S. Duesbery (North-Holland, Amsterdam, 1996) p.443-504 ]
- [17] J.P. Hirth, J. Lothe [ *Theory of Dislocations* (Wiley-Interscience, 1982) ]
- [18] P.B. Hirsch [ *J. Phys. C (France)* vol.40 (1979) p.117-21 ]
- [19] R. Jones [ *Philos. Mag. B (UK)* vol.42 (1980) p.213-9 ]
- [20] H.R. Kolar, J.C.H. Spence, H. Alexander [ *Phys. Rev. Lett. (USA)* vol.77 (1996) p.4031-4 ]
- [21] A. George, C. Escaravage, W. Schröter, G. Champier [ *Cryst. Lattice Defects (UK)* vol.4 (1973) p.29-36 ]
- [22] H.-J. Möller, H. Ewaldt, P. Haasen [ *Phys. Status Solidi A (Germany)* vol.55 (1979) p.469-78 ]
- [23] A. Ourmazd, D. Cherns, P.B. Hirsch [ *Inst. Phys. Conf. Ser. (UK)* no.60 (1981) p.39-44 ]
- [24] J. Thibault-Desseaux, H.O.K. Kirchner, J.L. Putaux [ *Philos. Mag. A (UK)* vol.60 (1989) p.385-400 ]
- [25] K. Minowa, I. Yonenaga, K. Sumino [ *Mater. Lett. (Netherlands)* vol.11 (1991) p.164-70 ]

## CHAPTER 4

### THERMAL PROPERTIES (*Edited by M.R. Brozel*)

- 4.1 Specific heats of c-Si and molten Si
- 4.2 Thermal expansion coefficients of c-Si
- 4.3 Melting points of Si
- 4.4 Phonon spectrum of c-Si
- 4.5 Thermal conductivity of c-Si
- 4.6 Thermal diffusivity of c-Si
- 4.7 Surface tension of liquid Si
- 4.8 Heat of fusion of Si

## 4.1 Specific heats of c-Si and molten Si

H.-M. Kagaya and T. Soma (updated by M.R. Brozel)

April 1998

### A SPECIFIC HEAT OF c-Si

Data relevant to the specific heat at constant pressure ( $c_p$ ) of Si are given in [1–6]. Recommended data are summarised in TABLE 1 together with the Debye temperature ( $\theta$ ).

TABLE 1 Specific heat and Debye temperature data.

T (K)	$c_p$ (J g <sup>-1</sup> K <sup>-1</sup> )	$\theta$ (K)	T (K)	$c_p$ (J g <sup>-1</sup> K <sup>-1</sup> )	$\theta$ (K)
5	$0.340 \times 10^{-4}$	641	280	0.691	645
10	$0.276 \times 10^{-3}$	631	300	0.713	643
20	$0.341 \times 10^{-2}$	545	400	0.785	650
40	$0.441 \times 10^{-1}$	463	500	0.832	653
60	0.115	492	600	0.849	654
80	0.188	535	700	0.866	
100	0.259	572	800	0.883	655
120	0.328	599	900	0.899	
140	0.395	617	1000	0.916	656
160	0.456	629	1100	0.933	
180	0.511	637	1200	0.950	
200	0.557	643	1300	0.967	
220	0.597	647	1400	0.983	
240	0.632	648	1500	1.000	
260	0.665	647	1600	1.017	

Notes (O: observed, Th: theoretical and E: extrapolated)

1. Extrapolation of the specific heat to the melting point (1687 K) gives 1.032 J g<sup>-1</sup> K<sup>-1</sup> (E).
2. The Debye temperature extrapolated to T = 0 K gives 645 K and reaches about 657 K at the melting point (E).
3. The Debye temperature has a minimum value of 463 K at T = 39 K (O).
4. At low temperatures below 5 K [2], the specific heat is given by:  
 $c_p = (0.716 T + 0.243 T^3) \times 10^{-6}$  within  $\pm 0.002 \times 10^{-6}$  J g<sup>-1</sup> K<sup>-1</sup> (Th).
5. Above 5 K the ratio  $c_p/T^3$  has a maximum at 39 K [2,4] and decreases rapidly with the approximate dependence of  $T^{-2.22}$  from 100 K to 500 K (Th).
6. Above 500 K the tabulated data are given by:  
 $c_p = 0.748 + 0.000168 T$  within  $\pm 0.004$  (Th).

#### *4.1 Specific heats of c-Si and molten Si*

7. Anharmonic contributions to the specific heat and the difference between the specific heat at constant pressure and that at constant volume of Si are appreciable at high temperatures (see [7–10]) (Th).

### **B SPECIFIC HEAT OF MOLTEN SILICON**

Using a high temperature electrostatic levitator it has recently been possible to measure the constant-pressure specific heat of molten Si both at temperatures above 1687 K (the melting point) and under considerable supercooling.  $c_p$  drops non-linearly from  $\sim 34 \text{ J mole}^{-1} \text{ K}^{-1}$  at 1360 K to  $25 \text{ J mole}^{-1} \text{ K}^{-1}$  at 1800 K. The authors note that this non-linear behaviour contrasts with the linear behaviour observed in many pure metals [11].

### **REFERENCES**

- [1] C.T. Anderson [ *J. Am. Chem. Soc. (USA)* vol.52 (1930) p.2301 ]
- [2] N. Pearlmon, P.H. Keesom [ *Phys. Rev. (USA)* vol.88 (1952) p.398, and vol.85 (1952) p.730 ]
- [3] P.V. Gul'tyaev, A.V. Petrov [ *Sov. Phys.-Solid State (USA)* vol.1 (1959) p.330 ]
- [4] P. Flubacher, A.I. Leadbetter, J.A. Morrison [ *Philos. Mag. (UK)* vol.4 (1959) p.273 ]
- [5] P.B. Kantor, O.M. Kisel, E.M. Fomichev [ *Ukr. Fiz. Zh. (USSR)* vol.5 (1960) p.358 ]
- [6] H.R. Shanks, P.D. Maycock, P.H. Sidles, G.C. Danielson [ *Phys. Rev. (USA)* vol.130 (1963) p.1743 ]
- [7] M.E. Fine [ *J. Chem. Phys. (USA)* vol.21 (1953) p.1427 ]
- [8] D.M.T. Newsham [ *Phys. Rev. (USA)* vol.152 (1966) p.841 ]
- [9] P.C. Trivedi, H.O. Sharma, L.S. Kothari [ *J. Phys. C (UK)* vol.10 no.18 (1977) p.3487-97 ]
- [10] P.C. Trivedi [ *J. Phys. C (UK)* vol.18 no.5 (1985) p.983 ]
- [11] W.K. Rhim, S.K. Chung, A.J. Rulison, R.E. Spjut [ *Int. J. Thermophys. (USA)* vol.18 no.12 (1997) p.489 ]

## 4.2 Thermal expansion coefficients of c-Si

T. Soma and H.-M. Kagaya (updated by M.R. Brozel)

April 1998

Data relevant to the linear thermal expansion coefficient  $\alpha$  ( $K^{-1}$ ) of Si are given in [1–14]. Recommended data are summarized in TABLE 1.

TABLE 1 Thermal expansion coefficient data.

T (K)	$\alpha$ ( $10^{-6} K^{-1}$ )	T (K)	$\alpha$ ( $10^{-6} K^{-1}$ )	T (K)	$\alpha$ ( $10^{-6} K^{-1}$ )
5	$0.6 \times 10^{-4}$	180	1.061	700	4.016
10	$0.48 \times 10^{-3}$	200	1.406	800	4.151
20	$-0.29 \times 10^{-2}$	220	1.715	900	4.185
40	-0.164	240	1.986	1000	4.258
60	-0.400	260	2.223	1100	4.323
80	-0.472	280	2.432	1200	4.384
100	-0.339	300	2.616	1300	4.442
120	-0.057	400	3.253	1400	4.500
140	0.306	500	3.614	1500	4.556
160	0.689	600	3.842	1600	4.612

Notes (O: observed, Th: theoretical and E: extrapolated)

1. Extrapolation to the melting point (1687 K) gives  $4.661 \times 10^{-6} K^{-1}$  (E).

2. The thermal expansion coefficient has a minimum at 80 K (O).

3. Below 14 K, the tabulated data are given by:

$$\alpha = 4.8 \times 10^{-13} T^3 \text{ within } \pm 0.01 \times 10^{-8} K^{-1} [12] \text{ (Th).}$$

4. From 120 K to 1500 K, a smooth curve of the linear thermal expansion coefficient given by:

$$\alpha = 3.725 \times 10^{-6} [1 - \exp(-5.88 \times 10^{-3} (T-124))] + 5.548 \times 10^{-10} T \text{ within } \pm 2 \times 10^{-7} K^{-1} \text{ has been proposed [14] (Th).}$$

5. Above 1000 K the tabulated data are given by:

$$\alpha = (3.684 + 0.00058 T) \times 10^{-6} \text{ within } \pm 0.004 \times 10^{-6} K^{-1} \text{ (Th).}$$

6. Above 600 K, the tabulated values obey the Gruneisen relation in which the ratio of thermal expansion coefficient to specific heat is  $(1.101 \pm 0.022) \times 10^{-6} \text{ g/cal}$  (Th).

7. The fact that there is a systematic difference in lattice parameters between powder and single-crystal samples has been experimentally reported [14] (O).

## 4.2 Thermal expansion coefficients of c-Si

### REFERENCES

- [1] D.F. Gibbons [ *Phys. Rev. (USA)* vol.112 (1958) p.136 ]
- [2] S.I. Novikova, P.G. Strelkov [ *Sov. Phys.-Solid State (USA)* vol.1 (1960) p.1687 ]
- [3] S.I. Novikova [ *Sov. Phys.-Solid State (USA)* vol.6 (1964) p.269 ]
- [4] D.N. Batchelder, R.O. Simmons [ *J. Chem. Phys. (USA)* vol.41 (1964) p.2324 ]
- [5] R.H. Carr, R.D. McCammon, G.K. White [ *Philos. Mag. (UK)* vol.12 (1965) p.157 ]
- [6] P.W. Sparks, C.A. Swenson [ *Phys. Rev. (USA)* vol.163 (1967) p.779 ]
- [7] V.V. Zhdanova, M.G. Kekua, T.Z. Samaclashvill [ *Inorg. Mater. (USA)* vol.3 (1967) p.1112 ]
- [8] A.P. Nasekows'kii [ *Ukr. Fiz. Zh. (USSR)* vol.12 (1967) p.1352 ]
- [9] H. Ibach [ *Phys. Status Solidi B (Germany)* vol.31 (1969) p.625 ]
- [10] G.K. White [ *J. Phys. D (UK)* vol.6 (1973) p.2070 ]
- [11] M.A. Norton, J.W. Berthold III, S.F. Jacobs, W.A. Plummer [ *J. Appl. Phys. (USA)* vol.47 no.4 (1976) p.1683-5 ]
- [12] K.G. Lyon, G.L. Salinger, C.A. Swenson, G.K. White [ *J. Appl. Phys. (USA)* vol.48 no.3 (1977) p.865-8 ]
- [13] R.B. Roberts [ *J. Phys. D (UK)* vol.14 (1981) p.L163 ]
- [14] Y. Okada, Y. Tokumaru [ *J. Appl. Phys. (USA)* vol.56 no.2 (1984) p.314-20 ]

## **4.3 Melting points of Si**

J.C. Brice (updated by M.R. Brozel)

April 1998

### **A INTRODUCTION**

The accurate measurement of temperatures at about 1400°C is far from easy (see [1–3]). Temperature transducers require careful calibration and have poor ageing characteristics. In this range the transducers are usually thermocouples (comprising platinum group metals). The majority show negative ageing: the output falls by of the order of the equivalent of 3 degrees after about 1000 hours at temperature. Temperature cycling, which is an essential part of the usual method (differential thermal analysis) of measuring melting points, increases the ageing rate. Thus thermocouples need to be calibrated regularly. Early workers in the field (prior to 1948) had the added problem that there was no universally accepted temperature scale in this range. This may account for some of the scatter of results from early work which gave a scatter of recommended melting point values over the range 1400 to 1420°C. Individual results spread over a bigger range (1396 to 1444°C) (see the early results reported in [4–6]). These early results will be ignored here. The later data given in [4–6] and in [7] and [8] show a much smaller scatter. See TABLE 1 and the other data given below.

Measuring the melting point of silicon presents two particular problems:

- (a) Silicon, particularly when molten, is very reactive and most, if not all, impurities depress the melting point. The usual choice of material to contain the melt and protect the thermocouple is vitreous silica but this dissolves slowly in silicon leading to contamination by oxygen which lowers the melting point by about 1 degree for each atom per cent in the melt (see the phase diagram in [9]).
- (b) Spontaneously nucleated silicon is bounded by (111) facets and to achieve a reasonable growth rate a measurable supercooling is needed (a growth rate of 2 mm/min requires a supercooling of about 2 degrees—Takao Abe, private communication). Thus thermal arrests on cooling curves will occur at temperatures below the melting point and the average of arrests on heating and cooling will be depressed.

In 1948 the International Practical Temperature Scale (IPTS-48) was published. This scale was revised in 1968 leading to the current scale (IPTS-68). At 1400°C, these scales differ by 2.0 degrees (see [10, p.4–6]). Adding 2.0 degrees to an IPTS-48 value yields an IPTS-68 value. In what follows, this has been done when necessary so that from here on all temperatures are on the 1968 scale.

### **B PREVIOUS RECOMMENDATIONS**

In 1950 a value of 1412°C was recommended in a US Atomic Energy Commission report [11]. In 1952 NBS published its Circular 500 [12] which also gave 1412°C. In 1968 Hultgren et al [14] gave 1414°C and this value was given again in 1973 [15].

### **C SOME DATA AND DISCUSSION**

Post 1948 data from [4–8] are summarised in TABLE 1 which gives the number of times a value has been reported.

### 4.3 Melting points of Si

TABLE 1 Melting temperatures.

Temperature (°C)	1408	1410	1412	1414	1416
Number of reports	1	1	7	8	3

The mean of these data is 1413.1°C with a standard error of 0.31 degrees. However, as discussed in the introduction, all the likely errors are negative so that the mean is likely to be below the true value. Thus a better choice would be the median (i.e. 1414°C). This has a standard error of about 0.4 degrees. Note that 1414°C is also the value most frequently observed.

### D RECOMMENDATION

A safe choice (half way between the previous recommendations) would be 1413 ±2°C. However, on the basis of the evidence, a reasonable recommendation is 1414.0°C with an uncertainty of 0.9 degrees corresponding to a 90% confidence level.

### E RECENT OBSERVATIONS

Recently the occurrence of an intermediate metastable phase close to the melting temperature has been discussed [16,17]. Its appearance may have contributed to some of the uncertainties alluded to in the previous section. A similar observation relating to a quadratic dependence of the density of molten Si on temperature,

$$\rho(T) = \rho_m - 1.69 \times 10^{-4} (T - T_m) - 1.75 \times 10^{-7} (T - T_m)^2$$

where  $\rho(T)$  is the density in  $\text{g cm}^{-3}$ ,  $T_m = 1687 \text{ K}$  (1414°C) and  $\rho_m$  is the density at  $T_m$  ( $2.56 \text{ g cm}^{-3}$ ), has been discussed in terms of bond breaking and the possible loss of short range order [18].

### F PRESSURE DEPENDENCE

Under a pressure of about one atmosphere, silicon melts at 1414.0°C (1687.1 K). The effect of pressure on the melting point is easily calculated using the Clausius–Clapeyron equation which shows that

$$dT_m/dP = T_m[V_l - V_s]/H \quad (1)$$

where  $V_s$  and  $V_l$  are given by  $M/\rho(l)$  and  $M/\rho(s)$  and  $P$  is the pressure. The other symbols are explained in TABLE 2 which gives the values found in [19].

From EQN (1), the rate of fall of  $T_m$  with pressure is

$$-dT_m/dP = 3.3 \times 10^{-8} \text{ K/Pa}$$

or since 1 atmosphere = 101325 Pa

$$dT_m/dP = -0.0034 \text{ K/atmosphere}$$

Note that the accuracy of this result depends critically on the accuracy of the density values. With the values used here, the result is very uncertain: errors of 10 to 50% are probable. It must be emphasised

### 4.3 Melting points of Si

that this estimate applies at low pressures. At high pressures, it is necessary to take account of the compressibilities of the solid and the liquid when estimating  $V_s$  and  $V_l$ .

TABLE 2 Values of parameters used to describe pressure dependence.

Symbol	Parameter	Value	Units
H	Latent heat of fusion	$5.066 \times 10^4$	J mole <sup>-1</sup>
T <sub>m</sub>	Melting point	1687.0	K
M	Atomic weight	$28.086 \times 10^{-3}$	kg mole <sup>-1</sup>
$\rho(s)$	Density of solid at T <sub>m</sub> *	$2.30 \times 10^3$	kg m <sup>-3</sup>
$\rho(l)$	Density of liquid at T <sub>m</sub> †	$2.51 \times 10^3$	kg m <sup>-3</sup>
V <sub>s</sub>	Molar volume of solid	$1.22 \times 10^{-5}$	m <sup>3</sup> mole <sup>-1</sup>
V <sub>l</sub>	Molar volume of liquid	$1.12 \times 10^{-5}$	m <sup>3</sup> mole <sup>-1</sup>

\* Calculated from the room temperature density ( $2.34 \times 10^3$  kg m<sup>-3</sup>) and the thermal expansion coefficient, assumed to be  $8 \times 10^{-6}$  K<sup>-1</sup> on average.

† A more recent measurement is  $2.56 \times 10^3$  kg m<sup>-3</sup> [18].

According to Landolt-Bornstein [20], T<sub>m</sub> = 1190°C at P = 40 kb. This gives an average dT<sub>m</sub>/dP of -0.0057 K/atmosphere in the range 1 to 40 kb and suggests that dT<sub>m</sub>/dP is a decreasing function of pressure.

## G CONCLUSION

The balance of recent and older data on the melting point of silicon suggests a value of  $1414.0 \pm 0.9^\circ\text{C}$ , at one atmosphere pressure. The rate of fall of this temperature with increasing pressure can be calculated, to within large error bounds, with the Clausius-Clapeyron equation, although at high pressures it is necessary to take into account the solid and liquid compressibilities.

## REFERENCES

- [1] ASTM [ *Manual on the Use of Thermocouples in Temperature Measurement* (ASTM, Philadelphia, 1981) ]
- [2] J.V. Nicholas, D.R. White [ *Traceable Temperatures* (DSIR, New Zealand, 1982) ]
- [3] T.J. Quinn [ *Temperature* (Academic Press, London, 1983) ]
- [4] M. Hansen [ *Constitution of Binary Alloys* (McGraw-Hill, New York, 1958) ]
- [5] R.P. Elliott [ *Constitution of Binary Alloys: First Supplement* (McGraw-Hill, New York, 1959) ]
- [6] F.A. Shunk [ *Constitution of Binary Alloys: Second Supplement* (McGraw-Hill, New York, 1969) ]
- [7] E.A. Brandes [ *Smithells Metals Reference Book* (Butterworth, London, 1983) ]
- [8] W.G. Moffatt [ *The Handbook of Binary Phase Diagrams* (Genium Publishing Corp., Schenectady, 1976) ]
- [9] J.C. Brice [ *Curr. Top. Mater. Sci. (Netherlands)* vol.4 (1980) ch.5 ]
- [10] D.W. Gray [ *American Institute of Physics Handbook* (McGraw-Hill, New York, 1972) ]
- [11] US Atomic Energy Commission [ *Report ANL-5750*, cited by Hodgman in *Handbook of Chemistry and Physics* (Chemical Rubber Publishing, Cleveland, 1960) p.1870-1 ]
- [12] F.D. Rossini, D.D. Wagman, W.H. Evans, S. Levine, I. Jaffe [ *Selected Values of Chemical Thermodynamics Properties* (NBS Circular 500, Washington, 1952) ]
- [13] H.L. Anderson [ *Physics Vade Mecum* (AIP, New York, 1981) ]

#### 4.3 Melting points of Si

- [14] R.R. Hultgren, R.L. Orr, F.D. Anderson, K.K. Kelley [ *Selected Values of Thermodynamic Properties of Metals and Alloys* (Wiley, New York, 1968) ]
- [15] R.R. Hultgren, P.O. Desai, D.T. Hawkins, K.K. Kelley, D. Wagman [ *Selected Values of Thermodynamic Properties of Elements* (Wiley, New York, 1973) ]
- [16] K. Yamamoto, T. Abe, S. Takasu [ *Jpn. J. Appl. Phys. I (Japan)* vol.30 (1991) p.2423-6 ]
- [17] P. Tchofo Dinda, G. Vlastou-Tsinganos, N. Flytzanis, A.D. Mistriotis [ *Phys. Rev. B Condens. Matter (USA)* vol.51 no.19 (1995) p.13697-704 ]
- [18] W.K. Rhim, S.K. Chung, A.J. Rulison, R.E. Spjut [ *Int. J. Thermophys. (USA)* vol.18 (1997) p.459-69 ]
- [19] E.A. Brandes [ *Smithells Metals Reference Book* (Butterworth, London, 1983) p.3-1, 8-3, 14-2 and 14-8 ]
- [20] Landolt-Bornstein [ *Numerical Data and Functional Relationships in Sci. & Tech. (New Series)* vol.III/17a (Springer Verlag, Berlin, 1982) section B1 ]

## 4.4 Phonon spectrum of c-Si

M.N. Wybourne (updated by M.R. Brozel)

June 1998

### A INTRODUCTION

This Datareview presents the results of inelastic neutron scattering, Raman spectroscopy and infrared spectroscopy measurements of the phonon spectrum of silicon. New data are also presented from theoretical work on crystalline silicon and surfaces and both theoretical and experimental work on heterostructures.

### B PHONON SPECTRUM

Details of the phonon spectrum of silicon have been studied primarily by the techniques of inelastic neutron scattering, Raman spectroscopy and infrared spectroscopy. Some of the earliest inelastic neutron scattering measurements of the phonon dispersion were reported by Brockhouse [1]. Later, with improved resolution and calibration, Dolling [2] presented dispersion curve data at 300 K for the three directions  $[\zeta 0 0]$ ,  $[\zeta \zeta \zeta]$ , and  $[0 \zeta \zeta]$ . For the two high symmetry directions  $[\zeta 0 0]$  and  $[\zeta \zeta \zeta]$ , the modes are strictly longitudinal (L) or transverse (T), while in the  $[0 \zeta \zeta]$  direction symmetry restrictions only require that the polarisation vector of the modes is in the  $[0 1 1]$  mirror plane.

Some of the phonon frequencies, with polarisation type, are given in TABLE 1.

TABLE 1 Phonon frequencies.

Reduced wavevector co-ordinates	Acoustic (THz)		Optical (THz)	
	T	L	T	L
0.0 0.0 0.0				$15.53 \pm 0.23$
0.2 0.0 0.0	$2.00 \pm 0.08$	$3.20 \pm 0.12$	$15.40 \pm 0.36$	$15.55 \pm 0.38$
0.4 0.0 0.0	$3.45 \pm 0.06$	$6.10 \pm 0.15$	$14.65 \pm 0.33$	$15.15 \pm 0.35$
0.6 0.0 0.0	$4.27 \pm 0.10$	$8.50 \pm 0.20$	$14.18 \pm 0.35$	$14.60 \pm 0.35$
0.8 0.0 0.0	$4.46 \pm 0.07$	$10.60 \pm 0.20$	$13.95 \pm 0.34$	$13.60 \pm 0.27$
1.0 0.0 0.0	$4.49 \pm 0.06$	$12.32 \pm 0.20$	$13.90 \pm 0.30$	$12.32 \pm 0.20$
0.1 0.1 0.1	$1.53 \pm 0.03$	$3.00 \pm 0.13$	$15.40 \pm 0.37$	$15.45 \pm 0.35$
0.2 0.2 0.2	$2.62 \pm 0.05$	$5.60 \pm 0.15$	$15.10 \pm 0.30$	$14.78 \pm 0.30$
0.3 0.3 0.3	$3.22 \pm 0.05$	$8.03 \pm 0.15$	$14.83 \pm 0.30$	$14.13 \pm 0.30$
0.4 0.4 0.4	$3.41 \pm 0.05$	$10.12 \pm 0.20$	$13.78 \pm 0.27$	$13.30 \pm 0.22$
0.5 0.5 0.5	$3.43 \pm 0.05$	$11.35 \pm 0.30$	$14.68 \pm 0.30$	$12.60 \pm 0.32$
0.0 0.2 0.2	$2.91 \pm 0.07$	$4.55 \pm 0.10$		$15.10 \pm 0.35$
0.0 0.4 0.4	$5.11 \pm 0.09$	$7.60 \pm 0.20$	$14.80 \pm 0.40$	$13.87 \pm 0.28$
0.0 0.5 0.5	$6.06 \pm 0.12$	$8.60 \pm 0.18$	$14.55 \pm 0.38$	$12.83 \pm 0.27$
0.0 0.75 0.75	$6.56 \pm 0.14$	$10.85 \pm 0.30$	$14.40 \pm 0.38$	$11.15 \pm 0.30$
0.0 0.85 0.85	$5.60 \pm 0.11$	$11.70 \pm 0.30$	$14.20 \pm 0.34$	$11.70 \pm 0.30$

Inelastic neutron scattering measurements have also been made by Nilsson and Nelin [3] to study the homology of the phonon dispersion relations of silicon and germanium. These authors presented data

#### 4.4 Phonon spectrum of c-Si

at 300 and 80 K with less uncertainty than the results of Dolling [2]; however, there are no significant differences between these sets of data.

Many different models have been used to describe the neutron scattering data, the earliest being the shell model of Cochran [4]. One of the best fits to the measured phonon frequencies (approximately 2%) is given by the Weber adiabatic bond-charge model [5]. Other calculations using the electron-ion Hamiltonian of the system have also been developed to model the phonon dispersion. These calculations treat the Hamiltonian in two ways, one in which the phonons are considered as small perturbations of the system [6] and the other in which the total energy of the lattice containing ‘frozen-phonons’ of arbitrary displacements is calculated [7]. Results of such calculations model the phonon frequencies to within ~5%, but are only tractable at the Brillouin zone centre and at points of high symmetry. A new ab initio approach to calculating the phonon characteristics was presented by Kunc and Martin [8] in which the force constants in real space are determined directly. Fleszar and Resta [9] have used this technique for silicon and have reported convergence to better than 3% for both the optical and acoustic phonon frequencies.

The Raman spectrum of silicon has been thoroughly studied by many authors and, with the help of the inelastic neutron scattering data, the interpretation is well understood. The diamond structure of silicon allows only one first-order Raman active phonon at the Brillouin zone centre. The first-order Raman spectrum has been investigated by Russell [10], Parker et al [11], Hart et al [12] and Chang et al [13], and the zone centre optical phonon frequency has been determined to be  $15.56 \pm 0.03$  THz. The second order Raman spectrum has been studied by Weinstein and Cardona [14] and Temple and Hathaway [15]. Using different polarisations, these workers were able to separate the independent components of the Raman tensor so that a comparison with the theoretical Raman spectrum [16], together with the unambiguous assignment of the spectral features, was possible. Weinstein and Cardona, and Temple and Hathaway have also discussed the comparison of the two phonon Raman spectrum intensity with the calculated phonon density of states for silicon [17].

The infrared absorption spectrum of silicon was first studied by Johnson [18] before neutron-scattering data were available. Further measurements and assignments of the spectral features were made later by Johnson and Loudon [19] and Balkanski and Nusimovici [20]. A comparison of the phonon frequencies obtained at high symmetry points in the Brillouin zone by neutron-scattering [2], Raman spectroscopy [15] and infrared spectroscopy [20] is given in TABLE 2.

TABLE 2 Phonon frequencies from infrared and Raman spectroscopies and neutron scattering.

Critical points		Phonon frequencies (THz)		
	Mode	Infrared [20]	Raman [15]	Neutron [2]
$\Gamma$		$15.50 \pm 0.06$	$15.56 \pm 0.03$	$15.53 \pm 0.09$
	TO	$13.46 \pm 0.09$	$13.79 \pm 0.06$	$13.91 \pm 0.30$
X	TA	$4.65 \pm 0.15$	$4.53 \pm 0.06$	$4.50 \pm 0.06$
	TO	$14.78 \pm 0.06$	$14.69 \pm 0.06$	$14.69 \pm 0.30$
L	TA	$3.39 \pm 0.06$	$3.39 \pm 0.06$	$3.42 \pm 0.06$
	TO	$14.33 \pm 0.39$	$14.09 \pm 0.06$	$14.42 \pm 0.39$
W				

Stress-induced changes in the phonon spectrum offer a convenient method by which to study anharmonic effects and to study the lattice dynamic models of silicon. Weinstein and Piermarini [21] have studied the first and second order Raman spectra of silicon under large applied hydrostatic pressures. The general effect of the pressure on the phonon dispersion near the zone edge was found to be that the transverse acoustic modes softened while the optical modes shifted to higher energies. The best fit to the pressure dependence of the first order Raman peak is

$$\Omega = 15.56 \pm 0.03 \text{ THz} + (15.6 \pm 0.9 \text{ GHz/kbar})P + (-21 \pm 6 \text{ MHz/kbar}^2) P^2$$

where P is the pressure. Estel et al [22] have reported phonon frequency changes in the  $\zeta\zeta\zeta$  transverse acoustic branch, with applied uniaxial stress, studied by inelastic neutron scattering. With a stress of 1.01 GPa in the [1 1 1] direction, the energy shifts reported are from +0.5% near the zone centre to -1.2% at the zone edge.

The internal stress of silicon deposited epitaxially onto sapphire has been studied using Raman spectroscopy to measure the shift in the zone-centre optical phonon frequency. In this way, Englert et al [23] were able to determine an internal stress of about  $7.0 \pm 0.3$  kbar for [001] silicon layers on [1012] sapphire substrates. Subsequently, this technique has been used to study the stress relief of deposited films that have been annealed [24] or silicon implanted and then annealed [25].

## C UPDATE

Since the previous edition of this book, there have been many advances in this subject, both in the fields of phonons in bulk crystalline Si and also in surface effects and heterostructures.

### C1 Bulk Crystalline Si (Theory)

Calculations of phonon spectra have been considered from a cluster approach [26], from a pseudo potential method and local-density approximation [27], or using density-functional theory and the adiabatic approximation [28]. Each of these approaches has reported good agreement with experiment. Anharmonic effects have been studied in silicon (and diamond) by Wang et al [29]. Similar work is reported by Narasimhan and Van der Bilt [30]. Monte-Carlo calculations have been employed by Hinckley and Singh [31] to predict ohmic hole mobility in Si and Ge and by Tamura [32] to describe quasi-diffusive phonon propagation in Si. Electron-phonon interactions have been studied by Tamura et al [33] and Revinskii [34]. Considerations of phonon spectra have been used by Omini and Sparavigna [35] to predict thermal conductivity, by Koskowich et al [36] to model near-infrared photon absorption due to phonon-assisted scattering and by Panzarini and Colombo [37] to study the diffusion of hydrogen in Si, the latter paper using a tight binding approach within a method based on molecular dynamics.

Considerations of the phonon spectrum involvement in the transport parameters has led Behnen [38] to estimate the Seebeck coefficient of Si.

### C2 Surface Effects (Theory)

Generally, surface phonons have been modelled on the (111) exposure although there is interest in the (110) surface. The surface phonon spectrum has been considered by Stich and Terakura, Jeongnim Kim et al and Stich et al [39–41] for the  $7 \times 7$  reconstructed (111) surface. The latter paper considers anharmonic effects.

The  $2 \times 1$  reconstruction of the (111) surface using an ab-initio approach is able to predict both the surface phonon spectrum and resulting dipole activity [42]. A similar system is reported by Ancilotto et al [43]. The (001) surface has been studied by Mele [44] assuming a surface dimer reconstruction.

There has been similar effort in modelling the Si surface with important chemical layers. The phonon spectrum of Si(111) covered with a monolayer of hydrogen is reported in [45–47], the last of these

#### 4.4 Phonon spectrum of *c*-Si

studies also considering a monolayer covering of As. This Si-As surface is also reported in [48] and [49]. The surface phonon spectrum of H on Si(110) has been reported by Graschus et al [50].

### C3 Heterostructures Involving Si (Theory and Experiment)

The importance of the Si/Si<sub>1-x</sub>Ge<sub>x</sub> systems has resulted in several attempts at modelling the phonon spectra. The simplest of these heterostructures is the Si/Ge system [51–55]. The more general problem of modelling the Si/Si<sub>1-x</sub>Ge<sub>x</sub> systems has been approached by [55–57]. Using the planar force constant model Zi and Ludwig [58] have addressed the problem of Si/(III-V) superlattices, while Ghislotti and Bottani [59] have investigated the Si/SiO<sub>2</sub>/Si bilayer.

There have been experimental contributions to the understanding of phonon spectra in these heterostructures. Kuznetsov et al [60] and Schorer et al [61] have measured the phonon spectra in Si/Ge while Pusep et al [62] and Talochkin et al [63] have measured the phonon spectra in Si<sub>0.5</sub>Ge<sub>0.5</sub>/Si superlattices, obtaining data relating to photo-electric constants, velocity of sound and Raman data.

### C4 Miscellaneous Work (Experiment)

The reflection and transmission of thermal phonon pulses in bulk Si have been measured by Muller and Weis [64,65]. The effects of channelling of acoustic phonons on electron scattering have been studied [66]. Phonon focusing leading to mode conversion has been reported [67]. Phonon assisted production of electrical current has been used to detect  $\alpha$ -particles [68,69] and X-rays [70]. With regard to specific impurity effects, the influence of ion implantation on phonon scattering is reported by Strickland et al [71] and the influence of dissolved oxygen on the propagation of high frequency phonons is discussed in [72]. In a similar vein, the influence of the atoms absorbed on the Si surface on the phonon spectrum has been measured under optical excitation. Strong confinement of the phonons to the surface is reported.

## D CONCLUSION

Experimental values of the phonon spectrum from inelastic neutron scattering, Raman spectroscopy and infrared spectroscopy measurements are presented. Several more recent theoretical treatments of phonon spectra in silicon are described and the results agree with experiment. Surface phonons have been theoretically modelled on the (111) and (110) surfaces. New data are now becoming available on Si/Ge heterostructures. Some miscellaneous observations are also reported.

## REFERENCES

- [1] B.N. Brockhouse [ *Phys. Rev. Lett. (USA)* vol.2 (1959) p.256 ]
- [2] G. Dolling [ *Symp. Inelastic Scattering of Neutrons in Solids and Liquids* (IAEA, Vienna, 1963) vol.2 p.37 ]
- [3] G. Nilsson, G. Nelin [ *Phys. Rev. B (USA)* vol.6 (1972) p.3777 ]
- [4] W. Cochran [ *Proc. R. Soc. Lond. A. (UK)* vol.253 (1959) p.260 ]
- [5] W. Weber [ *Phys. Rev. B (USA)* vol.15 (1977) p.4789 ]
- [6] R.M. Pick, M.H. Cohen, R.M. Martin [ *Phys. Rev. B (USA)* vol.1 (1970) p.910 ]
- [7] J. Ihm, M.T. Yin, M.L. Cohen [ *Solid State Commun. (USA)* vol.37 (1981) p.491 ]
- [8] K. Kunc, R.M. Martin [ *Phys. Rev. Lett. (USA)* vol.48 (1982) p.406 ]
- [9] A. Fleszar, R. Resta [ *Phys. Rev. B (USA)* vol.34 (1986) p.7140 ]
- [10] J.P. Russell [ *J. Phys. Radium* vol.26 (1965) p.620 ]

#### 4.4 Phonon spectrum of c-Si

- [11] J.H. Parker Jr., D.W. Feldman, M. Ashkin [ *Phys. Rev. (USA)* vol.155 (1967) p.712 ]
- [12] T.R. Hart, R.L. Aggarwal, B. Lax [ *Phys. Rev. B (USA)* vol.1 (1970) p.638 ]
- [13] R.K. Chang, J.M. Ralston, D.E. Keating [ in *Light Scattering Spectra of Solids* Ed. G.B. Wright (Springer-Verlag, 1969) p.369 ]
- [14] B.A. Weinstein, M. Cardona [ *Solid State Commun. (USA)* vol.10 (1972) p.961 ]
- [15] P.A. Temple, C.E. Hathaway [ *Phys. Rev. B (USA)* vol.7 (1973) p.3685 ]
- [16] R.A. Cowley [ *J. Phys. (France)* vol.26 (1965) p.659 ]
- [17] G. Dolling, R.A. Cowley [ *Proc. Phys. Soc. (UK)* vol.88 (1966) p.463 ]
- [18] F.A. Johnson [ *Proc. Phys. Soc. (UK)* vol.73 (1959) p.265 ]
- [19] F.A. Johnson, R. Loudon [ *Proc. R. Soc. Lond. A (UK)* vol.281 (1964) p.274 ]
- [20] M. Balkanski, M. Nusimovici [ *Phys. Status Solidi (Germany)* vol.5 (1964) p.635 ]
- [21] B.A. Weinstein, G.J. Piermarini [ *Phys. Rev. B (USA)* vol.12 (1975) p.1172 ]
- [22] J. Estel, J. Kalus, L. Pintschovius [ *Phys. Status Solidi B (Germany)* vol.126 (1984) p.121 ]
- [23] Th. Englert, G. Abstreiter, J. Pontcharra [ *Solid-State Electron. (UK)* vol.23 (1980) p.31 ]
- [24] G.A. Sai-Halasz, F.F. Fang, T.O. Sedgwick, A. Segmuller [ *Appl. Phys. Lett. (USA)* vol.36 (1980) p.419 ]
- [25] Y. Ohmura, T. Inoue, T. Yoshii [ *J. Appl. Phys. (USA)* vol.54 (1983) p.6779 ]
- [26] R. Jones [ *J. Phys. C (UK)* vol.20 no.14 (1987) p.L271-3 ]
- [27] S. Wei, M.Y. Chou [ *Phys. Rev. B (USA)* vol.50 no.4 (1994) p.221-6 ]
- [28] R.D. King-Smith, R.J. Needs [ *J. Phys., Condens. Matter (UK)* vol.2 no.15 (1990) p.3431-44 ]
- [29] C.Z. Wang, C.T. Chan, K.M. Ho [ *Phys. Rev. B, Condens. Matter (USA)* vol.42 no.17 (1990) p.11276-83 ]
- [30] S. Narasimhan, D. Vanderbilt [ *Phys. Rev. B, Condens. Matter (USA)* vol.43 no.5 (1991) p.4541-4 ]
- [31] J.M. Hinckley, J. Singh [ *J. Appl. Phys. (USA)* vol.76 no.7 (1994) p.4192-200 ]
- [32] S. Tamura [ *Phys. Rev. B, Condens. Matter (USA)* vol.48 no.18 (1993) p.13502-7 ]
- [33] S. Tamura, J.A. Shields, J.P. Wolfe [ *Phys. Rev. B, Condens. Matter (USA)* vol.44 no.7 (1991) p.3001-11 ]
- [34] A.F. Revinskii [ *Physics of the Solid State (USA)* vol.37 no.9 (1995) p.1567-8 ]
- [35] M. Omini, A. Sparavigna [ *Nuovo Cimento D (Italy)* vol.19D no.10 (1997) p.1537-63 ]
- [36] G.N. Koskowich, M. Soma, R.B. Darling [ *Phys. Rev. B, Condens. Matter (USA)* vol.41 no.5 (1990) p.2944-7 ]
- [37] G. Panzarini, L. Colombo [ *Phys. Rev. Lett. (USA)* vol.73 no.12 (1994) p.1636-9 ]
- [38] E. Behnen [ *J. Appl. Phys. (USA)* vol.67 no.1 (1990) p.287-92 ]
- [39] I. Stich, K. Terakura [ *Phys. Rev. Lett. (USA)* vol.74 no.22 (1995) p.4491-4 ]
- [40] Kim Jeongnim, Yeh Mei-Ling, F.S. Kahn, J.W. Wilkins [ *Phys. Rev. B, Condens. Matter (USA)* vol.52 no.20 (1995) p.14709-18 ]
- [41] I. Stich, J. Kohanoff, K. Terakura [ *Phys. Rev. B, Condens. Matter (USA)* vol.54 no.4 (1996) p.2642-53 ]
- [42] F. Ancilotto, A. Selloni, W. Andreoni, S. Baroni, R. Car, M. Parrinello [ *Phys. Rev. B, Condens. Matter (USA)* vol.43 no.11 (1991) p.8930-3 ]
- [43] F. Ancilotto, W. Andreoni, A. Selloni, R. Car, M. Parrinello [ *Phys. Rev. Lett. (USA)* vol.65 no.25 (1990) p.3148-51 ]
- [44] E.J. Mele [ *Surf. Sci. (Netherlands)* vol.278 no.1-2 (1992) p.L135-40 ]
- [45] B. Sandfort, A. Mazur, J. Pollmann [ *Phys. Rev. B, Condens. Matter. (USA)* vol.51 no.11 (1995) p.7139-49 ]
- [46] V.A. Ermoshin, A.K. Kazanski, K.A. Smirnov, D. Bougeard [ *J. Chem. Phys. (USA)* vol.105 no.20 (1996) p.9371-4 ]
- [47] R. Honke, P. Pavone, U. Schroder [ *Surf. Sci. (Netherlands)* vol.367 no.1 (1996) p.75-86 ]
- [48] D.C. Morse, E.J. Mele [ *Phys. Rev. B, Condens. Matter (USA)* vol.40 no.5 (1989) p.3465-8 ]

- [49] P. Santini, R. Ruggerone, L. Miglio, R.B. Doak [ *Phys. Rev. B, Condens. Matter (USA)* vol.46 no.15 (1992) p.9865-8 ]
- [50] V. Graschus, A. Mazur, J. Pollmann [ *Phys. Rev. B, Condens. Matter (USA)* vol.56 no.11 (1997) p.6482-5 ]
- [51] E. Molinari, A. Fasolino [ *Appl. Phys. Lett. (USA)* vol.54 no.11 (1989) p.1220-2 ]
- [52] S. Wilke, J. Masec, B. Velicky [ *Phys. Rev. B, Condens. Matter (USA)* vol.41 no.6 (1990) p.3769-77 ]
- [53] I. Lee, C.Y. Fong [ *Superlattices Microstruct. (UK)* vol.7 (1990) p.153-9 ]
- [54] A. Qteish, E. Molinari [ *Phys. Rev. B, Condens. Matter (USA)* vol.42 no.11 (1990) p.7090-6 ]
- [55] J. Zi, K. Zhang, Xie Xide [ *Phys. Rev. B, Condens. Matter (USA)* vol.45 no.16 (1992) p.9447-50 ]
- [56] N.W.C. Dharma-Wardana, P.X. Zhang, D.J. Lockwood [ *Phys. Rev. B, Condens. Matter (USA)* vol.48 no.16 (1993) p.11960-4 ]
- [57] A. Ben Amar, A. Qteish, N. Meskini [ *Phys. Rev. B, Condens. Matter (USA)* vol.53 no.9 (1996) p.5372-8 ]
- [58] J. Zi, W. Ludwig [ *J. Phys., Condens. Matter (UK)* vol.6 no.18 (1994) p.3291-300 ]
- [59] G. Ghislotti, C.E. Bottani [ *Phys. Rev. B, Condens. Matter (USA)* vol.50 no.16 (1994) p.12131-7 ]
- [60] O.A. Kuznetsov et al [ *Physics of the Solid State (USA)* vol.36 no.3 (1994) p.398-403 ]
- [61] R. Schorer, G. Abstreiter, S. de Gironcoli, E. Molinari, H. Kibbel, H. Presting [ *Phys. Rev. B, Condens. Matter (USA)* vol.49 no.8 (1994) p.5406-14 ]
- [62] Yu.A. Pusep, M.P. Sinyukov, A.B. Talochkin, M. Cardona, V.A. Markov, O.P. Pchelyakov [ *Sov. Phys. - Solid State (USA)* vol.34 no.4 (1992) p.599-603 ]
- [63] A.B. Talochkin, V.A. Markov, I.G. Neizvestnyi, O.P. Pchelyakov, M.P. Sinukov, S.I. Stenin [ *Sov. Phys. - Solid State (USA)* vol.33 no.6 (1991) p.954-5 ]
- [64] G. Muller, O. Weis [ *Z. Phys. B, Condens. Matter (Germany)* vol.80 no.1 (1990) p.25-38 ]
- [65] G. Muller, O. Weis [ *Z. Phys. B, Condens. Matter (Germany)* vol.80 no.1 (1990) p.15-23 ]
- [66] J.A. Shields, J.P. Wolfe, Shin-Ichiro Tamura [ *Z. Phys. B, Condens. Matter (Germany)* vol.76 no.3 (1989) p.295-301 ]
- [67] A.G. Every, W. Sachse, K.Y. Kim, M.O. Thompson [ *Phys. Rev. Lett. (USA)* vol.65 no.12 (1990) p.1446-9 ]
- [68] Th. Lange, E. Umlauf, W. Zulehner [ *Solid State Commun. (USA)* vol.71 no.8 (1989) p.697-700 ]
- [69] B.A. Young, B. Cabrera, A.T. Lee [ *Phys. Rev. Lett. (USA)* vol.64 no.23 (1990) p.2795-8 ]
- [70] B.A. Young, B. Cabrera, A.T. Lee, C.J. Martoff, B. Neuhauser, J.P. McVittie [ *IEEE Trans. Magn. (USA)* vol.25 no.2 (1989) p.1347-50 ]
- [71] K.R. Strickland, S.C. Edwards, J.K. Wigmore, R.A. Collins, C. Jeynes [ *Surf. Interface Anal. (UK)* vol.18 no.8 (1992) p.631-6 ]
- [72] U. Werling, K.F. Renk [ *Jpn. J. Appl. Phys. (Japan)* vol.26 suppl. 26-3 pt.1 (1987) p.671-2 ]

## 4.5 Thermal conductivity of c-Si

M.N. Wybourne (updated by M.R. Brozel)

April 1998

### A INTRODUCTION

This Datareview presents data on the thermal conductivity of single crystal silicon over a wide temperature range from 2 K to above the melting point. Two regions can be separated: below 200 K and above this temperature. Results are also presented for silicon doped with boron and oxygen.

### B EXPERIMENTAL RESULTS

The thermal conductivity of single crystal silicon has been measured over a wide temperature range and on a variety of samples by many workers [1–9]. One of the earliest measurements was by Koenigsberger and Weiss [10] who found a value of  $0.84 \text{ W cm}^{-1} \text{ K}^{-1}$  at 290 K for an impure sample. Recently, a number of measurements have been presented and compared in graphical form by Beadle et al [11]. Rowe and Bhandari [12] have reviewed the techniques used to measure the thermal conductivity of semiconductors and have also discussed the data for doped silicon reported by Steigmeier [13], Holland and Neuringer [8] and Slack [9].

In general, the thermal conductivity of single crystal silicon exhibits a temperature dependence characteristic of single crystal dielectric materials. For the purest silicon samples, the thermal conductivity goes through a maximum at a temperature of about 22 K. Above this temperature the conductivity falls as the phonon mean-free-path is reduced by phonon-phonon scattering processes. At temperatures below the maximum the absolute value of the conductivity is highly dependent on the sample but, in broad terms, it falls with a temperature dependence close to that of the specific heat of the lattice ( $T^3$ ).

For the purpose of this Datareview it is convenient to consider two temperature regions, one from 200 K to the melting point of silicon and the other up to 200 K. Above 200 K the thermal conductivity is largely independent of the particular sample specifications and the various reported data coalesce to be in agreement to within a factor of two. Representative data in this temperature range are taken from the measurements by Glassbrenner and Slack [7] and are presented in TABLE 1.

TABLE 1 Thermal conductivity values.

T (K)	K ( $\text{W cm}^{-1} \text{ K}^{-1}$ )	T (K)	K ( $\text{W cm}^{-1} \text{ K}^{-1}$ )
200	2.66	1000	0.31
300	1.56	1100	0.28
400	1.05	1200	0.26
500	0.80	1300	0.25
600	0.64	1400	0.24
700	0.52	1500	0.23
800	0.43	1600	0.22
900	0.36	1681	0.22

Note: These measurements were made on a [111] axis cylindrical sample 130 mm long and 26 mm in diameter. The sample was grown by the float-zone process in an argon atmosphere. The sample

#### 4.5 Thermal conductivity of *c*-Si

was n-type with a room-temperature resistivity of  $440 \Omega \text{ cm}$  and a carrier concentration of  $1.27 \times 10^{13} \text{ cm}^{-3}$ .

A recent measurement of the thermal conductivity of solid and liquid silicon at the melting temperature (1687 K) using a laser flash method reports values of  $273 \pm 0.3 \text{ W m}^{-1} \text{ K}^{-1}$  and  $56 \pm 1 \text{ W m}^{-1} \text{ K}^{-1}$ , respectively. These values appear to be inconsistent with those of Glassbrenner and Slack [7] and may be associated with the appearance of a new phase just above the melting point [23].

In the temperature range up to 200 K details of the temperature dependence of the thermal conductivity, together with position and magnitude of the conductivity maximum, are sensitive to the size, perfection, doping level and type, oxygen concentration [14], orientation [15] and surface quality [16] of the sample. It is only possible, therefore, to provide illustrative data in this temperature range (TABLE 2) [8].

TABLE 2 Thermal conductivity values.

T (K)	K ( $\text{W cm}^{-1} \text{ K}^{-1}$ )	T (K)	K ( $\text{W cm}^{-1} \text{ K}^{-1}$ )
150	4.10	20	47.7
100	9.13	10	24.0
50	28.0	8	16.4
40	36.6	6	8.99
30	44.2	4	3.11
		2	0.44

Note: These measurements were made on a bar sample 31.75 mm long and  $6.30 \times 6.07 \text{ mm}^2$  in cross-section. The sample was grown by the float-zone process and contained a boron concentration of  $1.0 \times 10^{13} \text{ cm}^{-3}$ .

In TABLE 3 we present data from the measurements of Holland and Neuringer [8] as a guide to the dependence of the maximum thermal conductivity on the concentration of boron impurities. It should be noted that the presence of oxygen impurities causes resonant phonon scattering at about 40 K [17] which suppresses both the magnitude and the temperature of the maximum for a given boron concentration.

TABLE 3 Maximum thermal conductivity versus concentration of boron impurities.

Boron concentration ( $\text{cm}^{-3}$ )	Thermal conductivity		Sample cross-section ( $\text{mm}^2$ )
	Maximum ( $\text{W cm}^{-1} \text{ K}^{-1}$ )	Temperature (K)	
$1.0 \times 10^{13}$	48	22	$6.30 \times 6.07$
$4.2 \times 10^{14}$	43	25	$6.17 \times 6.32$
$4.2 \times 10^{14}$	38	26	$3.45 \times 3.50$
$1.0 \times 10^{15}$	43	25	$6.19 \times 6.32$
$4.0 \times 10^{15}$	33	27	$5.86 \times 5.86$
$4.0 \times 10^{16}$	18	37	$6.24 \times 6.27$

Finally, thermal conductivity measurements of doped silicon samples have been used as a technique to study the nature of the impurities themselves [18–21]. Many of these studies have been reviewed elsewhere [22].

## C CONCLUSION

Thermal conductivity data have been presented from 2 to 1681 K. The variation from 200 to 1681 K is from 2.66 to 0.22 W cm<sup>-1</sup> K<sup>-1</sup>. A maximum value of ~47 W cm<sup>-1</sup> K<sup>-1</sup> is reached at 20 K and then the value decreases to 0.44 at 2 K. Values decrease as the boron concentration increases, at low temperatures.

## REFERENCES

- [1] B.B. Kuprovski, P.V. Geld [ *Fiz. Met. Metalloved. (USSR)* vol.3 (1956) p.182 ]
- [2] W.D. Kingery [ *J. Am. Ceram. Soc. (USA)* vol.42 (1959) p.617 ]
- [3] H. Mette, W.W. Gartner, C. Loscoe [ *Phys. Rev. (USA)* vol.117 (1960) p.1491 ]
- [4] A.D. Stuckes [ *Philos. Mag. (UK)* vol.5 (1960) p.84 ]
- [5] R.G. Morris, J.G. Hust [ *Phys. Rev. (USA)* vol.124 (1961) p.1426 ]
- [6] R.G. Morris, J.J. Martin [ *J. Appl. Phys. (USA)* vol.34 (1963) p.2388 ]
- [7] C.J. Glassbrenner, G.A. Slack [ *Phys. Rev. (USA)* vol.134 (1964) p.A1058 ]
- [8] M.G. Holland, L.G. Neuringer [ *Proc. Int. Conf. Physics of Semiconductors*, Exeter, England, 1962 (Inst. Phys., Bristol, 1962) p.474 ]
- [9] G.A. Slack [ *J. Appl. Phys. (USA)* vol.35 (1964) p.3460 ]
- [10] J. Koenigsberger, J. Weiss [ *Ann. d. Physik (Germany)* vol.35 (1911) p.1-46 ]
- [11] W.E. Beadle, J.C.C. Tsai, R.D. Plummer [ *Quick Reference Manual for Silicon Integrated Circuit Technology* (John Wiley & Sons, 1985) p.2-64 to 2-66 ]
- [12] D.M. Rowe, C.M. Bhandari [ *Prog. Cryst. Growth Charact. (UK)* vol.13 (1986) p.233 ]
- [13] E.F. Steigmeier [ in *Thermal Conductivity* vol.2 Ed. R.P.Tye (Academic Press, 1969) ]
- [14] D. Fortier, H. Djersassi, K. Suzuki, H.J. Albany [ *Phys. Rev. B (USA)* vol.9 (1974) p.4340 ]
- [15] A.K. McKurdy, H.J. Maris, C. Elbaum [ *Phys. Rev. B (USA)* vol.2 (1970) p.4077 ]
- [16] W.S. Hurst, D.R. Frankl [ *Phys. Rev. (USA)* vol.186 (1969) p.801 ]
- [17] A.M. de Goer, M. Locatelli, K. Lassmann [ *J. Phys. Colloq. (France)* vol.42 (1981) p.235 ]
- [18] D. Fortier, K. Suzuki [ *J. Phys. (France)* vol.37 (1976) p.143 ]
- [19] D. Fortier, K. Suzuki [ *Phys. Rev. B (USA)* vol.9 (1974) p.2530 ]
- [20] A. Adolf, D. Fortier, J.H. Albany, K. Suzuki, M. Locatelli [ in *Phonon Scattering in Condensed Matter* Ed. H.J. Maris (Plenum Press, 1980) p.421 ]
- [21] K.A. Adilov et al [ *Sov. Phys.-Solid State (USA)* vol.28 (1986) p.1070 ]
- [22] L.J. Challis, A.M. de Goer [ in *The Dynamical Jahn-Teller effect in Localized Systems* Eds Y.E. Perlin, M. Wagner (Elsevier, 1984) p.533 ]
- [23] K. Yamamoto, T. Abe, S. Takasu [ *Jpn. J. Appl. Phys. 1 (Japan)* vol.30 (1991) p.2423-6 ]

## 4.6 Thermal diffusivity of c-Si

M.N. Wybourne (updated by M.R. Brozel)

April 1998

### A INTRODUCTION

This Datareview presents data on the thermal diffusivity of single crystal silicon over a wide temperature range from 50 K to near to the melting point. Data are available for two regions: below 250 K and above 300 K. Indications also are given for heavily doped silicon.

### B EXPERIMENTAL RESULTS

Some of the earliest measurements of the thermal diffusivity of single-crystal silicon were reported by Shanks et al [1]. Using the method of Kennedy et al [2] these workers measured the thermal diffusivity of a (111) orientation  $107 \Omega \text{ cm}$  p-type sample over the temperature range 300–1400 K (TABLE 1). Shanks et al also presented data for two n-type samples of resistivity 33 and  $1010 \Omega \text{ cm}$  with orientations (111) and (100) respectively. The data from all three samples agreed to within the accuracies of the experiment. In the temperature range 300–900 K, the values of the thermal conductivity derived from these data are approximately 10% below those obtained from direct measurement [3]. Above 1000 K, direct measurements show that the thermal conductivity continues to decrease with temperature up to almost the melting point [3]. This is inconsistent with the thermal diffusivity measurements which suggest that the thermal conductivity should be temperature independent in this temperature range. The discrepancy is about 20% at 1400 K and is of unknown origin.

TABLE 1 Thermal diffusivity values.

T (K)	D ( $\text{cm}^2 \text{ s}^{-1}$ )	T (K)	D ( $\text{cm}^2 \text{ s}^{-1}$ )
300	0.86	800	0.19
400	0.52	900	0.16
500	0.37	1000	0.14
600	0.29	1200	0.12
700	0.24	1400	0.12

The values of thermal conductivity obtained from thermal diffusivity measurements made by Abeles et al [4] on a  $100 \Omega \text{ cm}$  silicon sample over the temperature range 300–1200 K are between those of Glassbrenner and Slack [3] and Shanks et al [1].

More recent measurements of the thermal diffusivity of silicon have been made by Turkes [5] using an ion-implanted resistor as the thermal transient sensor. This technique removed the problems associated with the thermal response time of sensors used in transient methods of determining the diffusivity. Turkes studied two samples, a  $6 \Omega \text{ cm}$  phosphorus doped sample and a  $1 \times 10^{17} \text{ cm}^{-3}$  aluminium doped sample. Data were taken in the range 20–250 K. Above 50 K, the diffusivity was sample independent and had a temperature dependence governed by the phonon-phonon scattering rate (TABLE 2). Below 50 K, the phonon-phonon interaction is not predominant and the temperature dependence of the diffusivity is determined by a combination of isotope, impurity and boundary scattering rates. Note that at the lowest temperatures where the phonon scattering rate is solely

dominated by the boundaries of the sample, the diffusivity will be dependent on the sample geometry and will be temperature independent.

Ebrahimi [6] has developed a technique to measure the thermal diffusivity of small silicon chips. Two bipolar transistors on the silicon chip are used as a thermal source and a thermal detector with the spacing between the devices acting as a thermal delay. Using a simplification of Angstrom's method [7], the diffusivity can be determined from the phase difference between the devices. Measurements were made over a limited temperature range, 220–380 K, and the values of the diffusivity obtained were approximately 15% higher than those obtained by Shanks et al [1].

TABLE 2 Thermal diffusivity values.

T (K)	D ( $\text{cm}^2 \text{s}^{-1}$ )	T (K)	D ( $\text{cm}^2 \text{s}^{-1}$ )
50	63.5	100	11.3
60	37.6	150	4.24
70	24.8	200	2.23
80	17.1	250	1.23
90	14.4		

The data given here refer to relatively lightly doped samples. Thermal conductivity data show that the diffusivity of highly doped silicon will be lower by a significant amount. For example, at 100 K a sample doped to over  $10^{20} \text{ cm}^{-3}$  would have a diffusivity that is an order of magnitude below the value for a lightly doped sample (TABLE 2). At 300 K, this reduction has fallen to a factor of two.

Rowe and Bhandari [8] reviewed thermal conductivity data and the methods for measuring both the conductivity and the diffusivity of doped semiconductors. They point out that both random and systematic errors occur in these measurements. Most authors quote only two significant figures implying an error between 0.5 and 5%. For the data given here, errors of the order of 5% should be assumed.

## C CONCLUSION

Thermal diffusivity data have been presented from 50 to 1400 K. The variation from 300 to 1400 K is from  $0.86$  to  $0.22 \text{ cm}^2 \text{s}^{-1}$ . A maximum value of  $\sim 64 \text{ cm}^2 \text{s}^{-1}$  is reached at 50 K and then the value decreases to 1.23 at 250 K. Values decrease markedly as the doping concentration increases to over  $10^{20} \text{ cm}^{-3}$ . Values are believed to be accurate to within the order of 5%.

## REFERENCES

- [1] H.R. Shanks, F.D. Maydock, P.H. Sidles, G.C. Danielson [ *Phys. Rev. (USA)* vol.130 (1963) p.1743 ]
- [2] W.L. Kennedy, P.H. Sidles, G.C. Danielson [ *Adv. Energy Convers. (UK)* vol.2 (1962) p.53 ]
- [3] C.J. Glassbrenner, G.A. Slack [ *Phys. Rev. (USA)* vol.134 (1964) p.A1058 ]
- [4] B. Abeles, D.S. Beers, G.D. Cody, J.P. Dismukes [ *Phys. Rev. (USA)* vol.125 (1962) p.44 ]
- [5] P. Turkes [ *Phys. Status Solidi A (Germany)* vol.75 no.2 (1983) p.519-23 ]
- [6] J. Ebrahimi [ *J. Phys. D (UK)* vol.3 (1970) p.236 ]
- [7] H.S. Carslaw, J.C. Jaeger [ *Conduction of Heat in Solids* (Clarendon Press, Oxford, 1948) ch.4 ]
- [8] D.M. Rowe, C.M. Bhandari [ *Prog. Cryst. Growth Charact. (UK)* vol.13 (1986) p.233 ]

## 4.7 Surface tension of liquid Si

S.C. Hardy (updated by M.R. Brozel)

April 1998

In the previous edition of this book, the surface tension of liquid silicon at the melting point (1683 K) was reported to be 885 mJ/m<sup>2</sup> and to decrease linearly with slope -0.28 mJ/(m<sup>2</sup> K) as the temperature increases [1]. These values for the surface tension and its temperature coefficient were determined using the sessile drop technique in purified flowing argon. The silicon samples were supported in shallow boron nitride cups. Auger analysis of the solidified silicon drops found no evidence of contamination by the cup material. The oxygen partial pressure in these measurements was thought to be very low because the surface tension values were in good agreement with an earlier measurement at 1723 K in pure hydrogen [2]. Surface tension values found in a previous measurement were significantly lower than the above result, probably due to the presence of surface active impurities [3].

Recently there has been further interest in these measurements with an emphasis on removing effects due to the crucible or other means of supporting the molten Si. Electromagnetic levitation has been employed together with the oscillating drop method to measure both the surface tension and the temperature coefficient [4]. Similar mechanical oscillations were observed in a Si drop hanging from a SiC covered carbon rod [5,6]. The most recent estimations were made using an electrostatic levitator under high vacuum conditions [7]. This group was able to measure the surface tension at several temperatures and derived the relationship  $\sigma(T) = 875 - 0.22(T - T_m)$  where  $\sigma(T)$  is the surface tension in 10<sup>-3</sup> N m<sup>-1</sup> and  $T_m$  is the melting temperature. A table of values derived since 1984 is shown below.

TABLE 1 Surface tension values.

Surface tension ( $\sigma$ at $T_m$ ) (10 <sup>-3</sup> N m <sup>-1</sup> )	Temp. coefficient (N m <sup>-1</sup> K <sup>-1</sup> )	Ref
885	-0.28	[1]
783.5	-0.65	[4]
819	-0.308	[5]
875	-0.22	[7]

## REFERENCES

- [1] S.C. Hardy [ *J. Cryst. Growth (Netherlands)* vol.69 no.2/3 (1984) p.456-60 ]
- [2] W.D. Kingery, M. Humenik [ *J. Phys. Chem. (USA)* vol.57 (1953) p.359 ]
- [3] S.V. Lukin, V.I. Zhuchkov, N.A. Vatolin [ *J. Less-Common Met. (Switzerland)* vol.67 (1979) p.399 ]
- [4] M. Przyborowski, T. Hibiya, M. Eguchi, I. Egry [ *J. Cryst. Growth (Netherlands)* vol.151 no.1-2 (1995) p.60-5 ]
- [5] Chung Sang-Ik, K. Izunome, A. Yokotani, S. Kimura [ *Jpn. J. Appl. Phys. 2 (Japan)* vol.34 no.5B (1995) p.L631-4 ]
- [6] H. Sasaki, Y. Anzai, Huang Xinming, K. Terashima, S. Kimura [ *Jpn. J. Appl. Phys. 1 (Japan)* vol.34, no.2A (1995) p.414-8 ]
- [7] W.K. Rhim, S.K. Chung, A.J. Rulison, R.E. Spjut [ *Int. J. Thermophys. (USA)* vol.18 no.2 (1997) p.459-69 ]

## 4.8 Heat of fusion of Si

J.C. Brice (updated by M.R. Brozel)

April 1998

Little work on the heat of fusion of silicon has been published. Reports in 1950 [1] and 1952 [2] review early work in the field and suggest a 'doubtful' value of  $11.1 \text{ kcal mole}^{-1}$  ( $46.5 \text{ kJ mole}^{-1}$ ). Hultgren in 1968 [3] and again in 1973 [4] gives a recommended value of  $12.1 \text{ kcal mole}^{-1}$  ( $50.6 \text{ kJ mole}^{-1}$ ). This value should be reliable to of the order of 3%.

### REFERENCES

- [1] US Atomic Energy Commission [ *Report ANL-5750* cited by Hodgman in *Handbook of Chemistry and Physics* (Chemical Rubber Publishing, Cleveland, 1960) p.1870-1 ]
- [2] F.D. Rossini et al [ *Selected Values of Chemical Thermodynamic Properties* (NBS Circular 500, Washington, 1952) ]
- [3] R.R. Hultgren et al [ *Selected Values of Thermodynamic Properties of Metals and Alloys* (Wiley, New York, 1968) ]
- [4] R.R. Hultgren et al [ *Selected Values of the Chemical Thermodynamic Properties of Elements* (Wiley, New York, 1973) ]

## CHAPTER 5

### SURFACE PROPERTIES AND CLEANING *(Edited by R.J. Nemanich)*

- 5.1 Reconstruction of silicon (001), (111) and (110) surfaces
- 5.2 Structure of clean silicon surfaces: vicinal Si(001) and Si(111) surfaces
- 5.3 Electronic structure of c-Si surfaces
- 5.4 Electrical characterisation of c-Si surfaces
- 5.5 Passivation of c-Si surfaces
- 5.6 Wet chemical cleaning and surface preparation of Si
- 5.7 HF vapour cleaning of oxide on c-Si
- 5.8 Plasma and other in situ approaches to cleaning of c-Si surfaces

## **5.1 Reconstruction of silicon (001), (111) and (110) surfaces**

V. Zielasek, Feng Liu and M.G. Lagally

November 1998

### **A INTRODUCTION**

Starting with bulk silicon, the creation of any surface necessarily cuts some of the highly directional covalent bonds between Si atoms, leaving energetically unfavourable dangling bonds at the surface. To lower the surface energy, Si(001), Si(111) and Si(110) exhibit surface reconstructions, i.e. atomic rearrangements, that reflect the balance between a reduction of dangling bonds and the minimisation of surface stress [1].

The increasing importance of surfaces and interfaces in semiconductor devices has stimulated extensive studies of low-index silicon surfaces over the years. Their reconstructions not only determine the surface electronic structure in detail but are also important for elementary processes of epitaxial growth, like adsorption, surface diffusion, and island formation.

### **B Si(001)**

#### **B1 Dimerisation**

On a bulk-terminated (001) surface each atom of the topmost layer would have two dangling bonds, i.e.  $sp^3$  hybrid orbitals occupied by only one electron ('bulk-terminated' means all atoms forming the surface remain at positions they would occupy in the bulk). The formation of surface dimers, as first proposed by Schlier and Farnsworth [2] and first directly observed by means of scanning tunnelling microscopy (STM) [3,4], eliminates half of the dangling bonds and reduces the overall surface free energy by about 1 eV per surface atom [5–9]. The decrease in electronic energy by dimerisation (2 eV per atom [10]) is partly compensated by an increase in strain energy (1 eV per atom [11]) because the rebonding of the surface atoms distorts the bond angles. An ordering of the dimers into straight rows minimises the strain energy. The orientation of the dimer rows along either [110] or  $[1\bar{1}0]$  is uniquely determined for each terrace by the stacking of the underlying atomic layers (see FIGURE 1).

#### **B2 Dimer Buckling**

At room temperature low-energy electron diffraction (LEED) displays a (2×1) superstructure [2] and STM shows the dimers appearing as symmetric [4]. Symmetric dimers, however, lead to a metallic surface because of the degeneracy of the energy levels of both its dangling bonds. Consequently, it is unstable against Jahn-Teller distortion [12]. The formation of asymmetric (buckled) dimers (see side view in FIGURE 1(a)), i.e. one atom of a dimer moves down adopting a planar  $sp^2$ -like configuration while the other atom moves up adopting an  $s^2p^3$ -like configuration [1,9], reduces the energy. This rehybridisation removes the degeneracy of dangling bonds and induces a charge transfer from the lower dimer atom to the upper atom, resulting in a partially ionic bonding character and a bandgap between filled and empty electronic surface states. Ab initio calculations [9] show that a buckled dimer is 0.2 eV lower in energy than a symmetric dimer. The experimental observations of apparently symmetric dimers at room temperature result from buckled dimers that flip between both possible

### 5.1 Reconstruction of silicon (001), (111) and (110) surfaces

buckled configurations with oscillation frequencies not resolvable by LEED or STM [13]. The non-metallic character of the surface has been shown by photoemission [14] and STM spectroscopy [15].

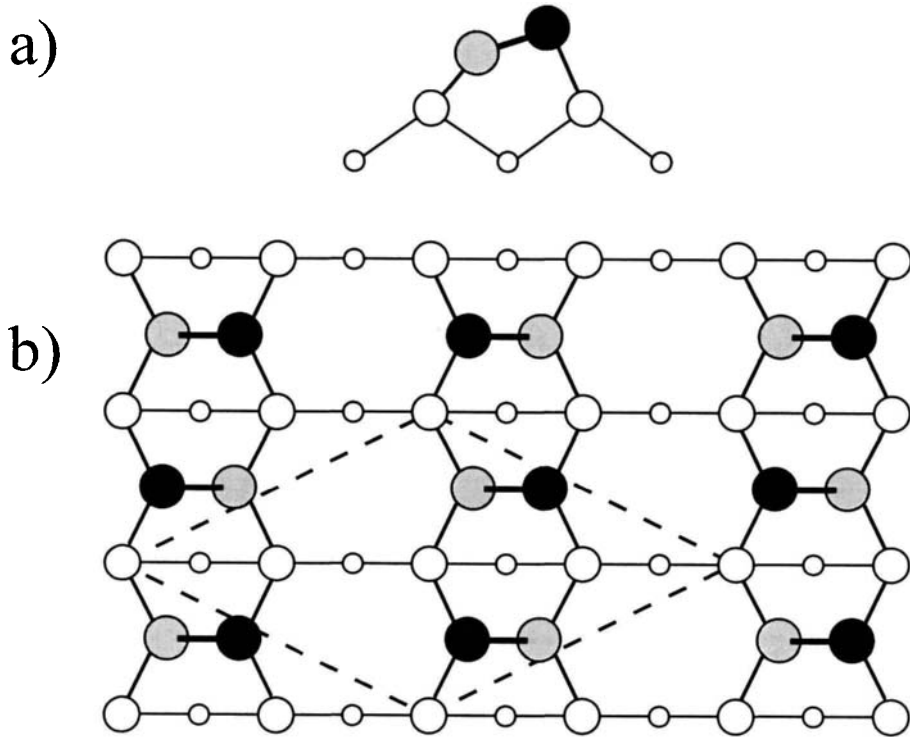


FIGURE 1 Ball-and-stick models of a buckled dimer and the Si(001)  $c(4\times 2)$  reconstructed surface. The dimer atoms are shown as black and grey circles, the second and third layer Si atoms as white circles; (a) side view of a buckled dimer showing schematically also its dangling bonds; (b) top view of the  $c(4\times 2)$  dimer reconstruction. The border of a single unit cell is depicted as a dashed line.

Like the dimerisation, dimer buckling decreases the electronic energy at the expense of increasing strain energy. Strain minimisation leads to alternate buckling directions along the dimer rows, giving rise to  $c(4\times 2)$  and, less often observed,  $p(2\times 2)$  reconstructions. These reconstructions have been observed by LEED at temperatures below 200 K [16] and by STM [4,17,18]. Also, ion scattering [19] and transmission electron diffraction [20] confirm the dimer buckling. FIGURE 1(b) shows a ball-and-stick model of the  $c(4\times 2)$  reconstruction.

LEED [16] finds a phase transition from the  $(2\times 1)$  superstructure to the  $c(4\times 2)$  reconstruction at temperatures between 150 and 250 K, in good agreement with theoretical calculations predicting a second-order phase transition from an ordered  $c(4\times 2)$  or  $p(2\times 2)$  reconstruction to a disordered  $(2\times 1)$  structure at a temperature between 200 and 250 K [21–23]. The results indicate a freezing in of the flipping motion at the phase transition. At room temperature, domains of static buckled dimers are often observed as pinned to defect sites [4,17] and on the upper terrace near to step edges [18], in particular  $S_A$  step edges (see next section).

Theoretical calculations yield a dimer bond length of 0.225–0.230 nm [1,24] and a tilt angle for buckled dimers in the range of 15–20° [1,13,24]. Experimental results for the dimer bond length,

### 5.1 Reconstruction of silicon (001), (111) and (110) surfaces

obtained by LEED [25], X-ray diffraction [26,27], and transmission electron diffraction [20] are within 0.220–0.247 nm. A recent surface X-ray diffraction study, measuring the in-plane and out-of-plane displacements of the atoms over 6 layers, finds the bond length as 0.237 nm ( $\pm 0.006$ ) and the buckling angle as 20° ( $\pm 3$ ) [27].

#### B3 c(4×4) Reconstruction

A c(4×4) reconstruction has been reported for clean Si(001) in the temperature range of 845 to 1050 K by several authors [28–32], notably often after exposing the silicon surface without native oxide to non-ultra-high vacuum conditions, e.g. during wet surface preparation processes or chemical vapour deposition. A study by secondary ion mass spectroscopy (SIMS) and reflection high-energy electron diffraction (RHEED) indicates that the c(4×4) reconstruction is caused by a slight carbon contamination in subsurface layers [32]. Details of the origin and atomic structure of the reconstruction, however, are not completely clear.

#### C Si(111)

##### C1 Cleavage Surface

Upon cleavage, silicon naturally forms (111) surfaces. Bulk-termination would yield one dangling bond per surface atom oriented perpendicular to the surface plane. Cleavage at temperatures between 9 K and room temperature yields Si(111) with (2×1) reconstructions [33]. The three-fold symmetry of the surface with respect to the underlying bulk may give rise to three different orientations of (2×1) domains. For a long time the doubling of periodicity was assumed to result from alternating rows of depressed and raised surface atoms (buckling model) [34], expected to lower surface energy by inducing a charge transfer from the downward atoms with p-like dangling bonds to the upward atoms with s-like dangling bonds. The model, however, is inconsistent with photoemission measurements of electronic surface properties, especially the core-level shifts of the surface atoms [35,36]. The  $\pi$ -bonded chain model, proposed by Pandey [37], has been in agreement with all experimental observations. Without reducing the number of dangling  $p_z$  bonds at the surface the surface energy is lowered by promoting some  $\pi$ -bonding among them. This is achieved by making them nearest neighbours within zig-zag chains of surface atoms that form along  $\{1\bar{1}0\}$  directions. Since the chains are connected by seven- and five-fold rings to the underlying bulk (see FIGURE 2), a complete breaking of Si–Si bonds in the second layer is required in order to form the structure out of the six-member rings that are characteristic of the diamond structure. As for the buckling of dimers, a tilting of the Si pairs forming the chains reduces the surface energy further as shown by both ab initio theories [38–42] and various experiments [43–48]. Overall, the energy gain of the  $\pi$ -bonded chain reconstruction is calculated to be about 0.3–0.4 eV per atom compared to the bulk-terminated surface. The formation barrier is calculated to be as low as  $\leq 0.03$  eV [38] which explains why the chain structure can be readily formed during cleavage at room temperature. The formation process may be mediated by the generation of stacking faults forming five- and seven-fold rings [49].

##### C2 Annealed or Epitaxial Si(111)

Both the (1×1) and the (2×1) reconstructions of cleavage Si(111) are metastable. The lowest-energy structure is a (7×7) reconstruction forming after annealing to temperatures higher than about 870 K or during Si(111) homoepitaxy. After it was first observed by Schlier and Farnsworth in 1959 [2] a complete model of the structure in agreement with all experimental observations was proposed by Takayanagi et al [50] about 25 years later.

### 5.1 Reconstruction of silicon (001), (111) and (110) surfaces

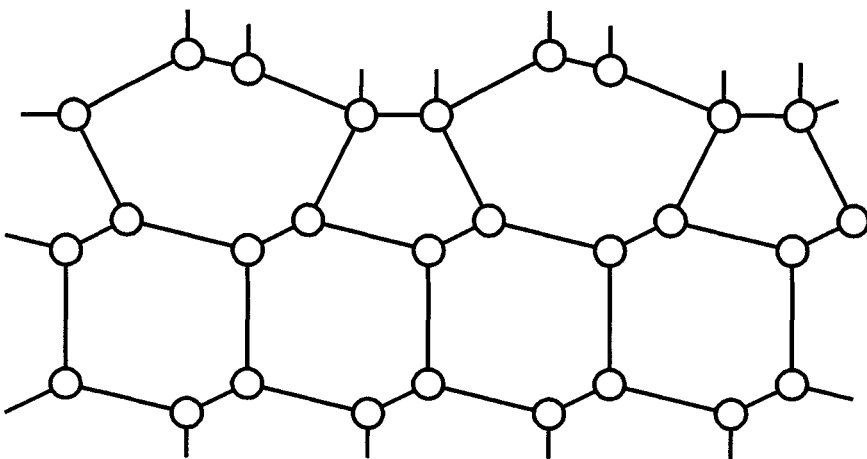


FIGURE 2 Side view of the cleavage Si(111) surface reconstructed according to the  $\pi$ -bonded chain model. The  $\pi$ -bonded chains form on top of the seven-member rings along  $(1\bar{1}0)$ .

The dimer-adatom-stacking fault (DAS) model (see FIGURE 3) is based on a transmission electron microscopy study and comprises several structural features that had been discovered by other groups. According to the DAS model, the  $(7\times 7)$  unit cell consists of two triangular sub-units. One of them contains a stacking fault as suggested by Bennett et al [51], producing wurtzite-type stacking of the outermost two double layers. The faulted and unfaulted sub-units are separated by a triangular network of partial dislocations. The dangling bonds along these dislocations are partially saturated by the formation of dimers as first suggested by McRae [52] and Himpel [53]. There are three dimers per triangle edge linked by eight-atom rings. Big holes (corner-holes) exposing large portions of the second double layer are at the corners of the unit cell, i.e. the crossing points of the dislocations. The atoms around the corner-holes form twelve-member rings.

Adatoms as another important feature of the reconstruction are the most effective way to reduce the dangling-bond density on a  $\{111\}$  surface of diamond structures [54]. There are six adatoms each in both triangular sub-units, located in a  $(2\times 2)$  arrangement on  $T_4$ -sites with bonds to three first-layer atoms. This arrangement has been seen directly by STM [55–57]. Overall, the number of dangling surface bonds is reduced by 2 per adatom as one dangling bond of each adatom remains unsaturated. Incorporation of adatoms introduces also large strain. Consequently there remain six rest atoms in each triangular sub-unit that are not bonded to adatoms. Ab initio theories [58–60] show that this arrangement balances the gain in electronic energy and the cost in strain energy best. All structural details, such as the rest atoms, the corner holes, and the asymmetry between the two triangle sub-units, have been revealed by STM equipped with spectroscopy [61]. The surface energy of the Si(111)-(7×7) reconstruction is calculated as 0.06 eV per  $(1\times 1)$  surface unit cell lower than that of the Si(111)-(2×1) reconstruction [62]. In-plane relaxations of the reconstructed layers with respect to the ideal DAS model have been obtained experimentally by a detailed analysis of X-ray diffraction data, showing adatom-induced strain fields and a general dilation to the borders of the  $(7\times 7)$  unit mesh [63].

Pathways for the transformation from the  $(2\times 1)$  reconstruction without adatoms to the  $(7\times 7)$  involve a  $(1\times 1)$  reconstruction with a disordered array of adatoms and structures related to the DAS model, most notably a  $(5\times 5)$  reconstruction. The energy of the  $(5\times 5)$  reconstruction has been shown to be

### 5.1 Reconstruction of silicon (001), (111) and (110) surfaces

only slightly higher than that of the (7×7). An STM study shows two different reaction pathways [64]. The reconstruction transforms from (2×1) to (5×5) at 623 K and from (5×5) to (7×7) at 873 K on wide terraces. Near to steps or domain boundaries which are assumed to provide extra adatoms the (2×1) transforms at about 572 K to domains of (7×7), (5×5) and a (1×1) reconstruction with a disordered array of adatoms. For temperatures higher than 673 K only the (7×7) reconstruction is observed in these regions.

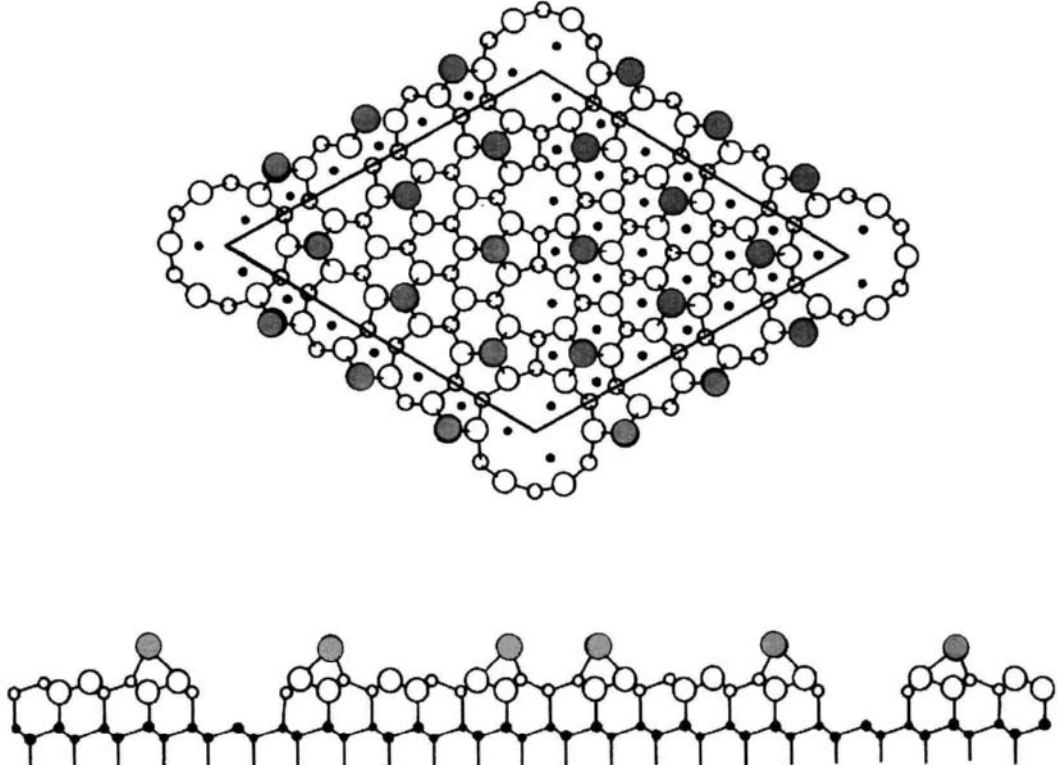


FIGURE 3 Top view (upper part) and cross-section along the long diagonal of the unit mesh (lower part) of the dimer-adatom-stacking fault (DAS) model of the Si(111)-(7×7) reconstruction. The adatom layer (shaded circles) and two double layers (open and solid circles) are depicted. The stacking fault is in the left half of the unit cell. (After [49].)

A first order phase transition from a (1×1) structure to the (7×7) reconstruction is observed at 1100 K [65,66]. Below the transition temperature low-energy electron microscopy (LEEM) [65] and STM [66] show the nucleation of triangular (7×7) reconstructed areas at step edges. Quenching the surface from temperatures above 1100 K can conserve (1×1) domains at room temperature.

### D Si(110)

The surface reconstruction of Si(110) sensitively depends on small amounts of contamination [67], as studies for different Ni coverages show. For contamination levels less than 0.5% two reconstructions are reported. According to the superstructures observed by RHEED they are called ‘16×2’ and ‘1×5’ [67–69]. However, a detailed analysis of the diffraction patterns and STM images shows that the exact description of the translation periodicity within the matrix notation is

$$\begin{pmatrix} -1 & 17 \\ -2 & 2 \end{pmatrix}$$

### 5.1 Reconstruction of silicon (001), (111) and (110) surfaces

for the ‘16×2’ structure (see FIGURE 4). For the ‘1×5’ structure the periodicity in the (001) direction is 5 whereas it is not well defined in the  $(\bar{1}\bar{1}0)$  direction.

The bulk-terminated Si(110) surface would consist of widely separated parallel zig-zag chains of Si atoms along  $[1\bar{1}0]$  with one dangling bond per surface atom. The ‘16×2’ structure consists of stripe-like domains that are separated by atomic-height steps [67] (see FIGURE 4). The direction of the stripes is  $[\bar{1}\bar{1}2]$  and the stripes are 2.5 nm wide. Adjacent steps can be either alternately up and down, as in FIGURE 4, or they can form [17,15,1] facets. Photoemission experiments provide evidence that the reconstruction involves adatoms [70], not shown in FIGURE 4. From STM measurements Packard and Dow [69] present a structure model involving adatoms in a distorted hexagonal array with each adatom being bonded to three atoms of the zig-zag chains.

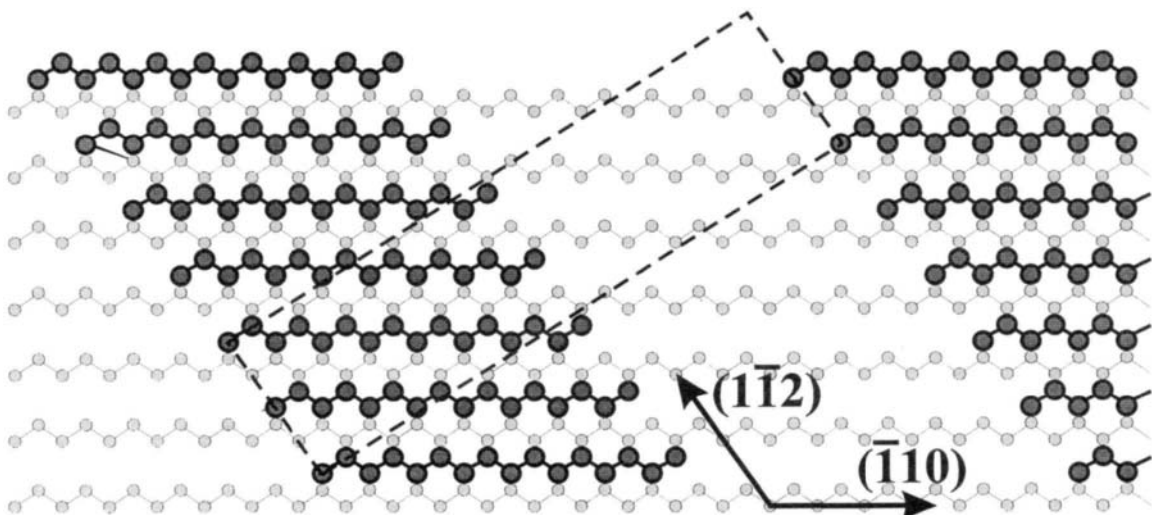


FIGURE 4 Schematic representation of the stripes of the Si(110)-‘16×2’ reconstruction. Atoms of the top-most regular layer are shown as shaded circles, atoms of the second layer as white circles. The dashed lines depict a unit cell of the reconstruction considering also the adatom arrangement that is not shown in the figure.

According to an STM study the ‘1×5’ reconstruction is formed by missing zig-zag rows in the  $[110]$  direction and involves adatoms [71]. Several models exist for the adatom arrangement [69,71,72] that appears not well ordered in STM images. The probable influence of very low surface contaminations on the formation of either the ‘16×2’ or the ‘1×5’ reconstruction is not clear.

## E CONCLUSION

All low-index silicon surfaces exhibit reconstructions that reduce the number of dangling bonds by dimerisation or by incorporating adatoms. On Si(001) the surface free energy is lowered by the formation of rows of asymmetric dimers that lead to the observation of (2×1), p(2×2), and c(4×2) superstructures. After annealing, or when grown epitaxially, Si(111) exhibits complex structures involving adatoms as well as dimers. The (7×7) reconstruction is the most stable at room temperature. The Si(110) reconstructions consist of stripe-like domains separated by atomic-height steps and most likely involve adatoms.

## 5.1 Reconstruction of silicon (001), (111) and (110) surfaces

### REFERENCES

- [1] G.P. Srivastava [ *Rep. Prog. Phys. (UK)* vol.60 (1997) p.561 ]
- [2] R.E. Schlier, H.E. Farnsworth [ *J. Chem. Phys. (USA)* vol.30 (1959) p.917 ]
- [3] R.M. Tromp, R.J. Hamers, J.E. Demuth [ *Phys. Rev. Lett. (USA)* vol.55 (1986) p.1303 ]
- [4] R.J. Hamers, R.M. Tromp, J.E. Demuth [ *Phys. Rev. B (USA)* vol.34 (1986) p.5343 ]
- [5] K.C. Pandey [ *Proc. 17<sup>th</sup> Int. Conf. on the Physics of Semiconductors* Eds. D.J. Chadi, W.A. Harrison (Springer, New York, 1985) p.55 ]
- [6] N. Roberts, R.J. Needs [ *Surf. Sci. (Netherlands)* vol.236 (1990) p.112 ]
- [7] S. Ihara, S.L. Ho, T. Uda, S. Hirao [ *Phys. Rev. Lett. (USA)* vol.65 (1990) p.1909 ]
- [8] J. Wang, T.A. Arias, J.D. Joannopoulos [ *Phys. Rev. B (USA)* vol.47 (1993) p.10497 ]
- [9] A. Ramstad, G. Brocks, P.J. Kelly [ *Phys. Rev. B (USA)* vol.51 (1995) p.14504 ]
- [10] W.A. Harrison [ *Phys. Rev. B (USA)* vol.24 (1981) p.5838 ]
- [11] P.N. Keating [ *Phys. Rev. (USA)* vol.145 (1966) p.637 ]
- [12] D.J. Chadi [ *Phys. Rev. Lett. (USA)* vol.43 (1979) p.43 ]; D.J. Chadi [ *J. Vac. Sci. Technol. (USA)* vol.16 (1979) p.1290 ]
- [13] J. Dabrowski, M. Scheffler [ *Appl. Surf. Sci. (Netherlands)* vol.56-58 (1992) p.15 ]
- [14] R.I.G. Uhrberg, G.V. Hansson, J.M. Nicholls, S.A. Flodstrom [ *Phys. Rev. B (USA)* vol.24 (1981) p.4684 ]
- [15] R.J. Hamers, U. Kohler [ *J. Vac. Sci. Technol. A (USA)* vol.7 (1989) p.2854 ]
- [16] T. Tabata, T. Aruga, Y. Murata [ *Surf. Sci. (Netherlands)* vol.179 (1987) p.L63 ]
- [17] R.A. Wolkow [ *Phys. Rev. Lett. (USA)* vol.68 (1992) p.2636 ]
- [18] D. Badt, H. Wengelnik, H. Neddermeyer [ *J. Vac. Sci. Technol. B (USA)* vol.12 (1994) p.2015 ]
- [19] R.M. Tromp, R.G. Smeenk, F.W. Saris [ *Phys. Rev. Lett. (USA)* vol.46 (1981) p.9392 ]
- [20] G. Jayaram, P. Xu, L.D. Mark [ *Phys. Rev. Lett. (USA)* vol.71 (1993) p.3489 ]
- [21] J. Ihm, D.H. Lee, J.D. Joannopoulos, J.J. Xiong [ *Phys. Rev. Lett. (USA)* vol.51 (1983) p.1872 ]
- [22] A. Saxena, E.T. Gawlinski, J.D. Gunton [ *Surf. Sci. (Netherlands)* vol.160 (1985) p.618 ]
- [23] V.E. Zubkus, P.J. Kundrotas, S.N. Molotkov, V.V. Zatarsi, E.E. Tornau [ *Surf. Sci. (Netherlands)* vol.243 (1991) p.295 ]
- [24] S.J. Jenkins, G.P. Srivastava [ *J. Phys., Condens. Matter (UK)* vol.8 (1996) p.6641 ]
- [25] B.W. Holland, C.B. Duke, A. Patton [ *Surf. Sci. (Netherlands)* vol.140 (1984) p.L267 ]
- [26] N. Jedrecy, M. Sauvage-Simkin, R. Pinchaux, J. Massiers, N. Greiser, V.H. Etgens [ *Surf. Sci. (Netherlands)* vol.230 (1990) p.197 ]
- [27] M. Takahashi, S. Nakatani, Y. Ito, T. Takahashi, X.W. Zhang, M. Ando [ *Surf. Sci. (Netherlands)* vol.338 (1995) p.L846 ]
- [28] R.N. Thomas, M.H. Francombe [ *Appl. Phys. Lett. (USA)* vol.11 (1967) p.108 ]
- [29] T. Sakamoto et al [ *Surf. Sci. (Netherlands)* vol.86 (1979) p.102 ]
- [30] R.I.G. Uhrberg, J.E. Northrup, D.K. Biegelsen, R.D. Brigans, L.-E. Swartz [ *Phys. Rev. B (USA)* vol.46 (1992) p.10251 ]
- [31] W.K. Liu, S.M. Mokler, N. Ohtani, C. Roberts, B.A. Joyce [ *Surf. Sci. (Netherlands)* vol.264 (1992) p.301 ]
- [32] K. Miki, K. Sakamoto, T. Sakamoto [ *Appl. Phys. Lett. (USA)* vol.71 (1997) p.3266 ]
- [33] V.A. Grazhulis, V.F. Kuleshov [ *Appl. Surf. Sci. (Netherlands)* vol.22-23 (1985) p.14 ]
- [34] D. Haneman [ *Phys. Rev. Lett. (USA)* vol.121 (1961) p.1093 ]
- [35] F.J. Himpsel, P. Heimann, T.-C. Chiang, D.E. Eastman [ *Phys. Rev. Lett. (USA)* vol.45 (1980) p.1112 ]
- [36] S. Brennan, J. Stohr, R. Jaeger, J.E. Rowe [ *Phys. Rev. Lett. (USA)* vol.45 (1980) p.1414 ]
- [37] K.C. Pandey [ *Phys. Rev. Lett. (USA)* vol.49 (1982) p.223 ]
- [38] J.E. Northrup, M.L. Cohen [ *Phys. Rev. Lett. (USA)* vol.49 (1982) p.1349 ]

### 5.1 Reconstruction of silicon (001), (111) and (110) surfaces

- [39] P. Badzigg, W.S. Verwoerd [ *Surf. Sci. (Netherlands)* vol.201 (1988) p.87 ]
- [40] F. Ancilotto, W. Andreoni, A. Selloni, R. Car, M. Parrinello [ *Phys. Rev. Lett. (USA)* vol.65 (1990) p.3148 ]
- [41] J.E. Northrup, M.S. Hybertsen, S.G. Louie [ *Phys. Rev. Lett. (USA)* vol.66 (1991) p.500 ]
- [42] N. Takeuchi, A. Selloni, A.I. Shkrebtii, E. Tosatti [ *Phys. Rev. B (USA)* vol.44 (1991) p.13611 ]
- [43] R.M. Tromp, L. Smit, J.F. van der Veen [ *Phys. Rev. Lett (USA)* vol.51 (1983) p.1672 ]
- [44] R. Feder, W. Monch [ *Solid State Commun. (USA)* vol.50 (1984) p.311 ]
- [45] F.J. Himpel, P.M. Marcus, R. Tromp, I.P. Batra, F. Jona, H. Liu [ *Phys. Rev. B (USA)* vol.30 (1984) p.2257 ]
- [46] H. Sakama, A. Kawazu, K. Ueda [ *Phys. Rev. B (USA)* vol.34 (1986) p.1367 ]
- [47] R.M. Feenstra, W.A. Thompson, A.P. Fein [ *Phys. Rev. Lett. (USA)* vol.56 (1986) p.608 ]
- [48] J.A. Stroscio, R.M. Feenstra, A.P. Fein [ *Phys. Rev. Lett. (USA)* vol.57 (1986) p.2579 ]
- [49] D. Reichardt [ *Prog. Surf. Sci. (UK)* vol.35 (1991) p.63 ]
- [50] K. Takayangi, Y. Tanishiro, M. Takahashi, S. Takahashi [ *Surf. Sci. (Netherlands)* vol.164 (1985) p.367 ]
- [51] P.A. Bennett, L.C. Feldman, Y. Kuk, E.G. McRae, J.E. Rowe [ *Phys. Rev. B (USA)* vol.28 (1983) p.3656 ]
- [52] E.G. McRae [ *Surf. Sci. (Netherlands)* vol.124 (1983) p.106 ]
- [53] F.J. Himpel [ *Phys. Rev. B (USA)* vol.27 (1983) p.7782 ]
- [54] W.A. Harrison [ *Surf. Sci. (Netherlands)* vol.55 (1976) p.1 ]
- [55] G. Binnig, H. Rohrer, Ch. Gerber, E. Weibel [ *Phys. Rev. Lett. (USA)* vol.50 (1983) p.120 and *Surf. Sci. (Netherlands)* vol.131 (1983) p.L379 ]
- [56] R.S. Becker, J.A. Golovchenko, B.S. Swartzentruber [ *Phys. Rev. Lett. (USA)* vol.54 (1985) p.2678 ]
- [57] R.J. Hamers, R.M. Tromp, J.E. Demuth [ *Phys. Rev. Lett. (USA)* vol.56 (1986) p.1972 ]
- [58] J.E. Northrup, M.L. Cohen [ *Phys. Rev. B (USA)* vol.29 (1984) p.1966 ]
- [59] J.E. Northrup [ *Phys. Rev. Lett. (USA)* vol.57 (1986) p.154 ]
- [60] R.D. Meade, D. Vanderbilt [ *Phys. Rev. B (USA)* vol.40 (1989) p.3905 ]
- [61] R.M. Tromp, R.J. Hamers, J.E. Demuth [ *Phys. Rev. Lett. (USA)* vol.55 (1986) p.1303 and *Science (USA)* vol.234 (1986) p.304 ]
- [62] K.D. Brommer, M. Needels, B.E. Larson, J.D. Joannopoulos [ *Phys. Rev. Lett. (USA)* vol.68 (1992) p.1355 ]
- [63] I.K. Robinson, W.K. Waskiewicz, P.H. Fuoss, N.J. Norton [ *Phys. Rev. B (USA)* vol.37 (1988) p.4325 ]
- [64] R.M. Feenstra, M.A. Lutz [ *Phys. Rev. B (USA)* vol.42 (1990) p.5391 ]
- [65] W. Telieps, E. Bauer [ *Surf. Sci. (Netherlands)* vol.162 (1985) p.163 ]
- [66] K. Miki et al [ *Ultramicroscopy (Netherlands)* vol.42-44 pt.A (1992) p.85 ]
- [67] Y. Yamamoto [ *Surf. Sci. (Netherlands)* vol.313 (1994) p.155 ]
- [68] A.J. Hoeven, D. Dijkkamp, E.J. van Loenen, P.J.G.M. van Hooft [ *Surf. Sci. (Netherlands)* vol.211/212 (1989) p.165 ]
- [69] W.E. Packard, J.D. Dow [ *Phys. Rev. B (USA)* vol.55 (1997) p.15643 ]
- [70] N. Safta et al [ *Nucl. Instrum. Methods Phys. Res. B (Netherlands)* vol.97 (1995) p.372 ]
- [71] R.S. Becker, B.S. Swartzentruber, J.S. Vickers [ *J. Vac. Sci. Technol. A (USA)* vol.6 (1988) p.472 ]
- [72] E.G. Keim, H. Wormeester, A van Silfhout [ *J. Vac. Sci. Technol. A (USA)* vol.8 (1990) p.2747 ]

## 5.2 Structure of clean silicon surfaces: vicinal Si(001) and Si(111) surfaces

V. Zielasek, Feng Liu and M.G. Lagally

November 1998

### A INTRODUCTION

Silicon surfaces are never perfectly flat but contain steps on a macroscopic scale. Atomic steps on low-index Si surfaces, acting, for instance, as nucleation centres in epitaxial growth or as scattering centres for charge transport near the surface, are not always considered as unwanted defects. Vicinal silicon surfaces, i.e. surfaces deliberately oriented slightly away from a low-index direction, are preferred substrates for the growth of smooth Si films because under appropriate conditions the film grows via step-flow: the steps proceed in the direction of the substrate miscut by incorporating adatoms. Regularly stepped Si surfaces also find applications as substrates for the growth of ordered low-dimensional nanostructures like arrays of quantum wires or dots. Knowing the atomic structure of steps and their interaction mechanisms is essential for their control.

### B VICINAL Si(001)

#### B1 Step Structure and Energy

Due to the symmetry of the diamond structure, the dimer row directions of terraces separated by an odd number of monatomic steps are perpendicular to each other, giving rise to both (2×1) and (1×2) domains at room temperature. All steps on Si(001) may be considered as a sequence of step segments oriented either along [110] or [1̄10]. Two different types of monatomic-height step segments exist: segments for which the upper-terrace dimer rows are parallel (perpendicular) to the step are called  $S_A$  ( $S_B$ ) [1]. Depending on the registry of the step edge with the dimer row reconstruction on the lower terrace,  $S_B$  steps can have two kinds of edge structure that are distinguished as rebonded or non-rebonded. The rebonded  $S_B$  step edge lowers the number of dangling bonds with respect to the non-rebonded step edge.

Although there can be two types of double steps ( $D_A$  and  $D_B$ ) [1], only  $D_B$  steps form [2,3]. Like  $S_B$  steps,  $D_B$  steps can have either a rebonded or non-rebonded structure. Experiments [2–4] show that on natural surfaces rebonded  $S_B$  and  $D_B$  step edges appear much more frequently than their non-rebonded counterparts, in agreement with total energy calculations [1]. The calculations yield as formation energy  $E$  per step atom:

$$\begin{aligned} E(S_A) &= 0.01(\pm 0.01) \text{ eV} \\ E(S_B) &= 0.15(\pm 0.03) \text{ eV} \\ E(D_A) &= 0.54(\pm 0.10) \text{ eV} \\ E(D_B) &= 0.05(\pm 0.02) \text{ eV} \quad (S_B \text{ and } D_B \text{ rebonded}) \end{aligned}$$

The energy of  $S_A$  steps is lowest because their formation induces neither extra dangling bonds nor extra stress due to step rebonding. FIGURE 1 shows the details of the atomic structure of  $S_A$  and rebonded  $S_B$  and  $D_B$  step segments in a perspective view.

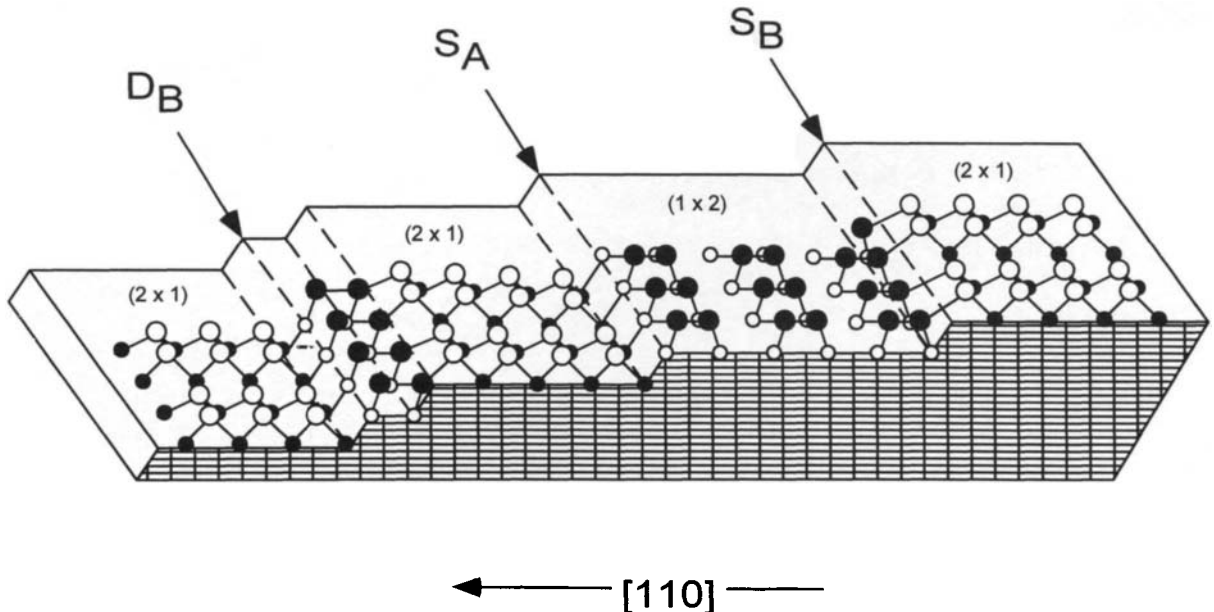


FIGURE 1 Ball-and-stick model of the most common step types on Si(001) in a perspective view.  $S_B$  and  $D_B$  steps are shown in their rebonded configuration, i.e. the step dimers of the top-most terrace bond to a dimer of the adjacent terrace or step and not to a single atom.

## B2 Miscut Angles Less than $1^\circ$

For miscut angles smaller than  $1^\circ$  only monatomic steps with a height of 0.136 nm are observed. Running nominally at  $45^\circ$  to the dimer row directions, steps on surfaces miscut toward a  $\{100\}$  direction are composed of equal numbers of  $S_A$  and  $S_B$  segments. On vicinal surfaces miscut towards a  $\{110\}$  direction  $S_A$  and  $S_B$  steps alternate (see FIGURE 1). Usually,  $S_A$  steps appear smooth in STM images while  $S_B$  steps appear rough, containing many kinks and segments of  $S_A$  termination [5]. There are more  $S_A$  kinks in an  $S_B$  step than  $S_B$  kinks in an  $S_A$  step because it costs less energy to create an  $S_A$  step segment. Analysing the  $S_A$  and  $S_B$  kink density in scanning tunnelling microscopy (STM) images, Swartzentruber et al [5] determined the energies  $E_{\text{exp}}$  per step atom required to form  $S_A$  and  $S_B$  segments experimentally as:

$$E_{\text{exp}}(S_A) = 0.028(\pm 0.002) \text{ eV}$$

$$E_{\text{exp}}(S_B) = 0.09(\pm 0.01) \text{ eV}$$

Monatomic steps separate surface stress domains because the in-plane stress of a dimerized terrace is anisotropic and the dimer row orientation rotates by  $90^\circ$  at the step edge [6]. At equilibrium the areas of both domains, i.e.  $(2 \times 1)$  and  $(1 \times 2)$  terraces, are nearly equal for surfaces with miscut angles smaller than  $0.3^\circ$ . As demonstrated by Men et al [7], uniaxial external strain applied to the surface in a  $\{110\}$  direction leads to step movement and the prevalence of either  $(2 \times 1)$  or  $(1 \times 2)$  domains because terraces with dimers oriented in the direction of higher compression are energetically favoured.

Low-energy electron microscopy (LEEM) of surfaces with miscuts smaller than  $0.2^\circ$  [8,9] has observed a surface transition from overall straight steps, randomly kinked and oriented according to the local miscut, to wavy steps with a macroscopic sinusoidal shape. These long-wavelength undulations of the steps are stabilised by a reduction of the size of surface-stress domains [10]. LEEM also shows that for miscuts smaller than  $0.03^\circ$  the surface separates in areas with straight steps and in

## 5.2 Structure of clean silicon surfaces: vicinal Si(001) and Si(111) surfaces

areas with hill-like structures, limiting the size of stress domains by increasing the step density over the value required to accommodate the miscut [9].

### B3 Miscut Angles Between 1° and 10°

If the surface is miscut by more than 1° towards {110} double-atomic-height steps begin to form and their fraction increases with increasing miscut angle [2,11–14]. The absence of  $D_A$  steps [2,3] leads to a predominance of  $D_B$  steps and terraces with dimer rows oriented in the direction of the miscut. Rebonded steps cause strain in the backbond of the upper terrace. The generated strain field, extending far from the step, leads to an attractive interaction between the  $S_B$  step and the adjacent lower  $S_A$  step [15], influencing the relative terrace width of (2×1) and (1×2) domains for steps as far as 8 nm apart [11]. The evolution of the surface structure with miscut has been studied by STM and electron diffraction [11,12,16] and is found to be a complex evolution led by the step-step interaction and the energy difference between an  $S_A$ - $S_B$  step pair and a rebonded  $D_B$  step. The dependence of the fraction  $f_{doub}$  of double steps on the miscut angle  $\alpha$  as determined by Swartzentruber et al [11] is shown in TABLE 1. Here  $f_{doub}$  is related to the total number of both single and double steps. The dependence of the step structure on the miscut azimuth has been studied by LEED on a lens-shaped sample [17]. On vicinal Si(001) miscut towards {100} only monatomic steps have been observed for miscut angles up to several degrees.

TABLE 1 Miscut angle versus  $f_{doub}$ .

$\alpha$ (deg)	$f_{doub}$
1.2	0.02
1.8	0.18
3.0	0.40
3.5	0.64

## C VICINAL Si(111)

### C1 Step Structure of Cleavage Surfaces

On cleaved surfaces the predominant step height is 0.314 nm, corresponding to the height of one double-layer, as suggested by the crystal structure and first shown by LEED [18]. Almost all steps are oriented along one of three equivalent directions with the outward normals along  $[2\bar{1}\bar{1}]$ ,  $[\bar{1}2\bar{1}]$ , or  $[\bar{1}\bar{1}2]$  [18,19]. For a bulk-terminated surface the step atoms of the upper terrace would have only two nearest neighbours and two dangling bonds. The (2×1) reconstructed surface can have its  $\pi$ -bonded chains running either parallel to the step edge or rotated by ±60°. Details of the step structures of the reconstructed surface have been studied by STM [19], showing that the (2×1) reconstruction extends right to the steps. The step atoms of the upper terrace rebond to the lower terrace with unit periodicity along the step edges, reducing the number of dangling bonds per step atom by one. FIGURE 2 shows two possible step structures as deduced from STM images by Feenstra and Stroscio [19].

### C2 Annealed or Epitaxial Si(111)

On carefully annealed Si(111) surfaces, i.e. tempered at 700°C for several hours and cooled down to room temperature slowly, the width of the (7×7) reconstructed terraces is quantised to units of half of

## 5.2 Structure of clean silicon surfaces: vicinal Si(001) and Si(111) surfaces

the  $(7 \times 7)$  mesh [20]. STM images by Becker et al [21] revealed that the reconstruction extends right to the steps and the steps run along the  $(7 \times 7)$  mesh edge through the corner holes of both upper and lower terrace. The terrace width quantisation, rendering the formation of kinks energetically extremely costly, has been used to promote the formation of arrays of perfectly straight steps over areas of more than  $100 \times 100 \text{ nm}^2$  [22]. On quickly cooled samples a quantisation of the terrace widths is not found and several shift vectors between the  $(7 \times 7)$  meshes on upper and lower terrace have been observed [20,23,24].

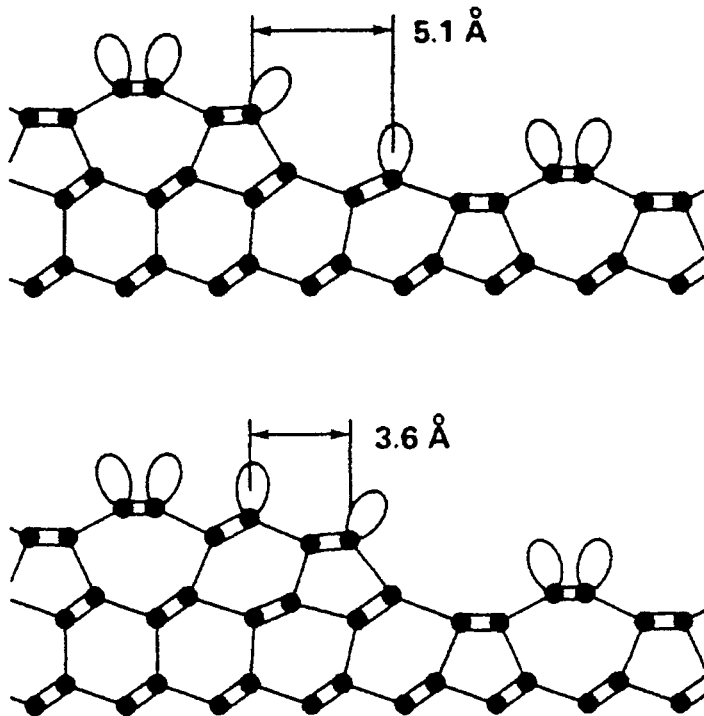


FIGURE 2 Side view of models for the step rebonding on cleavage Si(111), after [19]. The models include the  $(2 \times 1)$  reconstruction of the terrace and show the dangling bonds.

Besides steps with outward normals in the three equivalent  $\{2\bar{1}\bar{1}\}$  directions steps in the opposite directions are also found in STM images [23], in contrast to cleaved Si(111). The atomic configuration and the rebonding of both classes of steps is the same because the  $\{\bar{2}11\}$  steps form boundaries of those halves of the  $(7 \times 7)$  unit mesh that have a stacking fault in the topmost double layer whereas  $\{2\bar{1}\bar{1}\}$  steps form the boundary of unfaulted  $(7 \times 7)$  sections. Epitaxially grown Si islands on Si(111)-(7x7), however, exhibit preferentially a triangular shape with steps in the  $\{2\bar{1}\bar{1}\}$  directions [25].

Williams and co-workers [26,27] found a mixture of single-height ( $0.314 \text{ nm}$ ) and triple-height steps on annealed surfaces miscut towards  $(2\bar{1}\bar{1})$  and determined the dependence of the fraction  $f_{\text{trip}}$  of triple-height steps on the miscut angle  $\alpha$  (TABLE 2). The fraction  $f_{\text{trip}}$  is related to the total number of single and multiple steps. The abundance of triple-height steps increases with the miscut angle.

## 5.2 Structure of clean silicon surfaces: vicinal Si(001) and Si(111) surfaces

TABLE 2 Miscut angle versus  $f_{\text{trip}}$ .

$\alpha$ (deg)	$f_{\text{trip}}$
1.3( $\pm 0.1$ )	0.13( $\pm 0.02$ )
2.7( $\pm 0.3$ )	0.18( $\pm 0.01$ )
5.2( $\pm 0.4$ )	0.43( $\pm 0.03$ )
6.4( $\pm 0.6$ )	0.71( $\pm 0.06$ )

A faceting of the surface has been observed after annealing above the transition temperature between the (1×1) and the (7×7) reconstruction for samples miscut towards  $(\bar{2}11)$  or  $(1\bar{1}0)$  [28]. Above the transition temperature only monatomic height steps form for miscut angles up to 12°.

## D HIGH-INDEX SURFACES

No comprehensive surface energy diagram yet exists for silicon. In the range of orientations between (001) and (111) the morphology of a number of surfaces has been determined using diffraction and microscopy techniques ([29] and references therein). LEED experiments show that beyond 11° miscut away from the (001) orientation into the [110] direction (001) terraces with double height steps are admixed by (115) facets [17]. STM studies find that the (114) facet is the first stable surface close to (001) [29]. A structure model for the (2×1) reconstructed Si(114) facets involving dimers has been proposed, based on STM images and total-energy calculations [30]. For orientations between (114) and (113) the surfaces consist of (114) and (113) facets, forming a mesoscale sawtooth structure.

The bulk-terminated (113) surface would consist of alternating atomic rows with (001) and (111) orientations. Several structural models exist for the thermally very stable Si(113) surface showing a (3×2) reconstruction [31,32]. The surface energy is experimentally determined to be close to that of the Si(001) surface [33]. Calculations using the structure model of Dabrowski et al [32] based on dimers, rebonded step-like structure units, and interstitials yield a similarly low value.

For orientations from (113) to (5,5,12) the surface consists of mesoscale (113) and (5,5,12) facets with the (5,5,12) facets forming a (2×1) reconstruction with a  $0.77 \times 5.35 \text{ nm}^2$  large unit cell. A structural model consisting of tetramers and p-bonded chains is proposed, based on STM images [34]. In the orientation range between (5,5,12) and about (223) surfaces are composed of (5,5,12) and (111) facets [29]. Surfaces orientated in directions between (223) and (111) may be described as Si(111) terraces separated by single and triple atomic-height steps.

## E CONCLUSION

As for the terrace reconstructions the step structures of Si(001) and Si(111) are determined by the balance between the urge to reduce the number of dangling bonds and the cost of introducing additional surface stress. Strain induced by surface stress domains and by rebonding at step edges provides a mechanism for a step-step interaction ranging far beyond the local step area. On natural surfaces the fraction of multiple atomic-height steps increases with increasing miscut angle. All silicon surfaces in the range between (001) and (111) can generally be assembled from adatoms, dimers, rebonded steps, π-bonded chains, and tetramers.

## REFERENCES

- [1] D.J. Chadi [ *Phys. Rev. Lett. (USA)* vol.59 (1987) p.1691 ]
- [2] P.E. Wierenga, J.A. Kubby, J.E. Griffith [ *Phys. Rev. Lett. (USA)* vol.59 (1987) p.2169 ]

## 5.2 Structure of clean silicon surfaces: vicinal Si(001) and Si(111) surfaces

- [3] J.E. Griffith, G.P. Kochanski, J.A. Kubby, P.E. Wierenga [ *J. Vac. Sci. Technol. A (USA)* vol.7 (1989) p.1914 ]
- [4] N. Kitamura, B.S. Swartzentruber, M.G. Lagally, M.B. Webb [ *Phys. Rev. B (USA)* vol.48 (1993) p.5704 ]
- [5] B.S. Swartzentruber, Y.-W. Mo, R. Kariotis, M.G. Lagally, M.B. Webb [ *Phys. Rev. Lett. (USA)* vol.65 (1990) p.1913 ]
- [6] O.L. Alerhand, D. Vanderbilt, R.D. Meade, J.D. Joannopoulos [ *Phys. Rev. Lett. (USA)* vol.61 (1988) p.1973 ]
- [7] F.K. Men, W.E. Packard, M.B. Webb [ *Phys. Rev. Lett. (USA)* vol.61 (1988) p.2469 ]
- [8] R.M. Tromp, M.C. Reuter [ *Phys. Rev. Lett. (USA)* vol.68 (1992) p.820 ]
- [9] R.M. Tromp, M.C. Reuter [ *Phys. Rev. B (USA)* vol.47 (1986) p.7598 ]
- [10] J. Tersoff, E. Pehlke [ *Phys. Rev. Lett. (USA)* vol.68 (1992) p.816 ]
- [11] B.S. Swartzentruber, N. Kitamura, M.G. Lagally, M.B. Webb [ *Phys. Rev. B (USA)* vol.47 (1993) p.13432 ]
- [12] C.E. Aumann, J.J. de Miguel, R. Kariotis, M.G. Lagally [ *Surf. Sci. (Netherlands)* vol.275 (1992) p.1 ]
- [13] M. Schluter [ in *The Chemical Physics of Solid Surfaces and Heterogeneous Catalysis* Eds. D.A. King, D.P. Woodruff (Elsevier, Amsterdam, 1988) vol.5 p.37 ]
- [14] J.E. Griffith, G.P. Kochanski [ *CRC Crit. Rev. Solid State Mater. Sci. (USA)* vol.16 (1990) p.255 ]
- [15] E. Pehlke, J. Tersoff [ *Phys. Rev. Lett. (USA)* vol.67 (1991) p.465 ]
- [16] X. Tong, P.A. Bennett [ *Phys. Rev. Lett. (USA)* vol.67 (1991) p.101 ]
- [17] J. Wasserfall, W. Ranke [ *Surf. Sci. (Netherlands)* vol.315 (1994) p.227 ]
- [18] M. Henzler [ *Surf. Sci. (Netherlands)* vol.36 (1973) p.109 ]
- [19] R.M. Feenstra, J.A. Stroscio [ *Phys. Rev. Lett. (USA)* vol.59 (1987) p.2173 ]
- [20] J.L. Goldberg, X.S. Wang, J. Wei, N.C. Bartelt, E.D. Williams [ *J. Vac. Sci. Technol. A (USA)* vol.9 (1991) p.1868 ]
- [21] R.S. Becker, J.A. Golovchenko, E.G. McRae, B.S. Swartzentruber [ *Phys. Rev. Lett. (USA)* vol.55 (1985) p.2028 ]
- [22] J. Viernow, J.-L. Lin, D.Y. Petrovykh, F.M. Leibsle, F.K. Men, F.J. Himpsel [ *Appl. Phys. Lett. (USA)* vol.72 (1998) p.948 ]
- [23] H. Tochihara, W. Shimada, M. Itoh, H. Tanaka, M. Udagawa, I. Sumita [ *Phys. Rev. B (USA)* vol.45 (1992) p.11332 ]
- [24] Yafei Wang, Tien T. Tsong [ *Phys. Rev. B (USA)* vol.53 (1996) p.6915 ]
- [25] U. Kohler, J.E. Demuth, R.J. Hamers [ *J. Vac. Sci. Technol. A (USA)* vol.7 (1989) p.2860 ]
- [26] R.J. Phaneuf, E.D. Williams [ *Phys. Rev. B (USA)* vol.41 (1992) p.2991 ]
- [27] Jian Wei, X.S. Wang, J.L. Goldberg, N.C. Bartelt, E.D. Williams [ *Phys. Rev. Lett. (USA)* vol.68 (1992) p.2885 ]
- [28] R.J. Phaneuf, E.D. Williams [ *Phys. Rev. Lett. (USA)* vol.58 (1987) p.2563 ]; R.J. Phaneuf, E.D. Williams, N.C. Bartlet [ *Phys. Rev. B (USA)* vol.38 (1988) p.1984 ]
- [29] A.A. Baski, S.C. Erwin, L.J. Whitman [ *Surf. Sci. (Netherlands)* vol.392 (1997) p.69 ]
- [30] S.C. Erwin, A.A. Baski, L.J. Whitman [ *Phys. Rev. Lett. (USA)* vol.77 (1996) p.687 ]
- [31] W. Ranke [ *Phys. Rev. B (USA)* vol.41 (1990) p.5243 ]
- [32] J. Dabrowski, H.-J. Mussig, G. Wolff [ *Phys. Rev. Lett (USA)* vol.73 (1994) p.1660 ]
- [33] D.J. Eaglesham, A.E. White, L.C. Feldman, N. Moriya, D.C. Jacobson [ *Phys. Rev. Lett. (USA)* vol.70 (1993) p.1643 ]
- [34] A.A. Baski, S.C. Erwin, L.J. Whitman [ *Science (USA)* vol.269 (1995) p.1556 ]

## **5.3 Electronic structure of c-Si surfaces**

R.I.G. Uhrberg

November 1998

### **A INTRODUCTION**

The aim of this Datareview is to present the electronic band structure of Si surfaces based on the vast information which has appeared in the literature during the past 25 years. The review is basically restricted to experimental studies by angle-resolved photoemission and k-resolved inverse photoemission which give the surface band structure of the occupied and unoccupied surface states, respectively. Many surface states and surface resonances have been reported through the years especially for the Si(100)2×1 surface. The review is restricted to the most well established surface states and resonances. In some cases the surface state identification may still be considered uncertain, which is then pointed out in the text. A more detailed description of the surface electronic structure of the Si surfaces can be found in [1] and [2] which have extensive reference lists of the early photoemission studies.

### **B SURFACE ELECTRONIC STRUCTURE OF Si(100)**

The description of the Si(100) surface is based on [3] and the results presented in some later studies [4–7].

The clean Si(100) surface shows a 2×1 low energy electron diffraction (LEED) pattern at room temperature (RT) and a c(4×2) pattern below ~220 K when prepared in ultra high vacuum (UHV) [8]. The basic building blocks of these surfaces are the same, i.e. dimers on the surface. Each dimer atom makes two bonds with the underlying atoms (back-bonds) and one bond with the second atom of the dimer (dimer-bond). The fourth valence electron occupies a dangling-bond orbital. Based on this atomic structure we can expect to find several surface states, i.e. electronic states related to dangling-bonds, dimer-bonds and back-bonds which should all be located in the surface region. It has been under debate whether the dimers are tilted or not. The electronic structure observed by angle-resolved photoemission is, however, only consistent with tilted (asymmetric) dimers. The surface electronic structures of the room temperature 2×1 phase and the low temperature c(4×2) phase are very similar and they can both be explained by the c(4×2) periodicity. When interpreting the results of angle-resolved photoemission there are two things to be aware of. First, the on-axis Si(100) surface always has two 2×1/c(4×2) domains which differ in the orientation of the reconstruction by 90°. Secondly, a phase transition from 2×1 to c(4×2) occurs at ≈220 K. Since the asymmetric dimers are the basic ingredients of both phases the surface electronic structure should be very similar. The difference between the 2×1 and c(4×2) phases is just in the ordering of the tilt directions of the asymmetric dimers. In an idealised 2×1 reconstruction all dimers would be tilted in the same direction while in the c(4×2) reconstruction the dimers have an alternating tilt direction both parallel and perpendicular to the dimer rows. The size of the c(4×2) unit cell is twice the size of the 2×1 cell which means that the number of surface bands will be doubled for a c(4×2) surface compared to a surface with a true 2×1 periodicity.

Most of the studies of the surface electronic structure have been performed on on-axis Si(100) samples which show two-domain 2×1 LEED patterns. When probing the surface state dispersions along the  $\bar{\Gamma}$  –  $\bar{J}$  and  $\bar{\Gamma}$  –  $\bar{J}'$  symmetry axes one always obtains a superposition of these two symmetry

### 5.3 Electronic structure of *c*-Si surfaces

lines on a two-domain surface. The problem of superposition can be avoided by measuring along a direction in between these symmetry lines. Such a line corresponds to a [010] azimuthal direction. FIGURE 1 shows the  $2\times 1$  and  $c(4\times 2)$  surface Brillouin zones (SBZ) for the two orientations of the domains. The surface state dispersions are presented along the [010] direction in FIGURE 2 for a two domain surface. Although the [010] direction is not a symmetry line of the  $2\times 1$  or the  $c(4\times 2)$  reconstruction it serves as a good illustration of the surface band structure of the Si(100) surface.

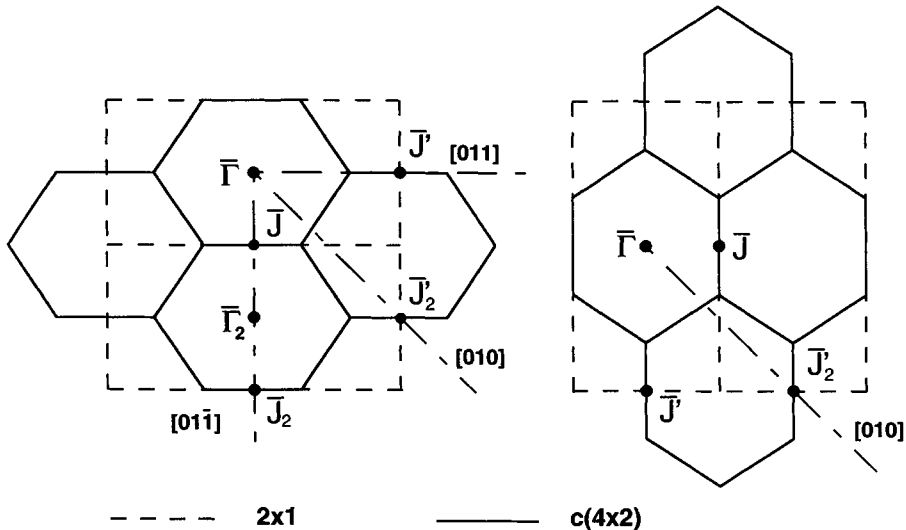


FIGURE 1 Surface Brillouin zones of the  $2\times 1$  and  $c(4\times 2)$  unit cells of Si(100). Left and right figures show the orientation of the SBZs for the two  $90^\circ$  rotated domains. The symmetry points refer to the  $2\times 1$  SBZ.

#### B1 Dangling-Bond Surface States

The experimental surface state dispersions labelled A and B have been identified as due to dangling-bond surface states. Comparisons with calculated surface band structures show that the dispersion A agrees very well with the theoretical predictions for a  $2\times 1$  reconstructed surface with asymmetric dimers. The dispersion B, which corresponds to a clear surface state peak in the angle-resolved photoemission spectra, cannot be explained by a  $2\times 1$  asymmetric dimer model. Various explanations have been proposed for the B structure but it is now clear that it is related to  $c(4\times 2)$  arrangements of the dimers on the surface. The B structure appears with the same intensity independent of the preparation of the Si(100) $2\times 1$  surface. Based on Si 2p core-level and valence band studies it has been concluded that the  $2\times 1$  surface at room temperature is to be regarded as a disordered  $c(4\times 2)$  surface [4–7,9]. A  $c(4\times 2)$  surface has two dangling-bond bands and the calculated dispersions [10] of these bands agree very well with the measured dispersions [7] for both the  $2\times 1$  (RT) and  $c(4\times 2)$  (low temperature) surfaces (see FIGURE 3).

The initial energies of the surface states vary, dependent on the doping level of the sample and the cleanliness of the surface. For samples with a moderate doping level, and just after cleaning, the energy position of A at  $\bar{\Gamma}$  is typically 0.5 eV below the Fermi level ( $E_F$ ) at room temperature (cold samples give a different value due to surface photovoltage shifts). The Fermi-level is located within the surface bandgap for such surfaces. The energy position of A at  $\bar{\Gamma}$  moves downward to a stable

### 5.3 Electronic structure of *c*-Si surfaces

position at  $\approx 0.7$  eV below  $E_F$  after a few hours in UHV. This corresponds to a situation where the Fermi-level is pinned at the minimum of the unoccupied dangling bond bands.

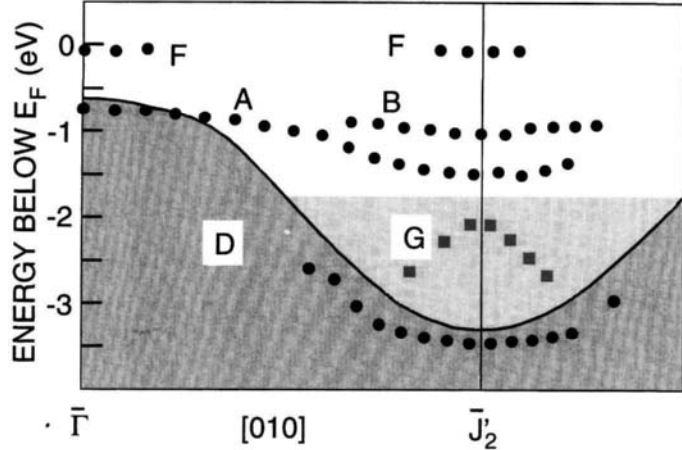


FIGURE 2 Dispersions of the surface states A, B, F and D along the [010] direction for a two-domain  $2 \times 1$  surface. The surface character of G is less well defined as discussed in the text. The shaded region is the bulk band structure projected on a  $1 \times 1$  SBZ and the lighter shaded area shows the additional projection due to the  $2 \times 1$  periodicity. A value of 0.6 eV was used for  $E_F - E_V$  [3].

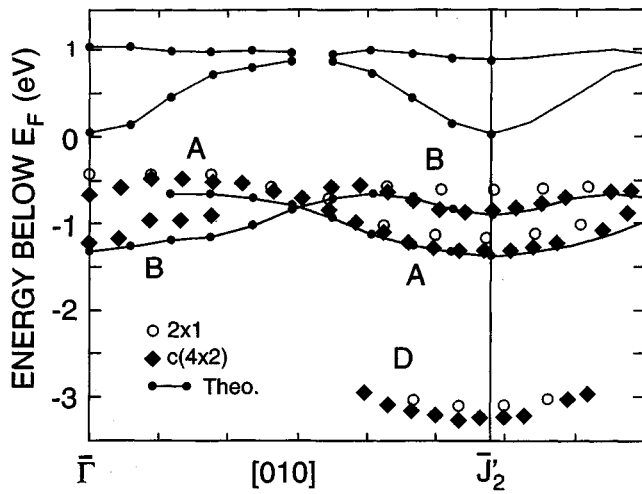


FIGURE 3 The experimental dispersions of the dangling-bond bands A and B obtained from both a  $2 \times 1$  and a  $c(4 \times 2)$  surface [7] are compared with calculated dispersions [10] for a  $c(4 \times 2)$  periodicity.

The surface state dispersions obtained from a single domain surface are shown in FIGURES 4 and 5. The single domain surface was obtained by using a  $4^\circ$  off-axis Si(l00) sample. Along  $\bar{\Gamma} - \bar{J}'$  in the [011] direction the A state disperses downwards similar to the case for the [010] direction. The B surface band is observed near  $\bar{J}'$  and it is almost flat in this region of the Brillouin zone. Along  $\bar{\Gamma} - \bar{J}$  in the  $[0\bar{1}\bar{1}]$  direction the A band is almost flat ( $\sim 0.1$  eV dispersion). The surface band B is more difficult to identify in this direction. A few data points around  $-1.0$  eV near  $\bar{\Gamma}_2$  are assigned to the B

### 5.3 Electronic structure of c-Si surfaces

band. The presence of two dangling bond bands is evidence for the existence of a  $c(4\times 2)$  periodicity on room temperature surfaces which exhibit a  $2\times 1$  LEED pattern. The existence of a second dangling-bond related state on single-domain  $2\times 1$  surfaces has been reported also in other studies [1,4].

The unoccupied part of the surface band structure can be studied with photoemission under certain conditions. By using n-type samples with a high doping concentration ( $\sim 1\times 10^{19} \text{ cm}^{-3}$ ), electrons from the bulk will accumulate on the surface leading to a band bending. The surface electrons occupy the lowest surface electronic states above the surface bandgap. If the occupation is of the order of a few percent the emission from these states can be observed in photoemission. For the room temperature  $2\times 1$  as well as for the  $c(4\times 2)$  surface obtained at low temperatures emission from states above the gap, F, can be observed at both the  $\bar{\Gamma}$  and the  $\bar{J}'$  points (see FIGURES 2–4). From the intensity of the photoemission peaks the minimum at  $\bar{\Gamma}$  seems to be slightly lower in energy than the minimum at the  $\bar{J}'$ -point. This is in good agreement with the calculated empty band dispersion for the  $c(4\times 2)$  periodicity in FIGURE 3, which shows minima at both the  $\bar{\Gamma}$  and the  $\bar{J}'$  points. The photoemission observation cannot be explained by a  $2\times 1$  periodicity since calculations give a dangling-bond band with only one minimum appearing at the  $\bar{J}'$  point.

The unoccupied part of the dangling-bond band structure has been studied more directly with inverse photoemission on a single domain  $2\times 1$  surface using a  $4^\circ$  off-axis sample [11]. The experimental dispersions of the empty bands are shown in FIGURES 4 and 5 along the  $\bar{\Gamma}-\bar{J}'$  and  $\bar{\Gamma}-\bar{J}$  symmetry lines of the  $2\times 1$  SBZ. Along the  $\bar{\Gamma}-\bar{J}-\bar{\Gamma}_2$  line two flat dangling-bond bands were observed. Along the  $\bar{\Gamma}-\bar{J}'$  line the two bands show dispersion with local minima at the  $\bar{\Gamma}$  and the  $\bar{J}'$  points. These minima are the same as those observed in direct photoemission, i.e. F in FIGURES 2 and 4. One would thus expect the minimum of the empty bands from inverse photoemission to coincide with the F peak from photoemission. The energy difference that is observed can be attributed to the problem of determining the energy of a structure close to the Fermi level in a spectrum. This difficulty is more apparent in inverse photoemission due to a lower energy resolution compared to photoemission. The solid lines show the calculated dispersion based on a  $2\times 1$  asymmetric dimer model [12]. The occupied dangling bond band associated with the up-atoms of the asymmetric dimers is labelled  $D_{\text{up}}$  while the empty dangling-bond band is denoted  $D_{\text{down}}$ . It is obvious that the  $2\times 1$  periodicity cannot explain the existence of two empty dangling-bond bands. The results of the inverse photoemission lead to the conclusion that also the empty dangling bond bands correspond to a  $c(4\times 2)$  periodicity of the asymmetric dimers.

The appearance of a second filled as well as empty dangling-bond surface band can in principle be explained by a  $p(2\times 2)$  periodicity since that unit cell has twice the area of a  $2\times 1$  cell. A possible  $p(2\times 2)$  origin of the second band has been discussed in different studies. Since the low temperature phase is  $c(4\times 2)$  it is natural to view the room temperature  $2\times 1$  phase as a disordered  $c(4\times 2)$  surface which still exhibits the  $c(4\times 2)$  surface electronic structure as is clearly demonstrated in FIGURE 3.

#### B2 Back-Bond Surface States

The surface state band D along the  $\bar{\Gamma}-\bar{J}'$  line ([010] direction) corresponds to a strong well-defined structure in the photoemission spectra. It is also observed in the [011] direction and by comparing with a calculated band structure for the  $2\times 1$  surface it can be assigned to a back-bond state ( $B_2$ ) associated with the up-atom of the dimer. Since the dangling-bond states show a  $c(4\times 2)$  character it would be more appropriate to compare with back-bond bands for a  $c(4\times 2)$  surface but no such dispersions have been published. In two studies a surface resonance at  $\sim -2$  to  $-3$  eV below  $E_F$  for

### 5.3 Electronic structure of c-Si surfaces

$\bar{k}_{\parallel}$ -values centred around the midpoint between  $\bar{\Gamma}$  and  $\bar{J}'_2$  has been identified [13,14]. Structure D and the surface resonance reported in these two studies correspond most likely to the same surface band. In the study by Johansson et al [3], the dispersion could be followed for a larger range of  $\bar{k}_{\parallel}$ -values. The full dispersion of D could not be determined in the previous studies due to technical constraints, i.e. too low photon energy [13] and too small light incidence angles [14] which made the emission intensity too low near  $\bar{J}'_2$ .

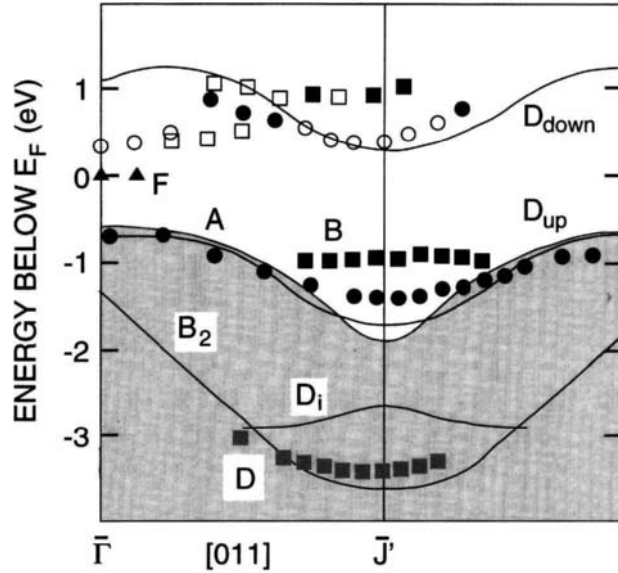


FIGURE 4 Dispersions of the surface states and resonances in the [011] direction on a single-domain Si(100)2×1 surface (A, B, F and D). Calculated surface bands ( $D_{up}$ ,  $D_{down}$ ,  $B_2$  and  $D_i$ ) based on an asymmetric dimer model are also shown [12]. The shaded region is the projected bulk band structure. Two empty bands from inverse photoemission are also included [11].

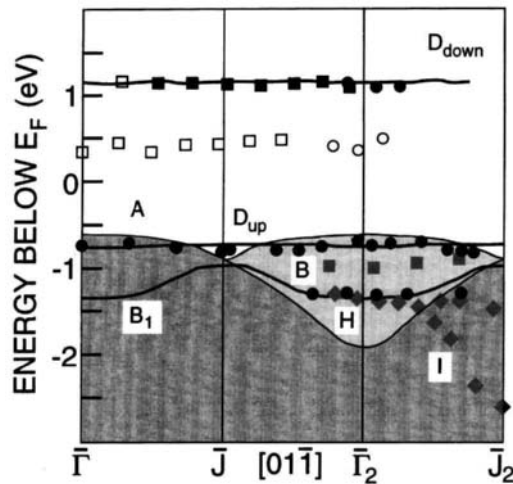


FIGURE 5 Dispersions of the surface states and resonances (A, B, H and I) in the  $[01\bar{1}]$  direction on a single-domain Si(100)2×1 surface [3]. Solid lines show two occupied surface bands ( $D_{up}$  and  $B_1$ ) and one empty band,  $D_{down}$  [12]. Two empty bands from inverse photoemission are also included [11].

### 5.3 Electronic structure of c-Si surfaces

Another surface band (H) is located at  $\sim -1.3$  eV near  $\bar{\Gamma}_2$  (see FIGURE 5). Beyond that point, it splits into two bands, one non-dispersive (H) and one steeply dispersing band (I). Both bands H and I were also present in the single-domain data presented by Enta et al [4]. However, only the band H was identified as a surface band in that study. Structure H coincides with the calculated back-bond band  $B_1$  near  $\bar{\Gamma}_2$ . There is, however, some uncertainty regarding the interpretation of this peak. The structure H may also correspond to the dangling-bond peak at  $\bar{J}'$  from the other domain which may exist on a minor fraction of the surface. This interpretation is, however, unlikely, since there was no indication of a contribution from the other domain in the [011] direction, at  $\bar{J}'$ , and since the LEED patterns were essentially single domain. It is therefore concluded, in agreement with the study by Enta et al [4] that structure H is intrinsic to the dominating domain. The explanation offered by the asymmetric  $2\times 1$  dimer model is then that structure H should be associated with the  $B_1$  back-bond. There is no theoretical information on the dispersion of  $B_1$  on a c( $4\times 2$ ) surface. Enta et al [4] instead interpreted feature H as the second dangling bond band due to the c( $4\times 2$ ) periodicity. It is here worth noting that structure B (see FIGURE 5) was not identified in their spectra.

The steeply dispersing structure I, which splits off from structure H beyond  $\bar{\Gamma}_2$ , cannot be associated with any calculated surface-resonance band. This structure was found to be highly sensitive to hydrogen adsorption and it has also been observed with overlapping dispersions for various photon energies (14, 16 and 19 eV) [3]. An assignment of I to a surface resonance state seems therefore very likely although no assignment of its origin has been possible.

#### B3 Dimer Bond State

Some candidates for a dimer bond state have been presented in the literature but they have been less well-defined than the A and B dangling-bond states, the D back-bond state and the F empty dangling-bond state.

The structure G (see FIGURE 2) has previously been identified as a surface state by Koke et al [14], Goldmann et al [15] and Johansson and co-workers [16,17]. Energetically, G is located in the bandgap of the  $1\times 1$  projected bulk band structure. The dispersion is symmetric with respect to the boundary of the  $2\times 1$  SBZ and it is also found to be invariant for the photon energies 15.0, 16.85 and 21.2 eV for which photoemission data are available [16,17]. The emission corresponding to structure G is not reduced to the same extent as the dangling-bond state when normal light incidence is used, which indicates a higher degree of  $p_x, p_y$  character for the G state.

The structure G has been associated with the dimer bond [16]. Although the energy position at  $\bar{J}'_2$  is about 0.6 eV higher than the position of the theoretical dimer band  $D_i$  at  $\bar{J}'$  (see FIGURE 4), there is a qualitative agreement between G and  $D_i$  in that both disperse to a maximum at  $\bar{J}'_2$  and  $\bar{J}'$ , respectively. The G and  $D_i$  dispersions cannot be compared in detail since no surface band structure calculation has been presented along the [010] direction for Si(100). In a theoretical study by Landmark et al [18] the dimer band was obtained for Ge(100) $2\times 1$  along the [010] direction. The theoretical dispersion for  $D_i$  on Ge is very similar to the experimental results for G on Si(100) $2\times 1$ .

In order to obtain more information about the nature of structure G Johansson et al [16] performed hydrogen chemisorption studies. For the monohydride phase, Si(100) $2\times 1$ :H, one expects that the dangling-bond state is removed due to the formation of Si-H bonds. After the dihydride phase, Si(100) $1\times 1$ :2H, has formed, one expects that also the dimer-bond is removed, since two hydrogen

### 5.3 Electronic structure of c-Si surfaces

atoms are supposedly bonded to each silicon atom and the dimer is broken up. For the monohydride phase the two uppermost surface states A and B as well as structure D are completely removed [3,16,17]. Structure G, however, is still present on the monohydride surface which suggests that it could be due to the dimer-bond. Furthermore, structure G was not observed for Si(100) surfaces showing 3×1 or 1×1 LEED patterns, which both correspond to higher hydrogen exposures. The surface state interpretation of G [14–17] has been questioned since an alternative explanation is possible [3]. It was pointed out by Johansson et al [3] that a structure with a very similar dispersion could arise from surface umklapp scattering of bulk direct transitions originating from  $\bar{k}_{\parallel}$ -points close to the  $\bar{J}'$  point in a <001> type of direction. Calculations of the  $E_i(\bar{k}_{\parallel})$  relations for the direct transition structures showed only a very weak dependence on the photon energy, which is in agreement with the experimental results for the dispersion of structure G. The absence of structure G on the 3×1:H and 1×1:H surfaces can be explained by the surface umklapp interpretation since there is no reciprocal surface lattice vector that connects  $\bar{k}_{\parallel}$ -points corresponding to the  $\bar{J}'$  points of the 2×1 SBZ in the [010] and [011] directions on these surfaces. Presently, the available data do not seem sufficient to conclusively determine the nature of G.

## C SURFACE ELECTRONIC STRUCTURE OF Si(111)

### C1 Si(111)7×7

The most stable reconstruction of the Si(111) surface has a 7×7 surface unit cell, i.e. the unit cell is 49 times larger than for the ideal unreconstructed 1×1 surface. The 7×7 reconstruction is obtained by annealing a clean Si(111) surface, where the details of the annealing procedure depend on whether the clean surface has been obtained by cleaving, sputtering or heat cleaning.

The dimer adatom stacking-fault model (DAS-model) which describes the atomic structure of the 7×7 surface was proposed by Takayanagi et al [19] based on transmission electron diffraction studies. This model is shown schematically in FIGURE 6. There are 12 adatoms, 6 rest atoms, 9 dimers and one corner hole per surface unit cell. In one half of the unit cell there is a stacking fault.

Throughout the last twenty years a large number of photoemission studies of the surface electronic structure on the Si(111)7×7 surface have been published as described in [1,2]. FIGURE 7 shows the surface state band structure obtained by angle-resolved photoemission and k-resolved inverse photoemission [20,21] along the  $\bar{\Gamma}-\bar{M}$  and  $\bar{\Gamma}-\bar{K}$  lines of the 1×1 SBZ (see FIGURE 8). The 7×7 surface exhibits three occupied surface states  $S_1$ ,  $S_2$  and  $S_3$ , in the energy range 0–2 eV below the Fermi level when studied at room temperature, and one unoccupied surface band,  $U_1$ . A strong support for the surface state interpretation of  $S_1$ ,  $S_2$  and  $S_3$  is given by the consistency of their dispersions for different photon energies, which is not found for the other structures in the spectra, and their sensitivity to contamination. A value of 0.63 eV for  $E_F-E_V$  was used to locate the top of the projected bulk bands. This value has been reported as an average for many 7×7 surfaces with a maximum spread of ≈0.15 eV [22].

The  $S_1$  surface state has a peak position that is  $\leq 0.2$  eV from the Fermi level and the high energy cut-off is very similar to the Fermi edge of a metal surface. This metallic character of the 7×7 surface has also been found in electron-energy-loss measurements, where it results in a very strong broadening of the elastic peak [23]. The emission intensity of the  $S_1$  surface state has a characteristic variation with the parallel wave vector,  $\bar{k}_{\parallel}$ , i.e. the emission intensity has a maximum approximately halfway between the  $\bar{\Gamma}$ -point and the SBZ boundary [24]. The points in FIGURE 7 show where the intensity

### 5.3 Electronic structure of *c*-Si surfaces

of  $S_1$  is high.  $S_1$  is also observed closer to  $\bar{\Gamma}$  but it is harder to determine the exact energy position since the intensity is rather low. It has been suggested that the  $S_1$  structure results from extrinsic effects [25], since it was seen with very low intensity in some studies. It is important to note that in those studies [25,26] the published spectra were all obtained at emission angles for which the intensity of  $S_1$  is low anyway, i.e. in the normal direction or at high emission angles. It is now generally accepted that  $S_1$  is an intrinsic surface state of the  $7\times 7$  surface.

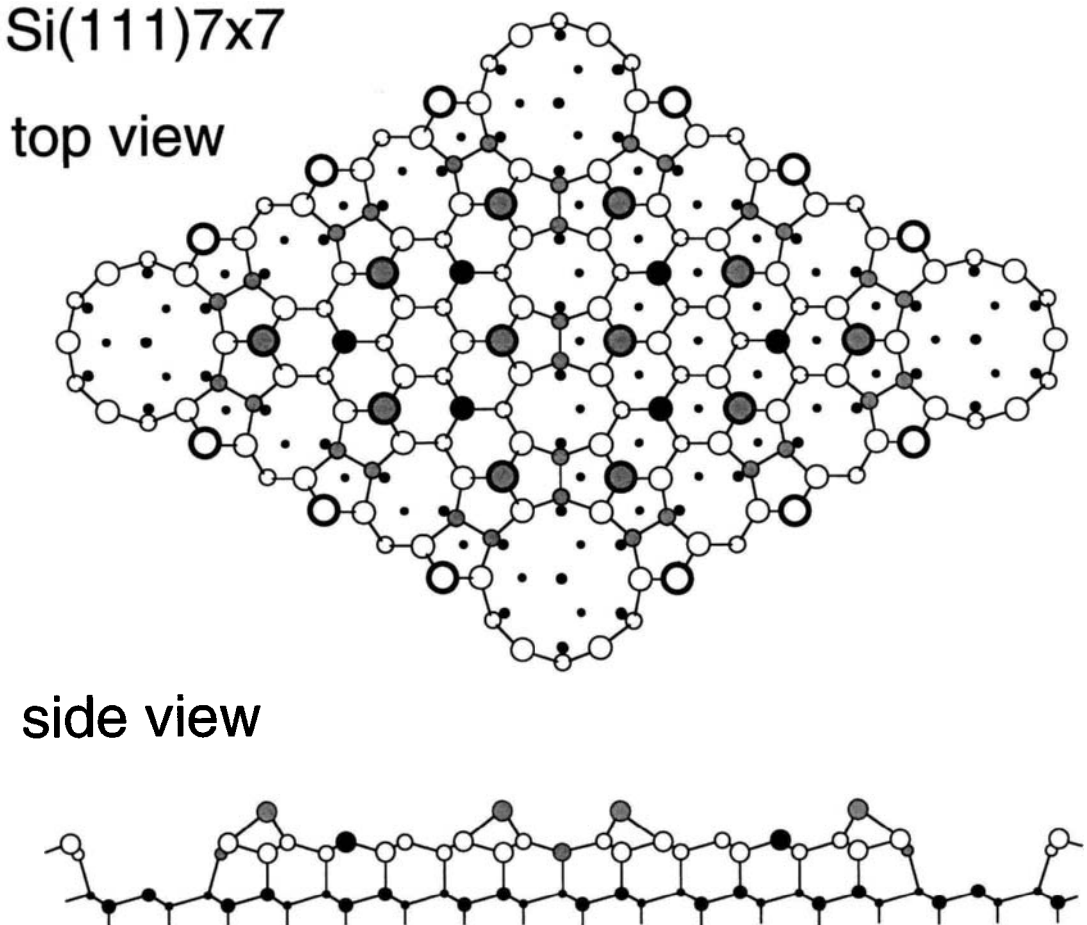


FIGURE 6 Dimer adatom stacking fault model (DAS model) of the Si(111) $7\times 7$  surface [19]. The large shaded circles represent the 12 adatoms per unit cell, and the 6 rest atoms are shown as solid circles. The left half of the unit cell contains the stacking fault.

The second surface state  $S_2$  can easily be followed throughout the  $1\times 1$  surface Brillouin zone. It has been described as a dispersionless feature; however, there is a small  $\sim 0.1$  eV positive dispersion from  $\bar{\Gamma}$  to 0.5 ( $\bar{\Gamma} - \bar{K}$ ). The energy of  $S_2$  is 0.8–0.9 eV below the Fermi level in the whole SBZ, which means that it is located in the projected bulk bandgap except close to the  $\bar{\Gamma}$ -point.

The  $S_3$  surface state is clearly observed in the photoemission spectra for  $\vec{k}_{\parallel}$ -values near the SBZ boundary. In the  $[10\bar{1}]$  azimuthal direction  $S_3$  has a negative dispersion of  $\sim 0.3$  eV for increasing emission angles and it falls within the  $1\times 1$  projected bulk bandgap in a large region around the

### 5.3 Electronic structure of *c*-Si surfaces

$\bar{K}$  – point as seen in FIGURE 7. In the  $[2\bar{1}\bar{1}]$  azimuth  $S_3$  disperses down to its absolute minimum energy, ~2.0 eV below  $E_F$ , at the  $\bar{M}$  – point, resulting in a total bandwidth of ~0.4 eV.

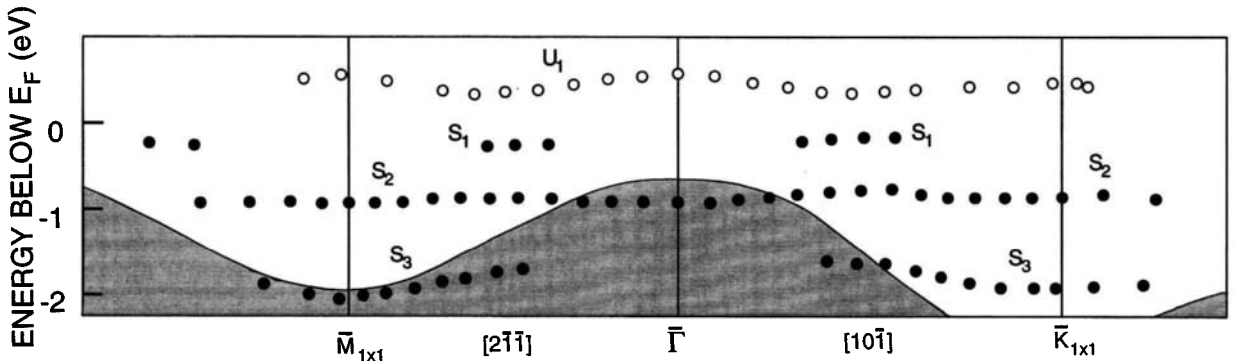


FIGURE 7 Dispersions of the adatom, rest atom and back-bond surface states ( $S_1$ ,  $S_2$  and  $S_3$ ) for Si(111)7×7 plotted in the 1×1 SBZ [20]. An empty surface band  $U_1$  has been identified by inverse photoemission [20,21]. For symmetry point labels see FIGURE 8.

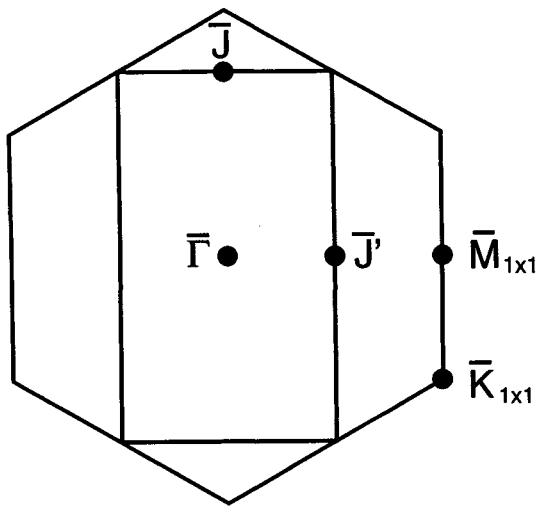


FIGURE 8 Surface Brillouin zones for a 1×1, unreconstructed, Si(111) surface and a 2×1 reconstructed surface. Symmetry points of the SBZs are indicated.

In inverse photoemission an empty band,  $U_1$ , was found in the whole SBZ along both the  $\bar{\Gamma} - \bar{M}$  and  $\bar{\Gamma} - \bar{K}$  lines. It shows a band width of ~0.2 eV with energy minima about halfway to the 1×1 SBZ boundary. This empty surface band has been assigned to adatom  $p_z$  orbitals involved in the coupling to second layer atoms [21].

Hamers et al [27] used current-imaging-tunnelling spectroscopy (CITS) to obtain energy-resolved real-space images of the filled and empty surface states of the Si(111)7×7 surface. It was shown, very convincingly, that the  $S_1$  surface state is localised on the positions in the 7×7 unit cell which correspond to the adatoms in the DAS model and that the  $S_2$  surface state is localised on the rest atom positions. Hamers et al [27] also found some evidence for tunnelling from a lower lying surface state, assigned to adatom back-bonds, which would correspond to the state  $S_3$ . There is presently a good understanding of the origin of the different surface states seen in the ARPES experiments on the

### 5.3 Electronic structure of *c*-Si surfaces

Si(111)7×7 surface. There are a few theoretical studies of the surface states on the 7×7 surface which give surface density of states that essentially reproduce the experimental results [28–30].

Very recently the Si(111)7×7 surface was re-examined in an angle-resolved photoemission study employing high-energy resolution at a low temperature (55 K) [31]. The spectra revealed a new surface state structure  $S'_1$  located at  $\sim -0.5$  eV. The twelve adatoms in the 7×7 unit cell are not all equivalent and the  $S_1$  and  $S'_1$  states were interpreted in terms of different kinds of adatoms. The low temperature study also provided a more detailed picture of the dispersions of the  $S_1$  and  $S_2$  surface states which are shown in FIGURE 9 together with the  $S'_1$  dispersion.

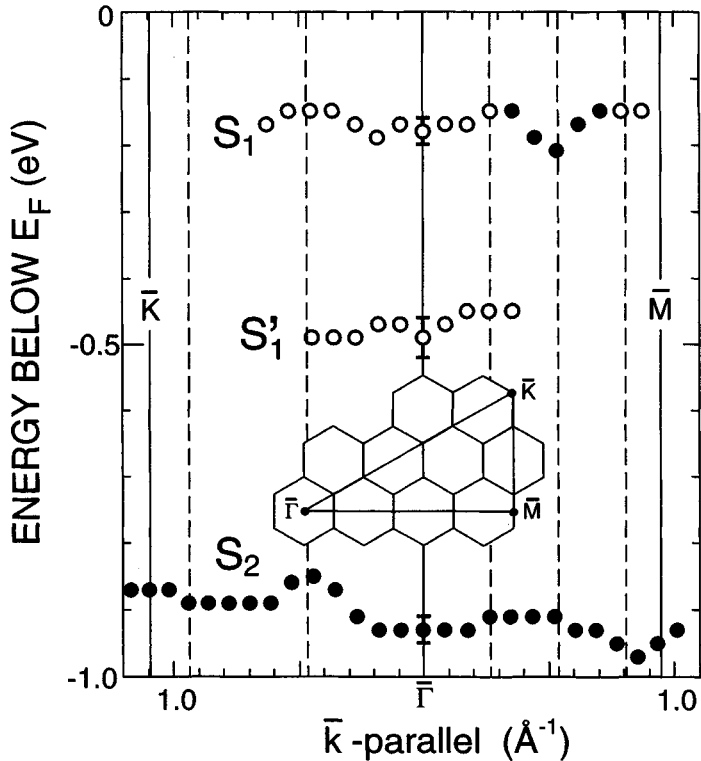


FIGURE 9 Dispersion of the  $S_1$ ,  $S'_1$  and  $S_2$  surface states along the  $\bar{\Gamma}-\bar{K}$  and  $\bar{\Gamma}-\bar{M}$  symmetry lines of the 1×1 SBZ. The inset shows the symmetry points of the 1×1 SBZ and several 7×7 SBZs. Dashed lines indicate the positions of  $\bar{\Gamma}_{7\times 7}$  points along the  $\bar{k}_\parallel$ -axis. Filled circles indicate strong emission intensity. The error bars at the  $\bar{\Gamma}$  point indicate the maximum uncertainty in the energy positions.

### C2 Si(111)5×5

Several groups have reported a 5×5 reconstruction which appears when a cleaved 2×1 reconstructed Si(111) surface is annealed to temperatures of 350–400°C [2]. This 5×5 reconstruction is stable up to annealing temperatures of 600–650°C, at which temperatures it completely converts to the 7×7 reconstruction. The electronic structure of this 5×5 reconstruction is very similar to that of the 7×7 surface which implies that the reconstructions are of the same type, i.e. they can both be described by the DAS-model. The surface states  $S_1$ ,  $S_2$  and  $S_3$  are all observed on the 5×5 surface [32]. There is no information on the unoccupied surface band at present. The strong similarity between the 5×5 and 7×7 reconstructions has been observed in STM studies by Feenstra and Lutz [33].

**C3 Si(111)2×1**

FIGURE 8 shows the surface Brillouin zones for both the unreconstructed  $1\times 1$  and the reconstructed  $2\times 1$  surface. There are three possible orientations of the  $2\times 1$  domains. In order to unambiguously determine the surface-state band structure with angle-resolved photoemission it is essential to study surfaces which exhibit only one of these domains.

A large number of angle-resolved photoemission studies of the Si(111)2×1 surface have been published during the last two decades and a detailed understanding of the electronic structure has emerged from these studies [1,2]. A summary of the surface electronic structure is given below.

In FIGURE 10 the dispersion of the surface-state band is shown relative to the edge of the projected bulk valence bands. The data points are from Uhrberg et al [34], Himpsel et al [35] and Martensson et al [36] and the included theoretical surface-state band dispersion comes from a calculation by Northrup and Cohen [37] using an energy-minimised version of the  $\pi$ -bonded chain model proposed by Pandey [38]. As seen in FIGURE 10 there is very good agreement between theory and experiment concerning the shape of the dispersion of the surface-state band. The strong positive dispersion found in the outer half of the  $\bar{\Gamma} - \bar{J}$  line is very significant for the understanding of the  $2\times 1$  reconstruction, since out of the many models investigated, only the  $\pi$ -bonded chain model has resulted in this kind of dispersion. The validity of this model has also been confirmed in later studies by STM [39].

According to the  $\pi$ -bonded chain model of the  $2\times 1$  reconstruction an empty antibonding surface-state band should be formed together with the filled bonding band. In the calculated energy band diagram in FIGURE 10 the minimum of this empty band is located at the  $\bar{J}$ -point  $\sim 0.2$  eV above the filled band. The antibonding band was directly observed with angle-resolved photoemission on highly n-doped samples by Martensson et al [36]. For the doping of  $8\times 10^{18}$  cm $^{-3}$  used, it could be estimated that there has to be an extra surface charge of approximately 0.01 electrons per surface atom to account for the observed band bending near the surface. In the  $2\times 1$  surface-state band structure one could thus expect that  $\sim 1\%$  of the antibonding band should be filled, starting from the minimum at  $\bar{J}$ . The minimum separation between the peaks from the bonding and the anti-bonding bands was 0.43 eV. The calculated bandgap is smaller by  $\sim 0.2$  eV which is consistent with the established fact that semiconductor bandgaps are underestimated in calculations using the local-density approximation. The surface bandgap was later very well reproduced in a many-body calculation by the same group [40]. The dispersion of the empty  $\pi^*$ -band obtained from inverse photoemission is also included in FIGURE 10 [41]. The dispersion of this  $\pi^*$ -band is also well reproduced by the calculation.

Besides the main surface-state band there is a small feature that has been assigned to a surface state, i.e. a shoulder A', found  $\approx 0.8$  eV below the strong surface-state peak near  $\bar{J}$ . The energy of this peak is within the projected bulk bandgap as shown in FIGURE 10. The weak shoulder has very consistently been reported near the  $\bar{J}$ -point in different studies [34–36,42]. The origin of this emission was a point of controversy for some time. However, the above mentioned consistency of the intensity of the shoulder indicates that it is a feature characteristic of a single-domain surface. An explanation of this second surface state, A', within the  $\pi$ -bonded chain model has been suggested through theoretical calculations by Selloni and Bertoni [43], who found a second surface state/resonance located below the dangling-bond band at  $\bar{k}_\parallel$ -points close to  $\bar{J}$ .

Through the years there have been many suggestions of back-bond surface states/resonances in ARPES experiments. The main support for these suggestions has been either an experimentally determined large contamination sensitivity or agreement with some calculated back-bond state

### 5.3 Electronic structure of c-Si surfaces

dispersions. However, no conclusive evidence for these back-bond resonances has been presented. Since emission from bulk direct transitions has been shown to be both intense and contamination sensitive [44] it is questionable whether any true back-bond surface resonances have been identified on the Si(111)2×1 surface.

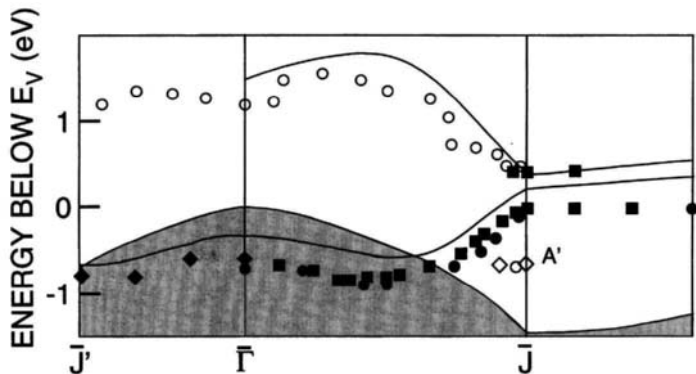


FIGURE 10 Occupied and empty dangling bond dispersions for Si(111)2×1. Photoemission data have been included from Uhrberg et al [34] • o, Himp sel et al [35] ♦◊ and Martensson et al [36] (filled square). The empty band dispersion was obtained by Perfetti et al [41] o. Solid lines show calculated dispersions [37] of the occupied ( $\pi$ ) and empty ( $\pi^*$ ) dangling bond bands for the  $\pi$ -bonded chain model of the 2×1 surface [38].

## D CONCLUSION

The dispersions of the dangling bond surface states have been presented for the different Si surfaces. These surface states are all well understood and the dispersions agree well with calculated dispersions for the Si(100) and Si(111)2×1 surfaces. There are not yet any calculated dispersion curves for the complex Si(111)7×7 surface. Other surface states/resonances have been treated and the experimental dispersions have been plotted for the various surfaces. In some cases the surface character is a little uncertain, and this has been discussed in the text.

## REFERENCES

- [1] G.V. Hansson, R.I.G. Uhrberg [ *Surf. Sci. Rep. (Netherlands)* vol.9 (1988) p.197 ]
- [2] R.I.G. Uhrberg, G.V. Hansson [ *CRC Crit. Rev. Solid State Mater. Sci. (USA)* vol.17 (1991) p.133 ]
- [3] L.S.O. Johansson, R.I.G. Uhrberg, P. Mårtensson, G.V. Hansson [ *Phys. Rev. B (USA)* vol.42 (1990) p.1305 ]
- [4] Y. Enta, S. Suzuki, S. Kono, T. Sakamoto [ *J. Phys. Soc. Jpn. (Japan)* vol.59 (1990) p.657 ]
- [5] Y. Enta, S. Suzuki, S. Kono [ *Phys. Rev. Lett. (USA)* vol.65 (1990) p.2704 ]
- [6] E. Landmark, C.J. Karlsson, Y.-C. Chao, R.I.G. Uhrberg [ *Surf. Sci. (Netherlands)* vol.287/288 (1993) p.529 ]
- [7] E. Landmark [ *Linköping Studies in Science and Technology*, Dissertation No.313 ]
- [8] T. Tabata, T. Aruga, Y. Murata [ *Surf. Sci. (Netherlands)* vol.179 (1987) p.63 ]
- [9] E. Landmark, C.J. Karlsson, Y.-C. Chao, R.I.G. Uhrberg [ *Phys. Rev. Lett. (USA)* vol.69 (1992) p.1588 ]
- [10] J.E. Northrup [ *Phys. Rev. B (USA)* vol.47 (1993) p.10032 ]
- [11] L.S.O. Johansson, B. Reihl [ *Surf. Sci. (Netherlands)* vol.269/270 (1992) p.810 ]

- [12] J. Pollmann, R. Kalla, P. Krüger, A. Mazur, G. Wolfgarten [ *Appl. Phys. A (Germany)* vol.4 (1986) p.1 ]; J. Pollmann, P. Krüger, A. Mazur [ *J. Vac. Sci. Technol. B (USA)* vol.5 (1987) p.945 ]
- [13] R.I.G. Uhrberg, G.V. Hansson, J.M. Nicholls, S.A. Flodström [ *Phys. Rev. B (USA)* vol.24 (1981) p.4684 ]
- [14] P. Koke, A. Goldmann, W. Mönch, G. Wolfgarten, J. Pollmann [ *Surf. Sci. (Netherlands)* vol.152/153 (1985) p.1001 ]
- [15] A. Goldmann, P. Koke, W. Mönch, G. Wolfgarten, J. Pollmann [ *Surf. Sci. (Netherlands)* vol.169 (1986) p.438 ]
- [16] L.S.O. Johansson, R.I.G. Uhrberg, G.V. Hansson [ *Surf. Sci. (Netherlands)* vol.189/190 (1987) p.479 ]
- [17] R.I.G. Uhrberg, L.S.O. Johansson, G.V. Hansson [ *Proc. 2<sup>nd</sup> Int. Conf. on the Structure of Surfaces*, Amsterdam, Holland, 22-25 June 1987, Eds. J.F. van der Veen, M.A. Van Hove (Springer Verlag, 1988) p.303 ]
- [18] E. Landemark, R.I.G. Uhrberg, P. Krüger, J. Pollmann [ *Surf. Sci. (Netherlands)* vol.236 (1990) p.359 ]
- [19] K. Takayanagi, Y. Tanishiro, M. Takahashi, S. Takahashi [ *J. Vac. Sci. Technol. A (USA)* vol.3 (1985) p.1502 ]; [ *Surf. Sci. (Netherlands)* vol.164 (1985) p.367 ]
- [20] P. Mårtensson, W.-X. Ni, G.V. Hansson, J.M. Nicholls, B. Reihl [ *Phys. Rev. B. (USA)* vol.36 (1987) p.5974 ]
- [21] J.M. Nicholls, B. Reihl [ *Phys. Rev. B (USA)* vol.36 (1987) p.8071 ]
- [22] F.J. Himpsel, G. Hollinger, R.A. Pollak [ *Phys. Rev. B (USA)* vol.28 (1983) p.7014 ]
- [23] U. Backes, H. Ibach [ *Solid State Commun. (USA)* vol.40 (1981) p.575 ]
- [24] F.J. Himpsel, D.E. Eastman, P. Heimann, B. Reihl, C.W. White, D.M. Zehner [ *Phys. Rev. B (USA)* vol.24 (1981) p.1120 ]
- [25] F. Houzay, G.M. Guichar, R. Pinchaux, Y. Petroff [ *J. Vac. Sci. Technol. (USA)* vol.18 (1981) p.860 ]
- [26] G.V. Hansson, R.Z. Bachrach, R.S. Bauer, D.J. Chadi, W. Göpel [ *Surf. Sci. (Netherlands)* vol.99 (1980) p.13 ]
- [27] R.J. Hamers, R.M. Tromp, J.E. Demuth [ *Phys. Rev. Lett. (USA)* vol.56 (1986) p.1972 ]
- [28] M. Fujita, H. Nagayoshi, A. Yoshimori [ *Surf. Sci. (Netherlands)* vol.242 (1991) p.229 ]
- [29] G.-X. Qian, D.J. Chadi [ *Phys. Rev. B (USA)* vol.35 (1987) p.1288 ]
- [30] K.D. Brommer, B.E. Larson, M. Needels, J.D. Joannopoulos [ *Jpn. J. Appl. Phys. (Japan)* vol.32 (1993) p.1360 ]
- [31] R.I.G. Uhrberg, T. Kaurila, Y.-C. Chao [ *Phys. Rev. B (USA)* vol.58 (1998) p.R1730 ]
- [32] R.I.G. Uhrberg, E. Landemark, L.S.O. Johansson [ *Phys. Rev. B (USA)* vol.39 (1989) p.13525 ]
- [33] R.M. Feenstra, M.A. Lutz [ *Phys. Rev. B (USA)* vol.42 (1990) p.5391 and *Surf. Sci. (Netherlands)* vol.243 (1991) p.151 ]
- [34] R.I.G. Uhrberg, G.V. Hansson, J.M. Nicholls, S.A. Flodström [ *Phys. Rev. Lett. (USA)* vol.48 (1982) p.1032 ]
- [35] F.J. Himpsel, P. Heimann, D.E. Eastman [ *Phys. Rev. B (USA)* vol.24 (1981) p.2003 ]
- [36] P. Mårtensson, A. Cricenti, G.V. Hansson [ *Phys. Rev. B (USA)* vol.32 (1985) p.6959 ]
- [37] J.E. Northrup, M.L. Cohen [ *Phys. Rev. Lett. (USA)* vol.49 (1982) p.1349 ]
- [38] K.C. Pandey [ *Phys. Rev. Lett. (USA)* vol.47 (1981) p.1913 ]
- [39] J.A. Stroscio, R.M. Feenstra, A.P. Fein [ *Phys. Rev. Lett. (USA)* vol.57 (1986) p.2579 ]
- [40] J.E. Northrup, M.S. Hybertsen, S.G. Louie [ *Phys. Rev. Lett. (USA)* vol.66 (1991) p.500 ]
- [41] P. Perfetti, J.M. Nicholls, B. Reihl [ *Phys. Rev. B (USA)* vol.36 (1987) p.6160 ]
- [42] F. Houzay et al [ *Surf. Sci. (Netherlands)* vol.132 (1983) p.40 ]
- [43] A. Selloni, C.M. Bertoni [ *Solid State Commun. (USA)* vol.45 (1983) p.475 ]
- [44] R.I.G. Uhrberg et al [ *Phys. Rev. Lett. (USA)* vol.52 (1984) p.2265 ]

## CHAPTER 6

### STRUCTURAL MODELLING (*Edited by M.I. Heggie*)

- 6.1 Approximate and parametrised quantum chemical methods for structural modelling of c-Si
- 6.2 Approximate and parametrised quantum mechanical methods for structural modelling of c-Si:  
the tight binding approximation
- 6.3 Electronic structure calculations of oxygen point defects in c-Si
- 6.4 Theoretical modelling of minor impurities in c-Si
- 6.5 c-Si surfaces - review of theoretical studies
- 6.6 Microscopic modelling of grain boundaries and stacking faults in c-Si
- 6.7 Vacancy defects in c-Si: electronic and ionic structures
- 6.8 Self-interstitials in c-Si: structure and migration mechanisms
- 6.9 Ab initio modelling techniques applied to c-Si
- 6.10 Modelling of dislocations in c-Si

## **6.1 Approximate and parametrised quantum chemical methods for structural modelling of c-Si**

P. Deák

March 1997

### **A INTRODUCTION**

Local deviations from the overall periodicity of the silicon crystal (i.e. bulk defects and surfaces) forfeit the principal basis for applying conventional band theory in structure calculations. Also, the use of the customary and otherwise very convenient plane wave expansion for one-electron states may prove to be very time consuming, especially for light impurities. Instead, localised states of the defect environment can be thought of as a ‘defect molecule’ [1], so invoking quantum chemistry, i.e. molecular physics, seems obvious. Of course, the defect molecule is embedded in an otherwise perfect crystalline environment. This can be taken into account in a simple way by adding a sizeable part of the nominally unperturbed portion of the lattice to the defect molecule, to form a so called cluster of atoms. The artificial states introduced into the ‘gap’ of the cluster by the dangling bonds on its surface should, however, be eliminated. One way to do that is to saturate the dangling bonds by hydrogen atoms: the resulting molecular cluster model (MCM) is very simple and has been widely used [2]. Another way is to choose the cluster in the form of a unit cell and to apply the Born–Kármán cyclic boundary conditions, without applying Bloch’s theorem [3,4]. With appropriate choice of the unit cell (to represent a special sampling of the primitive Brillouin zone [5]), and proper handling of the boundary condition, this cyclic cluster model (CCM) retains the full point group symmetry and enables good reproduction of the crystalline properties in a basically molecular calculation [6]. The MCM and the CCM form the basis for structure calculation of defects and surfaces on a localised basis. Ab initio solution of the cluster Schrödinger equation is very tedious, so often approximations are used. This Datareview deals with the so called ‘quantum chemical’ approximations. In Section B their derivation from ab initio Hartree–Fock theory is given and individual methods are described. Section C contains a short guide to application in silicon, with concluding remarks in Section D.

### **B ‘QUANTUM CHEMICAL’ APPROXIMATIONS TO AB INITIO ELECTRONIC STRUCTURE THEORY**

For determining structure and properties of defects and surfaces, the total energy of the model system has to be calculated, applying the adiabatic principle. The gradient of the total energy can then be used in molecular dynamics studies, or in a quasi-static approach to minimise the energy with respect to atomic co-ordinates. Regardless of using MCM or CCM, the Schrödinger equation of such large systems can only be solved in a one-electron approximation. There are two approaches to the problem: Hartree–Fock (HF) and density functional theory (DFT). The former expresses the total energy as a function of the many-electron wave function, constructed as a Slater-determinant of one-electron wave functions. The latter expresses the energy as a function of the electron density, constructed as a sum of squared one-electron wave functions. The one-electron wave functions are obtained in both cases from a pseudo-Schrödinger equation, which has to be solved iteratively (SCF procedure). If no further approximation is used, the method is termed ‘ab initio’ or (from) ‘first principles’. These words are often used in the meaning of exact but that is incorrect: both types of method have inherent errors. Apart from common problems with the breakdown of the adiabatic principle, HF results have to be corrected for electron correlation, and DFT results for electron self-interaction. In fact, to make DFT practical, an additional assumption has to be made for the form of the energy function (local density approximation, LDA). Still, the LDA is also regarded as ab initio.

Both ab initio theories apply an often-unmentioned further approximation, which is quite empirical in nature, in order to turn the pseudo-Schrödinger equation into a set of algebraic equations. The one-electron wave functions are expanded on a finite basis of known functions. For periodic systems a plane wave basis is appropriate, but this causes difficulties in localised systems. Instead, atomic-like functions (linear combination of ‘atomic’ orbitals: LCAO) can be used. Their choice is, however, somewhat arbitrary.

By definition, quantum chemical methods are those which can be and are used for molecules. In principle, both LDA and HF with LCAO expansions qualify. However, prior to relatively recent improvements in LDA, only HF or approximate HF methods were used. Therefore, for the purpose of this section, approximate and parametrised quantum chemical methods will be defined in the traditional sense, i.e. as ones derived from HF theory.

Expanding one-electron wave functions in terms of localised (real) functions  $v$ , centred on atom B,

$$\psi_i = \sum_B \sum_{v_B} c_{v_B i} v_B \quad (1)$$

The basic equation of HF theory is the Hartree–Fock–Roothaan (HFR) equation [7]. For a closed shell system (i.e. every one-electron state doubly occupied):

$$\sum_B \sum_{v_B} (F_{\mu_A v_B} - \epsilon_i S_{\mu_A v_B}) c_{v_B i} = 0 \quad (2)$$

Here

$$S_{\mu_A v_B} = \int \mu_A(1) v_B(1) dv_1 = \langle \mu_A | v_B \rangle \quad (3)$$

is the overlap matrix, and the Fock-matrix is given by

$$F_{\mu_A v_B} = H_{\mu_A v_B} + \sum_{C,D} \sum_{\lambda_C, \sigma_D} P_{\lambda_C \sigma_D} \left[ \langle \mu_A v_B | \lambda_C \sigma_D \rangle - \frac{1}{2} \langle \mu_A \sigma_D | \lambda_C v_B \rangle \right] \quad (4)$$

with two-electron integrals

$$\langle \mu_A v_B | \lambda_C \sigma_D \rangle = \iint \frac{\mu_A(1) v_B(1) \lambda_C(2) \sigma_D(2)}{r_{12}} dv_1 dv_2 \quad (5)$$

and bond order matrix

$$P_{\lambda_C \sigma_D} = 2 \sum_j^{N/2} c_{\lambda_C j} c_{\sigma_D j} \quad (6)$$

The one-electron, or core Hamiltonian matrix is:

$$H_{\mu_A v_B} = \int \mu_A(l) \left( -\frac{1}{2} \Delta + \sum_C V_C \right) v_B(l) dv_1 = \left\langle \mu_A \left( -\frac{1}{2} \Delta + \sum_C V_C \right) v_B \right\rangle \quad (7)$$

where  $V_C$  is the potential, or pseudopotential of atom C. (Atomic units have been used.)

Ab initio solution of the HFR equation is made difficult by the two-electron integrals of EQN (5) which may contain up to four centres and, therefore, have a number proportional to the fourth power of the number of electrons, N. The aim of all approximations is to reduce the number of explicitly calculated two-electron integrals. The basic criterion for selecting the two-electron integrals to be neglected is the magnitude of the overlap charge populations,  $\mu_A v_B$ , often called differential overlap (DO).

## B1 A Non-Empirical Approximation: PRDDO

The name PRDDO (partial retention of diatomic differential overlap [8]) is a reference to earlier ZDO methods (see Section B2): it emphasises the less approximate nature. PRDDO is an all-electron method, i.e. the core is treated explicitly. The minimal STO (Slater-type orbital) basis is used. The one-electron part of the Fock-matrix (EQN (7)) is properly calculated and transformed into a Löwdin-orthogonalised basis. The two-electron part is calculated directly on the orthogonalised basis set. (In fact, the orthogonalisation step is preceded by a transformation of the Slater-set to ensure orthogonality of core and valence orbitals and proper alignment of the orbitals along local principal axes). All four-centre integrals are neglected. One-centre integrals of the form

$$\langle \mu_A \mu_A | v_A v_A \rangle, \langle \mu_A v_A | \mu_A v_A \rangle, \langle \mu_A v_A | \lambda_A \lambda_A \rangle,$$

two-centre integrals of the form

$$\langle \mu_A \mu_A | v_B v_B \rangle, \langle \mu_A v_B | \mu_A v_B \rangle, \langle \mu_A v_B | \lambda_B \lambda_B \rangle,$$

as well as three-centre integrals of the form

$$\langle \mu_A v_B | \lambda_C \lambda_C \rangle$$

are retained and calculated in elaborate approximations using Gaussian-type orbitals (GTOs). Since the arising error is mainly systematic, correction factors have been introduced and adjusted to fit the calculated Fock-matrix elements to reference ab initio values.

PRDDO is, therefore, a strictly non-empirical approximation to HF theory. The results represent very good approximations to ab initio ones while the computational effort is reduced from  $\sim N^4$  to  $\sim N^3$ .

## B2 Semi-Empirical ZDO Methods

Despite the considerable gain, PRDDO is still quite time consuming for large systems. Drastic reduction in computational effort can only be achieved by a more wholesale reduction in the number of explicitly calculated two-electron integrals. Since that reduces accuracy considerably, the concept of ‘semi-empirical’ approximations has been introduced as a compromise. The error due to neglected integrals is compensated by the use of empirical data and adjustable parameters in analytical functions, substituting for some of the remaining terms in the Fock-matrix elements. This is in

## 6.1 Approximate and parametrised quantum chemical methods for structural modelling of c-Si

contrast to purely empirical methods—like empirical tight binding, ETB—where entire elements of the Hamiltonian matrix are substituted by empirical functions.

All semi-empirical quantum chemical methods are based on the zero differential overlap (ZDO) approximation. Since DOs are basically small, it is assumed that

- 1) the total charge in DOs is negligible, i.e. the basis is approximately orthogonal,

$$S_{\mu_A v_B} = \langle \mu_A | v_B \rangle \approx \delta_{\mu\nu} \delta_{AB} \quad (8)$$

- 2) all three- and four-centre integrals can be neglected.

Neither assumption is, in itself, really justified but it can be shown that they compensate for each other (see [9]). Since only one- and two-centre integrals remain, the required computational effort scales with  $\sim N^2$ .

### B2.1 The NDO methods of Pople et al

The neglect of differential overlap (NDO) methods [10] are based on neglecting also some of the one- and two-centre two-electron integrals between DOs. This is done at three consecutive levels:

I. NDDO: neglect of diatomic differential overlap, where only two-electron integrals between diatomic DOs are neglected:

$$\langle \mu_A v_B | \lambda_C \sigma_D \rangle = \langle \mu_A v_A | \lambda_C \sigma_C \rangle \delta_{AB} \delta_{CD} \quad (9)$$

II. INDO: intermediate neglect of differential overlap, where, in addition, two-electron integrals between monatomic DOs of different atoms are neglected:

$$\langle \mu_A v_A | \lambda_C \sigma_C \rangle = \begin{cases} \langle \mu_A v_A | \lambda_A \sigma_A \rangle \delta_{AC} \\ \langle \mu_A \mu_A | \lambda_C \lambda_C \rangle \delta_{\mu\nu} \delta_{\lambda\sigma} \end{cases} \quad (10)$$

III. CNDO: complete neglect of differential overlap, where, in addition, two-electron integrals between monatomic DOs on the same atom are neglected:

$$\langle \mu_A v_A | \lambda_A \sigma_A \rangle = \langle \mu_A \mu_A | \lambda_A \lambda_A \rangle \delta_{\mu\nu} \delta_{\lambda\sigma} \quad (11)$$

In order to preserve rotational invariance in INDO and CNDO, it is required that

$$\langle \mu_A \mu_A | \lambda_C \lambda_C \rangle = \gamma_{AC} \quad (12)$$

i.e. the value of two-centre two-electron integrals must not depend on the particular orbital, only on the atoms.

## 6.1 Approximate and parametrised quantum chemical methods for structural modelling of c-Si

These approximations are introduced on a valence shell STO basis. (In Si that means 3s, 3p, and 3d STOs.) In order to stay as close to ab initio HF as still possible, for  $\gamma_{AC}$  in EQN (12) the integral between the spherically symmetric charge distributions

$$\gamma_{AC} = \langle s_A s_A | s_C s_C \rangle \quad (13)$$

is used. Still, to compensate for the severe approximations in the two-electron part of the Fock matrix, parametrisation of the one-centre term (EQN (7)) is necessary. The following approximations have been introduced, in addition to ZDO:

$$H_{\mu_A v_A}^{\text{ZDO}} = \left\langle \mu_A \left( -\frac{1}{2} \Delta + V_A \right) v_A \right\rangle + \sum_{C \neq A} \langle \mu_A | V_C v_A \rangle \approx U_\mu^A \delta_{\mu v} + \sum_{C \neq A} V_{\mu v}^{AC} \quad (14)$$

$$H_{\mu_A v_B}^{\text{ZDO}} = \left\langle \mu_A \left( -\frac{1}{2} \Delta + V_A + V_B \right) v_B \right\rangle \approx \beta_{\mu_A v_A} S_{\mu_A v_A} \quad (15)$$

where the matrix element of the pseudopotential for atom C with effective core charge  $Z_C$  is

$$V_{\mu v}^{AC} = -Z_C \langle \mu_A v_A | s_C s_C \rangle \quad (16)$$

while  $U_\mu^A$ , the energy of an electron on a given atomic orbital, was determined from experimental data on free atoms, and  $\beta_{\mu_A v_A}$  was used as an adjustable parameter. Keeping faith with the HF theory,  $U_\mu^A$  has been expressed in terms of the calculated one-centre two-electron integrals and the spectroscopically determined Mullikan electron negativity,  $-[I_\mu + A_\mu]/2$ . Also the

$$\beta_{\mu_A v_A} = (\beta_A + \beta_B)/2 \quad (17)$$

parameters were used to fit calculated bond lengths to ones obtained from ab initio HF calculations. Actually, NDDO was never parametrised, while the standard parametrisation of CNDO became known as CNDO/2.

### B2.2 The role of correlation. NDO methods with spectroscopic or solid state parameters

The NDO methods of Pople aspired to give an economic approximation to ab initio HF theory and were very successful. For systems with  $\sim 100$  valence electrons, the results were typically well within 10% of the ab initio ones for about 0.01% of the computational cost. Of course, these methods cannot step over the limitations of HF theory itself. The configuration and geometrical data of a molecule (or a defect in an MCM) can be predicted accurately even if correlation (dependence of electronic interactions on the particular position of electrons) is neglected, because the correlation correction is roughly constant in the vicinity of the energy minimum for the ground state. However, in calculating heats of formation and reaction, energy of transition states, and ionisation and excitation energies, the changes of correlation energy cannot be neglected. Ab initio HF theory is usually extended with so called post-HF treatments to account for correlation. One way to do this is to construct a series of Slater-determinants by substituting some of the occupied HF one-electron states with unoccupied ones in the self-consistent Slater determinant of the ground state. Depending on the number of substitutions these are called singly, doubly, triply, etc. excited configurations. The many-electron wave function

can then be expanded on the basis of all such possible configurations, and the total energy is obtained as the expectation value of the many-electron Hamiltonian. This is the configuration interaction (CI) procedure. Only configurations with an even number of excitations contribute to the ground state, and only those with an odd number to the singly excited states. Often, configurations corresponding to triple excitations and higher are neglected, and only the single and double excitations with the lowest estimated energy are included (limited CI). Even so, the CI takes at least as much time as the SCF solution of the HFR equation.

The first attempt to include correlation at a semi-empirical level was the CNDO/S (spectroscopic) parametrisation [11], for the study of the excitation spectra of aliphatic molecules. One realises that fitting spectroscopic term values with both the  $U_{\mu}^A$  values and the one-centre two-electron interactions as empirical parameters [12] results in values for the latter which are considerably lower than the calculated integrals. This is a manifestation of intra-atomic correlation in the experimental results. Substituting two-centre two-electron integrals with an empirical function of the inter-atomic distance,  $R_{AB}$ , ensuring proper behaviour in infinity and smooth transition to the one-centre values at short distances, will, therefore, simulate the effect of inter-atomic correlation in the ground state of the molecule. In the CNDO/S parametrisation, instead of  $I_{\mu}$  and  $A_{\mu}$  values for the states of the free atom, valence state values were used. The one-centre two-electron integrals were approximated as  $(I_p - A_p)$ . The orbital degeneracy of the  $\beta$  parameters in EQN (17) was lifted and the values (as well as the exponents,  $\zeta_{\mu}$ , of the STOs in calculating EQN (15)) were fitted to reproduce experimental ionisation energies: another method of implicit inclusion of dynamic correlation. The parameters were not adjusted to reproduce bond lengths and angles, so experimental geometry had to be used. The excitations were then successfully calculated by a CI including a limited number of singly excited configurations.

The set of molecules included in determining the adjustable parameters in the original CNDO/S-CI scheme was limited to a few aliphatic molecules, and accordingly they did work well in saturated systems such as diamond crystal or silicon. For such studies the method has been reparametrised [13] using ionisation and excitation energies of saturated molecules of Si, C, O and H. This parametrisation has proven to be very useful in predicting the electronic structure of defects in silicon [6,14].

Harker and Larkins [15] have followed an even more direct approach in reparametrising CNDO for solid state studies.  $U_{\mu}^A$ ,  $\beta_{\mu}$  and  $\zeta_{\mu}$  were adjusted to fit calculated CCM results to crystalline properties (bond length, cohesive energy, bulk modulus and band structure) of silicon. Modelling of structural defects in the same CCM could then be performed. This parametrisation is also used in quantum mechanical molecular dynamics calculations [16].

An INDO/S-CI parametrisation also exists [17], and has recently been reparametrised by adjusting parameters to fit both molecular and crystalline data on silicon [18].

### B2.3 The modified methods of Dewar et al

#### MINDO/3 and MNDO

The intuitive ideas for implicit inclusion of dynamic correlation effects of the ground state into an HF derived theory were extended, generalised and—at least a posteriori—justified theoretically by Dewar and co-workers. Omitting CNDO, conceptual modifications were introduced subsequently to INDO

## 6.1 Approximate and parametrised quantum chemical methods for structural modelling of c-Si

and NDDO, producing the modified methods MINDO/3 [19] and MNDO [20] (the second D has been omitted from the name for convenience). The  $U_{\mu}^A$  and

$$g_{\mu\nu}^{A*} = g_{\mu\nu}^A - \frac{1}{2} h_{\mu\nu}^A \equiv \langle \mu_A \mu_A | v_A v_A \rangle - \frac{1}{2} \langle \mu_A v_A | \mu_A v_A \rangle$$

values obtained from Oleari's fit [12] to valence state ionisation energies were accepted also for the one-centre two-electron integrals, as indicated. The orbital and monatomic overlap populations ( $\mu_A \mu_A$  and  $\mu_A v_A$ , respectively) were described by fitted point charge configurations to the members of their dipole expansions and the two-centre two-electron integrals were calculated as interactions between these point charge configurations, using an analytical function (giving  $h_{\mu\nu}^A$  for  $R_{AB} \rightarrow 0$ , and  $1/R_{AB}$  for  $R_{AB} \rightarrow \infty$ ). In both methods the minimal valence basis (e.g. 3s and 3p STOs for Si) was used.

MINDO was, in fact, parametrised in three versions, MINDO/3 having been used generally. Since INDO has only two-centre two-electron integrals of the form of EQN (12), orbital populations were given by single point charges, and the interaction functions between them were fitted to an appropriate average of the one-centre parameters. Apart from the level of NDO, the main difference between MINDO/3 and MNDO is in EQN (15), and in the calculation of the core-core interaction,  $C_{AB}$ .

MINDO/3:

$$\beta_{\mu_A v_B} = \frac{1}{2} \beta_{AB} (I_{\mu}^A + I_{v}^B) \quad (18)$$

$$C_{AB} = Z_A Z_B \left[ \gamma_{AB} + \left( \frac{1}{R_{AB}} - \gamma_{AB} \right) \exp(-\alpha_{AB} R_{AB}) \right] \quad (19)$$

MNDO:

$$\beta_{\mu_A v_B} = \frac{1}{2} (\beta_{\mu_A} + \beta_{v_B}) \quad (20)$$

$$C_{AB} = Z_A Z_B \langle s_A s_A | s_B s_B \rangle [1 + \exp(-\alpha_A R_{AB}) + \exp(-\alpha_B R_{AB})] \quad (21)$$

The Slater-exponents in EQN (15) as well as the  $\beta$  and  $\alpha$  values have been adjusted to fit all types of calculated properties (geometry, heat of formation, ionisation potentials, dipole moments, transition states) to experimental data on a carefully selected and relatively large set of small organic molecules. (In MNDO, the  $U_{\mu}^A$  values have also been readjusted.) As a consequence of that and of the physics (chemistry) which is still embodied in the approximations, these methods worked very well for a wide range of molecules. Of course, the typical error was in the % range, and occasionally really large problems arose, but due to the availability of a large data bank on successes and failures in small systems (where experimental or ab initio results were available for comparison), these problems were mostly known in advance and mishaps could be avoided. This is an inherent advantage over fully empirical methods where the given parametrisation almost surely breaks down as the chemical bonding configuration changes, with no way of predicting the nature of the error.

## 6.1 Approximate and parametrised quantum chemical methods for structural modelling of c-Si

The diatomic parameters in EQNS (18) and (19) have lent extra power to MNDO/3 but also made the parametrisation very tedious. In fact, as far as silicon goes, Dewar's group determined it only for Si–Si and Si–H bonds [21], before switching to MNDO. (In addition, Si–O [22] and Si–S [23] values are available but those are less well tested.) In the framework of MNDO, Dewar's group published two sets of silicon parameters [24,25] but due to a small error in the original formulation, which affected third row elements of the periodic table especially [26], neither of them was too successful.

### AM1 and PM3

The parametrisations AM1 (Austin model [27]) and PM3 (parametrised model [28]) do not, in essence, differ much from MNDO. The only change concerns the pseudopotentials in the calculation of the core–core repulsion. Instead of Slater-type s orbitals, the more usual expansion into GTOs was used in both methods:

$$C_{AB} = Z_A Z_B (1 + f_A + f_B) \quad (22)$$

$$\begin{aligned} f_A &= \exp(-\alpha_A R_{AB}) + \sum_i k_A^i \exp\left[l_A^i (R_{AB} - m_A^i)^2\right] \\ f_B &= \exp(-\alpha_B R_{AB}) + \sum_j k_B^j \exp\left[l_B^j (R_{AB} - m_B^j)^2\right] \end{aligned} \quad (23)$$

with  $\alpha$ ,  $k$ ,  $l$  and  $m$  as adjustable parameters.

They represent, however, a shift in parametrisation strategy. AM1 was still parametrised by fitting to properties of a set of hand-picked molecules, constituting a well balanced sample of possible bonding situations. At the same time, the ‘generality’ was given up as far as properties were concerned. Notably, ionisation energies (crucial in modelling defects) were not considered. PM3, on the other hand, was parametrised using a large set of molecules on a ‘the more the better’ basis. As a consequence, AM1 works better in systems thought to be important by Dewar, and may fail in other cases (e.g. Si–O bonds), while PM3 looks to be more general, even if somewhat less accurate (and showing occasional unevenness due to the unbalanced set of molecules used for parametrisation). Both methods represent considerable improvement over MNDO/3 or MNDO. In addition, they are much better in describing vibrations.

In general—despite occasional problems with one or another bonding configuration which can mostly be anticipated—AM1 and PM3 come close in accuracy to ab initio LDA for a fraction of the cost. What is the theoretical justification for this success from many mostly intuitive approximations? The answer was found after the development of the theory of effective shell Hamiltonians (see [9] and references therein). Using a Green-function technique, the CI problem can be turned into a one-determinant eigenvalue equation with an effective valence Hamiltonian. The matrix elements of this Hamiltonian and their dependence on inter-atomic distance proved to be very similar to those of the MNDO Hamiltonian.

## C APPLICATION FOR STRUCTURAL MODELLING OF SILICON

The PRDDO program code is not generally available but was used very successfully for structural modelling of defects in silicon by Streicher et al (e.g. [29–31]).

All semi-empirical quantum chemical methods are incorporated into standard program codes and are available in the public domain [32]. One can easily obtain them and carry out MCM calculations

## 6.1 Approximate and parametrised quantum chemical methods for structural modelling of c-Si

without any programming or parametrisation work. A (beta) CCM version of the MOPAC 6.0 package [33] (capable of MNDO/3, MNDO, AM1, and PM3 calculations) and of the CNDO/S code [34] can be obtained from the present author. The molecular dynamics code [16] based on directly parametrised CNDO [15] is commercial.

The black box mode usage of semi-empirical methods is, however, dangerous. One has to be well aware of the overall performance of the particular method (parametrisation) for molecules related to the system under investigation, with respect to the properties in question. In the following, some comparisons are presented for some of the methods in the case of the silicon crystal. For modelling oxygen related defects, results on the Si–O–Si bond are also compared. It is recommended that such tests be performed before application of a given method (parametrisation) to a new problem is attempted.

TABLE 1 contains data for crystalline silicon from a CCM calculation with a 32 atom unit, using the most modern semi-empirical methods, AM1 and PM3 (with standard parameters [27,28]). The 32 atom CCM represents a nearly converged approximation to the band structure. CNDO results with ‘solid state’ parameters on a 64-atom unit cell are also presented [15,35].

TABLE 1 Calculated lattice parameter, bonding energy, ionisation threshold and Raman frequency of crystalline silicon.

Property	Exptl.	AM1	PM3	CNDO*
$a_0$ (Å)	5.431	5.429	5.461	5.45
$E_b$ (eV/bond)	2.34	2.37	2.63	2.4
$I_0$ (eV)	5.35	9.08	7.64	6.5
$\nu_{\text{Raman}}$ (cm <sup>-1</sup> )	518	491	484	544**

\* with the ‘solid state’ parameters of [15]

\*\* from [35]

FIGURE 1 shows the AM1, PM3 and CNDO/S band structures interpolated from the calculated electronic structure of the Si<sub>32</sub> CCM. The CNDO results of [15] on a 16-atom unit are also presented. TABLE 2 shows data for the Si–O–Si bond, obtained for the disiloxane molecule and from a CCM of  $\alpha$ -quartz, containing six primitive units.

TABLE 2 Calculated Si–O distance and Si–O–Si bond angle in disiloxane, as well as the binding energy of  $\alpha$ -quartz.

Property	Exptl.	AM1	PM3
$d_{\text{Si}-\text{O}}$ (Å) in H <sub>3</sub> SiOSiH <sub>3</sub>	1.63	1.73	1.68
$\theta_{\text{Si}-\text{O}-\text{Si}}$ (°) in H <sub>3</sub> SiOSiH <sub>3</sub>	145	150	118
$E_b$ (eV/bond) in $\alpha$ -SiO <sub>2</sub>	4.8	4.7	5.1

Although parametrised entirely on molecules, AM1 gives excellent values, with the exception of the Si–O bond length (which is also too long in the molecule) and the ionisation threshold of Si. Unfortunately, the whole AM1 band structure is grossly unrealistic (cf. omission of ionisation energies from parametrisation). Since many interesting defect complexes involve orbitals formed from

## 6.1 Approximate and parametrised quantum chemical methods for structural modelling of *c*-Si

band states (EMT orbitals), it is paramount that the band structure around the gap be qualitatively reproduced. In such cases AM1 can hardly be used. PM3, although generally somewhat less accurate than AM1, is acceptable in this respect. CNDO/S performs best, but of course it was intended specially for such purposes and is the only method using a full valence basis (3d orbitals for Si). A reasonable solution is to use PM3 for minimising the total energy, and CNDO/S to calculate the electronic structure at the equilibrium found by PM3 (e.g. [14]). A similar approach is used in the context of AM1 and INDO/S, reparametrising both [18].

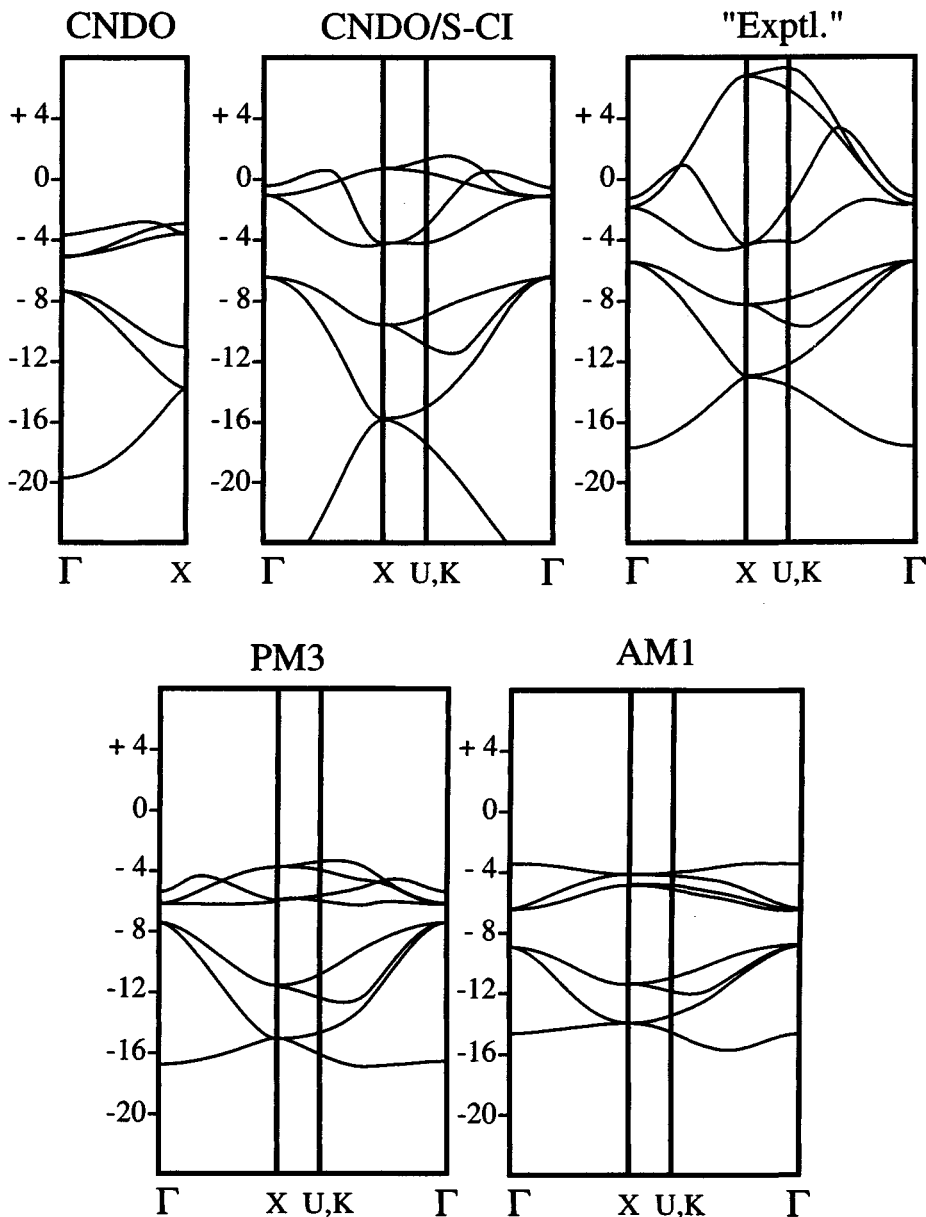


FIGURE 1 Semi-empirical band structure of crystalline silicon interpolated from the electronic structure of 32-atom (AM1, PM3, CNDO/S) and 16-atom (CNDO<sup>15</sup>) CCM calculations.

Finally, some words of caution with respect to electronic structure calculations of defects. Although the semi-empirical quantum chemical methods have been designed to account for ground state correlation in a basically HF scheme, excitation energies (e.g. the gap!) should be calculated by

accounting for changes in correlation energy properly. This means calculating the total energy of an excited state relative to the ground state and not simply subtracting the energy of the highest occupied orbital from that of the lowest unoccupied one. Another point is that the ZDO approximation has a different effect on orbitals with mainly s or mainly p character, over-stabilising the former (e.g. the  $\Gamma_2$  state in the conduction band of Si) if the system increases. This can be corrected for some CCMs [23]. The correction is less general but perhaps better justified than the ‘scissors operator’ used in ab initio LDA.

## D CONCLUSION

For modelling structural defects, light impurities and surfaces in silicon, CNDO (e.g. [35–37]) as well as MNDO/3 and PM3 (e.g. [14,23,38–40]) have been used widely in CCM calculations. MNDO and AM1 were used only in MCM for Si (e.g. [41–44]). Such studies have proven to be very useful in the pioneering work on defect and surface problems with many possible configurations or strong and complicated lattice relaxation. Semi-empirical quantum chemical methods, though less accurate than either ETB or LDA, have an advantage over ETB when unusual bonding situations might occur, and are more than  $10^3$  times faster than LDA. They can also be used efficiently as a forerunner to further LDA calculations [45], but using CNDO/S or INDO/S provides better excitation spectra. It is safe to say that semi-empirical methods have been and will be playing a useful role in structural modelling of silicon and silicon based systems in the ~100 atom range.

## REFERENCES

- [1] C.A. Coulson, M.J. Kearsley [ *Proc. Roy. Soc. A (UK)* vol. 241(1957) p.433-54 ]
- [2] A.M. Stoneham [ *Theory of Defects in Solids* (Clarendon Press, 1975) ]
- [3] A.J. Bennett, M. McCaroll, R.P. Messmer [ *Phys. Rev. B (USA)* vol.3 (1971) p.1397 ]
- [4] A. Zunger [ *J. Chem. Phys. (USA)* vol.63 (1975) p.1713 ]
- [5] R.A. Evarestov, V.A. Lovchikov, I.I. Tupitsin [ *Phys. Status Solidi B (Germany)* vol.117 (1983) p.417 ]
- [6] P. Deák, L.C. Snyder [ *Phys. Rev. B (USA)* vol.36 (1987) p.9619 ]
- [7] C.C.J. Roothaan [ *Rev. Mod. Phys. (USA)* vol.23 (1951) p.69 ]
- [8] T.A. Halgren, W.N. Lipscomb [ *J. Chem. Phys. (USA)* vol.58 (1973) p.1569 ]; D.S. Marynick, W.N. Lipscomb [ *Proc. Natl. Acad. Sci. USA (USA)* vol.79 (1982) p.1341 ]
- [9] W. Thiel [ *Tetrahedron (UK)* vol.44 (1988) p.7393 ]
- [10] J.A. Pople, D.L. Beveridge [ *Approximate Molecular Orbital Theory* (Academic Press, 1970) ]
- [11] J. Del Bene, H.H. Jaffe [ *J. Chem. Phys. (USA)* vol.48 (1968) p.1807 ]
- [12] L. Oleari, L. DiSipio, G. DeMichelis [ *Mol. Phys. (UK)* vol.10 (1966) p.97 ]
- [13] P. Deák [ *Int. J. Quantum Chem. (USA)* vol.23 (1983) p.1165 ]
- [14] P. Deák, L.C. Snyder, J.W. Corbett [ *Phys. Rev. B (USA)* vol.50 (1992) p.11612 ]
- [15] A.H. Harker, F.P. Larkins [ *J. Phys. C (UK)* vol.12 (1979) p.247 ]
- [16] D.S. Wallace, A.M. Stoneham, W. Hayes, A.J. Fisher, A.H. Harker [ *J. Phys., Condens. Matter (UK)* vol.3 (1991) p.3879 ]
- [17] J.E. Ridley, M. Zerner [ *Theor. Chim. Acta (Germany)* vol.32 (1973) p.11 ]
- [18] R.J. Baierle, M.J. Caldas, E. Molinari [ to be published ]
- [19] R.C. Bingham, M.J.S. Dewar, D.H. Lo [ *J. Am. Chem. Soc. (USA)* vol.97 (1977) p.1285 ]
- [20] M.J.S. Dewar, W. Thiel [ *J. Am. Chem. Soc. (USA)* vol.99 (1977) p.4899 ]
- [21] M.J.S. Dewar, D.H. Lo, C.A. Ramsden [ *J. Am. Chem. Soc. (USA)* vol.97 (1975) p.1311 ]
- [22] A.H. Edwards, W.B. Fowler [ *J. Phys. Chem. Solids (UK)* vol.46 (1985) p.841 ]
- [23] A.S. Yaspis, P. Deák, R.K. Singh, L.C. Snyder, J.W. Corbett [ *Phys. Rev. B (USA)* vol.38 (1988) p.9936 ]

## 6.1 Approximate and parametrised quantum chemical methods for structural modelling of c-Si

- [24] M.J.S. Dewar, M.L. McKee, H.S. Rzepa [ *J. Am. Chem. Soc. (USA)* vol.100 (1978) p.3607 ]
- [25] M.J.S. Dewar, F. Friedheim, G. Grady, E.F. Healy, J.J.P. Stewart [ *Organometallics (USA)* vol.5 (1986) p.375 ]
- [26] P. Deák, L.C. Snyder [ *Int. J. Quantum Chem. (USA)* vol.21 (1987) p.547 ]
- [27] M.J.S. Dewar, E.G. Zoebisch, E.F. Healy, J.J.P. Stewart [ *J. Am. Chem. Soc. (USA)* vol.107 (1985) p.3902 ]
- [28] J.J.P. Stewart [ *J. Comput. Chem. (USA)* vol.10 (1989) p.221 ]
- [29] S.K. Estreicher [ *Phys. Rev. B (USA)* vol.36 (1987) p.9122 ]
- [30] Dj.M. Maric, P.F. Meier, S.K. Estreicher [ *Phys. Rev. B (USA)* vol.47 (1993) p.3620 ]
- [31] M.A. Roberson, S.K. Estreicher, C.H. Chu [ *J. Phys., Condens. Matter (UK)* vol.5 (1994) p.8943-54 ]
- [32] Quantum Chemistry Program Exchange: qcpe@ucs.indiana.edu
- [33] J.J.P. Stewart [ *QCPE* vol.23 (1991) program 455 ]
- [34] J. Del Bene [ *QCPE* vol.11 (1970) program 174 ]
- [35] J.E. Smith, P.V. Symanszki, J.A.D. Matthew [ *Philos. Mag. B (UK)* vol.51 (1985) p.193 ]
- [36] A. Mainwood, A.M. Stoneham [ *J. Phys. C, Solid State Phys. (UK)* vol.17 (1984) p.2513 ]
- [37] A. Mainwood [ *Mater. Sci. Forum (Switzerland)* vol.196-201 (1995) p.1589 ]
- [38] P. Deák, L.C. Snyder, J.W. Corbett [ *Phys. Rev. B (USA)* vol.37 (1988) p.6887 ]
- [39] P. Badziag, W.S. Verwoerd, M.A. Van Hove [ *Phys. Rev. B (USA)* vol.43 (1991) p.2058-62 ]
- [40] B.I. Craig, P.V. Smith [ *Surf. Sci. (Netherlands)* vol.239 (1991) p.36 ]
- [41] G.G. De Leo, W.B. Fowler, G.D. Watkins [ *Phys. Rev. B (USA)* vol.29 (1984) p.3193 ]
- [42] G.G. De Leo, W.B. Fowler [ *Phys. Rev. B (USA)* vol.31 (1985) p.6861 ]
- [43] G.G. De Leo, W.B. Fowler [ *Phys. Rev. Lett. (USA)* vol.56 (1986) p.402 ]
- [44] R.J. Baierle, M.J. Caldas, E. Molinari, S. Ossicini [ *Braz. J. Phys. (Brazil)* vol.26 (1996) p.631 and *Solid State Commun. (USA)* to be published ]
- [45] C.P. Ewels, R. Jones, S. Öberg, J. Miro, P. Deák [ *Phys. Rev. Lett. (USA)* vol.77 (1996) p.865 ]

## **6.2 Approximate and parametrised quantum mechanical methods for structural modelling of c-Si: the tight binding approximation**

G. Jungnickel

April 1998

### **A INTRODUCTION**

Approximate quantum mechanical methods to determine the electronic structure of a system have been developed in the past to avoid or minimize certain efforts in difficult and demanding calculations for complex systems. In general, they solve the many-body Schrödinger equation by using several approximations considered not to be too serious. Since in many cases this is achieved by introducing empirical parameters or functionals into the scheme, such methods are also often referred to as semi-empirical methods.

One of these schemes which has been proven to be very successful in semiconductor research is the tight-binding model. It can be understood as the opposite extreme of the nearly free electron model and regards the solid as an assembly of weakly interacting neutral atoms. It basically considers the overlap of atomic orbitals in a bonded system as the source for (small) corrections of the isolated atom picture. Hereby, the atomic description is approximately preserved [1].

The tight-binding method is particularly attractive because it provides a direct understanding of chemical bonding in a covalent material in terms of occupied molecular orbitals constructed from overlapping atomic wave functions. In its standard forms the method is one of the fastest quantum-mechanically based electronic structure schemes and capable of analysing systems of a size considerably larger than can be managed with current full ab initio schemes. The tight-binding approximation provides a real space picture of the electronic interactions and is extremely useful in the study of changes in the band structure, the density of states, and related functions due to variations in the electronic configuration.

### **B TIGHT-BINDING METHODOLOGY**

To understand the various tight-binding schemes used throughout the literature one can start from the general problem of calculating the energy of a system of interacting atoms within density-functional theory. There, the Hamiltonian of a structure with M electrons at positions  $\vec{r}$  in the field of N nuclei at  $\vec{R}$

$$\hat{H} = \hat{T} + \hat{E}_{ee} + \hat{E}_{ei} + \hat{E}_{ii} \quad (1)$$

is written in terms of functionals of the electron density where  $\hat{T}$  denotes the kinetic energy operator and  $\hat{E}_{ee}$  the electron-electron,  $\hat{E}_{ei}$  the electron-ion and  $\hat{E}_{ii}$  the ion-ion interaction. This is based on the Hohenberg-Kohn theorem [2] that the electron density uniquely determines the total energy of a non-spin-polarized system. For this, it is assumed that due to the mass difference the electrons are always in their ground state and can instantaneously adjust to any change in nuclear positions. The many-body Schrödinger equation is then formally transformed by introducing a set of single particle wavefunctions  $\Psi_i$  that yield the electron density [3]. Integration of these equations results in one-

## 6.2 Methods for structural modelling of c-Si: the tight binding approximation

particle eigenvalues  $\varepsilon_i$  that may be used to substitute the kinetic energy expression in EQN (1). Finally, the total energy within density-functional theory may be written as

$$E_{\text{tot}} = \sum_i^{\text{occ}} \varepsilon_i - \frac{1}{2} \iint \frac{n(\vec{r})n(\vec{r}')}{|\vec{r} - \vec{r}'|} d\vec{r}d\vec{r}' + \frac{1}{2} \sum_{\alpha}^N \sum_{\beta}^N \frac{Z_{\alpha}Z_{\beta}}{|\vec{R}_{\alpha} - \vec{R}_{\beta}|} - \int n(\vec{r}) \frac{\delta E_{\text{xc}}[n(\vec{r})]}{\delta n(\vec{r})} d\vec{r} + E_{\text{xc}}[n(\vec{r})] \quad (2)$$

where the first term is a sum over the occupied Kohn–Sham eigenvalues and generally called the band structure term. The second term is a correction for counting the electron–electron interaction twice in the band structure term, the third term is the ion–ion core repulsion, and the last terms are double counting corrections related to exchange-correlation effects which describe the quantum mechanical nature of the electron interaction. The approach of most tight-binding schemes is to conserve the band structure sum and to treat the other terms as a classical potential  $V_{\text{rep}}$  which is essentially a short-ranged, repulsive two-body interaction

$$E_{\text{tot}} = \sum_i^{\text{occ}} \varepsilon_i + \sum_{\alpha}^N \sum_{\beta}^N V_{\text{rep}}(\vec{R}_{\alpha} - \vec{R}_{\beta}) \quad (3)$$

The formal solution of the Kohn–Sham equations (see e.g. [1]) takes advantage of the expansion of the single particle wave functions  $\Psi_i$  in terms of localized atomic orbitals  $\Phi_v$  (based on the assumption that these are only slightly perturbed in the solid state)

$$\Psi_i = \sum_v^L C_v^i \Phi_v \quad (4)$$

As a result of this linear combination of atomic orbitals (LCAO) method, the Kohn–Sham equations are transformed into the set of characteristic secular equations which can be solved in principle. In standard tight-binding schemes this is done non-self-consistently, e.g. by diagonalization, and yields the expansion coefficients of the molecular orbitals  $C_v^i$  and the associated one-electron eigenvalues  $\varepsilon_i$

$$\sum_v (H_{\mu\nu} - \varepsilon_i S_{\mu\nu}) C_v^i = 0 \quad (5)$$

Two matrices  $H$  and  $S$ , called the Hamiltonian and Overlap matrices, enter the eigenvalue problem and are given in the basis of the localized atomic orbitals as

$$H_{\mu\nu}(\vec{R}) = \int \Phi_{\mu}^{*}(\vec{r} - \vec{R}) \hat{H} \Phi_{\nu}(\vec{r}) d\vec{r} \quad S_{\mu\nu} = \int \Phi_{\mu}^{*}(\vec{r} - \vec{R}) \Phi_{\nu}(\vec{r}) d\vec{r} \quad (6)$$

where  $\hat{H}$  denotes the Hamiltonian operator for the solid state. If the atomic orbitals are transformed to form a basis set of orthogonalized functions the Overlap matrix becomes the unity matrix which is a frequently used, but not strictly necessary, simplification within numerous tight-binding schemes. The estimation of the Hamiltonian matrix elements is complicated because the atomic orbitals may be located at two different sites which in turn may be different from the origin of the operator  $\hat{H}$ . Such terms are called the three-centre integrals which for simplicity are usually neglected compared to two-centre contributions according to Slater and Koster [4]. A further reduction of the complexity of these

## 6.2 Methods for structural modelling of *c*-Si: the tight binding approximation

integrals is achieved if they are considered to be adjustable interaction parameters between nearest neighbours as will be discussed below. One-centre contributions are referred to as the on-site or (free) atomic orbital energies.

A detailed analysis of the relationship between the tight-binding model and density-functional theory has been given by Harris [5], Foulkes and Haydock [6], Sutton et al [7], and Sankey and Niklewski [8]. These authors showed rigorously that the method is a stationary approximation to self-consistent density-functional theory with an appropriate guess of the electron density. This directly yields the energy expression in EQN (3) and justifies the pairwise interaction assumed to model the ion–ion core repulsion together with the double counting corrections. It is necessary to require that such a density should not be too remote from the true self-consistent solution. The basic tight-binding idea that the interaction in the solid is a weak perturbation of the Hamiltonian for free atoms leads one to choose the charge density to be a superposition of atomic charge densities which are not allowed to respond to the condensation of separated atoms: see [7].

The various tight-binding methods essentially differ in the treatment of the Hamiltonian and Overlap matrix elements and in the functional forms proposed for the short-ranged repulsive potential. The diverse modifications are primarily caused by the goal of obtaining a highly transferable scheme that works well for all atomic arrangements of a given material independent of the number of atoms interacting with each other. It should be equally well applicable to molecules, clusters, condensed ordered and disordered solids, and even fluids. The simplest tight-binding algorithms suffer from a problem which is well known from the classical potential approach: that is a failure to describe a variation in the local coordination accurately enough. Hence, more sophisticated tight-binding representations [8,9] have been developed to optimize the predictive power of the method while still being much more efficient than other quantum-mechanically based techniques especially for increasing system size.

Secondly, a number of modifications have been introduced to reduce the effort required for solving the secular EQN (5) which is a matrix equation of size  $NL \times NL$  where  $L$  is the number of atomic orbitals considered in the wave function expansion. Using a conventional diagonalization scheme, the time to compute the eigenvalues is proportional to  $(NL)^3$ . Therefore,  $O(N)$  methods to avoid these time consuming diagonalization steps have been proposed [10–16]. Alternatively, the size of the matrices can be drastically reduced by exploiting a minimal basis set, thus minimizing  $L$ . The latter approximation emphasises the vast importance of valence orbital overlap.

### B1 Empirical Parametrisation of the Hamiltonian Matrix

To completely avoid calculating the integrals (EQN (6)) within a certain basis of localized orbitals, one can treat the matrix elements of the Hamiltonian and Overlap matrices as parameters for a given type and distance of atoms that can be fitted to representative band structure measurements or calculations. This very simple method has been widely used and mostly considers the interaction in a system as being due to nearest neighbour overlap only. The problem in this scheme is to define a certain distance dependence of the matrix elements and to establish a suitable repulsive potential which is usually considered to be of pairwise interactions only.

#### B1.1 Simple orthogonal parametrisation schemes

One of the first successful parametrisation schemes for crystals in the diamond and zincblende structure is due to Chadi and co-workers [17,18] which was based on the simplified LCAO scheme of Slater and Koster [4] and extended the nearest neighbour orbital overlap scheme discussed by Weaire and Thorpe [19] to include more distant neighbours. For silicon their method employed a minimal

## 6.2 Methods for structural modelling of c-Si: the tight binding approximation

basis of one 3s and three 3p functions. Retaining one-centre and two-centre interactions only they proved that at least one second nearest neighbour interaction is needed compared to the Weaire and Thorpe scheme to obtain reasonable valence band structures and related densities of states. Since these are the occupied states they will be most relevant for the total energy calculations.

Chadi and Cohen showed that there is a simple relationship to Hirabayashi's version [20] that invokes a basis of directed hybridised  $sp^3$  orbitals. Within these minimal basis schemes four Hamiltonian matrix elements and two on-site energies turn out to be sufficient to accurately describe the band structure of the diamond topology. The atomic orbitals are assumed to be orthogonal and do not enter the scheme explicitly. Rather, the Overlap matrix is a nearest neighbour map and the Hamiltonian matrix elements were fitted to band structure calculations within the empirical pseudo-potential method [21–24] (Section C) and the valence band structure could be reproduced to within a few tenths of an eV. This basic scheme has been used in several studies of the band structure [17], the lattice dynamics [25], and surface properties [26] of silicon. For this, the repulsive potential has been modelled to be a polynomial expansion of the fractional change of the bond length [18,26]. The silicon parameters defined in [26] have been widely used [11,27–29]: see also TABLE 1.

TABLE 1 Commonly used nearest-neighbour interaction parameters for Si in eV.  $E_s$  and  $E_p$  designate one-centre  $V(ss\sigma)$ ,  $V(sp\sigma)$ ,  $V(pp\sigma)$  and  $(Vpp\pi)$ , two-centre integrals for the minimal basis approach.  $V_1$  and  $V_2$  are defined as in Harrison's bond-orbital approximation and shown for comparison.

Ref	$E_p^*$	$E_s - E_p = 4 V_1$	$V_2$	$V(ss\sigma)$	$(Vsp\sigma)$	$V(pp\sigma)$	$(Vpp\pi)$
[32]	—	7.04	3.00	—	—	—	—
[33]	—	5.64	2.20	—	—	—	—
[34]	—	7.16	4.42	—	—	—	—
[17]	—	7.20	6.13	-2.03	2.55	4.55	-1.09
[11,26–29]	1.20	6.45	4.28	-1.94	1.75	3.05	-1.08
[30]	—	5.88	3.61	-1.92	1.92	1.96	-0.54
[37]	—	7.21	6.03	-1.93	2.54	4.46	-1.12
[43]**	1.20	6.45	4.08	-2.04	1.75	2.75	-1.08
[60]	—	5.30	3.67	-1.74	2.09	1.90	-1.14
[5]*****	-2.28	6.24	5.11	-3.28	3.27	1.95	-1.03
[53,54]*****	-6.52	7.03	5.26	-2.37	2.52	3.32	-1.07
[63]*****	-4.17	6.66	7.11	-2.92	3.83	4.08	-1.28

\* arbitrary if not given

\*\* with many-body interaction

\*\*\* non-orthogonal scheme

The solution of the Kohn–Sham equations need not necessarily be sought within a basis of atomic orbitals. As already mentioned it is possible and suitable especially for covalently bonded materials to transform the basis set into a basis of hybridised orbitals. Using such a scheme Pandey and Phillips [30] investigated the relaxation and surface states of the Si(111) surface. A similar treatment yields the bond-orbital model [31–34] if simultaneously the overlap between orbitals not directed in one and the same bond is neglected. This is an extremely simple description of a bond retaining only two parameters for Si ( $V_1$  and  $V_2$  in TABLE 1) but focuses on its chemical characterisation in the terms of covalency, metallicity and polarity.

Harrison [35] empirically found that the Hamiltonian matrix elements for a variety of crystals can be chosen as a universal constant times the inverse of the atomic distance squared. Froyen and Harrison [36] showed that this behaviour is due to the fact that the true valence bands in covalent solids still resemble free-electron bands and gave a method to roughly estimate interaction parameters from free-electron behaviour: see also [37].

## 6.2 Methods for structural modelling of *c*-Si: the tight binding approximation

Harrison [37] and Newman [38] both focused on improving the minimal basis approach by inclusion of antibonding s-states in order to improve the dispersion and position of conduction bands that are typically rather poor using interacting valence orbitals only. This is essential if one wants to calculate optical properties or concentrate on impurity levels in solids [38].

A number of studies were dedicated to the particular problem of obtaining reasonable binding energies over a range of structures with varying bond distances. The Hamiltonian matrix elements must be appropriately scaled in this case which is often done with Harrison's scaling as mentioned above. However, most of the uncertainties arise from the repulsive potential part. This has been taken by Tomanek and Schlüter [27] to be dependent on the number of bonds in a structure compared to the number of atoms. Their potential was parametrised to reproduce the energetics of the Si dimer and bulk structures with different coordination numbers and finally applied to study small silicon clusters. Wang et al [28] used a third-order polynomial fitted to total energy curves obtained from self-consistent field calculations and applied their tight binding model to study the temperature dependence of anharmonic vibrational effects in molecular-dynamics studies of silicon [28,39]. Another form of the matrix elements and simultaneously the repulsive potential has been obtained using the rescaling method [40,41]. With the expressions given there Xu et al [42] improved their scheme with the focus being on carbon and chose the repulsive potential to be a fourth-order polynomial where the argument itself is a complex exponential function. The idea behind this is to incorporate a stronger dependency of the local coordination into the repulsive potential. A transferable tight-binding model of this type for silicon has been presented by Kwon et al [43].

Finally, there are further modifications of the total energy expression (EQN (3)) necessary in the case of polar materials or strong charge transfer for example in the presence of dangling orbitals. Lee and Joannopoulos [44] added a long range term to the repulsive forces to explicitly model electrostatic multipole interactions between atoms in SiC. Harrison [45] introduced a Coulomb interaction energy that was modelled by Alerhand and Mele [46] by a Hubbard-like term. These authors studied the consequences of such forces for surface reconstructions and vibrational excitations of Si(100).

### B1.2 The non-orthogonal TB method

The orthogonal treatment of the atomic orbitals is based on ideas developed for the Hückel theory [47] where effects of non-orthogonality can be absorbed in a pseudo-potential. In turn, taking such effects into account yields the standard Hückel-type formulation that Overlap matrix elements are roughly proportional to Hamiltonian matrix elements as has been used for band structure calculations of silicon in the atom superposition and electron delocalisation (ASED) band theory [48]. Applied to the bond-orbital tight-binding formalism this results in an additional parameter (the orthogonality coefficient which is a proportionality factor between Overlap and Hamiltonian matrix elements) and shifts the energy levels somewhat modifying the cohesive energies [33,34,49]. The extension to a larger basis set and a full parametrisation of both the Hamiltonian and Overlap matrix elements for Si has been proposed by Lancaster and Dy [50].

The electronic properties of stacking fault geometries in silicon have been studied by Mattheis and Patel [51] also using an accurate parametrisation of all minimal basis matrix elements that enter the theory. In this particular case they additionally included interactions and overlap over three shells of neighbours yielding a total of 26 parameters defined by a least-squares fit to the bands obtained within the empirical pseudo-potential method [21–24]. The repulsive potential was chosen in a simple polynomial form of the fractional change in bond length. A highly transferable parametrisation for Si and the minimal basis has been published by Allen et al [52] who used self-consistent linear muffin tin orbital (LMTO) energy bands as a reference to fit the matrix elements for four different crystalline Si structures dependent on the distance between atoms. In this way they proved that the integrals in

## 6.2 Methods for structural modelling of *c*-Si: the tight binding approximation

EQN (6) follow very nearly the same distance dependency no matter what local geometry is present in Si.

In an attempt to avoid extensive parametrisation and to simplify the tight-binding scheme as much as possible Menon and Subbaswamy [53] went back to the universal scaling regime proposed by Harrison and the Hückel approach for the overlap matrix. They used a very simple repulsive potential but introduced an explicit distance dependency of the non-orthogonality coefficient. Aside from a few *a priori* parameters they are left with only three adjustable ones. In related studies of the geometries of small Si clusters the same authors and Ordejon et al [54] used the coordination-dependent repulsive potential of Tomanek and Schlüter [27] and a constant non-orthogonality coefficient. It turned out that the simplest repulsive potential one can think of is suitable to describe Si band structures, phase diagrams and bulk phonons as well as small clusters, provided that corrections due to non orthogonality of orbitals are included in the sum of the single-particle eigenvalues of the Kohn–Sham equations.

### B1.3 The bond order potential method

The band structure energy may alternatively be represented by the expression

$$E_{bs} = \sum_{i\alpha} \int_{-\infty}^{E_F} E n_{i\alpha}(E) dE \quad (7)$$

where  $n_{i\alpha}(E)$  is the local density of states of orbital  $\alpha$  at atom  $i$ . A number of methods have been found to calculate this local density of states without explicitly sampling the eigenvalues of the Kohn–Sham equations. These schemes include the method of moments [55], the recursion method [10,56,57], and related variants [10]. The basic idea is that  $n_{i\alpha}(E)$  can be expressed as a functional of only the Hamiltonian and Overlap matrix elements. Hence, EQN (5) need not be solved by the time-consuming diagonalization process.

In particular, Pettifor [58] and Aoki [59] showed that the density matrix or bond order can be easily evaluated within such a scheme. The total energy can then be expressed as a functional of the bond order. It turns out that for most applications the bond order depends on only a few moments of the density of states and converges rapidly. Utilizing fast recursion algorithms and nearest neighbour overlap yields a very efficient tight-binding method where the computational effort in principle is  $O(N)$ .

## B2 Parameter-Free Construction of the Hamiltonian Matrix

All the models described so far suffer from a more or less difficult parametrisation of the integrals in EQN (6). This has been done primarily to make the tight-binding scheme as transparent and simple as possible. However, the numerous attempts to improve transferability of the tight-binding energy expression show how problematic the task is for very different local environments. The greatest difficulties arise from the assumed distance dependence of the Hamiltonian and Overlap matrix elements. The attempt by Allen et al [52] to parametrise the matrix elements over a wide range of distances for several crystalline structures and to set up a universal functional form is an important step forward.

Mercer and Chou [60] followed a similar idea when they fitted the Hamiltonian matrix elements in an orthogonal minimal basis approach to self-consistent local-density calculations performed for Si

## 6.2 Methods for structural modelling of c-Si: the tight binding approximation

crystals as a function of volume. Interestingly, the distance dependence was not consistent with the long-standing rule of inverse bond distance squared and rather followed the functional form

$$H_{\mu\nu} = \frac{\alpha |\vec{r}|^{-\beta}}{1 + e^{\gamma(|\vec{r}| - r_0)}} \quad (8)$$

where  $H_{\mu\nu}$  stands for the Hamiltonian matrix elements and  $\alpha$ ,  $\beta$ ,  $\gamma$  and  $r_0$  are adjustable values. The repulsive interatomic potential has been chosen in exponential form and the amplitude was defined to be dependent on the bond angles to third neighbours which effectively goes beyond a pairwise interaction. However, this method is completely adjusted to a more sophisticated self-consistent field approach and was shown to be valid for a variety of Si structures.

### B2.1 The density-functional based tight-binding method

A step further has been taken by Seifert et al [61] and Porezag and co-workers [9] who developed a scheme that has been given the name density-functional based tight-binding (DF-TB) method. Here, the matrix elements are explicitly calculated for a given pair of atoms with an accurate self-consistent local-density calculation exploiting Slater-type atomic orbitals. The two-centre integrals in EQN (6) are stored as a function of atomic distances and the mesh can be interpolated in a non-orthogonal tight-binding approach by superposing the atomic potentials to get an estimate of the many-body potential. The repulsive part of the energy expression (EQN (3)) is a simple polynomial and fitted to reproduce self-consistent field results for the binding energy of respective dimers and bulk moduli of crystals.

The key idea to ensure that the two-centre approximation can still be used in the calculations of the matrix elements is to contract the wave function of the free atoms somewhat making them more ‘localized’. This in a sense postpones a behaviour in the final atomic compound and has been proven to work well for a variety of materials and in fact better than using true ground state atomic wave functions. It ensures that the matrix elements become short ranged. As a result the method can take all interactions even to distant neighbours into account. It is as fast as any other tight-binding scheme since all complicated computations are done separately. It is, therefore, suitable for accurate molecular dynamics simulations.

### B2.2 The ab initio multicentre tight-binding method

Inclusion of three-centre terms in the calculation of Hamiltonian matrix elements within a minimal basis set of similar contracted pseudo-atomic orbitals yields the most sophisticated density-functional based tight-binding approach to date invented by Sankey and Niklewski [8]. This scheme also attempts to compute the contributions to the repulsive potential explicitly exploiting pseudopotentials for the ion cores. It cannot deal with all matrix elements that appear in advance and, hence, is quite time-consuming but still faster than self-consistent schemes. Also, it does not require periodicity and can be used within molecular dynamics applications. It does not need any experimental input and is entirely first principles.

### B2.3 The Hartree–Fock based tight-binding method

Another parameter-free non-orthogonal tight-binding method has been introduced by Artacho and Yndurain [62] for investigating local and extended defects in semiconductors. There, the Hamiltonian parameters are calculated within the Hartree–Fock approximation for representative small clusters. The matrix elements obtained are transferred to larger crystalline systems by utilizing a Green’s

## 6.2 Methods for structural modelling of c-Si: the tight binding approximation

function method based on a minimal basis wave function expansion. The secular equations are transformed into a recursion relation that exploits the matrix elements between a one-particle propagator and the non-orthogonal basis set. These can be evaluated by splitting the full Hamiltonian into a part which is invariant under translations and can be solved analytically and a local perturbation that requires the inversion of a matrix with a reduced dimension. The particular method has been successfully used to study interstitial oxygen and hydrogen-passivated substitutional boron in bulk silicon as well as arsenic deposition onto silicon surfaces [62].

### C PARAMETRISED PSEUDOPOTENTIAL METHODOLOGY

A semi-empirical method which attacks the band structure problem from an entirely different point of view is the parametrised pseudopotential methodology [21–24]. In its essence it starts from the nearly free electron picture and introduces a weak periodic pseudopotential to remove large wave function oscillations in the core regions. As a result the Schrödinger equation for a valence pseudo-wave-function has to be solved by expanding the pseudopotential into plane waves. The expansion coefficients are expressed in terms of a structure factor multiplied by an atomic form factor which is fitted to experimental optical data. This method has been used to very accurately calculate the band structure of covalent materials and as mentioned above was frequently used as a reference to find tight-binding parameters.

### D CONCLUSION

The tight-binding approximation has been reviewed and shown to be extremely useful in studies of band structure, density of states and related functions. It considers the overlap of atomic orbitals in a bonded system as the source for small corrections to the view of atoms as being isolated. The general methodology has been outlined and various schemes, including empirical parametrisation of the Hamiltonian matrix, parameter-free construction of the Hamiltonian matrix and the parametrisation pseudopotential methodology, have been described in detail. The various approaches within the first two methods differ in the way they treat the Hamiltonian and Overlap matrix elements. The parametrisation pseudopotential methodology is a semi-empirical approach which starts from the nearly free electron picture and introduces a weak periodic pseudopotential. The latter has been used as a reference to find tight-binding parameters.

### REFERENCES

- [1] N.W. Ashcroft, N.D. Mermin [ *Solid State Physics* (Saunders College Publications, New York, 1976) ]
- [2] P. Hohenberg, W. Kohn [ *Phys. Rev. (USA)* vol.136 (1964) p.B864 ]
- [3] W. Kohn, L.J. Sham [ *Phys. Rev. (USA)* vol.140 (1965) p.A1133 ]
- [4] J.C. Slater, G.F. Koster [ *Phys. Rev. (USA)* vol.94 (1954) p.1498 ]
- [5] J. Harris [ *Phys. Rev. B (USA)* vol.31 (1985) p.1770 ]
- [6] W.M.C. Foulkes, R. Haydock [ *Phys. Rev. B (USA)* vol.39 (1989) p.12520 ]
- [7] A.P. Sutton, M.W. Finnis, D.G. Pettifor, Y. Ohta [ *J. Phys. C, Solid State Phys. (UK)* vol.21 (1988) p.35 ]
- [8] O.F. Sankey, D.J. Niklewski [ *Phys. Rev. B (USA)* vol.40 (1989) p.3979 ]
- [9] D. Porezag, Th. Frauenheim, Th. Köhler, G. Seifert, R. Kaschner [ *Phys. Rev. B (USA)* vol.51 (1995) p.12947 ]
- [10] R. Haydock, V. Heine, M.J. Kelly [ *J. Phys. C, Solid State Phys. (UK)* vol.5 (1972) p.2845 ]
- [11] K. Laasonen, R.M. Nieminen [ *J. Phys., Condens. Matter (UK)* vol.2 (1990) p.1509 ]
- [12] X.-P. Li, R.W. Nunes, D. Vanderbilt [ *Phys. Rev. B (USA)* vol.47 (1993) p.10891 ]
- [13] M.S. Daw [ *Phys. Rev. B (USA)* vol.47 (1993) p.10895 ]

## 6.2 Methods for structural modelling of c-Si: the tight binding approximation

- [14] F. Mauri, G. Galli, R. Car [ *Phys. Rev. B (USA)* vol.47 (1993) p.9973 ]
- [15] F. Mauri, G. Galli [ *Phys. Rev. B (USA)* vol.50 (1994) p.4316 ]
- [16] P. Ordejon, D.A. Drabold, M.P. Grumbach, R.M. Martin [ *Phys. Rev. B (USA)* vol.48 (1993) p.14646 ]
- [17] D.J. Chadi, M.L. Cohen [ *Phys. Status Solidi B (Germany)* vol.68 (1975) p.405 ]
- [18] D.J. Chadi, R.M. Martin [ *Solid State Commun. (USA)* vol.19 (1976) p.643 ]
- [19] D. Weaire, M.F. Thorpe [ *Phys. Rev. B (USA)* vol.4 (1971) p.2508 ]
- [20] K. Hirabayashi [ *J. Phys. Soc. Jpn. (Japan)* vol.27 (1969) p.1475 ]
- [21] J.D. Joannopoulos, M.L. Cohen [ *Phys. Rev. B (USA)* vol.7 (1973) p.2644 ]
- [22] J. Chelikowski, D.J. Chadi, M.L. Cohen [ *Phys. Rev. B (USA)* vol.8 (1973) p.2786 ]
- [23] J. Chelikowski, M.L. Cohen [ *Phys. Rev. B (USA)* vol.14 (1976) p.556 ]
- [24] J. Chelikowski, T.J. Wagener, J.H. Weaver, A. Jin [ *Phys. Rev. B (USA)* vol.40 (1989) p.9644 ]
- [25] D.J. Chadi [ *Phys. Rev. B (USA)* vol.19 (1979) p.2074 ]
- [26] D.J. Chadi [ *Phys. Rev. B (USA)* vol.29 (1984) p.785 ]
- [27] D. Tomanek, M.A. Schlüter [ *Phys. Rev. B (USA)* vol.36 (1987) p.1208 ]
- [28] C.Z. Wang, C.T. Chan, K.M. Ho [ *Phys. Rev. B (USA)* vol.39 (1989) p.8586 ]
- [29] R. Biswas, C.Z. Wang, C.T. Chan, K.M. Ho, C.M. Soukoulis [ *Phys. Rev. Lett. (USA)* vol.63 (1989) p.1491 ]
- [30] K.C. Pandey, J.C. Phillips [ *Solid State Commun. (USA)* vol.14 (1974) p.439 ]
- [31] W.A. Harrison [ *Electronic Structure and the Properties of Solids* (Freeman, San Francisco, 1980) ]
- [32] W.A. Harrison [ *Phys. Rev. B (USA)* vol.8 (1973) p.4487 ]
- [33] W.A. Harrison, S. Ciraci [ *Phys. Rev. B (USA)* vol.10 (1974) p.1516 ]
- [34] W.A. Harrison [ *Phys. Rev. B (USA)* vol.27 (1983) p.3592 ]
- [35] W.A. Harrison [ in *Festkörperprobleme* Ed. J. Treusch (Vieweg, Braunschweig, 1977) p.135 ]
- [36] S. Froyen, W.A. Harrison [ *Phys. Rev. B (USA)* vol.20 (1979) p.2420 ]
- [37] W.A. Harrison [ *Phys. Rev. B (USA)* vol.24 (1981) p.5835 ]
- [38] K.E. Kewman, J.D. Dow [ *Phys. Rev. B (USA)* vol.30 (1984) p.1929 ]
- [39] C.H. Xu, C.Z. Wang, C.T. Chan, K.M. Ho [ *J. Phys., Condens. Matter (UK)* vol.4 (1992) p.6047 ]
- [40] L. Goodwin, A.J. Skinner, D.G. Pettifor [ *Europhys. Lett. (Switzerland)* vol.9 (1989) p.701 ]
- [41] L. Goodwin [ *J. Phys., Condens. Matter (UK)* vol.3 (1991) p.3869 ]
- [42] C.H. Xu, C.Z. Wang, C.T. Chan, K.M. Ho [ *Phys. Rev. B (USA)* vol.43 (1991) p.5024 ]
- [43] I. Kwon, R. Biswas, C.Z. Wang, C.T. Chan, K.M. Ho, C.M. Soukoulis [ *Phys. Rev. B (USA)* vol.49 (1994) p.7242 ]
- [44] D.H. Lee, J.D. Joannopoulos [ *Phys. Rev. Lett. (USA)* vol.48 (1982) p.1846 ]
- [45] W.A. Harrison [ *Phys. Rev. B (USA)* vol.31 (1985) p.2121 ]
- [46] O.L. Alerhand, E.J. Mele [ *Phys. Rev. B (USA)* vol.35 (1987) p.5533 ]
- [47] P.W. Anderson [ *Phys. Rev. (USA)* vol.181 (1969) p.181 ]
- [48] K. Nath, A.B. Anderson [ *Solid State Commun. (USA)* vol.66 (1988) p.277 ]
- [49] M. van Schilfgaarde, W.A. Harrison [ *Phys. Rev. B (USA)* vol.33 (1986) p.2653 ]
- [50] J. Lancaster, K.S. Dy [ *Phys. Rev. B (USA)* vol.14 (1976) p.583 ]
- [51] L.F. Mattheis, J.R. Patel [ *Phys. Rev. B (USA)* vol.23 (1981) p.5384 ]
- [52] P.B. Allen, J.Q. Broughton, A.K. McMahan [ *Phys. Rev. B (USA)* vol.34 (1986) p.859 ]
- [53] M. Menon, K.R. Subbaswamy [ *Phys. Rev. B (USA)* vol.47 (1993) p.12754 ]
- [54] P. Ordejon, D. Lebedenko, M. Menon [ *Phys. Rev. B (USA)* vol.50 (1994) p.5645 ]
- [55] F. Cyrot-Lackmann [ *Adv. Phys. (UK)* vol.16 (1967) p.393 ]
- [56] M.J. Kelly [ *J. Non-Crystal Solids (Netherlands)* vol.18 (1975) p.55 ]
- [57] R. Haydock, V. Heine, M.J. Kelly [ *J. Phys. C, Solid State Phys. (UK)* vol.8 (1975) p.2591 ]
- [58] D.G. Pettifor [ *Phys. Rev. Lett. (USA)* vol.63 (1989) p.2480 ]

- [59] M. Aoki [ *Phys. Rev. Lett. (USA)* vol.71 (1993) p.3842 ]
- [60] J.L. Mercer, M.Y. Chou [ *Phys. Rev. B (USA)* vol.47 (1993) p.9366 ]
- [61] G. Seifert, D. Porezag, Th. Frauenheim [ *Int. J. Quantum Chem. (USA)* vol.98 (1996) p.185 ]
- [62] E. Artacho, F. Yndurain [ *Phys. Rev. B (USA)* vol.44 (1991) p.6169 ]
- [63] A. Sieck [ private communication ]

## CHAPTER 7

### BAND STRUCTURE (*Edited by R.J. Turton*)

- 7.1 Band structure of Si: Overview
- 7.2 Calculational methods for determining the band structure of bulk c-Si
- 7.3 Spin-orbit splitting in bulk c-Si
- 7.4 Variation of bandgap with temperature in c-Si
- 7.5 Variation of bandgap with doping in c-Si
- 7.6 Variation of bandgap with pressure in bulk c-Si
- 7.7 Band structure and bandgaps in strained bulk c-Si
- 7.8 Effective masses of electrons and holes in c-Si

## 7.1 Band structure of Si: Overview

R.J. Turton

October 1997

The band structure of bulk silicon has probably been the subject of more studies, both experimental and theoretical, than that of any other semiconductor. The Datareviews in this chapter cover various aspects of the band structure of crystalline bulk silicon.

Silicon is an indirect gap semiconductor, as can be seen from FIGURE 1. The lowest energy interband transition occurs between the valence band maximum at  $\Gamma$  and the six-fold degenerate conduction band minima which occur at approximately 0.84 ( $2\pi/a$ ) along the [100] and equivalent axes. The heavy and light hole states are degenerate at the top of the valence band at  $\Gamma$ , with the split off state slightly lower in energy. These states have  $\Gamma_8$  and  $\Gamma_7$  symmetry, respectively. However, since the spin-orbit splitting is very small in silicon (see Datareview 7.3), it is usual to assume that the state is three-fold degenerate and it is denoted by the single group notation as  $\Gamma_{25}$ . The single group symmetry labels are used in FIGURE 1 and TABLE 1. Other conduction minima occur at the L and  $\Gamma$  points, lying at approximately 1 eV and 2 eV above the conduction band edge, respectively. The  $\Gamma_{15c}$  minimum is three-fold degenerate and the slightly higher lying  $\Gamma_{2c}$  state is singly degenerate.

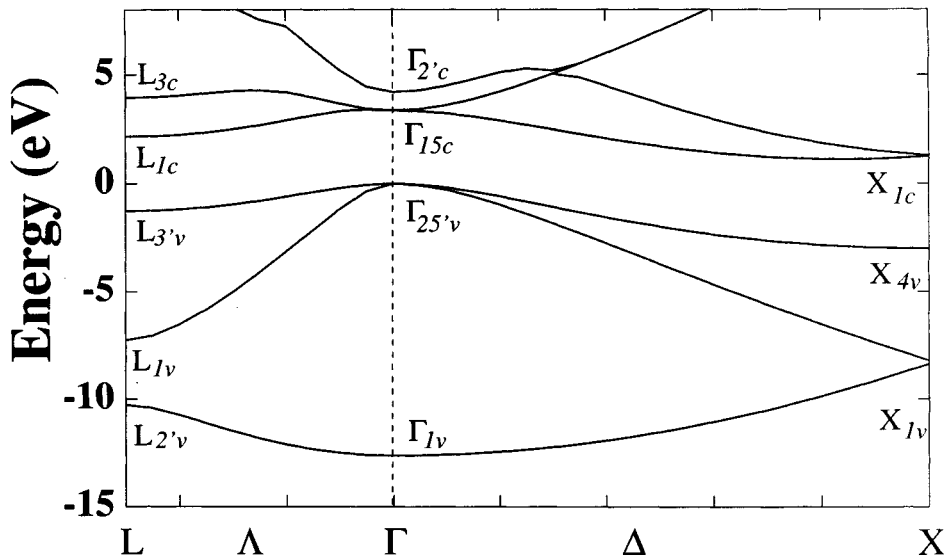


FIGURE 1 Band structure of silicon.

The energies of some of the main symmetry points, as determined by various experimental techniques, are given in TABLE 1. The energies are measured relative to the valence band maximum at  $\Gamma$ . The presence of two values for the conduction states should be explained. The earlier (left column) data were obtained by measuring the energy difference between the valence and conduction bands, whilst the more recent (right column) data were obtained by the method of inverse photoemission which measures the energy of the conduction states relative to the vacuum level. The discrepancy between the two columns of results is attributed to excitonic effects which are predicted to lower the energy of the  $E_1$  transition ( $L_{3v} - L_{3c}$ ), for example, by as much as 0.5 eV [11]. The

### 7.1 Band structure of Si: Overview

energies in the left column therefore correspond to the energies observed in optical transitions, whereas those in the right column correspond to the quasi-particle energies. Theoretical values for the energies of these symmetry points are given in TABLE 1 of Datareview 7.2.

The variation of the indirect bandgap as a function of temperature, doping and hydrostatic pressure is dealt with by Datareviews 7.4, 7.5 and 7.6, respectively, and the effects of uniaxial and biaxial strain are dealt with in Datareview 7.7. Note that in the presence of uniaxial and biaxial stress the symmetry of the band structure is also affected. The effective masses of the electrons and holes are reviewed in Datareview 7.8.

TABLE 1 Experimentally determined energies (in eV) of symmetry points in the band structure of Si (measured from the valence band maximum,  $\Gamma_{25v}$ ).

$E(\Gamma_{1v})$	$-12.4 \pm 0.6^a$	
$E(\Gamma_{25v})$	0.0	
$E(\Gamma_{15c})$	$3.40^b$	$3.05^c$
$E(\Gamma_{2c})$	$4.185 \pm 0.010^d$ $4.229 \pm 0.010^d$	$4.1^c$
$E(X_{4v})$	$-2.5 \pm 0.3^e$	
$E(X_{1c})$	$1.25^f$	$1.25^c$
Conduction minima	$1.17^g$	
$E(L_{2v})$	$-9.3 \pm 0.4^e$	
$E(L_{1v})$	$-6.4 \pm 0.4^a$	
$E(L_{3v})$	$-1.2 \pm 0.2^h$	
$E(L_{1c})$	$2.06 \pm 0.03^i$	$2.40 \pm 0.15^j$
$E(L_{3c})$	$3.9 \pm 0.1^h$	$4.15 \pm 0.10^j$

<sup>a</sup> [1]

<sup>b</sup> [2]

<sup>c</sup> [3]

<sup>d</sup> [4] Note - values are given for  $E_0$  and  $E_0 + \Delta_0$ .

<sup>e</sup> [5]

<sup>f</sup> [6] Estimated from the indirect gap.

<sup>g</sup> [7]

<sup>h</sup> [8]

<sup>i</sup> [9]

<sup>j</sup> [10]

### REFERENCES

- [1] W.D. Grobman, D.E. Eastman [ *Phys. Rev. Lett. (USA)* vol.29 (1972) p.1508 ]
- [2] R.R.L. Zucca, Y.R. Shen [ *Phys. Rev. B (USA)* vol.1 (1970) p.2668 ]
- [3] J.E. Ortega, F.J. Himpsel [ *Phys. Rev. B (USA)* vol.47 (1993) p.2130 ]
- [4] D.E. Aspnes, A.A. Studna [ *Solid State Commun. (USA)* vol.11 (1972) p.1375 ]
- [5] L. Ley, S. Kowalczyk, R. Pollak, D.A. Shirley [ *Phys. Rev. Lett. (USA)* vol.29 (1972) p.1088 ]
- [6] K.L. Shaklee, R.E. Nahory [ *Phys. Rev. Lett. (USA)* vol.24 (1970) p.942 ]
- [7] W. Bludau, A. Onton, W. Heinke [ *J. Appl. Phys. (USA)* vol.45 (1974) p.1846 ]
- [8] W.E. Spicer, R.C. Eden [ *Proc. 9th Int. Conf. on Physics of Semiconductors*, Moscow 1968, Eds. S.M. Ryvkin et al (Nauka, Leningrad, 1968) vol.1 p.65 ]
- [9] R. Hulthen, N.G. Nilson [ *Solid State Commun. (USA)* vol.18 (1976) p.1341 ]
- [10] D. Straub, L. Ley, F.J. Himpsel [ *Phys. Rev. Lett. (USA)* vol.54 (1985) p.142 ]
- [11] D. Straub, L. Ley, F.J. Himpsel [ *Phys. Rev. B (USA)* vol.33 (1986) p.2607 ]

## **7.2 Calculational methods for determining the band structure of bulk c-Si**

R.J. Turton

October 1997

### **A INTRODUCTION**

A wide range of techniques have been employed to calculate the energy band dispersion curves of semiconductors and insulators. Because silicon has a very simple crystal structure, it is often used as a test case, and so many of these methods have been applied to silicon. Rather than trying to list all of the different methods (and variations on these methods), this Datareview concentrates on identifying and describing the main types of approach that are used for generating silicon band structures.

At the coarsest level of categorisation we can distinguish between empirical and ab initio methods of calculation. Empirical methods typically rely on using a small number of adjustable parameters to obtain a fit to certain known features of the bulk band structure, whereas ab initio methods determine the band structure (and other properties) from first principles and require no experimental input.

The most popular empirical methods are based on pseudopotential or tight-binding models. These methods are generally simple to implement. In their most basic form they require only 100 or so lines of computer code, and can generate a band structure for a bulk semiconductor in a matter of seconds on a personal computer.

In contrast, a first principles program typically involves several tens of thousands of lines of computer code and makes much greater demands on computing resources. Nevertheless, for a simple crystal, such as bulk silicon, an ab initio approach based on the local density approximation (LDA) can be performed with ease on a fairly modest computer. Other methods which go beyond the local density approximation, such as quasiparticle and quantum Monte Carlo calculations, require state-of-the-art computing platforms.

### **B EMPIRICAL METHODS**

#### **B1 The Empirical Tight-Binding Method**

The tight-binding approximation is described in detail by Harrison [1] and Bullett [2], and is also dealt with more briefly in some solid state physics textbooks (e.g. Ashcroft and Mermin [3]).

In the tight-binding theory of Slater and Koster [4] the silicon crystal wavefunctions are constructed from a linear combination of atomic orbitals (LCAO), usually one s-like and three p-like functions per atom. This produces four valence (bonding) and four conduction (anti-bonding) bands.

The standard formulation involves two-centre matrix elements of the form

$$H_{ss\sigma}(R) = \int \psi_s^*(r - R) \hat{H} \psi_s(r) dr \quad (1)$$

where  $ss\sigma$  denotes that both orbitals are  $s\sigma$  orbitals. Since the only non-zero matrix elements occur between components of the same bonding orbital type (e.g. a  $\sigma$  orbital on both atoms), there are only

## 7.2 Calculational methods for determining the band structure of bulk c-Si

four matrix elements to be evaluated:  $H_{ss\sigma}$ ,  $H_{sp\sigma}$ ,  $H_{pp\sigma}$  and  $H_{pp\pi}$ . In the empirical tight-binding method these matrix elements are treated as adjustable parameters and are used to fit the calculated band structure to certain known features.

Although the basic tight-binding method gives a good description of the valence band states, the conduction bands are poorly represented. For example, in the calculation of Chadi and Cohen [5] the bandgap of silicon is about 3 eV! This suggests that it is necessary to use a larger basis set, but in practice good conduction bands have been obtained using the simple four state per atom basis set by introducing variations on the standard tight-binding scheme [6–8].

One disadvantage of the method is that the parameters are generally not transferable, i.e. a different set of parameters is required if, for example, the structure of the crystal is altered. There have, however, been many attempts to obtain tight-binding parameters which exhibit a degree of transferability. For example, Allen et al [9] have obtained parameters which reproduce silicon band structures for hypothetical simple cubic, face centred cubic and body centred cubic crystals.

### B2 The Empirical Pseudopotential Method

Whereas the tight-binding approach concentrates on the atomic orbitals, the pseudopotential method is derived from the assumption that the electrons in the interstitial regions behave in an approximately free-electron-like manner.

Earlier attempts at describing the crystal states in terms of plane waves, such as the augmented plane wave (APW) method of Slater [10] and the orthogonalised plane wave (OPW) method of Herring [11], ran into complications when describing the strong ionic potential which produces rapid oscillations of the wavefunctions in the core region.

It was suggested by Phillips and Kleinman [12] that the valence states of the crystal could be accurately described if the potential in the core is replaced by a much weaker pseudopotential,  $V_p$ . This gives rise to wavefunctions which are slowly varying, even in the core, and so convergence can be achieved using a relatively small number of plane waves. In many cases it is assumed that the pseudopotential is a function of position only. This is a local pseudopotential which can be expanded as

$$V_p(r) = \sum_G V(G) e^{iG \cdot r}$$

For silicon (and other elements which crystallise in the diamond structure) many of the Fourier coefficients  $V(G)$  are zero by symmetry. If plane waves up to a cutoff value of  $|G| < 4(2\pi/a)$  are used in the expansion, it turns out that there are only three non-zero coefficients.

Cohen and Bergstresser [13] used these three values as adjustable parameters to fit the band structure for Si and thirteen other semiconductors. The fit is very successful over a wide range of energies. In fact, it has recently been shown by Chelikowsky et al [14] that, by using three slightly different values for these parameters, it is possible to obtain a good fit to the band structure for energies up to 20 eV above the valence band maximum.

Spin-orbit splitting can be incorporated by including a fourth parameter, although in the case of silicon this effect is not usually included because of the small magnitude of the splitting (see Datareview 7.3).

## 7.2 Calculational methods for determining the band structure of bulk c-Si

One limitation of the local empirical pseudopotential model is that the valence charge densities are slightly incorrect. To rectify this problem, Chelikowsky and Cohen [15,16] incorporated a non-local correction term to take account of the energy dependence of the pseudopotential. It can be seen from TABLE 1 that the local and non-local methods produce very similar eigenvalues, at least for the states near the bandgap.

TABLE 1 Calculated energies (in eV) of symmetry points in the band structure of Si (measured from the valence band maximum,  $\Gamma_{25v}$ ). The local and non-local empirical pseudopotential (EPM) data are from Chelikowsky and Cohen [16], the APW and pseudopotential (PP) results are from Bachelet et al [28], the LMTO data are from Glötzel et al [22] and the full and model quasiparticle (QP) values are from Zhu and Louie [37]. These values should be compared with the experimental data in TABLE 1 of Datareview 7.1.

	Local EPM	Non-local EPM	APW LDA	PP LDA	LMTO LDA	Full QP	Model QP
$E(\Gamma_{1v})$	-12.53	-12.36	-12.02	-11.95	-11.87	-11.98	-12.30
$E(\Gamma_{25v})$	0.0	0.0	0.0	0.0	0.0	0.0	0.0
$E(\Gamma_{15c})$	3.43	3.43	2.49	2.54	2.59	3.43	3.43
$E(\Gamma_{2c})$	4.17	4.10	3.18	3.39	3.88	4.13	4.23
$E(X_{1v})$	-8.27	-7.69	-7.84	-7.80	-7.75	-7.97	-8.15
$E(X_{4v})$	-2.99	-2.86	-2.82	-2.92	-2.72	-2.95	-3.02
$E(X_{1c})$	1.22	1.17	0.55	0.62	0.62	1.53	1.47
$E(L_{2v})$	-10.17	-9.55	-9.64	-9.57	-9.53	-9.74	-9.98
$E(L_{1v})$	-7.24	-6.96	-7.06	-7.01	-6.93	-7.12	-7.28
$E(L_{3v})$	-1.22	-1.23	-1.16	-1.23	-1.05	-1.25	-1.28
$E(L_{1c})$	2.15	2.23	1.40	1.52	1.57	2.34	2.36
$E(L_{3c})$	4.00	4.34	3.37	3.37	3.51	4.30	4.30

Although empirical pseudopotentials are generally not transferable, some attempts have been made to produce empirical pseudopotentials which work in various different circumstances. For example, the pseudopotentials of Friedel et al [17] produce good deformation potentials and therefore can be used to model the behaviour of the states close to the bandgap under different strain conditions.

A detailed review of the theory and use of pseudopotentials is given in [18,19].

## C FIRST PRINCIPLES METHODS

Attempts to calculate the band structure of a solid from first principles can be divided into four approaches:

- (i) Hartree-Fock methods. These are usually restricted to few-atom systems and so we will not discuss them further here.
- (ii) Density functional theory. This is the ‘standard’ first principles approach for solids, usually employing the local density approximation (LDA) to evaluate the exchange-correlation contribution.
- (iii) Green’s function methods. These usually employ the GW approximation to calculate the quasiparticle energies.
- (iv) Quantum Monte Carlo methods. The most recent approach, with stochastic methods being used to solve the many-body equations.

## C1 Local Density Approximation Methods

A calculation of the properties of a bulk crystal—a system of about  $10^{23}$  interacting electrons and ions—from first principles seems a daunting prospect. However, two crucial steps towards making this calculation feasible were made by Hohenberg and Kohn [20] and Kohn and Sham [21] in 1964 and 1965, respectively. They showed that the problem of finding the ground state of the many-body system can be transformed into a series of one-electron equations in which the electrons are subject to a local effective potential  $V_{\text{eff}}(r)$ . This is known as density functional theory (DFT) because the total energy of the ground state is shown to be a functional of the electron charge density. The charge density of this new system is exactly the same as the ground state charge density of the real system. The one-electron energies  $\epsilon_i$  are given by the equation

$$\left[ -\frac{\hbar^2}{2m} \nabla^2 + V_{\text{eff}}(r) \right] \psi_i(r) = \epsilon_i \psi_i(r) \quad (2)$$

The effective potential is given by

$$V_{\text{eff}}(r) = V(r) + \frac{e}{4\pi\epsilon_0} \int \frac{\rho(r')}{|r - r'|} dr + \frac{\delta E_{\text{xc}}[\rho]}{\delta \rho(r)} \quad (3)$$

where  $\rho(r)$  is the electron charge density. Since the effective potential is dependent on the charge density, these equations must be solved self-consistently.

The main difficulty with these equations is in evaluating the exchange-correlation energy  $E_{\text{xc}}$  because this term contains the many-body interactions. Kohn and Sham [21] used the local density approximation (LDA) to approximate this term,

$$E_{\text{xc}} \approx E_{\text{xc}}^{\text{LDA}} = \int \epsilon_{\text{xc}}(n(r)) n(r) dr \quad (4)$$

where  $\epsilon_{\text{xc}}(n)$  is the exchange-correlation energy of a homogeneous electron gas of density  $n$ .

Various methods employing the local density approximation have been used to calculate the bulk band structure of silicon. For example, a number of calculations have been performed using linear muffin tin orbitals (LMTO) [22], non-muffin-tin augmented plane wave (APW) [23,24], and Gaussian orbitals [25]. However, the most popular approach for LDA calculations is a plane wave approach based on the pseudopotential approximation. This is largely due to the introduction of norm-conserving pseudopotentials [26,27] which have excellent transferability properties. Calculations on bulk silicon using norm-conserving pseudopotentials have been presented in several papers, e.g. [28,29].

The results in TABLE 1 show that these different methods produce very consistent results, with the eigenvalues of most symmetry points being identical to within  $\pm 0.1$  eV. However comparison with the empirical pseudopotential and quasiparticle results (which are in excellent agreement with experimental data) reveals that the energies of the conduction states are seriously in error. We will discuss this in the following section.

## C2 The LDA Bandgap Problem

Despite the remarkable success of the LDA method in calculating the ground state properties of a wide range of materials, one of the main problems with this approach is that it severely underestimates the magnitude of the bandgap—typically by about 50% in the case of silicon. (The problem is much worse in germanium where LDA calculations predict a zero bandgap [30].)

The simplest way to correct the bandgap is to perform a ‘scissors operation’, i.e. to rigidly shift the conduction band upwards by the required amount. This appears to work very well in the case of silicon since the magnitude of the error is approximately the same for the  $\Gamma$ , X and L minima (see column 3 of TABLE 2). However, this approach is less successful in certain other materials, notably diamond. It should also be pointed out that the scissors operation is not in keeping with the philosophy of the first principles approach because it requires empirical data to determine the true value of the bandgap.

TABLE 2 Calculated and experimental energies (in eV) for transitions across the bandgap from the valence band maximum at  $\Gamma_{25^\circ\text{v}}$  to the conduction band minima at  $\Gamma$ , X and L. LDA results are from Bachelet et al [28], the full quasiparticle (QP) values are from Zhu and Louie [37], the modified LDA (MLDA) values are from Bylander and Kleinman [33] and the screened-exchange LDA (sX-LDA) results are from Seidl et al [34]. More information on the experimental data is given in Datareview 7.1.

	LDA	QP	(QP-LDA)	MDLA	eX-LDA	Expt.
$\Gamma_{25^\circ\text{v}} \rightarrow \Gamma_{15\text{c}}$	2.54	3.43	0.89	3.34	3.37	$3.40^{\text{a}}, 3.05^{\text{b}}$
$\Gamma_{25^\circ\text{v}} \rightarrow X_{1\text{c}}$	0.62	1.47	0.85	1.48	1.55	$1.25^{\text{b,c}}$
$\Gamma_{25^\circ\text{v}} \rightarrow L_{1\text{c}}$	1.52	2.36	0.84	2.12	2.18	$2.06^{\text{d}}, 2.40^{\text{e}}$

<sup>a</sup>[38], <sup>b</sup>[39], <sup>c</sup>[40], <sup>d</sup>[41], <sup>e</sup>[42]

Various methods have been used to try to improve the bandgaps by making modifications to the local density approximation whilst keeping within the density functional framework. However, in 1988, Godby et al [31] showed that the main part of the bandgap error remains even in an exact solution of the Kohn-Sham equations. In other words, the error is inherent in the DFT approach. The reason is due to the discontinuity in the exchange-correlation energy when an electron is added to the system, i.e. the difference between the ground states of a system of N electrons and one with N + 1 electrons.

In the light of this discovery, there have been several attempts to incorporate the discontinuity by including additional terms in an otherwise standard LDA calculation. These have produced bandgaps which are much closer to the quasiparticle bandgaps [32,33]. An alternative approach is to reformulate the density functional method. These generalised Kohn-Sham methods also result in vastly improved bandgaps [34]. The cross-gap transition energies predicted by these methods are compared with quasiparticle and experimental values in TABLE 2.

## C3 Green’s Function Methods

A full first principles calculation of the quasiparticle energies can be obtained if the electron self-energy  $\Sigma$  is calculated in the GW approximation of Hedin [35]. Note that in these cases the LDA band structure is generally used as a starting point for the calculation. There are many reported calculations of bulk silicon band structures using this method, e.g. [31,36] and references in [36]. The calculations require enormous computational effort; however, this can be reduced significantly by using a model dielectric matrix instead of dealing with  $\Sigma$  directly [37].

Eigenvalues for the full and model dielectric methods are given in TABLE 1.

#### C4 Quantum Monte Carlo Methods

An alternative method of dealing with the exchange-correlation problem is to use stochastic methods. Reviews of how these methods can be applied to electronic structure calculations are given by Martin and Natoli [43] and Mitas [44].

In the variational Monte Carlo (VMC) approach a trial many-body wavefunction with several adjustable parameters is used. Monte Carlo methods are used to solve the multi-dimensional integrals in order to optimise the wavefunction. Such methods have been applied to silicon using non-local pseudopotentials [45].

In contrast, the Green's function and diffusion Monte Carlo (DMC) methods allow the exact many-body ground state to be sampled. Although a difficulty exists when applying this approach to systems of fermions, calculations for silicon have also been reported using this method [46].

#### D CONCLUSION

There are several methods for calculating the band structure of silicon, each having various advantages and disadvantages. Empirical methods are the fastest and simplest which can be run on more or less any computing platform, but generally are not transferable. LDA calculations provide the benchmark for first principles calculations. LDA calculations can be performed relatively easily on most modern computers, and several commercial packages are available. The valence band structure is very reliable, as are the cohesive and structural properties. The main problem is in calculating the energies of the conduction band states. Other methods have been investigated which avoid this problem, but these programs are not widely available and generally require powerful supercomputers.

#### REFERENCES

- [1] W.A. Harrison [ *Electronic Structure and the Properties of Solids* (Freeman, 1980) ]
- [2] D.W. Bullett [ *Solid State Phys. (USA)* vol.35 (1980) p.129 ]
- [3] N.A. Ashcroft, N.D. Mermin [ *Solid State Physics* (Holt-Saunders, 1976) ch.10 ]
- [4] J.C. Slater, G.F. Koster [ *Phys. Rev. (USA)* vol.94 (1954) p.1498 ]
- [5] D.J. Chadi, M.L. Cohen [ *Phys. Status Solidi B (Germany)* vol.11 (1975) p.732 ]
- [6] D.J. Chadi [ *Phys. Rev. B (USA)* vol.16 (1977) p.3572 ]
- [7] L.F. Mattheiss, J.R. Patel [ *Phys. Rev. B (USA)* vol.23 (1981) p.5384 ]
- [8] D.A. Papaconstantopoulos [ *Phys. Rev. B (USA)* vol.22 (1980) p.2903 ]
- [9] P.B. Allen, J.Q. Broughton, A.K. McMahan [ *Phys. Rev. B (USA)* vol.34 (1986) p.859 ]
- [10] J.C. Slater [ *Phys. Rev. (USA)* vol.51 (1937) p.151 ]
- [11] C. Herring [ *Phys. Rev. (USA)* vol.57 (1940) p.1169 ]
- [12] J.C. Phillips, L. Kleinman [ *Phys. Rev. (USA)* vol.116 (1959) p.287 ]
- [13] M.L. Cohen, T.K. Bergstresser [ *Phys. Rev. (USA)* vol.141 (1966) p.789 ]
- [14] J.R. Chelikowsky, T.J. Wagener, J.H. Weaver, A. Jin [ *Phys. Rev. B (USA)* vol.40 (1989) p.9644 ]
- [15] J.R. Chelikowsky, M.L. Cohen [ *Phys. Rev. B (USA)* vol.10 (1974) p.5095 ]
- [16] J.R. Chelikowsky, M.L. Cohen [ *Phys. Rev. B (USA)* vol.14 (1976) p.556 ]
- [17] P. Friedel, M.S. Hybertsen, M. Schlüter [ *Phys. Rev. B (USA)* vol.39 (1989) p.7974 ]
- [18] W.A. Harrison [ *Pseudopotentials in the Theory of Metals* (Benjamin, 1966) ]

## 7.2 Calculational methods for determining the band structure of bulk c-Si

- [19] H. Ehrenreich, F. Seitz, D. Turnbull (Eds.) [ *Solid State Physics* vol.24 (Academic Press, 1970) ]
- [20] P. Hohenberg, W. Kohn [ *Phys. Rev. B (USA)* vol.136 (1964) p.864 ]
- [21] W. Kohn, L.J. Sham [ *Phys. Rev. A (USA)* vol.140 (1965) p.1133 ]
- [22] D. Glötzel, B. Segall, O.K. Andersen [ *Solid State Commun. (USA)* vol.36 (1980) p.403 ]
- [23] F. Szmulowicz [ *Phys. Rev. B (USA)* vol.23 (1981) p.1652 ]
- [24] D.R. Hamann [ *Phys. Rev. Lett. (USA)* vol.42 (1979) p.662 ]
- [25] C.S. Wang, B.M. Klein [ *Phys. Rev. B (USA)* vol.24 (1981) p.3393 ]
- [26] D.R. Hamann, M. Schlüter, C. Chiang [ *Phys. Rev. Lett. (USA)* vol.43 (1979) p.1494 ]
- [27] G.B. Bachelet, D.R. Hamann, M. Schlüter [ *Phys. Rev. B (USA)* vol.26 (1982) p.4199 ]
- [28] G.B. Bachelet, H.S. Greenside, G.A. Baraff, M. Schlüter [ *Phys. Rev. B (USA)* vol.24 (1981) p.4745 ]
- [29] P.J.H. Denteneer, W. van Haeringen [ *J. Phys. C (UK)* vol.18 (1985) p.4127 ]
- [30] G.B. Bachelet, N.E. Christensen [ *Phys. Rev. B (USA)* vol.31 (1985) p.879 ]
- [31] R.W. Godby, M. Schlüter, L.J. Sham [ *Phys. Rev. B (USA)* vol.37 (1988) p.10159 ]
- [32] F. Gygi, A. Baldereschi [ *Phys. Rev. Lett. (USA)* vol.62 (1989) p.2160 ]
- [33] D.M. Bylander, L. Kleinman [ *Phys. Rev. B (USA)* vol.41 (1990) p.7868 ]
- [34] A. Seidl, A. Görling, P. Vogl, J.A. Majewski, M. Levy [ *Phys. Rev. B (USA)* vol.53 (1996) p.3764 ]
- [35] L. Hedin [ *Phys. Rev. (USA)* vol.139 (1965) p.A976 ]
- [36] M.S. Hybertsen, S.G. Louie [ *Phys. Rev. Lett. (USA)* vol.55 (1985) p.1418 ]
- [37] X. Zhu, S.G. Louie [ *Phys. Rev. B (USA)* vol.43 (1991) p.14142 ]
- [38] R.R.L. Zucca, Y.R. Shen [ *Phys. Rev. B (USA)* vol.1 (1970) p.2668 ]
- [39] J.E. Ortega, F.J. Himpsel [ *Phys. Rev. B (USA)* vol.47 (1993) p.2130 ]
- [40] K.L. Shaklee, R.E. Nahory [ *Phys. Rev. Lett. (USA)* vol.24 (1970) p.942 ]
- [41] R. Hulthen, N.G. Nilson [ *Solid State Commun. (USA)* vol.18 (1976) p.1341 ]
- [42] D. Straub, L. Ley, F.J. Himpsel [ *Phys. Rev. Lett. (USA)* vol.54 (1985) p.142 ]
- [43] R.M. Martin, V.D. Natoli [ in *Computational Approaches to Novel Condensed Matter Systems* Eds. D. Neilson, M.P. Das (Plenum Press, New York, 1995) p.7-35 ]
- [44] L. Mitas [ *Physica B (Netherlands)* vol.237-238 (1997) p.318 ]
- [45] S. Fahy, X.W. Wang, S.G. Louie [ *Phys. Rev. B (USA)* vol.42 (1990) p.3503 ]
- [46] X.P. Li, D.M. Ceperley, R.M. Martin [ *Phys. Rev. B (USA)* vol.44 (1991) p.10929 ]

## **7.3 Spin-orbit splitting in bulk c-Si**

B. Schmiedeskamp

September 1997

### **A INTRODUCTION**

Spin-orbit interaction in solids results in a splitting of some of the bands in the electronic band structure. Most important for the properties of semiconductors is the spin-orbit splitting of the valence bands (the lowest conduction band is not spin-orbit split). The size  $\Delta$  of the valence-band splitting depends strongly on the atomic number of the material and shows also a small dependence on the wave-vector  $\vec{k}$ . Typical values of  $\Delta$  are about 0.8 eV for InSb and 0.3 eV for GaAs and Ge. For silicon,  $\Delta$  is smaller than 50 meV and therefore usually not considered in theoretical and experimental work.

### **B AVAILABLE THEORETICAL AND EXPERIMENTAL DATA**

#### **B1 Theoretical Data**

To the author's knowledge relativistic band structure calculations for silicon (which would automatically yield values for the spin-orbit splitting) do not yet exist in the literature.

#### **B2 Experimental Data**

The spin-orbit splitting  $\Delta$  of the silicon valence bands at the  $\Gamma$ -point has been determined in [1] and [2] and found to be 44 meV. For different  $\vec{k}$  - values away from  $\Gamma$  in the  $\Lambda$ -direction  $\Delta$  turns out to be smaller (between 20 and 35 meV [3]).

### **C CONCLUSION**

This Datareview has covered the limited experimental and theoretical data on the spin-orbit splitting in bulk silicon. Values range from 44 meV at the  $\Gamma$ -point to 20–35 meV away from this point in the  $\Lambda$ -direction.

### **REFERENCES**

- [1] S. Zwerdling, K.J. Button, B. Lax, L.M. Roth [ *Phys. Rev. Lett. (USA)* vol.4 (1960) p.173 ]
- [2] G.L. Bona, F. Meier [ *Solid State Commun. (USA)* vol.55 (1985) p.851 ]
- [3] B. Schmiedeskamp, B. Vogt, U. Heinzmann [ *Solid State Commun. (USA)* vol.76 (1990) p.1391 ]

## 7.4 Variation of bandgap with temperature in c-Si

J. Weber

October 1997

### A INTRODUCTION

The variation of the energy gap with temperature originates from two different processes. The first one arises from the change in bond lengths with temperature and can be related to the pressure coefficient of the energy gap through the compressibility and the thermal expansion coefficient [1]. The second contribution is due to the electron-phonon interaction. The latter dominates at elevated temperatures ( $T \approx 100$  K), decreasing the bandgap energy with temperature. The electron-phonon contribution can be calculated at different levels of approximation. At high temperatures, theory predicts a linear energy shift of the bandgap with temperature, while at low temperatures the dependence is strongly nonlinear. This behaviour is reflected in the various semi-empirical analytical expressions used to fit the experimental data.

Four different analytical equations exist in the literature, which allow fits to the experimental data with three or four parameters.

$$E_g(T) = E_g(0) + \alpha T^2/(T + \beta) \quad (1)$$

$$E_g(T) = E_B - a_B[1 + 2/(\exp(\theta/T) - 1)] \quad (2)$$

$$E_g(T) = E_g(0) + BT + CT^2 \quad (3)$$

$$E_g(T) = E_g(0) - \frac{\alpha\theta}{2} \left[ \sqrt[3]{1 + \left( \frac{2T}{\theta} \right)^3} - 1 \right] \quad (4)$$

The most popular empirical relation EQN (1) was derived by Varshni [2]. More recently, the semi-empirical Bose-Einstein expression EQN (2) has been proposed, where the energy gap at  $T = 0$  is given by  $E_g(T) = E_B - a_B$  [3]. O'Donnell and Chen [4] proposed an equation, which is identical to EQN (2). A polynomial fit (EQN (3)) was used by Bludau et al [5] to fit their data. EQN (4) was recently proposed by Pässler [6], to achieve a better fit to the experimental data at lower temperatures.

The main difference between the two most used relations EQNS (1) and (2) is in the low-temperature region ( $T < 50$  K): the quadratic dependence given in EQN (1) is replaced in EQN (2) by an exponential dependence. The high temperature trend, however, is linear in both cases.

The effects of thermal expansion and the electron-phonon interaction are not explicitly considered or separately taken into account in all the empirical relations; therefore the physical meaning of the parameters appearing in them is not transparent. Collins et al [7] proposed a more elaborate procedure, which includes explicitly the lattice expansion and the distribution of phonon frequencies. The fits to the experimental data are, however, poor and the high numerical effort is not suitable for easy use [7].

## B THE FUNDAMENTAL INDIRECT BANDGAP IN SILICON

The optical transitions of the fundamental indirect gap take place between the top of the valence band  $\Gamma_{25}$  and the electron valleys located at about  $k = (2\pi/a) (0.84, 0, 0)$ . Experimental data for the energy of the indirect bandgap in Si exist today in the temperature range from 1.5 to 750 K. Absorption or photoluminescence measurements involving the participation of momentum conserving photons were analysed to yield the energy gap. Three independent data sets exist for the bandgap energy with temperature [5,8,9]. However, only in [5,8] are tables given with the numerical data of the energy gap at different temperatures. A first representative collection of earlier experimental  $E_g(T)$  data and a fit according to Varshni's EQN (1) was presented by Thurmond [10]. Even at the highest temperatures the optical properties are dominated by excitonic processes. MacFarlane et al [8] measured the excitonic absorption with high optical resolution up to  $T = 415$  K. The excitonic energies were derived from a fit to the absorption curves. Bludau et al [5] omitted the fitting procedure: the derivative of the free exciton absorption coefficient has a well defined singularity, which can be detected by wavelength modulation spectroscopy. Bludau et al give simple polynomial fits to their data (EQN (3)), which are valid in different temperature regimes. Green [11] has corrected the data of MacFarlane et al [8] by using an appropriate conversion factor between wavelength and energy and by including the exciton binding energy. After these corrections agreement with the data of Bludau et al [5] is found within 1 meV. Green also proposes a linear fit (EQN (5)) to the high temperature data of MacFarlane et al and Bludau et al. Absorption measurements at  $1.152 \mu\text{m}$  for temperatures up to 1140 K strongly support the validity of Thurmond's fit [12]. Alex et al [9] measured the near bandgap photoluminescence in the temperature range up to 1000 K and the position of the excitonic gap was derived from a line shape analysis.

In order to obtain the energy gap from the optical data, the free exciton binding energy  $E_{bx}$  and the energy of the momentum conserving phonons have to be known. The widely accepted value for the exciton binding energy is  $E_{bx} = (14.7 \pm 0.4)$  meV which corresponds to the ionisation of the  $\Delta_6$  ground-state of the free exciton [13–15]. There are no data available on the temperature dependence of  $E_{bx}$ ; however, a small increase with temperature is expected due to the change of the effective masses. This increase in  $E_{bx}$  should be only a few meV and is usually neglected. The dominant optical transition involves a momentum conserving TO phonon with energy  $E(\text{TO}) = (57.3 \pm 0.4)$  meV [13]. The weak temperature dependence of the phonon energies in this temperature regime is known from Raman measurements ( $\sim 2$  meV for TO phonons from 0 to  $900^\circ\text{C}$  [16]) and not included in the analysis of the optical data.

Low temperature PL measurements give the most accurate determination of the bandgap:  $E_g(1.8 \text{ K}) = 1.1695 \text{ eV}$  [13,14].

## C COMPILATION OF FIT PARAMETERS

Fits using EQN (1):

T range (K)	$E_g(0)$ (meV)	$\alpha$ (eV/K)	$\beta$ (K)	Error	Ref fit	Ref data set
0–750	1169.2	$4.9 \pm 0.2 \times 10^{-4}$	$655 \pm 40$	$\pm 0.5 \text{ meV}$	[9]	[9]
2–300	$1170 \pm 1$	$4.73 \pm 0.25 \times 10^{-4}$	$636 \pm 50$	$\pm 0.6 \text{ meV}$	[10]	[8]
2–300	11708	$5.367 \times 10^{-4}$	745.8		[6]	[5,8]

#### 7.4 Variation of bandgap with temperature in c-Si

Fits using EQN (2):

T range (K)	$E_B$ (meV)	$a_B$ (MeV)	$\theta$ (K)	Ref fit	Ref data set
0–300	1218.3	49.3	349.7	[6]	[5,8]

Fits using EQN (3):

T range (K)	$E_g(0)$ (meV)	B (eV/K)	C (eV/K <sup>2</sup> )	Error	Ref fit	Ref data set
0–190	1170.0	$1.059 \times 10^{-5}$	$-6.05 \times 10^{-7}$	$\pm 0.2$ meV	[5]	[5]
150–300	1178.5	$-9.025 \times 10^{-5}$	$-3.05 \times 10^{-7}$	$\pm 0.2$ meV	[5]	[5]
250–415	1206	$-2.73 \times 10^{-4}$	0	$\pm 1$ meV	[11]	[5]

Fits using EQN (4):

T range (K)	$E_g(0)$ (meV)	$\alpha\theta/2$ (meV/K)	$\theta$ (K)	p	Ref fit	Ref data set
0–300	1170.01	64.4	405.6	2.33	[6]	[5,8]

## D CONCLUSION

The indirect bandgap of crystalline Si was experimentally determined in the temperature range from 2 to 750 K. The most popular fit to the data according to Varshni's equation gives a deviation of  $\pm 1$  meV from the experimental data below 50 K, and less than  $\pm 0.5$  meV between 50 K and 600 K. Above 600 K the scatter in the experimental data increases with a standard deviation of 4 meV. More precise fits of the data either involve more fitting parameters or are valid only in certain temperature regimes.

## REFERENCES

- [1] P. Lautenschlager, P.B. Allen, M. Cardona [ *Phys. Rev. B (USA)* vol.31 (1985) p.2163 ]
- [2] Y.P. Varshni [ *Physica (Netherlands)* vol.34 (1967) p.149 ]
- [3] L. Viña, S. Logothetidis, M. Cardona [ *Phys. Rev. B (USA)* vol.30 (1984) p.1979 ]
- [4] K.P. O'Donnell, X. Chen [ *Appl. Phys. Lett. (USA)* vol.58 (1991) p.2924 ]
- [5] W. Bludau, A. Onton, W. Heinke [ *J. Appl. Phys. (USA)* vol.45 (1974) p.1846 ]
- [6] R. Pässler [ *Solid State Electron. (UK)* vol.39 (1996) p.1311 ]
- [7] A.T. Collins, S.C. Lawson, G. Davies, H. Kanada [ *Phys. Rev. Lett. (USA)* vol.65 (1990) p.891 ]
- [8] G.G. MacFarlane, T.P. McClean, J.E. Quarrington, V. Roberts [ *Phys. Rev. (USA)* vol.111 (1958) p.1245 ]
- [9] V. Alex, S. Finkbeiner, J. Weber [ *J. Appl. Phys. (USA)* vol.79 (1996) p.6943 ]
- [10] C.D. Thurmond [ *J. Electrochem. Soc. (USA)* vol.122 (1975) p.1133 ]
- [11] M.A. Green [ *J. Appl. Phys. (USA)* vol.67 (1990) p.2944 ]
- [12] G.E. Jellison Jr., D.H. Lowndes [ *Appl. Phys. Lett. (USA)* vol.41 (1982) p.594 ]
- [13] K.L. Shaklee, R.E. Nahory [ *Phys. Rev. Lett. (USA)* vol.24 (1970) p.942 ]
- [14] T. Nishino, M. Takeda, Y. Hamakawa [ *Solid State Commun. (USA)* vol.12 (1973) p.1137 ]
- [15] N.O. Lipari, M. Altarelli [ *Solid State Commun. (USA)* vol.32 (1979) p.171 ]
- [16] R. Tsu, J.G. Hernandez [ *Appl. Phys. Lett. (USA)* vol.41 (1982) p.1016 ]

## 7.5 Variation of bandgap with doping in c-Si

H.S. Bennett and R.J. Turton

March 1998

### A INTRODUCTION

The doping dependence of the indirect energy gap of silicon has received considerable experimental and theoretical attention. Many of these efforts are motivated by the need to describe the effects of high doping concentrations on the performance of electronic, optoelectronic and microwave devices.

The dependence of the indirect energy gap of silicon on doping density is usually expressed in terms of the bandgap change,

$$\Delta E_g(N) = E_g(N) - E_g(N = 0; \text{intrinsic}) \quad (1)$$

where N is the doping density for uncompensated material. Several determinations of the bandgap change for n-type and p-type silicon appear in the literature. The methods of obtaining these results may be categorised as:

- (i) electrical measurements at room temperature [1–5];
- (ii) photoluminescence (PL) and photoluminescence excitation (PLE) at low temperatures and at 300 K [6–12];
- (iii) optical and infrared absorption measurements at low temperatures and room temperature [13–15]; and
- (iv) theoretical calculations at low temperatures and at 300 K [16–24].

Statistical analyses of these data [25] show that bandgap changes determined by:

- (1) electrical measurements [1–5] and optical measurements [6–8,10–15] are not consistent with each other;
- (2) low temperature optical absorption measurements [13–15] and photoluminescence measurements [6–8,10–12] are consistent with each other when the physically correct, distorted densities of states are used to interpret the experimental data; and
- (3) absorption measurements [13–15] are consistent at both 300 K and at temperatures below 35 K with theoretical calculations [19–23].

Photoluminescence data show more apparent bandgap narrowing than the low temperature optical absorption data. However, this difference is reconciled by the fact that these two methods are sensitive to different regions of the distorted densities of states. Other discrepancies have been observed among the bandgap narrowing results obtained by the above measurement techniques. These arise from the various methods used to interpret the measurements. For example, electrical measurements give values of the apparent bandgap narrowing. When great care is used concerning the density of states in the majority-carrier band and concerning the interpretation of the PL data, then these electrically derived values may be reconciled with PL data [9].

## B ELECTRICAL MEASUREMENTS AT ROOM TEMPERATURE

There are two common methods [1–3] based on compact-analytic device models which use electrical measurements to obtain an ‘effective bandgap’ change as a function of the donor or acceptor density. Both methods involve building either a diode structure or a bipolar transistor. The latter may be either lateral or vertical.

The first method [1] is based on measuring the minority carrier current injected from a lightly doped emitter into a uniformly heavily doped substrate. This measurement has many uncertainties since the minority carrier current must be isolated from other current components. Also, since the compact-analytic models used to interpret the measurements are usually one-dimensional, the effects due to surface and sidewall currents must be known. Additional measurements are then required to obtain values for the minority carrier diffusion coefficient and diffusion length. The measurements are interpreted in terms of a compact-analytic device model that contains the effective intrinsic carrier concentration. An ‘effective bandgap’ change that is, in fact, simply a fitting parameter which has the units of energy is then inferred from this effective intrinsic carrier concentration. This fitting parameter, which frequently is confused with the physical bandgap change, contains the effects of everything not considered elsewhere in the device model. These effects include carrier-dopant-ion interactions, carrier-carrier interactions, degeneracy, minority mobilities which are not equal to majority mobilities, and physical lifetimes which are different from the empirical ones assumed in device models.

The second method [2,3] is based upon measuring the collector current of a bipolar transistor. Ancillary measurements then include the ‘average’ minority carrier diffusion coefficient or mobility and the area of the emitter. As in the first method, these measurements are then interpreted in terms of a compact-analytic device model which contains the effective intrinsic carrier concentration.

The interpretations of many electrical measurements contain the assumption that minority and majority mobilities are equal at the same doping density. However, this assumption is not correct [5,26], particularly in silicon doped above  $10^{19} \text{ cm}^{-3}$ . Many interpretations also assume uniform doping and this may not be valid for the devices on which the measurements were made.

## C PHOTOLUMINESCENCE MEASUREMENTS AT LOW TEMPERATURES AND AT 300 K

Photoluminescence experiments usually involve immersing the doped silicon samples in liquid helium between 2.4 K and 4 K and exciting them with light, for example, with 514.5 nm (2.409 eV) photons from an Ar-ion laser. Even though the quantum efficiencies are small for indirect bandgap semiconductors, photoluminescence spectra from the recombination of the electrons and holes can be obtained. Some measurements have been done at 20 K and 300 K [8,19].

Three main uncertainties exist in the interpretation of photoluminescence spectra from indirect bandgap semiconductors. These are associated with: (1) the initial and final states of the carriers; (2) the appropriate admixture of phonon-assisted transitions included in the calculated photoluminescence spectra for which the bandgap and Fermi energy are parameters; and (3) the Fermi energy and distorted densities of states used in the calculated photoluminescence spectra.

## D OPTICAL ABSORPTION MEASUREMENTS AT 300 K AND AT LOW TEMPERATURES

The optical or infrared absorption coefficients,  $\alpha$ , are obtained usually from measurements of the transmission coefficient  $T$  by inverting the relation

$$T = \frac{(1-R)^2 \exp(-\alpha d)}{1 - R^2 \exp(-2\alpha d)} \quad (2)$$

where  $R$  is the reflection coefficient and  $d$  is the sample thickness [13–15]. Separate measurements of  $d$  and  $R$  then give experimental curves for the absorption coefficients as a function of the absorbed photon energies. Such data have been obtained for a range of temperatures from 4 K to 300 K in heavily doped silicon. The interpretation of the absorption coefficients to yield the bandgap values and the bandgap changes involve similar uncertainties to those mentioned in the previous section.

## E THEORY AT 300 K AND 0 K

Bandgap narrowing is due to the carrier-dopant interaction and many-body effects. The former results in bound states at low doping concentrations. It leads to the formation of an impurity band as the doping concentration is increased and then band tailing as the impurity and continuum bands merge. The latter takes into account the exchange and correlation interactions among the carriers which become important at very high doping densities.

Several detailed many-body calculations have been performed to determine the magnitude of the bandgap narrowing in heavily doped silicon [17–19], but these calculations assume a temperature of 0 K and are strictly applicable only in the degenerate case. Since the variation of bandgap narrowing with temperature is not well understood, it is not possible to use the results to make accurate comparisons with experimental measurements made at room temperature.

Jain and Roulston [24] used simple analytic expressions and empirical assumptions with fitting parameters for the exchange, correlation and carrier-impurity interaction terms at a temperature of absolute zero. They obtained expressions for bandgap changes over a limited range of doping densities for both n-type and p-type silicon.

Another approach based on partial-wave scattering has been used by Lowney and Bennett [20]. This method has the advantage of being applicable at different temperatures, but is only valid for a rather narrow range of doping concentrations, particularly in the case of p-type silicon [21]. An alternative method using the multiple-scattering theory of Klauder [27], which is valid for all doping concentrations, has also been applied to the problem. A temperature dependent screening radius and Fermi-Dirac statistics are used to give room temperature results [22,23]. Bennett [29] has reported the first use of one theory, which is based on the Klauder fifth level of approximation, to treat both sides of the Mott transition in  $\text{Ga}_{1-y}\text{Al}_y\text{As}$  at 300 K. The mole fraction of AlAs is  $y$ . The results reported in [29] for p-type  $\text{Ga}_{1-y}\text{Al}_y\text{As}$  are expected to be qualitatively similar, but not quantitatively similar, for both p-type and n-type silicon. Calculations of bandgap narrowing and other quantities for silicon at 300 K are in progress [30].

## F APPLICATIONS TO DEVICE SIMULATION

In conventional device physics, the parameters used to describe high concentration effects on the band structure are determined from interpretations of electrical measurements on the devices being

modelled. Unless great care is taken, ambiguous results may occur when extracting such parameters from electrical measurements on devices. Such extractions for model parameters usually are based on a lower level device model and hence become dependent on that lower level device model itself. Conventional procedures give acceptable predictions for the effects of small variations in processing and in device geometry and dimensions. However, models built in this way may not lead to a fundamental understanding of the physical mechanisms responsible for the performance of the device, particularly when dimensions are less than a micrometre.

When possible, it is preferable to obtain parameters for high concentration effects by calculations based on quantum mechanics or by alternative measurements such as optical absorption or photoluminescence. The latter measurements do not require as much care in their interpretations to yield bandgap narrowing values as do electrical measurements. First-principles procedures give acceptable results for larger changes in fabrication processes and in device geometry and dimensions than do empirical procedures. They also have a much higher probability of leading to a fundamental understanding of device behaviour. However, it is important to remember that most calculations and interpretations of measurements assume uniform doping. The physics may be altered substantially in regions of steep doping gradients [27].

## G CONCLUSION

This Datareview has summarised the data available on the dependence of the indirect bandgap of silicon on doping concentration. Experimental values come from electrical measurements, photoluminescence, photoluminescence excitation, and optical and infrared absorption measurements, most at room temperature and some at low temperature. The bandgap narrowing at low temperature measured by photoluminescence, optical absorption and electrical measurements can be reconciled, when proper care is taken. Theoretical studies of bandgap narrowing cannot be compared accurately with experimental data at room temperature and work is continuing in this area. Simulations of device performance can give reasonable predictions of small variations in device geometry and dimensions but may not lead to fundamental understanding, particularly at small sizes.

## REFERENCES

- [1] R.P. Mertens, J.L. Van Meerbergen, J.F. Nijs, R.J. Van Overstraeten [ *IEEE Trans. Electron Devices (USA)* vol.ED-27 (1980) p.949 ]
- [2] D.D. Tang [ *IEEE Trans. Electron Devices (USA)* vol.ED-27 (1980) p.563 ]
- [3] W. Slotboom, H.C. deGraaff [ *Solid-State Electron. (UK)* vol.19 (1976) p.586 ]
- [4] A.W. Wieder [ in *Proceedings of the International Electron Devices Meeting* (1978) p.460 and *IEEE Trans. Electron Devices (USA)* vol.ED-27 (1980) p.1402 ]
- [5] J. del Alamo, S. Swirhun, R.M. Swanson [ in *Proceedings of the International Electron Devices Meeting* (1985) p.290 and *Solid-State Electron. (UK)* vol.28 (1985) p.47 ]
- [6] W.P. Dumke [ *Appl. Phys. Lett. (USA)* vol.42 (1983) p.196 ]. In Table I, ' $E_G + E_F$ ' should read ' $E_G + E_F - \hbar\omega_p$ '.
- [7] W.P. Dumke [ *J. Appl. Phys. (USA)* vol.54 (1983) p.3200 ]
- [8] J. Wagner [ *Solid-State Electron. (UK)* vol.28 (1985) p.25 and *Phys. Rev. B (USA)* vol.32 (1985) p.1323 ]
- [9] J. Wagner, J.A. del Alamo [ *J. Appl. Phys. (USA)* vol.63 (1988) p.425 ]
- [10] P.E. Schmid, M.L.W. Thewalt, W.P. Dumke [ *Solid State Commun. (USA)* vol.38 (1981) p.1091 ]
- [11] R.R. Parson [ *Solid State Commun. (USA)* vol.29 (1979) p.763 ]
- [12] A. Selloni, S.T. Pantelides [ *Phys. Rev. Lett. (USA)* vol.49 (1982) p.586 ]
- [13] P.E. Schmid [ *Phys. Rev. (USA)* vol.23 (1981) p.5531 ]

## 7.5 Variation of bandgap with doping in c-Si

- [14] A.A. Vol'fson, V.K. Subashiev [ *Sov. Phys.-Semicond. (USA)* vol.1 (1967) p.327 ]
- [15] M. Balkanski, A. Aziza, E. Amzallag [ *Phys. Status Solidi (Germany)* vol.31 (1969) p.323 ]
- [16] G.D. Mahan [ *J. Appl. Phys. (USA)* vol.51 (1980) p.2364 ]
- [17] R.A. Abramm, G.N. Childs, P.A. Saunderson [ *J. Phys. C (UK)* vol.17 (1984) p.6105 ]
- [18] A. Ghazali, J. Serre [ *Phys. Rev. Lett. (USA)* vol.48 (1982) p.886 and *Solid-State Electron. (UK)* vol.28 (1985) p.145 ]
- [19] K.F. Berggren, B.E. Sernelius [ *Phys. Rev. B (USA)* vol.24 (1981) p.1971 and *Solid-State Electron. (UK)* vol.28 (1985) p.11 ]
- [20] J.R. Lowney, H.S. Bennett [ *J. Appl. Phys. (USA)* vol.53 (1982) p.433 ]
- [21] H.S. Bennett [ *IEEE Trans. Electron Devices (USA)* vol.ED-30 (1983) p.920 ]
- [22] H.S. Bennett [ *J. Appl. Phys. (USA)* vol.59 (1986) p.2837 ]
- [23] J.R. Lowney [ *J. Appl. Phys. (USA)* vol.59 (1986) p.2049 ]
- [24] S.C. Jain, D.J. Roulston [ *Solid-State Electron. (UK)* vol.34 (1991) p.453 ]
- [25] H.S. Bennett, C.L. Wilson [ *J. Appl. Phys. (USA)* vol.55 (1984) p.3582 ]
- [26] H.S. Bennett [ *Solid-State Electron. (UK)* vol.26 (1983) p.1157 ]
- [27] J.R. Klauder [ *Ann. Phys. (Germany)* vol.14 (1961) p.43 ]
- [28] J.R. Lowney, H.S. Bennett [ *J. Appl. Phys. (USA)* vol.65 (1989) p.4823 ]
- [29] H.S. Bennett [ *J. Appl. Phys. (USA)* vol.83 (1998) p.3102 ]
- [30] H.S. Bennett [ to be published 1998 ]

*Contribution of the US National Institute of Standards and Technology and not subject to copyright.*

## 7.6 Variation of bandgap with pressure in bulk c-Si

R.J. Turton

April 1997

### A INTRODUCTION

It was first noted by Paul in 1958 [1] that the pressure coefficients of the energies of various symmetry points are approximately the same for all zincblende and diamond structure semiconductors, and silicon is no exception to this rule. Generally, it is found that the indirect gap from  $\Gamma_v$  to  $X_c$  (or to  $\Delta_c$  in the case of Si and Ge, where  $\Delta \approx 0.85X$ ) decreases for increasing pressure, whilst the direct bandgaps from  $\Gamma_v$  to  $\Gamma_c$  and from  $L_v$  to  $L_c$  increase. In gallium arsenide this leads to a transition from a direct to an indirect gap system as the pressure increases [2], whilst in germanium the lowest conduction state changes from L to X [3]. In silicon no such change occurs because the  $\Delta$  minimum is already the lowest energy conduction state at zero pressure.

### B EXPERIMENTAL RESULTS

Experimental measurements of the change in bandgap with pressure have been made using a number of techniques, including electrical transport [4], optical transmission [3], optical absorption [5] and electroreflectance [6]. Values are given in TABLE 1. Note that the  $\Gamma_v \rightarrow \Delta_c$  coefficient given by Slykhause and Drickamer [3] is noticeably larger than the other experimental and theoretical values. This is attributed to the fact that data up to 140 kbar were used—but it is now known that silicon undergoes a structural transition from diamond to  $\beta$ -Sn at a pressure of  $120 \pm 5$  kbar [5]. The most accurate experimental value for this coefficient is generally believed to be that due to Welber et al [5].

TABLE 1 Theoretical and experimental values of the pressure coefficients for various bandgaps in bulk silicon. The units are meV/kbar.

	LDA <sup>a</sup>	LDA <sup>b</sup>	QP <sup>b</sup>	LCGO <sup>c</sup>	Expt.
$\Gamma_{25}v \rightarrow \Delta_c$	-1.6	-1.41	-1.32	-1.43	$-1.5^d, -2.0^e, -1.41 \pm 0.06^f$
$\Gamma_{25}v \rightarrow \Gamma_{15}c$	0.5	0.58	0.53	1.39	$1 \pm 1^g$
$\Gamma_{25}v \rightarrow \Gamma_2c$	11.6	11.9	12.2		
$L_3v \rightarrow L_1c$	3.8	3.95	4.06		$6.2 \pm 0.4^g, 5.2 \pm 0.5^h$

<sup>a</sup>[9], <sup>b</sup>[10], <sup>c</sup>[11], <sup>d</sup>[4], <sup>e</sup>[3], <sup>f</sup>[5], <sup>g</sup>[6], <sup>h</sup>[8]

From the experimental measurements, Welber et al [5] concluded that in silicon the change in bandgap is a linear function of both pressure and lattice constant. (This differs from Ge and GaAs where quadratic terms are required [7]—the non-linearity in these materials is attributed to the presence of the d-core electrons.) However, recent calculations have shown that the bandgap varies non-linearly as a function of pressure (see below), but the effect may be too small to observe in an experiment. So, for the purposes of this Datareview we will assume that  $dE/dP$  is a constant.

Many theoretical calculations of the pressure coefficients for silicon have been reported in the literature. Here we concentrate only on the most recent, and, in principle, most accurate calculations. Results from first principles calculations employing the local density approximation (LDA) have been reported by Chang et al [9] and Zhu et al [10] (see TABLE 1). Although the LDA method is known to severely underestimate the bandgap (see Datareview 7.2) - by about 50% in the case of silicon at zero

## 7.6 Variation of bandgap with pressure in bulk c-Si

pressure - it is generally believed that the pressure coefficients of the bandgaps are well represented. This is confirmed by comparison with the results of first principles quasiparticle (QP) calculations [10] which are known to predict accurate bandgaps at zero pressure.

Comparing these results with experimental data it is found that:

- (a) the calculated pressure coefficients for the indirect transition ( $\Gamma_v \rightarrow \Delta_c$ ) are in good agreement with the experimental results of Welber et al [5];
- (b) the calculated coefficients for the direct transition to the p  $\Gamma$  state ( $\Gamma_v \rightarrow \Gamma_{15c}$ ) are within the rather wide error bars of the experimental result;
- (c) the calculated coefficients for the  $L_v \rightarrow L_c$  transition are not within the error bounds of the experimental data.

Although there appear to be no experimental results for the direct transition to the s  $\Gamma$  state ( $\Gamma_v \rightarrow \Gamma_{2c}$ ) for silicon, the calculated results are close to the measured values for this transition in Ge (as would be expected from the empirical theory of Paul [1]).

Some other points are worth noting regarding these first principles calculations. The calculations determine the energy gap as a function of lattice constant. The corresponding pressure P is obtained by using the Murnaghan equation of state (see [10])

$$P = \frac{B_0}{B'_0} \left[ 1 - \left( \frac{V}{V_0} \right)^{B'_0} \right] \quad (1)$$

where  $B_0$  is the bulk modulus,  $B'_0$  is the derivative of the bulk modulus with respect to pressure, and  $V_0$  is the crystal volume at zero pressure. Although the change in bandgap is found to be linear with respect to the lattice constant, the non-linearity of the Murnaghan equation of state means that the bandgap does not vary linearly with pressure. The effect becomes significant at pressures greater than about 50 kbar.

The calculations of Zhu et al [10] show that the pressure coefficients are virtually identical for three different choices of exchange-correlation potential, despite the fact that the magnitude of the bandgap is quite sensitive to the form of this potential.

The calculations of Ghahramani and Sipe [11] employ a linear combination of Gaussian orbitals (LCGO) scheme which gives good values for the bandgaps at zero pressure, but is conceptually simpler, and computationally far less demanding than the quasiparticle method. The results are in good agreement with the first principles calculations for the  $\Gamma_v \rightarrow \Delta_c$  coefficient, although there is a larger discrepancy in the  $\Gamma_v \rightarrow \Gamma_{15c}$  value.

## C CONCLUSION

The indirect bandgap of silicon, from  $\Gamma_v$  to  $X_c$ , decreases with increasing pressure, while the direct bandgap from  $\Gamma_v$  to  $\Gamma_c$  increases. Electrical transport, optical transmission, optical absorption and electroreflectance techniques have been used to determine the change and values are given. The change with pressure is measured to be a linear function of both pressure and lattice constant, but recent calculations suggest there may be a small non-linearity. Theoretical values for the pressure

## 7.6 Variation of bandgap with pressure in bulk c-Si

coefficient for the indirect transition agree with the experimental values, as do the values for the direct transition, albeit within wider error bars.

### REFERENCES

- [1] W. Paul [ *J. Phys. Chem. Solids (UK)* vol.8 (1958) p.196 ]
- [2] A.R. Goñi, G. Strössner, K. Syassen, M. Cardona [ *Phys. Rev. B (USA)* vol.36 (1987) p.1581 ]
- [3] T.E. Slykhouse, H.G. Drickamer [ *J. Phys. Chem. Solids (UK)* vol.7 (1958) p.210 ]
- [4] W. Paul, D.M. Warschauer [ *J. Phys. Chem. Solids (UK)* vol.5 (1958) p.102 ]
- [5] B. Welber, C.K. Kim, M. Cardona, S. Rodriguez [ *Solid State Commun. (USA)* vol.17 (1975) p.1021 ]
- [6] E. Schmidt, K. Vedam [ *Solid State Commun. (USA)* vol.9 (1971) p.1187 ]
- [7] B. Welber, M. Cardona, Y.F. Tsay, B. Bendow [ *Phys. Rev. B (USA)* vol.15 (1977) p.875 ]
- [8] R. Zallen, W. Paul [ *Phys. Rev. (USA)* vol.155 (1967) p.703 ]
- [9] K.J. Chang, S. Froyen, M.L. Cohen [ *Solid State Commun. (USA)* vol.50 (1984) p.105 ]
- [10] X. Zhu, S. Fahy, S.G. Louie [ *Phys. Rev. B (USA)* vol.39 (1989) p.7840 ]
- [11] E. Ghahramani, J.E. Sipe [ *Phys. Rev. B (USA)* vol.40 (1989) p.12516 ]

## 7.7 Band structure and bandgaps in strained bulk c-Si

G. Theodorou

June 1998

### A INTRODUCTION

Silicon, coherently grown on a substrate with a lattice constant different from its own, is under biaxial strain, while pressure along a particular direction produces a uniaxial strain. The biaxial strain arises from the fact that the lattice constant in the grown plane has to adjust to that of the substrate, producing also strain in the growth direction perpendicular to the growth plane. Uniaxial and biaxial strain are characterised by the strain direction, which denotes either the direction of growth for the biaxial strain or the direction of pressure for the uniaxial pressure. Even though uniaxial and biaxial strain have different hydrostatic components, they are equivalent from the symmetry point of view. For that reason we treat them together. The strain is described by the strain tensor  $[\varepsilon]$ , which for strain along the [001], [111] and [110] directions is given by [1–3],

$$[\varepsilon]_{[001]} = \begin{pmatrix} \varepsilon_{xx} & 0 & 0 \\ 0 & \varepsilon_{xx} & 0 \\ 0 & 0 & \varepsilon_{zz} \end{pmatrix}, [\varepsilon]_{[111]} = \begin{pmatrix} \varepsilon_{xx} & \varepsilon_{xy} & \varepsilon_{xy} \\ \varepsilon_{xy} & \varepsilon_{xx} & \varepsilon_{xy} \\ \varepsilon_{xy} & \varepsilon_{xy} & \varepsilon_{xx} \end{pmatrix}, \text{ and } [\varepsilon]_{[110]} = \begin{pmatrix} \varepsilon_{xx} & \varepsilon_{xy} & 0 \\ \varepsilon_{xy} & \varepsilon_{xx} & 0 \\ 0 & 0 & \varepsilon_{zz} \end{pmatrix}$$

with the convention that the x, y and z directions denote the conventional crystallographic axes of the diamond structure. The matrix elements for the strain tensor,  $\varepsilon_{ij}$ , are given in the following subsections.

#### A1 For Biaxial Strain

(1) Growth along the [001] direction:

$$\varepsilon_{xx} = \varepsilon', \quad \text{and} \quad \varepsilon_{zz} = -2 \frac{C_{12}}{C_{11}} \varepsilon'$$

(2) Growth along the [111] direction:

$$\varepsilon_{xx} = \frac{4C_{44}}{4C_{44} + C_{11} + 2C_{12}} \varepsilon', \quad \text{and} \quad \varepsilon_{xy} = -\frac{(C_{11} + 2C_{12})}{4C_{44} + C_{11} + 2C_{12}} \varepsilon'$$

(3) Growth along the [110] direction:

$$\varepsilon_{xx} = \frac{2C_{44} - C_{12}}{2C_{44} + C_{11} + C_{12}} \varepsilon', \quad \varepsilon_{zz} = \varepsilon', \quad \text{and} \quad \varepsilon_{xy} = -\frac{(C_{11} + 2C_{12})}{2C_{44} + C_{11} + C_{12}} \varepsilon'$$

with  $\varepsilon' = (a_s - a_0)/a_0$ , where  $a_s$  and  $a_0$  are the lattice constants of the substrate and unstrained Si, respectively, and  $C_{11}$ ,  $C_{12}$  and  $C_{44}$  are the elastic constants of Si, given by [4]

$$C_{11} = 1.675 \text{ Mbar}, C_{12} = 0.650 \text{ Mbar}, \text{ and } C_{44} = 0.801 \text{ Mbar}.$$

## A2 For Uniaxial Pressure

In this case, the strain tensor matrix elements are given by [1]:

- (1) Pressure along the [001] direction:

$$\varepsilon_{xx} = S_{12}X, \text{ and } \varepsilon_{zz} = S_{11}X$$

- (2) Pressure along the [111] direction:

$$\varepsilon_{xx} = \frac{1}{3}(S_{11} + 2S_{12})X, \text{ and } \varepsilon_{xy} = \frac{1}{6}S_{44}X$$

- (3) Pressure along the [110] direction:

$$\varepsilon_{xx} = \frac{1}{2}(S_{11} + 2S_{12})X, \quad \varepsilon_{zz} = S_{12}X, \quad \text{and} \quad \varepsilon_{xy} = \frac{1}{6}S_{44}X$$

with X the applied pressure, with the convention that it is negative when the sample is compressed and  $S_{ij}$  are the compliance constants, given by

$$S_{11} = \frac{C_{11} + C_{12}}{(C_{11} - C_{12})(C_{11} + 2C_{12})}, \quad S_{12} = \frac{-C_{12}}{(C_{11} - C_{12})(C_{11} + 2C_{12})}, \quad \text{and} \quad S_{44} = \frac{1}{C_{44}}$$

Uniaxial and biaxial strain affect the band structure as well as the bandgaps of Si. The band structure of strained bulk Si has been calculated in [5,6]. The important band edges are the valence band maxima at the  $\Gamma$  point of the Brillouin zone, the conduction band minima in the  $\Delta$  direction and the band edges along the  $\Lambda$  direction and near the L point. The effect of strain on the bands near these points is described by the deformation potentials.

## B STRAIN EFFECTS ON THE VALENCE BAND MAXIMA

In the absence of spin-orbit coupling, the top of the valence band of bulk Si is located at the  $\Gamma$ -point of the Brillouin zone and is triply degenerate. Spin-orbit coupling splits the states of the unstrained material, by moving two states up by an amount of  $\Delta_0/3$  (states  $V_1$  and  $V_2$  of heavy-hole and light-hole, respectively) and one state down by an amount of  $-2\Delta_0/3$  (spin split-off state). The combination of spin-orbit coupling and strain produces the following shifts in the states  $V_1$ ,  $V_2$  and  $V_3$ .

### B1 Strain Along the [001] and [111] Directions

$$\Delta E_{V_1} = \delta E_h - \frac{1}{6}\Delta_0 + \frac{1}{4}\delta E + \frac{1}{2}\sqrt{\Delta_0^2 + \Delta_0(\delta E) + \frac{9}{4}(\delta E)^2} \quad (1)$$

$$\Delta E_{V_2} = \delta E_h + \frac{1}{3}\Delta_0 - \frac{1}{2}\delta E \quad (2)$$

## 7.7 Band structure and bandgaps in strained bulk c-Si

$$\Delta E_{V_3} = \delta E_h - \frac{1}{6} \Delta_0 + \frac{1}{4} \delta E - \frac{1}{2} \sqrt{\Delta_0^2 + \Delta_0 (\delta E) + \frac{9}{4} (\delta E)^2} \quad (3)$$

with  $\delta E_h = a^v \text{Tr} [\epsilon]$  the hydrostatic component of the shift,  $a^v$  the hydrostatic deformation potential, and  $\text{Tr} [\epsilon]$  the trace of the strain tensor [1–3]. The quantity  $\delta E$  is given by

(1) for strain along the [001] direction

$$\delta E = \delta E_{001} = 2b(\epsilon_{zz} - \epsilon_{xx}) \quad (4)$$

(2) for strain along the [111] direction

$$\delta E = \delta E_{111} = 2\sqrt{3}d\epsilon_{xy} \quad (5)$$

$b$  is the deformation potential for strain of tetragonal symmetry and  $d$  the corresponding one for trigonal symmetry. Values for the deformation potentials  $b$  and  $d$  are given in TABLE 1.

TABLE 1 Experimental and theoretical values for spin-orbit coupling constant  $\Delta_0$ , and deformation

potentials  $b$ ,  $d$ ,  $\Xi_d^\Delta + \frac{1}{3} \Xi_u^\Delta - a^v$  and  $\Xi_u^\Delta$  for Si. All values are in eV.

	Experimental values	Theoretical values
$\Delta_0$	0.04 <sup>[a]</sup>	
$b$	$-2.10 \pm 0.10$ <sup>[b]</sup>	$-2.35$ <sup>[c]</sup> , $-2.21$ <sup>[d]</sup>
$d$	$-4.85 \pm 0.15$ <sup>[b]</sup>	$-5.32$ <sup>[c]</sup> , $-4.04$ <sup>[e]</sup>
$\Xi_d^\Delta + \frac{1}{3} \Xi_u^\Delta - a^v$	$1.50 \pm 0.30$ <sup>[b]</sup>	$1.72$ <sup>[c]</sup>
$\Xi_u^\Delta$	$8.6 \pm 0.4$ <sup>[b]</sup>	$9.16$ <sup>[c]</sup> , $8.86$ <sup>[d]</sup>

<sup>a</sup>Landolt-Börnstein ([8]).

<sup>b</sup>Laude et al ([9]).

<sup>c</sup>Van de Walle and Martin ([10]).

<sup>d</sup>Tserbak et al ([5]).

<sup>e</sup>Tserbak and Theodorou ([6]).

## B2 Strain Along the [110] Direction

In this case, there is no analytic expression for the splitting of the three upper valence states at  $\Gamma$ . The energies of these states can be obtained by the diagonalisation of the following Hamiltonian matrix [1,4]:

$$\begin{bmatrix} \delta E_h + \Delta_0 / 3 - A & -\sqrt{3}B & \sqrt{6}B \\ -\sqrt{3}B & \delta E_h + \Delta_0 / 3 + A & \sqrt{2}A \\ \sqrt{6}B & \sqrt{2}A & \delta E_h - 2\Delta_0 / 3 \end{bmatrix} \quad (6)$$

with  $A = (\delta E_{001} + 3(\delta E_{111}))/8$  and  $B = (\delta E_{001} - \delta E_{111})/8$ , where now  $\delta E_{001} = 4b(\epsilon_{xx} - \epsilon_{zz})$  and  $\delta E_{111} = (4/\sqrt{3})d\epsilon_{xy}$ .

## C STRAIN EFFECTS ON THE CONDUCTION BAND MINIMA

The influence of strain on the conduction band minima is given in [7].

### C1 Strain Along the [001] Direction

In this case, the six equivalent  $\Delta$  minima split into two groups, one that includes the four  $\Delta$  minima along the x and y directions and the other that includes the two minima along the z direction, with the following energy shifts:

$$\delta E(\Delta_{x,y}) = \left( \Xi_d^\Delta + \frac{1}{3} \Xi_u^\Delta \right) \text{Tr}[\epsilon] - \frac{1}{3} \Xi_u^\Delta (\epsilon_{zz} - \epsilon_{xx}) \quad (7)$$

$$\delta E(\Delta_z) = \left( \Xi_d^\Delta + \frac{1}{3} \Xi_u^\Delta \right) \text{Tr}[\epsilon] + \frac{2}{3} \Xi_u^\Delta (\epsilon_{zz} - \epsilon_{xx}) \quad (8)$$

$\Xi_d^\Delta + \frac{1}{3} \Xi_u^\Delta$  is the hydrostatic part of the deformation potential for the conduction band minima and

$\Xi_u^\Delta$  the uniaxial part. Values for the deformation potentials  $a_g = \Xi_d^\Delta + \frac{1}{3} \Xi_u^\Delta - a^v$  and  $\Xi_u^\Delta$  are given in

TABLE 1. The deformation potential  $a_g$  describes the behaviour under hydrostatic strain of the fundamental gap of Si.

### C2 Strain Along the [111] Direction

In this case, all  $\Delta$  minima remain equivalent, and their displacement has only a hydrostatic part which is given by

$$\delta E(\Delta) = \left( \Xi_d^\Delta + \frac{1}{3} \Xi_u^\Delta \right) \text{Tr}[\epsilon] \quad (9)$$

### C3 Strain Along the [110] Direction

In this case, the six  $\Delta$  minima split into two groups, one that includes the four minima along the x and y directions and the other which includes the two minima along the z direction, with the following energy shifts:

$$\delta E(\Delta_{x,y}) = \left( \Xi_d^\Delta + \frac{1}{3} \Xi_u^\Delta \right) \text{Tr}[\epsilon] - \frac{1}{3} \Xi_u^\Delta (\epsilon_{zz} - \epsilon_{xx}) \quad (10)$$

and

$$\delta E(\Delta_z) = \left( \Xi_d^\Delta + \frac{1}{3} \Xi_u^\Delta \right) \text{Tr}[\epsilon] + \frac{2}{3} \Xi_u^\Delta (\epsilon_{zz} - \epsilon_{xx}) \quad (11)$$

## D STRAIN EFFECTS ON THE E<sub>1</sub> AND E<sub>1</sub> + Δ<sub>1</sub> CRITICAL POINTS

Transitions contributing to the critical points E<sub>1</sub> and E<sub>1</sub> + Δ<sub>1</sub> are connected to direct transitions along the Λ direction, near the L point. Uniaxial and biaxial strain change their energies, and their values can be expressed in terms of the deformation potentials D<sub>j</sub><sup>i</sup>, as follows [1]:

### D1 Strain Along the [001] Direction

$$E_{\pm} = E_1(0) + \delta_H + \frac{1}{2}\Delta_1 \pm \frac{1}{2}\sqrt{\Delta_1^2 + 4\delta_S^2} \quad (12)$$

with  $\delta_H = (3)^{-1/2} D_1^1 \text{Tr}[\epsilon]$ ,  $\delta_S = \sqrt{2/3} D_3^3 (\epsilon_{zz} - \epsilon_{xx})$ , Δ<sub>1</sub> is the spin-orbit splitting, and the plus sign corresponds to the E<sub>1</sub> + Δ<sub>1</sub> transition while the minus corresponds to the E<sub>1</sub>. In these relations, D<sub>1</sub><sup>1</sup> describes the hydrostatic shift, and D<sub>3</sub><sup>3</sup> the intraband splitting of the valence band. Only the absolute value of D<sub>3</sub><sup>3</sup> can be obtained from EQN (12), while its sign is determined, from the strain dependence of the transition intensities, to be negative [11]. The values of the deformation potentials D<sub>1</sub><sup>1</sup> and D<sub>3</sub><sup>3</sup> are given in TABLE 2.

TABLE 2 Experimental and theoretical values for deformation potentials D<sub>i</sub><sup>j</sup> for Si. All values are in eV.

	Experimental values	Theoretical values
D <sub>1</sub> <sup>1</sup>	-9.8 ± 1.3 <sup>[a]</sup> , -8 ± 1 <sup>[b]</sup> , -9.72 ± 0.56 <sup>[c]</sup>	-8.5 <sup>[d]</sup> , -9.31 <sup>[e]</sup>
D <sub>3</sub> <sup>3</sup>	4.7 ± 0.5 <sup>[a]</sup> , 5 ± 1 <sup>[b]</sup> , 4.36 ± 0.62 <sup>[c]</sup>	2.3 <sup>[d]</sup> , 4.3 <sup>[e]</sup>
Sign of D <sub>3</sub> <sup>3</sup>		Negative <sup>[d]</sup>
D <sub>1</sub> <sup>5</sup>	6.5 ± 1.4 <sup>[a]</sup> , 10 ± 2 <sup>[b]</sup> , 7.83 ± 0.55 <sup>[c]</sup>	12 <sup>[d]</sup> , 7.05 <sup>[e]</sup>
D <sub>3</sub> <sup>5</sup>	3.0 ± 1.7 <sup>[a]</sup> , 4 ± 1 <sup>[b]</sup> , 5.04 ± 0.87 <sup>[c]</sup>	6.5 <sup>[d]</sup> , 6.28 <sup>[e]</sup>
Sign of D <sub>3</sub> <sup>5</sup>		Negative <sup>[d]</sup>

<sup>a</sup>Kondo and Moritani ([12]).

<sup>b</sup>Pollak and Rubloff ([13]).

<sup>c</sup>Etchegoin et al ([14]).

<sup>d</sup>Theodorou and Tsegas ([11]).

### D2 Strain Along the [111] Direction

Strain along the [111] direction causes the splitting of the L-point into the singlet [111] valley and the triplet [1̄1̄1], [1̄1̄1̄] and [1̄1̄1̄] valleys. This splitting, together with the intraband splitting of the valence bands, gives rise to four different transitions, namely E<sub>±</sub><sup>s</sup> for the singlet valley, and E<sub>±</sub><sup>t</sup> for the triplet valleys. Their transition energies in terms of the deformation potentials are given by

$$E_{\pm}^s = E_1(0) + \frac{1}{2}\Delta_1 + \delta_H + \frac{1}{2}\delta_S' \pm \frac{\Delta_1}{2} \quad (13)$$

$$E_{\pm}^t = E_1(0) + \frac{1}{2}\Delta_1 + \delta_H - \frac{1}{6}\delta_S \pm \frac{1}{6}\sqrt{9\Delta_1^2 + 16\delta_S^2} \quad (14)$$

where  $\delta_S = 2\sqrt{3}D_1^5\epsilon_{xy}$  and  $\delta_{S'} = \sqrt{6}D_3^5\epsilon_{xy}$ , and the notation that the plus sign corresponds to the  $E_1 + \Delta_1$  transition and the minus to the  $E_1$ . The  $D_1^5$  deformation potential gives the interband contribution while  $D_3^5$  describes the intraband contribution. The sign of  $D_3^5$  once again cannot be determined from the energies; it is found, from the strain-dependence of the transition intensities, to be negative [11]. The values of the deformation potentials  $D_1^1$  and  $D_3^3$  are given in TABLE 2.

## E CONCLUSION

Heteroepitaxy of silicon produces biaxial strain and pressure in a given direction produces uniaxial strain. Strain is described by the strain tensor and this Datareview has summarised these tensors in the [001], [111] and [110] directions. Strain also causes shifts in band extrema and critical point energies and these variations are also described.

## REFERENCES

- [1] F.H. Pollak, M. Cardona [ *Phys. Rev. (USA)* vol.172 (1968) p.816 ]
- [2] G.L. Bir, G.E. Pikus [ *Symmetry and Strain-Induced Effects in Semiconductors* (Wiley, New York, 1974) ]
- [3] M. Chandrasekhar, F.H. Pollak [ *Phys. Rev. B (USA)* vol.15 (1977) p.2127 ]
- [4] C.G. Van de Walle [ *Phys. Rev. B (USA)* vol.39 (1989) p.1871 ]
- [5] C. Tserbak, H.M. Polatoglou, G. Theodorou [ *Phys. Rev. B (USA)* vol.47 (1993) p.7104 ]
- [6] C. Tserbak, G. Theodorou [ *Phys. Rev. B (USA)* vol.52 (1995) p.12232 ]
- [7] C. Herring, E. Vogt [ *Phys. Rev. (USA)* vol.101 (1956) p.944 ]
- [8] O. Madelung, H. Schulz, K. Weiss (Eds.) [ *Landolt-Bornstein Numerical Data and Functional Relationships in Science and Technology, New Series* (Springer, Berlin, 1982) vol.17a ]
- [9] L.D. Laude, F.H. Pollak, M. Cardona [ *Phys. Rev. B (USA)* vol.3 (1971) p.2623 ]
- [10] C.G. Van de Walle, R.M. Martin [ *Phys. Rev. B (USA)* vol.34 (1986) p.5621 ]
- [11] G. Theodorou, G. Tsegas [ *Phys. Status Solidi B (Germany)* vol.207 (1998) p.541 ]
- [12] K. Kondo, A. Moritani [ *Phys. Rev. B (USA)* vol.14 (1976) p.1577 ]
- [13] F.H. Pollak, G.W. Rubloff [ *Phys. Rev. Lett. (USA)* vol.29 (1972) p.789 ]
- [14] P. Etchegoin, J. Kircher, M. Cardona [ *Phys. Rev. B (USA)* vol.47 (1993) p.10292 ]

## 7.8 Effective masses of electrons and holes in c-Si

D.J. Dunstan

January 1998

### A INTRODUCTION

The top of the valence band in silicon is typical of the tetrahedral semiconductors. The  $J = 3/2$  states are degenerate at the Brillouin zone centre and are spin-orbit split from the lower-lying  $J = 1/2$  states. Away from the zone centre, the fourfold  $J = 3/2$  degeneracy is not allowed by symmetry and the splitting can be described in terms of a heavy-hole band and a light-hole band [1,2]. The lowest conduction band minima are away from the Brillouin zone centre, at approximately 85% of the way to the zone edge along the  $(k, 0, 0)$  directions. Thus none of the band extrema are spherical and so effective masses are approximations appropriate for some purposes only. Moreover, the spin-orbit splitting is small (see Datareview 7.3) so that non-parabolicity is important in the valence band.

### B EXPERIMENTAL RESULTS

Cyclotron resonance gives the best values of effective masses. Early measurements [3,4] gave the electron longitudinal and transverse masses as 0.98 and 0.19. Later work using uniaxial strain to lift the valley degeneracy [5,6] improved the accuracy. Green [7] gave a comprehensive review of the data and its interpretation. Best values for the electron effective masses at helium temperature are those of Hensel et al [5,6].

$$m_t^* = 0.1905(1)$$

$$m_l^* = 0.9163(4)$$

while at 300 K the transverse mass increases to 0.198. These values correspond to a density of states effective mass [7] of

$$m_{dc}^* = 6^{2/3} (m_t^2 m_l)^{1/3} = 1.062$$

increasing to 1.09 at 300 K. They also give a thermal velocity effective mass [7] of

$$m_{tc}^* = 0.27$$

Ning and Sah [8] used the values of Hensel et al to derive an equivalent  $m^* = 0.2982$  for calculating binding energies in a single spherical valley approximation, and this value agrees well with the value of 0.23 obtained by Lawaetz [9] on theoretical grounds.

Away from the conduction band minima, the electron effective mass increases (non-parabolicity). This effect can be parametrised using

$$m(E) = m_0 (1 + 2AE)$$

where  $m_0$  is the value at the bottom of the band. For the silicon band edge, A has the value  $0.5 \text{ eV}^{-1}$  [10]. Consequently, all the effective masses increase with doping and with temperature; for details see [11].

The valence band is fully described by three parameters obtained from cyclotron resonance. For a full discussion, see Green [7] and Humphreys [12]. From early data [3], Cardona [13] obtained heavy- and light-hole masses of 0.52 and 0.16. From the later more accurate data [4,5], Barber [14] obtains

$$m_{hh}^* = 0.537$$

$$m_{lh}^* = 0.153$$

$$m_{so}^* = 0.234$$

as zone-centre effective masses at low temperature. From the same data, Green [7] obtains temperature-dependent density-of-states and thermal velocity effective masses of

$$\begin{aligned} m_{dv}^* &= 0.59 \text{ (4 K)} \\ &= 1.15 \text{ (300 K)} \end{aligned}$$

$$\begin{aligned} m_{tv}^* &= 0.37 \text{ (4 K)} \\ &= 0.41 \text{ (300 K)} \end{aligned}$$

Effective masses may also be derived from k.p theory [9] from which the heavy and light masses at the zone centre are 0.49 and 0.16. Going away from the zone-centre, the heavy-hole band is most non-parabolic in the (110) directions and the light-hole band in the (111) directions. In the region of the spin-orbit splitting energy, 44 meV, the bands are not parabolic and an effective mass is not an appropriate approximation. At much higher energies, the bands are again approximately parabolic, with effective masses [10] of 1.26 (heavy-hole) and 0.36 (light-hole).

## C CONCLUSION

Effective masses in silicon are approximations and are measured best by cyclotron resonance. Values for electron effective masses at helium temperature are given, and are noted to increase away from the conduction band minimum (non-parabolicity). Heavy- and light-hole masses are listed and again non-parabolicity occurs in certain directions.

## REFERENCES

- [1] G.F. Koster, J.O. Dimmock, R.G. Wheeler, H. Statz [ *Properties of the 32 Point Groups* (MIT Press, MA, USA, 1963) ]
- [2] R.A. Smith [ *Semiconductors* (Cambridge University Press, 1978) ]
- [3] G. Dresselhaus, A.F. Kip, C. Kittel [ *Phys. Rev. (USA)* vol.98 (1955) p.368 ]
- [4] R.N. Dexter, H.J. Zeiger, B. Lax [ *Phys. Rev. (USA)* vol.104 (1956) p.637 ]
- [5] J.C. Hensel, G. Feher [ *Phys. Rev. (USA)* vol.129 (1963) p.1041 ]
- [6] J.C. Hensel, H. Hasegawa, M. Nakayama [ *Phys. Rev. (USA)* vol.138 (1965) p.A225 ]
- [7] M.A. Green [ *J. Appl. Phys. (USA)* vol.67 (1990) p.2944 ]
- [8] T.H. Ning, C.T. Sah [ *Phys. Rev. B (USA)* vol.4 (1971) p.3468 ]
- [9] P. Lawaetz [ *Phys. Rev. B (USA)* vol.4 (1971) p.3460 ]
- [10] C. Jacoboni, L. Reggiani [ *Rev. Mod. Phys. (USA)* vol.55 (1983) p.645; and *Adv. Phys. (UK)* vol.28 (1979) p.493 ]
- [11] O. Madelung (Ed.) [ *Data in Science and Technology. Semiconductors: Group IV Elements and III-V Compounds* (Springer-Verlag, Berlin 1991) ]
- [12] R.G. Humphreys [ *J. Phys. C (UK)* vol.14 (1981) p.2935 ]
- [13] M. Cardona [ *J. Phys. Chem. Solids (UK)* vol.24 (1963) p.1543 ]
- [14] H.D. Barber [ *Solid-State Electron. (UK)* vol.10 (1967) p.1039 ]

## CHAPTER 8

### ELECTRICAL PROPERTIES (*Edited by S.H. Jones*)

- 8.1 Resistivity and carrier concentrations of doped c-Si, and sheet resistance of ion-implanted bulk Si
- 8.2 Piezoresistance of c-Si
- 8.3 Electron mobility, diffusion and lifetime in c-Si
- 8.4 Hole mobility, diffusion and lifetime in c-Si
- 8.5 Carrier ionization: field, temperature and orientation dependence
- 8.6 Modelling equations and parameters for numerical simulation

## **8.1 Resistivity and carrier concentrations of doped c-Si, and sheet resistance of ion-implanted bulk Si**

**M. Pawlik, D. Schechter and K.H. Nicholas**

[ Datareviews from 'Properties of Silicon' (INSPEC, IEE, London, UK, 1988) are combined here for the reader's convenience and presented in improved format. ]

### **A RESISTIVITY OF n- AND p-TYPE Si, DOPING DEPENDENCE**

The relationship between resistivity and dopant density has been systematically measured in boron and phosphorus doped silicon [A1]. Bulk silicon slices were used having dopant densities in the range  $3 \times 10^{13}$  to  $1 \times 10^{20} \text{ cm}^{-3}$  for n-type and  $1 \times 10^{14}$  to  $1 \times 10^{20} \text{ cm}^{-3}$  for p-type. The techniques of capacitance voltage (C-V) for densities less than  $1 \times 10^{18} \text{ cm}^{-3}$  and Hall effect for densities greater than  $1 \times 10^{18} \text{ cm}^{-3}$  were used in conjunction with four point probe measurements of resistivity. Additional data points from other published sources have been added to extend the range of validity. Estimates of the self consistency of the conversion between resistivity and dopant concentration and vice versa are given and vary over the range  $1 \times 10^{12}$  to  $1 \times 10^{21} \text{ cm}^{-3}$  for boron and  $1 \times 10^{12}$  to  $5 \times 10^{20} \text{ cm}^{-3}$  for phosphorus, being at worst 4.5%.

It is emphasised that there is conversion between dopant density and resistivity and not carrier concentration and resistivity. No account has been taken of possible incomplete ionisation although in the range of direct measurement deviations are expected to be small or non-existent.

These data have been tabulated and presented in graphical form [A2], together with estimates of the deviation from the other much quoted work of Irvin [A3]. The deviation is found to be as large as 60% over a part of the range. TABLE A1 shows data at convenient values of resistivity and TABLE A2 shows data at convenient values of dopant concentration.

TABLE A1.

Resistivity (ohm cm)	Dopant density ( $\text{cm}^{-3}$ )	
	n-type	p-type
$10^{-4}$	$1.6 \times 10^{21}$	$1.2 \times 10^{21}$
$10^{-3}$	$7.38 \times 10^{19}$	$1.17 \times 10^{20}$
$10^{-2}$	$4.53 \times 10^{18}$	$8.49 \times 10^{18}$
$10^{-1}$	$7.84 \times 10^{16}$	$2.77 \times 10^{17}$
1	$4.86 \times 10^{15}$	$1.46 \times 10^{16}$
$10^1$	$4.45 \times 10^{14}$	$1.34 \times 10^{15}$
$10^2$	$4.27 \times 10^{13}$	$1.33 \times 10^{14}$
$10^3$	$4.2 \times 10^{12}$	$1.3 \times 10^{13}$
$10^4$	$4.0 \times 10^{11}$	$1.3 \times 10^{12}$

TABLE A2.

Dopant density (cm <sup>-3</sup> )	Resistivity (ohm cm)	
	n-type	p-type
10 <sup>12</sup>	$4.3 \times 10^3$	$1.3 \times 10^4$
10 <sup>13</sup>	$4.3 \times 10^2$	$1.3 \times 10^3$
10 <sup>14</sup>	$4.29 \times 10$	$1.31 \times 10^2$
10 <sup>15</sup>	4.48	$1.33 \times 10$
10 <sup>16</sup>	$5.23 \times 10^{-1}$	1.44
10 <sup>17</sup>	$8.38 \times 10^{-2}$	$2.02 \times 10^{-1}$
10 <sup>18</sup>	$2.36 \times 10^{-2}$	$4.35 \times 10^{-2}$
10 <sup>19</sup>	$5.78 \times 10^{-3}$	$8.87 \times 10^{-3}$
10 <sup>20</sup>	$7.70 \times 10^{-4}$	$1.17 \times 10^{-3}$
10 <sup>21</sup>	$1.6 \times 10^{-4}$	$1.3 \times 10^{-4}$

A number of possible interferences may arise which can affect these conversions. Primary amongst these is the compensation of silicon through the presence of impurities other than the majority dopant density impurity. Normally these are unintentionally introduced dopants of opposite polarity, and similar effects due to the presence of deep level impurities, crystalline defects, interstitials and lattice damage by radiation are observed.

At high doping levels, the possibility of the formation of compounds and complexes arises and such effects prevent some dopant atoms from being electrically active. This is particularly likely in phosphorus or arsenic doped silicon above the limit of solid solubility. Since bulk silicon material with dopant densities greater than  $1 \times 10^{20}$  cm<sup>-3</sup> is not available, measurements in this range are made on ion implanted or diffused material. Differences are observed depending on the method of preparation of the samples, in particular the method of annealing, and no universal agreement has been reached about the conversion or mobility changes. The paper of Masetti et al [A4] describes attempts to determine mobility and carrier concentration relationships.

## REFERENCES TO SECTION A

- [A1] W.R. Thurber, R.L. Mattis, Y.M. Liu, J.J. Filliber [ *National Bureau of Standards, Special Publication SP400-64* (National Bureau of Standards, Washington, USA, 1981) ]
- [A2] [ *ASTM Standard Practice, Designation F723-82, Annual Book of Standards* vol.10.05 (Philadelphia, USA, 1984) p.598-614 ]
- [A3] J.C. Irvin [ *Bell Syst. Tech. J. (USA)* vol.41 (1962) p.387-410 ]
- [A4] G. Masetti, M. Severi, S. Solmi [ *IEEE Trans. Electron Devices (USA)* vol.T-ED-30 no.7 (1983) p.764-9 ]

## B CARRIER CONCENTRATIONS IN LIGHTLY- AND MODERATELY-DOPED Si

### B1 Symbols

The following symbols are used in this section:

- E<sub>a</sub> = acceptor binding energy
- E<sub>c</sub> = energy of conduction band edge
- E<sub>d</sub> = donor binding energy
- E<sub>f</sub> = Fermi energy

## 8.1 Resistivity and carrier concentrations; sheet resistance of ion-implanted bulk Si

$E_v$  = energy of valence band edge

$g_1$  = acceptor degeneracy

$g_2$  = donor degeneracy

$k$  = Boltzmann constant

$n$  = density of electrons in the conduction band

$n_2$  = density of electrons bound to donors

$N_a$  = density of acceptors

$N_c$  = effective density of states in conduction band

$N_d$  = density of donors

$N_v$  = effective density of states in valence band

$p$  = density of holes in the valence band

$p_1$  = density of holes bound to acceptors

$T$  = temperature in K

### B2 Lightly Doped Silicon ( $<1 \times 10^{16} \text{ cm}^{-3}$ )

Carrier concentrations in lightly-doped material at thermal equilibrium and in the absence of applied fields are calculated by assuming charge neutrality [B1].

$$p + p_1 + N_d = n + n_2 + N_a$$

For parabolic bands [B2]

$$p = N_v \exp[(E_v - E_f)/kT]$$

$$n = N_c \exp[-(E_c - E_f)/kT]$$

$$n_2 = N_d/[1 + (1/g_2) \exp((E_d - E_f)/kT)]$$

$$p_1 = N_a/[1 + (1/g_1) \exp((E_f - E_a)/kT)]$$

The effective densities of states in silicon are

$$N_v = 1.04 \times 10^{19} \times (T/300)^{(3/2)} \text{ cm}^{-3}$$

$$N_c = 2.8 \times 10^{19} \times (T/300)^{(3/2)} \text{ cm}^{-3}$$

### B3 Moderately Doped Silicon ( $<1 \times 10^{18} \text{ cm}^{-3}$ )

All of the above relations hold reasonably well up to doping levels of about  $1 \times 10^{16} \text{ cm}^{-3}$ . Many of these relationships must be modified in more heavily doped materials. A practical model for treating heavier donor dopings, up to about  $1 \times 10^{18} \text{ cm}^{-3}$ , has been devised by Lee and McGill [B3,B4]. The random electric fields of the ionised impurities (in n-type materials all of the acceptors are ionised) cause various effects—a shift in the conduction band edge, conduction band tailing (so that the conduction band edge is no longer sharply defined), and a random shift in the binding energy of the various donor impurity atoms. In addition, the overlap of the impurity electron wavefunctions of adjacent donor impurities produces a further random shift in donor binding energies. These random shifts in donor binding energies result in the donor energy lying within a range, rather than having a sharply defined value, and hence one speaks of an impurity band.

## 8.1 Resistivity and carrier concentrations; sheet resistance of ion-implanted bulk Si

In this model, the number of electrons in the conduction band is given by

$$n = \int_{-\infty}^{\infty} \frac{N_c(E) dE}{1 + \exp[(E - E_f)/kT]}$$

where  $N_c(E)$  is a suitably modelled average density of conduction band states that results from the conduction band tailing.

The density of ionised donors in this model is given by

$$\begin{aligned} N_d^+ &= N_d - n_2 \\ &= \int_{-\infty}^{\infty} \frac{\rho(i)(E - E'_d) dE}{1 + 2 \exp[(E_f - E)/kT]} \end{aligned}$$

where  $\rho(i)(E - E'_d)$  is a suitably modelled impurity band density of states and  $E'_d$  is the average shifted donor binding energy.

The procedure for calculating the carrier concentration using this model is analogous to that for lightly doped material. The Fermi energy is iterated until charge neutrality is satisfied, the difference being that the charge neutrality computations are much more complicated since the conduction band density of states and the impurity band density of states depend on the carrier concentration and the extent of ionisation of the donors, which in turn depends on the Fermi level. Hence these computations must be done self-consistently.

Based on the available experimental data, the Lee-McGill model appears to be quite successful at describing n-type silicon up to a maximum donor concentration of about  $10^{18} \text{ cm}^{-3}$ . This author has published detailed computations of activation energy and carrier concentration [B4]. TABLES B1 and B2 give carrier concentration as a function of donor and compensating acceptor doping level in As doped Si at temperatures of 80 K and 300 K, respectively. Carrier concentrations were also computed at 10 K, but the number of carriers was so small that the results were not tabulated.

Computations were also carried out in the doping range  $10^{15} \text{ cm}^{-3} < N_d < 10^{16} \text{ cm}^{-3}$  to compare the dilute and Lee-McGill models. At a temperature of 300 K the two models agreed within 1% for all three shallow group V impurities (P, As and Sb) for  $N_d = 10^{16} \text{ cm}^{-3}$ . This agreement held for P and Sb doped material down to  $N_d = 2 \times 10^{15} \text{ cm}^{-3}$ . For As doped Si the agreement steadily decreased as  $N_d$  decreased below  $10^{16} \text{ cm}^{-3}$ . For all dopants, the Lee-McGill model ceased to give reasonable results for  $N_d < 2 \times 10^{15} \text{ cm}^{-3}$ .

As the temperature is decreased, the agreement between the two models also decreases. At 80 K, the two models agree to about 20% at  $N_d = 10^{16} \text{ cm}^{-3}$ . As  $N_d$  is decreased, the percentage difference decreased steadily to about 5% at  $N_d = 2 \times 10^{15} \text{ cm}^{-3}$  (12% for As doped material). At this temperature, the Lee-McGill model again fails for  $N_d < 2 \times 10^{15} \text{ cm}^{-3}$ . For all dopants the carrier concentration calculated by the Lee-McGill model at low temperatures exceeded that calculated by the dilute model.

### 8.1 Resistivity and carrier concentrations; sheet resistance of ion-implanted bulk Si

TABLE B1 Carrier concentration in As doped Si at 80 K.

$N_d$ (cm $^{-3}$ )	$N_a$ (cm $^{-3}$ )				
	$1 \times 10^{12}$	$1 \times 10^{13}$	$1 \times 10^{14}$	$1 \times 10^{15}$	$1 \times 10^{16}$
$1 \times 10^{14}$	$8.9 \times 10^{13}$	$8.1 \times 10^{13}$	-	-	-
$2 \times 10^{14}$	$1.6 \times 10^{14}$	$1.6 \times 10^{14}$	$8.1 \times 10^{13}$	-	-
$5 \times 10^{14}$	$3.5 \times 10^{14}$	$3.4 \times 10^{14}$	$2.7 \times 10^{14}$	-	-
$1 \times 10^{15}$	$5.8 \times 10^{14}$	$5.7 \times 10^{14}$	$5.1 \times 10^{14}$	-	-
$2 \times 10^{15}$	$9.2 \times 10^{14}$	$9.2 \times 10^{14}$	$8.6 \times 10^{14}$	$3.7 \times 10^{14}$	-
$5 \times 10^{15}$	$1.6 \times 10^{15}$	$1.6 \times 10^{15}$	$1.6 \times 10^{15}$	$1.1 \times 10^{15}$	-
$1 \times 10^{16}$	$3.0 \times 10^{15}$	$3.0 \times 10^{15}$	$2.9 \times 10^{15}$	$2.6 \times 10^{15}$	-
$2 \times 10^{16}$	$4.6 \times 10^{15}$	$4.6 \times 10^{15}$	$4.6 \times 10^{15}$	$4.3 \times 10^{15}$	$2.0 \times 10^{15}$
$5 \times 10^{16}$	$8.1 \times 10^{15}$	$8.1 \times 10^{15}$	$8.0 \times 10^{15}$	$7.8 \times 10^{15}$	$6.3 \times 10^{15}$
$1 \times 10^{17}$	$1.2 \times 10^{16}$	$1.2 \times 10^{16}$	$1.2 \times 10^{16}$	$1.2 \times 10^{16}$	$1.1 \times 10^{16}$
$2 \times 10^{17}$	$1.9 \times 10^{16}$	$1.9 \times 10^{16}$	$1.9 \times 10^{16}$	$1.9 \times 10^{16}$	$1.9 \times 10^{16}$
$5 \times 10^{17}$	$3.8 \times 10^{16}$	$3.8 \times 10^{16}$	$3.8 \times 10^{16}$	$3.8 \times 10^{16}$	$3.9 \times 10^{16}$
$1 \times 10^{18}$	$7.1 \times 10^{16}$	$7.1 \times 10^{16}$	$7.1 \times 10^{16}$	$7.2 \times 10^{16}$	$7.5 \times 10^{16}$

Note - carrier concentrations are expressed in units of cm $^{-3}$ .

TABLE B2 Carrier concentration in As doped Si at 300 K.

$N_d$ (cm $^{-3}$ )	$N_a$ (cm $^{-3}$ )				
	$1 \times 10^{12}$	$1 \times 10^{13}$	$1 \times 10^{14}$	$1 \times 10^{15}$	$1 \times 10^{16}$
$1 \times 10^{14}$	$9.9 \times 10^{13}$	$9.0 \times 10^{13}$	-	-	-
$2 \times 10^{14}$	$2.0 \times 10^{14}$	$1.9 \times 10^{14}$	$1.0 \times 10^{14}$	-	-
$5 \times 10^{14}$	$5.0 \times 10^{14}$	$4.9 \times 10^{14}$	$4.0 \times 10^{14}$	-	-
$1 \times 10^{15}$	$1.0 \times 10^{15}$	$9.9 \times 10^{14}$	$9.0 \times 10^{14}$	-	-
$2 \times 10^{15}$	$2.0 \times 10^{15}$	$2.0 \times 10^{15}$	$1.9 \times 10^{15}$	$1.0 \times 10^{15}$	-
$5 \times 10^{15}$	$5.0 \times 10^{15}$	$5.0 \times 10^{15}$	$4.9 \times 10^{15}$	$4.0 \times 10^{15}$	-
$1 \times 10^{16}$	$9.9 \times 10^{15}$	$9.9 \times 10^{15}$	$9.8 \times 10^{15}$	$8.9 \times 10^{15}$	-
$2 \times 10^{16}$	$2.0 \times 10^{16}$	$2.0 \times 10^{16}$	$2.0 \times 10^{16}$	$1.9 \times 10^{16}$	$9.9 \times 10^{15}$
$5 \times 10^{16}$	$4.9 \times 10^{16}$	$4.9 \times 10^{16}$	$4.9 \times 10^{16}$	$4.8 \times 10^{16}$	$3.9 \times 10^{16}$
$1 \times 10^{17}$	$9.6 \times 10^{16}$	$9.6 \times 10^{16}$	$9.6 \times 10^{16}$	$9.5 \times 10^{16}$	$8.7 \times 10^{16}$
$2 \times 10^{17}$	$1.9 \times 10^{17}$	$1.9 \times 10^{17}$	$1.9 \times 10^{17}$	$1.9 \times 10^{17}$	$1.8 \times 10^{17}$
$5 \times 10^{17}$	$4.4 \times 10^{17}$	$4.4 \times 10^{17}$	$4.4 \times 10^{17}$	$4.4 \times 10^{17}$	$4.3 \times 10^{17}$
$1 \times 10^{18}$	$8.1 \times 10^{17}$	$8.1 \times 10^{17}$	$8.1 \times 10^{17}$	$8.1 \times 10^{17}$	$8.0 \times 10^{17}$

Note - carrier concentrations are expressed in units of cm $^{-3}$ .

### REFERENCES TO SECTION B

- [B1] W. Shockley [ in *Electrons and Holes in Semiconductors* (D. Van Nostrand, 1950) p.465-71 ]
- [B2] K. Seeger [ *Semiconductor Physics* (Springer-Verlag, 1973) p.35-45 ]
- [B3] T.F. Lee, T.C. McGill [ *J. Appl. Phys. (USA)* vol.46 no.1 (1975) p.373-80 ]
- [B4] D. Schechter [ *J. Appl. Phys. (USA)* vol.61 no.2 (1987) p.591-8 ]

## C SHEET RESISTANCE OF ION-IMPLANTED BULK Si

The accurate control of the dose of dopant ions and the ability to implant through a passivating layer make ion implantation an attractive technique for forming doped layers for use as resistors or as layers in active devices. Special electrical properties can also be achieved by ion implantation.

The sheet resistance of a uniformly doped fully annealed ion implanted layer is identical with that of such a layer produced by diffusion or growth. The dopant species used for fully annealed layers are generally those used in other doping methods (elements of groups III and V). There are, however, some features specific to implanted layers and some species not generally considered for diffusion (In, N, etc.) can be incorporated by ion implantation.

The concentration profile of an implanted layer is well defined [C1] and controlled, and full activation can be achieved without seriously degrading the profile. The sheet resistance can then be calculated from standard bulk concentration versus resistivity data [C2]. Often, a Gaussian profile can be assumed as the resistance is not very sensitive to small amounts of channelling. Standard computer models, e.g. SUPREM (Stanford, USA) and ICECREM (IFT Munich, Germany) can be used to obtain accurate values. An approximate value can be obtained from the simple formula  $R = KD^{-0.7}S^{-0.3}$  [C3] where R is the sheet resistance, D the implant dose, S the standard deviation of the implanted profile and K a constant. For a p-type dopant such as boron K has the value  $1 \times 10^{11}$  ohm/cm<sup>1.1</sup> while for n-type dopants it is  $5.8 \times 10^{10}$  ohm/cm<sup>1.1</sup>. The formulae give a first approximation ( $\pm 10\%$  B,  $\pm 20\%$  P and As) between doses of  $3 \times 10^{12}$  /cm<sup>2</sup> and  $10^{15}$  /cm<sup>2</sup>. If the anneal does not cause significant diffusion the value of S can be related to the implant energy. For implant energies of 30 to 200 keV the following formulae can be used:

$$\text{Boron} \quad S = 2.64 \times 10^{-6} (\ln E) - 4.6 \times 10^{-6}$$

$$\text{Phosphorus} \quad S = 1.56 \times 10^{-6} (\ln E)^2 - 9.5 \times 10^{-6} (\ln E) + 1.66 \times 10^{-5}$$

$$\text{Arsenic} \quad S = 8.5 \times 10^{-7} (\ln E)^2 - 5.7 \times 10^{-6} (\ln E) + 1.07 \times 10^{-5}$$

where E is the implant energy in keV. Agreement with standard tables [C1] is to better than 5%. Resistors with sheet resistance greater than about 50 kohm/sq tend to be non-linear with voltage and sensitive to surface related charges and substrate doping. The special resistors described later can ease the problem. The lower limit is set by the solid solubility of impurities and acceptable layer depth. It can be difficult to reduce resistance much below 10 ohm/sq without the special annealing techniques described later. There is some evidence that at very high concentrations mobilities in p- and n-type layers converge [C4] but at fairly high concentrations those for different n-type species diverge [C2,C16].

The temperature necessary for complete annealing (removal of damage effects on mobility and reaching activation levels as in thermal equilibrium) depends on dose, species and other factors. Some general trends can, however, be given provided the silicon has not been rendered amorphous by the implantation damage: (a) the higher the dose the higher the temperature of anneal required (typically 500°C to 950°C); (b) the higher the temperature of implant the less the damage and lower the minimum anneal temperature (provided it does not prevent amorphisation); and (c) oxidising atmospheres during annealing can cause defects to grow rather than anneal out [C5].

If the layer has become amorphous, regrowth can take place at temperatures as low as 650°C [C6]. Redistribution of dopant can occur and so the sheet resistance estimates are not necessarily valid. For

## *8.1 Resistivity and carrier concentrations; sheet resistance of ion-implanted bulk Si*

high doses of certain dopants, loss of dopant to the surface can be significant, particularly with (111) material which does not regrow so rapidly as (100) material.

Resistors with markedly different properties can be made by incomplete or rapid annealing. An anneal temperature of 500°C is high enough to stabilise the layer and the sheet resistance is not generally very sensitive to anneal time and temperature [C7]. There is often a minimum in sheet resistance against anneal temperature plots at 500°C particularly for p-type layers. Anneals at 500°C therefore tend to give stable resistors of reproducible value while being compatible with aluminium and silicide layers.

The temperature coefficients of resistance of fully annealed implanted layers are similar to those of diffused layers. They are always positive. Residual damage tends to lead to effective dopant level depths deeper in the bandgap than without damage. This leads to a more negative temperature coefficient of resistance [C8]. By adjusting the amount of damage temperature coefficients near zero can be obtained as are desired for resistors in linear integrated circuits [C9]. The damage can be adjusted by the choice of annealing temperature and extra damage can be produced by implanting a species neutral in silicon [C10].

To make reproducible high value resistors the sensitivity to oxide charge and to depletion at the junction with the substrate must be reduced. This can be achieved by reducing carrier mobility or deepening the dopant energy depth.

The smaller the mobility the smaller the change in resistance for a given change in oxide or depleted charges. The mobility is lower for p-type layers and can be reduced further by compensation [C11] or damage [C10]. Ion implantation is ideal for making compensated resistors because of the good control of dose. Even greater improvements can be achieved by implantation damage.

Only a small fraction of dopant atoms are ionised at room temperature for deep level dopants but all are ionised in depletion layers. Thus for a given change in depletion layer charge the number of ionised dopants, and so carriers, changes by a much smaller amount. There are p-type dopants with deeper energy levels (In, Tl [C12]) and ion implantation helps in avoiding any problems due to their diffusion in oxides. Implantation damage also causes the effective energy depth of p- and n-type dopants to be deeper.

High value resistors can therefore be made by damaging implants into boron doped layers or just implants of neutral ions (such as Ne) [C13] which give p-type activity with an acceptor depth of 0.25 eV. In this way resistors with a sheet resistance of 250 kohm/sq can be made. The temperature coefficient of such layers is strongly negative because of the dopant energy depth. Linearity of resistors of a given value is also improved by damage because of the reduced sensitivity to depletion at the junction with the substrate.

Rapid annealing (1000°C for less than a minute) can lead to supersaturation of dopant atoms for high doses. Concentrations well above solid solubility can be achieved. Mobilities tend to be low because of ionised impurity scattering but sheet resistances much lower than with thermal equilibrium anneals can be achieved [C14]. Rapid annealing techniques can be divided into those in which the slice as a whole reaches a uniform temperature and those so rapid that heating is localised laterally and in depth. Strip heaters [C15], optical heating [C16] and electron beam annealing [C17] generally give uniform slice temperatures. The sheet resistances for implant doses below those causing supersaturation are then in good agreement with the calculations mentioned earlier because diffusion is negligible in terms of its effect on sheet resistance. The advantage of these forms of rapid annealing is the full activation with limited diffusion at a relatively low cost compared to the localised annealing

## 8.1 Resistivity and carrier concentrations; sheet resistance of ion-implanted bulk Si

techniques. Pulsed laser [C18] or electron beam annealing can involve local melting of the crystal surface. The implant profile is then altered to provide a rectangular profile for high frequency emitters [C19] etc. The sheet resistance can also be slightly lower than with other rapid annealing techniques.

### REFERENCES TO SECTION C

- [C1] B.J. Smith [ *Ion Implantation Range Data for Silicon and Germanium Technologies* (GB Learned Information Ltd., Europe, 1977) ]
- [C2] G. Masetti, M. Severi, S. Solmi [ *Ext. Abstr. Electrochem. Soc. (All Div.) (USA)* vol.83-1 (1983) p.639 ]
- [C3] K.H. Nicholas [ *Radiat. Eff. (UK)* vol.28 (1976) p.177 ]
- [C4] C. Hill [ *Inst. Phys. Conf. Ser. (UK)* vol.69 (1983) p.172 ]
- [C5] I.R. Sanders, P.S. Dobson [ *Philos. Mag. (UK)* vol.20 (1969) p.881 ]; P. Ashburn, C. Bull, K.H. Nicholas, G.R. Booker [ *Solid-State Electron. (UK)* vol.9 (1977) p.731 ]
- [C6] L. Csepregi, W.K. Chu, H. Muller, J.W. Mayer, T.W. Sigmon [ *Radiat. Eff. (UK)* vol.28 (1976) p.277 ]
- [C7] J.M. Shannon, R.A. Ford, R.A. Gard [ *Radiat. Eff. (UK)* vol.6 (1970) p.217 ]
- [C8] D.P. Oostkoek, J.A. den Boer, W.K. Hofker [ *European Conf. on Ion Implantation* Reading, UK, 7-9 Sept. 1970 (PPL, Stevenage, UK, 1970) p.88 ]
- [C9] G. Kelson, H.H. Stellrecht, D.S. Perloff [ *IEEE J. Solid-State Circuits (USA)* vol.SC-8 (1973) p.336 ]
- [C10] B.A. Maciver [ *Electron. Lett. (UK)* vol.11 (1975) p.484 ]
- [C11] J.D. MacDougal, K.E. Manchester, P.E. Roughan [ *Proc. IEEE (USA)* vol.57 (1969) p.1538 ]
- [C12] K.R. Whight, P. Blood, K.H. Nicholas [ *Solid-State Electron. (UK)* vol.19 (1976) p.1021 ]
- [C13] K.H. Nicholas, R.A. Ford [ *Proc. 2nd Int. Conf. Ion Implantation in Semiconductors* (Springer-Verlag, Berlin, 1971) p.357-61 ]
- [C14] W.K. Hofker, G.E.J. Eggermont, K. Tamminga, D.P. Oosthoek [ *Laser-Solid Interactions and Laser Processing* (New York, USA, 1979) p.425-8 ]
- [C15] B.-Y. Tsaur, J.P. Donnelly, J.C.C. Fan, M.W. Geis [ *Appl. Phys. Lett. (USA)* vol.39 (1981) p.93 ]
- [C16] G.K. McGinty, K.H. Nicholas [ *ESSDERC 1983 Europhysics Conf. Abs.* vol.F7 (EPS, Switzerland, 1983) p.159-61 ]
- [C17] H.J. Smith, E. Ligeon, A. Bontemps [ *Appl. Phys. Lett. (USA)* vol.39 (1981) p.93 ]
- [C18] D.H. Austin, C.M. Surka, T.N.C. Venkatesen, R.E. Slushier, J.A. Golovchenko [ *Appl. Phys. Lett. (USA)* vol.33 (1978) p.437 ]
- [C19] C. Hill [ *Laser Solid Interactions and Transient Thermal Processing of Materials* (North Holland, New York, USA, 1983) p.381 ]

## 8.2 Piezoresistance of c-Si

M.V. Chaparala and B.S. Shivaram

June 1998

### A INTRODUCTION

The phenomenon of piezoresistance, i.e. change in the electrical resistance of a material when subjected to external stress, has been known since it was first discovered by Lord Kelvin [1] in 1856 while investigating the effect of stress in metallic wires. His work was continued by his pupil Tomlinson [2], and was further explored by others during the 1920s and 1930s [3–6]. The piezoresistive effect in silicon was discovered by Smith [7] in 1954. With the rise of semiconductor technology during the mid century, this research was extended by many others [8–17].

While the principal application of piezoresistance is for strain gauges which can be discrete or integrated devices with on chip signal processing, other physical and thermodynamic quantities can also be measured by converting changes in the parameter of interest to strain. Further, progress in circuit integration has added to the importance of a detailed understanding of piezoresistivity, as electrical signal processing is highly susceptible to a trace of strain in the substrates. Integrated circuits (IC) including IC strain gauges, pressure sensors and Hall effect devices have great potential for application in various fields. The performance of such devices may be seriously affected by encapsulation stress. A thermal mismatch between the mounting material and the chip produces stress in the IC die resulting in considerable piezo effects which make it difficult to predict the circuit parameters. Thus it is technologically important to understand the piezoresistive effects in silicon and other semiconductors. This survey concentrates on the piezoresistive effect in single crystal silicon, although polycrystalline silicon and silicon on insulator are touched upon as well.

To understand the origins of the piezoresistive effect consider the simple case of a bar of length  $\ell$ , cross-sectional area  $A = x \times y$ , and resistivity  $\rho$ . The fractional change in resistance  $dR/R$  due to an externally imposed stress is given by

$$\frac{dR}{R} = \frac{d\ell}{\ell} - \frac{dx}{x} - \frac{dy}{y} + \frac{d\rho}{\rho} \quad (1)$$

where the first term is due to the elongation of the material, the second and third terms are due to the thinning of the material, and the last term is due to change in the specific resistivity of the material and is sometimes referred to as the electronic contribution to the piezoresistive effect. The electronic contribution has its origins in the band structure of the material and among other things is a function of the carrier mobility, carrier type, carrier concentration, temperature, etc.

Crystalline silicon is anisotropic, meaning that the elastic constants [18] and the piezoresistive coefficients [7,16] are different along the various crystal orientations. Hence, tensor notation is appropriate to express the piezoresistivity in silicon. Using tensors the change in the specific resistivity can be written as

$$\frac{d\rho_i}{\rho} = \sum_j \pi_{ij} S_j + \sum_{j,k} \pi_{ijk} S_j S_k + \sum_{j,k,l} \pi_{ijkl} S_j S_k S_l + \dots \quad (2)$$

## 8.2 Piezoresistance of c-Si

where the single suffixes replace the double suffixes of the full tensor notation and run from 1 to 6 as 1 = xx , 2 = yy , 3 = zz , 4 = yz , 5 = zx , 6 = xy . S<sub>j</sub>, S<sub>k</sub> and S<sub>l</sub> are the stress components and  $\pi_{ij}$  and  $\pi_{ijk}$  are the first and second order piezoresistive (PR) coefficients. From symmetry considerations it can be shown that for silicon (which has cubic symmetry) there are 3 first order [7], 9 second order [19] and 20 third order [20] independent nonzero piezoresistive coefficients. The first order (linear) terms which are members of a fourth rank tensor, account for about 80–90% of the total contribution due to changes in specific resistivity, while the higher order terms are used to account for the observed nonlinearity in the piezoresistance at higher strains.

Smith measured the three independent terms of the first order PR coefficients. For most strain gauge applications the linear coefficients are sufficient. Ignoring the non-linearities due to the higher order terms, the above tensor equation can be reduced to a scalar equation by choosing a specific crystal orientation and specifying that the applied stress is purely uniaxial. There are several different terms used in the literature when discussing piezoresistivity. The scalar equations provide the simplest intuitive description of the various terms. Most are related to each other through the Young's modulus of the material Y given by  $Y = S/\varepsilon$ , where S is the stress applied and  $\varepsilon = d\ell/\ell$  is the strain produced. The following list gives the definitions of, and the relationships between, some of the most common terms:

- Piezoresistivity coefficient ( $\pi$ , units = m<sup>2</sup>/N): fractional change in resistivity per unit stress.

$$\pi = \frac{\frac{d\rho}{\rho}}{S} = \frac{\frac{d\rho}{\rho}}{Y\varepsilon} \quad (3)$$

For an anisotropic material such as silicon the three independent linear PR coefficients are represented by  $\pi_{11}$  or  $\pi_L$ ,  $\pi_{12}$  or  $\pi_T$ , and  $\pi_{44}$ , where,  $\pi_{11}$  and  $\pi_{12}$  denote the fractional change in resistivity for a stress parallel to and perpendicular to the current flow respectively, while  $\pi_{44}$  represents a voltage measured perpendicular to the current flow for a shear stress. This is sometimes confusingly referred to as the piezo-Hall effect. However, it should be noted that the true Hall coefficients (which are a measure of the perpendicular voltage when there is an external magnetic field) in silicon are also piezo sensitive and the term piezo-Hall effect is more commonly used to refer to this latter phenomenon. Readers interested in the experimental and theoretical results on the piezo-Hall effects in silicon are referred to articles [29] and [30], respectively.

- Elastoresistance coefficient (m, units = dimensionless): fractional change in resistivity per unit strain.

$$m = \frac{\frac{d\rho}{\rho}}{\varepsilon} = \frac{\frac{d\rho}{\rho}}{S} Y = Y\pi \quad (4)$$

For the anisotropic case, the directional components of the elastoresistance coefficients and gauge factors are defined in a manner similar to that described earlier for the piezoresistivity coefficients.

- Gauge factor (G or K-factor, units = dimensionless): this figure of merit refers to the fractional change in resistance per unit strain. Combining the geometrical terms in EQN (1) by using Poisson's ratio  $\nu$ , we write G as:

## 8.2 Piezoresistance of *c*-Si

$$G = \frac{dR/R}{\epsilon} = \frac{dR/R}{d\ell/\ell} = 1 + 2v + \frac{dp/p}{d\ell/\ell} = 1 + 2v + m = 1 + 2v + Y\pi \quad (5)$$

For most materials the Poisson's ratio is a number between 0 and 0.5. Hence, the gauge factor change due to changes in the physical dimensions of the material alone will lie in the range of 1 to 2. In silicon the measured gauge factors range from -102 to 135, implying that the electronic piezoresistivity is the most dominant contribution to the piezoresistance in these materials. This can be seen from the gauge factors given in TABLE 1 [21–23].

TABLE 1 Gauge factors of some common materials.

Material	Gauge factor
Nichrome V	2.1
Cu	1.6
Ni	-12.62
Al	1.4
Pt	2.60
Fe	0.44
Co	0.84
Mo	0.80
Ta	1.30
W	1.16
Sn	3.34
Bi	-11.36
Si <sub>Single Crystal</sub>	-102 to 135
Si <sub>Poly-crystalline</sub>	-30 to 40
Si <sub>SOI</sub>	30 to 110

## B SINGLE CRYSTAL SILICON

The piezoresistive effect in single crystal silicon was first discovered by Smith [7] in 1954 and was later studied by many researchers [8–13].

### B1 Linear Piezoresistive Coefficients

The experimental values of the linear piezoresistive coefficients (first order piezoresistive coefficients) from Smith [7] are still widely used today and are given in TABLE 2. The elastoresistive coefficients were calculated from Smith's data [7] by using the compliance coefficients in TABLE 3 [18,24] and the formulae in TABLE 4 [25]. All coefficients in TABLE 2 refer to currents along the <110> axes, applied stress in the range 1 to 10 MPa, sample resistivities in the range 11.7 to 18.6 ohm cm for n-type and 7.8 to 22.7 ohm cm for p-type, and temperature 298 K.

## 8.2 Piezoresistance of *c*-Si

TABLE 2 Piezoresistive and elastoresistive coefficients for single crystal silicon [7].

	Piezoresistive coefficients $\times 10^{-11}$ (m <sup>2</sup> /N)			Elastoresistive coefficients (dimensionless)		
	$\pi_{11}$	$\pi_{12}$	$\pi_{44}$	$m_{11}$	$m_{12}$	$m_{44}$
n-type	-102.2	53.4	-13.6	-101.1	57.3	-10.8
p-type	6.6	-1.1	138.1	9.5	1.7	109.6

TABLE 3 Compliance and stiffness coefficients for silicon [18,24].

Compliance coefficient $\times 10^{-11}$ (m <sup>2</sup> /N)			Stiffness coefficient $\times 10^{11}$ (N/m <sup>2</sup> )		
$s_{11}$	$s_{12}$	$s_{44}$	$c_{11}$	$c_{12}$	$c_{44}$
0.768	-0.214	1.26	1.657	0.639	0.796

TABLE 4 Expressions for some common piezoresistive and elastic coefficients [18,25].

Linear piezoresistive coefficients	
$\pi_{11}$	$s_{11} m_{11} + 2s_{12} m_{12}$
$\pi_{12}$	$s_{11} m_{12} + s_{12} (m_{11} + m_{12})$
$\pi_{44}$	$s_{44} m_{44}$
Linear elastic coefficients	
Young's modulus (Y)	$1/s_{11}$
Poisson's ratio ( $\nu$ )	$-s_{12}/s_{11}$

TABLES 2 and 3 show the various coefficients related to the principal axes. For a cubic system such as silicon the matrix of 2-subscript piezoresistance coefficients, referred to the crystallographic axes, has the form shown below:

$$\left( \begin{array}{cccccc} \pi_{11} & \pi_{12} & \pi_{12} & 0 & 0 & 0 \\ \pi_{12} & \pi_{11} & \pi_{12} & 0 & 0 & 0 \\ \pi_{12} & \pi_{12} & \pi_{11} & 0 & 0 & 0 \\ 0 & 0 & 0 & \pi_{44} & 0 & 0 \\ 0 & 0 & 0 & 0 & \pi_{44} & 0 \\ 0 & 0 & 0 & 0 & 0 & \pi_{44} \end{array} \right) \quad (6)$$

However, all of the 36 coefficients may be nonzero when referred to a Cartesian system of arbitrary orientation relative to the crystallographic orientation. In a highly anisotropic material such as silicon any of the coefficients can be made large by choosing an appropriate orientation. The piezoresistance and elastic coefficients for alternative directions [12,16,18,26] can be calculated from a tensor transformation for the particular orientation. The relevant transformation from the crystal axes ( $x_i$ ) to an arbitrary coordinate system ( $x'_i$ ) is described by  $x'_i = l_{ij}x_j$ , where  $l_{ij}$  are the direction cosines of the transformation. TABLE 5 gives the calculated values for a few orientations in the  $<100>$  plane, which highlight the extreme anisotropy found in silicon.

It should be noted that the gauge factors can be either positive or negative. For example the transverse gauge factor for n-type material along the  $<110>$  direction is negative, while for p-type material it is positive for the  $<100>$  direction.

## 8.2 Piezoresistance of c-Si

TABLE 5 Extremal values of PR and elastic constants in the <100> plane.

	n-Type				p-Type			
	Maximum		Minimum		Maximum		Minimum	
	Magnitude	Direction	Magnitude	Direction	Magnitude	Direction	Magnitude	Direction
$\pi_{11} \times 10^{-11} (\text{m}^2\text{N}^{-1})$	-102.2	<100>	-31.2	<110>	71.8	<100>	6.6	<100>
$\pi_{12} \times 10^{-11} (\text{m}^2\text{N}^{-1})$	53.4	<100>	0.0 -17.6	<110> <sup>A</sup> <110>	-66.3	<110>	-1.1	<100>
$G_L^*$	-131.3	<100>	-51.6	<110>	122.4	<110>	10.2	<100>
$G_T^*$	71.1	<100>	0.0 -28.6	<110> <sup>A</sup> <110>	-110.9	<110>	0 0.125	<100> <sup>B</sup> <100>
$Y \times 10^{11} (\text{N m}^{-2})$	1.69	<110>	1.30	<100>	1.69	<110>	1.30	<100>
$v$	0.28	<100>	0.064	<110>	0.28	<100>	0.064	<110>

<sup>A</sup> Represents a direction 14.93° from the <110> direction.

\* Gauge factor calculations include the volumetric effect 1+2v.

<sup>B</sup> Represents a direction 1.09° from the <100> direction.

### B2 Impurity and Temperature Dependence of Piezoresistance

In general, the piezoresistive coefficient ( $\pi$ ) is a function of the impurity concentration (N) and temperature (T). It is a decreasing function of concentration and temperature. A simple model due to Kanda [16] predicts that the piezoresistive coefficients vary with the Fermi level in the manner described by the following two equations:

$$\begin{aligned} \pi(N, T) &= P(N, T) \times \pi(300 \text{ K}) \\ P(N, T) &= \frac{300}{T} \frac{F'_{s+1/2}(\eta)}{F_{s+1/2}(\eta)} \end{aligned} \quad (7)$$

where  $\pi(300 \text{ K})$  is the first order piezoresistive coefficient from Smith's data [7]. The doping and temperature dependence is expressed via the piezoresistance coefficient  $P(N, T)$ .  $F_r(\eta)$  is the Fermi-Dirac integral, with the prime representing the derivative of the Fermi-Dirac integral,  $\eta$  representing the Fermi energy measured from the band edge in units of  $k_B T$  and  $s$  depending on the scattering type, i.e. 3/2 for impurity scattering, -1/2 for acoustic phonon scattering and 0 for optical phonon scattering. In the present case only acoustic phonon scattering is applicable. TABLE 6 illustrates the sensitivity of the piezoresistance factor to doping concentration at 300 K. Although the above formula gives good results in n-type silicon, with p-type silicon Kanda [16] quotes a deviation of calculated values from experimental values of +13% and -21% at doping concentrations of  $5 \times 10^{18} \text{ cm}^{-3}$  and  $3 \times 10^{19} \text{ cm}^{-3}$ , respectively.

TABLE 6 Longitudinal piezoresistance factor as a function of doping concentration.

Doping concentration ( $\text{cm}^{-3}$ )	$1 \times 10^{18}$	$5 \times 10^{18}$	$1 \times 10^{19}$	$5 \times 10^{19}$	$1 \times 10^{20}$
P (n-type) (%)	98	92	85	52	34
P (p-type) (%)	95	80	66	28	20

## 8.2 Piezoresistance of c-Si

The calculation of the temperature dependence of the piezoresistive coefficients from EQN (7) is tedious, and often it is convenient to look up the temperature coefficients of piezoresistance in a table. The temperature coefficients of resistance and piezoresistance as a function of doping concentration are shown in TABLE 7 [16,27].

TABLE 7 Temperature coefficients of resistance (TCR) and piezoresistance (TCP) as a function of doping concentration.

Doping concentration ( $\text{cm}^{-3}$ )	n-Type		p-Type	
	TCR (%/K)	TCP (%/K)	TCR (%/K)	TCP (%/K)
$5 \times 10^{18}$	0.01	-0.28	0.0	-0.27
$1 \times 10^{19}$	0.05	-0.27	0.01	-0.27
$3 \times 10^{19}$	0.09	-0.19	0.06	-0.18
$1 \times 10^{20}$	0.19	-0.12	0.17	-0.16

The small temperature coefficients of the elastic constants have also been measured and are shown in TABLE 8 [28].

TABLE 8 Temperature coefficients of elastic constants [28].

TC of $c_{11}$ (%/K)	TC of $c_{12}$ (%/K)	TC of $c_{44}$ (%/K)
-0.0075	-0.0025	-0.0056

### B3 Higher Order Piezoresistive Coefficients

In the above discussion of the anisotropy, impurity doping dependence and temperature dependence of the piezoresistive coefficients we implicitly neglected the higher order terms in EQN (2). The nonlinear terms become important at higher stresses. Theoretical interpretation of the higher order terms requires a more thorough treatment which is important for calculating the characteristics of micromachined sensors. Discussions on the second order piezoresistive coefficients in n- and p-type silicon and the determination of the nine independent second order tensor components of  $\pi_{ijk}$  can be found in [25,56]. Theoretical work by Ohmura [20] on the third order piezoresistivity coefficients for p-type silicon establishes the twenty independent nonzero components of the piezoresistivity tensor in EQN (2). Experimental work on the nonlinearity in the piezoresistivity coefficients due to higher order stress terms can be found in [31]. A recent review of the theoretical work on silicon with emphasis on the calculation of the nonlinear part of the piezoresistive coefficients is given in [58].

## C POLYCRYSTALLINE SILICON

Polycrystalline silicon or polysilicon consists of small single crystal silicon grains separated by a thin amorphous grain boundary. Piezoresistivity in polysilicon has been investigated by many researchers [32–41]. In theoretical treatments the grains and grain boundary regions have been modelled as a single crystal and Schottky barrier [42–44]. The inhomogeneous structure of a polysilicon film comprising crystalline and grain boundary regions is characterized by grain size, grain orientation, doping level and annealing treatments, which have a significant effect on the piezoresistive properties of the film. Thus the piezoresistive properties of the polysilicon film depend on the growth process employed and the gauge factors can vary from -30 to 50. In a similar fashion the temperature coefficients of resistivity (TCR) and piezoresistivity (TCP) are also growth dependent. While growth dependent variations in TCR can be as large as 100% of the value in single crystal silicon, the

## *8.2 Piezoresistance of c-Si*

changes in TCP from the single crystal values are smaller (of the order of 30%). For a given film the piezoresistivity shows the same temperature and doping dependence as the single crystal silicon.

### **D SOI**

Thin piezoresistive elements are easily realized with silicon on insulator technology (SOI). For large dimensions, the piezoresistive coefficients in SOI are comparable to bulk values [23].

### **E SIZE EFFECTS**

Piezoresistive sensors are increasingly being used in sensing and control applications along with IC circuitry to fabricate micro electromechanical systems (MEMS). Several effects begin to manifest themselves as these devices are miniaturized from the micro to sub-micro to nano metre length scales. As the dimensions are shrunk the surface to volume ratio diverges and the surface contribution to electronic properties including piezoresistance begins to dominate. For example, it has been observed that the piezoresistance coefficient is reduced in deep submicron transistors [55]. Also, size reduction makes quantum effects, i.e. discreteness of electronic energy levels, more apparent. Apart from these two consequences other effects which in principle could be eliminated also arise. For example, the probability of device failure due to the presence of single crystal defects within the domain of the device would increase.

### **F THEORY AND MODELLING**

The earliest models of the piezoresistance in n- and p-type silicon have been based on the multi-valley model involving anisotropic scattering of the carriers [9,11]. According to this model the predominant contributions come from (a) the strain induced change in the relative populations of the different valleys, and (b) intervalley scattering processes where the initial and final electron states are in different valleys.

In p-type silicon additional effects arise due to the bands at  $k = 0$ . Here the bands are not parabolic and the light and heavy hole bands are degenerate. The lifting of degeneracy by the applied strain causes additional scattering due to transfer of the holes between the two bands [57]. A recent review of the theoretical work on silicon with emphasis on the calculation of both the nonlinear part of the piezoresistive coefficients as well as the anisotropic effects is given in [58].

Apart from these traditional explanations, mention should also be made of the significant theoretical progress that has been made in recent years in understanding carrier transport in doped semiconductors in terms of localization and electron-electron correlation effects [59]. Including the effects of strain in the context of these recent theories appears to have been little investigated.

Based on the extensive theoretical and experimental work done on piezoresistance in silicon several workers [60] have attempted to predict the behaviour of real devices by simulation and modelling. Such an approach is likely to prove increasingly important as devices of complex geometries capitalising on the extreme anisotropy of silicon become available.

### **G APPLICATIONS**

Piezoresistance in single crystal, SOI and polycrystalline silicon has been used in the design and fabrication of many sensing and control applications. Both active and passive sensing elements can be used, as bipolar and MOS transistors are known to be strain sensitive [47,48]. Pressure [49], angular

## 8.2 Piezoresistance of c-Si

rate [55], flow [53], position-force [50,51], optical [54] and magnetic [52] measurements and control systems are a few common applications where piezoresistance based sensors have been used.

### REFERENCES

- [1] W. Thompson [ *Trans. R. Soc. (UK)* vol.146 (1856) p.649 ]
- [2] H. Tomlinson, [ *Trans. R. Soc. (UK)* vol.174 (1883) p.1 ]
- [3] J.A. Donaldson, R. Wilson [ *Proc. R. Soc. Lond. (UK)* vol.27 (1907) p.18 ]
- [4] P.W. Bridgman [ *Proc. Am. Acad. Arts Sci. (USA)* vol.59 (1923) p.117 ]
- [5] H. Rolnick [ *Phys. Rev. (USA)* vol.36 (1930) p.506 ]
- [6] M. Allen [ *Phys. Rev. (USA)* vol.42 (1942) p.848 ]
- [7] C.S. Smith [ *Phys. Rev. (USA)* vol.94 (1954) p.42 ]
- [8] E.N. Adams [ *Phys. Rev. (USA)* vol.96 (1954) p.803 ]
- [9] C. Herring, E. Vogt [ *Phys. Rev. (USA)* vol.101 (1956) p.944 ]
- [10] W.P. Mason, R.N. Thurston [ *J. Acoust. Soc. Am. (USA)* vol.32 (1957) p.1906 ]
- [11] R.W. Keyes [ *Solid State Phys. (USA)* vol.11 (1960) p.149 ]
- [12] W.G. Pfann, R.N. Thurston [ *J. Appl. Phys. (USA)* vol.32 (1961) p.2008 ]
- [13] O.N. Tufte, E.L. Stelzer [ *J. Appl. Phys. (USA)* vol.34 (1963) p.313 ]
- [14] J. Kinoshita [ *J. Phys. Soc. Jpn. (Japan)* vol.33 (1972) p.743 ]
- [15] J.Y.W. Seto [ *J. Appl. Phys. (USA)* vol.47 (1976) p.4780 ]
- [16] Y. Kanda [ *IEEE Trans. Electron Devices (USA)* vol.ED-29 (1982) p.64 ]
- [17] P.J. French, A.G.R. Evans [ *Solid-State Electron. (UK)* vol.32 (1989) p.1 ]
- [18] J.J. Wortman, R.A. Evans [ *J. Appl. Phys. (USA)* vol.36 (1965) p.153 ]
- [19] J.T. Lenkeri [ *Phys. Status Solidi B (Germany)* vol.136 (1986) p.373 ]
- [20] Y. Ohmura [ *Jpn. J. Appl. Phys. (Japan)* vol.33 (1994) p.3314 ]
- [21] J.W. Dally, W.F. Riley [ *Experimental Stress Analysis* (McGraw-Hill, 1978) ]
- [22] G.C. Kuczynsk [ *Phys. Rev. (USA)* vol.94 (1954) p.61 ]
- [23] P.M. Zavracky, K. Warner, I. Lasic, J. Green [ *J. Micromech. Microeng. (UK)* vol.3 (1993) p.96 ]
- [24] W.P. Mason [ *Physical Acoustics and the Properties of Solids* (D. Van Norstrand Company, Inc., Princeton, New Jersey, 1958) ]
- [25] K. Matsuda, K. Suzuki, K. Yamamura, Y. Kanda [ *J. Appl. Phys. (USA)* vol.73 (1993) p.1838 ]
- [26] Y. Kanda [ *Jpn. J. Appl. Phys. (Japan)* vol.26 (1987) p.1031 ]
- [27] W.M. Bullis et al [ *Solid-State Electron. (UK)* vol.11 (1968) p.639 ]
- [28] H.J. McSkimin, W.L. Bond, E. Buckler, G.K. Teal [ *Phys. Rev. (USA)* vol.83 (1951) p.1080 ]
- [29] B. Hälg [ *J. Appl. Phys. (USA)* vol.64 (1988) p.276 ]
- [30] A. Nathan, T. Manku [ *Appl. Phys. Lett. (USA)* vol.62 (1993) p.2947 ]
- [31] K. Yamada et al [ *IEEE Trans. Electron Devices (USA)* vol.ED-29 (1982) p.71 ]
- [32] Y. Onuma, K. Sekiya [ *Jpn. J. Appl. Phys. (Japan)* vol.11 (1972) p.420 ]
- [33] J.Y.W. Seto [ *J. Appl. Phys. (USA)* vol.47 (1976) p. 4780 ]
- [34] H. Mikoshiba [ *Solid-State Electron. (UK)* vol.24 (1981) p.221 ]
- [35] W. Germer, W. Todt [ *Sens. Actuators (Switzerland)* vol.4 (1983) p. 183 ]
- [36] J.C. Erskine [ *IEEE Trans. Electron Devices (USA)* vol.ED-30 (1983) p.796 ]
- [37] P.J. French, A.G.R. Evans [ *Electron. Lett. (UK)* vol.20 (1984) p. 999 ]
- [38] J. Detry, D. Koneval, S. Blackstone [ *Proc. Transducers '85 Conf. 1985 Int. Conf. on Solid-State Sensors and Actuators*, Philadelphia, Pa, USA, 11-14 June 1985 (IEEE, New York, USA, 1985) p.278-80 ]
- [39] P.J. French, A.G.R. Evans [ *Sens. Actuators (Switzerland)* vol.15 (1988) p.257 ]
- [40] V.A. Gridchin, V.M. Lubimsky, M.P. Sarina [ *Sens. Actuators A (Switzerland)* vol. 49 (1995) p.67 ]

## 8.2 Piezoresistance of c-Si

- [41] M. Le Berre et al [ *Sens. Actuators A (Switzerland)* vol.54 (1996) p.700 ]
- [42] P.J. French, A.G.R. Evans [ *Solid-State Electron. (UK)* vol.32 (1989) p.1 ]
- [43] M.M. Mandurah, K.C. Saraswat, T.I. Kamins [ *IEEE Trans. Electron Devices (USA)* vol.ED-28 (1981) p.1163 ]
- [44] S.N. Singh, R. Kishore, P.K. Singh [ *J. Appl. Phys. (USA)* vol.57 (1985) p.2793 ]
- [45] K. Yasumura et al [ *Bull. Am. Phys. Soc. (USA)* vol.43 (1998) p.370 ]
- [46] R. Degraeve, G. Groeseneken, I. De Wolf, H.E. Maes [ *IEEE Trans. Electron Devices (USA)* vol.ED-44 (1997) p.943 ]
- [47] W. Sansen, P. Vandelooy, B. Puers [ *Sens. Actuators (Switzerland)* vol.3 (1983) p.343 ]
- [48] A.P. Dorey, T.S. Madden [ *Solid-State Electron. (UK)* vol.12 (1969) p.185 ]
- [49] B. Folkmer, P. Steiner, W. Lang [ *Sens. Actuators A (Switzerland)* vol.54 (1996) p.488 ]
- [50] S.R. Manalis, S.C. Minne, C.F. Quate [ *Appl. Phys. Lett. (USA)* vol.68 (1996) p.871 ]
- [51] W.L. Jin, C.D. Mote Jr. [ *Sens. Actuators A (Switzerland)* vol.65 (1998) p.89 ]
- [52] H. Nakane, H. Adachi, M. Walker, U. Klein [ *Transducers 97. 1997 Int. Conf. on Solid-State Sensors and Actuators*, Chicago, IL, USA, 16-19 June 1997 (IEEE, New York, 1997) p.405 ]
- [53] N. Svedin, E. Stemme, G. Stemme [ *Transducers 97. 1997 Int. Conf. on Solid-State Sensors and Actuators*, Chicago, IL, USA, 16-19 June 1997 (IEEE, New York, 1997) p.145 ]
- [54] M. Ikeda et al [ *Proc. SPIE (USA)* vol.3008 (1997) p.111 ]
- [55] R. Voss et al [ *Transducers 97. 1997 Int. Conf. Solid-State Sensors and Actuators*, Chicago, IL, USA, 16-19 June 1997 (IEEE, New York, 1997) p.879 ]
- [56] Y. Ohmura, W. Morinaga [ *Jpn. J. Appl. Phys. (Japan)* vol.35 (1996) p.L280 ]
- [57] J.A. Chroboczek, F.H. Pollack, H.F. Staunton [ *Philos. Mag. B (UK)* vol.50 (1984) p.113 ]
- [58] S. Durand, C.R. Tellier [ *J. Phys. III (France)* vol.6 (1996) p.237 ]
- [59] P.A. Lee, T.V. Ramakrishnan [ *Rev. Mod. Phys. (USA)* vol.57 (1985) p. 287 ]
- [60] Z.Z. Wang, J. Suski, D. Collard [ *Sens. Actuators A (Switzerland)* vol.47 (1996) p.628 ]

## **8.3 Electron mobility, diffusion and lifetime in c-Si**

**P.J. Mole, J.M. Rorison, J.A. del Alamo and D. Lancefield**

[ Datareviews from 'Properties of Silicon' (INSPEC, IEE, London, UK, 1988) are combined here for the reader's convenience and presented in improved format. ]

### **A ELECTRON MOBILITY IN BULK Si**

#### **A1 Introduction**

The mobility of majority carrier electrons in bulk silicon is considered over a temperature range of 200 to 400 K, where the models presented for the mobility are claimed to be accurate to about 5%. This temperature range includes that over which silicon devices are used. The mobility outside this range is also given in some of the references cited. In addition, the mobility of electrons when they are minority carriers (typical of high injection conditions) and their mobility at high electric fields are considered in separate sections.

#### **A2 Intrinsic Mobility, Temperature Dependence**

The intrinsic mobility of silicon is limited by scattering of the electrons by lattice vibrations (phonons). This gives rise to a mobility which falls rapidly as the temperature increases (as this increases the density of phonons present). Historically, the model for the mobility is based on experimental measurement of the Hall mobility [A1,A2]; subsequently [A3,A4], the measurements have been corrected for the Hall coefficient and the model presented here is for the conductivity mobility. The simplest model for the intrinsic mobility is:

$$\mu_L = \mu_o (T/T_o)^{-\alpha}$$

In [A5,A6], the parameters for the model are calculated to be  $\mu_o = 1430 - 1448 \text{ cm}^2/\text{V s}$  at  $T_o = 300 \text{ K}$  and  $\alpha = 2.20 - 2.33$ .

The simplicity of this model belies the complexity of the phonon scattering processes which contribute to the carrier scattering. In effect there will be contributions from acoustic and optic phonons via inter and intra valley scattering processes. This added complexity is rarely necessary for the analysis of silicon devices; however, details can be found in [A7,A8].

#### **A3 Effect of Lattice Strain on Mobility**

The effect of strain on mobility is notable in devices where the silicon is processed or packaged in a manner which introduces strain, for example hetero-epitaxy as is commonly used in silicon-on-sapphire devices. This is elegantly illustrated in [A9] where the Hall mobility in a silicon-on-sapphire film is measured as a function of the lattice stress (determined by Raman spectroscopy). A compressive stress of  $5 \times 10^9 \text{ dyne/cm}^2$  reduces the mobility by about 30%. This figure can only be used as a guide since the mobility in silicon-on-sapphire is also reduced by film defects and so cannot be compared directly to intrinsic silicon.

#### A4 Effect of Electrically Active Impurities on Mobility

The deliberate introduction of electrically active impurities into silicon allows the control of silicon devices. Over the temperature range of interest, it will be assumed that these impurities are fully active and therefore neutral impurity scattering will be ignored [A10]. Donors (usually phosphorus or arsenic) give up a valence electron and introduce a fixed positive electronic charge density,  $N_d$  ( $\text{cm}^{-3}$ ) into the silicon. Acceptors (usually boron) accept an electron and introduce a fixed negative electronic charge density,  $N_a$  ( $\text{cm}^{-3}$ ), into the silicon. These charge centres will introduce coulombic scattering which in the presence of a high mobile carrier density will be reduced by screening.

In [A11] the following model for the doping dependence of mobility at 300 K was introduced:

$$\mu = \mu_{\min} + \frac{\mu_o - \mu_{\min}}{1 + \left( \frac{N_d + N_a}{N_{\text{ref}}} \right)^{\alpha}}$$

Reference [A12] gives  $\mu_{\min} = 92 \text{ cm}^2/\text{V s}$ ,  $\mu_o = 1360 \text{ cm}^2/\text{V s}$ ,  $\alpha = 0.91$  and  $N_{\text{ref}} = 1.3 \times 10^{17} \text{ cm}^{-3}$  with a mean square error of 6%.

These values, however, do not allow simple prediction of mobility over a range of temperatures. In [A13] an attempt is made to introduce a temperature dependence of the mobility parameters above. However, an alternative approach is to derive an expression based on the Brooks–Herring formula for impurity scattering as in [A5,A6]. Firstly, a contribution to the scattering due to impurity scattering is introduced:

$$\mu_I = \frac{AT^{3/2}}{N_{\text{scat}}} \left[ \ln \left( 1 + \frac{BT^2}{N_{\text{car}}} \right) - \frac{BT^2}{N_{\text{car}} + BT^2} \right]^{-1}$$

The parameters are given by  $A = 4.61 \times 10^{17}/\text{cm/V/s/K}^{3/2}$

$$B = 1.52 \times 10^{15}/\text{cm}^3/\text{K}^2$$

and the distinction introduced in [A6] between the number of scattering sites introduced by the impurities ( $N_{\text{scat}} = N_d + N_a$ ) and the number of free carriers available for screening ( $N_{\text{car}} = N_d - N_a$ ) is made.

The contribution to the mobility from impurity scattering can then be combined with that from phonons using the approach of [A14] and the approximation in [A5]:

$$\mu = \mu_L f(x)$$

where  $f(x)$  can be approximated by

$$f(x) \approx \frac{1.025}{\left[ 1 + \left( \frac{x}{1.68} \right)^{1.43} \right]} - 0.025$$

and

$$x = \sqrt{6\mu_L / \mu_I}$$

At high doping levels ( $>10^{19} \text{ cm}^{-3}$ ) the above approaches still cannot account for all the effects of impurities. The presence of such a high concentration of impurity introduces several effects. Not all the electrically active impurity atoms surrender their electrons to the conduction band. This gives rise to a reduced number of charged impurity scattering sites and correspondingly increases the number of neutral scattering centres [A10]. This is most significant at the lower temperatures. The conduction band and the band of states generated by the impurities merge, complicating the band structure and leading to the dependence of the scattering on donor type. The electron gas will become degenerate and the form of the scattering will change accordingly, e.g. [A17]. At high concentrations the impurities precipitate becoming electrically inactive and provide additional scattering centres; the degree of precipitation will depend on the dopant type and the processing history (see section 13 of [A17]). In practice there is no tendency for the mobility to reach a minimum at high concentrations and a distinct dependence on dopant type is reported [A15]. This can be modelled at 300 K by [A15]:

$$\mu = \mu_o + \frac{\mu_{max} - \mu_o}{1 + (p/C_r)^\alpha} - \frac{\mu_I}{1 + (C_s/p)^\beta}$$

where  $p$  is the carrier concentration.

TABLE A1 Parameters calculated for the data measured on both arsenic and phosphorus doped samples [A15].

Parameter	Phosphorus	Arsenic	Units
$\mu_o$	68.5	52.2	$\text{cm}^2/\text{V s}$
$\mu_{max}$	1414	1417	$\text{cm}^2/\text{V s}$
$\mu_I$	56.1	43.4	$\text{cm}^2/\text{V s}$
$C_r$	$9.20 \times 10^{16}$	$9.68 \times 10^{16}$	$\text{cm}^{-3}$
$C_s$	$3.41 \times 10^{20}$	$3.41 \times 10^{20}$	$\text{cm}^{-3}$
$\alpha$	0.711	0.680	
$\beta$	1.98	2.00	

## A5 Effect of Material Quality on Mobility

There is no detailed report of variation of mobility with material preparation. It therefore seems reasonable to assume that current crystal growth techniques and epitaxial layer growth techniques do not introduce significant densities of carrier scattering defects. However current hetero-epitaxy techniques, e.g. silicon-on-sapphire [A9] and other new ‘silicon-on-alternative substrate’ growth techniques, cannot be guaranteed to reduce the carrier scattering defects to such levels. Thus the application of all the data presented here to silicon films with abnormally high defect levels must be made with care.

## A6 A More Accurate Determination of Mobility

For certain applications a more accurate knowledge of the mobility is required over a wider temperature range. The models described in [A16] are extensions to the models above which give a greater accuracy, except at high doping levels where the corrections discussed in [A15] are not included. The reader is referred directly to them.

## REFERENCES TO SECTION A

- [A1] G.L. Pearson, J. Bardeen [ *Phys. Rev. (USA)* vol.75 (1948) p.865 ]
- [A2] F.J. Morin, J.P. Maita [ *Phys. Rev. (USA)* vol.96 (1954) p.28 ]
- [A3] D. Long [ *Phys. Rev. (USA)* vol.120 (1960) p.2024 ]
- [A4] P. Norton, T. Bragginnis, H. Levinstein [ *Phys. Rev. B (USA)* vol.8 (1973) p.5632 ]
- [A5] J.M. Dorkel, Ph. Lureeq [ *Solid-State Electron. (UK)* vol.24 (1981) p.821 ]
- [A6] N.D. Arora, J.R. Hauser, D.J. Roulston [ *IEEE Trans. Electron Devices (USA)* vol.ED-29 (1982) p.292 ]
- [A7] K. Seeger [ *Semiconductor Physics* (Springer, 1973) ISBN 3-211-81186-9 ]
- [A8] C.T. Sah, P.C.H. Chan, C.K. Wang, R.L. Sah, K.A. Yamakawa, R. Lutwack [ *IEEE Trans. Electron Devices (USA)* vol.ED-28 (1981) p.304 ]
- [A9] Y. Kobayashi, M. Nakamura, T. Suzuki [ *Appl. Phys. Lett. (USA)* vol.40 no.12 (1982) p.1040-2 ]
- [A10] S.S. Li, W.R. Thurber [ *Solid-State Electron. (UK)* vol.20 no.7 (1977) p.609-16 ]
- [A11] D.M. Caughey, R.E. Thomas [ *Proc. IEEE (USA)* vol.55 (1967) p.2192 ]
- [A12] G. Baccarani, P. Ostoja [ *Solid-State Electron. (UK)* vol.18 (1975) p.579 ]
- [A13] S. Selberherr [ *Analysis and Simulation of Semiconductor Devices* (Springer, 1984) ISBN 3-211-81800-6 ]
- [A14] P.P. Debye, E.M. Conwell [ *Phys. Rev. (USA)* vol.93 (1954) p.693 ]
- [A15] G. Masetti, M. Severi, S. Solmi [ *IEEE Trans. Electron Devices (USA)* vol.ED-30 no.7 (1983) p.764-9 ]
- [A16] R.D. Larrabee, W.R. Thurber, W.M. Bullis [ *A FORTRAN Program for Calculation of the Electrical Parameters of Extrinsic Silicon* (NBS Special publ. 400-63, 1980) ]
- [A17] C. Herring, E. Vogt [ *Phys. Rev. (USA)* vol.101 (1986) p.944 ]

## B ELECTRON MOBILITY AT A (100) Si SURFACE

The reader is referred to Datareview 5.2 (p.128-30) of *Properties of Silicon* (INSPEC, IEE, London, UK, 1988). The book is out of print but a free copy of 5.2 will be supplied on application by e-mail to [jsears@iee.org.uk](mailto:jsears@iee.org.uk). It is also the intention of the publishers to make 5.2 available free on the world wide web at <http://www.iee.org.uk/publish/books/emis.html>.

## C ELECTRON MOBILITY IN 2D n-TYPE Si: THEORETICAL ASPECTS

The reader is referred to Datareview 5.3 (p.131-5) of *Properties of Silicon* (INSPEC, IEE, London, UK, 1988). The book is out of print but a free copy of 5.3 will be supplied on application by e-mail to [jsears@iee.org.uk](mailto:jsears@iee.org.uk). It is also the intention of the publishers to make 5.3 available free on the world wide web at <http://www.iee.org.uk/publish/books/emis.html>.

## D ELECTRON MOBILITY IN n-TYPE BULK Si, ELECTRIC FIELD DEPENDENCE

### D1 Introduction: The Basic Model

For extrinsic semiconductors the conduction is determined by the acceleration of the excess carriers, in the case of n-type materials electrons, and the scattering processes which arrest their motion. For n less than about  $10^{18} \text{ cm}^{-3}$  at 300 K, Maxwell-Boltzmann (non-degenerate) statistics are appropriate to describe the electrons' behaviour, while for higher carrier densities Fermi-Dirac (degenerate) statistics are needed. This reflects the transition from semiconductor to metallic-like behaviour as the doping level is increased. In the absence of an external field, either an electric field E or a

### 8.3 Electron mobility, diffusion and lifetime in c-Si

concentration gradient  $\nabla n$ , the electrons move with a random thermal velocity  $v_{th}$  which depends on their thermal energy  $\epsilon_{th}$  according to:

$$\epsilon_{th} = \frac{m^* [v_{th}]^2}{2} = \frac{3}{2} kT \quad (D1)$$

where  $m^*$  is the electron effective mass of the conduction band,  $k$  is Boltzmann's constant and  $T$  is the temperature. The effect of introducing an electric field  $E$  is to distort this velocity distribution, imparting a drift velocity  $v_d$  to this 'gas' of electrons. For linear response, valid at low field, the mobility  $\mu$  of the electrons is defined as

$$\mu = \frac{v_d}{E} \quad (D2)$$

The mobility  $\mu$  can be related to the scattering processes through the relation:

$$\mu = \frac{e\tau'}{m^*} = \frac{el'}{m^* v'} \quad (D3)$$

where  $e$  is the electron charge,  $\tau'$  and  $l'$  are the mean time and length between collisions respectively and  $v'$  is the effective velocity including field effects (heating). EQN (D2) is written in the most general form where  $\mu$  is, in general, a tensor but for cubic semiconductors it is scalar in the linear regime and is usually generalised to be a scalar outside this regime as well. This approach leads to a current defined for the electrons of

$$j_e = en\mu E \quad (D4)$$

where  $n$  is the carrier concentration.

The response of electrons to a concentration gradient is defined [D1] in terms of a diffusion coefficient  $D$  as

$$j_D = -eD\nabla n \quad (D5)$$

where  $D$  is a scalar at low  $E$  field.

At equilibrium  $\mu$  and  $D$  are connected by the Einstein relation

$$D = \frac{\mu kT}{e} \quad (D6)$$

where  $T$  is the thermal temperature.

The equation for the total current  $j$  is the sum of  $j_D$  and  $j_e$  which is known as the drift diffusion equation and is valid for low electric field with  $\mu$  and  $D$  taken as scalars. In general, both  $\mu$  and  $D$  are field dependent tensors outside the low field region, but we will only focus on the electric field dependence of  $\mu$  and  $v_d$ .

### D1.1 General results

The band structure of the material can be seen to enter into the mobility in  $m^*$  using effective mass theory which is suitable for low field. The band structure details will also be important in the evaluation of the individual scattering processes. Certain general features have been found for covalent semiconductors independent of the details of the material. These are [D1]:

- (i) The mobility goes down as the electric field increases.
- (ii) The average energy  $\langle \epsilon \rangle$  increases slowly at low field and more quickly as the field increases.
- (iii) D increases slowly with increasing field.

These results are linked to the general results that for covalent semiconductors the scattering mechanisms become more effective as the electron energy increases.

The resulting behaviour for drift velocity and mobility for silicon and n-silicon at room temperature as a function of field is [D1]:

- (i) low field:  $v_d$  is linear and  $\mu$  is a constant  $\mu_0$  (ohmic behaviour);
- (ii) warm field ( $E < 10^3$  V/cm):  $v_d$  is sub-linear due to acoustic and intervalley scattering and  $\mu$  is well described by the expression  $\mu(E) = \mu_0[1 + \beta E^2]$  where  $\beta$  is termed the warm electron coefficient;
- (iii) intermediate field ( $10^3$  V/cm  $< E$ ):  $v_d$  is increasingly sub-linear due to the increasing role of longitudinal optical phonons resulting in a decreasing  $\mu(E)$ ;
- (iv) high field ( $E > 10^4$  V/cm):  $v_d$  saturates to  $v_s$  through the dominance of longitudinal optical phonon scattering;

$$v_s \approx \sqrt{8 E_o / 3\pi m^*}$$

where  $E_o$  is the energy of the longitudinal optical phonon

$$\frac{\hbar\omega_o}{2\pi}$$

- (v) very high field ( $E > 10^5$  V/cm): is characterised by rapid carrier heating and breakdown.

This gradual increase to velocity saturation for silicon is in sharp contrast to gallium arsenide where intervalley effects produce negative differential mobility (NDM). In addition, the lower  $m^*$  of gallium arsenide results in a higher velocity for low field than in silicon. For high n-type silicon  $v_d$  is always lower for the same electric field compared with pure silicon. It saturates at a higher field and to a lower  $v_s$  which decreases with  $n$  as shown in Jacoboni et al [D2].

### D2 Modelling Electron Transport

Simple empirical or semi-empirical treatments for electron velocity or mobility as a function of  $E$ ,  $T$  and  $n$  in bulk semiconductors are useful for device simulation. For n-type silicon simple modelling of  $\mu(E)$  by parametrising or analysing  $\beta$  [D3–D8] are reasonably successful.

A very commonly used empirical expression for  $v_d$  as a function of  $E$  and  $n$  for  $T = 300$  K is the Scharfetter and Gummel expression [D9]

$$v_d = \frac{\mu_o E}{\left[ 1 + \frac{N}{\frac{N_{ref}}{S} + N_{ref}} + \frac{(E/A)^2}{(E/A + F)} + \left(\frac{E}{B}\right)^2 \right]^{\frac{1}{2}}}$$

where  $\mu_o = 1400 \text{ cm}^2/\text{V s}$ ,  $N_{ref} = 3 \times 10^{16} \text{ cm}^{-3}$ ,  $S = 350$ ,  $A = 3.5 \times 10^3 \text{ V/cm}$ ,  $F = 8.8$  and  $B = 7.4 \times 10^3 \text{ V/cm}$ .

To attain more understanding of the physics of electron transport it is usual to go to a semi-classical approach in which the electron is treated classically within a Boltzmann equation formalism while the scattering events are treated quantum mechanically. This approach only yields analytical results usually employing a heated Maxwellian distribution [D1] for very simple models. Numerical methods, chiefly Monte Carlo simulation techniques [D1,D2,D10,D11], have been used to derive results. This approach simulates the path of an electron through many scattering events in a probabilistic approach and results in a mean energy  $\langle \epsilon \rangle$  and mean velocity  $\langle v_d \rangle$ . It is also possible to derive a distribution function from this approach.

## D2.1 Scattering processes

Detailed understanding of the scattering processes involved are needed for this approach. Scattering can occur from phonon deformation of the lattice (deformation potential interaction) or from the electrostatic field set up by these phonons (piezoelectric interaction). It is important to distinguish the difference between these two types of scattering as the latter type will be screened very efficiently by electrons for n-type systems reducing their effect. The screening due to electrons denoted as  $\epsilon_{ee}(q,\omega)$  is both wavevector ( $q$ ) and frequency ( $\omega$ ) dependent [D12] although a static approximation  $\omega = 0$  or a long wavelength approach  $q = 0$  is often made. The role of electrons in screening scattering processes and also in relaxing the distribution function towards a Maxwellian form is an area under investigation [D13].

The scattering processes are derived independently of the electric field and are usually divided into intravalley and intervalley scattering. The important scattering processes for n-silicon are: intravalley acoustic deformation potential scattering, intervalley phonon scattering, ionised impurity scattering\*, neutral impurity scattering\* and electron-electron scattering\*. (Those marked with \* will be screened efficiently by the electrons.) These processes are dealt with in detail in [D1] in terms of the physics and derivation of the scattering matrix elements. Values of these parameters are given in [D2]. Good agreement of theory and experiment can be derived through analysis of the details of the scattering processes when the anisotropy and anharmonicity of the band structure of silicon are included [D2].

At room temperature and low electric field the acoustic deformation potential and intervalley phonon scattering are the most important scattering mechanisms. Whilst acoustic phonon scattering is well understood the identification of the type of phonons involved in intervalley phonon scattering has been the subject of much work [D14,D15] and is still unresolved.

At low temperatures and low fields ionised impurity scattering becomes an important scattering mechanism and reduces  $\mu$ . Impurity scattering can be treated within the Brooks-Herring or Conwell-Weiskoff formalisms which have been reconciled by Ridley [D16]. The effect of  $n$  on  $\mu$  as a function of  $T$  for low  $T$  is given in Jacoboni et al [D2]. At room temperature if  $n > 10^{16} \text{ cm}^{-3}$  impurity scattering again becomes significant [D2]. The temperature dependence of the mobility at low  $T$

### 8.3 Electron mobility, diffusion and lifetime in c-Si

( $T < 50$  K) is due to acoustic phonons while at higher  $T$  ( $T > 50$  K) intervalley phonon scattering becomes important. A room temperature  $\mu(T)$  behaviour of  $T^{-2.42}$  is found empirically which deviates from the  $T^{-1.50}$  behaviour expected for purely acoustic phonon scattering [D2].

For higher fields there is a deviation from Ohm's law which occurs at lower fields as  $T$  decreases which makes  $v_d(E)$  become sub-linear. In addition, for higher fields ( $E > 10$  V/cm at 8 K,  $E > 10^2$  V/cm at 77 K,  $E > 2 \times 10^3$  V/cm at 300 K [D2])  $v_d$  exhibits anisotropy behaviour with respect to the orientation of the electric field on the crystal. The anisotropy is due to a repopulation of the valleys [D17]. When  $E$  is parallel to  $<111>$  the six valleys are equally orientated with respect to  $E$  but for  $E$  parallel to  $<100>$  two valleys exhibit  $m_l^*$  in the direction of the field while the remaining four exhibit  $m_t^*$  where  $m_t^* < m_l^*$ . Electrons in transverse valleys therefore have a higher mobility and are heated to a greater extent by the field and transfer electrons to the colder and slower valleys. The net result is a lower  $v_d$  for  $E$  parallel to  $<100>$ . The effect becomes stronger as the temperature falls since relaxation effects are less effective at low  $T$ . For  $T < 45$  K negative differential mobility (NDM) occurs for  $20$  V/cm  $< E < 60$  V/cm. For the high field limit the anisotropy disappears. Experimental results of  $v_d(E,T)$  are given in [D2]. The role of optical phonon (deformation potential) scattering becomes important as the field increases and results in the saturation of the velocity of the electrons. Detailed theories show that the other scattering processes also contribute to  $v_s$  and that band non-parabolicity is also important. For  $T < 45$  K,  $v_s = 1.3 - 1.4 \times 10^7$  cm/s independent of  $T$  [D2]. For higher  $T$ ,  $v_s(T)$  decreases steadily as  $T$  increases and at room temperature  $v_s \sim 1 \times 10^7$  cm/s [D2]. In general the mobility of electrons in bulk silicon is well understood as a function of electric field, temperature and impurity content.

### D3 Experimental Comparisons

Experimental measurements of  $v_d$  and  $D$  result from conductivity measurements, microwave techniques and time of flight techniques [D1,D2]. Conductivity methods have been used since the 1950s and are based on measurement of the current density which flows through a sample of extrinsic semiconductor when the current is as in EQN (D3). By knowing the carrier concentration (Hall effect)  $v_d$  can be determined. Microwave techniques can be applied in two ways; either the electrons are heated by a pulsed  $E$  field and their mobility is determined by measurement of the attenuation of a low microwave field or the charge carriers are heated by a large pulsed microwave field and their mobility is determined with the aid of a low DC electric field. The former method is useful in the determination of the energy relaxation time. Time of flight techniques involve measurement of the drift velocity which is a variation of the Hayes and Shockley experiment. The measurement of  $v_s$  can be achieved by analysis of one carrier injection current under space charge limited conditions at high field. A detailed comparison of experimental results for  $v_d$  as a function of  $E$  for electrons at 77 K and 300 K using the different experimental techniques is given in Jacoboni et al [D2].

### REFERENCES TO SECTION D

- [D1] C. Jacoboni, L. Reggiani [ *Adv. Phys. (UK)* vol.28 no.4 (1979) p.493-553 ]
- [D2] C. Jacoboni, C. Canali, G. Ottaviani, A. Alberigi Quaranta [ *Solid-State Electron. (UK)* vol.20 (1977) p.77 ]
- [D3] C. Canali, G. Majni, R. Minder, G. Ottaviani [ *Electron. Lett. (UK)* vol.10 no.24 (1974) p.523-4 ]
- [D4] C. Canali, G. Majni, R. Minder, G. Ottaviani [ *IEEE Trans. Electron Devices (USA)* vol.ED-22 no.11 (1975) p.1045-7 ]
- [D5] G. Bosman, R.J.J. Zijlstra, F. Nava [ *Solid-State Electron. (UK)* vol.24 no.1 (1981) p.5-9 ]
- [D6] N. Ahmad, V.K. Arora [ *IEEE Trans. Electron Devices (USA)* vol.ED-33 no.7 (1986) p.1075-7 ]

### 8.3 Electron mobility, diffusion and lifetime in c-Si

- [D7] S.A. Schwarz, S.E. Russek [ *IEEE Trans. Electron Devices (USA)* vol.ED-30 no.12 (1983) p.1629-33 ]
- [D8] S.A. Schwarz, S.E. Russek [ *IEEE Trans. Electron Devices (USA)* vol.ED-30 no.12 (1983) p.1634-9 ]
- [D9] D.L. Scharfetter, H.K. Gummel [ *IEEE Trans. Electron Devices (USA)* vol.ED-16 (1969) p.64 ]
- [D10] P.J. Price [ *Semicond. Semimet. (USA)* vol.14 (1979) ch.4 p.249-308 ]
- [D11] C. Jacoboni, L. Reggiani [ *Rev. Mod. Phys. (USA)* vol.55 (1983) p.645 ]
- [D12] J.M. Rorison, D.C. Herbert [ *J. Phys. C (UK)* vol.19 no.21 (1986) p.3991-4010 ]
- [D13] P. Lugli, D.K. Ferry [ *Physica B & C (Netherlands)* vol.129 no.1-3 (1985) p.532-6 ]
- [D14] M.H. Jorgensen, N.O. Gram, N.I. Meyer [ *Solid State Commun. (USA)* vol.10 (1972) p.337 ]
- [D15] J.G. Nash, J.W. Holm-Kennedy [ *Appl. Phys. Lett. (USA)* vol.24 no.3 (1974) p.139-41 ]
- [D16] B.K. Ridley [ *J. Phys. C (UK)* vol.10 (1977) p.1589 ]
- [D17] W. Sasaki, M. Shibuya, K. Mizouguchi, G.M. Hatoyama [ *J. Phys. Chem. Solids (UK)* vol.8 (1959) p.250 ]

## E ELECTRON MOBILITY IN n-TYPE EPITAXIAL Si

Electron mobilities in epitaxially grown n-type Si have to be compared with mobilities measured in bulk doped as-grown Si [E1]. These bulk mobilities are, within experimental error, identical to those obtained in ion-implanted or diffused layers up to solid solubility values [E2]. A small dependence on the dopant species is observed for doping levels higher than about  $1 \times 10^{19} \text{ cm}^{-3}$ .

A word of caution is required when comparing reported mobility data. Mobility is usually measured using the Hall technique. The result of this measurement is the Hall mobility which is related to the conductivity mobility (the parameter of most interest in device applications) through the Hall factor. Systematic measurements of the Hall factor have been carried out for phosphorus-doped Si [E3]. In spite of it not actually being the case [E3], most authors assume a Hall factor of unity or, in other words, they assume that the Hall and conductivity mobilities are identical. This review will therefore address Hall mobilities measured in epitaxial layers grown by various techniques.

- (a) Vapour Phase Epitaxy (VPE). Systematic measurements of electron mobility in P-doped Si grown in an  $\text{H}_2/\text{SiH}_4/\text{PH}_3$  gas system at  $1050^\circ\text{C}$  have been reported in the doping range of  $2.5 \times 10^{17}$  to  $1.6 \times 10^{20} \text{ cm}^{-3}$  [E4,E5]. At all doping levels electron mobilities within 4% of the Si bulk values were obtained.
- (b) Low Pressure Vapour Phase Epitaxy (LPVPE). LPVPE-growth of P-doped Si using the  $\text{H}_2/\text{SiCl}_2\text{H}_2/\text{PH}_3$  gas system in the temperature range  $785 - 933^\circ\text{C}$  have been reported [E6,E7]. The maximum doping level is  $5 \times 10^{18} \text{ cm}^{-3}$ . Mobilities identical to bulk Si values have been measured down to  $823^\circ\text{C}$ . Unintentionally doped n-type layers at the  $1 \times 10^{16} \text{ cm}^{-3}$  level show mobilities of about 90% of the bulk values.
- (c) Molecular Beam Epitaxy (MBE). MBE growth of P-, As-, and Sb-doped Si has been extensively studied. In P-doped Si, doping levels up to  $1.5 \times 10^{19} \text{ cm}^{-3}$  have been obtained [E8]. Within the experimental error, the mobility is identical to that of bulk Si at 300 K and 77 K. In As-doped Si, mobility values have been reported for doping levels up to  $8 \times 10^{19} \text{ cm}^{-3}$  [E9]. The best values in [E9] and those of other authors at lower doping levels [E8] are essentially identical to bulk values. Sb-doped Si layers have been grown with doping levels up to  $1 \times 10^{20} \text{ cm}^{-3}$  [E10]. Again identical results to those for bulk Si were obtained [E8,E10,E11].

## REFERENCES TO SECTION E

- [E1] W.R. Thurber, R.L. Mattis, Y.M. Liu, J.J. Filliben [ *J. Electrochem. Soc. (USA)* vol.127 no.8 (1980) p.1807-12 ]
- [E2] G. Masetti, M. Severi, S. Solmi [ *IEEE Trans. Electron Devices (USA)* vol.ED-30 no.7 (1983) p.764-9 ]
- [E3] J.A. del Alamo, R.M. Swanson [ *J. Appl. Phys. (USA)* vol.57 no.6 (1985) p.2314-7 ]
- [E4] J.A. del Alamo, R.M. Swanson [ *J. Appl. Phys. (USA)* vol.56 no.8 (1984) p.2250-2 ]; Erratum in [ *J. Appl. Phys. (USA)* vol.57 no.6 (1985) p.2346 ]
- [E5] J.A. del Alamo, R.M. Swanson [ *J. Electrochem. Soc. (USA)* vol.132 no.12 (1985) p.3011-6 ]
- [E6] L. Vescan, H. Beneking, O. Meyer [ *Mater. Res. Soc. Symp. Proc. (USA)* vol.71 (1986) p.133-8 ]
- [E7] L. Vescan, U. Breuer, Ch. Werres, H. Beneking [ *Proc. Int. Symp. on Trends and New Applications in Thin Films* Strasbourg, France, 10-13 March 1987, p.217-21 ]
- [E8] R.A.A. Kubiak, S.M. Newstead, W.Y. Leong, R. Houghton, E.H.C. Parker, T.E. Whall [ *Appl. Phys. A (Germany)* vol.42 no.3 (1987) p.197-200 ]
- [E9] T. Sugiyama, T. Itoh [ *J. Electrochem. Soc. (USA)* vol.133 no.3 (1986) p.604-9 ]
- [E10] Y. Shiraki [ *Prog. Cryst. Growth Charact. (UK)* vol.21 no.1-4 (1986) p.45-66 ]
- [E11] R.A.A. Kubiak, W.Y. Leong, E.H.C. Parker [ *J. Electrochem. Soc. (USA)* vol.132 no.11 (1985) p.2738-42 ]

## F ELECTRON MOBILITY IN Si, PRESSURE DEPENDENCE

The mobility of electrons in silicon is found to increase with increasing hydrostatic pressure at room temperature. For a sample with  $n = 10^{16} \text{ cm}^{-3}$ ,  $\mu = 1000 \text{ cm}^2/\text{V s}$  and  $\frac{\partial(\ln \mu)}{\partial P} = 2.5 \times 10^{-3}/\text{kbar}$  [F1].

This is in contrast to Ge and the direct gap III-V semiconductors where the mobility generally decreases with increasing pressure because of the dominant effect of the pressure dependence of the electron effective mass [F2].

From a consideration of the band structure of silicon, and its pressure dependence, the pressure dependence of the density of states effective mass is predicted to be small, i.e.  $\frac{\partial(\ln m^*)}{\partial P}$  up to  $3 \times 10^{-4}/\text{kbar}$ , compared to Ge where it is predicted to be almost an order of magnitude larger. Consequently, at room temperature where intervalley phonon scattering is dominant it is the pressure induced increase in the phonon energies, causing a reduction in the phonon population, that causes the mobility to increase.

## REFERENCES TO SECTION F

- [F1] D. Lancefield [ PhD Thesis, University of Surrey, Guildford, Surrey, UK (1985) ]
- [F2] D. Lancefield, A.R. Adams, M.A. Fisher [ *J. Appl. Phys. (USA)* vol.62 (1987) p.2342 ]

## G MINORITY CARRIER ELECTRON MOBILITY IN p-TYPE Si

The reader is referred to Datareview 5.7 (p.145-6) of *Properties of Silicon* (INSPEC, IEE, London, UK, 1988). The book is out of print but a free copy of 5.7 will be supplied on application by e-mail to [jsears@iee.org.uk](mailto:jsears@iee.org.uk). It is also the intention of the publishers to make 5.7 available free on the world wide web at <http://www.iee.org.uk/publish/books/emis.html>.

## H MINORITY CARRIER ELECTRON DIFFUSION LENGTH IN p-TYPE Si

The electron diffusion length in p-type silicon,  $L_e$ , is related to the electron lifetime,  $\tau_e$ , and the electron mobility,  $\mu_e$ , through the equation:

$$L_e = \sqrt{\left(\frac{kT}{q}\right) \mu_e \tau_e} \quad (H1)$$

where  $k$  is the Boltzmann constant,  $T$  is the absolute temperature and  $q$  is the electron charge. The electron diffusion length can therefore be computed at any doping level using the available experimental data for  $\mu_e$  and  $\tau_e$  given in Sections G and I.

In lightly doped unprocessed p-type Si grown by the float-zone technique, electron diffusion lengths as high as 3000 microns have been measured [H1]. In Czochralski-grown Si, and after processing,  $L_e$  is usually much smaller than the above value due to the sensitivity of  $\tau_e$  to contaminants and crystal defects.

As the acceptor concentration increases beyond about  $1 \times 10^{16} \text{ cm}^{-3}$ ,  $L_e$  starts to decrease. In comparison to n-type silicon, systematic measurements of  $L_e$  as a function of  $N_a$  in p-type silicon are very scarce [H2]. An approximate fit to the measurements of [H2] for doping levels over  $1 \times 10^{18} \text{ cm}^{-3}$  is

$$L_e = (7.13 \times 10^{14}) N_a^{-0.923} \text{ cm} \quad (H2)$$

with  $N_a$  in  $\text{cm}^{-3}$ . Because the material used in [H2] was unprocessed, to compare EQN (H2) with the data collected in Sections G and I, the linear term of EQN (I1) in Section I should be dropped. Even in this case the agreement is no better than about a factor of 3 in the  $10^{18} - 10^{20} \text{ cm}^{-3}$  regime. More measurements are certainly needed in this range.

No temperature dependent measurements of  $L_e$  are known to this author.

## REFERENCES TO SECTION H

- [H1] D. Huber, A. Bachmeier, R. Wahlich, H. Herzer [ *Proc. Conf. Semiconductor Silicon 1986* Eds H.R. Huff, T. Abe, B. Kobessen (Electrochemical Society, USA, 1986) p.1022-32 ]
- [H2] L. Passari, E. Susi [ *J. Appl. Phys. (USA)* vol.54 no.7 (1983) p.3935-7 ]

## I MINORITY CARRIER ELECTRON LIFETIME IN p-TYPE Si

In high purity p-type silicon, the electron lifetime  $\tau_e$  is independent of the acceptor concentration but is sensitive to other impurities (like O, Fe or C), the degree of crystal perfection (stacking faults, dislocation loops, point defects), and the cleanliness and thermal history of the fabrication procedures. The highest reported values of electron lifetime in unprocessed p-type silicon fabricated by the float-zone technique are of the order of 20 ms [I1]. These high lifetimes were also found to be insensitive to gettering techniques that usually improve the lifetime of lower quality material. The data presented in [I1] may then constitute a fundamental upper limit for electrons, restricted by an intrinsic defect like a vacancy.

### 8.3 Electron mobility, diffusion and lifetime in c-Si

Beyond an acceptor impurity concentration of about  $1 \times 10^{17} \text{ cm}^{-3}$  the electron lifetime begins to decrease as the acceptor density,  $N_a$ , increases. The rate of decrease also increases with doping level. Time decay measurements of  $\tau_e$  in as-grown Czochralski [I2,I3] and epitaxially grown and processed silicon [I4] have yielded different results in the moderate doping regime. In the latter, a fit to the obtained data valid for  $N_a > 1 \times 10^{17} \text{ cm}^{-3}$  is [I4]:

$$\frac{1}{\tau_e} = [(3.45 \times 10^{-12} N_a) + (9.5 \times 10^{-32} N_a^2)] \text{ s}^{-1} \quad (\text{I1})$$

with  $N_a$  in  $\text{cm}^{-3}$ .

In unprocessed Czochralski-grown silicon only the quadratic term in EQN (I1) is required to acceptably fit the experimental data in this doping regime. The value of the constant is, however, essentially identical to the one given in EQN (I1). The Auger coefficient in heavily doped p-type silicon appears then to be  $C_{ae} = 9.5 \times 10^{-32} \text{ cm}^6/\text{s}$ .

The temperature dependence of the electron lifetime in lightly doped p-type silicon around room temperature has been explained by invoking a Shockley–Read–Hall recombination mechanism. The energy position above the valence band of the trap responsible appears to change with doping from 45 meV [I5] to 180 meV [I6]. In intentionally Au-contaminated moderately doped ( $N_a = 2 \times 10^{17} \text{ cm}^{-3}$ ) Si,  $\tau_e$  was observed to depend quadratically on the absolute temperature [I7]. In the heavily-doped regime, the Auger coefficient  $C_{ae}$  increases with temperature from a value of  $7.8 \times 10^{-32} \text{ cm}^6/\text{s}$  at 77 K to  $1.2 \times 10^{-31} \text{ cm}^6/\text{s}$  at 400 K [I3].

In highly excited Si (when both the hole and electron concentrations are equal and exceed the background doping level), lifetimes of 40 ms have recently been measured [I8]. Measurements of the sum of the hole and electron Auger coefficients,  $C_{ah} + C_{ae}$ , have also been carried out in this regime. By comparing data (at room temperature) from a number of authors (see TABLE II),  $C_{ah} + C_{ae}$  is found to decrease as the carrier concentration increases. The value at the highest carrier concentrations [I9,I11] is close to the sum of  $C_{ah}$  and  $C_{ae}$  of heavily doped n- and p-type silicon ( $2.75 \times 10^{-31} \text{ cm}^6/\text{s}$ ).

TABLE II Sum of Auger coefficients in highly injected Si.

Ref	$n$ ( $\text{cm}^{-3}$ )	$C_{ae} + C_{ah}$ ( $\text{cm}^6/\text{s}$ )
Yablonovitch & Gmitter [I8]	$4 \times 10^{16}$	$2 \times 10^{-30}$
Sinton & Swanson [I10]	$6 \times 10^{16}$	$1.7 \times 10^{-30}$
Svantesson & Nilsson [I11]	$2.5 \times 10^{18}$	$3.4 \times 10^{-31}$
Fauchet & Nighan [I9]	$3 \times 10^{20}$	$2 \times 10^{-31}$

This highly excited Auger coefficient was found by Svantesson and Nilsson [I12] to be approximately proportional to  $T^{0.6}$  in the temperature interval 195 – 372 K.

## REFERENCES TO SECTION I

- [I1] D. Huber, A. Bachmeier, R. Wahlich, H. Herzer [ *Proc. Conf. Semiconductor Silicon 1986* Eds H.R. Huff, T. Abe, B. Kobesssen (Electrochemical Society, USA, 1986) p.1022-32 ]
- [I2] J.D. Beck, R. Conradt [ *Solid State Commun. (USA)* vol.13 no.1 (1973) p.93-5 ]
- [I3] J. Dziewior, W. Schmid [ *Appl. Phys. Lett. (USA)* vol.31 no.5 (1977) p.346-8 ]

- [I4] S.E. Swirhun, Y.-H. Kwark, R.M. Swanson [ *Proc. Int. Electron Device Meeting* Los Angeles, CA, USA, December 1986 (IEEE, USA, 1986) p.24-7 ]
- [I5] A. Ohsawa, K. Honda, R. Takizawa, N. Toyokura [ *Rev. Sci. Instrum. (USA)* vol.54 no.2 (1983) p.210-2 ]
- [I6] P.C. Mathur, R.P. Sharma, P. Saxena, J.D. Arora [ *J. Appl. Phys. (USA)* vol.52 no.5 (1981) p.3651-4 ]
- [I7] W. Schmid, J. Reiner [ *J. Appl. Phys. (USA)* vol.53 no.9 (1982) p.6250-2 ]
- [I8] E. Yablonovitch, T. Gmitter [ *Appl. Phys. Lett. (USA)* vol.49 no.10 (1986) p.587-9 ]
- [I9] P.M. Fauchet, W.L. Nighan Jr. [ *Appl. Phys. Lett. (USA)* vol.48 no.11 (1986) p.721-3 ]
- [I10] R. Sinton, R.M. Swanson [ *IEEE Trans. Electron Devices (USA)* vol.ED-34 no.6 (1987) p.1380-9 ]
- [I11] K.G. Svantesson, N.G. Nilsson [ *Solid-State Electron. (UK)* vol.21 no.11-12 (1978) p.1603-8 ]
- [I12] K.G. Svantesson, N.G. Nilsson [ *J. Phys. C (UK)* vol.12 no.18 (1979) p.5111-20 ]

## CHAPTER 9

### IMPURITIES IN SILICON (*Edited by S.J. Pearson*)

- 9.1 Diffusion of O in c-Si
- 9.2 Segregation coefficient of O in c-Si
- 9.3 Solubility of O in c-Si
- 9.4 O-related IR absorption in c-Si
- 9.5 Precipitation, segregation and IR absorption of O in c-Si
- 9.6 Segregation coefficient, solubility and IR absorption of C in c-Si
- 9.7 Diffusion of C in c-Si
- 9.8 Hydrogen diffusion and solubility in c-Si
- 9.9 Hydrogen-containing point defects in c-Si
- 9.10 Nitrogen in c-Si
- 9.11 Solubility and diffusion of transition metal impurities in c-Si
- 9.12 Deep levels of transition metal impurities in c-Si
- 9.13 Electronic states of chalcogen-related donors in c-Si
- 9.14 Properties of rare-earth doped c-Si
- 9.15 Alkali impurities (Na, K, Li) in c-Si

## 9.1 Diffusion of O in c-Si

B. Pajot

March 1998

### A INTRODUCTION

The diffusion of a foreign element in a crystal is the thermally activated motion of an entity involving this element, from which a distribution profile obtained at a given temperature can be fitted to a simple Arrhenius law of the form:

$$D(T) = D_0 \exp(-E_{\text{diff}}(K)/T) \text{ cm}^2 \text{s}^{-1} \quad (1)$$

In silicon, the isolated forms of oxygen are:

- 1) interstitial oxygen ( $O_i$ ), an O atom bonded to two nearest neighbour (NN) Si atoms in a near bond-centre location,
- 2) the oxygen-vacancy centre (OV), where a missing NN of O allows re-bonding to a next nearest neighbour (NNN) Si atom. It is produced by irradiation with high-energy particles.

Below the melting point, as-grown Czochralski (CZ) silicon is supersaturated with  $O_i$ . The bond-centre location of  $O_i$  increases the distance between the two NN Si atoms from 0.236 to ~0.32 nm, resulting in an expansion of the lattice in the  $\langle 111 \rangle$  directions. Thus, precipitation of  $\text{SiO}_2$  reduces the  $O_i$  concentration and allows some lattice relaxation. Points to remember are that diffusion of  $O_i$  is already detected near 400°C and that an O atom can form complexes with defects, dopants, foreign atoms and, presumably, with another O atom.

The diffusion coefficient  $D_{\text{oxy}}$  of O in silicon has been measured by different methods and a good account of this complex subject is given in the review by Newman and Jones [1]. Many diffusion results can be understood by assuming as an elementary step the thermally assisted jump of an O atom between two adjacent bond-centred sites. The substantial increase of the diffusion coefficient measured in some determinations in the 450–650°C region has been explained by postulating the existence of an oxygen dimer diffusing more rapidly than  $O_i$ . Finally, it is now well established that the presence of hydrogen in silicon can enhance the diffusion coefficient of O by factors which can reach two orders of magnitude. A summary of these points is presented below.

### B NORMAL DIFFUSION

$D_{\text{oxy}}$  can be measured at high temperature from the O profiles after diffusion or out diffusion of O between 700 and 1200°C [2–4] and from the dependence on temperature of the absorption of a fixed ultrasonic frequency in CZ samples. In the latter case, an increase of the absorption is observed near 1030°C, at resonance with the jump frequency of an O atom between two equivalent locations in the crystal [5,6]. The values obtained match reasonably with low-temperature results (~300–450°C) obtained from the annealing of the stress-induced dichroism of the 9 μm absorption band of  $O_i$ , due also to a jump of  $O_i$  between two equivalent sites [7,8].

TABLE 1 gives a summary of the values of the parameters  $D_0$  and  $E_{\text{diff}}$  of EQN (1), obtained by different methods, which give reasonably comparable results. Note the consistency of the results on standard CZ material based on the determination of reorientation of the O atom, but also significant

### 9.1 Diffusion of O in c-Si

differences using the same method (diffusion of  $^{18}\text{O}$  in FZ silicon) with different detection methods. The formation of O precipitates reduces the O concentration able to out diffuse and also the diffusivity, as reported by Shimura et al [9] for 64 hr at a temperature of 1000°C. This clearly shows that the results obtained from profiles implying the diffusion of  $\text{O}_i$  have to be considered carefully.

TABLE 1 Values of the pre-exponential factor and of the activation energy for the diffusion of O in silicon determined by different techniques.

$D_0 (\text{cm}^2 \text{s}^{-1})$	$E_{\text{diff}} (\text{K})$ $10^4$	Method	Ref
0.23	2.97	Annealing of stress-induced dichroism (IR)	[7]
0.17	2.95	"	[8]
0.21	2.96	Internal friction	[5,6]
0.14	2.95	Out diffusion profile (SIMS)	[4]
0.07	2.83	Diffusion of $^{18}\text{O}$ in FZ silicon (SIMS)	[2]
22.6	3.66	" (nuclear detection)	[3]
0.091	2.8	O-induced lattice strain (X-rays)	[10]
0.11	2.91	IR (dichroism), SANS and IR (LHeT)	[11]
0.033	2.82	Growth kinetics of platelets	[12]

Mikkelsen [13] and Newman and Jones [1] have drawn very similar composite plots of different experimental determinations of  $D_{\text{oxy}}$  vs  $T^{-1}$  giving for the so-called 'normal' diffusion coefficient:

$$D_{\text{oxy}} = 0.13 \exp(-2.94 \times 10^4 (K/T)) \text{ cm}^2 \text{s}^{-1}$$

or an activation energy  $E_{\text{diff}}$  of 2.53 eV.

Indirect determinations of  $D_{\text{oxy}}$  are based on an evaluation of the effect of temperature on the size and concentration of the O precipitates, plus some assumptions on their composition, assuming that  $\text{O}_i$  diffusion is the limiting process to the growth rate of the precipitates. For  $T > 650^\circ\text{C}$ , the modelling of the data still yields the 'normal' value of  $D_{\text{oxy}}$ . Below 650°C, information on the precipitates comes from high-resolution transmission electron microscopy (TEM). The need to invoke an enhancement of  $D_{\text{oxy}}$  by a factor of  $\sim 10^4$  at 485°C by Bergholz et al [14] to explain the growth of coesite precipitates was removed when these precipitates were re-ascribed to other materials, but the explanation of the results is not definitive [1]. The extrapolation of the high-temperature data on the average number of O atoms/precipitate to 450°C predicts that 2  $\text{O}_i$  should coalesce to form an O dimer. This dimer is usually labelled  $\text{O}_2$  and this is unfortunate because if it exists, it is very probably not an oxygen molecule. Determinations of  $D_{\text{oxy}}$  from a measurement of  $\text{O}_i$  loss near 500°C, based on a model of  $\text{O}_2$  formation, give values  $\sim 5$  times lower than 'normal'  $D_{\text{oxy}}$  [15]. The formation of 450°C thermal donors (TDs) is one consequence of  $\text{O}_i$  diffusion between  $\sim 380$  and 500°C and these TDs are known to incorporate small O clusters [16].  $D_{\text{oxy}}$  has been obtained from high-temperature O diffusion profiles measured electrically after generation of TDs by an additional annealing at 450°C, using a calibration between [TD] and [ $\text{O}_i$ ] [17]. The production of O precipitates during the cooling-down from the diffusion step cannot be excluded [9] while the TDs are produced only from  $\text{O}_i$  so that values obtained using this kind of detection of O must be taken with care. Moreover, as will be seen later, the diffusion of  $\text{O}_i$  at low temperature and the TD generation can be enhanced [18] so that even a reliable detection of  $\text{O}_i$  present at high temperature from the production of TDs at 450°C seems to be questionable.

## C ENHANCED DIFFUSION

### C1 Effect of Intrinsic Defects

Loss of stress-induced dichroism of  $O_i$  in pre-stressed silicon is observed after room temperature electron-irradiation while it occurs near 300°C in un-irradiated silicon [19]. This difference, first attributed to radiation-enhanced diffusion of  $O_i$ , is now explained by a two-step process: first, the capture of a vacancy (V) by  $O_i$  (creation of OV) with internal reorientation of the O atom at room temperature, followed by the recombination of OV with an interstitial Si atom ( $Si_i$ ), leaving  $O_i$  with an orientation different from the initial one. This radiation-induced jump does not contribute to O diffusion, but produces a loss of the stress-induced dichroism. There seems to be no evidence of a role of  $Si_i$  on  $D_{oxy}$  [1].

### C2 The Oxygen Dimer

This  $O_2$  dimer has already been mentioned above. Its existence is also predicted from theoretical analyses [1]. Rapid diffusion of di-oxygen ‘molecules’ was proposed by Gösele and Tan [20] to explain by a combination of two di-oxygens the rate of formation of TDs, found by Kaiser et al [21] to be proportional to  $[O_i]^4$ , at a time when TDs were thought to have a core made of four O atoms. The existence of this dimer was also invoked by Gösele et al [22] to explain the rapid out diffusion of  $^{16}O$  from CZ silicon heated in the range 500–650°C and implying enhancement of  $D_{oxy}$  by factors of up to  $10^4$ , as reported by Lee et al [23,24]. Similar rapid out diffusion of O at 450°C implying comparable enhancement of  $D_{oxy}$  was also reported by Gaworzewski and Ritter [18] and as a rule, it seems that the values of  $D_{oxy}$  deduced from the out diffusion measurements in the low-temperature domain are much larger than the normal value of  $D_{oxy}$ . No satisfactory explanation of this has been given yet.

### C3 Effect of Carbon

From the comparison of the out diffusion profiles of O in CZ silicon with low C (LC) and high C (HC) contents by Shimura [9] at 750 and 1000°C, it seems that ‘normal’  $D_{oxy}$  is valid at 1000°C for LC and HC and at 750°C for LC, but that at 750°C the diffusion coefficient of O in HC is higher by a factor of about 3 than the ‘normal’ value. This last point can be related to a higher diffusivity of the  $O_iC_i$  complexes formed in HC.

### C4 Effect of Hydrogen

The presence in CZ silicon of hydrogen introduced by heating at high temperature in an  $H_2$  or  $D_2$  atmosphere and quenching or by heating in a hydrogen plasma enhances the TD production rate [25,26] and the loss rate of stress-induced dichroism [27] in a reproducible way. The H-induced enhancement of  $D_{oxy}$  between 250 and 400°C deduced from the TD production rate can be quantified [1] as:

$$D_{oxy}(enh) = 2.3 \times 10^{-6} \exp(-2.0 \times 10^4(K)/T) \text{ cm}^2\text{s}^{-1}$$

The value of  $2.0 \times 10^4$  K (1.7 eV) for  $E_{diff}(enh)$  is somewhat lower than the one ( $2.3 \times 10^4$  K or 2.0 eV) deduced from the loss of stress-induced dichroism. The presence or the introduction in CZ silicon of transition metals such as Ni, Fe or Cu has been pointed out as a source for the enhancement of  $D_{oxy}$  [28], but in these experiments, H was also introduced with the metals. Thus, it is very likely that the effect observed was due to H [1].

## D CONCLUSION

Diffusion coefficients of O in silicon have been determined using different modellings of the diffusion mechanisms and of the aggregation of O. Direct methods have allowed us to establish a ‘normal’ value of  $D_{oxy}$ , but they have also shown that  $D_{oxy}$  could be enhanced by external factors. More assumptions had to be made with indirect methods, but their use has generally provided the ‘normal’ value of  $D_{oxy}$  in the high-temperature region. Indirect determinations in the low-temperature region have produced values of  $D_{oxy}$  enhanced with respect to the ‘normal’ value. They are explained by the presence of fast-diffusing species like the O dimer, whose existence is also predicted from several calculations (evidence of the existence of two close O<sub>i</sub> atoms, which could act as a dimer, has recently been provided [29]). It has been also shown that the diffusion of O at low-temperature was enhanced by the presence of H and theoretical modelling has been of great help in understanding the underlying mechanism. The complete understanding of the diffusion of O at low-temperature is, however, interwoven with that of a microscopic description of the formation and dissociation kinetics of the TDs and there are many unanswered questions remaining.

## REFERENCES

- [1] R.C. Newman, R. Jones [ *Semicond. Semimet.* vol.42 (Academic Press, San Diego, 1994) p.289-352 ]
- [2] J.C. Mikkelsen Jr. [ *Appl. Phys. Lett. (USA)* vol.40 (1982) p.336 ]
- [3] J. Gass, H.H. Muller, H. Stussi, S. Schweitzer [ *J. Appl. Phys. (USA)* vol.51 (1980) p.2030 ]
- [4] S.-T. Lee, D. Nichols [ *Appl. Phys. Lett. (USA)* vol.47 (1985) p.1001 ]
- [5] C. Hass [ *J. Phys. Chem. Solids (UK)* vol.15 (1960) p.108 ]
- [6] P.D. Southgate [ *Proc. Phys. Soc. Lond. (UK)* vol.36 (1960) p.385 ]
- [7] G.D. Watkins, J.W. Corbett, R.S. McDonald [ *J. Appl. Phys. (USA)* vol.53 (1982) p.7097 ]
- [8] M. Stavola, J.R. Patel, L.C. Kimerling, P.E. Freedland [ *Appl. Phys. Lett. (USA)* vol.42 (1983) p.73 ]
- [9] F. Shimura, T. Higuchi, R.S. Hockett [ *Appl. Phys. Lett (USA)* vol.53 (1988) p.69 ]
- [10] Y. Takano, M. Maki [ *Electrochem. Soc. Proc. Vol. (USA)* vol.PV-73 (1973) p.469 ]
- [11] F.M. Livingston et al [ *J. Phys. C, Solid State Phys. (UK)* vol.17 (1984) p.6253 ]
- [12] K. Wada, N. Inoue [ *J. Cryst. Growth (Netherlands)* vol.71 (1985) p.111 ]
- [13] J.C. Mikkelsen Jr. [ *Mater. Res. Soc. Symp. Proc. (USA)* vol.59 (1986 p.19 ]
- [14] W. Bergholz, J.L. Hutchison, P. Pirouz [ *J. Appl. Phys. (USA)* vol.58 (1985) p.3419 ]
- [15] S.A. McQuaid, M.J. Binns, C.A. Londos, J.H. Tucker, A.R. Brown, R.C. Newman [ *J. Appl. Phys (USA)* vol.77 (1995) p.1427 ]
- [16] J. Michel, J.R. Niklas, J.M. Spaeth [ *Phys. Rev. B (USA)* vol.40 (1989) p.1732 ]
- [17] R.A. Logan, A.J. Peters [ *J. Appl. Phys (USA)* vol.30 (1959) p.1627 ]
- [18] P. Gaworowski, G. Ritter [ *Phys. Status Solidi A (Germany)* vol.67 (1981) p.511 ]
- [19] R.C Newman, J.H. Tucker, F.M. Livingston [ *J. Phys. C, Solid State Phys. (UK)* vol.16 (1983) p.L151 ]
- [20] U. Gösele, T.Y. Tan [ *Appl. Phys. A (Germany)* vol.28 (1982) p.79 ]
- [21] W. Kaiser, H.L. Frisch, H. Reiss [ *Phys. Rev. (USA)* vol.112 (1958) p.1546 ]
- [22] U. Gösele, K.Y. Ahn, B.P.R. Marioton, T.Y. Tan, S.-T. Lee [ *Appl. Phys. A (Germany)* vol.48 (1989) p.219 ]
- [23] S.-T. Lee, P. Fellinger [ *Appl. Phys. Lett. (USA)* vol.49 (1986) p.1793 ]
- [24] S.-T. Lee, P. Fellinger, S. Chen [ *J. Appl. Phys. (USA)* vol.63 (1988) p.1924 ]
- [25] C.S. Fuller, R.A. Logan [ *J. Appl. Phys. (USA)* vol.28 (1957) p.1427 ]
- [26] R.C. Newman, J.H. Tucker, A.R. Brown, S.A. McQuaid [ *J. Appl. Phys. (USA)* vol.70 p.3061 ]

### *9.1 Diffusion of O in c-Si*

- [27] S.A. McQuaid, R.C. Newman, J.H. Tucker, E.C. Lightowers, A. Kubiak, M. Goulding [ *Appl. Phys. Lett. (USA)* vol.58 (1991) p.2933 ]
- [28] A.K. Tipping, R.C. Newman, D.C. Newton, J.H. Tucker [ *Mater. Sci Forum (Switzerland)* vol.10-12 (1986) p.887 ]
- [29] L.I. Murin, T. Hallberg, V.P. Markevich, J.L. Lindström [ *Phys. Rev. Lett (USA)* vol.80 (1998) p.93 ]

## 9.2 Segregation coefficient of O in c-Si

B. Pajot

April 1997

### A INTRODUCTION

The equilibrium segregation coefficient  $k_0$  of a solute in a substance is the ratio of its equilibrium concentration  $C_{0s}/C_{0l}$  in the solid and the liquid near the liquid/solid interface. In the growth of silicon crystals from the melt by the Czochralski (CZ) method, the concentration  $C_s(x)$  along the crystal axis of usual group III and group V dopants added to the melt follows the normal freezing law modelled by Pfann [1]:

$$C_s(x) = C_i k (1 - x)^{1-k} \quad (1)$$

where  $C_i$  is the initial dopant concentration in the melt and  $x$  the fraction of the melt solidified. As pointed out by Lin [2] the strong thermal convection in the silicon melt and small growth rates ensure that the measured segregation coefficient  $k$  for these dopants is usually the equilibrium value, except for elements with a high vapour pressure like Sb. For larger growth rates and for dopants with  $k_0 < 1$ , the value of the segregation coefficient has been found to increase. This is due to the large dopant concentration in the liquid near the solidification front, resulting from the segregation in the solid phase, which cannot readjust instantly to the equilibrium value. It has indeed been shown [3] that an effective segregation coefficient  $k_{eff}$  larger than  $k_0$  could be derived from the diffusion boundary layer thickness  $\zeta$ , the growth rate  $f$  and the diffusion coefficient  $D_t$  of the dopant in the melt as:

$$k_{eff} = k_0 (k_0 + (1 - k_0) \exp(-\zeta f / D_t))^{-1} \quad (2)$$

The thickness of the boundary layer can be expressed in terms of  $D_t$ , the kinematic viscosity of the melt  $v$  and the crystal rotation rate  $\omega$  as:

$$\zeta = 1.6 D_t^{1/3} v^{1/6} \omega^{-1/2} \quad (3)$$

and it shows that when the term in the exponent of EQN (2) increases from zero,  $k_{eff}$  gradually changes from  $k_0 (<1)$  to a limiting value near unity. This demonstrates the role of the growth conditions on the measured values of the segregation coefficient. By contrast, for  $k_0 = 1$ , no change of  $k$  with the growth rate is expected.

The situation for O is different from that for the shallow dopants: molten silicon continuously dissolves the silica of the crucible at a typical rate of 10  $\mu\text{m/h}$  [4]. Part of the oxygen produced evaporates from the melt as  $\text{SiO}$  but, as a result of the balance between thermal and forced convective, it is also transported near the liquid/solid interface, where it is incorporated into the crystal as interstitial oxygen ( $O_i$ ). It thus follows from the way O is introduced in the melt that its axial distribution in the crystal does not follow EQN (1). The actual O distribution and concentration in the melt depend mainly on the relative directions and rates of the rotations of the crucible and of the crystal and on the evaporation of  $\text{SiO}$  from the melt.

The segregation coefficient of oxygen in silicon is usually measured by determining the  $O_i$  concentration in the crystal and in the quenched melt or in crystals obtained under different growth

## 9.2 Segregation coefficient of O in c-Si

conditions. Other methods have also been described by Barraclough [5]. The O<sub>i</sub> concentration is usually obtained from the room temperature absorption coefficient of the 9 μm infra-red (IR) band of the CZ silicon crystal. Silica precipitates may be present in the crystal for very high oxygen concentrations. They can alter the measurement as they show absorption in the same 9 μm region as the O<sub>i</sub> band, but the presence of these bands can be easily recognised. An alternative in that case is to measure a weak absorption band of O<sub>i</sub> at 5.81 μm or 1720 cm<sup>-1</sup> in wavenumber, which is free of interference with the absorption of the precipitates. Within ±3%, there is now a world-wide agreement on the value of the factor to convert the absorption coefficient of the 9 μm band into an O<sub>i</sub> concentration [6], but the actual value of this factor has no effect on the value of the O segregation coefficient when the method used requires only the determination of the ratios of the O<sub>i</sub> concentrations in the frozen melt and in the crystal. Secondary ion mass spectroscopy (SIMS) using an O-implanted sample as a reference and charged-particle activation analysis have also been used to measure O concentrations. Unlike the IR method, these two latter methods measure the overall O concentration whatever the configuration of O in the crystal.

## B VALUES OF THE SEGREGATION COEFFICIENT

The first evaluations of k(ox) were made between 1955 and 1960: a value <1 is suggested from the tentative eutectic Si-O phase diagram given by Sosman [7], but in their seminal paper on O in silicon, Kaiser and Keck [8] noted that the O<sub>i</sub> content along a CZ crystal did not change when the growth rate was abruptly changed. From this fact, these authors concluded that the segregation coefficient was of the order of unity. A value of k(ox) near 0.5 was reported by Trumbore [9], determined by vacuum fusion analysis on quenched silicon samples melted in a silica tube. The next attempt was reported in 1973 and the values of k(ox) measured from that time are summarised in TABLE 1. They vary between 0.25 and 1.4 with a clustering near unity.

The most significant result of Harada et al [10] was obtained under growth conditions where the normal freezing law of EQN (1) should be verified (encapsulation of the melt preventing the evaporation of SiO and the supply of O and no rotation of the crystal). No variation of [O] with the fraction solidified was observed, indicating a value of k<sub>0</sub>(ox) near unity. The origin of the longitudinal oxygen striations observed with changes in the growth rate was ascribed by Lin and Hill [11] to a segregation coefficient of O less than unity (0.3). Barraclough [5] has re-ascribed these striations to the result of O concentration changes in the melt originating from temperature fluctuations during the changes of the growth rate. Series and Barraclough [12] have reported that in a somewhat similar experiment, where the temperature of the melt was kept constant, no O striations were observed, indicating a segregation coefficient of unity. This seems to be in agreement with the thermodynamic calculations of Carlberg [13], which predict a value of k(ox) slightly less than unity.

## C CONCLUSION

The most recent determinations of k(ox) give a value very close to unity while the Si/SO phase diagram construction gives a value slightly less than unity, but this latter value is qualitative. It has been pointed out that a value of k(ox) strictly equal to unity would correspond to the merging of the liquidus and solidus regions in the phase diagram, a situation not consistent with the phase rule [2]. However, in the absence of an accurate determination of the deviation of k(ox) from unity, a value of k(ox) equal to one should be recommended.

## 9.2 Segregation coefficient of O in c-Si

TABLE 1 Values of the segregation coefficient  $k_{\text{ox}}$  of O in silicon determined by different techniques.

$k_{\text{ox}}$	Method	Techniques	Remarks and ref	Year
$1.2 \pm 0.2$	Analysis of liquid and solid solubilities of O by freezing of a molten zone	CPAA and IR absorption	FZ material in an $\text{O}_2$ atmosphere [14]	1973
$1.4 \pm 0.3$	"	"	" [15]	1974
$>1$	Analysis of the growth rate dependence on the swirl distribution and $\text{O}_i$ microsegregation	Interface demarcation IR absorption Spreading resistance X-ray topography	CZ crystals with diameters of 20 and 75 mm [16]	1979
$\sim 0.3$	Analysis of the $\text{O}_i$ axial distribution for different pulling rates using EQN (2)	IR absorption	CZ crystals with diameters small compared to that of the crucible [10]	1983
$\sim 0.25$	Analysis of the effect of the growth rate on the axial striation pattern	Local IR absorption with $\text{CO}_2$ laser Spreading resistance	" [17]	1985
1	Comparison of the $\text{O}_i$ and P axial distributions	SIMS calibrated by IR and CPAA Spreading resistance	Si melt fully encapsulated by the crystal (no $\text{SiO}$ loss) [10]	1985
1	Comparison of the O and P distributions on facets	"	"	"
1	Comparison of the O and Sb distribution across twin boundary	"	"	"
1	Comparison of the O and P distribution across growth striations	"	"	"
slightly <1	Si,O phase diagram calculated from thermodynamic data		[13]	1986
$1 \pm 0.1$	Analysis of the O axial distribution for different growth rates		Melt temperature kept constant. Sb-doped [12]	1987

## REFERENCES

- [1] W.G. Pfann [ *Zone Melting* (John Wiley & Son, New York, 1965) ]
- [2] W. Lin [ in *Semicond. Semimet. (USA)* vol.42 (1994) p.9-52 ]
- [3] J.A. Burton, R.C. Prim, W.P. Slichter [ *J. Chem. Phys. (USA)* vol.21 (1953) p.1987 ]
- [4] A. Seidl, R. Marten, G. Müller [ *J. Electrochem. Soc. (USA)* vol.141 (1994) p.2564 ]
- [5] K.G. Barracough [ in *Properties of Crystalline Si, 1<sup>st</sup> Edition.* (INSPEC, IEE, London, UK, 1988) p.291 ]
- [6] B. Pajot [ Datareview in this book: 9.4 O-related IR absorption in c-Si ]
- [7] R.B. Sosman [ *Trans. J. Br. Ceram. Soc. (UK)* vol.54 (1955) p.655 ]
- [8] W. Kaiser, P.H. Keck [ *J. Appl. Phys. (USA)* vol.28 (1957) p.882 ]
- [9] F.A. Trumbore [ *Bell Syst. Tech. J. (USA)* vol.39 (1960) p.205 ]
- [10] H. Harada, T. Itoh, N. Ozawa, T. Abe [ *Proc. 3rd Int. Symp. VLSI Sci. & Technol.* Toronto, Ont., Canada, 13-16 May 1985, Eds. W.M. Bullis, S. Broyda (Electrochem. Soc., Pennington, NJ, USA 1985) p.526 ]
- [11] W. Lin, D. W. Hill [ *J. Appl. Phys. (USA)* vol.54 (1983) p.1082 ]

## 9.2 Segregation coefficient of O in c-Si

- [12] R.W. Series, K.C. Barraclough [ *Extended Abst. Electrochem. Soc. Fall Meeting 1987* Honolulu, Hawaii, 18-23 October 1987 (Electrochem. Soc., Pennington, NJ, USA 1987) ]
- [13] T. Carlberg [ *J. Electrochem. Soc. (USA)* vol.139 (1986) p.1940 ]
- [14] Y. Yatsurugi, N. Akiyama, Y. Endo, T. Nozaki [ *J. Electrochem. Soc. (USA)* vol.120 (1973) p.975 ]
- [15] T. Nozaki, Y. Yatsurugi, N. Akiyama, Y. Endo, Y. Makide [ *J. Radioanal. Chem. (Switzerland)* vol.19 (1974) p.109 ]
- [16] A. Murgai, H.C. Gatos, W.A. Westdorp [ *J. Electrochem. Soc. (USA)* vol.126 (1979) p.2240 ]
- [17] W. Lin, M. Stavola [ *J. Electrochem. Soc. (USA)* vol.132 (1985) p.1412 ]

## 9.3 Solubility of O in c-Si

B. Pajot

April 1997

### A INTRODUCTION

In the Czochralski (CZ) growth, O is introduced in molten silicon from the dissociation of silica from the crucible. It can also be introduced during float-zoned (FZ) growth when O-bearing gases are used, or by solid state diffusion.

The measurement of a solubility is that of a maximum concentration of isolated O in liquid or solid silicon under equilibrium with silicon oxides at a given temperature. Direct measurements of the O concentration in molten silicon contained in a silica crucible have recently been made using an electrochemical O sensor [1,2]. Common methods used to derive an O concentration are applicable only for the solid state. They are:

- Charged particle activation analysis (CPAA)
- Secondary ion mass spectroscopy (SIMS)
- Gas fusion analysis (GFA)
- Infrared (IR) absorption

CPAA, SIMS and GFA allow the determination of the overall O concentration. IR absorption is used to measure the concentration of interstitial oxygen atoms bonded to two nearest neighbour Si atoms ( $O_i$ ). The IR method is based on the fact that the normal cooling rate of CZ silicon is too fast for noticeable precipitation of silicon oxides to occur so that metastable  $O_i$  concentrations comparable to the ones near the melting point (1413°C) are measured. The  $O_i$  concentration is determined from the room temperature absorption coefficient of an  $O_i$  vibration–rotation band at 9.04  $\mu\text{m}$  using a suitable calibration factor. Within  $\pm 3\%$ , there is now a world-wide agreement on a value of  $3.1 \times 10^{17} \text{ cm}^{-2}$  for this factor [3]. Silica precipitates may be present in the crystal for very high oxygen concentrations or after some annealing treatments. They can alter the measurement as they show absorption in the same spectral region as the  $O_i$  band. An alternative in that case is to measure the absorption near liquid helium temperature (LHeT) [4]. Another one is to measure at room temperature a weak absorption band of  $O_i$  at 5.81  $\mu\text{m}$  or  $1720 \text{ cm}^{-1}$  in wavenumber, which is free of interference with the absorption of the precipitates [5]. Another method for  $O_i$  determination is to measure, by an X-ray technique, the average lattice expansion due to the presence of  $O_i$  in the crystal [6]. The lattice expansion coefficient  $\beta$  can be expressed in terms of the increase  $\Delta a_0$  of the lattice constant due to an increase  $\Delta N$  of the concentration of a foreign atom as  $\Delta a_0/(a_0 \Delta N)$ . For  $O_i$ , a reliable value of  $\beta$  is  $(4.4 \pm 0.2) \times 10^{-24} \text{ cm}^3$  [7].

### B LIQUID SOLUBILITY

A determination of the liquid solubility from thermodynamic calculations has been made by Carlberg [8]. It is based on an experimental value of the standard free-energy of solution of oxygen in liquid silicon in equilibrium with  $\text{SiO}_2$ . The solubility is thermally activated and can be expressed as  $[O_{\text{eq}}]_{\text{liq}} = 1.3 \times 10^{24} \exp(-22370(\text{K})/\text{T}) \text{ cm}^{-3}$ . The value at the melting point is found to be  $2.1 \times 10^{18} \text{ cm}^{-3}$  and the activation energy 2.0 eV. Ekhult and Carlberg [9] have also shown the importance of the Si/SiO equilibrium in melts with a lower O content. Comparable results have been obtained experimentally by GFA of quenched melts contained in a silica tube by Hirata and

### 9.3 Solubility of O in c-Si

Hoshikawa [10], who derived  $[O_{eq}]_{liq} = 4.0 \times 10^{23} \exp(-2.0 \times 10^4(K)/T) \text{ cm}^{-3}$ . Huang et al [11] used GFA and SIMS to evaluate the O concentration in samples very similar to those of [8]. The main difference in their results is a much weaker temperature dependence of the solubility (if any). A value of the solubility in the melt near the melting point between  $2$  and  $3 \times 10^{18} \text{ cm}^{-3}$  seems a reasonable estimation.

The absolute values of the O concentrations obtained by direct measurements in a melt contained in a regular CZ crucible with an electrochemical O sensor [1] are larger than expected by about a factor of three. These values are very probably related to the method used, but the method gives significant evidence of an O concentration gradient related to the rotation of the crucible and to the O source (the concentration is larger near to the walls of the crucible than near to the centre). The existence of an O concentration gradient due to the rotation of the crucible is confirmed by IR determination of the radial distribution of O in different frozen melts by Togawa et al [12].

## C SOLID SOLUBILITY

As-grown or as-quenched CZ silicon is oversaturated with O<sub>i</sub> at room temperature and the concentration measured is a good evaluation of the concentration near to the melting point. A reasonable order of magnitude of the solid solubility at the melting point can already be derived from the results of the quenched melt experiments in sealed quartz tubes indicating O<sub>i</sub> concentrations in the vicinity of  $2 \times 10^{18} \text{ cm}^{-3}$ . This figure has also been obtained from the construction of the Si-O phase diagram in the Si-rich region by Carlberg [8]. The O<sub>i</sub> concentration in CZ materials depends strongly on the growth parameters and it is generally less than the equilibrium solubility at the melting point. Precise adjustment of the growth parameters allows production of CZ silicon crystals with fairly uniform and controlled O concentrations. A review by Lin [13] on the incorporation of O shows that if usual growth parameters allow production of O<sub>i</sub> concentrations between about  $5$  and  $12 \times 10^{17} \text{ cm}^{-3}$ , O<sub>i</sub> concentrations near to the solubility limit have been found in crystals grown with large crucible rotation rates ( $\sim 30$  rpm) or by applying a vertical magnetic field to the melt. The solubility is expected to decrease with temperature. Its measurement requires a physical situation where thermal equilibrium is reached at a given temperature. This has been typically done by annealing a CZ material at a given temperature to produce internal precipitation of silicon oxides or by making O diffuse at a given temperature in silicon with an initial low O<sub>i</sub> content, e.g. FZ silicon. The thermally activated solubility is expressed as:

$$[O_{eq}]_{sol} = C_{so} \exp(-E_s(K)/T) \text{ cm}^{-3} \quad (1)$$

where C<sub>so</sub> is a constant related to the entropy of solution and E<sub>s</sub> the heat of solid solution in Kelvin ( $E_s(\text{eV}) = 8.617 \times 10^{-5} E_s(\text{K})$ ). A summary of the results is presented in TABLE 1.

Part of the spreading of the experimental results has been analysed by Wilkes [22] as due to a combination of different factors including:

1. The difficulty in discriminating between the IR signatures of O<sub>i</sub> and of the precipitates.
2. Contamination of the samples.
3. Measurements performed while equilibrium was not reached.
4. Different IR calibration factors.

In 1986, Mikkelsen [23] proposed a composite solubility curve yielding a heat of solution of 1.52 eV by bringing together experimental data from different origins. It corresponds to:

$$[O_{eq}]_{sol} = 9.0 \times 10^{22} \exp(-1.76 \times 10^4(K)/T) \text{ cm}^{-3} \quad (2)$$

### 9.3 Solubility of O in c-Si

To obtain this expression, the data using IR measurements were replotted using a common IR calibration factor ( $3.03 \times 10^{17} \text{ cm}^{-2}$ ) very close to the one recommended above. Thus, EQN (2) is recommended for the solubility of O in silicon, with a domain of validity between the silicon melting point and about 850°C. For these limits, the solubilities derived from EQN (2) are  $2.58 \times 10^{18}$  and  $1.36 \times 10^{16} \text{ cm}^{-3}$ , respectively. Between 850 and 700°C, the apparent solubility versus  $T^{-1}$  shows a flattening and Newman [24] even reports an increase of the solubility below 700°C to about  $10^{17} \text{ cm}^{-3}$  near 500°C. This is due to the combined increase of the concentration of oxide precipitates and to a decrease of their sizes and this must be considered as a pseudo-equilibrium situation.

TABLE 1 Summary of data relating to O solid solubility.  $E_s$  should be multiplied by  $8.617 \times 10^{-5}$  to read in eV.

$E_s$ $10^4 \text{ (K)}$	$C_s$ $10^{22} \text{ (cm}^{-3}\text{)}$	Temp. range (°C)	Method	Detection	Ref
1.09	0.12	1000–1250	O precipitation	IR (LHeT)	[14]
2.67	18	1250–1400	Thermal donors	Spreading resistance	[15]
1.82	12	1100–1200	O precipitation	IR (77 K)	[16]
1.39	0.82	"	O diffusion	X-rays	[6]
1.15	0.19	780–1100	O precipitation	IR (77 and 300 K)	[17]
1.24	0.28	1000–1280	O diffusion	CPAA	[18]
1.20	0.2		O precipitation in neutron-irradiated silicon	IR (300 K)	[19]
1.18	0.064	600–1240	O diffusion	SIMS and IR (300 K)	[20]
1.39	0.71	650–1050	O precipitation	IR (LHeT and 300 K)	[4]
1.40	0.95	1000–1375	O diffusion	CPAA	[21]
2.54	740	near 1413	O-Si phase diagram	-	[8]
1.62	2.6	850–1200	Composite from [4], [16] and [20]	-	[4]

A decrease of the O solubility in n<sup>+</sup> Sb-doped CZ silicon has been reported [25]. Possible reasons are: 1) a reduction of the O solubility in the melt due to antimony, 2) an increase of the O evaporation through Sb-containing oxides and 3) a decrease of the segregation of O. The measurements by Huang et al [11] of the O concentration in frozen melts containing increasing Sb concentrations show that for [Sb] < 1% at, the O solubility is unchanged, but when [Sb] increases, the O solubility increases to reach about  $10^{19} \text{ cm}^{-3}$  for [Sb] near 2% at. These results seem to rule out the first assumption.

## D CONCLUSION

A composite value of the O solubility in solid silicon  $[O_{eq}]_{sol}$  at the melting point is  $2.6 \times 10^{18} \text{ cm}^{-3}$ , but in most CZ crystals, the maximum  $[O_i]$  measured in as-grown CZ silicon is  $1.2\text{--}1.4 \times 10^{18} \text{ cm}^{-3}$  with a small concentration of precipitated [O] and TDs. Values near or slightly above the solubility limit have been found only in some ‘magnetic’ crystals [13], and this means that for most other CZ materials, the solubility limit is not reached. The above value of  $[O_{eq}]_{sol}$  agrees acceptably with the value of  $2.0 \times 10^{18} \text{ cm}^{-3}$  obtained from a determination of the Si/SiO<sub>2</sub> phase diagram.

## REFERENCES

- [1] A. Seidl, R. Marten, G. Müller [ *J. Electrochem. Soc. (USA)* vol.141 (1994) p.2564 ]
- [2] K.-W. Yi et al [ *J. Electrochem. Soc. (USA)* vol.143 (1996) p.722 ]
- [3] W.M. Bullis [ in *Semicond. Semimet. (USA)* vol.42 (1994) p.95-152 ]

### 9.3 Solubility of O in c-Si

- [4] F.M. Livingston et al [ *J. Phys. C (UK)* vol.17 (1984) p.6253 ]
- [5] Y. Kitagawara, H. Kubota, M. Tamatsuka, T. Takenaka, K. Takamizawa [ US Patent no. 5,368,118 (1995) ]
- [6] Y. Takano, M. Maki [ *Semiconductor Silicon 1973; Proc. Electrochem. Soc. (USA)* vol.PV-73 (1973) p.469 ]
- [7] D. Windisch, P. Becker [ *Phys. Status Solidi A (Germany)* vol.118 (1990) p.379 ]
- [8] T. Carlberg [ *J. Electrochem. Soc. (USA)* vol.136 (1989) p.1940 ]
- [9] U. Ekhult, T. Carlberg [ *J. Electrochem. Soc. (USA)* vol.133 (1986) p.551 ]
- [10] H. Hirata, K. Hoshikawa [ *J. Cryst. Growth (Netherlands)* vol.106 (1990) p.657 ]
- [11] X. Huang et al. [ *Jpn. J. Appl. Phys. (Japan)* vol.32 (1993) p.3671 ]
- [12] S. Togawa, Y. Shiraishi, K. Terashima, S. Kimura. [ *J. Electrochem. Soc. (USA)* vol.142 (1995) p.2839 ]
- [13] W. Lin [ in *Semicond. Semimet. (USA)* vol.42 (1994) p.9-52 ]
- [14] H.J. Hrostowski, W. Kaiser [ *J. Phys. Chem. Solids (UK)* vol.9 (1959) p.214 ]
- [15] R.A. Logan, A.J. Peters [ *J. Appl. Phys. (USA)* vol.30 (1959) p.1627 ]
- [16] A.R. Bean, R.C. Newman [ *J. Phys. Chem. Solids (UK)* vol.32 (1971) p.1211 ]
- [17] K. Tempelhoff, F. Spiegelberg, R. Gleichmann [ *Semiconductor Silicon 1977; Proc. Electrochem. Soc. (USA)* vol.PV 77-2 (1977) p.585 ]
- [18] J. Gass, H.H. Müller, H. Stussi, S. Schweitzer [ *J. Appl. Phys. (USA)* vol.51 (1980) p.2030 ]
- [19] R.A. Craven [ *Semiconductor Silicon 1981; Proc. Electrochem. Soc. (USA)* vol.PV 81-5 (1981) p.254 ]
- [20] J.C. Mikkelsen Jr. [ *Appl. Phys. Lett. (USA)* vol.40 (1982) p.336 ]
- [21] Y. Itoh, T. Nozaki [ *Jpn. J. Appl. Phys. (Japan)* vol.279 (1985) p.279 ]
- [22] J.G. Wilkes [ in *Properties of Crystalline Si, 1<sup>st</sup> Edition* EMIS Datareviews Series no. 4 (INSPEC, IEE, London, UK, 1988) p.300 ]
- [23] J.C. Mikkelsen [ *Mater. Res. Soc. Symp. Proc. (USA)* vol.59 (1986) p.19 ]
- [24] R.C. Newman [ in *Materials Modelling: From Theory to Technology* (IOP Publishing, Bristol, 1992) p.309 ]
- [25] K.G. Barraclough [ *J. Cryst. Growth (Netherlands)* vol.99 (1990) p.654 ]

## 9.4 O-related IR absorption in c-Si

B. Pajot

March 1998

### A INTRODUCTION

Oxygen is present in all silicon crystals, either pulled from a melt contained in a  $\text{SiO}_2$  crucible (Czochralski or CZ silicon) or grown by the float-zone (FZ) method. With the latter method, the O concentration is typically  $10^{15} \text{ cm}^{-3}$  or 20 ppba, compared to about  $10^{18} \text{ cm}^{-3}$  in most CZ crystals. At room temperature, as-grown CZ crystals are supersaturated with isolated oxygen ( $\text{O}_i$ ) which is the dominant form, but due to the reactivity of oxygen, complexes of O with some foreign atoms are also found. Irradiation of silicon with energetic particles or photons also produces complexes between oxygen and lattice defects and foreign atoms. O-related electrically active thermal donors (TDs) are produced by annealing CZ silicon from approximately 400 to 550°C. Various forms of O precipitates are formed by annealing, the morphology and composition depending mainly on the annealing temperature. Above 1100°C, the precipitates begin to dissolve when the solubility of oxygen becomes comparable with the  $\text{O}_i$  concentration in the material.

Vibrational absorption due to  $\text{O}_i$ , O-related complexes and defects and silica precipitates are observed in the mid IR. Low-temperature electronic absorption due to TDs can also be observed in the same spectral region and at lower frequencies, depending on the location of the Fermi level. The creation of localised excitons bound to O-related complexes can also be produced by IR absorption in the near IR and their annihilation detected by photoluminescence (PL). Detailed presentations of the different topics mentioned below can be found in [1].

### B INTERSTITIAL OXYGEN

$\text{O}_i$  is an O atom nearly bond-centred between two nearest neighbour (NN) Si atoms and chemically bonded to these atoms. The most recent calculations agree with an extreme excursion of O giving a Si–O–Si bond angle of near 160°, but they show that the probability of the presence of the O atom is maximum at the bond centre [2]. A broad absorption band near  $1106 \text{ cm}^{-1}$  (9  $\mu\text{m}$ ) near 300 K has long been ascribed to  $\text{O}_i$  [3]. The observation of other  $\text{O}_i$ -related bands at 514 and  $1206 \text{ cm}^{-1}$  led Hrostowski and Kaiser [4] to point out the analogy between these modes and those of a Si–O–Si quasi-molecule. Later, Hrostowski and Alder [5] attributed the temperature dependence of the 9  $\mu\text{m}$  band to the hindered rotation of the O atom about the Si–Si axis. Direct evidence for some kind of rotation of the O atom was given by Bosomworth et al [6] from IR absorption at liquid helium temperature (LHeT). The present understanding of the dynamics of  $\text{O}_i$  is still based on a molecular analogy, where the observed IR features are attributed to some modes of the inner linear part of a  $\text{Si}_3\equiv\text{Si}-\text{O}-\text{Si}\equiv\text{Si}_3$  quasi-molecule, combined with rotation of the O atom [7,9]. One missing feature is the symmetric breathing mode of Si–O–Si, which is not IR active and has not yet been detected by Raman scattering.

The modes related to the  $\text{Si}_3\equiv\text{Si}-\text{O}-\text{Si}\equiv\text{Si}_3$  quasi-molecule with symmetry  $D_{3d}$  are: one asymmetric  $A_{2u}$  mode giving the 9  $\mu\text{m}$  band, one symmetric  $A_{1g}$  IR inactive mode and a doubly degenerate  $E_u$  mode. The  $514 \text{ cm}^{-1}$  absorption can be considered as a silicon phonon mode perturbed by  $\text{O}_i$ , with symmetry  $E_u$ , rather than the  $E_u$  mode of the quasi-molecule. The 2D low-frequency motion (2DLM) of the O atom giving the far IR features at LHeT cannot be described by the above molecular model since it

#### 9.4 O-related IR absorption in c-Si

does not allow for the motion of the O atom perpendicular to the Si–Si axis. The characteristics of the IR features of O<sub>i</sub> at room temperature are given in TABLE 1.

TABLE 1 Positions, relative absorptions and full widths at half-maximum (FWHM) of the O<sub>i</sub>-related absorptions in silicon at 293 K.

Position (cm <sup>-1</sup> )	Attribution	Relative absorption	FWHM (cm <sup>-1</sup> )	Ref
514	O <sub>i</sub> -induced Si transverse mode	0.2	7.6	[8]
[612]	A <sub>1g</sub> ( <sup>16</sup> O <sub>i</sub> )	IR inactive		[2]
1059	A <sub>2u</sub> ( <sup>18</sup> O <sub>i</sub> )	-	29	[8]
1108	A <sub>2u</sub> ( <sup>16</sup> O <sub>i</sub> )	1	33	"
1227	A <sub>2u</sub> + 2DLFM ( <sup>16</sup> O <sub>i</sub> )	1.1 × 10 <sup>-2</sup>	22	"
1720	A <sub>2u</sub> + A <sub>1g</sub>	1.1 × 10 <sup>-2</sup>	31	"

When the temperature is lowered near to LHeT, the IR bands resolve into lines which can show Si and O isotope effects (<sup>28</sup>Si: 92.2%, <sup>29</sup>Si: 4.7%, <sup>30</sup>Si: 3.1% and <sup>16</sup>O: 99.76%, <sup>17</sup>O: 0.04%, <sup>18</sup>O: 0.20% are the natural abundances) and 2DLFM is observed in the far IR. For weak features, isotope effects due to <sup>17</sup>O and <sup>18</sup>O can only be seen with samples enriched with these isotopes [7]. TABLE 2 gives the LHeT frequencies for different isotopic combinations. Some of them are identified by a state labelling |k, ℓ, N>, where k describes the radial dependence of the 2DLFM, ℓ its angular dependence and N the high-frequency A<sub>2u</sub> mode [9].

TABLE 2 Frequencies (cm<sup>-1</sup>) at LHeT of the O<sub>i</sub>-related transitions from the ground state for different O and Si isotopes. When relevant, they are labelled by the final state (see text).

The <sup>29</sup>Si<sub>2</sub>O and <sup>28</sup>SiO<sup>30</sup>Si transitions are nearly coincident, but the first is 30 times less intense and it is not detected.

Si combination	Attribution	<sup>16</sup> O	<sup>17</sup> O	<sup>18</sup> O	Ref
No dependence on the Si mass	0, ±1, 0>	29.3	28.2	27.2	[6,7]
<sup>28</sup> Si <sub>2</sub> O	O <sub>i</sub> -induced Si mode	517.8	517.8	517.8	[7]
<sup>30</sup> Si <sub>2</sub> O	0, 0, 1> or A <sub>2u</sub>	1129.2	-	-	"
<sup>29</sup> SiO <sup>30</sup> Si	"	1130.8	-	-	"
<sup>28</sup> SiO <sup>30</sup> Si	"	1132.7	1105.8	1181.2	"
<sup>28</sup> SiO <sup>29</sup> Si	"	1134.5	1107.6	1083.0	"
<sup>28</sup> Si <sub>2</sub> O	"	1136.4	1109.5	1085.0	"
Mainly <sup>28</sup> Si <sub>2</sub> O	1, 0, 1>	1205.7	1176.7	1151.1	"
<sup>28</sup> SiO <sup>30</sup> Si	A <sub>2u</sub> + A <sub>1g</sub>	1735.4	-	-	"
<sup>28</sup> SiO <sup>29</sup> Si	"	1742.2	-	-	"
<sup>28</sup> Si <sub>2</sub> O	"	1748.6	1720.4	1696.0	"

Above LHeT, the progressive thermalisation of levels related to the 2DLFM produces ‘hot’ lines, already visible at 10 K and their position is given in TABLE 3.

The quantitative measurement of the IR absorption of O<sub>i</sub> is a method to determine [O<sub>i</sub>] in silicon and this point is discussed in Section E.

TABLE 3 Frequencies ( $\text{cm}^{-1}$ ) of  $\text{O}_i$  lines due to transitions from excited levels observed above 10 K.

Initial state	Final state	$^{16}\text{O}$	$^{17}\text{O}$	$^{18}\text{O}$	Ref
$ 0, \pm 1, 0\rangle$	$ 0, \pm 2, 0\rangle$	37.8		35.3	[6]
"	$ 1, 0, 0\rangle$	49.0			[6]
"	$ 0, \pm 1, 1\rangle$	1128.3	1101.3	1077.6	[10]
"	$ 1, \pm 1, 1\rangle$	1216.7	1192.6		"
$ 0, \pm 2, 0\rangle$	$ 0, \pm 3, 0\rangle$	43.3			[6]
"	$ 0, \pm 2, 1\rangle$	1121.9	1095.1	1071.8	[10]

## C OXYGEN-RELATED DEFECTS

### C1 Irradiation Defects

Complexes between O and intrinsic defects are caused by irradiation of CZ silicon with high-energy particles or  $\gamma$ -rays and during the annealing of the as-irradiated crystals. These centres usually produce local vibrational modes (LVMs). EPR spectroscopy can allow us to determine the symmetry of some of them and DLTS their electrical activity. The annihilation or the creation of excitons bound to some of these complexes produces photoluminescence or absorption lines in the near IR, whose isotope effects or sidebands help to obtain a more accurate picture of these centres. The O-vacancy (OV or A centre) is formed when a mobile vacancy is trapped by  $\text{O}_i$ . In the OV, the O atom is bonded to two NNN Si atoms. It is electrically active with two well-established charge states ( $\text{OV}^0$  and  $\text{OV}^-$ ), paramagnetic when negative and stable up to about 500 K [11,12]. Its annealing near 550 K nearly coincides with the growth of a mode at  $889 \text{ cm}^{-1}$  [13]. The related centre could be  $\text{O}_2\text{V}$ , a vacancy decorated with two non-interacting O atoms [13,14] or a trivacancy decorated with one O ( $\text{OV}_3$ ) [15]. Annealing of the  $889 \text{ cm}^{-1}$  LVM produces other LVMs at higher frequency. Complexes between O and Si interstitials ( $\text{Si}_i$ ) are produced by irradiation at low-temperature and they are usually not stable above room temperature. Irradiation centres involving O and C or P are known. The  $\text{O}_i\text{C}_i$  centre has been studied by different experimental methods and by ab initio calculations and its structure is understood, but much remains to be done for the other centres. Exciton lines related to irradiation defects involving O have also been reported. They are included in TABLE 4 which gives a summary of the most prominent IR features related to different kinds of irradiation centres.

### C2 Complexes with Foreign Atoms

Li, an interstitial fast-diffusing donor, can form several donor complexes with  $\text{O}_i$ , and for low [Li], the most abundant is a shallow  $\text{Li}_i\text{O}_i$  donor [16]. Electrically neutral substitutional C and Ge and the interstitial N pair can form with  $\text{O}_i$  neutral centres [17,18]; in some conditions H can also interact with  $\text{O}_i$  [19]. In all these centres, there is no direct bonding between  $\text{O}_i$  and the foreign atom, but the  $\text{O}_i$  modes are perturbed. TABLE 5 gives the positions of these  $\text{O}_i$  modes.

#### 9.4 O-related IR absorption in c-Si

TABLE 4 Positions of the most intense absorption bands or lines due to intrinsic and extrinsic O-related irradiation defects. Correlation with EPR signatures is indicated. PL is for photoluminescence.

Position ( $\text{cm}^{-1}$ )		Attribution	EPR label of the centre	Remarks	Ref
~300 K	LHeT				
830 (791)	836 (798)	$^{16}\text{OV}^0$ ( $^{18}\text{OV}^0$ )		Anneals out at 300°C	[11,14,20]
877	885	$^{16}\text{OV}^-$	B1 or A	"	[14,12]
	841	$\text{OV}_2$ ?		After 100°C anneal	[21]
889 (850)	895	$^{16}\text{O}_2\text{V}$ ( $^{18}\text{O}_2\text{V}$ ) or $^{16}\text{OV}_3$ ( $^{18}\text{OV}_3$ )	P4	After 300°C anneal	[13,14,22]
905, 969	910, 976	$\text{O}_3\text{V}$ or $\text{O}_2\text{V}_3^*$	A15*	After 450°C anneal	[14,22]
1000		$\text{O}_3\text{V}$ or $\text{O}_2\text{V}_2^*$	P2*		[14,23]
	936 (80 K)	$\text{O}_i\text{S}_i$ ?	A17	Anneals out at 100°C	[24–26]
	845/856 (80 K)	$\text{O}_i\text{S}_i$ -like 2 charge states	A18 ?	Anneals out at 25°C	[24,26]
529, 550, 742, 865 and 1115 (LHeT)		$\text{O}_i\text{C}_i$	G15	C modes higher than the O modes	[27,28]
~859 / 910	864 / 916	(P,O,V) <sup>0</sup> / (P,O,V) <sup>-</sup>	ODMR	After 200°C anneal	[29]
861.5 / 908	866 / 915	Same with As		After 200°C anneal	[30]
861 / 905	867 / 913	Same with Sb		After 200°C anneal	"
	3942 (488.8 meV)	COV ? Monoclinic I		Also in PL $^{18}\text{O}$ : 3941 $\text{cm}^{-1}$	[31]
	6187.8 (767.3 meV)	(O,C)		Also in PL (P line) After 350°C anneal	[32,33]
	6368.6 (789.7 meV)	$\text{O}_i\text{C}_i$	G15	Also in PL (C line) $^{13}\text{C}$ : 6369.3 $\text{cm}^{-1}$	[27,28,34]

TABLE 5 Position ( $\text{cm}^{-1}$ ) at LHeT of the  $\text{A}_{2u}$   $\text{O}_i$  mode perturbed by foreign atoms. For the (NN,O) centres, the positions of the  $\text{O}_i$  modes at 77 K are 1030, 1028, 1028 and 1013  $\text{cm}^{-1}$  for  $^{14}\text{N}_2^{16}\text{O}$ ,  $^{15}\text{N}_2^{16}\text{O}$ ,  $^{14}\text{N}^{15}\text{N}^{16}\text{O}$  and  $^{14}\text{N}_2^{17}\text{O}$ , respectively [18].

Foreign atom	H	D	Li	C	Ge
Position ( $\text{cm}^{-1}$ )	1075.1	1076.3	1016	1105, 1052	1118, 1130
Ref	[19]	[19]	[35]	[36]	[37]

#### D OXYGEN-RELATED PRECIPITATES AND THERMAL DONORS

The nature of the precipitates and their vibrational absorption depends on the growth conditions of CZ. Detailed studies of the correlation between IR absorption and transmission electron microscopy (TEM) of O-related precipitates have been made by Shimura and Tsuya [38] and by Gaworzewski et al [39]. Between about 500 and 750°C, O precipitates give a broad ( $\sim 150 \text{ cm}^{-1}$ ) band whose peak frequency increases from  $\sim 1030$  to  $1110 \text{ cm}^{-1}$ . At 600°C, precipitation of oxygen is nearly total for  $\sim$  a 250 hour-annealing. The corresponding precipitates seem to be small  $\text{a-SiO}_x$  ( $1 < x \leq 2$ ) clusters. For 250 hour-annealings between 750 and 1000°C, the features change progressively to two bands at  $\sim 1120$  and  $1225 \text{ cm}^{-1}$  (the latter is not to be confused with the weak  $\text{O}_i$  band of TABLE 1 at the same frequency). Several interpretations of these two bands have been proposed. A convincing interpretation is that the  $1120 \text{ cm}^{-1}$  band is due to globular-like precipitates while tabular-like precipitates would be responsible for the band near  $1225 \text{ cm}^{-1}$  and for another one near  $1080 \text{ cm}^{-1}$ . For annealing near to 1000°C and up to 1150°C, besides a band nearly coincident with the  $\text{O}_i$  mode at  $1107 \text{ cm}^{-1}$ , a weaker band at  $470 \text{ cm}^{-1}$  has also been reported [38]. They are ascribed to small

#### 9.4 O-related IR absorption in c-Si

octahedral precipitates of stoichiometric SiO<sub>2</sub>. A component of the feature at 470 cm<sup>-1</sup> could be related to a weak band at 810 cm<sup>-1</sup>, both tentatively attributed to a-SiO<sub>2</sub> [38].

The 450°C thermal donors (TDs) are the first centres formed by the aggregation of O atoms. About 10 different TDs have been identified at LHeT by their double donor He-like electronic spectra and more than 80 related transitions have been identified between 350 and 1200 cm<sup>-1</sup> [40]. Their exact microscopic structure is still debated 40 years after having first been observed [41] and a review of their widely-investigated properties is given in [42]. The two simplest TDs, TD1 and TD2, are bistable and they are electrically inactive when in their metastable state [40]. The core of the TDs contains 2 O atoms but the exact number of O atoms for each TD is not known with certainty. LVMs related to O in TDs have been reported recently [43,44]. Their positions, which do not show much dependence on temperature and on the charge state of the TDs, are given in TABLE 6.

TABLE 6 Positions of <sup>16</sup>O-related LVMs observed in CZ samples containing TDs. X1 and X2 label the metastable states of TD1 and TD2. NL10 is the label of an EPR signature due to one or several O-related centres produced in the same temperature range as the TDs.

Position (cm <sup>-1</sup> )	Correlation with	Remarks	Ref
975/1020	TD1/X1		[44]
988/1020	TD2/X2	<sup>18</sup> O : 945 cm <sup>-1</sup>	[44]
999	TD3	<sup>18</sup> O : 955 cm <sup>-1</sup>	[44]
1006	TDn	<sup>18</sup> O : 965 cm <sup>-1</sup>	[44]
1012	NL10 ?	<sup>18</sup> O : 969 cm <sup>-1</sup>	[44]
724	TD2	Observed with the 988 cm <sup>-1</sup> LVM	[44]
728	TD3	Observed with the 999 cm <sup>-1</sup> LVM	[44]
734	TDn	Observed with the 1006 cm <sup>-1</sup> LVM	[44]
744	NL10 ?	Observed with the 1012 cm <sup>-1</sup> LVM	[44]

The mode at 1012 cm<sup>-1</sup> has also been attributed to O<sub>i</sub> because it can be observed in CZ silicon after heating at 1350°C and quenching [8]. This seems now unlikely, but the presence of NL10 after such a thermal treatment is not obvious and the attribution of the mode has to be confirmed. TDs are converted into an electrically inactive form near 600°C, but ‘new’ thermal donors (NDs) associated with extended defects and Si/SiO<sub>2</sub> precipitate interfaces are formed near 650°C [42]. These NDs do not seem to produce a distinctive IR absorption.

#### E CALIBRATION OF THE IR ABSORPTION

The intensity of the absorption of the O<sub>i</sub> features is proportional to the O<sub>i</sub> concentration. Many calibration factors between the peak absorption coefficient of the 9 μm band at room temperature and [O<sub>i</sub>] have been proposed, based on a determination of the total [O] using mainly charged particle activation analysis and/or gas fusion analysis (for a review, see Bullis [45]). Between 1983 and 1996, eight of the ten independent determinations of the calibration factor have given values between 6.0 and 6.28 ppma cm. The most recent values of the calibration factor are 6.04 and 6.21 ppma cm [46,47] and the methodology of the IR measurements for these two certifications of reference silicon materials seems to reduce the risk of systematic errors. I recommend here as a calibration factor the average of these two values, 6.13 ppma cm or  $3.07 \times 10^{17}$  cm<sup>-2</sup> and this factor is valid between 295 and 310 K.

At LHeT, the FWHP of the intense O<sub>i</sub> line at 1136 cm<sup>-1</sup> is 0.6 cm<sup>-1</sup> so that a spectral resolution of ~0.2 cm<sup>-1</sup> or less is necessary to measure the true peak absorption. When this is met, the ratio of  $\alpha_{\max}(1106)$  at room temperature to the peak absorption of the 1136 cm<sup>-1</sup> line,  $\alpha_{\max}(1136)$ , at LHeT is

0.028. The calibration factor for the peak absorption at  $1136\text{ cm}^{-1}$  is thus 172 ppba cm or  $8.60 \times 10^{15}\text{ cm}^{-2}$ . Above 8 K, the intensity of the line starts decreasing because of thermalisation so that a sample temperature below 8 K is mandatory for a quantitative determination. Measurements have shown that the ratio of  $\alpha_{\max}(1106)$  to the integrated absorption  $I_A$  of the whole isotopic structure near  $1136\text{ cm}^{-1}$  is 0.03 cm below 8 K [48]. Thus, the calibration factor between  $[\text{O}_i]$  and  $I_A$  is  $9.2 \times 10^{15}\text{ cm}^{-1}$  and it should be independent of the spectral resolution. When it is necessary to determine  $[\text{O}_i]$  in samples containing O precipitates, the interference between the bands of the precipitates and the  $\text{O}_i$  band at  $1107\text{ cm}^{-1}$  produces a large uncertainty. In that case, the measurement can be performed near LHeT, where the broad precipitate bands can be easily discriminated from the sharp  $\text{O}_i$  lines. An alternative, in that case, is to measure at room temperature the weak combination band of  $\text{O}_i$  at  $1720\text{ cm}^{-1}$  in wavenumber, which is free of interference with the absorption of the precipitates, but at the expense of sensitivity [49]. The accuracy or even the use of these methods of determination of  $[\text{O}_i]$  is limited by the absorption of free or bound carriers and these points are discussed in [45].

## F CONCLUSION

Vibrational IR absorption has helped to identify many O-related centres in silicon. The IR results presented here are reasonably up to date, but the list of lines is certainly not exhaustive and I have omitted the electronic absorption lines of the TDs, known to be related to O, as well as those of the shallow thermal donors (STDs), possibly due to some (O,N) complexes [50,51]. A good account of the O-related PL centres in silicon can be found in the review by Lightowlers and Davies [52]. The existence of an oxygen dimer has been predicted from O diffusion results and from theory [53]. Very recent results convincingly show that weak LVMs at  $1012$ ,  $1060$  and  $1105\text{ cm}^{-1}$  (LHeT) are indeed related to an oxygen dimer made of two nearby  $\text{O}_i$  atoms [54].

## REFERENCES

- [1] R.K. Willardson, A.C. Beer, E.R. Weber (Eds) [ *Semicond. Semimet. (USA)* vol.42 (1994) ]
- [2] E. Artacho, F. Ynduráin [ *Mater. Sci. Forum (Switzerland)* vol.196-201 (1996) p.103 ]
- [3] W. Kaiser, P.H. Keck, C.F. Lange [ *Phys. Rev. (USA)* vol.101 (1956) p.1264 ]
- [4] H.J. Hrostowski, R.H. Kaiser [ *Phys. Rev. (USA)* vol.107 (1957) p.966 ]
- [5] H.J. Hrostowski, B.J. Alder [ *J. Chem. Phys. (USA)* vol.33 (1960) p.980 ]
- [6] D.R. Bosomworth, W. Hayes, A.R.L. Spray, G.D. Watkins [ *Proc. R. Soc. Lond. A. (UK)* vol.317 (1970) p.133 ]
- [7] B. Pajot, E. Artacho, C.A.J. Ammerlaan, J.M. Spaeth [ *J. Phys., Condens. Matter (UK)* vol.7 (1995) p.7077 ]
- [8] B. Pajot, H.J. Stein, B. Cales, C. Naud [ *J. Electrochem. Soc. (USA)* vol.132 (1985) p.3034 ]
- [9] H. Yamada-Kanata, C. Kaneta, T. Ogawa [ *Phys. Rev. B (USA)* vol.42 (1990) p.9650 ]
- [10] B. Pajot [ *Semicond. Semimet. (USA)* vol.42 (1994) p.191-249 ]
- [11] J.W. Corbett, G.D. Watkins, R.M. Chrenko, R.S. McDonald [ *Phys. Rev. (USA)* vol.121 (1961) p.1015 ]
- [12] G.D. Watkins, J.W. Corbett [ *Phys. Rev. (USA)* vol.121 (1961) p.1001 ]
- [13] J.W. Corbett, G.D. Watkins, R.S. McDonald [ *Phys. Rev. (USA)* vol.135 (1964) p.A1381 ]
- [14] J.L. Lindström, B.G. Svensson [ *Mater. Res. Soc. Symp. Proc. (USA)* vol.59 (1986) p.45 ]
- [15] G. Davies, E.C. Lightowlers, R.C. Newman, A.S. Oates [ *Semicond. Sci. Technol. (UK)* vol.2 (1987) p.524 ]
- [16] A.K. Ramdas, S. Rodriguez [ *Rep. Prog. Phys. (UK)* vol.44 (1981) p.1297 ]
- [17] R.C. Newman [ *Infrared Studies of Crystal Defects* (Taylor and Francis, 1973) ]
- [18] F. Berg Rasmussen et al [ in *Early Stages of Oxygen Precipitation in Silicon* Ed. R. Jones (Kluwer Academic Publishers, 1996) p.319-27 ]

- [19] V.P. Markevich, M. Suezawa, K. Sumino [ *Mater. Sci. Forum (Switzerland)* vol.196-201 (1995) p.915 ]
- [20] F.A. Abou-el-Fotouh, R.C. Newman [ *Solid State Commun. (USA)* vol.15 (1974) p.1409 ]
- [21] A.K. Ramdas, M.G. Rao [ *Phys. Rev. (USA)* vol.142 (1966) p.451 ]
- [22] H.J. Stein [ *Appl. Phys. Lett. (USA)* vol.48 (1986) p.1540 ]
- [23] Y.-H Lee, J. W. Corbett [ *Phys. Rev. B (USA)* vol.13 (1976) p.2653 ]
- [24] R.E. Whan [ *Phys. Rev. (USA)* vol.140 (1965) p.A690 ]
- [25] A. Brelot, J. Charlemagne [ in *Radiation Effects in Semiconductors* Eds J.W. Corbett, G.D. Watkins (Gordon & Breach, New York, USA, 1971) p.161 ]
- [26] Y.H. Lee, J. C. Corelli, J. W. Corbett [ *Phys. Lett. A (Netherlands)* vol.60 (1977) p.55 ]
- [27] G. Davies et al [ *J. Phys. C (UK)* vol.19 (1985) p.841 ]
- [28] G.D. Watkins [ in *Early Stages of Oxygen Precipitation in Silicon* Ed. R. Jones (Kluwer Academic Publishers, 1996) p.1-18 ]
- [29] J.L. Lindström, B.G. Svensson, W.M. Chen [ *Mater. Sci. Forum (Switzerland)* vol.83-87 (1992) p.333 ]
- [30] T. Hallberg, J.L. Lindström, B.G. Svensson, K. Swiatek [ *Mater. Sci. Forum (Switzerland)* vol.143-147 (1994) p.1239 ]
- [31] G. Davies, E.C. Lightowers, M. Stavola, K. Bergman, B. Svensson [ *Phys. Rev. B (USA)* vol.2755 (1987) p.2755 ]
- [32] M. Tajima, P. Stallhofer, D. Huber [ *Jpn. J. Appl. Phys. (Japan)* vol.22 (1983) p.L586 ]
- [33] B. Pajot, J. von Bardeleben [ *Proc. 13<sup>th</sup> ICDS*, Coronado, California, 12-17 August 1984, Eds. L.C. Kimerling, J.M. Parsey Jr. (Metallurgical Society AIME, 1985) p.685 ]
- [34] K. Thonke, G.D. Watkins, R. Sauer [ *Solid State Commun. (USA)* vol.51 (1984) p.127 ]
- [35] R.M. Chrenko, R.S. McDonald, E.M. Pell [ *Phys. Rev. A (USA)* vol.138 (1966) p.1775 ]
- [36] R.C. Newman [ *Mater. Res. Soc. Symp. Proc. (USA)* vol.59 (1986) p.403 ]
- [37] H. Yamada-Kaneta, C. Kaneta, T. Ogawa [ *Phys. Rev. B (USA)* vol.47 (1993) p.9338 ]
- [38] F. Shimura, H. Tsuya [ *J. Electrochem. Soc. (USA)* vol.129 (1982) p.2089 ]
- [39] P. Gaworzecki, E. Hild, F.-G. Kirscht, L. Vecsernyès [ *Phys. Status Solidi A (Germany)* vol.85 (1984) p.133 ]
- [40] P. Wagner, J. Hage [ *Appl. Phys. A (Germany)* vol.49 (1989) p.123 ]
- [41] W. Kaiser, H.L. Frisch, H. Reiss [ *Phys. Rev. (USA)* vol.112 (1958) p.1456 ]
- [42] J. Michel, L.C. Kimerling [ *Semicond. Semimet. (USA)* vol.42 (1994) p.261-87 ]
- [43] J.L. Lindström, T. Hallberg [ *Phys. Rev. Lett (USA)* vol.72 (1994) p.2729 ]
- [44] J.L. Lindström, T. Hallberg [ in *Early Stages of Oxygen Precipitation in Silicon* Ed. R. Jones (Kluwer Academic Publishers, 1996) p.41-60 ]
- [45] W.M. Bullis [ *Semicond. Semimet. (USA)* vol.42 (1994) p.95-152 ]
- [46] R. Murray et al [ *J. Electrochem. Soc. (USA)* vol.139 (1992) p.3582 ]
- [47] B.G. Rennex, J.R. Ehrstein, R.I. Scace [ *J. Electrochem. Soc. (USA)* vol.143 (1996) p.258 ]
- [48] B. Pajot [ unpublished results ]
- [49] Y. Kitagawara, H. Kubota, M. Tamatsuka, T. Takenaka, K. Takamizawa [ US Patent no. 5,368,118 (1995) ]
- [50] M. Suezawa [ in *Early Stages of Oxygen Precipitation in Silicon* Ed. R. Jones (Kluwer Academic Publishers, 1996) p.207-21 ]
- [51] A. Gali, J. Miro, P. Deák [ in *Early Stages of Oxygen Precipitation in Silicon* Ed. R. Jones (Kluwer Academic Publishers, 1996) p.419-25 ]
- [52] E.C. Lightowers, G. Davies [ in *Early Stages of Oxygen Precipitation in Silicon* Ed. R. Jones (Kluwer Academic Publishers, 1996) p.303-18 ]
- [53] R.C. Newman [ in *Early Stages of Oxygen Precipitation in Silicon* Ed. R. Jones (Kluwer Academic Publishers, 1996) p.19-39 ]
- [54] L.I. Murin, T. Hallberg, V.P. Markevich, J.L. Lindström [ *Phys. Rev. Lett (USA)* vol.80 (1998) p.93 ]

## 9.5 Precipitation, segregation and IR absorption of O in c-Si

S.J. Pearton

May 1997

### A INTRODUCTION

The Si melts used in bulk Czochralski growth contain a significant concentration of oxygen unintentionally incorporated from the  $\text{SiO}_2$  crucible [1,2]. In the molten solution growth, the O concentration in the solidified Si differs from that in solution. The ratio of the impurity concentration in the solids ( $C_s$ ) to that in liquid melt ( $C_o$ ) at a given temperature is referred to as the segregation coefficient or equilibrium distribution coefficient  $K_{\text{Ox}}$ . In general, the segregation coefficient can be estimated theoretically from thermodynamics [3], i.e. at equilibrium, the partial molar Gibbs free energies of the oxygen in the solid must equal that in the melt. One of the key parameters is the heat of solution, which has a strong influence on the resulting segregation coefficient. For dopant impurities or metallic ions the calculated values agree well with experiment but this is not the case for O, N and C. Empirically it is found that the segregation coefficients  $K_o$  for dopants or metals are related to the maximum molar solid solubility  $X_M$  by the Fischler rule [4]

$$X_M = 0.1K_o \quad (1)$$

This is shown in FIGURE 1 (upper line), where the line represents EQN (1) and the points are experimental values [5]. Note, however, that oxygen does not obey the Fischler rule (lower line of FIGURE 1).

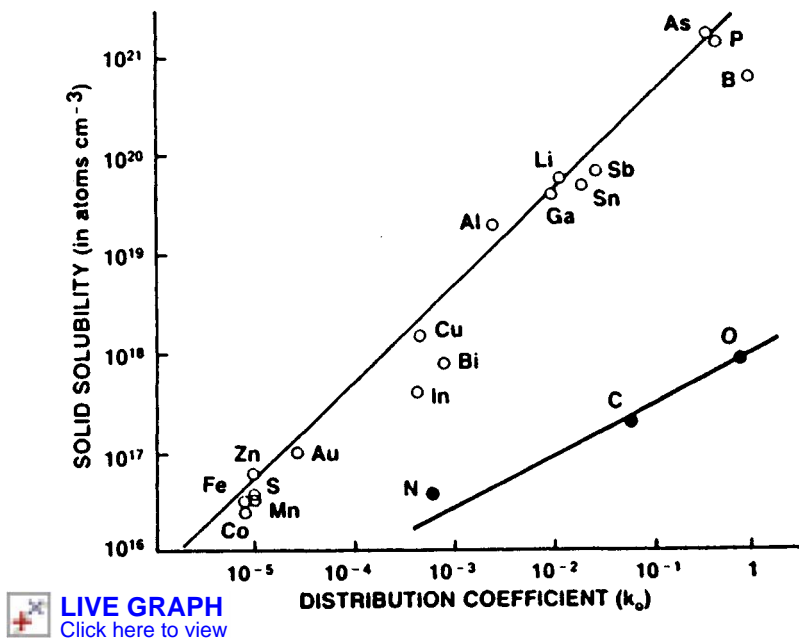


FIGURE 1 Segregation or distribution coefficient as a function of maximum impurity solubility (after [3,5]).

Oxygen is transported to the Si melt as  $\text{SiO}$  through the following reaction of the quartz crucible and the molten Si [6]



The high vapour pressure of SiO ( $2 \times 10^{-3}$  atm at the melting point of Si) leads to most of it re-evaporating from the melt, but  $1.27 \times 10^{18}$  oxygen  $\text{cm}^{-3}$  remains in the solid [7]. Oxygen-related thermal donors can be generated from this incorporated oxygen by heat treatments around  $450^\circ\text{C}$ , and these can be annihilated by treatment at still higher temperatures ( $\sim 650^\circ\text{C}$ , 30 min). At temperatures above  $\sim 750^\circ\text{C}$ , oxygen outdiffusion from the surface and precipitation to form  $\text{SiO}_2$  precipitates in the bulk occur, with beneficial effects of the latter because of their gettering action for metallic impurities. The desirable range of initial oxygen concentrations in device-grade Si wafers is  $0.9\text{--}1.18 \times 10^{18} \text{ cm}^{-3}$ . Lower values do not allow the  $\text{SiO}_2$  precipitation to occur and thus the internal gettering mechanism is ineffective, while higher values may lead to wafer warpage during heat treatments.

## B SEGREGATION COEFFICIENT

Since oxygen is continuously evaporating from the melt during growth, its content in the solid is not solely determined by the usual relationship

$$C_s = K C_o (1 - g)^{K-1} \quad (3)$$

where  $g$  is the fraction of melt pulled. For a typical condition of constant rotation rates for crucible and crystal, the oxygen concentration is higher in the seed end of the crystal and in the centre of the wafers. The distribution of carbon is generally found to be the inverse of that of oxygen in both the radial and axial directions.

The primary factors affecting the oxygen concentration in the crystal are the temperature at the crucible wall and the ratio of surface area between the crucible/melt interface and melt free surface because the concentration in the melt is the difference between the dissolution rate of the  $\text{SiO}_2$  crucible and the evaporation rate of SiO. Silicon ingots with very low oxygen concentrations ( $< 10^{16} \text{ cm}^{-3}$ ) can be grown from non-oxide crucibles (e.g. silicon nitride [8]). Uniform, high oxygen concentrations can be obtained by adding  $\text{SiO}_2$  rings or rods to the bottom of the crucible.

Many reports exist of attempts to measure the effective segregation coefficient of oxygen in Si [9–11]. In general, oxygen concentration in the melt cannot be directly measured in such experiments; the results lead to an effective value only and assumptions must be made concerning the behaviour at the solid/melt interface. Yatsurugi et al [7] reported  $K_{\text{OX}} = 1.2 \pm 0.17$  based on charged particle activation analysis of the total oxygen present in float-zone crystals doped with oxygen from the gas phase, and IR measurement of the interstitial oxygen ( $9 \mu\text{m}$ ) band. Additional evidence for a  $K_{\text{OX}}$  value near unity has come from a variety of other experiments [12–14] and calculations [13]. Literature values range from 0.25 to 3, but many of the extreme values at either end of this range appear to result from large experimental uncertainties.

## C IR ABSORPTION

IR absorption at  $9 \mu\text{m}$  is the most commonly used method for measuring the interstitial oxygen concentration in Si. The conversion of peak intensity into concentration (conversion factor  $3.14 \times 10^{17} \text{ cm}^{-3}$  or 6.28 ppma) [15] works well for lightly-doped Si, but free carrier absorption in heavily doped material requires other techniques such as the gas-fusion method [16] or electron bombardment of the Si to reduce the carrier density [17]. It is important to note that the amount of

## 9.5 Precipitation, segregation and IR absorption of O in c-Si

oxygen incorporated into Si is above the solid solubility at typical device process temperatures of 400–1200°C and thus the dissolved oxygen may change state to become incorporated into donor complexes, precipitates, stacking faults and so on.

The IR spectrum of Si shows a series of lines due to vibrations of the lattice itself, plus bands at 1106 cm<sup>-1</sup> (9 μm) due to interstitial oxygen and a much smaller (typically ~16 times) band at 513 cm<sup>-1</sup> (19 μm). The absorption coefficient x depends on oxygen concentration C<sub>OX</sub> and sample thickness t through the relationship

$$x = \frac{1}{t} \log(aC_{OX}) \quad (4)$$

where a is the absorptivity. The American Society for Testing and Materials (ASTM) and Japan Electronic Industry Development Association (JEIDA) issue standards for the calibration of the 9 μm absorption coefficient for determining the concentration of oxygen in Si. The best value is probably that from an interlaboratory consortium, which determined the calibration factor at room temperature to be 6.28 ±0.18 ppm cm [18], also designated the International Oxygen Coefficient 1988.

It is important to remember that the absorption at 9 μm yields only the interstitial oxygen concentration, and does not represent the total oxygen present in all forms. The 9 μm band is due to oxygen at an interstitial site, bonded to two neighbouring Si atoms and forming a non-linear Si–O–Si structure. At low temperatures and high resolution the 9 μm band may show fine structure due to the presence of multiple groundstates, and isotopic effects (<sup>28</sup>Si, <sup>29</sup>Si, <sup>30</sup>Si, <sup>16</sup>O, <sup>17</sup>O, <sup>18</sup>O) [19–25]. The 19 μm band is thought to be due to symmetric vibration of oxygen, while the 9 μm band results from antisymmetric vibrations. Rotational transitions of the Si–O–Si structure can be found in the far IR (i.e. 27–49 cm<sup>-1</sup>) [19–25].

Irradiation of oxygen-rich Si produces a variety of oxygen-vacancy and oxygen-silicon and impurity interstitial complexes, most of whose microstructure and exact chemical composition is not firmly established. The best known of these complexes is the so-called A-centre, an O–V defect where the oxygen still forms two bridging bonds with neighbouring silicon atoms, but is in a near-substitutional position [26,27]. This leads to an electrical level in the bandgap at E<sub>C</sub>–0.18 eV, detectable by deep level transient spectroscopy (DLTS), and to absorption bands at 830 and 877 cm<sup>-1</sup> (neutral and negative charge states).

The strength of the oxygen-related IR bands is strongly reduced by annealing as the oxygen transforms from isolated interstitials into clusters, defect complexes and SiO<sub>x</sub> phases. For extended 450°C annealing absorption lines in the regions 200–550 cm<sup>-1</sup> and 700–1200 cm<sup>-1</sup> appear that correspond to the thermal donors [28–31].

## D CONCLUSION

The segregation coefficient for O in Si appears to be close to unity, and measurement of the 9 μm absorption band intensity gives a concentration for interstitial oxygen.

## REFERENCES

- [1] See for example H.R. Huff, T. Abe, B. Kolbeson (Eds.) [ *Semiconductor Silicon 1986* (Electrochemical Society, Pennington, NJ, 1986) ]

### 9.5 Precipitation, segregation and IR absorption of O in c-Si

- [2] W.C. O'Mara, R.B. Herring, L.P. Hunt (Eds.) [ *Handbook of Semiconductor Si Technology* (Noyes Publications, Park Ridge, NJ, USA, 1990) ]
- [3] R.J. Jaccodine, C.W. Pearce [ in *Defects in Si* Eds. W.M. Bullis, L.C. Kimerling (Electrochemical Society, Pennington, NJ, USA, 1983) p.115-9 ]
- [4] S. Fischler [ *J. Appl. Phys. (USA)* vol.33 (1962) p.1615 ]
- [5] F.A. Trumborn [ *Bell Syst. Tech. J. (USA)* vol.39 (1960) p.205 ]
- [6] H. Ming Lauw [ in *Handbook of Semiconductor Si Technology* Eds. W.C. O'Mara, B. Herring, L.P. Hunt (Noyes Publications, Park Ridge, NJ, USA, 1990) ]
- [7] Y. Yatsurugi, N. Aikayama, Y. Endo, T. Nozaki [ *J. Electrochem. Soc. (USA)* vol.120 (1973) p.975 ]
- [8] M. Watanabe, T. Usami, S. Takasu, S. Matsuo, E. Toji [ *Jpn. J. Appl. Phys. (Japan)* vol.22-1 (1982) p.185 ]
- [9] H.M. Lauw [ *Microelectron. J. (UK)* vol.12 (1981) p.33 ]
- [10] R.W. Series, K.G. Barraclough [ *J. Cryst. Growth (Netherlands)* vol.60 (1982) p.212 ]
- [11] K.G. Barraclough [ in *Properties of Si* (INSPEC, IEE, London, UK, 1988) ]
- [12] H. Harada, T. Itoh, N. Ozawa, T. Abe [ *Proc. 3rd Symp. VLSII Sci. and Technol.* Eds. W.M. Bullis, S. Broyda (Electrochem. Soc., Pennington, NJ, USA, 1985) p. 526 ]
- [13] T. Carlberg [ *J. Electrochem. Soc. (USA)* vol.133 (1986) p.1940 ]
- [14] W.C. O'Mara [ in *Handbook of Semiconductor Si Technology* Eds. W.C. O'Mara, R.B. Herring, L.P. Hunt (Noyes Publications, Park Ridge, NJ, USA, 1990) ]
- [15] W.M. Bullis et al [ *Electrochem. Soc. Meeting Extended Abstracts (USA)* vol.86-1 (1986) p.196 ]
- [16] M. Walitzki, H.J. Rath, J. Reffle, S. Pahlke, M. Blatte [ in *Semiconductor Silicon* Eds. H.R. Huff, T. Abe, B. Kolbesen (Electrochemical Society, Pennington, NJ, 1986) p.86-99 ]
- [17] H. Tsuya, M. Kanamori, M. Takeda, K. Yasuda [ in *VLI Science and Technology* Eds. W.M. Bullis, S. Broydo (Wiley, NY, USA, 1985) p.517-25 ]
- [18] A. Baghdadi et al [ *J. Electrochem. Soc. (USA)* vol.136 (1989) p.2015 ]
- [19] M. Stavola [ *Appl. Phys. Lett. (USA)* vol.44 (1984) p.514 ]
- [20] B. Pajot, H.J. Stein, B. Cales, C. Nared [ *J. Electrochem. Soc. (USA)* vol.732 (1985) p.3034 ]
- [21] H.J. Hrostowski, B.J. Adler [ *J. Chem. Phys. (USA)* vol.33 (1960) p.980 ]
- [22] B. Pajot [ *J. Phys. Chem. Solids (UK)* vol.28 (1967) p.73 ]
- [23] D.R. Bosomworth, W. Hayes, A.R.L. Spray, G.D. Watkins [ *Proc. R. Soc. Lond. A (UK)* vol.317 (1970) p.133 ]
- [24] R.C. Newman [ *Infrared Studies of Crystal Defects* (Taylor and Francis, London, 1973) p. 88 ]
- [25] B. Pajot, B. Cales [ *Mater. Res. Soc. Symp. Proc. (USA)* vol.59 (1986) p.39 ]
- [26] G.D. Watkins, J.W. Corbett [ *Phys. Rev. (USA)* vol.121 (1961) p.1001 ]
- [27] J.W. Corbett, G.D. Watkins, R.M. Chrenko, R.S. McDonald [ *Phys. Rev. (USA)* vol.121 (1961) p.1015 ]
- [28] R. Oeder, P. Wagner [ in *Defects in Semiconductors II* Eds. S. Mahajan, J.W. Corbett (North-Holland, The Netherlands, 1983) p. 14 ]
- [29] M. Suezawa, K. Sumino [ *Phys. Status Solidi A (Germany)* vol.83 (1984) p.235 ]
- [30] M. Stavola, K.M. Lee [ *Mater. Res. Soc. Symp. Proc. (USA)* vol.59 (1986) p.95 ]
- [31] R.C. Newman [ *J. Phys. C (UK)* vol.18 (1985) p.L967 ]

## 9.6 Segregation coefficient, solubility and IR absorption of C in c-Si

S.J. Pearton

May 1997

### A INTRODUCTION

The light element impurities C, O and N in Si do not follow the empirical Fischler rule that relates maximum molar solid solubility  $X_M$  to segregation coefficient  $K_O$ , i.e.  $X_M = 0.1K_O$  [1]. The major sources of carbon contamination in Si crystals are the graphite heater (an extruded or moulded graphite cylinder into which the  $\text{SiO}_2$  crucible is placed) and accessories such as heat shields which may react with  $\text{O}_2$ ,  $\text{H}_2\text{O}$  or  $\text{SiO}$  gases or the  $\text{SiO}_2$  crucible itself to form gaseous carbon compounds that are incorporated into the melt through vapour phase transport [2]. It is not expected that the polySi charge is a significant source of carbon, because the latter typically contains  $2 \times 10^{15}$ – $8 \times 10^{16}$  carbon  $\text{cm}^{-3}$ , while typical single crystals have higher concentrations,  $10^{16}$ – $4 \times 10^{17}$   $\text{cm}^{-3}$  [3–5]. Moreover, the segregation coefficient of carbon is only 0.07 [3].

The carbon impurities are generally incorporated on substitutional sites which leads to a decrease in local lattice parameter and the presence of stresses. While carbon is electrically inactive it may influence the behaviour of oxygen, e.g. inhibiting thermal donor formation at  $450^\circ\text{C}$  [16] and enhancing  $\text{SiO}_2$  nucleation and precipitation rates [7–9]. To reduce the carbon concentration the graphite parts in a crystal puller may be coated with chemical vapour deposition (CVD) SiC [2], which can produce carbon levels  $<10^{16}$   $\text{cm}^{-3}$  in the crystal.

Carbon produces an IR peak at  $605 \text{ cm}^{-1}$ , on the edge of a strong lattice band at  $610 \text{ cm}^{-1}$  [10]. The standard calibration factor is 1.7–2.0 ppma  $\text{cm}$  [11,12]. The standard method requires that the measurements be made with double-side polished, parallel side samples. The absorption coefficient  $\alpha$  is obtained from the transmittance  $T$  according to the relationship

$$T = \frac{I}{I_0} = \frac{(1-R)^2 \exp(-\alpha d)}{1-R^2 \exp(-2\alpha d)} \quad (1)$$

where  $I_0$  is the base intensity,  $I$  the relative transmitted intensity at the wavelength of the absorption peak,  $d$  the sample thickness and  $R$  the reflectance of Si (0.3 at these wavelengths).

### B SEGREGATION COEFFICIENT

The most reliable values come from Nozacki et al [13],  $k_C = 0.07 \pm 0.01$ , and Kolbesen and Muhlbauer [7],  $k_C = 0.058 \pm 0.005$ . These are equilibrium values obtained under low growth rate conditions. At high growth rates the effective segregation coefficient may be much higher, leading to dissolved carbon concentrations well in excess of the normal solubility. The small segregation coefficient may also lead to microscopic inhomogeneities in carbon inclusion. Series and Barraclough [5] found an effective segregation coefficient  $K_e$  of 0.1, which is equivalent to an equilibrium segregation coefficient  $K_O$  of 0.06–0.07.

## C SOLUBILITY

The equilibrium solubility in liquid Si is  $4 \times 10^{18} \text{ cm}^{-3}$  [13] while that in solid Si is  $3.5 \times 10^{17} \text{ cm}^{-3}$  [3] at the melting point. The solid solubility  $C_S$  varies with temperature as [14]

$$C_S = 4 \times 10^{24} \exp(-2.4\text{eV}/kT) \text{ cm}^{-3} \quad (2)$$

If the carbon level exceeds the solubility in dislocation-free crystals, SiC particles may form and produce polycrystalline growth. SiC precipitates may impair the electrical quality of junction devices. The maximum solubility of carbon in oxygen-rich pulled ingots may be  $\sim 10^{18} \text{ cm}^{-3}$ , and it is found that  $\text{SiO}_2$  precipitates may act as nucleation sites for SiC precipitation.

## D IR ABSORPTION

The IR absorption due to isolated carbon is fairly straightforward with a single localized vibrational mode at  $605 \text{ cm}^{-1}$  at 300 K ( $607.5$  at 77 K), the so-called 16.5 micron band [15]. Weak lines may also be seen at  $586.3 \text{ cm}^{-1}$  due to  $^{13}\text{C}$ , and at  $1169.0$  and  $1205.8 \text{ cm}^{-1}$  due to second harmonics of  $^{13}\text{C}$  and  $^{12}\text{C}$ , respectively. The intensity of the  $605 \text{ cm}^{-1}$  line is proportional to the dissolved carbon concentration, with

$$C_S = \alpha \times 0.83 \times 10^{17} \text{ carbon cm}^{-3} \quad [16]$$

$$C_S = \alpha \times 1.0 \times 10^{17} \text{ carbon cm}^{-3} \quad [17]$$

being the most widely used conversions. The position of the IR band is well explained by models taking into account lattice distortion by the small C atoms [18]. Irradiation of Si may lead to a variety of C-related defect absorption bands thought to contain oxygen or silicon interstitials in addition to carbon [19]. Prolonged annealing of carbon-rich Si also leads to a reduction in the intensity of the  $605 \text{ cm}^{-1}$  band—at high temperatures ( $>1000^\circ\text{C}$ ), the most likely cause is precipitation to form SiC, whereas at lower temperatures the carbon is basically immobile and therefore the loss of signal is due to complexing reactions with other impurities like oxygen.

## E CONCLUSION

Carbon is a generally benign impurity in terms of effects on ICs [20]. Its solubility at the melt temperature is  $\sim 3.5 \times 10^{17} \text{ cm}^{-3}$ , its segregation coefficient is 0.067–0.07 and it has a well-defined infra-red signature at  $605 \text{ cm}^{-1}$ .

## REFERENCES

- [1] R.J. Jaccodine, C.W. Pearce [ in *Defects in Si* Eds. W.M. Bullis, L.C. Kimerling (The Electrochemical Society, Pennington, NJ, USA, 1983) p.115-9 ]
- [2] H.M. Liaw [ in *Handbook of Semiconductor Si Technology* Eds. W.C. O'Mara, R.B. Herring, L.P. Hunt (Noyes Publications, Park Ridge, NJ, USA, 1990) ]
- [3] T. Nozaki, Y. Yatsurugi, N. Akiyama [ *J. Electrochem. Soc. (USA)* vol.117 (1970) p.1566 ]
- [4] H.M. Liaw [ *Microelectron. J. (UK)* vol.12 (1981) p.33 ]
- [5] R.W. Series, K.G. Barraclough [ *J. Cryst. Growth (Netherlands)* vol.60 (1982) p.212 ]
- [6] J. Leroueille [ *Phys. Status Solidi A (Germany)* vol.67 (1981) p.177 ]
- [7] B.O. Kolbesen, A. Muhlbauer [ *Solid-State Electron. (UK)* vol.25 (1982) p.759 ]
- [8] H. Foll, U. Gosele, B.O. Kolbesen [ *J. Cryst. Growth (Netherlands)* vol.49 (1977) p.90 ]

## 9.6 Segregation coefficient, solubility and IR absorption of C in c-Si

- [9] K.G. Barracough, J.G. Wilkes [ in *Semiconductor Si 1986* Eds. H.R. Huff, T. Abe, B. Kolbesen (The Electrochemical Society, Pennington, NJ, USA, 1986) ]
- [10] R.C. Newman, J.B. Willis [ *J. Phys. Chem. Solids (UK)* vol.26 (1965) p.373 ]
- [11] W.M. Bullis [ in *Handbook of Semiconductor Si Technology* Eds. W.C. O'Mara, R.B. Herring, L.P. Hunt (Noyes Publications, Park Ridge, NJ, USA, 1986) ]
- [12] N. Inoue, T. Arai, T. Nozacki, R. Endo, K. Mizuma [ in *Emerging Semiconductor Technology ASTM STP 960* Eds. D.C. Gupta, P.H. Langer (American Society for Testing and Materials, Philadelphia, PA, USA, 1986) ]
- [13] T. Nozacki, Y. Yatsurugi, N. Akiyama, Y. Endo, Y. Makida [ *J. Radioanal. Chem. (Switzerland)* vol.19 (1974) p.109 ]
- [14] A.R. Bean, R.C. Newman [ *J. Phys. Chem. Solids (UK)* vol.32 (1971) p.1211 ]
- [15] R.C. Newman, R.S. Smith [ *J. Phys. Chem. Solids (UK)* vol.30 (1969) p.1493 ]
- [16] [ *ASTM Method F 123-81*, Philadelphia, PA, USA (1981) ]
- [17] J.L. Regolini, J.P. Stoguert, C. Ganter, P. Siffert [ *J. Electrochem. Soc. (USA)* vol.133 (1986) p.2165 ]
- [18] C.S. Chen, D.K. Schroder [ *Phys. Rev. B (USA)* vol.35 (1987) p.713 ]
- [19] L. Canham [ in *Properties of Si* EMIS Datareview Series no.4 (INSPEC, IEE, London, UK, 1988) ]
- [20] B.O. Kolbesen [ in *Aggregation Phenomena of Point Defects in Silicon* Eds. E. Sirtl, J. Goorissen (Electrochemical Society, Pennington, NJ, USA, 1983) p.155-175 ]

## 9.7 Diffusion of C in c-Si

K.G. Barraclough and R.C. Newman

March 1997

### A INTRODUCTION

Carbon impurity atoms occupying substitutional lattice sites are commonly found in single crystal silicon grown from either the melt (e.g. Czochralski (CZ) and floating-zone (FZ) silicon) or from the vapour phase (e.g. chemical vapour phase epitaxy and molecular beam epitaxy). The diffusion coefficient ( $D_c$ ) and the diffusion mechanism of carbon control the rate and type of defects formed during the high temperature heat treatments required for device processing. Diffusion coefficient data are available for the temperature range from 800°C to 1400°C and, in general, independent investigations using different techniques are in good agreement. Published data have been obtained for dislocation-free Si, plastically deformed Si, CZ material and FZ crystals, but these variations do not lead to changes in  $D_c$  for the temperature range quoted. However, diffusion in a phosphorus ambient enhances  $D_c$ , while there is an indication that a nitrogen ambient reduces  $D_c$ .

Substitutional carbon atoms are ejected into bonded interstitial sites ( $C_i$ ) when they capture a rapidly diffusing self-interstitial (I-atom) produced by the displacement of lattice atoms by high energy irradiation (e.g. electron irradiation, neutron irradiation or ion implantation, etc.) or by the precipitation of  $\text{SiO}_2$  particles in CZ Si. The carbon interstitial may be present in a negative, neutral or positive charge state, depending upon the position of the Fermi level. These centres are highly mobile above room temperature and form complexes with remaining substitutional carbon, oxygen, boron and various other impurity atoms. The rapid diffusion of  $C_i$  leads to an explanation of the diffusion of substitutional carbon  $C_s$  at high temperatures in terms of a kick-out or a Frank-Turnbull dissociative mechanism.

### B EXPERIMENTAL RESULTS

Newman and Wakefield [1] determined  $D_c$  in dislocated, high resistivity (100  $\Omega$  cm) CZ Si using a radio-tracer technique with either barium carbonate or acetylene as a source of  $^{14}\text{C}$ . Silicon carbide ( $\text{Si}^{14}\text{C}$ ) was formed on the sample surface as a result of the reactions in sealed silica tubes containing the  $^{14}\text{C}$  source. Diffusion temperatures ranged from 1070 to 1402°C. Surface concentrations of  $^{14}\text{C}$  were measured directly using a Geiger counter, after removal of successive layers by grinding. Heating times were chosen to give measurable counting rates to depths of at least 60  $\mu\text{m}$ , thereby avoiding near-surface effects. Experiments with acetylene were considered to be more liable to error because of its low activity. Spurious data to a depth of 15  $\mu\text{m}$  from the original surface were observed for measurements with either source as a result of incomplete removal of small amounts of silicon carbide formed by the reaction with the source.

Experimental values are reproduced in TABLE 1, where it is seen that the data obtained by using acetylene as a source were in good agreement with corresponding measurements using  $\text{CO}_2$  derived from barium carbonate, despite the limitations described above. The data were re-analysed by Newman and Wakefield [2] to give:

$$D_c = 1.9 \exp [(-3.1 \pm 0.2) \text{ eV}/kT] \text{ cm}^2 \text{ s}^{-1}$$

## 9.7 Diffusion of C in c-Si

TABLE 1 Diffusion coefficient data for carbon in silicon.

Ref	Temp.	Time (hr)	Diffusion coefficient ( $\text{cm}^2 \text{s}^{-1}$ )	Anneal conditions
[1]	1402	1	$6.3 \times 10^{-10}$	$^{14}\text{C}$ in-diffusion <sup>#</sup>
[1]	1402	1	$7.1 \times 10^{-10}$	"
[1]	1390	3	$3.7 \times 10^{-10}$	"
[1]	1390	3	$3.0 \times 10^{-10}$	
[1]	1375	2	$3.9 \times 10^{-10}$	"
[1]	1350	3.9	$3.5 \times 10^{-10}$	"
[1]	1320	7.0	$2.1 \times 10^{-10}$	"
[1]	<sup>+</sup> 1314	10.2	$2.2 \times 10^{-10}$	
[1]	1314	15.8	$1.7 \times 10^{-10}$	"
[1]	1264	25	$1.2 \times 10^{-10}$	"
[1]	1264	24	$1.3 \times 10^{-10}$	"
[1]	*1250	43	$5.0 \times 10^{-11}$	"
[1]	1231	26	$5.6 \times 10^{-11}$	"
[1]	1210	64	$3.0 \times 10^{-11}$	"
[1]	1210	64	$2.4 \times 10^{-11}$	"
[1]	*1200	112	$2.6 \times 10^{-11}$	"
[1]	*1200	112	$2.2 \times 10^{-11}$	"
[1]	1150	168	$1.5 \times 10^{-11}$	"
[1]	1150	168	$1.7 \times 10^{-11}$	"
[1]	<sup>+</sup> 1109	309	$6.6 \times 10^{-12}$	"
[1]	<sup>+</sup> 1109	309	$5.2 \times 10^{-12}$	"
[1]	1109	309	$4.8 \times 10^{-12}$	"
[1]	1109	309	$9.1 \times 10^{-12}$	"
[1]	1070	403	$3.0 \times 10^{-12}$	"
[1]	1000	4	$5 \times 10^{-13}$	Nitrogen ambient
[5]	1000	2.5	$1.2 \times 10^{-12}$	Oxygen ambient
[5]	1000	0.66	$6 \times 10^{-12}$	Phosphorus ambient
[4]	900	2.66	$3 \times 10^{-14}$	Nitrogen ambient
[5]	900	20	$6 \times 10^{-14}$	Nitrogen ambient
[4]	900	2.66	$9 \times 10^{-14}$	Oxygen ambient
[4]	900	9.33	$9 \times 10^{-14}$	Oxygen ambient
[5]	900	20	$1.5 \times 10^{-13}$	Oxygen ambient
[5]	900	0.66	$2 \times 10^{-12}$	Phosphorus ambient
[4]	900	2.66	$1.3 \times 10^{-12}$	Phosphorus ambient
[5]	900	8	$0.4 \times 10^{-12}$	Phosphorus ambient
[4]	900	9.33	$0.6 \times 10^{-12}$	Phosphorus ambient
[5]	800	108	$6 \times 10^{-16}$	Nitrogen ambient
[5]	800	141	$1.4 \times 10^{-15}$	Nitrogen ambient
[5]	800	141	$7 \times 10^{-15}$	Oxygen ambient
[5]	800	7	$7 \times 10^{-14}$	Phosphorus ambient
[5]	800	88	$4 \times 10^{-15}$	Phosphorus ambient

<sup>+</sup> Plastically deformed prior to heating.

\* Experiments with acetylene as  $^{14}\text{C}$  source.

#Note:  $^{14}\text{C}$  in-diffusion was from  $\text{Si}^{14}\text{C}$  produced by decomposition of  $\text{Ba}^{14}\text{CO}_3$  in sealed silica tubes.

Gruzin et al [3] carried out similar experiments to those of Newman and Wakefield [1,2], using  $\text{Ba}^{14}\text{CO}_3$  as the source of  $^{14}\text{C}$ . High resistivity, dislocated ( $5 \times 10^4 \text{ cm}^{-2}$ ), n-type, low oxygen, FZ Si

## 9.7 Diffusion of C in c-Si

samples were used. Only four temperatures were investigated between 950 and 1100°C. The data were not tabulated, although it was stated that they were in close agreement with the earlier work.

More recently, Rollert et al [4] also carried out a large number of in-diffusion measurements. They used dislocation-free, plastically deformed, FZ, CZ (oxygen concentration of  $9 \times 10^{17} \text{ cm}^{-3}$ ), and pre-annealed CZ Si samples.  $^{14}\text{C}$  diffusion was from  $\text{CO}_2$  released from  $\text{BaCO}_3$  or from  $^{14}\text{C}$  graphite powder deposited on to the sample surface. The two procedures led to error function complement profiles and Gaussian distributions respectively. Values of  $D_c$  determined from these data were essentially identical to those reported in [1,2], and the quoted values of  $D_c$  were given by:

$$D_c = (0.95_{-0.33}^{+0.51}) \exp [(-3.04 \pm 0.05) \text{ eV}/kT] \text{ cm}^2 \text{ s}^{-1}$$

This study therefore extended the measurements to lower temperatures by 150°C.

It is known that the diffusion rate of substitutional dopant impurities in Si can be modified by the presence of excess vacancies (V) or I-atoms and a similar dependence was expected for the diffusion of  $\text{C}_s$  atoms. This dependence was considered in a series of papers [5–7]. Secondary ion mass spectrometry (SIMS) measurements of the carbon out-diffused profiles for high carbon dislocated ( $10^4\text{--}10^5 \text{ cm}^{-2}$ ) CZ Si crystals were made by Kalejs et al [5] who observed an enhanced diffusivity at 900°C after annealing samples in phosphine compared with nitrogen. This enhancement was attributed to the interactions of  $\text{C}_s$  atoms with I-atoms generated by the in-diffusion of phosphorus. Any small reduction in  $D_c$  in samples heated in  $\text{N}_2$  gas could be due to the injection of vacancies at the surface that would reduce the local equilibrium concentration of I-atoms.

In a later paper, Ladd et al [6] extended their studies [5] to include carbon-rich dislocated ( $10^6\text{--}10^7 \text{ cm}^{-2}$ ) silicon ribbon (low-oxygen) samples grown by the edge-defined film fed growth technique. Three different ambients at 900°C were also used, namely nitrogen, oxygen and phosphorus. Diffusion coefficient enhancement over the value for the nitrogen anneal was by a factor of 3 during oxidation and a factor of 40 during phosphorus in-diffusion.

In fitting the experimental data to theoretical out-diffusion plots, it was assumed that the equilibrium surface concentration was  $5 \times 10^{14} \text{ atoms cm}^{-3}$ , the equilibrium solubility at 900°C [8]. TABLE 1 includes the data from [6] and it is seen that an extended 9.33 hr phosphorus-anneal differs significantly from a 2.66 hr phosphorus-anneal, presumably due to the decrease in the generation rate of interstitials for the longer anneal.

The studies in [5] and [6] were extended in [7] by investigating different temperatures between 800 and 1100°C. Anneal times were chosen at each temperature to give an out-diffusion profile of at least 1  $\mu\text{m}$ , so that it could be readily measured by SIMS. At 1000°C, the nitrogen ambient produced the same results as an argon ambient. The diffusion data for the nitrogen anneals, phosphorus anneals and oxidations, (TABLE 1), converge at temperatures above about 1100°C, as expected if the self-interstitial supersaturation ratios for oxidation and phosphorus diffusions decrease with increasing temperature. If the original data in [1,2] are extrapolated below 1100°C then, within experimental error, they are in agreement with both nitrogen and oxygen-ambient data in [7]. The maximum diffusion enhancement of approximately a factor of 70 was observed for phosphorus diffusions at 800°C [7] (TABLE 1).

The identification and calibration of infrared (IR) vibrational lines at 922 and 932  $\text{cm}^{-1}$  for neutral interstitial  $\text{C}_i$  atoms produced by e-irradiation of carbon doped Si at a nominal 77 K (Bean and Newman [9]) led to a procedure to determine the diffusion coefficient  $D_{\text{CI}}$  of interstitial carbon atoms.

## 9.7 Diffusion of C in c-Si

High resistivity ( $500 \Omega \text{ cm}$ ) FZ crystals containing carbon at a concentration  $[C_s] = 2 \times 10^{17} \text{ cm}^{-3}$  were irradiated with 2 MeV electrons to cause a loss of  $\Delta[C_s] = 3 \times 10^{16} \text{ cm}^{-3}$ . On annealing at a temperature in the range 297–331 K, the  $C_i$  atoms diffused and were trapped by remaining  $C_s$  atoms that were assumed to have a capture radius of 10 Å. Since  $[C_i] = \Delta[C_s]$  was significantly smaller than ( $[C_s] - \Delta[C_s]$ ), first order kinetics were assumed and then verified by the measurements. Values of  $D_{Ci}$  were obtained with the further assumption that  $C_i$  atoms were not trapped and lost at vacancy-related radiation centres (Tipping and Newman [10]).

The  $C_i$  defect is, in reality, a bonded structure, known as a split-interstitial so that a  $C_i$  and a Si atom share one lattice site with the two atoms aligned along one of the three  $<001>$  directions (Watkins and Brower [11]). The  $C_i^+$  and  $C_i^-$  centres both show electron paramagnetic resonance (EPR) spectra with  $C_{2v}$  symmetry [11,12]. Alignment of a particular  $[001]$  axis can be achieved at low temperatures by the application of a uniaxial stress and the time constant  $\tau_0$  for the loss of this alignment during an isothermal anneal can then be determined by EPR when the stress is removed. For the temperature range 211 to 222 K, Watkins and Brower [11] found values of  $\tau_0$  for  $C_i^+$  of  $1.1 \times 10^{-16} \text{ s}$  and  $E = 0.88 \text{ eV}$  compared with

$$\tau_0 = 1.6 \times 10^{-15} \exp(0.80 \text{ eV/kT}) \text{ s}$$

obtained by Song and Watkins [12]. Equivalent data for  $C_i^-$  gave [12]

$$\tau_0 = 3 \times 10^{-16} \exp(0.77 \text{ eV/kT}) \text{ s}$$

from EPR measurements but a higher value of  $E = 0.85 \text{ eV}$  was obtained from DLTS measurements (Benton et al [13]). EPR measurements cannot be made for the neutral defect. However, it is apparent that the diffusion barrier is hardly changed when the charge state of the  $C_i$  defect is changed. Tipping and Newman [10] therefore combined IR and EPR data for  $C_i^+$  to obtain the diffusion coefficient:

$$D_i = 0.44 \exp(-0.87 \text{ eV/kT}) \text{ cm}^2 \text{ s}^{-1}$$

over 7 orders of magnitude. Later measurements of Chappell et al [14] yielded an activation energy of  $0.86 \pm 0.01 \text{ eV}$ .

In the  $C_i$ -limited mode of both the kick-out and the dissociative mechanism of diffusion, we have:

$$D_{i(\text{eff})} = [C_i]_{\text{eq}} D_i / [C_s]_{\text{eq}}$$

as discussed in [4]. Combining the data for  $D_i$  with the value of  $D_s = D_{i(\text{eff})}$ , we find

$$[C_i]_{\text{eq}} / [C_s]_{\text{eq}} = 2.16 \exp(-2.17 \text{ eV/kT})$$

in agreement with the observations that the overwhelming majority of carbon atoms occupy substitutional sites in as-grown silicon. Further data and discussion are given by Davies and Newman [15].

## C CONCLUSION

Carbon is commonly found on substitutional sites in all forms of single crystal silicon. Diffusion data exist for temperatures from 800 to 1400°C, where values are independent of the type of silicon. Enhanced diffusion is seen in phosphorus-doped material, but nitrogen may decrease the diffusion

rate. Interstitial carbon atoms capture self-interstitials (from irradiation or implantation or SiO<sub>2</sub> precipitation). These highly mobile bonded interstitials diffuse by a kick-out or a Frank-Turnbull dissociative mechanism.

## REFERENCES

- [1] R.C. Newman, J. Wakefield [ *J. Phys Chem Solids (UK)* vol.19 (1961) p.230-4 ]
- [2] R.C. Newman, J. Wakefield [ in *Metallurgy of Semiconductor Materials* Ed. J.B. Schroeder (Interscience, New York, 1962) vol.15 p.201-8 ]
- [3] P.L. Gruzin, S.V. Zemskii, A.D. Bulkin, N.M. Makarov [ *Sov. Phys.-Semicond. (USA)* vol.7 (1974) p.1241 ]
- [4] F. Rollert, N.A. Stolwijk, H. Mehrer [ *Mater. Sci. Forum (Switzerland)* vol.38-41 (1989) p.753-8 ]
- [5] J.P. Kalejs, L.A. Ladd, U. Gösele [ *Appl. Phys. Lett. (USA)* vol.45 (1984) p.268-9 ]
- [6] L.A. Ladd, J.P. Kalejs, U. Gösele [ *Mater. Res. Soc. Symp. Proc. (USA)* vol.36 (1985) p.89-94 ]
- [7] L.A. Ladd, J.P. Kalejs [ *Mater. Res. Soc. Symp. Proc. (USA)* vol.59 (1986) p.445-50 ]
- [8] A.R. Bean, R.C. Newman [ *J. Phys. Chem. Solids (UK)* vol.32 (1971) p.1211-9 ]
- [9] A.R. Bean, R.C. Newman [ *Solid State Commun. (USA)* vol.8 (1970) p. 175-7 ]
- [10] A.K. Tipping, R.C. Newman [ *Semicond. Sci. Technol. (UK)* vol.2 (1987) p. 315-7 ]
- [11] G.D. Watkins, K.L. Brower [ *Phys. Rev. Lett. (USA)* vol.36 (1976) p. 1329-32 ]
- [12] L.W. Song, G.D. Watkins [ *Phys. Rev. B. (USA)* vol.42 (1990) p.5759-64 ]
- [13] J.L. Benton, M.T. Asom, R. Sauer, L.C. Kimerling [ *Mater. Res. Soc. Symp. Proc. (USA)* vol.104 (1988) p.85-91 ]
- [14] S.P. Chappell, G. Davies, E.C. Lightowers, R.C. Newman [ *Mater. Sci. Forum (Switzerland)* vol.38-41 (1989) p.481-5 ]
- [15] G. Davies, R.C. Newman [ *Carbon in Monocrystalline Silicon: Handbook on Semiconductors* vol.3, Eds. T. S. Moss, S. Mahajan (Elsevier, 1994) p.1557-635 ]

## CHAPTER 10

### DOPANTS IN SILICON (*Edited by K. Jones*)

- 10.1 Diffusion of Al, Ga, In and Tl in c-Si
- 10.2 Diffusion of P, As and Sb in c-Si
- 10.3 Boron-interstitial clustering in c-Si
- 10.4 Solubility of B, Al, Ga, In, Tl, P, As and Sb in c-Si
- 10.5 Ion implantation of B and P in c-Si

## 10.1 Diffusion of Al, Ga, In and Tl in c-Si

D. de Cogan and Y.M. Haddara (Updated by K. Jones)

October 1998

### A INTRODUCTION

This Datareview presents data on the diffusion behaviour of the acceptors Al, Ga, In and Tl in crystalline silicon. A range of impurity sources and diffusion conditions have been employed for each of the impurities considered. Sequential diffusions of acceptor and donor impurities are also described. Both silicon oxide and nitride have been used as mask materials during diffusion processes and the advantages/disadvantages of each are outlined

### B DIFFUSION OF Al IN c-Si

The interest in aluminium as an impurity arises from the fact that it diffuses faster than other acceptors. The solubility limit is, in most cases, low, which reduces dislocation formation and there is no evidence of intermetallic reactions with the host element.

The diffusion properties can be characterised by either monitoring junction depth (using a bevel and stain technique) or by means of a complete profile determination. The standard method which was used by Fuller and Ditzenberger [B1] consists of measuring sheet resistance again. Other techniques, such as Hall effect and spreading resistance, are sometimes used.

The early studies of aluminium diffusion were the subject of much controversy. Values of diffusion constant differed by up to two orders of magnitude. TABLE B1 provides data on the pre-exponential and activation terms in  $D = D_0 \exp(-E/kT)$  quoted by different authors. The diffusion constant at 1200°C is given for the purposes of comparison.

TABLE B1 Diffusion parameters for Al in Si.

$D_0$ (cm <sup>2</sup> /s)	E (eV)	D (1200°C)	Ref
8	3.47	$9.24 \times 10^{-12}$	[B1]
2800	3.8	$1.28 \times 10^{-10}$	[B2]
4.8	3.36	$1.58 \times 10^{-11}$	[B3]
0.5	3.0	$2.74 \times 10^{-11}$	[B4]
1.38	3.41	$3.00 \times 10^{-12}$	[B5]
1.8	3.2	$2.04 \times 10^{-11}$	[B6]

These differences were largely due to the nature of the impurity sources and diffusion conditions. Fuller and Ditzenberger [B1] used aluminium metal in an evacuated sealed tube. Goldstein [B2] placed an aluminium silicon button on top of the silicon substrate within an evacuated sealed tube. Miller and Savage [B3] attempted to avoid any reaction between the quartz tube and the samples. Accordingly, the substrate and source were placed inside a silicon boat held within a tantalum tube which acted as a getter. The assembly was heated in an open arrangement using helium or argon at the rate of 2.5 l/min. Navon and Chernyshov [B7] have re-examined Goldstein's [B2] work and obtained results which are more in line with those of Fuller and Ditzenberger [B1]. Klein [B8] has evaporated and alloyed aluminium into silicon. Diffusion was then performed from the alloy front. The results

## 10.1 Diffusion of Al, Ga, In and Tl in c-Si

were reported to confirm Goldstein's values. Ghoshtagore [B5] has deposited an aluminium rich epitaxial layer as the diffusing source. Trimethyl aluminium was used in the epilayer. There have been several other suggestions for diffusion sources. Chang and Roesch [B9], in a German patent, propose using aluminium coated wafers in an open tube as a vapour source. In a European patent application Chang et al [B10] suggest that aluminium oxide or sapphire could be used as a source in an open tube with argon or hydrogen as the ambient. Nisnevich [B11] has used aluminium doped silica in an open tube and has obtained a value of  $D = 3.01 \times 10^{-11} \text{ cm}^2/\text{s}$  at  $1250^\circ\text{C}$ .

Bullough et al [B12] have shown that the free energies for the formation of silica and alumina are such that any aluminium coming into contact with silica will bring about a redox reaction: silica is reduced and aluminium is oxidised. They suggest therefore that the silica tube makes a significant contribution. Rai-Choudhury et al [B13] presented thermochemical data to show the effect of silica and water vapour during aluminium diffusion. The aluminium partial pressure is reduced and the formation of a stable alumina skin seals the source. They have shown that if residual water vapour can be reduced to less than 0.01 ppm then liquid aluminium and solid alumina can co-exist and a lower diffusion temperature is favoured. This minimises source oxidation. If, however, a quartz diffusion system has a high vapour content then a high diffusion temperature is preferred, although the source will oxidise and lead to reproducibility problems. They suggest the use of alumina or zirconia boats and point to the fact that Kao [B4] obtained an aluminium surface concentration close to the solubility limit by allowing his quartzware to be passivated by the formation of a layer of silicon and alumina prior to diffusion. The use of passivation is recommended. Rosnowski [B6] has used passivated quartz in an open tube, high vacuum system. The absence of argon as a carrier or backfill gas raises the aluminium partial pressure. He found that a metallic source tended to cause sample degradation due to alloying on the substrate surface. For this reason the use of a silicon-aluminium alloy source was recommended. There is the added advantage that in an alloyed source it is not possible for an impervious oxide skin to form. This might explain why Goldstein [B2] obtained a larger value for the diffusion coefficient than many other workers at that time.

The effects of subsequent oxidation on the diffusion of aluminium in silicon have been studied by Mizuo and Higuchi [B14]. In the range  $950\text{--}1150^\circ\text{C}$  diffusion in (100) silicon is enhanced. The diffusion in (111) silicon is enhanced at low temperatures and retarded at high temperatures. These effects are totally inhibited by the addition of HCl to the oxidising ambient.

The reaction between aluminium and oxide normally inhibits the use of silica as a mask. However, Rosnowski [B15], in a US patent, describes how a  $4 \mu\text{m}$  layer of silica can be used for selective masking. The reaction to form silicon and alumina on the silica surface effectively masks against aluminium diffusion. The method proposed by Jayant-Baliga [B16] involves the use of silicon nitride. As interfacial stresses can lead to cracking in nitride films a multilayer mask is recommended.  $100\text{--}2000 \text{ \AA}$  of silica are grown on the silicon surface. A layer of nitride is deposited on top of this ( $500\text{--}3000 \text{ \AA}$ ) and that is followed by  $1500 \text{ \AA}$  of CVD silicon oxide. Diffusion depths of up to  $35 \mu\text{m}$  were achieved at  $1250^\circ\text{C}$ . Although the cover oxide (necessary for gallium diffusions) was attacked, there was no evidence of reaction between the dopant and the nitride layer. The ratio of lateral diffusion depth to junction depth was unity.

In their work on the effects of oxidation on aluminium diffusion Mizuo and Higuchi [B14] used a pre-deposit of  $10^{15} \text{ cm}^{-2}$  aluminium implanted at 150 keV. Leroy et al [B17] have used a  $10^{15} \text{ cm}^{-2}$  100 keV implant as a preliminary to their study of diffusion of aluminium in silicon by semi-continuous laser annealing. The diffusion constant was similar to that reported by others and an activation energy of 3.4 eV was observed. Baranova et al [B18] describe the technique of transmission ion (recoil atom) bombardment of thin films of aluminium.  $2.3 \times 10^{15} \text{ cm}^{-2}$  50 keV argon ions were used and a diffusion constant of  $4.5 \times 10^{14} \text{ cm}^2/\text{s}$  was measured following a one hour anneal at  $800^\circ\text{C}$ .

## REFERENCES TO SECTION B

- [B1] C.S. Fuller, J.A. Ditzenberger [ *J. Appl. Phys. (USA)* vol.27 (1956) p.544 ]
- [B2] B. Goldstein [ *Bull. Am. Phys. Soc. Ser. II (USA)* vol.1 (1956) p.145 ]
- [B3] R.C. Miller, A.J. Savage [ *J. Appl. Phys. (USA)* vol.27 (1956) p.1430 ]
- [B4] Y.C. Kao [ *Electro-Technol. (USA)* vol.5 (1967) p.90 ]
- [B5] R.N. Ghoshtagore [ *Phys. Rev. B (USA)* vol.3 (1971) p.2507 ]
- [B6] W. Rosnowski [ *J. Electrochem. Soc. (USA)* vol.125 (1978) p.957-62 ]
- [B7] D. Navon, V. Chernyshov [ *J. Appl. Phys. (USA)* vol.28 (1957) p.823 ]
- [B8] T. Klein [ *Mullard Research Labs. (UK) Rp8-28 CVD Annual Report December 1962 (W) AD 295065* ]
- [B9] M.F. Chang, A. Roesch [ German Patent 2 932 432 (20 March 1980) ]
- [B10] M.F. Chang, R.F. Kennedy, D.K. Hartmann, A. Roesch, H.B. Assalit [ European Patent Application 19 272 (26 November 1980) p.272 ]
- [B11] Ya.D. Nisnevich [ *Izv. Akad. Nauk. SSSR Neorg. Mater. (Russia)* vol.19 (1983) p.853-6 ]
- [B12] R. Bullough, R.C. Newman, J. Wakefield [ *Proc. IEE (UK)* no.106B (1959) p.277 ]
- [B13] P. Rai-Choudhury, R.A. Selim, W.J. Takei [ *J. Electrochem Soc. (USA)* vol.124 (1977) p.762-6 ]
- [B14] S. Mizou, H. Higuchi [ *Jpn. J Appl. Phys. (Japan)* vol.21 (1982) p.56-60 ]
- [B15] W. Rosnowski [ US Patent 4 029 528 (12 June 1977) ]
- [B16] B. Jayant-Baliga [ *J. Electrochem Soc. (USA)* vol.126 (1979) p.292-6 ]
- [B17] C. Leroy, J.E. Bouree, M. Rodot [ *J. Phys. Colloq. (France)* vol.44 (1983) p.235-40 ]
- [B18] A.S. Baranova, D.I. Tetel'baum, E.I. Zorin, P.V. Pavlov, E.V. Dobrokhotov, A.K. Kuritsyna [ *Sov. Phys.-Semicond. (USA)* vol.7 (1974) p.1151-3 ]

## C DIFFUSION OF Ga IN c-Si

The earliest studies of diffusion of gallium in silicon were carried out by Fuller and Ditzenberger [C1] using a sealed tube arrangement. Characterisation was undertaken using successive lapping and sheet resistance measurements. It was found that the diffusion constant could be described by

$$D = 3.6 \exp(-3.5 \text{ eV}/kT) \text{ cm}^2/\text{s}$$

in the range 1105–1360°C. Gallium (III) oxide was used as the source. Frosch and Derick [C2] used an open tube system with a similar source and wet hydrogen as the carrier gas. Kurtz and Gravel [C3] employed metallic gallium in an open tube system with argon. It was found that the diffusion constant was dependent on the dopant concentration. Diffusion from a radioactive metallic source was first studied by Kren et al [C4]. Makris and Masters [C5] have used gallium doped silicon powder as a source in sealed tube experiments at 900–1050°C. It was found that the diffusion coefficient of gallium in boron doped silicon increased linearly with boron concentration at boron levels below about  $10^{19} \text{ cm}^{-3}$ . They found that the diffusion coefficient fitted the expression

$$D = 60 \exp(-3.89 \text{ eV}/kT) \text{ cm}^2/\text{s}$$

Sordevall et al [C30] performed tracer diffusion studies using SIMS, in the temperature range 850–1150°C and reported

$$D = 6.5 \exp(-3.59 \pm 0.1 \text{ eV}/kT) \text{ cm}^2/\text{s}$$

### *10.1 Diffusion of Al, Ga, In and Tl in c-Si*

Boltaks and Dzhafarov [C6] have heat treated antimony doped wafers in an atmosphere of gallium vapour in the range 1180–1340°C, and found that the presence of antimony accelerated the diffusion of gallium compared with control samples where  $D = 2.1 \exp(-3.51 \text{ eV}/kT)$ . According to Nakajima and Ohkawa [C7] the simultaneous diffusion of gallium and phosphorus into silicon is retarded by the presence of arsenic vapour in the range 1000–1150°C. They attribute this to the interactions between the internal electric fields of the impurities. No interaction between phosphorus and gallium was observed in the absence of arsenic. The interactions between sequential gallium-arsenic diffusions in silicon have been studied by Jones and Willoughby [C8], who have also compared sequential gallium-arsenic diffusions with sequential gallium-phosphorus diffusions [C9]. They found that at high concentration phosphorus enhanced the gallium diffusion. The effects of arsenic (enhancement or retardation) depended on the experimental conditions. This is largely in accord with the work of Okamura [C10] who has, however, noted [C11] that profiles determined by neutron activation analysis give higher gallium concentrations than that suggested by standard lapping/resistance techniques. This effect is attributed to gallium precipitation during cooling.

The effect of the diffusion source has received considerable attention. Fuller and Ditzenberger [C1] used the tri-valent oxide. The wet-hydrogen technique of Frosch and Derick [C2] is thought to involve the reduction of gallium oxide to the more volatile gallium (I) oxide. This has been the subject of a German patent by Popp and Held [C12]. Ghoshtagore [C13] has a German patent for a two-zone heat treatment of gallium (II) oxide in an open tube system involving a stream of argon and carbon monoxide. He has shown [C14] that wet carbon monoxide leads to a reduction of the oxide so that metallic gallium is the volatile species. He has also shown [C15] that the presence of traces of oxygen can have profound effects on the diffusion of gallium. For this reason he has grown a gallium-rich epitaxial layer on clean silicon. He quotes an intrinsic bulk diffusion coefficient  $D = 0.374 \exp(-3.39 \text{ eV}/kT)$ . It is suggested that the bulk diffusion occurs by acceptor–vacancy pair formation and migration. The correlation between activation energy and covalent radius for gallium is in agreement with the results for other acceptors. Gallium can also be diffused from a composite source consisting of gallium and 60% gallium (III) oxide formed by the thermal decomposition of gallium acetylacetone at 400°C in 10 mtorr of oxygen [C16]. Haridos et al [C17] have performed sealed tube measurements using pure gallium metal in the range 700–1100°C. They have found that the diffusion coefficient is given by  $D = 0.05 \exp(-2.7 \text{ eV}/kT)$  which is significantly less than the previously quoted values. The difference is attributed to the absence of intrinsic effects in their experiments, which is consistent with the observations of Ghoshtagore [C15].

Martin and Reuschel [C18] have outlined a technique for obtaining a uniform distribution of gallium impurity by neutron irradiation of a mixed crystal of silicon containing less than 10% germanium.

It has been found that silica is ineffective for masking silicon during gallium diffusion [C2,C19]. Gallium diffuses faster in silica than in silicon. Diffusion studies of gallium in silica have been undertaken by Grove et al [C20]. Nakajima and Ohkawa [C21] have studied the effect of silicon crystal orientation on gallium diffusion through an oxide layer. Junction depths were independent of oxide thickness in the range 500–5000 Å. Jain et al [C22] have compared diffusions into bare and oxide covered silicon. At 1035°C the junction depth under oxide exceeds that in bare silicon. They have shown that enhancement and retardation effects depend on the relative temperature of oxide formation and gallium diffusion. They propose a model based on strain gradients at the interface. The experimental observations have been confirmed by Mizuo and Higuchi [C23] who note that these effects are reduced by the addition of HCl to the oxidising ambient.

Silicon nitride has been suggested as a diffusion mask for gallium [C24]. However, Jayant-Baliga [C25] mentions that this is effective only for shallow diffusion. The nitride layer can either crack or react with the gallium so that it cannot be subsequently removed. To overcome this he proposes a

## 10.1 Diffusion of Al, Ga, In and Tl in c-Si

sandwich structure. A layer of oxide between the silicon and nitride inhibits cracking and a layer of oxide over the nitride prevents attack by gallium. Using this arrangement it has been possible to achieve junction depths of 275 µm. Dumas [C26] describes a modification of this approach in a US patent.

The effects of 45 keV gallium implantation (dose  $10^{15} \text{ cm}^{-2}$ ) have been studied by Bamo et al [C27]. An enhanced diffusion was observed at implant temperatures of 150–700°C. This was independent of temperature and rate over this range. Gyulai et al [C28] have implanted gallium at 80 keV. They used both CVD oxide and nitride as encapsulants. Almost all gallium diffused into the oxide and no snowplough effect was observed. With nitride there was very rapid gallium diffusion which was probably due to strain damage at the interface.

It has been observed that gold and copper are gettered during gallium diffusion [C29]. Gold is gettered regardless of the cooling conditions. Most copper near the surface layer is removed during diffusion. Bulk copper is gettered during slow cooling.

## REFERENCES TO SECTION C

- [C1] C.S. Fuller, J.A. Ditzenberger [ *J. Appl. Phys. (USA)* vol.27 (1956) p.544 ]
- [C2] C.J. Frosch, L. Derick [ *J. Electrochem. Soc. (USA)* vol.104 (1957) p.547 ]
- [C3] A.D. Kurtz, C.L. Gravel [ *J. Appl. Phys. (USA)* vol.29 (1958) p.1456 ]
- [C4] J.G. Kren, B.J. Masters, E.S. Wajda [ *Appl. Phys. Lett. (USA)* vol.5 (1964) p.49 ]
- [C5] J.S. Makris, B.J. Masters [ *J. Appl. Phys. (USA)* vol.42 (1971) p.3750 ]
- [C6] B.I. Boltaks, T.D. Dzhafarov [ *Sov. Phys.-Solid State (USA)* vol.5 (1964) p.2649 ]
- [C7] Y. Nakajima, S. Ohkawa [ *Jpn. J. Appl. Phys. (Japan)* vol.10 (1971) p.1745 ]
- [C8] C.L. Jones, A.F.W. Willoughby [ *Proc. Electrochem. Soc. (USA)* vol.77 (1977) p.684 ]
- [C9] C.L. Jones, A.F.W. Willoughby [ *Inst. Phys. Conf. Ser. (UK)* no.31 (1977) p.194 ]
- [C10] M. Okamura [ *Jpn. J. Appl. Phys. (Japan)* vol.7 (1968) p.1067 ]
- [C11] M. Okamura [ *Jpn. J. Appl. Phys. (Japan)* vol.10 (1979) p.434 ]
- [C12] G. Popp, G. Held [ German Patent 2 751 163 (17 May 1979) ]
- [C13] R.N. Ghoshtagore [ German Patent 2 644 879 (21 April 1977) ]
- [C14] R.N. Ghoshtagore [ *Solid-State Electron. (UK)* vol.22 (1979) p.877 ]
- [C15] R.N. Ghoshtagore [ *Phys. Rev. B (USA)* vol.3 (1971) p.2507-14 ]
- [C16] G. Mermant [ *3rd Colloq. Int. Appl. Tech. Vide. Ind. Semicond. Composants Electron. Microelectron (AVISEM 71)* (1971) p.72 ]
- [C17] S. Haridos, F. Beniere, M. Gauneau, A. Rupert [ *J. Appl. Phys. (USA)* vol.51 (1980) p.5833 ]
- [C18] J. Martin, K. Reuschel [ German Patent 2 407 697 (Sept 1975) ]
- [C19] F.K. Heumann, D.M. Brown, E. Mets [ *J. Electrochem Soc. (USA)* vol.115 (1968) p.99 ]
- [C20] A.S. Grove, O. Leistikko, C.T. Sah [ *J. Phys. Chem. Solids (UK)* vol.25 (1964) p.985 ]
- [C21] Y. Nakajima, S. Ohkawa [ *Jpn. J. Appl. Phys. (Japan)* vol.11 (1972) p.1742 ]
- [C22] G.C. Jain, A. Prasad, B.C. Chakravarty [ *Phys. Status Solidi A (Germany)* vol.46 (1978) p.151 ]
- [C23] S. Mizou, H. Higuchi [ *Denki Kagaku (Japan)* vol.50 (1982) p.338-43 ]
- [C24] V.Y. Doo [ *IEEE Trans. Electron. Devices (USA)* vol.ED-13 (1966) p.561 ]
- [C25] B. Jayant-Baliga [ *J. Electrochem Soc. (USA)* vol.126 (1979) p.292-6 ]
- [C26] G.H. Dumas [ US Patent 3 895 976 (22 July 1975) ]
- [C27] K. Bamo et al [ *Jpn. J. Appl. Phys. (Japan)* vol.12 (1973) p.735 ]
- [C28] J. Gyulai, L. Csepregi, T. Nagy, J.W. Mayer, H. Muller [ *Vide (France)* no.174 (1974) p.146 ]
- [C29] N. Momma, H. Taniguchi, M. Ura, T. Ogawa [ *J. Electrochem. Soc. (USA)* vol.125 (1975) p.963 ]

## 10.1 Diffusion of Al, Ga, In and Tl in c-Si

- [C30] U. Sordevall, M. Fiesel, A. Lodding [ *J. Chem. Soc. Faraday Trans. (UK)* vol.86 (1990) p.1293 ]

### D DIFFUSION OF IN IN c-Si

Fuller and Ditzenberger [D1] using a lap and sheet resistance technique have measured the diffusion coefficient of indium in silicon and find that it can be described by  $D = 16.5 \exp(-3.9 \text{ eV}/kT) \text{ cm}^2/\text{s}$ . Ghoshtagore [D2] has obtained  $D = 0.785 \exp(-3.63 \text{ eV}/kT) \text{ cm}^2/\text{s}$  using indium rich implanted layers and spreading resistance measurement. He has shown that most acceptors have an activation energy which is proportional to the impurity covalent radius. Indium fits this relationship very well and an indium–vacancy pair migration mechanism is proposed.

It had been thought that indium might constitute an alternative acceptor impurity for VLSI technology. For this reason much work has concentrated on the properties of implanted layers. To a first approximation the diffusion constant is the same as that of an ordinary diffusion in an inert atmosphere [D3]. However, at higher dose levels there are differences due to field aided diffusion [D4].

$$D (10^{13} \text{ cm}^{-2}) = 169 \exp(-4.19 \text{ eV}/kT)$$

$$D (10^{14} \text{ cm}^{-2}) = 204 \exp(-4.22 \text{ eV}/kT)$$

Gamo et al [D5] have observed that there is an enhanced diffusion of indium when the implantation temperature is in the range 250–700°C. The effect is independent of temperature and dose rate over the range and an interstitial diffusion mechanism is suggested.

Antoniadis and Moskowitz [D6] have compared the drive-in properties of implanted indium in dry nitrogen and dry oxygen. An oxygen enhanced diffusion is observed which at 1000°C is almost identical to that for boron. Cerofolini et al [D3] report that the segregation between silicon and oxide favours the former. In the initial stages, indium can be incorporated in the oxide because of the high growth rate compared with the low diffusivity. After that, a snowplough effect gives rise to indium accumulation at the silicon surface.

According to Schroder et al [D7] the determination of indium doping concentration by Hall measurements appears to give erroneously high results. Capacitance–voltage and junction breakdown techniques are more reliable.

### REFERENCES TO SECTION D

- [D1] C.S. Fuller, J.A. Ditzenberger [ *J. Appl. Phys. (USA)* vol.27 (1956) p.544 ]
- [D2] R.N. Ghoshtagore [ *Phys. Rev. B (USA)* vol.3 (1971) p.2507-14 ]
- [D3] G.F. Cerofolini, G.U. Pignateli, F. Riva, G. Ferla, G. Ottaviani [ *Thin Solid Films (Switzerland)* vol.101 (1983) p.137-44 ]
- [D4] G.F. Cerofolini, G. Ferla, G.U. Pignateli, F. Riva, [ *Thin Solid Films (Switzerland)* vol.101 (1983) p.275-83 ]
- [D5] K. Gamo et al [ *Jpn. J. Appl. Phys. (Japan)* vol.12 (1973) p.735 ]
- [D6] D.A. Antoniadis, I. Moskowitz [ *J. Appl. Phys. (USA)* vol.53 (1982) p.9214 ]
- [D7] D.K. Schroder, T.T. Braggins, H.M. Hobgood [ *J. Appl. Phys. (USA)* vol.49 (1978) p.5256-9 ]

## 10.1 Diffusion of Al, Ga, In and Tl in c-Si

### E DIFFUSION OF Tl IN c-Si

According to Shulman [E1] thallium is a deep acceptor in silicon. The energy level lies at 0.26 eV above the valence band. It has a very high vapour pressure at the melting point of silicon (it boils at 1490°C). Shulman encountered considerable problems in incorporating it into growing crystals.

There is only limited information available on the diffusion of thallium into silicon. Fuller and Ditzenberger [E2] have used the oxide as the source in evacuated sealed tube experiments. Profiles were obtained using successive lap and sheet resistance measurements. TABLE E1 summarises their results which can be described by the equation  $D = 16.5 \exp(-3.9 \text{ eV}/kT) \text{ cm}^2/\text{s}$ . Within the limits of their experimental error this is identical to the equation for indium.

TABLE E1 Diffusion data for Tl in Si.

T (°C)	D (cm <sup>2</sup> /s)
1360	$2.03 \times 10^{-11}$
1320	$1.2 \times 10^{-11}$
1255	$8.6 \times 10^{-12}$
1170	$5.0 \times 10^{-13}$
1105	$8.0 \times 10^{-14}$

Data from Fuller and Ditzenberger [E2]

Ghoshtagore [E3] has used a doped silicon epitaxial layer as a source. Unlike his work on gallium and aluminium, it was not possible to use an organo-thallium compound during epi-growth on account of its vapour pressure and stability. Accordingly, he used a 99.9999% pure metal source on the susceptor during growth. He was only able to determine the diffusion properties at a single value of surface concentration. Profiles were obtained using spreading resistance techniques. He estimated that the diffusion constant could be described by the equation  $D = 1.37 \exp(-3.7 \text{ eV}/kT) \text{ cm}^2/\text{s}$  in the range 1244–1338°C, which fits in well with his correlation between activation energy and impurity tetrahedral radius. Differences between his results and those of Fuller and Ditzenberger were attributed to oxidation-reduction reactions on the silicon surface.

Thallium has several oxides which may contribute in varying degrees to the dopant partial pressure over the diffusion temperature range 800–1350°C. According to [E4] thallium (+3) oxide decomposes to thallium (+1) oxide at 875°C (at atmospheric pressure). At 1080°C thallium (+1) oxide further decomposes to metallic thallium.

A recent study by Dedekaev et al [E5] estimates a very much higher activation energy, namely 4.62 eV. The reported pre-exponential factor is  $9.37 \times 10^{10} \text{ cm}^2/\text{s}$ . These results appear to be quite different from anything quoted previously and the authors do not offer any explanation.

### REFERENCES TO SECTION E

- [E1] R.G. Shulman [ *J. Phys. Chem. Solids (UK)* vol.2 (1957) p.115 ]
- [E2] C.S. Fuller, J.A. Ditzenberger [ *J. Appl. Phys. (USA)* vol.27 (1956) p.544 ]
- [E3] R.N. Ghoshtagore [ *Phys. Rev. B (USA)* vol.3 (1971) p.2507-14 ]
- [E4] [ *Handbook of Chemistry & Physics* 64<sup>th</sup> edn (CRC Press, 1983) p.B-147 ]
- [E5] T.T. Dedekaev, V.V. Eliseev, D.Kh. Lagkuev, V.A. Fidarov [ *Sov. Phys.-Solid State (USA)* vol.27 (1985) p.1699-700 ]

**F CONCLUSION**

Aluminium is the fastest diffusing of the commonly used acceptors in silicon. Oxidation and temperature both affect the diffusion coefficient. A silica/nitride multilayer can be used as a diffusion mask. Sequential diffusions of gallium and various dopant species show enhancement/retardation depending on donor species and experimental conditions. Again a mixed oxide/nitride layer can be used as a mask. Indium diffusion has been studied mainly in implanted layers. Various values for the diffusivity of Tl in silicon have been reported.

## **10.2 Diffusion of P, As and Sb in c-Si**

A.A. Brown, P.B. Moynagh, P.J. Rosser and Y.M. Haddara  
(Updated by K. Jones)

October 1998

### **A INTRODUCTION**

This Datareview describes the diffusion behaviour of the donors P, As and Sb in crystalline silicon. Diffusion occurs by donor/vacancy pairs and donor/interstitial pairs, and is hence complex in nature. For each impurity element the following sections outline the inert intrinsic situation and the more general case.

### **B DIFFUSION OF P IN c-Si**

#### **B1 Inert Intrinsic Phosphorus Diffusion**

The mathematical basis for the diffusion process was laid by Fick whose first law sets forward the hypothesis that the rate of transfer of a diffusing particle through unit area is proportional to the magnitude of the gradient normal to that area, i.e. in the x-direction

$$J = -D \frac{dC}{dx}$$

where the proportionality constant, D ( $m^2/s$ ), is known as the diffusion constant or the diffusivity. The diffusion process occurs because of the random walk of the impurity atoms and is therefore a thermally activated process. The temperature dependence of the diffusion coefficient is Arrhenius in nature:

$$D = D_0 \exp(-E/kT)$$

where E is the activation energy (which, for the common dopants in silicon, is about 4 eV).

Due to the low concentration of stable point defects in silicon, it has not been possible to determine directly whether vacancies or self-interstitials are dominant in diffusion processes. Numerous kinds of indirect observations have been made to build cases for vacancies and for self-interstitials. The current belief is that both types of point defect exist somewhat independently [B1] and that both influence diffusion. Under diffusive conditions where the silicon is intrinsically doped and where no surface reaction is taking place, the vacancy and self-interstitial concentrations are temperature dependent only and are described approximately by the equilibrium concentrations:

$$C_v^* = C_{ov} \exp(-E_v/kT)$$

$$C_i^* = C_{oi} \exp(-E_i/kT)$$

Dopant diffusion takes place in the silicon by interacting with these point defects so that the diffusing species are the phosphorus/vacancy pair, PV, and the phosphorus/Si-interstitial pair, PI. The intrinsic

## 10.2 Diffusion of P, As and Sb in c-Si

diffusivity due to the vacancy mechanism is referred to as  $D_V^*$  and that due to the interstitialcy mechanism as  $D_I^*$ . The intrinsic, inert ambient diffusivity is therefore given by the sum of the equilibrium diffusivities due to the vacancy and the self-interstitial components:

$$D^* = D_V^* + D_I^*$$

The wide energy range available to the Fermi level in silicon leads to a given lattice defect (i.e. a vacancy or Si-interstitial) appearing in a variety of ionised states [B2]. As such, the dopant/point-defect pairs exist as, for example,  $P^+V^-$  which we will denote by  $PV^-$ . The intrinsic, inert ambient diffusivity can therefore be written:

$$D^* = D_{V^+}^* + D_{V^0}^* + D_{V^-}^* + D_{V^{--}}^* + D_{I^+}^* + D_{I^0}^* + D_{I^-}^* + D_{I^{--}}^*$$

where the intrinsic diffusivity of the phosphorus diffusing as  $PV^-$  is given by  $D_{V^-}^*$ , etc.

The diffusion coefficient in crystals with a cubic lattice should be isotropic. For phosphorus doping levels of less than about  $10^{20} \text{ cm}^{-3}$  with no surface reaction taking place this is indeed the case [B3,B4]. The diffusion coefficient is therefore given by:

$$D = D_n \exp(-E_n / kT)$$

TABLE B1 Diffusivities for inert diffusion of phosphorus in single crystal (100), (110), (111) Si.

Temperature (°C)	$D_n (\text{cm}^2/\text{s})$	$E_n (\text{eV})$	Ref
800–1300	3.85	3.66	[B5]
950–1150	3.62	3.61	[B6]
1100–1300	3.7	3.69	[B7]
1100–1200	1.3	3.5	[B8]
950–1250	5.3	3.69	[B9]
1000–1200		3.7	[B10]
840–1150	0.6	3.51	[B4]

## B2 Phosphorus Diffusion, the General Case

As shown above, the inert intrinsic situation gives rise to a single diffusion coefficient that is a function of temperature only. To model diffusion under inert intrinsic conditions, we need not know any of the details of the diffusion mechanisms. Conversely, experiments conducted under inert intrinsic conditions yield no information as to the details of the diffusion mechanisms. In contrast, since diffusion involves the interaction of dopant atoms with native point defects (as mentioned above), and since these species are charged species, deviations from point defect equilibrium (i.e. non-inert conditions) and changes to the Fermi level (i.e. extrinsic conditions) cause the diffusion coefficient to behave in a complex manner. Currently, there is agreement that most situations of practical interest may be modelled by writing the diffusion coefficient as:

$$D = D^* \left[ f_I \frac{C_I}{C_I^*} + (1 - f_I) \frac{C_V}{C_V^*} \right]$$

## 10.2 Diffusion of P, As and Sb in c-Si

where  $f_i$  is the fraction of dopant diffusing by a substitutional-interstitial(cy) mechanism and  $D^*$  is the equilibrium diffusivity given by:

$$D^* = D^0 + \sum_i \left[ D_{+i} \left( \frac{p}{n_i} \right)^i + D_{-i} \left( \frac{n}{n_i} \right)^i \right]$$

where  $p$  and  $n$  are the hole and electron concentrations, respectively, and the different  $D$ s are the diffusivities of corresponding charged species.

For phosphorus, there is strong evidence in the literature that  $f_i$  is 1 so that there is no vacancy-mediated component to the diffusion [B9–B11]. Furthermore, the general consensus is that the diffusing species is a PI pair with the  $I^0$ ,  $I^-$  and  $I^{--}$  species playing the important roles in the diffusion. This allows us to write:

$$D_p = \left[ D^0 + D^- \left( \frac{n}{n_i} \right) + D^{--} \left( \frac{n}{n_i} \right)^2 \right] \cdot \frac{C_1}{C_i^*}$$

with:

$$D_v(0)[\text{eq}] = 3.85 \exp(-3.66/kT) \text{ cm}^2/\text{s}$$

$$D_v(-)[\text{eq}] = 4.44 \exp(-4.00/kT) \text{ cm}^2/\text{s}$$

$$D_v(--)[\text{eq}] = 44.2 \exp(-4.37/kT) \text{ cm}^2/\text{s}$$

Modelling diffusion under a given situation then becomes a matter of determining the correct values for the electron concentration and the interstitial supersaturation. Oxidation of silicon and nitridation of silicon dioxide are known to introduce interstitial supersaturation of the order of 10. Ion implantation introduces interstitial supersaturation of the order of  $10^3$ – $10^4$ . Nitridation of silicon introduces a vacancy supersaturation (and hence an interstitial undersaturation through Frenkel pair recombination) of the order of 10. There is a considerable body of literature on the modelling of diffusion under these conditions (see e.g. [B12,B13] and references therein).

## REFERENCES TO SECTION B

- [B1] D.A. Antoniadis et al [ *J. Appl. Phys. (USA)* vol.53 (1982) p.6788-96 ]
- [B2] R.B. Fair [ *Diffus. Defect Data (Switzerland)* vol.37 (1984) p.1-24 ]
- [B3] T.C. Chan et al [ *Proc. IEEE (USA)* vol.58 (1970) p.588-9 ]
- [B4] C. Hill [ in *Semiconductor Silicon 1981* Eds H.R. Huff, J. Kriegler, Y. Takeishi (Electrochem. Soc., Princeton, 1981) ]
- [B5] R.B. Fair, J.C.C. Tsai [ *J. Electrochem. Soc. (USA)* vol.122 (1975) p.1689-96 ]
- [B6] Y. Ishikawa, Y. Sakina, H. Tanaka, S. Matsumoto, T. Nimi [ *J. Electrochem. Soc. (USA)* vol.129 (1982) p.644-8 ]
- [B7] R.N. Ghoshtagore [ *Solid-State Electron. (UK)* vol.15 (1972) p.1113 ]
- [B8] G. Massetti, S. Solmi, G. Soncini [ *Solid-State Electron. (UK)* vol.16 (1973) p.1491-21 ]
- [B9] J.S. Makris, B.J. Masters [ *J. Electrochem. Soc. (USA)* vol.120 (1973) p.1252-3 ]
- [B10] M.L. Barry [ *J. Electrochem. Soc. (USA)* vol.117 (1970) p.1405-10 ]
- [B11] T.Y. Tan, U.M. Gösele [ *Appl. Phys. A (Germany)* vol.37 (1985) p.1 ]
- [B12] T. Shimizu et al [ *Jpn. J Appl. Phys. (Japan)* vol.37 (1998) p.1184 ]

## 10.2 Diffusion of P, As and Sb in c-Si

- [B13] P.B. Moynagh, P.J. Rosser [ *19<sup>th</sup> Eur. Solid State Devices Research Conf.* (1989) p.291-6 ]
- [B14] E. Chason et al [ *J. Appl. Phys. (USA)* vol.81 (1997) p.6513 ]
- [B15] S.M. Hu [ *Mater. Sci. Eng. R (Switzerland)* vol.13 (1994) p.1054 ]

### C DIFFUSION OF As IN c-Si

#### C1 Inert Intrinsic Arsenic Diffusion

The mathematical basis for the diffusion process was laid by Fick whose first law sets forward the hypothesis that the rate of transfer of a diffusing particle through unit area is proportional to the magnitude of the gradient normal to that area, i.e. in the x-direction

$$J = -D \frac{dC}{dx}$$

where the proportionality constant, D ( $m^2/s$ ), is known as the diffusion constant or the diffusivity. The diffusion process occurs because of the random walk of the impurity atoms and is therefore a thermally activated process. The temperature dependence of the diffusion coefficient is Arrhenius in nature:

$$D = D_0 \exp(-E/kT)$$

where E is the activation energy (which, for the common dopants in silicon, is about 4 eV).

Due to the low concentration of stable point defects in silicon, it has not been possible to determine directly whether vacancies or self-interstitials are dominant in diffusion processes. Numerous kinds of indirect observations have been made to build cases for vacancies and for self-interstitials. The current belief is that both types of point defect exist somewhat independently [C1] and that both influence diffusion. Under diffusive conditions where the silicon is intrinsically doped and where no surface reaction is taking place, the vacancy and self-interstitial concentrations are temperature dependent only and are described approximately by the equilibrium concentrations:

$$C_V^* = C_{oV} \exp(-E_V/kT)$$

$$C_I^* = C_{oI} \exp(-E_I/kT)$$

Dopant diffusion takes place in the silicon by interacting with these point defects so that the diffusing species are the arsenic/vacancy pair, AV, and the arsenic/Si-interstitial pair, AI. The intrinsic diffusivity due to the vacancy mechanism is referred to as  $D_V^*$  and that due to the interstitial mechanism as  $D_I^*$ . The intrinsic, inert ambient diffusivity is therefore given by the sum of the equilibrium diffusivities due to the vacancy and the self-interstitial components:

$$D^* = D_V^* + D_I^*$$

The wide energy range available to the Fermi level in silicon leads to a given lattice defect (i.e. a vacancy or Si-interstitial) appearing in a variety of ionised states [C2]. As such, the dopant/point-defect pairs exist as, for example,  $As^+V^-$  which we will denote by  $AV^-$ . The intrinsic, inert ambient diffusivity can therefore be written:

## 10.2 Diffusion of P, As and Sb in c-Si

$$D^* = D_{V^+}^* + D_{V^0}^* + D_{V^-}^* + D_{V^{--}}^* + D_{I^+}^* + D_{I^0}^* + D_{I^-}^* + D_{I^{--}}^*$$

where the intrinsic diffusivity of the arsenic diffusing as  $AV^-$  is given by  $D_{V^-}^*$ , etc.

The diffusion coefficient in crystals with a cubic lattice should be isotropic. For arsenic doping levels of less than about  $10^{20}$  cm $^{-3}$  with no surface reaction taking place this is indeed the case [C3]. The diffusion coefficient is therefore given by:

$$D = D_n \exp(-E_n / kT)$$

Literature diffusivities for inert diffusion of arsenic in single crystal silicon are listed in TABLE C1.

TABLE C1 Diffusivities for inert diffusion of arsenic in single crystal (100), (110), (111) Si.

Temperature (°C)	$D_n$ (cm $^2$ /s)	$E_n$ (eV)	Ref
900–1250	22.9	4.1	[C4]
1050–1200	59	4.2	[C5]
1000–1300	24	4.08	[C6]
840–1250	13	4.05	[C3]
950–1150	35.3	4.11	[C7]
1050–1400	102.8	4.27	[C8]
1167–1394	0.0655	3.44	[C9]
950–1150	2870	4.58	[C10]
1100–1400	1.218	3.75	[C11]

There are also literature values for the contribution to this inert diffusivity from the As(+)V(0) pair and the As(+)V(–) pair. Ho et al [C12] have found:

$$D_V(0)[eq] = 0.0114 \exp(-3.44/kT) \text{ cm}^2/\text{s}$$

$$D_V(-)[eq] = 30.0 \exp(-4.15/kT) \text{ cm}^2/\text{s}$$

and Colclaser [C13] reported:

$$D_V(0)[eq] = 0.38 \exp(-3.58/kT) \text{ cm}^2/\text{s}$$

$$D_V(-)[eq] = 22.9 \exp(-4.1/kT) \text{ cm}^2/\text{s}$$

## C2 Arsenic Diffusion, the General Case

As shown above, the inert intrinsic situation gives rise to a single diffusion coefficient that is a function of temperature only. To model diffusion under inert intrinsic conditions, we need not know any of the details of the diffusion mechanisms. Conversely, experiments conducted under inert intrinsic conditions yield no information as to the details of the diffusion mechanisms. In contrast, since diffusion involves the interaction of dopant atoms with native point defects (as mentioned above), and since these species are charged species, deviations from point defect equilibrium (i.e. non-inert conditions) and changes to the Fermi level (i.e. extrinsic conditions) cause the diffusion coefficient to behave in a complex manner. Currently, there is agreement that most situations of practical interest may be modelled by writing the diffusion coefficient as:

$$D = D^* \left[ f_I \frac{C_I}{C_I^*} + (1 - f_I) \frac{C_V}{C_V^*} \right]$$

where  $f_I$  is the fraction of dopant diffusing by a substitutional-interstitial(cy) mechanism and  $D^*$  is the equilibrium diffusivity given by:

$$D^* = D^0 + \sum_i \left[ D_{+i} \left( \frac{p}{n_i} \right)^i + D_{-i} \left( \frac{n}{n_i} \right)^i \right]$$

where  $p$  and  $n$  are the hole and electron concentrations, respectively, and the different  $D$ s are the diffusivities of corresponding charged species.

For arsenic, there is general agreement that only two terms in this general expression are sufficient to model the diffusion so that we may write:

$$D_{As} = \left[ D^0 + D^- \left( \frac{n}{n_i} \right) \right] \cdot \left[ f_I \frac{C_I}{C_I^*} + (1 - f_I) \frac{C_V}{C_V^*} \right]$$

with literature values for  $D^0$  and  $D^-$  given in the previous section. Modelling diffusion under a given situation then becomes a matter of determining the correct values for the electron concentration and the interstitial and vacancy supersaturations (provided a value is given for  $f_I$ ; this is further discussed below). Oxidation of silicon and nitridation of silicon dioxide are known to introduce interstitial supersaturations of the order of 10. Ion implantation introduces interstitial supersaturation of the order of  $10^3$ – $10^4$ . Nitridation of silicon introduces a vacancy supersaturation (and hence an interstitial undersaturation through Frenkel pair recombination) of the order of 10. There is a considerable body of literature on the modelling of diffusion under these conditions (see e.g. [C14,C15] and references therein).

However, there is strong disagreement in the literature as to the value of  $f_I$ . Fahey et al [C16] found that results obtained under oxidising conditions and those obtained under nitriding conditions produced inconsistent results. Vandebossche and Baccus [C17] used a more complex model, taking into account two reactions that could produce a dopant–interstitial pair and two that could produce a dopant–vacancy pair (as opposed to one reaction each as the simplest picture proposes). With this hypothesis, they were able to model As diffusion with  $f_I = 0.21$ . The only problem with this model is that it introduces two new fitting parameters for each dopant. With many more parameters than sets of unique experimental conditions, the conclusions become less reliable. One alternative explanation of the inconsistent results obtained by Fahey et al is the clustering behaviour of As which has not yet been adequately modelled. In spite of the disagreement on the exact value of  $f_I$  for As, most work to date has produced estimates in the range of 0.2–0.5. Hence, there is general agreement that both the vacancy and the interstitial are important to As diffusion in Si.

## REFERENCES TO SECTION C

- [C1] D.A. Antoniadis, I. Moskowitz [ *J. Appl. Phys. (USA)* vol.53 (1982) p.6788-96 ]
- [C2] D. Anderson, K.O. Jeppson [ *J. Electrochem. Soc. (USA)* vol.131 (1984) p.2675-9 ]
- [C3] C. Hill [ *Semiconductor Silicon 1981* Eds H.R. Huff, J. Kriegler, Y. Takeishi (Electrochem. Soc., Princeton, 1981) p.988-1006]

## 10.2 Diffusion of P, As and Sb in c-Si

- [C4] R.B. Fair, J.C.C. Tsai [ *J. Electrochem. Soc. (USA)* vol.122 (1975) p.1689-96 ]
- [C5] G.F. Cerofolini [ *Thin Solid Films (Switzerland)* vol.135 (1986) p.59-72 ]
- [C6] S. Matsumoto, J.F. Gibbons, V. Deline, C.A. Evans Jr. [ *Appl. Phys. Lett. (USA)* vol.37 (1980) p.821-4 ]
- [C7] Y. Ishikawa, Y. Sakina, H. Tanaka, S. Matsumoto, T. Nimi [ *J. Electrochem. Soc. (USA)* vol.129 (1982) p.644-8 ]
- [C8] B.J. Masters et al [ *J. Appl. Phys. (USA)* vol.40 (1969) p.2390-4 ]
- [C9] R.N. Ghoshtagore [ *Phys. Rev. B (USA)* vol.3 (1971) p.397-401 ]
- [C10] D.P. Kennedy et al [ *Proc. IEEE (USA)* vol.59 (1971) p.335-6 ]
- [C11] D.L. Kendall et al [ *Semiconductor Silicon 1969* Eds R.R. Halbrecht, E.L. Kern (Electrochem. Soc., Princeton, 1969) ]
- [C12] C.P. Ho et al [ *Tech. Report* no.SEL 84-001, Stanford Electronics Labs, Stanford University, California, USA (1984) ]
- [C13] R.A. Colclaser [ *Microelectronics: Processing and Device Design* (John Wiley and Sons, 1980) ]
- [C14] E. Chason et al [ *J. Appl. Phys. (USA)* vol.81 (1997) p.6513 ]
- [C15] S.M. Hu [ *Mater. Sci. Eng. R (Switzerland)* vol.13 (1994) p.105 ]
- [C16] P.M. Fahey, P.B. Griffin, J.D. Plummer [ *Rev. Mod. Phys. (USA)* vol.61 (1989) p.289 ]
- [C17] E. Vandebossche, B. Baccus [ *J. Appl. Phys. (USA)* vol.72 (1992) p.447 ]

### **D DIFFUSION OF Sb IN c-Si**

#### **D1 Inert Intrinsic Antimony Diffusion**

The mathematical basis for the diffusion process was laid by Fick whose first law sets forward the hypothesis that the rate of transfer of a diffusing particle through unit area is proportional to the magnitude of the gradient normal to that area, i.e. in the x-direction

$$J = -D \frac{dC}{dx}$$

where the proportionality constant, D ( $m^2/s$ ), is known as the diffusion constant or the diffusivity. The diffusion process occurs because of the random walk of the impurity atoms and is therefore a thermally activated process. The temperature dependence of the diffusion coefficient is Arrhenius in nature:

$$D = D_0 \exp(-E/kT)$$

where E is the activation energy (which, for the common dopants in silicon, is about 4 eV).

Due to the low concentration of stable point defects in silicon, it has not been possible to determine directly whether vacancies or self-interstitials are dominant in diffusion processes. Numerous kinds of indirect observations have been made to build cases for vacancies and for self-interstitials. The current belief is that both types of point defect exist somewhat independently [D1] and that both influence diffusion. Under diffusive conditions where the silicon is intrinsically doped and where no surface reaction is taking place, the vacancy and self-interstitial concentrations are temperature dependent only and are described approximately by the equilibrium concentrations:

$$C_v^* = C_{ov} \exp(-E_v/kT)$$

## 10.2 Diffusion of P, As and Sb in c-Si

$$C_i^* = C_{oi} \exp(-E_i / kT)$$

Dopant diffusion takes place in the silicon by interacting with these point defects so that the diffusing species are the antimony/vacancy pair, SbV, and the antimony/Si-interstitial pair, SbI. The intrinsic diffusivity due to the vacancy mechanism is referred to as  $D_v^*$  and that due to the interstitial mechanism as  $D_I^*$ . The intrinsic, inert ambient diffusivity is therefore given by the sum of the equilibrium diffusivities due to the vacancy and the self-interstitial components:

$$D^* = D_v^* + D_I^*$$

The wide energy range available to the Fermi level in silicon leads to a given lattice defect (i.e. a vacancy or Si-interstitial) appearing in a variety of ionised states [D2]. As such, the dopant/point-defect pairs exist as, for example,  $Sb^+V^-$  which we will denote by  $SbV^-$ . The intrinsic, inert ambient diffusivity can therefore be written:

$$D^* = D_{V^+}^* + D_{V^0}^* + D_{V^-}^* + D_{V^{--}}^* + D_{I^+}^* + D_{I^0}^* + D_{I^-}^* + D_{I^{--}}^*$$

where the intrinsic diffusivity of the antimony diffusing as  $SbV^-$  is given by  $D_{V^-}^*$ , etc.

The diffusion coefficient in crystals with a cubic lattice should be isotropic. For antimony doping levels of less than about  $10^{20} \text{ cm}^{-3}$  with no surface reaction taking place this is indeed the case [D3,D4]. The diffusion coefficient is therefore given by:

$$D = D_n \exp(-E_n / kT)$$

Under intrinsic diffusive conditions, antimony dopant profiles show excellent Fickian-type behaviour [D5].

Literature diffusivities for inert diffusion of antimony in single crystal silicon are listed below.

Fair [D6] describes the intrinsic diffusivity of antimony in a manner which physically accounts for the fact that antimony diffuses by interaction with neutral vacancies  $Sb(+)V(0)$ , and with singly negatively charged vacancies,  $Sb(+)V(-)$ .

$$\begin{aligned} D^* &= D_{V^0}^* + D_{V^-}^* \\ &= (1.284 \times 10^9) \exp(-3.65 \text{ eV}/kT) + (1.0 \times 10^{10}) \exp(-4.08 \text{ eV}/kT) \mu\text{m}^2/\text{min} \end{aligned}$$

Colclaser [D7] reported:

$$\begin{aligned} D^* &= D_{V^0}^* + D_{V^-}^* \\ &= 0.214 \exp(-3.65 \text{ eV}/kT) + 13 \exp(-4.0 \text{ eV}/kT) \text{ cm}^2/\text{s} \end{aligned}$$

Ghoshtagore [D5] describes the intrinsic diffusivity of antimony as

$$\begin{aligned} D^* &= D_n \exp(-E_n / kT) \\ &= 0.214 \exp(-3.65 \text{ eV}/kT) \text{ cm}^2/\text{s} \end{aligned}$$

## D2 Antimony Diffusion, the General Case

As shown above, the inert intrinsic situation gives rise to a single diffusion coefficient that is a function of temperature only. To model diffusion under inert intrinsic conditions, we need not know any of the details of the diffusion mechanisms. Conversely, experiments conducted under inert intrinsic conditions yield no information as to the details of the diffusion mechanisms. In contrast, since diffusion involves the interaction of dopant atoms with native point defects (as mentioned above), and since these species are charged species, deviations from point defect equilibrium (i.e. non-inert conditions) and changes to the Fermi level (i.e. extrinsic conditions) cause the diffusion coefficient to behave in a complex manner. Currently, there is agreement that most situations of practical interest may be modelled by writing the diffusion coefficient as:

$$D = D^* \left[ f_l \frac{C_l}{C_l^*} + (1 - f_l) \frac{C_v}{C_v^*} \right]$$

where  $f_l$  is the fraction of dopant diffusing by a substitutional-interstitial(cy) mechanism and  $D^*$  is the equilibrium diffusivity given by:

$$D^* = D^0 + \sum_i \left[ D_{+i} \left( \frac{p}{n_i} \right)^i + D_{-i} \left( \frac{n}{n_i} \right)^i \right]$$

where  $p$  and  $n$  are the hole and electron concentrations, respectively, and the different  $D$ s are the diffusivities of corresponding charged species.

For antimony, there is strong agreement that  $f_l \approx 0$  so that the vacancy contribution is the dominant one [D9–D12]. Additionally, there is general agreement that only two terms in this general expression are sufficient to model the diffusion so that we may write:

$$D_{\text{Sb}} = \left[ D^0 + D^- \left( \frac{n}{n_i} \right) \right] \cdot \frac{C_v}{C_v^*}$$

where literature values for the two contributions have been given above. Modelling diffusion under a given situation then becomes a matter of determining the correct values for the electron concentration and the interstitial and vacancy supersaturations. Oxidation of silicon and nitridation of silicon dioxide are known to introduce interstitial supersaturations of the order of 10. Ion implantation introduces interstitial supersaturation of the order of  $10^3$ – $10^4$ . Nitridation of silicon introduces a vacancy supersaturation (and hence an interstitial undersaturation through Frenkel pair recombination) of the order of 10. There is a considerable body of literature on the modelling of diffusion under these conditions (see e.g. [D12,D13] and references therein).

## REFERENCES TO SECTION D

- [D1] D.A. Antoniadis, I. Moskowitz [ *J. Appl. Phys. (USA)* vol.53 (1982) p.6788-96 ]
- [D2] R. Francis, P.S. Dobson [ *J. Appl. Phys. (USA)* vol.50 (1979) p.280-4 ]
- [D3] T.C. Chan et al [ *Proc. IEEE (USA)* vol.58 (1970) p.588-9 ]
- [D4] C. Hill [ *Semiconductor Silicon 1981* Eds H.R. Huff, J. Kriegler, Y. Takeishi (Electrochem. Soc., Princeton, 1981) p.988-1006]

- [D5] R.N. Ghoshtagore [ *Phys. Rev. B (USA)* vol.3 (1971) p.397-401 ]
- [D6] R.B. Fair [ *Impurity Doping Processes in Silicon* Ed. F.Y.Y. Wang (North-Holland, 1981) ]
- [D7] R.A. Colclaser [ *Microelectronics: Processing and Device Design* (John Wiley and Sons, 1980) p.123 ]
- [D8] H.-J. Gössmann et al [ *Appl. Phys. Lett. (USA)* vol.71 (1997) p.3862 ]
- [D9] P.M. Fahey, P.B. Griffin, J.D. Plummer [ *Rev. Mod. Phys. (USA)* vol.61 (1989) p.289 ]
- [D10] T. Shimizu et al [ *Jpn. J. Appl. Phys. (Japan)* vol.37 (1998) p.1184 ]
- [D11] P.B. Moynagh, P.J. Rosser [ *19<sup>th</sup> Eur. Solid State Devices Research Conf.* (1989) p.291-6 ]
- [D12] E. Chason et al [ *J. Appl. Phys. (USA)* vol.81 (1997) p.6513 ]
- [D13] S.M. Hu [ *Mater. Sci. Eng. R (Switzerland)* vol.13 (1994) p.105 ]

## E CONCLUSION

Inert intrinsic conditions produce a single diffusion coefficient which is only temperature dependent. Deviations from point defect equilibrium (non-inert) and changes to the Fermi level (extrinsic conditions) lead to complex diffusion behaviour in donor impurity incorporation in silicon. It is believed that phosphorus diffuses predominantly via phosphorus/interstitial pairs and both oxidation and nitridation affect the interstitial supersaturation. Both vacancies and interstitials are thought to play a role in As diffusion. Vacancy/antimony pairs appear to dominate the diffusion of antimony in silicon.

## CHAPTER 11

### DEFECT LEVELS IN SILICON

(Edited by H. Grimmeis)

- 11.1 Vacancies and interstitials and their interactions with impurities in c-Si
- 11.2 Electrical and optical properties of dislocations in c-Si
- 11.3 Shallow thermal donors in c-Si
- 11.4 Thermal double donors in c-Si
- 11.5 Double donors and acceptors in c-Si

## **11.1 Vacancies and interstitials and their interactions with impurities in c-Si**

G.D. Watkins

September 1997

### **A INTRODUCTION**

There are two fundamental native defects in silicon—the lattice vacancy and the silicon interstitial. Each is present in thermodynamic equilibrium at any finite temperature  $T$ , its concentration being proportional to  $\exp(-W/kT)$ , where  $W$  is its formation energy. At elevated temperatures, therefore, each provides a mechanism for normal thermally activated diffusion of the substitutional host and impurity atoms. In addition, non-equilibrium conditions produced during device processing such as oxidation, annealing of plasma etching, ion implantation damage, etc., can serve to provide a temporary release of these defects, which, in turn, can cause anomalous transient enhanced diffusion phenomena.

In addition, these defects, whether isolated or complexed with other defects or impurities, represent a disruption of the normal bonding structure of the lattice, and therefore can introduce electrically active levels into the forbidden gap. They therefore directly affect the electrical properties of the material. This also means that the defects can take on several charge states, each potentially with a different structural arrangement in the lattice, different diffusional properties, different interactions with other defects, etc. Determining, therefore, their electronic and physical properties, and the relationship of these to their local structural arrangements in the lattice, is essential to understanding their role in silicon device technology.

In this Datareview, we will summarize briefly what is presently believed to be established concerning the isolated intrinsic defects and their interactions with impurities in silicon [1–3]. Although there have been many experiments that directly or indirectly reflect the properties and/or effects of these defects, it has been primarily through the use of electron paramagnetic resonance (EPR) to identify the defects, and high energy electron irradiation to produce them in a cold lattice, that reliable information has been obtained. In addition, local vibrational mode (LVM) spectroscopy has, in some recent cases, provided reliable defect identification for intrinsic defects trapped by lighter impurity atoms. As a result, we will treat here primarily the results of such studies, or, in a few cases, those using other experimental techniques that reliably correlate with the EPR or LVM identifications. In addition, we will also consider with caution some recent state-of-the-art theoretical results concerning the defects, in those cases where it may be helpful in partially filling in the experimental gaps.

### **B THE LATTICE VACANCY**

#### **B1 Structure and Electrical Properties**

The isolated lattice vacancy has been identified by EPR in both its paramagnetic single positive ( $V^+$ ) and negative ( $V^-$ ) charge states immediately after *in situ* electron irradiation at cryogenic temperatures (4.2 K, 20.4 K). From detailed studies monitoring these spectra, it has been established that the vacancy can actually take on five different charge states in the silicon bandgap, ( $V^{++}$ ,  $V^+$ ,  $V^0$ ,  $V^-$ ,  $V^{- -}$ ), i.e. it introduces four levels into the gap [2,3]. This is summarized in FIGURE 1, (a) and (b), which illustrate also the near neighbour relaxations that occur for the two observed charge states as the

## 11.1 Vacancies and interstitials and their interactions with impurities in c-Si

broken bonds partially reconstruct by pairs. In the case of  $V^-$ , the structure has also been probed and confirmed in great detail by electron-nuclear double resonance (ENDOR) of silicon neighbours in many shells of surrounding lattice sites [4]. The positions of the two (donor) levels close to the valence band have been firmly established [5], as shown. In this case, their level position ordering is reversed from normal for a double donor, a rare phenomenon known as ‘negative-U’, where the second trapped electron (or hole) is bound more strongly than the first [6]. This has been shown to result from the increasing energy gained in the dangling bond reconstructions (a Jahn–Teller effect) as the vacancy picks up electrons [7]. The positions of the other two (acceptor) levels have not yet been established, except for the tentative conclusion that the double acceptor level is deeper than 0.17 eV from the conduction band edge [8].

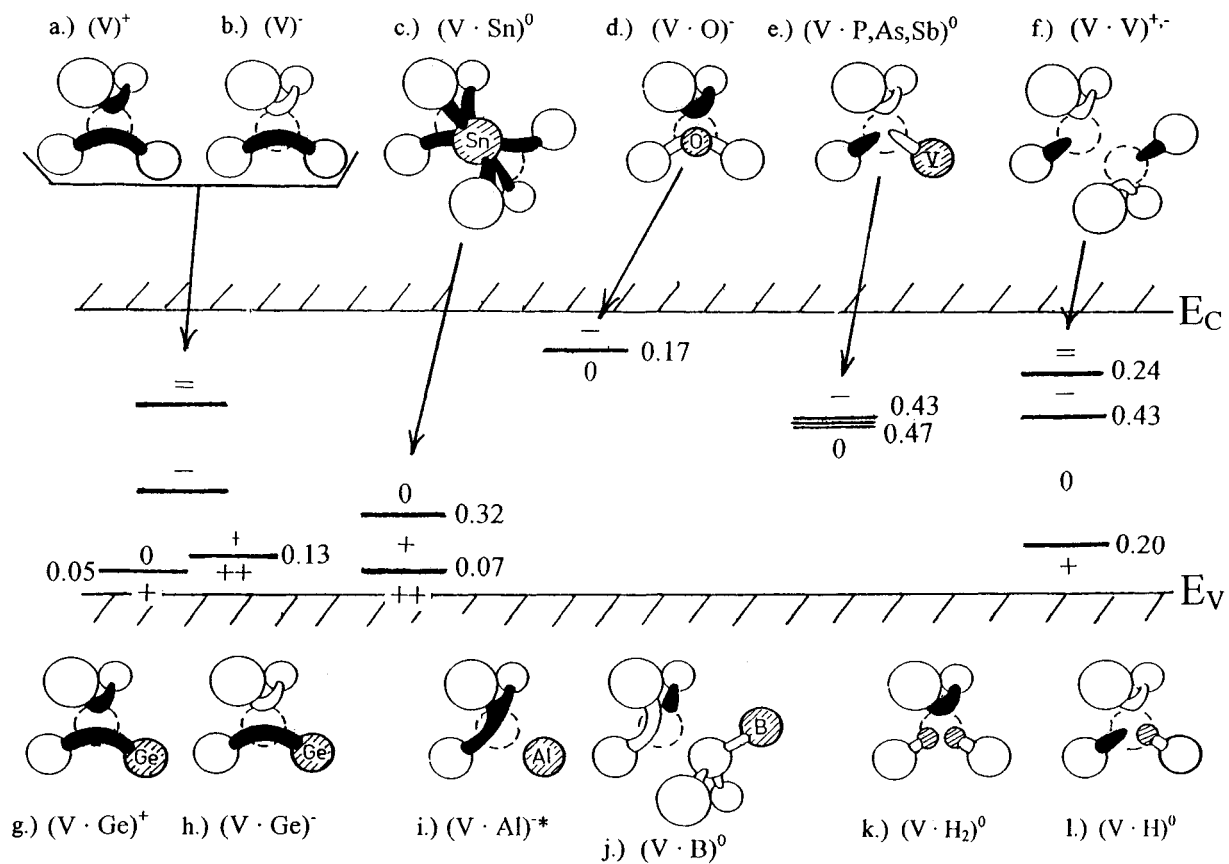


FIGURE 1 Structures of isolated and trapped vacancies and their identified electrical levels (in eV from the closest band edge). The electrically active dangling and/or reconstructed bonds are shown in black.

## B2 Vacancy Diffusion

The vacancy spectra disappear in a 15 min isochronal annealing sequence at  $\sim 70$  K in n-type,  $\sim 150$  K in p-type, and  $\sim 200$  K in high resistivity material [2,3]. The simultaneous growth of new spectra that have been identified as vacancies paired with other defects establishes unambiguously that the annealing process is the result of long range diffusion of the vacancy. The kinetics of the processes have been determined giving for the vacancy migration activation energy,  $0.18 \pm 0.02$  eV in n-type,  $0.45 \pm 0.04$  eV in high resistivity, and  $0.32 \pm 0.02$  eV in p-type material [2,3]. These presumably reflect

### 11.1 Vacancies and interstitials and their interactions with impurities in c-Si

the different properties of the  $V^-$ ,  $V^0$ , and  $V^{++}$  charge states, which are dominant in each of the respective cases.

In addition, it has been established that the vacancy migration and trapping processes can also be made to occur even at 4.2 K under optical excitation or electrical injection, as well as partially also by the ionization accompanying the electron irradiation [3,9]. The vacancy is therefore a very fragile defect, displaying also athermal recombination-enhanced motion. This has been interpreted to result from the changes in the near neighbour lattice relaxation associated with the broken bond reconstruction versus charge state, which serves to dump energy into the vibrational modes of the defect upon electron and hole capture. At elevated temperatures where diffusion is normally studied, all charge states can exist as the vacancy traps and emits the thermally generated electrons and holes, and each of the above processes will be simultaneously occurring to various degrees. In detail, therefore, the vacancy migration process is very complicated, but, in practical terms, it has the simple result that the contribution of its migration barrier to the activation energy for diffusion is very small. The principal contribution must come from its formation energy.

#### B3 Vacancy Interactions with Impurities and Other Defects

In FIGURE 1, we show, in addition to the isolated vacancy, the structures deduced for various identified trapped vacancies [2,3], as well as the electrical levels which have been determined for them. When trapped by substitutional Sn, the large Sn atom moves into a position halfway into the vacancy, producing, for the neutral state, what can be considered an Sn atom in the centre of a divacancy, as illustrated in (c). Its single and double donor states are now in normal positive-U ordering [8], as shown. Interstitial oxygen is an effective trap, moving into the vacancy, as shown in (d), and bonding strongly to two of the vacancy neighbours. The remaining two dangling bonds form an acceptor level at  $E_C - 0.17$  eV [10]. Vacancies trapped by the substitutional group-V atoms P, As or Sb take on the configuration shown in (e), introducing a single acceptor level at  $E_C - 0.43$ ,  $E_C - 0.47$ , or  $E_C - 0.44$  eV, respectively [8]. The divacancy results from pairing of two vacancies during vacancy anneal, and its structure is shown in (f). It can take on four charge states in the gap,  $(VV)^+$ ,  $(VV)^0$ ,  $(VV)^-$ , and  $(VV)^{--}$ , depending upon whether there are one, two, three, or four electrons trapped into the well separated remaining two dangling bonds, with the measured level positions [11], as indicated.

In the case of the Ge-vacancy pair, the electrical level positions have not been directly measured. However, its dangling bond reconstructions, shown in (g) and (h), reveal an only slightly perturbed vacancy, and its general behaviour versus Fermi level, optical excitation, etc., appears identical to that of the isolated vacancy. This suggests a very similar level structure (including negative-U), as indicated in the figure for the isolated vacancy. The level positions have also not been conclusively identified for vacancies trapped by aluminium or boron. Their structures have, however, been determined, with the aluminium atom as nearest neighbour, (i), and the boron atom as next nearest neighbour, (j).

On the above defects, ENDOR studies of surrounding silicon neighbour shells have also been performed, confirming the structures in detail for  $(V\cdot O)^-$ ,  $(V\cdot V)^{+-}$ , and  $(V\cdot B)^0$  [4]. EPR of an excited triplet ( $S = 1$ ) state of  $(V\cdot O)^0$  has also been observed [12].

Shown also in FIGURE 1, (l) and (k), are a single vacancy containing one, and two, hydrogen atoms, respectively, which have also been identified by EPR techniques. The neutral two-hydrogen complex was identified by optical detection of EPR of its  $S = 1$  triplet state in luminescence [13], and was formed by the trapping of the vacancy after electron irradiation in previously hydrogen-soaked material. The neutral single hydrogen atom defect was identified recently in hydrogen-implanted

material [14]. Combined with the rich variety of hydrogen local vibrational mode absorption spectra observed in hydrogen-implanted material, it has been possible to detect and identify the signatures of the complete set, VH, VH<sub>2</sub>, VH<sub>3</sub>, and VH<sub>4</sub> [15,16]. All are stable at room temperature. All except VH<sub>4</sub> will have dangling bonds and should be electrically active. No information concerning their electrical level positions is yet available, but, as suggested by their structures, the electrical properties of V·H<sub>2</sub> can reasonably be expected to be similar to those of V·O, and, similarly, those of V·H to those of V·P.

In FIGURE 2, the stability of the vacancy and several of the first generation vacancy-defect pairs is summarized schematically, as has been observed in ~15–30 min isochronal annealing studies [2,3,15].

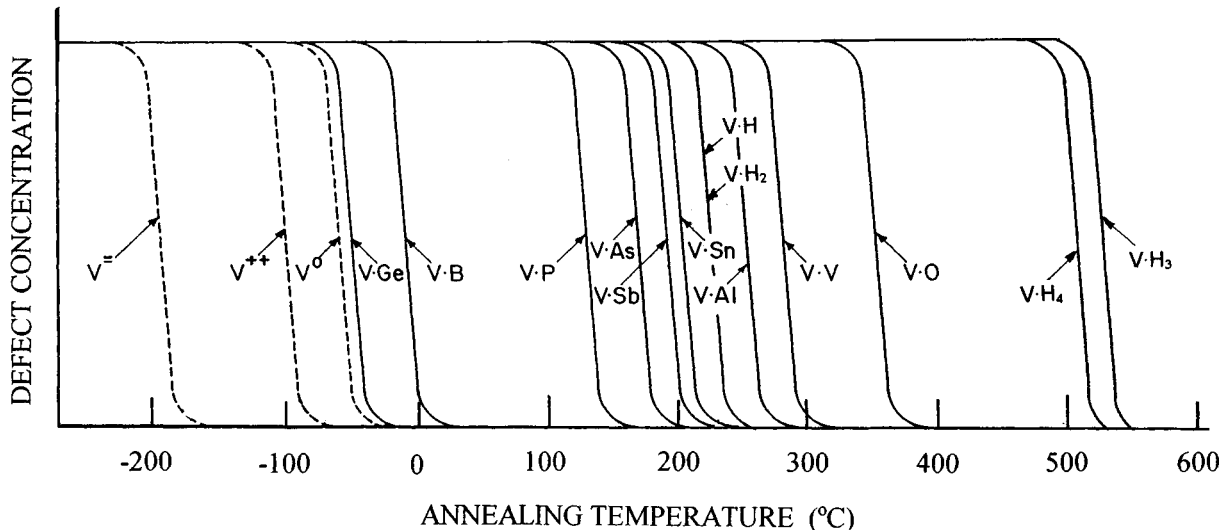


FIGURE 2 Schematic of vacancy and vacancy-defect pair annealing stages (~15–30 min isochronal).

## C THE SILICON INTERSTITIAL

### C1 Mobility

In p-type silicon, no EPR evidence of an isolated silicon atom has been observed after in situ electron irradiation at cryogenic temperatures. Instead, only defects which are identified as interstitials trapped at impurities are observed, and in ~ 1:1 concentration to that of the isolated vacancies. From this, it has been concluded that the isolated interstitial atoms must be highly mobile under the electron irradiation conditions in p-type material, even at 4.2 K [2]. In n-type silicon, defect production is observed to be much lower at cryogenic temperatures, making these experiments much more difficult, but the evidence there indicates that migration may not occur until annealing to ~150–175 K [17], where the trapped interstitial configurations are observed to emerge. In either case, however, high mobility for the interstitial is indicated, it having executed long range motion at least by ~175 K. Again, therefore, as for the vacancy, the activation energy for its contribution to diffusion processes must come primarily from its formation energy. In contrast to the vacancy, however, there is unfortunately no direct experimental evidence of its structure or electrical properties.

### C2 Trapped Interstitials

The structure and properties of the trapped interstitials are of interest, both because the defects are important by themselves, but also for the possible clues they contain concerning the properties of the isolated silicon interstitial, before it is trapped. In FIGURE 3, (a) – (c), we show the rich variety of

## 11.1 Vacancies and interstitials and their interactions with impurities in c-Si

structures deduced from the EPR studies for three of the identified trapped interstitials [2], along with the corresponding level positions that have been determined for them. As trapped by substitutional aluminium, FIGURE 3(a), the interstitial silicon atom has traded places, ejecting the Al atom into the high symmetry tetrahedral interstitial site, as seen in its  $\text{Al}_i^{++}$  EPR-active charge state, and also by ENDOR [18,19]. It is a donor, with its second donor level [20] as indicated. On the other hand, originally substitutional boron finds itself displaced into a position slightly off from a bond-centred position between two silicon atoms, as observed in its neutral  $\text{B}_i^0$  EPR-active charge state, FIGURE 3(b). Its electrical levels have been determined as shown [21], its acceptor level being substantially below its donor level in negative-U ordering. Different again is the trapping by substitutional carbon, FIGURE 3(c), which ends up in a split- $\langle 100 \rangle$  configuration sharing a lattice site with a silicon atom. For it, the electrical levels are in normal ordering, as shown [22,23]. In this case, all three available charge states retain this configuration, as evidenced by the EPR studies of its positive ( $\text{C}_i^+$ ) and negative ( $\text{C}_i^-$ ) states, and by infrared carbon local mode studies of its neutral ( $\text{C}_i^0$ ) state [24].

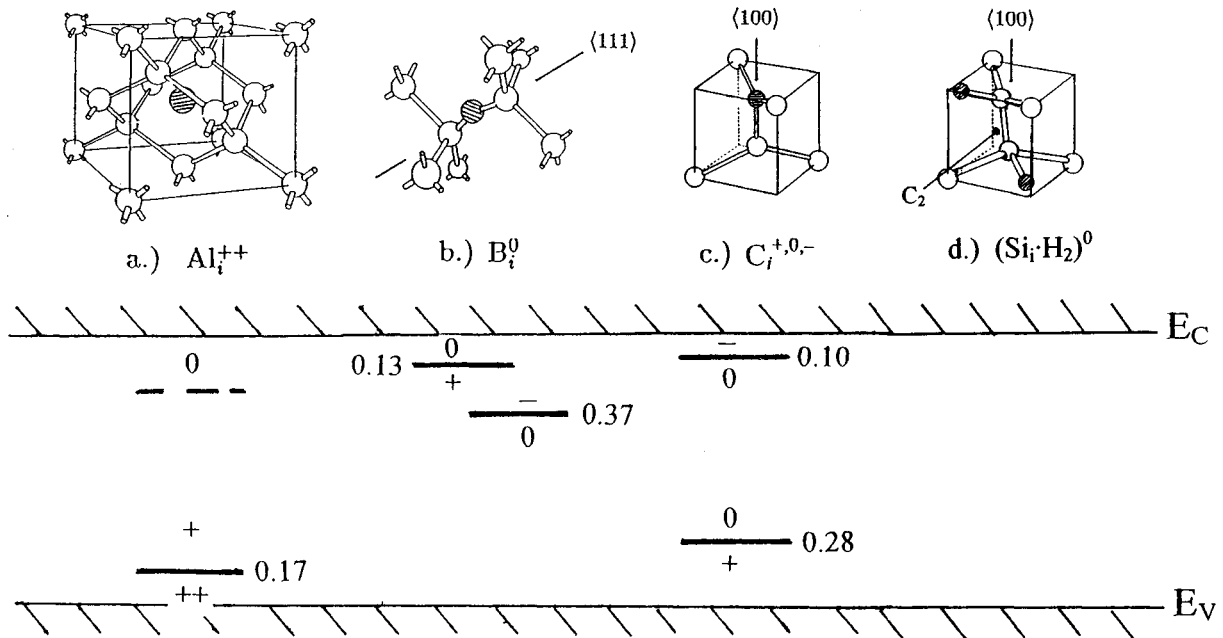


FIGURE 3 Trapped interstitials and their identified level positions. The cross-hatched atoms represent the trapping impurities.

Finally, we include in FIGURE 3(d) the configuration for interstitial silicon paired with two hydrogen atoms, recently identified from LVM studies [15,25]. Here, the presence of the two bonding hydrogens causes the silicon split-interstitial configuration to rotate to an orientation intermediate between a  $\langle 100 \rangle$  and  $\langle 110 \rangle$  split, while remaining in the plane perpendicular to the  $\langle 100 \rangle$  axis indicated as  $\text{C}_2$  in the figure (the defect retains  $180^\circ$  rotation symmetry around this axis). This configuration, predicted theoretically first by Deák et al [26], has been subsequently confirmed and studied in greater detail using state of the art ab initio local density methods [27]. The symmetry and the directions of the various hydrogen stretch vibrational modes determined in the LVM study agree in remarkable detail with the calculated lattice positions for the atomic constituents, providing convincing evidence of the identification and the detailed model for the defect configuration. In the model, the hydrogen atoms serve to complete the four-fold bonding of the two silicons, and, in so doing, remove the electrical activity of the defect. Although observed in this study after hydrogen implantation, these characteristic LVM bands had previously been observed, but not identified at the

### 11.1 Vacancies and interstitials and their interactions with impurities in c-Si

time, after electron irradiation of silicon grown in a hydrogen atmosphere [28]. By analogy with V·H<sub>2</sub>, therefore, it can be produced by interstitial trapping in hydrogen-soaked material.

#### C3 The Isolated Silicon Interstitial

Hence, one might expect a variety of possible bonding and/or non-bonding configurations available to the isolated interstitial silicon as well. Theory appears to confirm this. Combining the results of two independent research groups [29–31] leads to the prediction that Si<sub>i</sub><sup>++</sup> sits in the undistorted tetrahedral interstitial position, Si<sub>i</sub><sup>+</sup> in a bond-centred position, and Si<sub>i</sub><sup>0</sup> in a split-<110> configuration where it shares a lattice site with another silicon atom. (The split-<110> configuration for Si<sub>i</sub><sup>0</sup> has been confirmed by several more recent theoretical studies [27,32,33].) These results were obtained from ab initio total energy calculations involving the local density approximation and are therefore presumably representative of current state-of-the-art capabilities. Of course, the results must still be taken with a certain amount of caution, but there are several features to them which makes one feel that they may be essentially correct. (1) The different configurations predicted for each charge state follow reasonably closely the pattern of the impurity-trapped interstitials. (Si<sub>i</sub><sup>++</sup> is isoelectronic with Al<sub>i</sub><sup>+</sup>, which with its closed 3s atomic orbital shell should experience no instability in the symmetric tetrahedral interstitial position. Si<sub>i</sub><sup>+</sup> is isoelectronic to B<sub>i</sub><sup>0</sup> (a single atomic p-electron that likes to form bonds) which is also bond-centred. Si<sub>i</sub><sup>0</sup> is isoelectronic to C<sub>i</sub><sup>0</sup> (two atomic p-orbitals), which enters also a symmetric, albeit <100> rather than <110>, split interstitial arrangement.) (2) Each of the predicted configurations is a saddle point for migration between either of the other two, providing a natural explanation for its athermal mobility in the presence of ionization, as the defect changes its charge state upon capture of electrons and holes. (3) Low barriers for migration are predicted even without charge state change. (4) Like interstitial boron, negative-U electrical properties are predicted as the defect distorts out of the tetrahedral position with the bond-centred intermediate configuration metastable.

In spite of the fact therefore that the isolated interstitial atom has not been directly observed, we have reason to feel that we may understand it reasonably well.

#### C4 Interstitial-Related Interactions

In FIGURE 4, we illustrate schematically the hierarchy of annealing reactions for the various interstitial-related defects, as would be seen in a ~15–30 min isochronal annealing sequence [2,22]. In this case, in contrast to FIGURE 2, we follow the annealing also through the second generation defects as the first generation trapped interstitials (B<sub>i</sub>, C<sub>i</sub>, Al<sub>i</sub>), in turn, migrate over long distances and pair with other defects. Here, we have added results deduced from LVM spectroscopy and DLTS measurements for which there has been no direct EPR or firm LVM identification (shaded boxes). These include the trapping and relatively low temperature re-release of interstitial silicon from interstitial oxygen [17,34], as well as the various interactions of B<sub>i</sub> as it begins to migrate [22]. These have been included because they represent a logical extension from the EPR-confirmed DLTS signatures of C<sub>i</sub> and B<sub>i</sub> in a systematic study versus doping concentration of the relevant trapping impurities, and one can be reasonably confident of the conclusions.

The kinetics for the migration of the first generation defects have also been determined. For C<sub>i</sub>, the diffusional activation energy has been measured to be 0.80–0.88 eV [35]. The activation barrier for B<sub>i</sub> migration has been determined to be 0.6 eV [36]. For Al<sub>i</sub>, it is 1.2 eV [20]. However, for both B<sub>i</sub> and Al<sub>i</sub>, the effective barrier is reduced under injection conditions, to zero (athermal) for B<sub>i</sub> [36,37], and 0.3 eV for Al<sub>i</sub> [20]. This large recombination enhancement argues strongly for configurational changes versus charge state for them also, as pointed out in the above references. Consistent with this, subsequent theoretical studies have also come to similar conclusions [38,39]. In fact, the behaviour of

### 11.1 Vacancies and interstitials and their interactions with impurities in c-Si

the three defects can be understood on the basis of a very simple physical argument: making the reasonable assumption, as we did in the previous section, that one mechanism for the effect is the conversion from the tetrahedral site for the  $s^2$  ion to a bonded configuration when it picks up an electron to become  $s^2p^1$ , one predicts the conversion to occur for both  $Al_i$  and  $B_i$  as they go from the singly positive to the neutral state, and not to occur for  $C_i$ , for which all three available charge states have at least one p-electron.

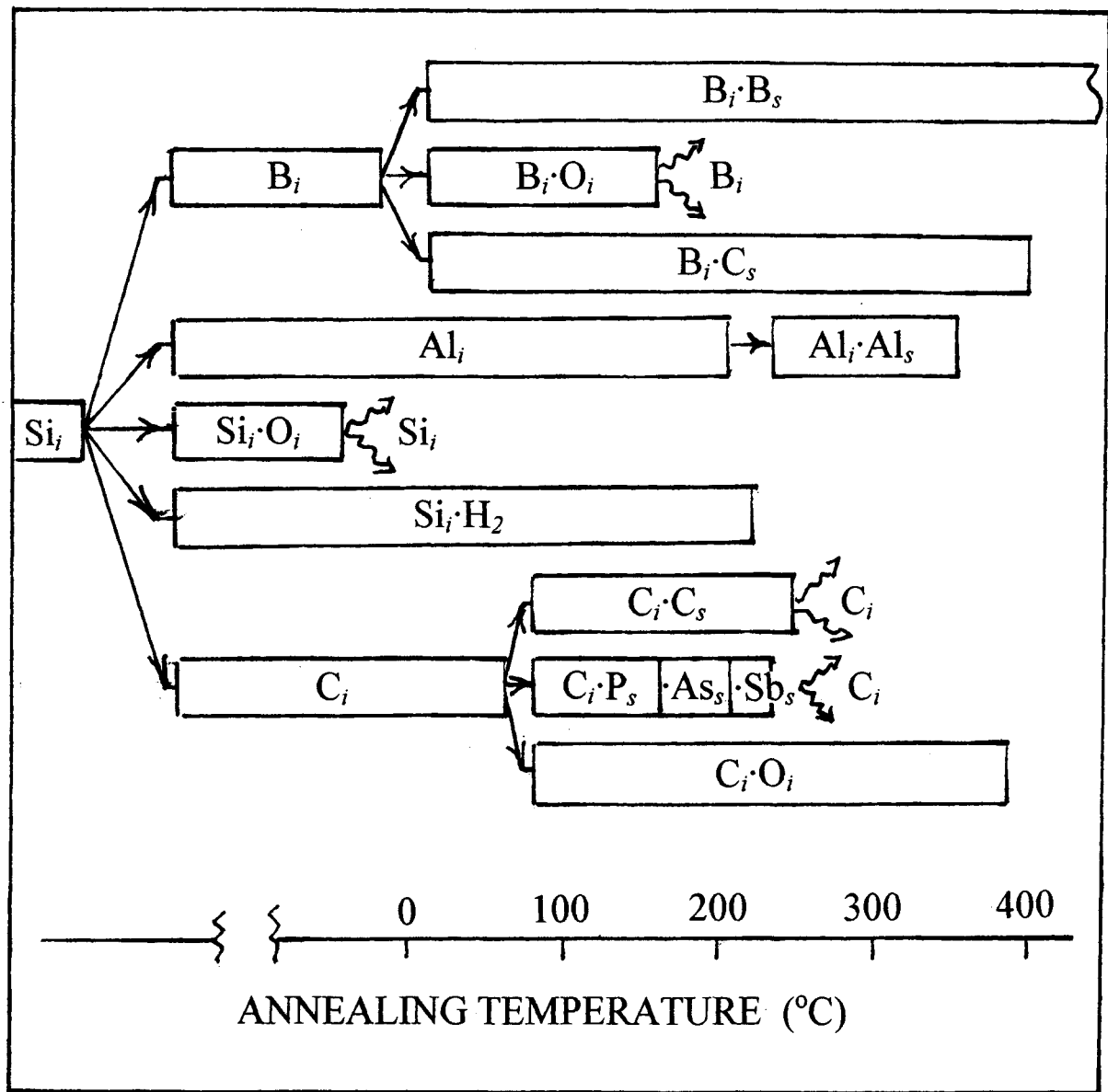


FIGURE 4 Schematic of annealing stages for interstitial-related defects (~15–30 min isochronal). The cross-hatched blocks have been indirectly deduced from DLTS studies; the remainder have been directly identified and followed by EPR or LVM spectroscopy.

Understanding this evolution of both the first and second generation interstitial-related defects turns out to be essential in understanding much of the transient-enhanced diffusion that occurs in wafer processing for two reasons: 1) the second generation annealing involves long range motion of the

### *11.1 Vacancies and interstitials and their interactions with impurities in c-Si*

impurity, as well, and 2) most of the device processing steps are believed to involve the release of excess interstitials.

## **D CLOSE FRENKEL PAIRS**

In the interpretation of the above results, it has been commonly assumed that competition between annihilation and separation of the close vacancy-interstitial (Frenkel) pairs is occurring during a low temperature irradiation, and that only the separated pairs survive [2,3]. In this model, the strong Fermi level dependence of defect production, described briefly in Section C1, can be explained in terms of the relative effect of charge state upon the two processes. However, using X-ray diffraction techniques, Erhart and Zillgen [40] have concluded very recently that, instead, the escaped vacancies and interstitials can comprise only a small fraction of the pairs produced, whose production rate is independent of Fermi level, and whose presence they continue to detect frozen into the lattice, presumably electrically inactive, and annealing out only slowly in the range up to room temperature. This is a very interesting new result, and, if correct, must force a reconsideration of the basic processes occurring during the primary damage event. It should have no effect, however, upon the understanding that we have obtained concerning the escaped isolated interstitials and vacancies.

## **E OTHER SPECTROSCOPIC PROBES**

Other spectroscopic techniques have become reliable and important probes for monitoring the defects, once a detailed correlation has been made with EPR identifications. An obvious case is DLTS, which can recognize a defect from its energy level positions, once established. Infrared LVM spectroscopy is another example, only briefly considered here for the specific case of intrinsic defects trapped by hydrogen, where uniaxial stress measurements and selective isotope substitution provided, without EPR, the necessary symmetry information for defect modelling. Correlated with EPR identifications, it has been successfully used also for some of the defects incorporating the other lighter atom impurities, such as C [24,35], and O [41]. For some of the defects, optical electronic spectra have also been identified. These include, for the vacancy-related defects, the divacancy [42] and the three group-V-atom-vacancy pairs [43]. For the first and second generation interstitial-related defects, sharp optical spectra associated with  $C_i$ ,  $C_iC_s$ , and  $C_iO_i$  have been identified [35]. In many cases, these probes have served to provide, in turn, important supplemental information concerning the defects, as well as to provide an independent monitor to follow the production and further evolution of the defects. This additional information has been incorporated into the descriptions of several of the defects described above, as noted.

## **F CONCLUSION**

We have reviewed the established information concerning the lattice vacancy and interstitial in silicon, and their interactions with other impurities and defects. The isolated defects are highly mobile and their individual contributions to the activation energy for high temperature diffusion processes must come primarily from their formation energies. Their high mobilities mean, in turn, that they are not stable at ambient temperatures and exist only in their trapped states. The identity and properties of the important trapped states, and their evolution as the material is annealed, are, for the most part, well established, providing much of the information necessary to unravel the various transient-enhanced annealing processes that are observed to occur in silicon device processing.

## ACKNOWLEDGEMENTS

Support for the preparation of this review, as well as for the relevant research at Lehigh over the past two decades, has been given by continuing grants over this period from the US Office of Naval Research.

## REFERENCES

- [1] For an extensive review of research results prior to 1990, with more complete references, particularly to the EPR literature of that period, see [2] and [3] below. Here we will supply detailed references for that period primarily to those studies relevant to the electrical and migrational properties of the defects.
- [2] G.D. Watkins [ in *Materials Science and Technology* vol.4 (VCH, Weinheim, 1991) ch.3 ]
- [3] G.D. Watkins [ in *Deep Centers in Semiconductors* Ed. S.T. Pantelides (Gordon and Breach, 1986) ch.3 ]. This deals with the vacancy only, but in greater detail.
- [4] A review of ENDOR studies, including their application to the intrinsic defects and their progeny, can be found in C.A.J. Ammerlaan [ *Mater. Res. Soc. Symp. Proc. (USA)* vol.46 (1985) p.227 ]
- [5] J.L. Newton, A.P. Chatterjee, R.D. Harris, G.D. Watkins [ *Physica B (Netherlands)* vol.116 (1983) p.219 ]
- [6] G.D. Watkins [ in *Festkörperprobleme XXIV (Advances in Solid State Physics)* Ed. P. Grosse (Viewig, Braunschweig 1984) p.164 ]
- [7] G.A. Barraff, E.O. Kane, E.O. Schlüter [ *Phys. Rev. B (USA)* vol.21 (1980) p.5662 ]
- [8] J.R. Troxell [ PhD dissertation, Lehigh Univ., 1979, unpublished ]
- [9] G.D. Watkins, A.P. Chatterjee, R.D. Harris, J.R. Troxell [ *Semicond. Insul. (UK)* vol.5 (1983) p.321 ]
- [10] G.D. Watkins, J.W. Corbett, R.M. Walker [ *J. Appl. Phys. (USA)* vol.30 (1959) p.1198 ]
- [11] L.C. Kimerling [ *Inst. Phys. Conf. Ser. (UK)* no.46 (1977) p.221 ]
- [12] K.L. Brower [ in *Phys. Rev. B (USA)* vol.5 (1972) p.4274 ]
- [13] W.M. Chen, O.O. Awadelkarim, B. Monemar, J.L. Lindström, G.S. Oehrlein [ *Phys. Rev. Lett. (USA)* vol.64 (1990) p.3042 ]
- [14] B. Bech Nielsen, P. Johannessen, P. Stallinga, K. Bonde Nielsen [ *Phys. Rev. Lett. (USA)* vol.79 (1997) p.1507 ]
- [15] B. Bech Nielsen, L. Hoffmann, M. Budde, R. Jones, J. Goss, S. Öberg [ *Mater. Res. Forum (Switzerland)* vol.199-201 (1995) p.933 ]
- [16] G.R. Bai, J.K. Zhou, J.M. Chen, T.S. Shi, M.W. Qi, L.M. Xie [ *Sci. Sin. A (China)* vol.31 (1988) p.399 ]
- [17] R.D. Harris, G.D. Watkins [ *J. Electron. Mater. (USA)* vol.14 (1984) p.799 ]
- [18] K.L. Brower [ *Phys. Rev. B (USA)* vol.1 (1970) p.1908 ]
- [19] J.R. Niklas, J.-M. Spaeth, G.D. Watkins [ *Mater. Res. Soc. Symp. Proc. (USA)* vol.46 (1985) p.237 ]
- [20] J.R. Troxell, A.P. Chatterjee, G.D. Watkins, L.C. Kimerling [ *Phys. Rev. B (USA)* vol.19 (1979) p.5336 ]
- [21] R.D. Harris, J.L. Newton, G.D. Watkins [ *Phys. Rev. B (USA)* vol.36 (1987) p.1094 ]
- [22] L.C. Kimerling, M.T. Asom, J.L. Benton, P.J. Devrinsky, C.E. Caefter [ *Mater. Sci. Forum (Switzerland)* vol.38-41 (1989) p.141 ]
- [23] L.W. Song, G.D. Watkins [ *Phys. Rev. B (USA)* vol.42 (1990) p.5759 ]

## 11.1 Vacancies and interstitials and their interactions with impurities in c-Si

- [24] J.F. Zheng, M. Stavola, G.D. Watkins [ *22<sup>nd</sup> International Conference on the Physics of Semiconductors*, Vancouver, Canada, 15-19 Aug 1994, Ed. E.J. Lockwood (World Scientific, Singapore, 1995) p.2363 ]
- [25] M. Budde et al [ *19<sup>th</sup> International Conference on Defects in Semiconductors*, Aveiro, Portugal, July 21-25 1997, Eds. G. Davis, M.H. Nazaré (Mater. Res. Forum, in press) ]
- [26] P. Deák, L.C. Snyder, M. Heinrich, C.R. Ortiz, J.W. Corbett [ *Physica B (Netherlands)* vol.170 (1991) p.253 ]
- [27] C.G. Van de Walle, J. Neugebauer [ *Phys. Rev. B (USA)* vol.52 (1995) p.R14320 ]
- [28] T.S. Shi, G.R. Bai, M.W. Qi, J.K. Zhou [ *Mater. Res. Forum (Switzerland)* vol.10-12 (1986) p.597 ]
- [29] R. Car, P.J. Kelly, A. Oshiyama, S.T. Pantelides [ *13th Internatitonal Conference on Defects in Semiconductors*, Coronado, CA, 12-17 Aug 1984, Eds. L.C. Kimerling, J.M. Parsey Jr. (Metallurgical Society of AIME, Warrendale, PA, 1985) p.269 ]
- [30] T. Bar-Yam, J.D. Joannopoulos [ *13th Internatitonal Conference on Defects in Semiconductors*, Coronado, CA, 12-17 Aug 1984, Eds. L.C. Kimerling, J.M. Parsey Jr. (Metallurgical Society of AIME, Warrendale, PA, 1985) p.261 ]
- [31] For a more detailed discussion of the interstitial properties implied by [29,30], see G.D. Watkins [ *Mater. Res. Soc. Symp. Proc. (USA)* vol.469 (1997) p.139-50 ]
- [32] D.J. Chadi [ *Phys. Rev. B (USA)* vol.46 (1992) p.9400 ]
- [33] S. Libertino et al [ *Appl. Phys. Lett. (USA)* vol.71 (1997) p.389 ]
- [34] A. Brelot, J. Charlemagne [ *Radiat. Eff. (UK)* vol.8 (1971) p.61 ]
- [35] G. Davies, R.C. Newman [ *Handbook on Semiconductors* vol.3 (Elsevier Science B.V., Amsterdam, 1994) p.1557 ]. This contains a comprehensive review of the role of carbon in silicon, which combines information from EPR, DLTS, and optical studies.
- [36] J.R. Troxell, G.D. Watkins [ *Phys. Rev. B (USA)* vol.22 (1980) p.921 ]
- [37] R.D. Harris, G.D. Watkins, L.C. Kimerling [ *Mater. Sci. Forum (Switzerland)* vol.10-12 (1986) p.163 ]
- [38] G.A. Baraff, M. Schlüter [ *Phys. Rev. B (USA)* vol.30 (1984) p.3460 ]
- [39] E. Tarnow [ *Europhys. Lett. (Switzerland)* vol.16 (1991) p.449 ]
- [40] P. Erhart, H. Zillgen [ *Mater. Res. Soc. Symp. Proc. (USA)* vol.469 (1997) ]
- [41] R.C. Newman [ *Infra-red Studies of Crystal Defects* (Taylor and Francis, 1973) ]
- [42] L.J. Cheng, J.C. Corelli, J.W. Corbett, G.D. Watkins [ *Phys. Rev. (USA)* vol.103 (1966) p.761 ]
- [43] G.D. Watkins [ *Rad. Eff. Defects Solids (UK)* vol.111-112 (1989) p.487 ]

## 11.2 Electrical and optical properties of dislocations in c-Si

E.A. Steinman and E.B. Yakimov

December 1998

### A INTRODUCTION

Experiments already performed 20 years ago showed that plastic deformation decreases the carrier concentration in both n- and p-type Si crystals and that the type of conductivity in n-Si is changed at high dislocation densities [1]. In crystals which have been highly deformed at temperatures below 700°C, the Fermi level was found [1,2] to be pinned at dislocation levels located at 0.42–0.45 eV above the valence band. Similar energy levels were obtained by evaluating barrier heights formed near individual dislocations [3]. In addition to these main dislocation levels, further energy levels have been observed at  $E_v+0.27$ ,  $E_v+0.17$  [1] and  $E_c-0.4$  eV [2] in deformed crystals by Hall effect measurements.

In samples of high dislocation density, deep level transient spectroscopy (DLTS) studies [4,5] revealed five electron and eight hole traps with energy levels at  $E_c-0.18$ ,  $E_c-0.28$ ,  $E_c-0.41$ ,  $E_c-0.48$ ,  $E_c-0.63$  eV and  $E_v-0.09$ ,  $E_v-0.23$ ,  $E_v-0.26$ ,  $E_v-0.29$ ,  $E_v-0.35$ ,  $E_v-0.36$ ,  $E_v-0.40$ ,  $E_v-0.63$  eV. The number of dislocation related traps is considerably smaller in samples of low dislocation density (about  $10^5$ – $10^6$  cm $^{-2}$ ). In these crystals, four levels have been detected in the upper half of the energy gap ( $E_c-0.19$ ,  $E_c-0.29$ ,  $E_c-0.41$ ,  $E_c-0.54$  eV) [6] and three levels in the lower half (0.20, 0.38, 0.54 eV) [7,8]. Most of these centres show a logarithmic dependence of the capture coefficient on filling pulse duration which is explained by the influence of a barrier formed around dislocations in conjunction with the capture of majority carriers [5]. The relative concentration of different energy levels depends in a complex way on the impurity concentration of the initial sample, deformation temperature, dislocation density, etc., and can vary in a wide range. It should also be noticed that if all these centres are located in the vicinity of dislocations, filling of deeper lying levels may prevent the capture of carriers into shallower levels [9], which in turn leads to a decrease or even disappearance of peaks associated with shallower levels.

Scanning electron microscopy (SEM) in the electron beam induced current (EBIC) mode performed in semiconductor crystals reveals local regions with enhanced recombination velocities [10]. This technique therefore allows us to study not only the recombination activity of dislocations but also to demonstrate that most centres introduced in the crystals during plastic deformation are located near dislocations [10] or along their slip planes [11] and not distributed homogeneously through the crystal. In principle, the analysis of EBIC data could provide information on dislocation related energy levels. Unfortunately, the results of such analyses are rather controversial. Shallow levels (about 0.06 eV from both bands) due to 60° and screw dislocations were, for example, estimated from the temperature dependence of the EBIC contrast [12], whereas considerably deeper levels were obtained in [13] using other EBIC techniques.

Increasing the deformation temperature and/or the annealing temperature above 750°C is found [1] to result in a decrease of the acceptor properties of dislocations. It is also observed that the amplitudes of DLTS spectra at least partially decrease at these annealing temperatures [4,6,7]. On the other hand, the EBIC contrast of dislocations increases normally after high temperature annealing [14]. Although the acceptor properties of dislocations annealed at temperatures higher than 750°C deteriorate, it is interesting to observe that these properties can be restored by applying deformation temperatures

## *11.2 Electrical and optical properties of dislocations in c-Si*

above 1150–1190°C [15]. This behaviour has been explained by the release of oxygen from dislocations.

Diffusivities of transition metals in Si are rather high at temperatures usually used for deformation processes. Hence, unintentional contamination of samples during thermal treatment often can not be excluded. This is particularly true for experiments previously performed with deformation cells containing metal parts. It is therefore not unreasonable to assume that the results cited above may originate from contaminated dislocations. Results obtained on well characterized dislocations are described in the next section.

### **B INVESTIGATIONS OF CLEAN DISLOCATIONS**

Considerable improvements in sample preparation eventually allowed the study of dislocations introduced in samples of very low contamination level. It has been shown [16] that clean dislocations exhibit very low recombination activities which, however, increased as soon as the samples were contaminated. So far, it has not been possible to obtain DLTS signals from ‘clean’ partial dislocations [17]. An absence of DLTS signals was also reported in [18] for clean dislocations which were introduced during very short deformation periods resulting in short pathways. DLTS spectra were, however, clearly observed after subsequent thermal annealing or increasing the deformation time. In [19], for example, the authors reported that the DLTS and EPR signals in highly dislocated Si depended on the area covered by the moving dislocations which they explained by the creation of intrinsic point defects and complex defects (including these point defects) during the motion of dislocations.

### **C INVESTIGATION OF DISLOCATIONS INTERACTING WITH SPECIFIC IMPURITIES**

The impact of transition metals on the electronic properties of dislocations and their electrical activity has been studied in several papers, in particular by using the EBIC technique [1,13,16,20–22]. Cu passivation of dislocation-related deep levels was observed in [20]. The authors reported a decrease in the DLTS signal after Cu doping. Other studies showed [1] that interaction of dislocations with copper decreased the acceptor properties of both defects quite considerably. EBIC investigations demonstrated [13,16,21,22] that Cu, Ni, Fe and Au enhance the recombination properties of dislocations. Gettering of gold at dislocations was shown to increase the EBIC contrast value and to change its dependence on annealing temperature without changing the DLTS spectra originating from dislocations [21].

Several papers have been devoted to investigations of dislocations interacting with hydrogen because of the ability of hydrogen to passivate extended and point defects in semiconductor crystals. These DLTS and EBIC investigations have shown that hydrogen indeed decreases the EBIC contrast of the dislocations [25] and the amplitude of dislocation-related DLTS spectra [23,24]. The mechanism of such passivation processes is, however, not simple. It was, for example, observed that hydrogen diffused into Si crystals at room temperature without passivating dislocations [24,26]. Passivation was only successful if the temperature was increased to about 300°C.

Oxygen is one of the most important impurities in Si because it is present in all crystals and its concentration can be varied from  $10^{14}$  to about  $10^{18} \text{ cm}^{-3}$ , depending on the growth method. Interaction of dislocations with oxygen was shown to influence the mobility of dislocations [27] and to create the minimal starting stress [27,28] which is necessary to bring dislocations in motion. It was also shown [28] that oxygen can be gathered by moving dislocations and that the oxygen

## 11.2 Electrical and optical properties of dislocations in c-Si

concentration in dislocation atmospheres depends on the oxygen content as well as on the parameters of dislocation motion.

A common procedure to study the effect of oxygen on the electrical and optical properties of dislocations is to compare Si samples grown by the Czochralski (Cz) method with those grown by the floating zone (FZ) technique because the oxygen concentration in these two types of crystals can differ by more than two orders of magnitude. Both types of samples are then deformed under similar conditions. Such investigations have revealed significant differences in the EBIC contrast of individual dislocations and its dependence on the electron beam current between Cz and FZ Si crystals as well as between Cz crystals with different oxygen content. Differences were also observed in samples deformed under similar conditions but cooled at different rates [14]. The dislocation related EBIC contrast in Cz Si [29] depends non-monotonically on the annealing temperature exhibiting a minimum at 750–800°C and an increase at higher temperatures which is in anti-correlation with the charge carrier concentration observed in [1]. The effect of oxygen on the dislocation recombination activity was also studied by using laser beam induced current (LBIC) measurements of minority carrier diffusion lengths in plastically deformed Si [30].

The effect of dislocations on the charge carrier concentration in highly dislocated Si was found to be almost independent of the oxygen concentration [1]. Oxygen only slightly enhances the annealing of dislocation related acceptor centres at temperatures above 700–750°C and increases slightly the hole concentration. However, in samples of low dislocation density ( $N_D \approx 10^7 \text{ cm}^{-2}$ ) a pronounced difference between Cz and FZ samples has been observed [28]. In FZ n-Si, the electron concentration decreases monotonically with increasing dislocation density, whereas in Cz n-Si samples the electron concentration increases with increasing dislocation density, implying that shallow donors are introduced in such samples during plastic deformation at temperatures higher than 700°C [28,31]. At low dislocation densities, the concentration of these shallow donors is proportional to the dislocation density and most of the donors were found to be located near dislocations [28]. Further studies indicated that oxygen may be involved in the formation of these shallow donors in Cz samples. It should also be noticed that if the samples were quenched after deformation at 700°C neither starting stresses nor dislocation donors were observed. This shows that the defects discussed here are of complex nature and that particular reactions have to take place for their formation.

## D DISLOCATION-RELATED LUMINESCENCE

Four photoluminescence (PL) lines D1(0.81 eV), D2(0.87 eV), D3(0.94 eV), and D4(0.98 eV) known to originate from dislocation related centres [32] have been investigated quite extensively [33–36]. Several properties of these lines clearly show that they are correlated in pairs D1/D2 and D3/D4. Measurements performed after plastic deformation at low temperatures and high stresses [37] showed that the lines D3 and D4 strongly depend on particular dislocation morphologies [38]. The D4 line is substituted by two new recombination bands D5 and D6 with energies near 0.96 eV and 1.013 eV, respectively. The fine structure of the 0.96 eV emission is attributed to recombination processes of electrons and holes at Shockley partial dislocations split apart by different widths. Almost all glide dislocations in silicon are dissociated into partial dislocations of Shockley type, confining an intrinsic stacking-fault ribbon [37]. In equilibrium, the distance between two coupled partial dislocations is of the order of 5 nm. Low temperature high stress deformation and consequent cooling under applied stress leads to a freezing of non-equilibrium splittings which can be larger or smaller than the ones in equilibrium. Using these results and comparing data for germanium and silicon, the authors of [39,40] concluded that the fine structure of emission D5 originates from recombination processes at 90° partial dislocations of split 60° dislocations and that the potential of the second partial serves as a disturbance for the initial or final state, since the convergence of the fine structure is described by one and the same exponent. Hence, the distribution of the emission intensity through a set of narrow lines

## *11.2 Electrical and optical properties of dislocations in c-Si*

reflects the distribution of the widths of the split dislocations. In this model, the D6 line was linked to recombination processes at highly split  $60^\circ$  dislocations which coincide with recombination processes at isolated  $90^\circ$  partial dislocations. This conclusion is supported by the dependence of the position of the D4, D5 and D6 lines on uniaxial stress [38] and polarization measurements [41]. Most probably, the D3 line is the TO phonon replica of the D4 line.

The origin of the D1 and D2 line is, compared with the D3 and D4 line, less clear. Stacking faults between dislocations, impurity atoms in the strain field around dislocations, dislocation jogs and segments of dislocations of special type (like Lomer dislocations) are typical examples for the origin of the D1 and D2 lines suggested in the literature. Uniaxial stress measurements showed that defects responsible for these lines have tetragonal symmetry and are randomly distributed over all equivalent orientations [35]. This implies that D1 and D2 centres are not related to regular parts of dislocations. On the other hand, detailed polarization measurements on samples with a single slip system revealed that the polarization of the D1 and D2 lines is slightly different and forms a  $90^\circ$  angle with the slip plane [41]. This suggests a correlation of the orientational distribution of D1 and D2 centres with the slip plane and indicates a correlation between these centres and dislocations.

An important matter is the role of impurities in the formation of dislocation-related radiative centres. Here, transition metals should be considered in the first place taking into account that they are fast diffusers and are known to form deep levels which can readily affect the electrical and optical properties of bulk silicon. It has been demonstrated recently [42] that crystals not doped with transition metals ( $<10^{11} \text{ cm}^{-3}$ ) do not exhibit D-band luminescence or any contrast in EBIC measurements, while after deliberate Cu doping ( $\approx 10^{13} \text{ cm}^{-3}$ ) both luminescence and contrast are clearly observed. An interesting point is that similar results are obtained with other impurities such as Ni, Fe, Ag or Au [43]. It is therefore concluded that any influence of transition metals on the luminescence properties of dislocations must be indirect.

Interesting results have been reported on the temperature dependence of dislocation-related luminescence. Regarding the D4 and D3 lines, good agreement is obtained in different studies [34,35,44] which showed that the deactivation energy of these lines is in the range between 4 and 10 meV. Different or even controversial results have been reported for the D1 and D2 line. Whereas the authors of [34,35] obtained deactivation energies very close to the ones of the D4 and D3 lines, a value of 0.17 eV was reported in [44]. Based on the model applied in [44] and considering that the samples in [34,35] were deformed at much lower temperature than those in [44], a possible explanation for the discrepancy in the deactivation energy of the D1 line has been suggested by the authors of [44]. At low deformation temperatures, deep non-radiative recombination centres are generated at dislocations according to DLTS and EPR measurements. The lower the deformation temperature, the higher the concentration of these deep centres. According to [44], the excitation of carriers from D1 centres to any local mobility edge, which results in a movement of carriers along the dislocation, is accompanied by a decrease of luminescence since the carriers will be trapped at dangling bonds and other deep non-radiative centres. This implies that generation of dislocations at high temperatures should result in dislocation related luminescence at room temperature [44,45].

## **E CONCLUSION**

This Datareview has summarised the electrical and optical properties of dislocations in crystalline silicon. Several hole and electron traps have been revealed by DLTS measurements, while SEM and EBIC reveal local regions of enhanced recombination. The effects of specific impurities have been determined. Increased recombination occurs with Cu, Ni, Fe and Au, while H decreases recombination. Oxygen influences dislocation mobility and may form shallow donors near

dislocations. Several luminescence peaks have been associated with dislocations and their origins discussed.

## REFERENCES

- [1] V.G. Eremenko, V.I. Nikitenko, E.B. Yakimov [ *Sov. Phys.-JETP (USA)* vol.46 (1978) p.598-603 ]
- [2] V.A. Grazhulis, V.V. Kveder, V.Yu. Mukhina [ *Phys. Status Solidi A (Germany)* vol.43 (1977) p.407-15 ]
- [3] V.G. Eremenko, V.I. Nikitenko, E.B. Yakimov [ *Sov. Phys.-JETP (USA)* vol.42 (1976) p.503-7 ]
- [4] L.C. Kimerling, J.R. Patel [ *Appl. Phys. Lett. (USA)* vol.34 (1979) p.73-5 ]
- [5] V.V. Kveder, Yu.A. Osipyan, W. Schröter, G. Zoth [ *Phys. Status Solidi A (Germany)* vol.72 (1982) p.701-4 ]
- [6] P. Omling, E.R. Weber, L. Montelius, H. Alexander J. Michel [ *Phys. Rev. B (USA)* vol.32 (1985) p.6571-81 ]
- [7] V.V. Aristov, P. Werner, I.I. Snighireva, I.I. Khodos, E.B. Yakimov, N.A. Yarykin [ *Sov. Phys.-Semicond. (USA)* vol.20 (1986) p.571-3 ]
- [8] J.J. Simon, E. Yakimov, M. Pasquinelli [ *J. Phys. III (France)* vol.5 (1995) p.1327-36 ]
- [9] S.V. Koveshnikov, O.V. Feklisova, E.B. Yakimov, N.A. Yarykin [ *Phys. Status Solidi A (Germany)* vol.127 (1991) p.67-73 ]
- [10] E. Yakimov [ *Scanning Microsc. (USA)* vol.6 (1992) p.81-96 ]
- [11] I.E. Bondarenko, H. Blumtritt, J. Heydenreich, V.V. Kazimiruk, E.B. Yakimov [ *Phys. Status Solidi A (Germany)* vol.95 (1986) 173-7 ]
- [12] S. Kasanagi, T. Sekiguchi, B. Shen, K. Sumino [ *Mater. Sci. Technol. (UK)* vol.11 (1995) p.685-90 ]
- [13] T.S. Fell, P.R. Wilshaw, M.D. de Coteau [ *Phys. Status Solidi A (Germany)* vol.138 (1993) p.695-704 ]
- [14] I.E. Bondarenko, E.B. Yakimov [ *Phys. Status Solidi A (Germany)* vol.122 (1990) p.121-8 ]
- [15] E.B. Yakimov, N.A. Yarykin, V.I. Nikitenko [ *Phys. Status Solidi A (Germany)* vol.84 (1984) p.443-50 ]
- [16] M. Kittler, C. Ulhaq-Bouillet, V. Higgs [ *Mater. Sci. Eng. B (Switzerland)* vol.24 (1994) p.52 ]
- [17] A. Berg, I. Brough, J.H. Evans, G. Lorimer, A.R. Peaker [ *Semicond. Sci. Technol. (UK)* vol.7 (1992) p.A263-8 ]
- [18] O.V. Kononchuk, V.V. Nikitenko, V.I. Orlov, E.B. Yakimov [ *Phys. Status Solidi A (Germany)* vol.143 (1994) p.K5-7 ]
- [19] C. Kisielowski-Kemmerich, H. Alexander [ in *Defects in Crystals* Ed. E. Mizera (World Scientific, 1988) p.290-305 ]
- [20] W. Staiger, G. Pfeiffer, K. Weronek, A. Höpner, J. Weber [ *Mater. Sci. Forum (Switzerland)* vol.143-147 (1994) p.1571-5 ]
- [21] V.V. Aristov et al [ *Phys. Status Solidi A (Germany)* vol.102 (1987) p.687-95 ]
- [22] Z.J. Radzimski, T.Q. Zhou, A.B. Buczkowski, G.A. Rozgonyi [ *Appl. Phys. A (Germany)* vol.53 (1991) p.189-93 ]
- [23] M.N. Zolotukhin, V.V. Kveder, Yu.A. Osip'yan [ *Sov. Phys.-JETP (USA)* vol.55 (1982) p.1189 ]
- [24] S.V. Koveshnikov, S.V. Nosenko, E.B. Yakimov [ *Phys. Status Solidi A (Germany)* vol.120 (1990) p.391-5 ]
- [25] C. Dube, J.I. Hanoka [ *Appl. Phys. Lett. (USA)* vol.45 (1984) p.1135-7 ]
- [26] Yu.A. Osip'yan, A.M. Rtishchev, E.A. Steinman, E.B. Yakimov, N.A. Yarykin [ *Sov. Phys.-JETP (USA)* vol.55 (1982) p.294-7 ]

- [27] K. Sumino [ *NATO ASI Ser. B, Phys. (USA)* vol.202 (1988) p.77-94 ]
- [28] I.E. Bondarenko, V.G. Eremenko, V.I. Nikitenko, E.B. Yakimov [ *Phys. Status Solidi A (Germany)* vol.60 (1980) p.341-9 ]
- [29] E.B. Yakimov [ *Mater. Res. Soc. Symp. Proc. (USA)* vol.138 (1989) p.173-7 ]
- [30] S. Acerboni, S. Pizzini, S. Binetti, M. Acciarri, B. Pichaud [ *J. Appl. Phys. (USA)* vol.76 (1994) p.2703-10 ]
- [31] M. Koguchi, I. Yonenaga, K. Sumino [ *Jpn. J. Appl. Phys. (Japan)* vol.21 (1982) p.L411-3 ]
- [32] N.A. Drozdov, A.A. Patrin, V.D. Tkachev [ *Sov. Phys.-JETP Lett. (USA)* vol.23 (1976) p.597 ]
- [33] M. Suezawa, K. Sumino [ *Phys. Status Solidi A (Germany)* vol.78 (1983) p.639 ]
- [34] M. Suezawa, Y. Sasaki, K. Sumino [ *Phys. Status Solidi A (Germany)* vol.79 (1983) p.173 ]
- [35] R. Sauer, J. Weber, J. Stoltz, E.R. Weber, K.H. Kurster, H. Alexander [ *Appl. Phys. A (Germany)* vol.36 (1985) p.1 ]
- [36] V. Higgs, E.C. Lightowers, S. Tajbakhsh [ *Appl. Phys. Lett. (USA)* vol.61 (1992) p.1087 ]
- [37] K. Wessel, H. Alexander [ *Philos. Mag. (UK)* vol.35 (1977) p.1523 ]
- [38] R. Sauer, Ch. Kisielowski-Kemmerich, H. Alexander [ *Phys. Rev. Lett. (USA)* vol.57 (1986) p.1472 ]
- [39] A.N. Izotov, A.I. Kilubakin, S.A. Shevchenko, E.A. Steinman [ *Phys. Status Solidi A (Germany)* vol.130 (1992) p.193 ]
- [40] E.A. Steinman [ *Mater. Sci. Forum (Switzerland)* vol.143-147, part 1 (1994) p.537 ]
- [41] A.N. Izotov, Yu.A. Osip'yan, E.A. Steinman [ *Sov. Phys.-Solid State (USA)* vol.28 no.4 (1986) p.567-70 ]
- [42] V. Higgs, C.E. Norman, E.C. Lightowers, P. Kightley [ *Proc. 20th Int. Conf. on the Physics of Semiconductors* Eds. E.M. Anastassakis, J.D. Joannopoulos (World Scientific, Singapore, 1990) vol.1 p.706-9 ]
- [43] V. Higgs, M. Goulding, A. Brinklow, P. Kightley [ *Appl. Phys. Lett. (USA)* vol.60 (1992) p.1369-71 ]
- [44] V.V. Kveder, E.A. Steinman, S.A. Shevchenko, H.G. Grimmeiss [ *Phys. Rev. B (USA)* vol.51 (1995) p.10520-6 ]
- [45] E. Sveinbjörnsson, J. Weber [ *Appl. Phys. Lett. (USA)* vol.69 (1996) p.2686 ]

## CHAPTER 12

### OPTICAL PROPERTIES (*Edited by D.E. Aspnes*)

- 12.1 Optical properties of c-Si: general aspects
- 12.2 Optical functions of intrinsic c-Si for photon energies up to 7.5 eV: table
- 12.3 Optical functions of intrinsic c-Si for selected photon energies: table
- 12.4 Optical functions of liquid Si

## 12.1 Optical properties of c-Si: general aspects

D.E. Aspnes

March 1998

### A INTRODUCTION AND SUMMARY

This work is an update of my 1988 EMIS assessment of values of the complex dielectric function  $\epsilon = \epsilon_1 + i\epsilon_2$  and refractive index  $n = n + ik$  of crystalline (c-) Si [1]. Because these data are expected to be used primarily for optical modelling, such as the determination of thicknesses of oxide overlayers from ellipsometric spectra, I emphasize the spectral range 0.5 to 7.5 eV, discussing recent developments, measurement procedures, and selection criteria, and in Datareview 12.2 providing for modelling purposes a summary of preferred values from 0.0 to 7.5 eV in steps of 0.02 eV. To provide a more complete picture below 1.2 eV and information above 7.5 eV, in Datareview 12.3 I reproduce the listings of [1] in these ranges. A general discussion of the data in Datareview 12.3 is given in [1].

Since 1988 new data have indicated that improvements are needed in the earlier listing below 7.5 eV. In the quartz-optics range the spectroscopic ellipsometry (SE) results of Herzinger et al [2] replace the pseudodielectric function  $\langle\epsilon\rangle = \langle\epsilon_1\rangle + i\langle\epsilon_2\rangle$  spectra of Aspnes and Studna [3] taken with SE on nominally H-terminated (111) Si surfaces. From 6.0 to 6.5 eV the results of [2] replace the results of Philipp [4], obtained by a Kramers–Kronig (K–K) analysis of reflectance data from 0 to 25 eV on air-oxidized samples. The results of [2] also replace the previous extrapolation of  $n$  between 1.1 and 1.5 eV. Quartz-optics work since 1988 includes the 1992 results of Jellison [5], obtained from an analysis of SE spectra measured from 1.48 to 5.30 eV on air-oxidized samples, the 1992  $\langle\epsilon\rangle$  spectra of Nayar et al [6], obtained from 2.75 to 4.96 eV by SE on epitaxial (001) and (111) films freshly deposited by chemical vapour deposition, the 1994  $\langle\epsilon\rangle$  spectra of Yasuda and Aspnes [7], obtained from 1.5 to 6.0 eV by SE on nominally atomically flat H-terminated (111) Si samples prepared by NH<sub>4</sub>F etching, and the above-mentioned 1998 results of [2], obtained from a self-consistent analysis of SE spectra from 0.75 to 6.5 eV obtained on one air-oxidized and six thermally oxidized (001) wafers. In addition, Geist et al [8] performed transmission measurements to determine an accurate ( $\pm 2\%$ ) value of  $k$  at the HeNe laser wavelength of 6328 Å, providing an independent check on the SE results.

Specifically, the more recent data indicate that the values of  $\langle\epsilon_2\rangle$  reported in [3] are substantially larger than the true bulk values of  $\epsilon_2$  from 2.5 to 3.2 eV, below the onset of strong absorption, probably because a rotating-analyzer ellipsometer cannot measure small values of  $\langle\epsilon_2\rangle$  accurately. The newer results reported in [2] and [5] were taken independently with instruments not subject to this limitation, and the excellent agreement of their measured spectral dependences over this range is significant. Their absolute values were determined by comparison with absorption results, and hence cannot be used as an independent check. However, the interpolated value of  $k$  at 1.959 eV from [2], 0.01455, differs by only 7% from that given in [8], 0.01564. This modification to the previously listed values of  $\epsilon_2$  also impacts the value of  $\epsilon_1$  in the vicinity of the  $(E_0', E_1)$  complex near 3.4 eV. A second improvement is found at the  $E_2$  peak of  $\epsilon_2$  at 4.24 eV, where the value 48.3 obtained for  $\langle\epsilon_2\rangle$  in [7] exceeds by a substantial margin the value 46.8 reported in [3]. A higher value of  $\langle\epsilon_2\rangle$  implies a more abrupt transition between bulk and ambient, and hence an improved representation of the true bulk dielectric function  $\epsilon$  by the pseudodielectric function  $\langle\epsilon\rangle$  (see below).

## B MEASUREMENT AND ANALYSIS

It is virtually impossible to eliminate uncertainties in nominal bulk values of  $\epsilon$  determined by reflectance techniques (reflectometry and ellipsometry), which with the exception of [8] have been the recent methods of choice. Optical measurements do not measure  $\epsilon$  directly, so its determination by optical methods necessarily involves modelling and assumptions. At the sample and analysis levels one can either attempt to prepare atomically flat, perfectly terminated surfaces and calculate  $\langle\epsilon\rangle \approx \epsilon$  within the two-phase (substrate/ambient) model ignoring the effects of overayers, or prepare stable (usually oxidized) samples and reduce the data in the three- (substrate/overlayer/ambient) or four- (substrate/interface/overlayer/ambient) phase models taking the overayers and interfaces explicitly into account. With respect to measurement approaches, one can either perform a K–K analysis of reflectance data obtained over a suitably wide spectral range, as done in [4], or use SE to determine the complex reflectance ratio  $\rho$ , as done in [2], [3], and [7].

The two-phase model was used in [3], [6], and [7], with [3] introducing the use of the ellipsometer to monitor surface preparation in real time to obtain the most abrupt surface as determined by the maximal height of the  $E_2$  peak of  $\epsilon_2$ . Although a truly abrupt surface cannot be obtained, if for no other reason than that termination of the bulk lattice will affect atomic potentials to a depth of several monolayers, the closer this ideal is approached the closer  $\langle\epsilon\rangle$  approaches  $\epsilon$ . The atomically flat H-terminated (111) Si surfaces prepared by NH<sub>4</sub>F etching probably come as close to this ideal as possible, and as such have been suggested as reference standards for optical instruments [7]. The three-phase method was used in [4] and [5], and the four-phase approach in [2]. The disadvantages of the three- and four-phase approaches are that the thickness and dielectric response of the Si/oxide interface and probably that of the oxide overlayer itself are not well known. The nature of the interface remains a matter of contention, and it was noted in the multisample analysis of [2] that the value of the  $E_2$  peak in  $\epsilon_2$  could vary from 47.2 to 49.7 depending on the thickness and spectral response assumed for this interface. Also, air-oxidized overayers were assumed in [2] and [5] to be SiO<sub>2</sub>, whereas Philipp [4] found that these overayers are more accurately modelled as SiO. However, since both SiO<sub>2</sub> and SiO are transparent below about 6 eV, this should not make a major difference.

Further flexibility is possible in analysis. One can either reduce SE data directly on a wavelength-by-wavelength basis, or develop an analytic representation by fitting piecewise-continuous analytic functions that satisfy the necessary constraints of causality and linearity. The former approach is more direct but does not suppress noise and may yield results that are not fully K–K consistent. The latter approach eliminates these difficulties but imposes predetermined functional dependences that may not fully represent  $\epsilon$ . So far, regarding reference-quality data the latter approach has been used only in [2].

It is also becoming clear that we are reaching the point where remaining discrepancies, of the order of 1–2% in peak values, may be intrinsically unavoidable in reflectance-type measurements. These discrepancies originate from the localization of the excited states created during optical absorption in regions where materials are strongly absorbing, and result in effects such as apparent differences of the order of a few meV in critical point energies according to orientation and chemical termination [9]. These results imply that accurate modelling may require the use of  $\epsilon$  data for a specific orientation and termination, that is, the analysis of SiO<sub>2</sub> films on (001) samples should be done using  $\epsilon$  data determined on similar oxide-terminated (001) samples rather than using  $\epsilon$  data obtained on H-terminated (111) samples.

Future improvements will probably require different approaches, for example the use of transmission measurements as done in [8]. Transmission measurements have the obvious advantages of maximizing and minimizing the interactions of the light beam with the bulk and surfaces, respectively, and thereby

## 12.1 Optical properties of c-Si: general aspects

minimizing surface effects. However, the accuracy requirements in strongly absorbing regions of the spectrum are severe. First-order calculations show that an SiO<sub>2</sub> overlayer reduces the height of the E<sub>2</sub> peak of <ε<sub>2</sub>> by 0.56/Å. Thus the difference between the values of 47.6 and 48.3 obtained in [2] and [7], respectively, is equivalent to 1.2 Å of SiO<sub>2</sub>. To reduce this uncertainty to an equivalent thickness uncertainty of ±0.1 Å, a current metrology target, transmission measurements accurate to within 0.2%, or about 10 times better than that done in [8], would be required.

Fortunately, the situation improves substantially below 3 eV. In particular, a similar calculation shows that the ±2% uncertainty in κ reported at λ = 6328 Å in [8] translates into an SiO<sub>2</sub> thickness uncertainty of about 0.05 Å. Since κ is the crucial parameter for determining overlayer thicknesses by ellipsometry in this spectral range, the datum of [8] already permits SiO<sub>2</sub>-equivalent overlayer thicknesses to be determined to ±0.1 Å. In regions where Si is essentially transparent, similarly accurate values of n should be obtainable by the prism-coupling method. The use of these techniques to obtain accurate spectral values of ε would also enable us to obtain new insight into the nature of overlayers and interfaces on Si.

## C CONCLUSION

The above considerations are taken into account in Datareview 12.2, which covers the range from 0.00 to 7.50 eV in increments of 0.02 eV and is intended for modelling applications. The data were chosen as follows. (1) The values from 0.20 to 6.50 eV are the data of [2]. Although the values from 0.20 to 0.75 eV of [2] are an extrapolation, they agree excellently well with the data of Edwards and Ochoa [10] and Primak [11] in this spectral range. Also, although the effect of the Si/SiO<sub>2</sub> interface remains uncertain and a higher E<sub>2</sub> peak in <ε<sub>2</sub>> was reported in [7], the values of [2] are rigorously K–K consistent, contain no experimental noise, and are obtained on oxidized (001) Si samples, thereby meeting the criteria of [9] given the expected primary use of these results. (2) The value of ε<sub>1</sub> at 0.00 eV is that determined in [1]. (3) The values of ε<sub>1</sub> from 0.02 to 0.18 eV are an extrapolation of [2] constrained to pass through the value at 0.00372 eV determined in [12]. (4) The values of ε<sub>2</sub> from 0.00 to 0.20 eV are also those of [12]. (5) The values from 6.5 to 7.5 eV are extrapolations of [2] designed to pass through the values of ε<sub>1</sub> and ε<sub>2</sub> at 7.5 eV obtained in [4]. For ε<sub>2</sub> this extrapolation mainly smoothes the data of [4], whereas the natural extrapolation of the ε<sub>1</sub> data of [2] matches smoothly that of [4] at 7.5 eV.

Datareview 12.3 reproduces the listing of [1] to provide additional detail below 1.20 eV and information above 7.50 eV, and also includes the 1.959 eV value of κ determined by Geist et al [8]. Only values of n, κ and α are given, since in many cases not enough information is available to calculate ε. The sources of the data are indicated therein, and a general discussion of these data is given in [1].

The values listed are for nominally intrinsic material at room temperature. Although <ε> data for c-Si at various temperatures have been reported [13,14], a comprehensive list is beyond the scope of this summary. The term ‘room temperature’ is not well defined, but for most applications temperature effects are not expected to contribute significantly. Since the main consequence is a shift of critical point energies by about 0.4 meV/°C, temperature effects are easily estimated by adding the first energy derivative of the listed data multiplied by the shift of critical point energy. Not surprisingly, the largest effects are found at the (E<sub>0</sub>' E<sub>1</sub>) and (E<sub>2</sub>) critical points near 3.4 and 4.2 eV, respectively, where they are of the order of 0.07/°C and 0.08/°C in ε<sub>1</sub> and ε<sub>2</sub>. Doping effects are not modelled as easily, being manifest by increasing broadening that becomes noticeable at impurity levels of the order of 10<sup>18</sup> cm<sup>-3</sup> [15].

## REFERENCES

- [1] D.E. Aspnes [ in *Properties of Silicon* (INSPEC, IEE, London, UK, 1988) ch.2 p.59-80.  
Please E-mail jsears@iee.org.uk for a free copy of these pages. ]
- [2] C.M. Herzinger, B. Johs, W.A. McGahan, J.A. Woollam, W. Paulson [ *J. Appl. Phys. (USA)* vol.83 (1998) p.3323-36 ]
- [3] D.E. Aspnes, A.A. Studna [ *Phys. Rev. B (USA)* vol.27 (1983) p.985-1009 ]
- [4] H.R. Philipp [ *J. Appl. Phys. (USA)* vol.43 (1972) p.2835-9 ]
- [5] G.E. Jellison Jr. [ *Opt. Mater. (Netherlands)* vol.1 (1992) p.41-7 ]
- [6] V. Nayar, W.Y. Leong, C. Pickering, A.J. Piddock, R.T. Carline, D.J. Robbins [ *Appl. Phys. Lett. (USA)* vol.61 (1992) p.1304-6 ]
- [7] T. Yasuda, D.E. Aspnes [ *Appl. Opt. (USA)* vol.33 (1994) p.7435-8 ]
- [8] J. Geist, A.R. Schaefer, J.-F. Song, Y.H. Wang, E.F. Zalewski [ *J. Res. Natl. Inst. Stand. Technol. (USA)* vol.95 (1990) p.549-58 ]
- [9] K.A. Bell, L. Mantese, U. Rossow, D.E. Aspnes [ *J. Vac. Sci. Technol. B (USA)* vol. 15 (1997) p.1205-11 ]
- [10] D.F. Edwards, E. Ochoa [ *Appl. Opt. (USA)* vol.19 (1980) p.4130-1 ]
- [11] W. Primak [ *Appl. Opt. (USA)* vol.10 (1971) p.759-63 ]
- [12] E.V. Loewenstein, D.R. Smith, R.L. Morgan [ *Appl. Opt. (USA)* vol.12 (1973) p.398-406 ]
- [13] G.E. Jellison Jr., F.A. Modine [ *J. Appl. Phys. (USA)* vol.53 (1982) p.3745-53 ]
- [14] P. Lautenschlager, M. Garriga, L. Viña, M. Cardona [ *Phys. Rev. B (USA)* vol.36 (1987) p.4821-30 ]
- [15] L. Viña, M. Cardona [ *Phys. Rev. B (USA)* vol. 29 (1984) p.6739-51 ]
- [16] F.A. Johnson [ *Proc. Phys. Soc. Lond. (UK)* vol.73 (1959) p.265-72 ]
- [17] B. Bendow, H.G. Lipson, S.P. Yukon [ *Appl. Opt. (USA)* vol.16 (1977) p.2909-13 ]
- [18] A. Hordvik, L. Skolnik [ *Appl. Opt. (USA)* vol.16 (1977) p.2919-24 ]
- [19] G.D. Cody, B.G. Brooks [ private communication (1986) ]
- [20] W.C. Dash, R. Newman [ *Phys. Rev. (USA)* vol.99 (1955) p.1151-5 ]
- [21] W.R. Hunter [ listed in D.F. Edwards, in *Handbook of Optical Constants of Solids* Ed. E. Palik (Academic, New York, 1985) p.547-69 ]
- [22] E.O. Filatova, A.S. Vinogradov, I.A. Sorokin, T.M. Zimkina [ *Sov. Phys.-Solid State (USA)* vol.25 (1983) p.736-9 ]

## 12.2 Optical functions of intrinsic c-Si for photon energies up to 7.5 eV: table

D.E. Aspnes

March 1998

The data in this table were compiled as described in Datareview 12.1.

E (eV)	$\epsilon_1$	$\epsilon_2$	n	$\kappa$	$\alpha$ ( $\text{cm}^{-1}$ )
0.000	11.69640	0.00000	3.420	0.000	0.000E+00
0.020	11.69298	0.00000	3.419	0.000	0.000E+00
0.040	11.69640	0.00000	3.420	0.000	0.000E+00
0.060	11.69913	0.00171	3.420	0.000	0.152E+01
0.080	11.70119	0.00109	3.421	0.000	0.130E+01
0.100	11.70324	0.00116	3.421	0.000	0.172E+01
0.120	11.70597	0.00068	3.421	0.000	0.122E+01
0.140	11.70940	0.00048	3.422	0.000	0.994E+00
0.160	11.71350	0.00016	3.422	0.000	0.373E+00
0.180	11.71830	0.00015	3.423	0.000	0.401E+00
0.200	11.72309	0.00001	3.424	0.000	0.150E-01
0.220	11.72103	0.00000	3.424	0.000	0.000E+00
0.240	11.72691	0.00000	3.424	0.000	0.000E+00
0.260	11.73330	0.00000	3.425	0.000	0.000E+00
0.280	11.74021	0.00000	3.426	0.000	0.000E+00
0.300	11.74765	0.00000	3.427	0.000	0.000E+00
0.320	11.75561	0.00000	3.429	0.000	0.000E+00
0.340	11.76411	0.00000	3.430	0.000	0.000E+00
0.360	11.77313	0.00000	3.431	0.000	0.000E+00
0.380	11.78269	0.00000	3.433	0.000	0.000E+00
0.400	11.79279	0.00000	3.434	0.000	0.000E+00
0.420	11.80343	0.00000	3.436	0.000	0.000E+00
0.440	11.81462	0.00000	3.437	0.000	0.000E+00
0.460	11.82636	0.00000	3.439	0.000	0.000E+00
0.480	11.83865	0.00000	3.441	0.000	0.000E+00
0.500	11.85150	0.00000	3.443	0.000	0.000E+00
0.520	11.86491	0.00000	3.445	0.000	0.000E+00
0.540	11.87889	0.00000	3.447	0.000	0.000E+00
0.560	11.89344	0.00000	3.449	0.000	0.000E+00
0.580	11.90857	0.00000	3.451	0.000	0.000E+00
0.600	11.92429	0.00000	3.453	0.000	0.000E+00
0.620	11.94059	0.00000	3.456	0.000	0.000E+00
0.640	11.95750	0.00000	3.458	0.000	0.000E+00
0.660	11.97500	0.00000	3.460	0.000	0.000E+00
0.680	11.99311	0.00000	3.463	0.000	0.000E+00
0.700	12.01185	0.00000	3.466	0.000	0.000E+00
0.720	12.03120	0.00000	3.469	0.000	0.000E+00
0.740	12.05119	0.00000	3.471	0.000	0.000E+00
0.760	12.07181	0.00000	3.474	0.000	0.000E+00
0.780	12.09308	0.00000	3.478	0.000	0.000E+00
0.800	12.11502	0.00000	3.481	0.000	0.000E+00

12.2 Optical functions of intrinsic c-Si for photon energies up to 7.5 eV: table

E (eV)	$\epsilon_1$	$\epsilon_2$	n	$\kappa$	$\alpha (\text{cm}^{-1})$
0.820	12.13761	0.00000	3.484	0.000	0.000E+00
0.840	12.16089	0.00000	3.487	0.000	0.000E+00
0.860	12.18484	0.00000	3.491	0.000	0.000E+00
0.880	12.20950	0.00000	3.494	0.000	0.000E+00
0.900	12.23486	0.00000	3.498	0.000	0.000E+00
0.920	12.26095	0.00000	3.502	0.000	0.000E+00
0.940	12.28776	0.00000	3.505	0.000	0.000E+00
0.960	12.31533	0.00000	3.509	0.000	0.000E+00
0.980	12.34365	0.00000	3.513	0.000	0.000E+00
1.000	12.37275	0.00000	3.517	0.000	0.123E-06
1.020	12.40265	0.00000	3.522	0.000	0.289E-01
1.040	12.43336	0.00001	3.526	0.000	0.854E-01
1.060	12.46490	0.00002	3.531	0.000	0.232E+00
1.080	12.49731	0.00004	3.535	0.000	0.581E+00
1.100	12.53059	0.00008	3.540	0.000	0.133E+01
1.120	12.56479	0.00017	3.545	0.000	0.278E+01
1.140	12.59991	0.00033	3.550	0.000	0.532E+01
1.160	12.63595	0.00057	3.555	0.000	0.935E+01
1.180	12.67294	0.00091	3.560	0.000	0.152E+02
1.200	12.71086	0.00136	3.565	0.000	0.233E+02
1.220	12.74972	0.00194	3.571	0.000	0.336E+02
1.240	12.78952	0.00265	3.576	0.000	0.465E+02
1.260	12.83026	0.00348	3.582	0.000	0.620E+02
1.280	12.87196	0.00443	3.588	0.001	0.802E+02
1.300	12.91463	0.00552	3.594	0.001	0.101E+03
1.320	12.95828	0.00673	3.600	0.001	0.125E+03
1.340	13.00292	0.00808	3.606	0.001	0.152E+03
1.360	13.04857	0.00954	3.612	0.001	0.182E+03
1.380	13.09524	0.01114	3.619	0.002	0.215E+03
1.400	13.14295	0.01287	3.625	0.002	0.252E+03
1.420	13.19172	0.01472	3.632	0.002	0.292E+03
1.440	13.24157	0.01670	3.639	0.002	0.335E+03
1.460	13.29251	0.01881	3.646	0.003	0.382E+03
1.480	13.34457	0.02104	3.653	0.003	0.432E+03
1.500	13.39777	0.02340	3.660	0.003	0.486E+03
1.520	13.45214	0.02590	3.668	0.004	0.544E+03
1.540	13.50770	0.02851	3.675	0.004	0.606E+03
1.560	13.56447	0.03126	3.683	0.004	0.671E+03
1.580	13.62248	0.03413	3.691	0.005	0.741E+03
1.600	13.68177	0.03714	3.699	0.005	0.814E+03
1.620	13.74235	0.04027	3.707	0.005	0.892E+03
1.640	13.80427	0.04352	3.715	0.006	0.974E+03
1.660	13.86756	0.04691	3.724	0.006	0.106E+04
1.680	13.93224	0.05042	3.733	0.007	0.115E+04
1.700	13.99836	0.05406	3.741	0.007	0.125E+04
1.720	14.06597	0.05783	3.750	0.008	0.134E+04
1.740	14.13509	0.06173	3.760	0.008	0.145E+04
1.760	14.20577	0.06575	3.769	0.009	0.156E+04
1.780	14.27805	0.06990	3.779	0.009	0.167E+04
1.800	14.35198	0.07418	3.788	0.010	0.179E+04
1.820	14.42761	0.07859	3.798	0.010	0.191E+04
1.840	14.50499	0.08312	3.809	0.011	0.204E+04

12.2 Optical functions of intrinsic c-Si for photon energies up to 7.5 eV: table

E (eV)	$\epsilon_1$	$\epsilon_2$	n	$\kappa$	$\alpha$ (cm <sup>-1</sup> )
1.860	14.58417	0.08778	3.819	0.011	0.217E+04
1.880	14.66521	0.09257	3.830	0.012	0.230E+04
1.900	14.74816	0.09749	3.840	0.013	0.245E+04
1.920	14.83308	0.10254	3.851	0.013	0.259E+04
1.940	14.92004	0.10771	3.863	0.014	0.274E+04
1.960	15.00910	0.11301	3.874	0.015	0.290E+04
1.980	15.10034	0.11844	3.886	0.015	0.306E+04
2.000	15.19384	0.12400	3.898	0.016	0.323E+04
2.020	15.28968	0.12968	3.910	0.017	0.340E+04
2.040	15.38794	0.13549	3.923	0.017	0.357E+04
2.060	15.48873	0.14143	3.936	0.018	0.375E+04
2.080	15.59212	0.14750	3.949	0.019	0.394E+04
2.100	15.69824	0.15370	3.962	0.019	0.413E+04
2.120	15.80718	0.16002	3.976	0.020	0.433E+04
2.140	15.91908	0.16647	3.990	0.021	0.453E+04
2.160	16.03405	0.17305	4.004	0.022	0.473E+04
2.180	16.15224	0.17976	4.019	0.022	0.494E+04
2.200	16.27378	0.18659	4.034	0.023	0.516E+04
2.220	16.39887	0.19355	4.050	0.024	0.538E+04
2.240	16.52765	0.20064	4.065	0.025	0.560E+04
2.260	16.66031	0.20787	4.082	0.025	0.583E+04
2.280	16.79708	0.21522	4.099	0.026	0.607E+04
2.300	16.93813	0.22272	4.116	0.027	0.631E+04
2.320	17.08365	0.23038	4.133	0.028	0.655E+04
2.340	17.23393	0.23822	4.151	0.029	0.681E+04
2.360	17.38925	0.24628	4.170	0.030	0.707E+04
2.380	17.54991	0.25462	4.189	0.030	0.733E+04
2.400	17.71621	0.26331	4.209	0.031	0.761E+04
2.420	17.88853	0.27244	4.230	0.032	0.790E+04
2.440	18.06721	0.28215	4.251	0.033	0.821E+04
2.460	18.25261	0.29257	4.272	0.034	0.854E+04
2.480	18.44514	0.30386	4.295	0.035	0.889E+04
2.500	18.64519	0.31623	4.318	0.037	0.928E+04
2.520	18.85316	0.32989	4.342	0.038	0.971E+04
2.540	19.06947	0.34509	4.367	0.040	0.102E+05
2.560	19.29454	0.36208	4.393	0.041	0.107E+05
2.580	19.52880	0.38115	4.419	0.043	0.113E+05
2.600	19.77275	0.40264	4.447	0.045	0.119E+05
2.620	20.02687	0.42686	4.475	0.048	0.127E+05
2.640	20.29165	0.45420	4.505	0.050	0.135E+05
2.660	20.56762	0.48502	4.535	0.053	0.144E+05
2.680	20.85532	0.51976	4.567	0.057	0.155E+05
2.700	21.15532	0.55885	4.600	0.061	0.166E+05
2.720	21.46823	0.60275	4.634	0.065	0.179E+05
2.740	21.79470	0.65194	4.669	0.070	0.194E+05
2.760	22.13544	0.70694	4.705	0.075	0.210E+05
2.780	22.49115	0.76829	4.743	0.081	0.228E+05
2.800	22.86266	0.83654	4.782	0.087	0.248E+05
2.820	23.25086	0.91228	4.823	0.095	0.270E+05
2.840	23.65679	0.99612	4.865	0.102	0.295E+05
2.860	24.08159	1.08869	4.909	0.111	0.322E+05
2.880	24.52659	1.19066	4.954	0.120	0.351E+05

12.2 Optical functions of intrinsic c-Si for photon energies up to 7.5 eV: table

E (eV)	$\epsilon_1$	$\epsilon_2$	n	$\kappa$	$\alpha$ ( $\text{cm}^{-1}$ )
2.900	24.99333	1.30270	5.001	0.130	0.383E+05
2.920	25.48364	1.42552	5.050	0.141	0.418E+05
2.940	25.99970	1.55986	5.101	0.153	0.456E+05
2.960	26.54423	1.70647	5.155	0.166	0.497E+05
2.980	27.12064	1.86617	5.211	0.179	0.541E+05
3.000	27.73337	2.03987	5.270	0.194	0.589E+05
3.020	28.38838	2.22883	5.332	0.209	0.640E+05
3.040	29.09379	2.43518	5.399	0.226	0.695E+05
3.060	29.86039	2.66298	5.470	0.243	0.755E+05
3.080	30.70195	2.91991	5.547	0.263	0.822E+05
3.100	31.63452	3.21932	5.632	0.286	0.898E+05
3.120	32.67491	3.58228	5.725	0.313	0.990E+05
3.140	33.83825	4.03910	5.827	0.347	0.110E+06
3.160	35.13510	4.63036	5.940	0.390	0.125E+06
3.180	36.56792	5.40737	6.064	0.446	0.144E+06
3.200	38.12726	6.43242	6.197	0.519	0.168E+06
3.220	39.78669	7.77882	6.337	0.614	0.200E+06
3.240	41.49542	9.53092	6.483	0.735	0.241E+06
3.260	43.16604	11.78282	6.630	0.889	0.294E+06
3.280	44.65250	14.63067	6.769	1.081	0.359E+06
3.300	45.71726	18.14163	6.888	1.317	0.441E+06
3.320	46.01252	22.27232	6.969	1.598	0.538E+06
3.340	45.14623	26.74359	6.986	1.914	0.648E+06
3.360	42.89018	30.97944	6.921	2.238	0.762E+06
3.380	39.43012	34.27005	6.770	2.531	0.867E+06
3.400	35.39683	36.13890	6.557	2.756	0.950E+06
3.420	31.56288	36.61217	6.321	2.896	0.100E+07
3.440	28.44932	36.13536	6.101	2.962	0.103E+07
3.460	26.17564	35.24919	5.919	2.977	0.104E+07
3.480	24.58865	34.33495	5.780	2.970	0.105E+07
3.500	23.46292	33.56477	5.675	2.957	0.105E+07
3.520	22.61654	32.97390	5.595	2.947	0.105E+07
3.540	21.93482	32.54051	5.531	2.942	0.106E+07
3.560	21.35398	32.23106	5.478	2.942	0.106E+07
3.580	20.84009	32.01732	5.433	2.946	0.107E+07
3.600	20.37421	31.87942	5.395	2.955	0.108E+07
3.620	19.94437	31.80412	5.361	2.966	0.109E+07
3.640	19.54175	31.78222	5.332	2.981	0.110E+07
3.660	19.15935	31.80682	5.305	2.998	0.111E+07
3.680	18.79160	31.87234	5.282	3.017	0.113E+07
3.700	18.43413	31.97408	5.260	3.039	0.114E+07
3.720	18.08364	32.10813	5.241	3.063	0.116E+07
3.740	17.73778	32.27137	5.223	3.089	0.117E+07
3.760	17.39488	32.46141	5.207	3.117	0.119E+07
3.780	17.05380	32.67671	5.192	3.147	0.121E+07
3.800	16.71375	32.91648	5.178	3.178	0.122E+07
3.820	16.37410	33.18077	5.166	3.211	0.124E+07
3.840	16.03423	33.47041	5.155	3.246	0.126E+07
3.860	15.69330	33.78708	5.145	3.283	0.128E+07
3.880	15.35015	34.13324	5.137	3.322	0.131E+07
3.900	15.00304	34.51213	5.130	3.364	0.133E+07
3.920	14.64947	34.92782	5.125	3.408	0.135E+07

12.2 Optical functions of intrinsic c-Si for photon energies up to 7.5 eV: table

E (eV)	$\epsilon_1$	$\epsilon_2$	n	$\kappa$	$\alpha$ (cm <sup>-1</sup> )
3.940	14.28587	35.38511	5.121	3.455	0.138E+07
3.960	13.90737	35.88948	5.118	3.506	0.141E+07
3.980	13.50742	36.44709	5.117	3.561	0.144E+07
4.000	13.07737	37.06456	5.118	3.621	0.147E+07
4.020	12.60592	37.74894	5.119	3.687	0.150E+07
4.040	12.07826	38.50738	5.120	3.760	0.154E+07
4.060	11.47495	39.34658	5.122	3.841	0.158E+07
4.080	10.77033	40.27149	5.121	3.932	0.163E+07
4.100	9.93109	41.28283	5.118	4.033	0.168E+07
4.120	8.91525	42.37323	5.110	4.146	0.173E+07
4.140	7.67276	43.52166	5.092	4.273	0.179E+07
4.160	6.14868	44.68681	5.062	4.414	0.186E+07
4.180	4.29023	45.79979	5.015	4.567	0.194E+07
4.200	2.05976	46.75800	4.943	4.730	0.201E+07
4.220	-0.54428	47.42477	4.842	4.898	0.210E+07
4.240	-3.46083	47.64395	4.707	5.061	0.218E+07
4.260	-6.54704	47.27673	4.538	5.209	0.225E+07
4.280	-9.58721	46.25408	4.339	5.330	0.231E+07
4.300	-12.33997	44.61895	4.120	5.415	0.236E+07
4.320	-14.60856	42.53010	3.896	5.458	0.239E+07
4.340	-16.30187	40.21902	3.681	5.463	0.240E+07
4.360	-17.45708	37.91653	3.485	5.441	0.240E+07
4.380	-18.21227	35.77958	3.312	5.402	0.240E+07
4.400	-18.73818	33.85087	3.159	5.359	0.239E+07
4.420	-19.16030	32.07370	3.017	5.316	0.238E+07
4.440	-19.51426	30.35471	2.879	5.273	0.237E+07
4.460	-19.75949	28.63500	2.741	5.223	0.236E+07
4.480	-19.83543	26.92332	2.608	5.161	0.234E+07
4.500	-19.71484	25.27754	2.484	5.088	0.232E+07
4.520	-19.42037	23.76048	2.373	5.005	0.229E+07
4.540	-19.00558	22.40706	2.278	4.919	0.226E+07
4.560	-18.52617	21.21843	2.196	4.832	0.223E+07
4.580	-18.02222	20.17481	2.125	4.747	0.220E+07
4.600	-17.51554	19.25092	2.063	4.666	0.218E+07
4.620	-17.01513	18.42500	2.008	4.588	0.215E+07
4.640	-16.52373	17.68138	1.959	4.512	0.212E+07
4.660	-16.04209	17.00942	1.916	4.440	0.210E+07
4.680	-15.57095	16.40170	1.877	4.370	0.207E+07
4.700	-15.11136	15.85242	1.842	4.302	0.205E+07
4.720	-14.66470	15.35667	1.812	4.237	0.203E+07
4.740	-14.23237	14.90993	1.786	4.174	0.201E+07
4.760	-13.81570	14.50802	1.763	4.114	0.199E+07
4.780	-13.41580	14.14694	1.744	4.057	0.197E+07
4.800	-13.03354	13.82295	1.727	4.002	0.195E+07
4.820	-12.66961	13.53250	1.713	3.950	0.193E+07
4.840	-12.32443	13.27227	1.701	3.901	0.191E+07
4.860	-11.99824	13.03917	1.691	3.855	0.190E+07
4.880	-11.69105	12.83027	1.683	3.811	0.189E+07
4.900	-11.40275	12.64293	1.677	3.770	0.187E+07
4.920	-11.13305	12.47467	1.671	3.732	0.186E+07
4.940	-10.88156	12.32325	1.667	3.696	0.185E+07
4.960	-10.64778	12.18664	1.664	3.663	0.184E+07

12.2 Optical functions of intrinsic c-Si for photon energies up to 7.5 eV: table

E (eV)	$\epsilon_1$	$\epsilon_2$	n	$\kappa$	$\alpha$ ( $\text{cm}^{-1}$ )
4.980	-10.43110	12.06303	1.661	3.632	0.183E+07
5.000	-10.23088	11.95082	1.658	3.603	0.183E+07
5.020	-10.04647	11.84861	1.657	3.576	0.182E+07
5.040	-9.87720	11.75524	1.655	3.552	0.181E+07
5.060	-9.72247	11.66971	1.653	3.529	0.181E+07
5.080	-9.58175	11.59124	1.652	3.509	0.181E+07
5.100	-9.45463	11.51919	1.650	3.490	0.180E+07
5.120	-9.34085	11.45306	1.649	3.473	0.180E+07
5.140	-9.24036	11.39246	1.647	3.458	0.180E+07
5.160	-9.15335	11.33707	1.646	3.444	0.180E+07
5.180	-9.08034	11.28658	1.644	3.433	0.180E+07
5.200	-9.02229	11.24062	1.642	3.423	0.180E+07
5.220	-8.98076	11.19857	1.639	3.416	0.181E+07
5.240	-8.95798	11.15919	1.636	3.411	0.181E+07
5.260	-8.95690	11.11998	1.631	3.408	0.182E+07
5.280	-8.98064	11.07642	1.625	3.409	0.182E+07
5.300	-9.03124	11.02123	1.615	3.412	0.183E+07
5.320	-9.10778	10.94455	1.602	3.417	0.184E+07
5.340	-9.20421	10.83556	1.583	3.422	0.185E+07
5.360	-9.30847	10.68572	1.559	3.426	0.186E+07
5.380	-9.40405	10.49262	1.531	3.427	0.187E+07
5.400	-9.47398	10.26233	1.499	3.424	0.187E+07
5.420	-9.50607	10.00866	1.466	3.414	0.188E+07
5.440	-9.49651	9.74912	1.434	3.399	0.187E+07
5.460	-9.45015	9.49956	1.405	3.380	0.187E+07
5.480	-9.37746	9.27006	1.380	3.359	0.187E+07
5.500	-9.29016	9.06387	1.358	3.337	0.186E+07
5.520	-9.19764	8.87898	1.339	3.315	0.186E+07
5.540	-9.10560	8.71092	1.322	3.294	0.185E+07
5.560	-9.01644	8.55509	1.306	3.275	0.185E+07
5.580	-8.93052	8.40798	1.291	3.255	0.184E+07
5.600	-8.84730	8.26735	1.277	3.237	0.184E+07
5.620	-8.76612	8.13196	1.263	3.219	0.183E+07
5.640	-8.68646	8.00114	1.250	3.201	0.183E+07
5.660	-8.60800	7.87451	1.237	3.184	0.183E+07
5.680	-8.53057	7.75182	1.224	3.167	0.182E+07
5.700	-8.45410	7.63285	1.212	3.150	0.182E+07
5.720	-8.37856	7.51744	1.200	3.133	0.182E+07
5.740	-8.30394	7.40540	1.188	3.117	0.181E+07
5.760	-8.23025	7.29658	1.177	3.101	0.181E+07
5.780	-8.15751	7.19082	1.166	3.085	0.181E+07
5.800	-8.08572	7.08799	1.155	3.069	0.180E+07
5.820	-8.01487	6.98794	1.144	3.054	0.180E+07
5.840	-7.94504	6.89054	1.134	3.038	0.180E+07
5.860	-7.87624	6.79569	1.124	3.023	0.180E+07
5.880	-7.80849	6.70325	1.114	3.008	0.179E+07
5.900	-7.74179	6.61313	1.105	2.994	0.179E+07
5.920	-7.67614	6.52521	1.095	2.979	0.179E+07
5.940	-7.61156	6.43940	1.086	2.965	0.179E+07
5.960	-7.54805	6.35559	1.077	2.951	0.178E+07
5.980	-7.48562	6.27369	1.068	2.937	0.178E+07
6.000	-7.42427	6.19361	1.059	2.923	0.178E+07

12.2 Optical functions of intrinsic c-Si for photon energies up to 7.5 eV: table

E (eV)	$\epsilon_1$	$\epsilon_2$	n	$\kappa$	$\alpha$ (cm <sup>-1</sup> )
6.020	-7.36402	6.11525	1.051	2.910	0.178E+07
6.040	-7.30488	6.03852	1.042	2.897	0.177E+07
6.060	-7.24680	5.96335	1.034	2.884	0.177E+07
6.080	-7.18978	5.88964	1.026	2.871	0.177E+07
6.100	-7.13380	5.81732	1.018	2.858	0.177E+07
6.120	-7.07886	5.74630	1.010	2.846	0.177E+07
6.140	-7.02492	5.67652	1.002	2.833	0.176E+07
6.160	-6.97200	5.60789	0.994	2.821	0.176E+07
6.180	-6.92003	5.54035	0.986	2.809	0.176E+07
6.200	-6.86903	5.47383	0.978	2.798	0.176E+07
6.220	-6.81896	5.40826	0.971	2.786	0.176E+07
6.240	-6.76979	5.34358	0.963	2.774	0.176E+07
6.260	-6.72150	5.27973	0.955	2.763	0.175E+07
6.280	-6.67407	5.21665	0.948	2.752	0.175E+07
6.300	-6.62745	5.15429	0.940	2.741	0.175E+07
6.320	-6.58163	5.09258	0.933	2.730	0.175E+07
6.340	-6.53657	5.03149	0.925	2.719	0.175E+07
6.360	-6.49222	4.97095	0.918	2.708	0.175E+07
6.380	-6.44857	4.91094	0.910	2.698	0.174E+07
6.400	-6.40557	4.85139	0.903	2.687	0.174E+07
6.420	-6.36319	4.79228	0.895	2.677	0.174E+07
6.440	-6.32138	4.73356	0.888	2.666	0.174E+07
6.460	-6.28012	4.67520	0.880	2.656	0.174E+07
6.480	-6.23936	4.61716	0.873	2.646	0.174E+07
6.500	-6.19906	4.55942	0.865	2.636	0.174E+07
6.520	-6.15856	4.50096	0.857	2.626	0.174E+07
6.540	-6.11844	4.44304	0.849	2.615	0.173E+07
6.560	-6.07852	4.38212	0.841	2.605	0.173E+07
6.580	-6.03908	4.32548	0.833	2.595	0.173E+07
6.600	-6.00000	4.27000	0.826	2.585	0.173E+07
6.620	-5.96128	4.21568	0.819	2.575	0.173E+07
6.640	-5.92292	4.16252	0.811	2.565	0.173E+07
6.660	-5.88480	4.11160	0.804	2.556	0.173E+07
6.680	-5.84720	4.06040	0.797	2.546	0.172E+07
6.700	-5.81000	4.01000	0.790	2.537	0.172E+07
6.720	-5.77320	3.96040	0.784	2.527	0.172E+07
6.740	-5.73680	3.91160	0.777	2.518	0.172E+07
6.760	-5.70140	3.86420	0.770	2.509	0.172E+07
6.780	-5.66560	3.81680	0.763	2.500	0.172E+07
6.800	-5.63000	3.77000	0.757	2.491	0.172E+07
6.820	-5.59460	3.72380	0.750	2.481	0.172E+07
6.840	-5.55940	3.67820	0.744	2.472	0.171E+07
6.860	-5.52380	3.63320	0.737	2.463	0.171E+07
6.880	-5.48920	3.58880	0.731	2.454	0.171E+07
6.900	-5.45500	3.54500	0.725	2.445	0.171E+07
6.920	-5.42120	3.50180	0.719	2.437	0.171E+07
6.940	-5.38780	3.45920	0.712	2.428	0.171E+07
6.960	-5.35540	3.41840	0.706	2.420	0.171E+07
6.980	-5.32260	3.37660	0.700	2.411	0.171E+07
7.000	-5.29000	3.33500	0.694	2.402	0.170E+07
7.020	-5.25760	3.29360	0.688	2.394	0.170E+07
7.040	-5.22540	3.25240	0.682	2.385	0.170E+07

*12.2 Optical functions of intrinsic c-Si for photon energies up to 7.5 eV: table*

E (eV)	$\epsilon_1$	$\epsilon_2$	n	$\kappa$	$\alpha$ ( $\text{cm}^{-1}$ )
7.060	-5.19280	3.21020	0.675	2.377	0.170E+07
7.080	-5.16120	3.16980	0.669	2.368	0.170E+07
7.100	-5.13000	3.13000	0.663	2.360	0.170E+07
7.120	-5.09920	3.09080	0.657	2.352	0.170E+07
7.140	-5.06880	3.05220	0.651	2.344	0.170E+07
7.160	-5.04000	3.01360	0.645	2.336	0.170E+07
7.180	-5.01000	2.97640	0.639	2.328	0.169E+07
7.200	-4.98000	2.94000	0.634	2.320	0.169E+07
7.220	-4.95000	2.90440	0.628	2.312	0.169E+07
7.240	-4.92000	2.86960	0.623	2.304	0.169E+07
7.260	-4.88880	2.83560	0.618	2.296	0.169E+07
7.280	-4.85920	2.80240	0.612	2.288	0.169E+07
7.300	-4.83000	2.77000	0.607	2.280	0.169E+07
7.320	-4.80120	2.73840	0.603	2.272	0.169E+07
7.340	-4.77280	2.70760	0.598	2.265	0.169E+07
7.360	-4.74600	2.67760	0.593	2.258	0.168E+07
7.380	-4.71800	2.64840	0.588	2.250	0.168E+07
7.400	-4.69000	2.62000	0.584	2.243	0.168E+07
7.420	-4.66200	2.59240	0.580	2.236	0.168E+07
7.440	-4.63400	2.56560	0.576	2.228	0.168E+07
7.460	-4.60480	2.54080	0.572	2.221	0.168E+07
7.480	-4.57720	2.51520	0.568	2.214	0.168E+07
7.500	-4.55000	2.49000	0.564	2.206	0.168E+07

## 12.3 Optical functions of intrinsic c-Si for selected photon energies: table

D.E. Aspnes

March 1998

For a discussion of these data see Datareview 12.1 and reference [1] thereof. The cited references in this table refer to those listed in Datareview 12.1.

E (eV)	n	$\kappa$	$\alpha$ ( $\text{cm}^{-1}$ )
0.000	3.420 [1]	0	0
0.00372	3.4155 [12]	0	0
0.00496	3.4160		
0.00620	3.4165		
0.00744	3.4170		
0.00868	3.4175		
0.00992	3.4180		
0.01116	3.4182		
0.0124	3.4185		
0.0136	3.4188		
0.0149	3.4190		
0.0161	3.4191		
0.0174	3.4192		
0.0186	3.4194		
0.0198	3.4195		
0.0211	3.4195		
0.0223	3.4196		
0.0236	3.4197		
0.0248	3.4197		
0.0260	3.4198		
0.0273	3.4198		
0.0285	3.4198		
0.0297	3.4198		
0.0310	3.4199		
0.0322	3.4199		
0.0335	3.4200		
0.0347	3.4200		
0.0359	3.4200		
0.0372	3.4200		
0.0384	3.4200		
0.0397	3.4200		
0.0409	3.4200		
0.0421	3.4200		
0.0434	3.4200 [12]		
0.0496	3.4201 [10]	9.0E-5	0.5 [16]
0.0516	3.4202	1.1E-4	0.6
0.0539	3.4203	1.3	0.7
0.0563	3.4203	1.6	0.9
0.0590	3.4204	2.3	1.4
0.0620	3.4204	2.9	1.8

12.3 Optical functions of intrinsic c-Si for selected photon energies: table

E (eV)	n	$\kappa$	$\alpha (\text{cm}^{-1})$
0.0652	3.4205	3.2	2.1
0.0689	3.4205	3.7	2.6
0.0707		4.2	3.0
0.0729	3.4206	3.8	2.8
0.07513		9.9E-4	7.5
0.0762		1.22E-3	9.5
0.0775	3.4206	7.6E-4	6.0
0.0787		2.0	1.6
0.0800	3.4207	1.6	1.3
0.0826	3.4207	1.3	1.1
0.0855	3.4208	1.2	1.0
0.0868		1.0E-4	0.9
0.0885	3.4208	1.7	1.5
0.0918	3.4209	3.1	2.9
0.0921		3.1	3.1
0.0954	3.4209	2.3	2.3
0.0992	3.4210	1.9	1.9
0.0998		1.7	1.7
0.1016		2.0	2.1
0.1033	3.4211	1.6	1.7
0.1042		1.4	1.5
0.1078	3.4212	2.0	2.2
0.1103		2.1	2.3
0.1127	3.4213	1.8	2.1
0.1181	3.4214	1.3E-4	1.5
0.124	3.4215	7.E-5	0.9
0.130	3.4217	4.0	0.5
0.135		6.0	0.9 [16]
0.135		4.9	0.67 [17]
0.138	3.4219		
0.140		7.0	1.0 [16]
0.140		6.1	0.87 [17]
0.145		4.0	0.6 [16]
0.145		4.5	0.67 [17]
0.146	3.4221		
0.150		2.0	0.3 [16]
0.150		2.2	0.33 [17]
0.155	3.4224	1.5	0.24
0.160		2.3	0.36
0.165	3.4227	1.7	0.28
0.170		1.6	0.28
0.175		1.9	0.33
0.177	3.4231		
0.180		2. 2E-5	0.40
0.185		5.3E-6	0.10
0.190		1.1E-6	0.021
0.191	3.4236		
0.195		9.0E-7	0.018
0.200		7.4	0.015
0.205		6.1	0.018
0.207	3.4242		
0.210		4.2	0.0089

12.3 Optical functions of intrinsic c-Si for selected photon energies: table

E (eV)	n	$\kappa$	$\alpha$ ( $\text{cm}^{-1}$ )
0.215		4.1	0.0089
0.220		4.0	0.0089
0.225	3.4250	3.3	0.0075
0.230		3.0	0.0069
0.235		2.9	0.0069
0.240		2.8	0.0069
0.245		2.3	0.0058
0.248	3.4261		
0.250		1.9	0.0049
0.255		2.0	0.0052
0.260		2.0	0.0053
0.265		2.2	0.0058
0.270		2.3E-7	0.0063 [17]
0.275	3.4275		
0.291	3.4283		
0.310	3.4294		
0.326		1.3E-8	0.00042 [18]
0.354	3.4321		
0.363	3.4327		
0.375	3.4335		
0.413	3.4361		
0.457	3.4393		
0.459		2.6E-9	0.00012 [18]
0.496	3.4424		
0.509	3.4434 [10]		
0.574	3.443 [11]		
0.620	3.449		
0.689	3.458		
0.731	3.464		
0.775	3.471		
0.809	3.478		
0.885	3.489		
0.903	3.501 (?)		
1.015		1.6E-8	0.0017 [19]
1.020		4.1	0.0042
1.025		5.6E-8	0.0058
1.030		1.1E-7	0.011
1.033	3.519		
1.035		2.1	0.022
1.040		3.1	0.032
1.045		3.9	0.041
1.050		6.4E-7	0.064
1.055		1.4E-6	0.145
1.060		2.2	0.24
1.065		3.1	0.34
1.070		4.2	0.46
1.075		5.5	0.60
1.080		7.0	0.70
1.084	3.533		
1.085		8.8E-6	0.97
1.090		1.10E-5	1.26
1.095		1.33	1.48

12.3 Optical functions of intrinsic c-Si for selected photon energies: table

E (eV)	n	$\kappa$	$\alpha$ (cm $^{-1}$ )
1.100		1.54	1.72 [19]
1.100		0.85	0.95 [20]
1.105		1.77	1.99 [19]
1.107	3.536 [11]		
1.110		2.1	2.4
1.120		2.7	3.1
1.130		3.6	4.1
1.140		4.6	5.3
1.150		5.9	6.9 [19]
1.150		8.1	9.4 [20]
1.160		7.6E-5	8.9E0 [19]
1.170		1.00E-4	1.2E1
1.180		1.36	1.6
1.190		1.8	2.2
1.200		2.4E-4	2.9 [8]
1.959		(1.564±0.03)E-2 [8]	(3.105±0.062)E3 [8]
7.500	0.563 [4]	2.21 [4]	1.68E6 [4]
7.750	0.517	2.10	1.65
8.000	0.478	2.00	1.62
8.250	0.444	1.90	1.59
8.500	0.414	1.82	1.57
8.750	0.389	1.73	1.53
9.000	0.367	1.66	1.51
9.250	0.348	1.58	1.48
9.500	0.332	1.51	1.45
9.750	0.318	1.45	1.43
10.00	0.306	1.38	1.40
10.50	0.286	1.26	1.34
11.00	0.272	1.16	1.29
11.50	0.263	1.06	1.24
12.00	0.257	0.963	1.17
12.50	0.255	0.875	1.11
13.00	0.258	0.792	1.04E6
13.50	0.265	0.714	9.7E5
14.00	0.275	0.641	9.1
14.50	0.288	0.573	8.4
15.00	0.313	0.479	7.3
15.50	0.323	0.450	7.1
16.00	0.345	0.394	6.4
16.50	0.369	0.342	5.7
17.00	0.397	0.296	5.1
17.50	0.426	0.255	4.5
18.00	0.455	0.219	4.0
18.50	0.485	0.189	3.5
19.00	0.514	0.163	3.1
19.50	0.542	0.140	2.8
20.00	0.569 [4]	0.122 [4]	2.5
20.00	0.567 [21]	0.0835	1.7 [21]
21.01	0.627	0.058	1.2E5
22.14	0.675	0.0405	9.1E4
23.39	0.722	0.0292	6.9
24.31	0.752	0.0243	6.0

12.3 Optical functions of intrinsic c-Si for selected photon energies: table

E (eV)	n	$\kappa$	$\alpha$ ( $\text{cm}^{-1}$ )
25.30	0.778	0.0205	5.3
26.38	0.803	0.0178	4.8
27.55	0.824	0.0158	4.4
28.83	0.843	0.0147	4.3
30.24	0.860	0.0138	4.2
32.63	0.885	0.0128	4.2
34.44	0.899	0.0121	4.2
36.47	0.918	0.0113	4.2
38.75	0.925	0.0104	4.1
40.00	0.930	0.010	4.1
42.75	0.942	0.0090	3.9
45.92	0.952	0.00785	3.7
47.69	0.956	0.0073	3.5
51.66	0.964	0.0061	3.2
56.36	0.972	0.0050	2.9
61.99	0.978	0.00393	2.5
68.88	0.987	0.00297	2.1
77.49	0.991	0.00215	1.7
88.56	1.000 [21]	0.00143	1.3E4 [21]
98.5	1.003 [22]	0.011 [22]	1.1E5
99.0	1.006	0.011	1.1
99.5	1.014	0.014	1.4
100.0	1.016	0.022	2.2
100.3	1.030		
100.5	1.012	0.043	4.4
101.0	1.000	0.040	4.0
101.5	0.996	0.028	2.8
102.0	0.996	0.027	2.7
103.0	0.996	0.026	2.7
104.0	0.996	0.026	2.7
106.0	0.997	0.026	2.8
110	0.995	0.025	2.8
115	0.994	0.025	2.9
120	0.990	0.025	3.0
125	0.988	0.024	3.0
130	0.986	0.021	2.8
135	0.986	0.020	2.7
140	0.987	0.018	2.5
145	0.988	0.017	2.5
150	0.988	0.016	2.4
155	0.988	0.014	2.2
160	0.989	0.014	2.2
165	0.989	0.013	2.2
170	0.988	0.012	2.1
180	0.989	0.009	1.6
200	0.990	0.007	1.5E5
250	0.993	0.004	9E4
300	0.995	0.003	8
350	0.997	0.002	7
400	0.998 [22]	0.002 [22]	7E4

## 12.4 Optical functions of liquid Si

D.E. Aspnes

March 1998

The metallic character of liquid Si makes its optical response substantially different from that of the solid at temperatures above its 1410 K melting point, a property that is particularly useful for in-situ optical studies of laser annealing. The optical functions of liquid Si produced by pulsed laser melting of a wafer surface were recently determined at 632.8 nm (1.959 eV) and the six wavelengths of the Ar<sup>+</sup> ion laser by Jellison and Lowndes [1]. An ellipsometer with a nanosecond response time was used for the measurements, and estimated confidence limits were 0.05 on n and κ. The data, given in TABLE 1, were fitted to the Drude expression

$$\epsilon = 1 - \left( \frac{(35.1 \text{ eV})^2}{E(E + i8.2 \text{ eV})} \right)$$

which yields n and κ values within 15% of the data and also gives an estimated DC conductivity of 50 μΩ cm, in reasonable agreement with a measured value of 80 μΩ cm.

The results are also consistent with previous measurements of n and κ by Li and Fauchet [2] and of n by Shvarev et al [3]. The κ values of Shvarev et al [3] appear to be low by about 1.

TABLE 1 Optical functions of liquid Si according to [1].

E (eV)	n	κ	α (10 <sup>6</sup> cm <sup>-1</sup> )
1.959	3.80	5.20	1.03
2.409	3.11	4.89	1.19
2.540	2.94	4.99	1.29
2.707	2.74	4.96	1.36
3.407	1.93	4.32	1.49
3.531	1.80	4.26	1.53
3.711	1.74	4.09	1.54

### REFERENCES

- [1] G.E. Jellison Jr., D.H. Lowndes [ *Appl. Phys. Lett. (USA)* vol.51 (1987) p.352-4 ]
- [2] K.D. Li, P.M. Fauchet [ *Solid State Commun. (USA)* vol.61 (1987) p.207-9 ]
- [3] K.M. Shvarev, B.A. Baum, P.V. Gel'd [ *Sov. Phys.-Solid State (USA)* vol.16 (1975) p.2111-2 ]

## CHAPTER 13

### PHOTOCONDUCTIVITY AND PHOTOGENERATED CARRIERS (*Edited by M. Willander*)

- 13.1 Photoconductivity of c-Si: general remarks
- 13.2 Photoconductivity spectra of ion-implanted c-Si
- 13.3 Photoconductivity spectra of electron irradiated c-Si
- 13.4 Bulk lifetimes of photogenerated carriers in intrinsic c-Si
- 13.5 Bulk lifetimes of photogenerated carriers in doped and treated c-Si
- 13.6 Surface recombination velocity in c-Si
- 13.7 Mobility and diffusion of photogenerated carriers in intrinsic c-Si
- 13.8 Mobility and diffusion of photogenerated carriers in doped and treated c-Si

## 13.1 Photoconductivity of c-Si: general remarks

V. Grivickas, J. Vaitkus and M. Willander

January 1998

### A PHOTOCOCONDUCTIVITY PROPERTIES

Photoconductivity (PC) is related to the excess carrier concentration of free electrons and holes ( $\Delta n$ ,  $\Delta p$ ) through the equation

$$\sigma = q(\Delta n \mu_e + \Delta p \mu_h) \quad (1)$$

where  $q$  is the electron charge and  $\mu_e$ ,  $\mu_h$  are the corresponding drift mobilities. Excess carrier pairs can be created by a number of external stimuli, for example the absorption of electromagnetic radiation in the fundamental band with a photon energy  $h\nu \geq E_g$  where  $E_g$  is the forbidden gap energy. Either the excess electron or the excess hole can be created by excitation from the bound impurity levels in the forbidden gap (with a photon energy  $h\nu \leq E_g$ ) or by charge injection (extraction) through various types of rectifying contacts or in a forward-biased pn-junction. Carrier recombination lifetime and mobilities are semiconductor parameters that directly characterise PC for different injection levels. The recombination lifetime  $\tau$ , in general, is the average time an excess e-h pair exists. This is usually defined as the time required for the concentration to decay to  $1/e$  of its initial value according to

$$\tau(t) = -\Delta n / \frac{\partial \Delta n(t)}{\partial t} \equiv -\frac{\partial}{\partial t} \ln[\Delta n(t)] \quad (2)$$

It should be distinguished from the generation lifetime which is usually introduced for representation of thermally activated space-charge generation within the depletion region of Si devices [1,2]. Generation lifetime is presented in Datareview 13.5. Occasionally, so called electron and hole lifetime, or the minority-carrier lifetime, are further subdivided as a characteristic parameter for a specific relaxation process [3–5], but such finer subdivision is not done here. We will mostly use the general term to cover all of these possibilities.

The gradient of carrier concentration in a sample causes the diffusion current of density

$$J_D = qD \text{grad}(\Delta n) \quad (3)$$

where  $D$  is the diffusion coefficient.  $D$  also describes the range (called the diffusion length) which the carrier can diffuse during the time interval  $\Delta t$

$$l_D = \sqrt{D \cdot \Delta t} \quad (4)$$

At weak electric fields and low doping levels  $D_i$  and drift mobility  $\mu_i$  are related by the Einstein formula

$$D_i = (kT/q)\mu_i \quad i = e, h \quad (5)$$

### 13.1 Photoconductivity of c-Si: general remarks

where  $T$  is the temperature in K,  $k$  is the Boltzmann constant. Diffusion current indirectly determines PC in semiconductors since it couples carrier propagation for different regions of the sample. In this way, lifetime is mainly determined by the most effective recombination sink in the sample. As a consequence, the effect of surface or interface recombination typically complicates attempts to measure the true bulk lifetime. We shall present the concept of surface recombination velocity in Datareview 13.6 in the context of carrier diffusion and lifetime.

## B METHODS

PC measurements divide naturally into two categories: steady-state methods and dynamic methods. Steady-state methods depend on DC measurements or measurements under steady-state conditions. Dynamic methods depend on measuring either the decay of carrier density following an excitation pulse or the phase lag between a signal and a modulated excitation. Both categories can be developed for uniform and non-uniform samples. Steady-state PC methods are very effective for high resistance or highly compensated Si material and for structures with pn-junctions: see Datareviews 13.2 and 13.3. Some classical PC methods are described by the text books of Bube [3], Ryvkin [4] and Milnes [5]. Carrier lifetime measurement in Si by PC decay is appointed as the ASTM standard: see Blair and Seiler [6]. This method relies on a measurement of the change of the sample's resistivity when the optical excitation is terminated. Picosecond or subpicosecond PC are also available; however, under such conditions, the photoconductor should be regarded as a distributed circuit element, and the propagation of the wave through this region should be properly treated [7].

The constant-current steady state PC, based on the spectral absorption, is an excellent tool for monitoring deep energy levels in Si (Grimmeiss [8]). A typical example of monitoring shallow impurities at low temperatures in the case of Si:In is given by Peschel et al [9]. A variety of experimental techniques lead to indirect measurement of PC. For example, contactless PC measurement can be carried out from microwave reflectivity, radio frequency techniques, from photoluminescence, and from free carrier induced absorption or reflection, and by transient grating techniques. Several methods have been developed for measurement of Si devices directly. Among them, open circuit voltage decay, surface photovoltage or pulse MOS capacitor can be mentioned. A collection of various techniques is provided by Orton and Blood [10] and by Maracas and Schroder [11]. Accurate and fast recombination lifetime measurements are extremely important for material and processing specialists as a sensitive tool for monitoring lattice defects caused by contamination or improper treatment of Si material. For the complexity of measurement situations, however, the correlation of results obtained by different techniques should be undertaken with great care, relying on the fundamental, the phenomenological and the statistical basis of each method [12–14]. As pointed out by Hangleiter [15], care should be taken for lifetime interpretation in the case of unipolar Si devices in the absence of minority carrier injection (for example in DLTS measurement) compared with the case where some low-level junction occurs.

## C INJECTION LEVEL

The rate and duration of the photogeneration determine the net excess carrier injection level. Since PC parameters depend to some extent on the excess carrier concentration, injection level must be specified in the measurements. From the statistical basis of the Shockley-Read-Hall (SRH) recombination process and also for the Auger type process, high-level (HL) and low-level (LL) injection are usually introduced. These are classified with excess carrier concentration against the extrinsic equilibrium majority carrier concentration  $n_0$ : HL when  $\Delta n = \Delta p \gg n_0$  or LL when  $\Delta n = \Delta p \ll n_0$  ( $p_0$  should be used in p-type Si) [2]. This classification proceeds under most device operating conditions operating with LL and HL injection during current conduction (for example in power devices). At the same time this classification is valid for grouping of carrier mobility and

### 13.1 Photoconductivity of c-Si: general remarks

diffusion parameters: see Datareviews 13.7 and 13.8. In a specific case, however, HL and LL injection against the density of the recombination centre may be settled [3,4].

## REFERENCES

- [1] D.K. Schroder [ *Semiconductor Material and Device Characterisation* (J. Wiley and Sons, New York, USA, 1990) and in *Handbook of Semiconductor Silicon Technology* Eds. W. O'Mara et al (Noyes, Park Ridge, NJ, USA, 1990) ]
- [2] B.J. Baliga [ *Modern Power Devices* (J. Wiley and Sons, New York, USA, 1987) ]
- [3] R.H. Bube [ *Photoconductivity of Solids* (J. Wiley and Sons, New York, USA, 1960) ]
- [4] S.M. Ryvkin [ *Photoelectric Effects in Semiconductors* (Cons. Bureau, New York, USA, 1964) ]
- [5] A.G. Milnes [ *Deep Impurities in Semiconductors* (J. Wiley and Sons, New York, USA, 1973) ]
- [6] P.D. Blair, C.F. Seiler [ *Lifetime Factors in Silicon* Eds. J.B. Wheeler et al (ASTM STP 712, ASTM, Baltimore, USA, 1980) p.148 ]
- [7] C.H. Lee (Ed.) [ *Picosecond Optoelectronic Devices* (Academic Press, Orlando, USA, 1984) ]
- [8] H.G. Grimmeiss [ *Annu. Rev. Mater. Sci. (USA)* vol.7 (1977) p.341 ]
- [9] W. Peschel, R. Kuhnert, M. Shultz [ *Appl. Phys. A (Germany)* vol.30 (1983) p.59 ]
- [10] J.W. Orton, P. Blood [ *The Electric Characterization of Semiconductors: Measurement of Minority Carrier Properties* (Academic Press, London, UK, 1990) ]
- [11] G.N. Maracas, D. Schroder [ in *Characterization of Semiconductor Materials* Ed. G.E. McGuire (Noyes, Park Ridge, NJ, USA, 1990) vol.1 ch.1 ]
- [12] K. Graff, H. Fisher [ *Top. Appl. Phys. (Germany)* vol.31 (1979) p.173 ]
- [13] V. Grivickas et al [ *Lith. Phys. J. (USA)* vol.32 (1992) p.307 ]
- [14] W.M. Bullis, H.R. Huff [ *J. Electrochem. Soc. (USA)* vol.143 (1996) p.1399 ]
- [15] A. Hangleiter [ *Phys. Rev. B (USA)* vol.35 (1987) p.9149 ]

## 13.2 Photoconductivity spectra of ion-implanted c-Si

M. Willander and B.G. Svensson

January 1998

### A INTRODUCTION

Only a few reports exist in the literature on photoconductivity (PC) measurements of ion implanted silicon samples, and PC is a rare topic at international conferences on ion implantation and atomic collisions in solids. One reason may be that for commonly used ion doses ( $\geq 10^{14} \text{ cm}^{-2}$ ) large defect clusters are generated and as a result, well-defined energy levels are hard to observe. Similar ideas have been put forward by Kalma and Corelli [1] who found a broad ‘energy band’ overriding single defect levels in samples irradiated with 45 MeV electrons, which generate a considerable amount of complex defects. In contrast, for 1.5 MeV electrons, which predominantly give rise to ‘simple’ (isolated) point defects, single energy levels dominated and very little of the broad ‘energy band’ was observed.

However, in this context it should be mentioned that *in situ* conductivity measurements have recently been demonstrated to be a powerful tool for monitoring defect evolution in crystalline as well as in amorphous silicon during ion bombardment [2–4]. A similar exploration of the PC technique would be highly desirable, and in particular, this holds for an intermediate dose regime ( $\sim 10^{10} - 10^{13} \text{ cm}^{-2}$ ) where suitable tools for defect studies are scarce [5].

### B RESULTS AND DISCUSSION

Netange et al [6] implanted high-resistivity n- and p-type silicon samples with 100 keV B ions at room temperature (RT) to doses of about  $10^{14} \text{ cm}^{-2}$  and obtained spectra similar to those for electron-irradiated samples, i.e. a major level at 0.32 eV and an important increase of the photoconductivity at  $\sim 0.4$  eV. The level at 0.32 eV was attributed to a transition of the divacancy ( $V_2$ ) centre from a singly positive to a neutral charge state, in accordance with results for neutron-irradiated p-type samples [7]. Cheng [7] based his identification on similarities of the band shape and stress-induced dichroism of the 0.32 eV PC-band with the corresponding properties of  $V_2$  measured by other techniques (infrared absorption and electron paramagnetic resonance (EPR)). EPR and deep level transient spectroscopy (DLTS) measurements yield a bandgap position of 0.20 – 0.25 eV above the valence band edge ( $E_v$ ) for the transition from neutral to singly positive charge state of  $V_2$ ; this may, however, not be directly comparable to the 0.32 eV level because of the different excitation processes involved [7]. A distinct possibility would also be that the so-called C(3) centre plays a role since it is a dominating defect after implantation at RT [8]. The C(3) centre is associated with an interstitial carbon–interstitial oxygen pair and gives rise to a donor level at  $\sim 0.35$  eV above  $E_v$  [9], close to the position of the 0.32 eV PC-band.

Netange et al [6] attributed the sharp increase near 0.4 eV in the PC-spectra to the so-called Di-defects [10] (in this case interstitial boron,  $B_i$ ). However, its temperature stability (about 300°C) does not agree with that of  $B_i$  since interstitial boron atoms display long range migration at temperatures below RT [11] and form more stable complexes through reactions with other impurities and defects. Consequently, we conclude that the 0.4 eV transition is not due to  $B_i$ , but some other implantation induced defect. On the basis of results from other experimental techniques, e.g. DLTS [12], several energy levels assigned to different defects occur in the region around  $E_v + 0.4$  eV.

PC-spectra of silicon samples (p-type, 80–2000  $\Omega$  cm) implanted with  $10^{15}$   $\text{cm}^{-2}$  Se ions and subsequently annealed at 1200°C showed two of three well-known levels found in selenium diffused samples [13], namely the levels at ~0.19 eV (attributed to  $\text{Se}_2$ -centres) and ~0.27 eV below the conduction band edge ( $E_c$ ). Astrova et al [13] conducted their experiments using two different cooling procedures (rapid cooling in air and quenching in cooled water) and found a strong influence on the PC-spectra. A considerable reduction in the concentration of the two levels was observed in the quenched samples but no conclusive explanation was given. Furthermore, a numerical value of the photo-ionisation cross-section of the  $E_c - 0.19$  eV level was deduced and found to be about a factor of 100 smaller than that of the  $E_c - 0.27$  eV level.

Peschel et al [14] implanted In and Tl into silicon and, after annealing, the corresponding energy level positions were determined using PC. In order to increase the sensitivity of the measurements, a pn-junction was formed between the implanted thin film and the silicon substrate by an additional implant. During the PC-measurements the pn-junction was reverse biased by applying a voltage to the back-side contact, and as a result, an improvement of the sensitivity by 2–3 orders of magnitude was achieved. Good agreement was obtained between the implanted films and bulk wafers with respect to spectral sensitivity and positions of the levels. The ionisation energies were extracted by a novel concept where photothermal excitation, via excited bound states, was separated from direct photoexcitation into the band continuum, utilising the fact that the two processes exhibit different temperature dependence.

Finally, PC-spectra of silicon samples implanted with high doses of carbon ( $5.5 \times 10^{17}$   $\text{cm}^{-2}$ ) contain a dominant peak at 0.37 eV and two additional transitions at 0.73 and 1.0 eV [15]. After a 30 min anneal at 1100°C the peaks disappear. Akimchenko et al [15] assigned the 0.37 eV level to singly negatively charged  $\text{V}_2$  centres. Provided that the interaction takes place with the conduction band, this assignment is consistent with DLTS results showing that the transition  $\text{V}_2(0/-)$  occurs at  $\sim E_c - 0.42$  eV [12]. However, it must be emphasised that several defect levels exist close to  $E_c - 0.4$  eV, and the assignment of the PC-peak at 0.37 eV must be regarded as tentative, especially since the samples were reported to be p-type (hole conductive). The transition at 1.0 eV was attributed to interstitial carbon ( $C_i$ ), which is consistent with the acceptor level position of  $C_i$  at  $\sim E_c - 0.10$  eV [8] if the excitation occurs from the valence band. On the other hand,  $C_i$  is mobile at RT and forms stable complexes through pairing and/or reactions with other impurities and defects. Thus, isolated  $C_i$  atoms are not anticipated to be stable after implantation at RT (or elevated temperatures) [8], and therefore the 1.0 eV transition is believed to originate from some other implantation induced defect, possibly involving carbon.

## C CONCLUSION

There is little data on photoconductivity of ion implanted silicon, probably because high ion doses lead to defect clusters which make discrete energy levels difficult to observe. Nevertheless, data are presented for silicon implanted with B, Se, In, Tl and C, as measured by PC and other techniques.

## REFERENCES

- [1] A.H. Kalma, J.C. Corelli [ in *Radiation Effects in Semiconductors* Ed. F.L. Vook (Plenum Press, New York, 1968) p.153 ]
- [2] A. Battaglia, S. Coffa, F. Priolo, C. Spinella [ *Appl. Phys. Lett. (USA)* vol.65 (1994) p.306 ]
- [3] S. Coffa, F. Priolo, A. Battaglia [ *Phys. Rev. Lett. (USA)* vol.70 (1993) p.3756 ]
- [4] J.H. Shin, H.A. Atwater [ *Phys. Rev. B (USA)* vol.48 (1993) p.5964 ]
- [5] B.G. Svensson [ Datareview in this book: *14.5 Energy levels, structure and properties of point defects induced by ion implantation and electron irradiation of c-Si* ]

### 13.2 Photoconductivity spectra of ion-implanted c-Si

- [6] B. Netange, M. Cherki, P. Baruch [ *Appl. Phys. Lett. (USA)* vol.20 (1972) p.349 ]
- [7] L.J. Cheng [ in *Radiation Effects in Semiconductors* Ed. F.L. Vook (Plenum Press, New York, 1968) p.143 ]
- [8] J. Lalita, N. Keskitalo, A. Hallén, C. Jagadish, B.G. Svensson [ *Nucl. Instrum. Methods Phys. Res. B (Netherlands)* vol.120 (1996) p.27 ]
- [9] G. Davies, R.C. Newman [ in *Handbook of Semiconductors* Eds. T.S. Moss, S. Mahajan (Elsevier, Amsterdam, 1994) ch.21 p.1557 ]
- [10] M. Cherki, A.H. Kalma [ *Phys. Rev. B (USA)* vol.1 (1970) p.647 ]
- [11] G.D. Watkins [ *Phys. Rev. B (USA)* vol.12 (1975) p.5824 ]
- [12] L.C. Kimerling [ in *Radiation Effects in Semiconductors 1976* Eds. N.B. Urli, J.W. Corbett (Inst. Phys., Bristol, 1977) p.221 ]
- [13] E.V. Astrova, I.B. Bol'shakov, A.A. Lebedev, O.A. Mikhno [ *Sov. Phys.-Semicond. (USA)* vol.19 (1985) p.565 ]
- [14] W. Peschel, R. Kuhner, M. Schulz [ *Appl. Phys. A (Germany)* vol.30 (1983) p.59 ]
- [15] I.P. Akimchenko, K.V. Kisseleva, V.V. Krasnoperov, A.G. Touryanski, V.S. Vavilov [ *Radiat. Eff. (UK)* vol.48 (1980) p.7 ]

### 13.3 Photoconductivity spectra of electron irradiated c-Si

M. Willander and J.L. Lindström

January 1998

#### A INTRODUCTION

Many of the known defects in silicon introduced by electron irradiation have been investigated by photoconductivity (PC) measurements. The method is direct and sensitive. As these defects often are anisotropic and can be preferentially aligned by uniaxial stress it is often possible to get more detailed information about a defect using stress and polarised light in connection with PC [1]. When doing the measurements one has usually to vary the frequency of the chopped light to optimise the PC signal [2]. A possible influence from defects at the surface should also be considered. When interpreting the results there can be a problem in determining the background signal for a particular defect level since the PC signal is additive. The early work using PC on e-irradiated silicon has been summarised by Fan and Ramdas [3]. Later reviews have been done by Vavilov [4] and Curtis [5].

#### B RESULTS

TABLE 1 is a summary of the reported energy levels from PC on electron irradiated silicon.

TABLE 1 Energy levels in electron-irradiated silicon observed by photoconductivity measurements.

Position of level (eV)	Defect assignment	Ref
$E_c - 0.16$	vacancy-oxygen (A-centre)	[3,7,9]
$E_c - 0.36$	divacancy	[6]
$E_c - 0.39$	divacancy	[6,11]
$E_c - 0.43$	phosphorus-related	[7]
$E_c - 0.48$	arsenic-related	[7]
$E_c - 0.54$	divacancy	[6]
$E_v + 1.0$	unknown	[7]
$E_v + 0.53$	unknown	[7]
$E_v + 0.525$	unknown	[7]
$E_v + 0.445$	unknown	[7]
$E_v + 0.45$	unknown	[9]
$E_v + 0.430$	boron-related	[10]
$E_v + 0.39$	aluminium-related	[10]
$E_v + 0.35$	unknown	[10]
$E_v + 0.30$	interstitial-oxygen complex?	[7,9]
$E_v + 0.25$	divacancy	[7]

One of the most studied defects in silicon, the vacancy-oxygen centre (A-centre), appears in two charge states VO(0) and VO(-). It acts as an acceptor and gives rise to a level 0.16 - 0.18 eV below the conduction band. There is a spread in values reported from different experimental techniques (resistivity, Hall effect and PC). From PC the value  $E_c - 0.16$  eV is found: see TABLE 1. Since the formation of A-centres requires the presence of vacancies and oxygen atoms, a great variation in concentration can occur for a certain electron fluence depending upon the concentration of oxygen and dopants. Impurities trapping vacancies, like P and Sn, will lower the A-centre concentration, while the presence of traps for self-interstitials will suppress the vacancy-self-interstitial annihilation and therefore will give a higher concentration. Thus, the conditions for observing the A-centre with

### 13.3 Photoconductivity spectra of electron irradiated c-Si

PC are that the irradiation has to be performed on a suitable material and to an electron fluence so that the Fermi level is above  $E_c - 0.16$  eV.

Another important defect studied in PC is the divacancy. This defect appears in four different charge states. Levels at  $E_c - 0.36$ ,  $0.39$ ,  $0.54$  and  $E_v + 0.25$  eV have been associated with it [6,7]. With the Fermi level below  $E_c - 0.22$  eV only the  $0.54$  eV level could be observed [6]. Kalma and Corelli [6] used a technique reported by Cheng [8] to study the  $E_c - 0.39$  and  $E_c - 0.54$  eV levels using polarised light and stress induced dichroism.

They found excellent agreement with results from electron paramagnetic resonance (EPR) and IR-absorption measurements and concluded that the two levels are related to the same defect, the divacancy. Several defects formed by interaction between vacancies, interstitials and dopants have been reported.

In phosphorus doped material the strength of the level at  $E_c - 0.43$  eV increases with increasing phosphorus doping at constant electron fluence. The level has been assigned to the vacancy-phosphorus centre (E-centre) [7].

Since the mobility of the self-interstitial in silicon has a different temperature dependence from the mobility of the vacancy, experiments have been performed where the temperature of the sample during irradiation has been varied.

Vavilov et al [9] observed a continuous distribution of allowed levels introduced by electron irradiation at 80 K. When raising the temperature to 300 K they disappeared and new levels appeared at  $E_v + 0.45$  eV in boron-doped float-zoned (FZ) material and at  $E_c - 0.16$ ,  $E_v + 0.30$  and  $E_v + 0.45$  eV in high oxygen material.

Matsui and Baruch [7] found energy levels at  $0.29$ ,  $0.445$ ,  $0.525$  and  $1.0$  eV above the valence band in p-type material irradiated at 20 K by 1.5 MeV electrons. In n-type material levels at  $0.16$ ,  $0.43$  or  $0.48$  eV below the conduction band were observed.

Cherki and Kalma [10] investigated electron-irradiated boron and aluminium doped silicon irradiated at 4.2, 20.4, 77 and 300 K. They observed at all temperatures the same defect levels  $E_v + 0.43$  eV ( $\pm 0.005$  eV) in boron doped and  $E_v + 0.39$  eV ( $\pm 0.010$  eV) in aluminium doped silicon. Their conclusion was that, as only the self-interstitial is mobile at the lowest of these temperatures, the observed defects are formed when a self-interstitial changes place with a substitutional boron or aluminium atom. They also carried out stress-induced dichroism measurements and found a C<sub>3v</sub> symmetry of these defects. Both defects annealed in the temperature range of 250 to 300°C.

Li-doped silicon irradiated with 1.5 MeV electrons at 77 K was studied by Caillot et al [11]. In FZ material they observed at least four kinds of complexes. They discuss different formation and annealing mechanisms and found a Li-concentration dependence of the annealing. In pulled crystals they observed two different complexes which are stable up to  $>730$  K. These were interpreted as Li-O (or vacancy) complexes.

## C CONCLUSION

This Datareview has summarised the data available from photoconductivity measurements in electron irradiated silicon. Defects containing a vacancy with oxygen (A centre), divacancies, phosphorus-containing, arsenic-related, boron-related, aluminium-related and lithium-containing defects have all been identified. Other defects have been observed but not yet assigned.

## REFERENCES

- [1] J.W. Corbett [ *Electron Radiation Damage in Semiconductors and Metals*, Solid State Physics (USA) suppl.7 (Academic Press, New York, 1966) ]
- [2] P. Vajda, L.J. Cheng [ in *Radiation Effects in Semiconductors* Eds J.W. Corbett, G.D. Watkins (Gordon & Breach, New York, 1971) ]
- [3] Y.H. Fan, A.K. Ramdas [ *J. Appl. Phys. (USA)* vol.30 (1959) p.1127 ]
- [4] V.S. Vavilov [ *Radiation Damage in Semiconductors* (Dunod & Cie., Paris, 1965) p.115 ]
- [5] O.L. Curtis Jr. [ in *Point Defects in Solids* vol.2 Eds J.H. Crawford Jr., L.M. Slifkin (Plenum Press, New York-London, 1975) ]
- [6] A.H. Kalma, J.C. Corelli [ in *Radiation Effects in Semiconductors* Ed. F.L. Vook (Plenum, New York, 1968) p.153 ]
- [7] K. Matsui, P. Baruch [ *Lattice Defects in Semiconductors* (University of Tokyo Press, Tokyo, 1968) p.282 ]
- [8] L.J. Cheng [ *Phys. Lett. A (Netherlands)* vol.24 (1967) p.729 ]
- [9] V.S. Vavilov, S.I. Vintovkin, A.S. Lyutovich, A.F. Plotnikov, A.A. Sokolova [ *Sov. Phys.-Solid State (USA)* vol.7 (1965) p.399 ]
- [10] M. Cherki, A.H. Kalma [ *IEEE Trans. Nucl. Sci. (USA)* vol.NS-16 (1969) p.24 ]
- [11] M. Calliot, M. Cherki, A.H. Kalma [ *Phys. Status Solidi A (Germany)* vol.4 (1971) p.121 ]

## 13.4 Bulk lifetimes of photogenerated carriers in intrinsic c-Si

V. Grivickas and M. Willander

January 1998

### A INTRODUCTION

When excess e-h pairs recombine, they release energy by one of several distinct physical mechanisms. Three basic mechanisms are important for bulk Si. The recombination event can proceed through intermediate recombination centres (known as multiphonon recombination or the Shockley–Read–Hall (SRH) mechanism [1,2]) or it can proceed by a conduction band electron falling directly into a hole in the valence band by radiative and by Auger recombination. The bulk recombination lifetime for either injection level is:

$$\tau_b^{-1} = \tau_{\text{SRH}}^{-1} + \tau_{\text{rad}}^{-1} + \tau_{\text{Aug}}^{-1} \quad (1)$$

EQN (1) is an expression for parallel processes. In such an expression, the lowest of the three lifetimes dominates the recombination lifetime. In general, the SRH lifetime dominates at lower injections and dopings while Auger recombination dominates at high injection or high doping. For indirect bandgap Si, the radiative recombination is small compared to either the SRH or the Auger recombination [3].

In this Datareview the lifetime of excess carriers in intrinsic bulk Si will be considered. We define ‘intrinsic Si’ as a material without intentional or process-technology-dependent impurities or structural defects and with an extremely low contaminant concentration. In reality this means that shallow impurity density should be below  $10^{15} \text{ cm}^{-3}$ , most soluble heavy metal impurity density should be below  $10^{11} \text{ cm}^{-3}$  and the known structural imperfections of the crystal (volume or area defects) should be kept well below the  $10^3 \text{ cm}^{-2}$  limit [3]. These conditions are achievable in current high-purity (ULSI-grade) as-grown float zone (FZ)-Si and, to a lesser extent, in magnetic field-applied Czochralski (MCZ) grown Si. An ordinary Czochralski grown crystal also can satisfy some of these conditions. We somewhat artificially refer below to ‘electronic grade’ CZ-Si as a material used for the fabrication of microelectronics devices. For CZ as-grown material, which covers various contaminants of substantial amounts, used by the photovoltaics industry, we will use the term ‘solar-grade’ CZ-Si. For the purpose of comparison we also will present data in the block cast multicrystalline (mc)-Si which is also used for the commercial fabrication of some photovoltaic devices.

### B SRH-LIFETIME

In intrinsic Si, SRH lifetime depends on the density of residual recombination centres. In TABLE 1, the bulk SRH lifetime specification is provided for commercially available Si fabricated by various growth methods. In the first row we present data on an average LL-injection lifetime extracted in a number of SiN-film-passivated Si wafers, taken from a recent publication of Schmidt and Aberle [4]. In the second row we present (without a particular specification of the research group) the typical lifetime data in intrinsic Si reported during the last decade.

Due to the outstanding degree of purity a higher intrinsic SRH lifetime is observed in FZ-Si. In this material, SRH lifetime usually remains constant independent of shallow impurity doping

### 13.4 Bulk lifetimes of photogenerated carriers in intrinsic c-Si

concentration well above  $10^{16} \text{ cm}^{-3}$ . In as-grown MCZ- and electronic-grade CZ-Si it is found that the dominant recombination centre is a deep-level which is considered to be an oxygen-related defect complex. This reveals the lifetime dependence on the resistivity under the framework of the SRH relation [1,6] (see Datareview 13.5), and also manifests proportionality to the oxygen concentration. It was shown that, in these crystals, the effective density of recombination centres is proportional to the interstitial oxygen concentration in the range  $O_i = (5 - 25) \text{ ppma}$  [7,8].

TABLE 1 SRH lifetime of intrinsic as-grown Si.

	FZ-Si	MCZ-Si	CZ-Si, electr.-grade	CZ-Si, solar-grade	mc-Si
$\tau_{SRH}$ [4]	4 (1 – 10) ms	-	900 $\mu\text{s}$	200 $\mu\text{s}$	19 (4 – 30) $\mu\text{s}$
$\tau_{SRH}$ , typical range	(0.4 – 40) ms	(0.2 – 2) ms	100 – 1000 $\mu\text{s}$	(40 – 300) $\mu\text{s}$	15 – 200 $\mu\text{s}$ [5]

### C RADIATIVE LIFETIME

For electrons in the conduction band recombining with holes in the valence band, the radiative lifetime is given by

$$\tau_{rad} = \beta_{rad} (p_0 + n_0 + \Delta n + \Delta p)^{-1} \quad (2)$$

where  $\beta_{rad}$  is the radiative recombination coefficient, the equilibrium carrier concentrations are  $n_0$  and  $p_0$ , and the total concentrations are  $n = n_0 + \Delta n$  and  $p = p_0 + \Delta p$ . For HL injection conditions ( $\Delta n \approx \Delta p \gg n_0, p_0$ ), the radiative lifetime is inversely proportional to the excess carrier concentration. The radiative recombination coefficient has been determined as a function of temperature by Schlangenotto et al [9] who used electrical injection in the base of a thin p-i-n device and corrected the measured emission for reabsorption. In TABLE 2 the extracted  $\beta_{rad}$ , together with the calculated  $\tau_{rad}$  values for an arbitrary chosen HL injection of  $\Delta n = 10^{16} \text{ cm}^{-3}$ , are presented. In [8] it was shown quantitatively that the measured  $\beta_{rad}$  is Coulomb-enhanced due to so-called electron-hole (e-h) correlation terms [9]. The decrease of  $\beta_{rad}$  with increasing T by a factor of 30 in the range 100 K to 400 K, results mainly in the decrease of the exciton concentration.

TABLE 2 Radiative coefficient and radiative lifetime in intrinsic Si [9].

T (K)	101	128	153	183	213	243	273	303	333	365	393
$\beta_{rad} \times 10^{-14} (\text{cm}^3/\text{s})$	17.8	7.6	4.25	2.6	1.9	1.45	1.13	0.94	0.77	0.64	0.55
$\tau_{rad}$ (ms) at $\Delta n = 10^{16} \text{ cm}^{-3}$	0.56	1.32	2.35	3.85	5.26	6.90	8.85	10.6	13.0	15.6	18.2

For a single e-h pair which is, at low temperature, coupled into a single exciton, the radiative lifetime was estimated from the experiments in intrinsic Si at the cryogenic temperatures and is a value as high as  $\tau^{ex} = 100 \mu\text{s}$  [10]. (A constant value of about  $\tau^{ex} = 200 \mu\text{s}$  was found by Cuthbert [19].)

### D AUGER LIFETIME

From the reaction kinetics for Auger band-to-band recombination it is expected that the recombination lifetime for this three-particle process must follow the relation:

$$\tau_{Aug} = \frac{\Delta n}{\gamma_e (p^2 n - p_0^2 n_0) + \gamma_h (pn^2 - p_0 n_0^2)} \quad (3)$$

### 13.4 Bulk lifetimes of photogenerated carriers in intrinsic c-Si

where  $\gamma_n$  and  $\gamma_p$  are Auger recombination probabilities (coefficients) of the e-e-h and h-h-e Auger collision processes, providing the recombination energy is given to the third electron or hole, respectively. The Auger lifetime obeys an inverse-square law dependence on carrier density. This dependence can be simplified further for the HL injection of intrinsic Si:

$$\tau_{\text{Aug}} = [\gamma \times (\Delta n)^2]^{-1} \quad \gamma = \gamma_e + \gamma_h \quad \Delta n = \Delta p \gg p_0, n_0 \quad (4)$$

It was therefore shown experimentally that Auger coefficients, extracted from EQN (4), obey a fundamental injection dependence in Si [11]. Much higher Auger recombination coefficients later have been proven in various experiments for carrier concentrations below the excitonic Mott transition ( $\Delta n_{\text{Mott}} \approx 7 \times 10^{17} \text{ cm}^{-3}$  at 300 K) [7,12,13]. In this injection range, the Auger coefficient is decreasing with increasing temperature from T = 150 K down to 500 K [14]. Auger recombination enhancement has been explained quantitatively by Hangleiter and Hacker [15]. It was shown that, in similarity to radiative recombination as described above, Coulomb correlation factors enhance the Auger recombination lifetime. For numerical simulation of the overall effect, the injection dependence of the Auger coefficient in EQN (4) can be approximated at T = 300 K by the following formula [16]:

$$\gamma = \gamma_{\min} + (\gamma_{\max} - \gamma_{\min})/[1 + (\Delta n/n_{\text{ref}})^p] \quad (5)$$

with  $\gamma_{\min} = 4 \times 10^{-31} \text{ cm}^6 \text{ s}^{-1}$ ,  $\gamma_{\max} = 1.35 \times 10^{-30} \text{ cm}^6 \text{ s}^{-1}$ ,  $n_{\text{ref}} = 7 \times 10^{17} \text{ cm}^{-3}$  and  $p = 1$ . The temperature dependency of the four parameters entering EQN (5) is, however, not yet well defined.

At low temperatures (T < 23 K) and high excitation, e-h droplets are formed in Si, as an intrinsic excitation with an equal constant number of electrons and holes in a drop. Lifetime in e-h droplets is conditioned by band-to-band Auger processes. This lifetime has been determined experimentally to be  $\tau_{\text{dr}} = 137 \text{ ns}$  [17].

Localised band-to-band Auger processes also determine the extrinsic recombination of excitons bound to shallow neutral donor and acceptor impurities in Si. Since exciton radius decreases with increasing binding energy, the lifetime does not depend on the density of impurities but obeys a well defined constant and exponential lifetime which follows a universal power law:  $\tau \sim E_A^{-4.6}$  and  $\tau \sim E_D^{-3.9}$  where  $E_A$  and  $E_D$  are the binding energy of the acceptor hole and the donor electron. Lifetimes from the measurements performed at 4.2 K by Schmid [18] for different impurities are given in TABLE 3.

TABLE 3 Lifetimes for excitons bound to neutral shallow impurities in intrinsic Si [18].

Impurity $\tau_{\text{ba-ex}}$ (ns)	Acceptors				Donors		
	B	Al	Ga	In	Li	P	As
1055	76	77	2.7		1150	272	183

## E CONCLUSION

Bulk lifetime in silicon is dominated by Shockley–Read–Hall recombination at low injections and doping levels while band-to-band Auger recombination dominates at higher levels of both parameters. Data is presented for lifetimes in intrinsic silicon grown by a variety of processes. In electronic grade material, the deep level recombination centre is an oxygen related defect. Values for the lifetimes due to bound excitons linked to shallow impurities are also presented.

## REFERENCES

- [1] W. Shockley, W.T. Read [ *Phys. Rev. (USA)* vol.87 (1952) p.835 ]
- [2] N. Hall [ *Phys. Rev. (USA)* vol.87 (1952) p.387 ]
- [3] D.K. Schroder [ *Semiconductor Material and Device Characterization* (J. Wiley and Sons, New York, USA, 1990) and in *Handbook of Semiconductor Silicon Technology* Eds. W. O'Mara et al (Noyes, Park Ridge, NJ, USA, 1990) ]
- [4] J. Schmidt, A.G. Aberle [ *J. Appl. Phys. (USA)* vol.81 (1997) p.6186 ]
- [5] A. Cuevas, M. Stocks, S. Armand, M. Stuckings, F. Ferrazza [ *Appl. Phys. Lett. (USA)* vol.70 (1997) p.1017 ]
- [6] B.J. Baliga [ *Modern Power Devices* (J. Wiley and Sons, New York, USA, 1987) ]
- [7] S.K. Pang, A. Rohatgi [ *J. Electrochem. Soc. (USA)* vol.138 (1991) p.523 ]
- [8] Y. Kitagaware, T. Yoshida, T. Hamaguchi, T. Takenaka [ *J. Electrochem. Soc. (USA)* vol.142 (1995) p.3505 ]
- [9] H. Schlangenotto, H. Maeder, W. Gerlach [ *Phys. Status Solidi A (Germany)* vol.21 (1974) p.357 ]
- [10] R.B. Hammond, R.N. Silver [ *Appl. Phys. Lett. (USA)* vol.36 (1970) p.68 ]
- [11] J. Vaitkus, V. Grivickas [ *Sov. Phys.-Semicond. (USA)* vol.14 (1981) p.1102 ]
- [12] E. Yablonovich, T. Gmitter [ *Appl. Phys. Lett. (USA)* vol.49 (1986) p.587 ]
- [13] R.A. Sinton, R.M. Swanson [ *IEEE Trans. Electron Devices (USA)* vol.34 (1987) p.1380 ]
- [14] V. Grivickas, J. Linnros, A. Galeckas, V. Bikbajev [ *Proc. 23rd Int. Conf. on Physics of Semiconductors* (World Scientific, Singapore, 1996) vol.1 p.91 ]
- [15] A. Hangleiter, R. Häcker [ *Phys. Rev. Lett. (USA)* vol.65 (1990) p.215 ]
- [16] A. Galeckas, V. Grivickas, M. Petrauskas, L. Frank, J.A. Tellefsen [ *Thin Solid Films (Switzerland)* vol.191 (1990) p.37 ]
- [17] W. Schmid [ *Solid State Commun. (USA)* vol.19 (1976) p.347 ]
- [18] W. Schmid [ *Phys. Status Solidi B (Germany)* vol.84 (1977) p.529; *Solid-State Electron. (UK)* vol.21 (1978) p.1285 ]
- [19] J.D. Cuthbert [ *Phys. Rev. B (USA)* vol.1 (1970) p.1552 ]

## 13.5 Bulk lifetimes of photogenerated carriers in doped and treated c-Si

V. Grivickas and M. Willander

January 1998

### A INTRODUCTION

We define doped and treated Si as a material with intentional doping during crystal growth or processing. We shall consider bulk recombination data resulting from various impurity contamination and transformation of the defects. Treatments on temperature and irradiation will be specified separately. Note that an expression of the three main parallel recombination mechanisms, EQN (1) in Datareview 13.4, is also applicable for doped and treated Si. While the radiative recombination via impurities in Si is small compared with Shockley-Read-Hall (SRH) or Auger recombination, it is not zero. The emanating light is used in a number of measurements of temporal and spatial behaviour of defects at low temperatures [1]. We shall start with SRH lifetime since this mechanism is often used for the description of doped and treated VLSI-device Si material.

### B SRH-LIFETIME, INJECTION DEPENDENCE

Each energy level represents some type of imperfection characterised by energy,  $E_T$ , concentration,  $N_T$ , and electron and hole capture cross-sections,  $\sigma_n$  and  $\sigma_p$ . Experimentally determined  $\tau_{SRH}$  values lie in the range of 1–100  $\mu\text{s}$  for VLSI-device process cycled Si material [2]. In highly damaged silicon-on-sapphire films the SRH-lifetime can be as low as in the range 1–100 ps [3]. The large spread of values is governed, in general, by the different recombination centre concentrations involved. This presents an opportunity to use recombination lifetime monitoring for very sensitive control of material perfection or of cleanliness of the applied process on the basis of the ‘fingerprint’ detected on the lifetime map [4]. The variation in lifetime with injection level is important to bipolar devices operating over a very large range of injection levels [5].

In the classical interpretation of the SRH process, the energy is released as phonons or lattice vibrations. The recombination takes place in two distinct steps, when first an electron (or a hole) is captured by the same centre. The statistics account for the occupation probabilities, and the SRH lifetime is given by the expression [2]:

$$\tau_{SRH} = \frac{\tau_{p0} (n_0 + n_1 + \Delta n) + \tau_{n0} (p_0 + p_1 + \Delta p)}{p_0 + n_0 + \Delta n} \quad (1)$$

where  $\tau_{n0} = 1/(\sigma_n v_{th} N_T)$  and  $\tau_{p0} = 1/(\sigma_p v_{th} N_T)$  are the corresponding hole and electron minority carrier lifetimes and  $v_{th}$  is the thermal velocity of the holes and the electrons, respectively. The excess concentrations are approximately equal to each other ( $\Delta n \approx \Delta p$ ) under conditions of space charge neutrality and in the absence of trapping. The quantities  $n_1 = n_i \exp[(E_T - E_i)/kT]$  and  $p_1 = n_i \exp[(E_T - E_i)/kT]$  are defined for recombination centre energy  $E_T$  with respect to the intrinsic Fermi energy  $E_i$ .

From EQN (1), two concepts of recombination lifetimes are easily distinguished. The minority carrier lifetime dominates the recombination process under LL injection conditions when the minority carrier

concentration is low compared to the equilibrium majority carrier concentration. This LL SRH-lifetime is given by the expression:

$$\tau_{SRH}(LL) \approx \tau_{p0} \left[ 1 + \exp\left(\frac{E_T - E_F}{kT}\right) \right] + \tau_{n0} \exp\left(\frac{2E_i - E_T - E_F}{kT}\right) \quad (2)$$

When the injection level becomes very high, the lifetime from EQN (1) asymptotically approaches a constant HL-value which is given by the expression:

$$\tau_{SRH}(HL) \approx \tau_{p0} + \tau_{n0} (1 + \xi) \quad (3)$$

The HL SRH-lifetime is not dependent on the position of the recombination centre, nor on the temperature. However, it is directly dependent upon the capture cross-section ratio  $\xi = \sigma_n/\sigma_p$ .

The SRH-lifetime depends indirectly on the energy level  $E_T$  because the capture cross-section tends to be highest for most impurities with energy levels near the middle of the bandgap and lowest near the band edges. There is, however, no clear rule - only trends. So, the LL SRH-lifetime has its smallest value when the recombination centre lies in a broad range centred around mid gap. As the centre is shifted towards either the conduction or the valence band edges, the LL SRH-lifetime increases as a result of the decreasing probability of capturing either holes or electrons. In reality, the identification of various centres by the SRH recombination process through EQN (1) gives considerable scatter because of a number of non-trivial circumstances [6,7]:

- several effective SRH recombination centres can be involved simultaneously in the volume of material;
- the recombination constants can vary for centres that have amphoteric properties, with energy position depending on the number of captured electrons;
- various boundaries or barriers can disturb the condition of charge neutrality (this is particularly important for high resistivity irradiated Si under the low injection condition);
- the recombination centre can be metastable with respect to the measurement condition or with measurement temperature range;
- the sample or the carrier injection is non-homogeneous and the carrier diffusion modifies the rate equation.

Typical SRH injection dependencies in a wide injection range of  $10^{11} - 10^{18} \text{ cm}^{-3}$  for medium doped n- and p-Si have been determined by Linnros and co-workers [6]. The SRH lifetime changes after wafer sawing and polishing were observed in [6,7].

SRH generation is important for Si devices influencing carrier thermal excitation from centres into bands. In general, the correlation between  $\tau_g$  and  $\tau_r$  is observed at LL injection conditions. The experimental ratio of the generation lifetime to recombination lifetime is measured typically in the range  $\tau_g/\tau_r = 50-500$  for uniformly doped material with uniform centre densities. This ratio can exceed as high as  $\tau_g/\tau_r = 1500$  when the centre distribution in the material is non-uniform or contains a high concentration of oxygen, e.g. in CZ-grown Si after subsequent heat treatments (see Schroder [2] and references therein).

## C LIFETIME KILLERS, DEEP METAL IMPURITIES

The energy levels of some intrinsic metallic impurities (Fe, Cr, Cu, Au, Pt), metal-acceptor clusters (FeB, CrB) and a few structural imperfections (dislocations, E-centre, A-centre, divacancy, vacancy) are known as the most important SRH recombination centres in Si. The capture cross-sections vary over a wide range. For Coulomb-attractive centres they may be as high as  $10^{-13} \text{ cm}^{-2}$ , for neutral centres they are around  $10^{-15} \text{ cm}^{-2}$ , while they are as low as  $10^{-18} \text{ cm}^{-2}$  for Coulomb-repulsive centres. Abakumov et al [8], using cascade capture theory, have analysed most experimentally determined temperature dependencies for shallow impurity capture cross-sections in Si. The excitonic capture cross-section model of deep level recombination centres such as in Si:Fe and Si:B,Cr was motivated at lower temperatures by Hangleiter [1]. Typical values for the capture cross-sections of Si:Au were determined by Wu and Peaker [9]. Most deep impurities have the soluble concentration in Si of about  $10^{15} - 10^{16} \text{ cm}^{-3}$ , thus, the lowest values of carrier lifetimes are in a few ns range at 300 K [1,2,9,10]. An inverse linear dependency of carrier lifetime as a function of the Fe concentration in the range  $10^{11} - 10^{15} \text{ cm}^{-3}$  has been observed by Rotondaro et al [11]. It was shown that the impact of Fe on n-Si is at least one order of magnitude lower than on p-Si. On the other hand, Cu is highly detrimental to n-Si, but has no significant impact on the minority carrier properties of p-Si.

The effect of either dissociation or photodegradation of CrB and FeB pairs on the carrier lifetime in Si was recently reported by several authors [12–14]. A survey on metal impurities for previous carrier lifetime studies can be found in the book by Graff [15].

## D THE EFFECT OF TEMPERATURE TREATMENTS

Thermal donor clusters which occur in CZ-Si after long-term thermal treatments at 300 – 450°C have impact on long LL injection lifetime [16,17]. As shown by Glinchuk et al [16] the effect of persistent photoconductivity for tens of seconds is related to minority carrier recombination via two kinds of induced recombination centres. New oxygen donors which occur with annealing at 600–800°C have the usual impact on carrier lifetime reduction both for LL lifetime and for HL lifetime.

Two- or three-step high-temperature treatment procedures are often applied in order to utilise intrinsic gettering of CZ-grown Si material. Grivickas et al [18] have shown that HL injection lifetime in the gettered zone of CZ-Si decreases sublinearly from  $10^{-6}$  down to  $10^{-7}$  s with increasing bulk oxygen precipitate density in the range between  $10^6$  and  $10^8 \text{ cm}^{-2}$ . In contrast, the lifetime in the precipitate-free zone can exceed as high as a few tens of  $\mu\text{s}$ .

The characterisation of an oxide-induced stacking fault annular ring-pattern for a 12 hr anneal at 1140°C in CZ-grown Si has been made by PC lifetime mapping: see Raebuger et al [19]. It was shown that the gettering behaviour of the ring can be distinguished by carrier lifetime variation within the range 8–100  $\mu\text{s}$ .

The correlation between minority carrier lifetime and annealing in CZ- and FZ-Si during high temperature lamp heating was recently demonstrated by Poggi et al [20].

## E THE EFFECT OF IRRADIATION

For electron, proton, neutron or Co-60 gamma irradiated Si, the carrier lifetime is strongly dependent on the introduced radiation defects. This effect is usually described by the lifetime degradation factor K defined by

$$\tau^{-1} = \tau_b^{-1} + K\Phi \quad (4)$$

where  $\tau$  is the lifetime after irradiation,  $\tau_b$  is the bulk lifetime before irradiation and  $\Phi$  is the irradiation fluency of particles. Typical values of  $K$  vary between  $10^{-5}$  and  $10^{-9} \text{ cm}^2/\text{s}$  for fluency of  $\Phi = 10^{11}\text{--}10^{15} (\text{cm}^{-2})$ .  $K$  has dose, energy and doping dependencies of the particular particle [21,22]. Among recombination centres, the so-called A centre ( $E_c = 0.18 \text{ eV}$ ) with  $\sigma_n \approx 10^{-14} \text{ cm}^2$  and divacancy centre ( $E_c = 0.23 \text{ eV}$ ) with  $\sigma_n \approx 2 \times 10^{-15} \text{ cm}^2$  at 300 K are very active recombination centres responsible for the lifetime reduction. High energy electron or proton irradiation is used to control uniformity of carrier lifetime in Si material used for fabrication of thyristors. The temperature and the injection dependence of SRH lifetime in 15 MeV electron irradiated  $p^+ \text{-} n \text{-} n^+$  diodes was studied by Bleichner et al [23].

Radiation damage caused by ion-implantation changes the carrier lifetime by several orders of magnitude, and thus the lifetime can be as short as  $10^{-12} \text{ s}$  around the typical amorphisation dose [24,25].

## F AUGER LIFETIMES

For the LL injection of highly-doped Si the Auger lifetime (see Datareview 13.2) obeys an inverse-square law dependence on the equilibrium carrier density. Assuming constant Auger coefficients, this dependence can be expressed for e-e-h and h-h-e processes as

$$\begin{aligned} \tau_A &= \frac{1}{\gamma_h p_0^2}, \quad \Delta n = \Delta p \ll p_0 \text{ (LL injection, p-type Si)} \\ \tau_A &= \frac{1}{\gamma_e n_0^2}, \quad \Delta n = \Delta p \ll n_0 \text{ (LL injection, n-type Si)} \end{aligned} \quad (5)$$

The Auger recombination coefficient was determined in highly doped material ( $N > 5 \times 10^{18} \text{ cm}^{-3}$ ) by Dzievior and Schmidt [26]. These values are provided in TABLE 1. They are nearly independent of temperature in the range 77 – 400 K. Note that the sum of individual coefficients  $\gamma_n + \gamma_p$  agrees with the value of  $\gamma$  determined at the corresponding HL carrier injection level in intrinsic Si: see Datareview 13.4.

TABLE 1 Auger coefficients for highly doped Si (e-e-h and h-h-e processes) at different temperatures [26].

T	77 K	300 K	400 K
$\gamma_n (\text{cm}^6/\text{s}) \times 10^{-31}$	2.3	2.8	2.8
$\gamma_p (\text{cm}^6/\text{s}) \times 10^{-31}$	0.78	0.99	1.2

At carrier densities below  $5 \times 10^{18} \text{ cm}^{-3}$  Auger coefficients are enhanced because of e-h correlations. The appropriate Auger recombination lifetimes and enhancement factors  $g_{eeh}$  and  $g_{hhe}$  have been calculated by Hangleiter and Häcker [27]. The enhancement factors are higher at low temperatures. In addition, the sum of  $g_{eeh}\gamma_n + g_{hhe}\gamma_p$  is larger because of the enhancement  $(g_{eeh} + g_{hhe})\gamma$  which represents Auger recombination under the HL carrier injection in intrinsic Si: see Datareview 13.4.

Experimental proof of impurity-assisted Auger recombination in silicon was provided by Hangleiter [28]. Au, Fe or Cr were diffused into medium doped p-type Si at 850 – 950°C. This treatment resulted in recombination centres of density  $10^{13} – 10^{14} \text{ cm}^{-3}$  and in an LL injection lifetime of 10 – 100 ns at 80 K. The Auger process produced hot particles which have been identified by energetic shift from the carrier emission corresponding to the levels in the gap, i.e. at  $\hbar\nu_{\max} = 2E_g - E_T - \hat{\omega}\Omega$  where  $E_T$  is the trap level and  $\hat{\omega}\Omega$  is the phonon involved in the radiative transition.

## G CONCLUSION

This Datareview summarises the data on bulk lifetimes in doped treated silicon. The Shockley–Read–Hall lifetime under low injection conditions is governed by the recombination centre energy and temperature, while the corresponding values for high injection levels are independent of these two parameters but are dependent on the capture cross-section ratio. Effects of deep level metallic impurities are also summarised, where values of lifetime can be reduced to a few ns at 300 K. Various temperature treatments are utilised to modify the lifetimes via adjustment of the oxygen donor or oxygen precipitate levels. Lifetimes are reduced following various irradiation treatments (electron, proton, ion-implantation, etc.), often caused by A centre and divacancy centre defects. The Auger lifetime is inversely proportional to the carrier concentration, under low injection conditions, and is virtually temperature independent from 77 to 400 K in highly doped material. Auger lifetimes increase as the carrier density falls below  $\sim 5 \times 10^{18} \text{ cm}^{-3}$ . Auger recombination can be assisted by Au, Fe or Cr incorporation into silicon.

## REFERENCES

- [1] A. Hangleiter [ *Phys. Rev. B (USA)* vol.35 (1987) p.9149 and vol.37 (1988) p.2594 ]
- [2] D.K. Schroder [ *Semiconductor Material and Device Characterization* (J. Wiley and Sons, New York, USA, 1990) and in *Handbook of Semiconductor Silicon Technology* Eds. W. O'Mara et al (Noyes, Park Ridge, NJ, USA, 1990) ]
- [3] A. Galeckas, V. Grivickas, M. Petrauskas, L. Frank, J.A. Tellefsen [ *Thin Solid Films (Switzerland)* vol.191 (1990) p.37 ]
- [4] J. Linnros, R. Revsäter, L. Heijkenskjöld, P. Norlin [ *IEEE Trans. Electron Devices (USA)* vol.42 (1995) p.1174 ]
- [5] B.J. Baliga [ *Modern Power Devices* (J. Wiley and Sons, New York, USA, 1987) ]
- [6] J. Linnros [ *J. Appl. Phys. (USA)* (1998) in press ]; V. Grivickas, J. Linnros, A. Vigelis, J. Seckus, J.A. Tellefsen [ *Solid-State Electron. (UK)* vol.35 (1992) p.299 ]; V. Grivickas et al [ *Lith. Phys. J. (USA)* vol.32 (1992) p.307 ]
- [7] K. Graff, H. Piper [ *Top. Appl. Phys. (Germany)* vol.31 (1979) p.173 ]
- [8] V.N. Abakumov, V.I. Perel, I.N. Jassievic [ *Sov. Phys.-Semicond. (USA)* vol.12 (1978) p.1 ]
- [9] R.H. Wu, A.R. Peaker [ *Solid-State Electron. (UK)* vol.25 (1982) p.643 ]
- [10] W. Schmid, J. Reiner [ *J. Appl. Phys. (USA)* vol.53 (1982) p.6250 ]
- [11] A.L. Rotondaro et al [ *J. Electrochem. Soc. (USA)* vol.143 (1996) p.3014 ]
- [12] J.H. Reiss, R.R. King, K.W. Mitchell [ *Appl. Phys. Lett. (USA)* vol.68 (1996) p.3302 ]
- [13] K. Mishra [ *Appl. Phys. Lett. (USA)* vol.68 (1996) p.3281 ]
- [14] A. Kaniava, A.L. Rotondaro, J. Vanhellemont, U. Menczigar, E. Gaubas [ *Appl. Phys. Lett. (USA)* vol.68 (1995) p.3930 ]
- [15] K. Graff [ *Metal Impurities in Silicon-Device Fabrication* Springer Series Mater. Sci. vol.24 (Springer, Berlin, Germany, 1995) ]
- [16] K.D. Glinchuk, N.M. Litovchenko, V.Yu. Ptitsin [ *Cryst. Res. Technol. (Germany)* vol.24 (1989) p.1295 ]
- [17] V.B. Nelmash, M.G. Sosnin, V.I. Shakhovtsov, V.L. Shindich, I.I. Yaskovets [ *Sov. Phys.-Semicond. (USA)* vol.22 (1988) p.127 ]

### *13.5 Bulk lifetimes of photogenerated carriers in doped and treated c-Si*

- [18] V. Grivickas, V. Bikbajevas, J. Seckus, A. Vigelis, L. Frank [ *Phys. Status Solidi A (Germany)* vol.125 (1991) p.133 ]
- [19] J. Raebuger, A. Ramanowski, Q. Zhang, G. Razgonyi [ *Appl. Phys. Lett. (USA)* vol.69 (1996) p.3037 ]
- [20] A. Poggi, E. Susi, M.A. Butturi, M.C. Carotta [ *J. Electrochem. Soc. (USA)* vol.141 (1994) p.754 ]
- [21] S.D. Brotherton, P. Bradley [ *J. Appl. Phys. (USA)* vol.53 (1982) p.5720 ]
- [22] J. Linnros, P. Norlin, A. Hallen [ *IEEE Trans. Electron Devices (USA)* vol.40 (1993) p.2065 ]; A. Hallen, N. Keskitalo, F. Masszi, V. Nagl [ *J. Appl. Phys. (USA)* vol.79 (1996) p.3906 ]
- [23] H. Bleichner, P. Jonsson, N. Keskitalo, E. Nordlander [ *J. Appl. Phys. (USA)* vol.79 (1996) p.9142-8 ]
- [24] M. Willander [ *J. Appl. Phys. (USA)* vol.56 (1984) p.3006 ]
- [25] P.R. Smith, D.H. Auston, A.M. Johnson, W.M. Augustyniak [ *Appl. Phys. Lett. (USA)* vol.38 (1981) p.47 ]
- [26] J. Dzievior, W. Schmid [ *Appl. Phys. Lett. (USA)* vol.31 (1977) p.346 ]
- [27] A. Hangleiter, R. Häcker [ *Phys. Rev. Lett. (USA)* vol.65 (1990) p.215, *J. Appl. Phys. (USA)* vol.75 (1994) p.7570 ]
- [28] A. Hangleiter [ *Phys. Rev. Lett. (USA)* vol.55 (1985) p.2976 ]

## 13.6 Surface recombination velocity in c-Si

V. Grivickas, J.A. Tellefsen and M. Willander

January 1998

### A INTRODUCTION

When recombination events occur at the surface, they are characterised by the surface recombination velocity,  $S$ . In most cases for crystalline Si, surface recombination is explained by the Shockley–Read–Hall (SRH) recombination model via interface trap density  $D_{it}$  which is integrated over the energy of the bandgap states [1,2]. However, an effective surface recombination can be introduced equally well at a virtual surface within the sample positioned at the edge of the space charge or near to a damaged region. Since all Si wafers and most Si devices consist of regions with surfaces available for recombination, both bulk and effective surface recombination (or generation) take place simultaneously, and their separation sometimes is quite difficult [1,3]. In most practical cases, the decay time of the total number of excess carriers can be presented in a simplified form:

$$\tau^{-1}(t) = \tau_b^{-1}(t) + \tau_s^{-1}(t) \quad (1)$$

where  $\tau_s(t)$  is the decay time characterising surface recombination. The mode with the slowest decay is called the fundamental mode. It is the stationary carrier distribution evolving after the matching of diffusion and recombination flows in a volume [2–6]. This implies that the decay time from the fundamental mode is independent of time, so that the decay is exponential in time. This decay time is sometimes called the asymptotic or principal lifetime. In a Si wafer with two equal surface recombination rates on both surfaces, the fundamental lifetime can be expressed by a well-known dual solution for the cases of very strong ( $Sd/D \gg 1$ ) and very weak surface recombination ( $Sd/D \ll 1$ ):

$$\tau_s = \frac{d}{2S} + \frac{1}{D} \left( \frac{d}{\pi} \right)^2 \quad (2)$$

where  $d$  is the wafer thickness and  $D$  is the carrier diffusion coefficient. This is, in fact, a very good approximation, as the uncertainty is less than 4% across the complete range of  $S$  [4]. This approximation is a useful tool that allows rapid evaluation and visualisation of the effect of surface recombination when interpreting lifetime measurements for near bulk excitation. A similar formula holds for the case of very high asymmetry of  $S$  values on two surfaces, as given by Sproul [5]. With carrier excitation near an illuminated face, the main part of the decay takes place from higher modes and only a relatively small part of the decay occurs from the fundamental mode. Some solutions can be found for very high surface recombination velocities, given by Kunst and Sanders [7]. Analytical approximations of the continuity equation, using harmonic optical generation of various frequencies, have also been considered in detail by Otaradian [8].

### B DAMAGED SURFACES

A high value of the effective surface recombination can be obtained on both n- and p-type damaged Si surfaces, as shown in TABLE 1. Usually, for any values above  $S = 10^4$  cm/s recombination rates do not exhibit carrier injection-, temperature- or resistivity-dependence. Some further details can be

### 13.6 Surface recombination velocity in c-Si

found in [9–11]. On chemically polished Si lower averaged  $S_{ef}$  values are usually reported for the (100) surface with respect to the (111) surface.

TABLE 1 Effective surface recombination on typically damaged surfaces of crystalline Si.

Surface	Chemically polished	Chemically polished with native $\text{SiO}_2$	Lapped and polished	Sawn	Heavily implanted, not annealed
$S_{ef}$ (cm/s)	$5 \times 10^3 - 5 \times 10^4$	$(2 - 10) \times 10^3$	$1 \times 10^4 - 5 \times 10^5$	$\geq 5 \times 10^5$	$\geq 5 \times 10^5$

### C PASSIVATED SURFACES

The minimisation of surface recombination losses for both types of chemomechanically polished Si can be obtained by a few surface passivation schemes (see citations in [12]):

- high quality of thermal oxidation at high temperatures ( $\sim 1000^\circ\text{C}$ ), either without or with metal on the top;
- chemical passivation by hydrofluoric acid (HF);
- native  $\text{SiO}_2$  covered during ultraviolet (UV) illumination;
- chemical iodine ethanol-passivation from solution;
- low-temperature plasma chemical vapour deposition of  $\text{SiN}$ ;
- thermal  $\text{SiO}_2$  with field effect by means of a corona chamber discharge.

An outstanding degree of surface recombination reduction can be achieved, as evident from TABLE 2. In all cases with  $\text{SiO}_2$ , it is due to surface defect passivation and due to the surface band bending induced by the fixed charge density in  $\text{SiO}_2$  and acting on one type of carrier as a repulsion force from the surface. The disadvantage, however, is that  $S_{ef}$  becomes a complicated function of the type, the injection level and the resistivity of the material [13]. For passivation in HF acid, for  $\text{SiO}_2$  under UV illumination, and for  $\text{SiO}_2$  with corona chamber discharge, another disadvantage is that passivation is metastable in time, i.e. it proceeds after processing only for a duration ranging from a few seconds to hours [14,15]. If, after passivation, a steady bias light is used in carrier lifetime studies, some experiments show that the chemically passivated surface is not entirely inactive and the decay of excess carriers depends strongly on the injection level [16].

TABLE 2 Minimal reported effective surface recombination on a passivated surface of crystalline Si for mediate injection and high resistivity material.

Passivation scheme	Thermal $\text{SiO}_2$	HF acid	$\text{SiO}_2$ under UV illumination	Iodine ethanol	$\text{SiN}$ deposition	$\text{SiO}_2$ with corona
$S_{ef}$ (cm/s)	0.25 – 200	<50	<50	5 – 50	0.4 – 16	0.5 – 10

Si- $\text{SiO}_2$  interface recombination in the range  $S_{ef} = 50 - 400$  cm/s is reported for either high-quality silicon-on-insulator (SOI) [17,18] or a bonded Si-Si interface fabricated from wafers of (100) orientation [6].

Surface generation velocity in the passivated and depleted region of Si devices was determined to be typically in the range  $S_{gen} = 0.1 - 5$  cm/s [1,19].

## D DOPED SURFACES

The minority carrier surface recombination velocity of highly doped Si has been studied by King and co-workers for both n-type [20] and p-type material [21]. The main finding of these experiments is that  $S_{ef}$  of thermally oxidised Si increases with the doping density of n-type material and is essentially constant for p-type. The very recent results obtained by Cuevas et al [22] on phosphorus diffusions in n-type Si are summarised in TABLE 3. If, in addition, Al is deposited on the top of a thermally  $\text{SiO}_2$  passivated surface and annealed at 400°C in  $\text{N}_2 + \text{H}_2$ , it was shown that the corresponding surface velocities are lower, by a factor of 2 approximately [22].

TABLE 3 Minority-carrier surface recombination velocity of phosphorus diffused n-Si [22].

Surface condition	Thermally $\text{SiO}_2$ passivated	Unpassivated	Metal-coated
$S_{ef}$ (cm/s)	$S_{ef} = 10^{16} N_D$ (for $N_D > 10^{18} \text{ cm}^{-3}$ )	$2 \times 10^5$	$3 \times 10^6$

## E CONCLUSION

Surface recombination velocity can normally be explained by Shockley-Read-Hall recombination in silicon via an interface trap density. However, both bulk and surface recombination occur simultaneously and the decay time of excess carriers is a combination of both. A simple expression is given to relate surface recombination velocity to lifetime, wafer thickness and diffusion coefficient. High values of surface recombination velocity are obtained on damaged surfaces. Low values of surface recombination velocity are obtained on passivation using  $\text{SiO}_2$ . n-Type doping increases the surface recombination velocity but p-type doping does not.

## REFERENCES

- [1] D.K. Schroder [ *Semiconductor Material and Device Characterization* (J. Wiley and Sons, New York, USA, 1990) and in *Handbook of Semiconductor Silicon Technology* Eds. W. O'Mara et al (Noyes, Park Ridge, NJ, USA, 1990) ]
- [2] A.G. Aberle, S. Glunz, W. Warta [ *J. Appl. Phys. (USA)* vol.71 (1992) p.4422 ]
- [3] K.L. Luke, L.J. Cheng [ *J. Appl. Phys. (USA)* vol.61 (1987) p.2282 ]
- [4] V. Grivickas, D. Noreika, J.A. Tellefsen [ *Sov. Phys.-Collect. (USA)* vol.29 (1989) p.591 ]
- [5] A.B. Sproul [ *J. Appl. Phys. (USA)* vol.76 (1994) p.2851 ]
- [6] V. Grivickas, G. Thungström, V. Bikabajevas, J. Linnros, D. Noreika [ *Jpn. J. Appl. Phys. (Japan)* vol.34 (1995) p.L806 ]
- [7] M. Kunst, A. Sanders [ *Semicond. Sci. Technol. (UK)* vol.7 (1992) p.51 ]
- [8] T. Otaradian [ *Solid-State Electron. (UK)* vol.36 (1993) p.153 and p.163 ]
- [9] J. Waldmeyer [ *J. Appl. Phys. (USA)* vol.63 (1988) p.1977 ]
- [10] K. Graff, H. Fisher [ *Top. Appl. Phys. (Germany)* vol.31 (1979) p.173 ]
- [11] V. Grivickas, M. Willander, J.A. Tellefsen [ *J. Appl. Phys. (USA)* vol.55 (1984) p.3169 ]
- [12] J. Schmidt, A.G. Aberle [ *J. Appl. Phys. (USA)* vol.81 (1997) p.6186 ]
- [13] S.W. Glunz, A.B. Sproul, W. Warta, W. Wetling [ *J. Appl. Phys. (USA)* vol.75 (1994) p.1611 ]
- [14] M. Schüfthaler, R. Brendel, G. Langguth, J.H. Werner [ *Proc. 1st World Conf. on Photovoltaic Energy Conversion* Walkoloa, Hawaii, Dec. 1994 ]
- [15] M. Hirose, T. Yasaka, M. Takakura, S. Miyazaki [ *Solid State Technol. (USA)* vol.34 (1991) p.43 ]
- [16] T. Maekawa, Y. Shima [ *Jpn. J. Appl. Phys. (Japan)* vol.35 (1996) p.L133 ]

### *13.6 Surface recombination velocity in c-Si*

- [17] M. Ichimura, T. Makino, H. Asakura, A. Usami, E. Morita, E. Arai [ *Jpn. J. Appl. Phys. (Japan)* vol.36 (1997) p.L839 ]
- [18] Y.-S. Chang, S.S. Li, P.-C. Yang [ *Solid-State Electron. (UK)* vol.38 (1995) p.1359 ]
- [19] E. Simenon, J. Vanhellemont, C. Claeys, A. Kaniava, E. Gaubas [ *Semicond. Sci. Technol. (UK)* vol.11 (1996) p.1434 ]
- [20] R.R. King, R.A. Sinton, R.M. Swanson [ *IEEE Trans. Electron Devices (USA)* vol.37 (1990) p.365 ]
- [21] R.R. King, R.M. Swanson [ *IEEE Trans. Electron Devices (USA)* vol.38 (1991) p.1399 ]
- [22] A. Cuevas, P.A. Basore, G. Giroult-Matlakowski, C. Dubois [ *J. Appl. Phys. (USA)* vol.80 (1996) p.3370 ]

## 13.7 Mobility and diffusion of photogenerated carriers in intrinsic c-Si

V. Grivickas and M. Willander

January 1998

### A INTRODUCTION

The mobility of a particular type of carrier is usually introduced by a proportionality coefficient between the carrier drift velocity  $v_d$  and the electric field E and can be expressed as

$$\mu = |E| / |v_d| \equiv q\langle\tau\rangle / m \quad (1)$$

where q is the elementary charge, m is the effective mass of the carrier and  $\langle\tau\rangle$  is the average relaxation time in the carrier distribution function for the drift momentum loss. The mobility obtained by the Hall effect,  $\mu_H$ , is related to the drift mobility through the Hall factor  $r_H = \mu_H/\mu$  [1,2]. The corresponding carrier diffusivity is introduced by the proportionality between the diffusion current and the gradient of the carrier concentration:

$$J_{\text{dif}} = -qD \frac{d\Delta n}{dx} \quad (2)$$

Here, a minus sign means that the carrier moves out from the region of excess carrier concentration. In the general situation, for arbitrary injection conditions, the ambipolar diffusivity must be calculated from

$$D = (n + p) / \left[ \frac{n}{D_h} + \frac{p}{D_e} \right] \quad (3)$$

Physically, the ambipolar diffusivity arises from the fact that, due to the fast moving electrons, an electric field will develop with respect to the more slowly moving holes. This will tie electrons and holes together in a coupled diffusive motion.

Both physical quantities  $\mu$  and D can be theoretically calculated by solving the kinetic Boltzmann equation in the relaxation-time approximation [2] or, more generally, by hydrodynamic transport schemes applying Kohler's variational method [3,4].

### B LATTICE SCATTERING

The main scattering mechanism in intrinsic Si at low injection involves lattice vibrations, e.g. interband or intraband acoustic or optical phonon scattering [4]. Scattering by residual partially ionised or neutral impurities becomes important only in the low-temperature range  $T \leq 80$  K [2]. In TABLE 1, the mobility and diffusivity values are provided as typically reported at room temperature from measurements on FZ and CZ as-grown intrinsic Si (see [4-6] and references therein). The ambipolar diffusion coefficient was measured at moderately HL injection ( $n = p = 10^{15} \text{ cm}^{-3}$ ). Lattice

scattering determined carrier mobility and diffusion values agree according to the Einstein relation: see Datareview 13.1.

TABLE 1 The lattice scattering determined mobility and diffusivity values in high-resistivity intrinsic Si at  $T \approx 295$  K.

	$\mu_e$ ( $\text{cm}^2/\text{V s}$ )	$D_e$ ( $\text{cm}^2/\text{s}$ )	$\mu_h$ ( $\text{cm}^2/\text{V s}$ )	$D_h$ ( $\text{cm}^2/\text{s}$ )	$D_{\text{amb}}$ ( $\text{cm}^2/\text{s}$ )
FZ-Si	1350 – 1500	33 – 39	450 – 500	11 – 13.4	16.5 – 19.8
CZ-Si	1250 – 1400	32 – 36	420 – 480	11 – 12.8	15.5 – 17

The electron and the hole mobilities were measured in a very low doped base p-i-n diode ( $n^- = 4.5 \times 10^{11} \text{ cm}^{-3}$ ) at the HL injection of  $5 \times 10^{13} \text{ cm}^{-3}$  between 78 and 340 K by Misiakos and Tsamakis [7]. In the temperature range from 170 to 340 K the carrier mobilities vary as  $T^{-a}$ , where  $a = 2.34 \pm 0.08$  for electrons while for holes  $a = 2.85 \pm 0.05$ . Around 77.8 K the hole mobility is  $140\,000 \text{ cm}^2/\text{V s}$  while the electron mobility is  $24\,000 \text{ cm}^2/\text{V s}$ , and the temperature power coefficients are  $a \approx 2$  for both types of carrier.

## C INJECTION DEPENDENCE OF MOBILITY

When the excited carrier density is higher than a critical concentration,  $\Delta n_{\text{cr}}$ , a decrease of  $\mu_e + \mu_h$  is observed due to electron hole (e-h) scattering [8,9]. This dependence strongly affects the high current operation of bipolar power devices, such as p-i-n diodes and thyristors [10]. The decrease in mobility is more pronounced at low temperatures. As was shown by Grivickas et al [9] the empirical temperature dependence for  $\Delta n_{\text{cr}}$  is given by

$$\Delta n_{\text{cr}} = 10^{16} (\text{cm}^{-3}) \times (T/300 \text{ K})^{1.4} 1800/(\mu_e + \mu_h) \quad (4)$$

with T in the range 100 – 400 K and with mobilities in ( $\text{cm}^2/\text{V s}$ ). In the injection level interval of  $(10^{17} – 10^{19}) \text{ cm}^{-3}$ , the effects of carrier interactions are poorly modelled by the standard simulation algorithm which is using the expression either of Dorkel and Leturcq (D-L) or of Klaassen (K) [11,12]. Recently, attempts have been made to resolve this conflict including the effect of the randomisation of energy between carriers of the same type and accounting for the excitonic effects [13,14]. In this context, excitons being neutral particles cannot contribute to drift currents. As was shown in [15], therefore, up to the injection level of  $10^{18} \text{ cm}^{-3}$  the total mobility reduction can be empirically reproduced for 295 K by the modified D-L expression.

An increase of  $\mu_e + \mu_h$  in the degenerated region ( $\Delta n \geq 10^{19} \text{ cm}^{-3}$ ) has been reported by Auston et al [16]. This increase occurs due to an increase in the kinetic energy of the carriers. It can be modelled in the frame of Fermi-Dirac integrals [17].

## D INJECTION DEPENDENCE OF DIFFUSIVITY

In a diffusive flow, electrons and holes move in the same direction, so the net momentum of flow is not changed by e-h scattering. From thermodynamics arguments, an essentially constant diffusion mobility has been predicted for ambipolar injection (see [18,19] and references therein). At room temperature, the experimentally determined ambipolar diffusion coefficient, however, gradually reduces from  $16 \text{ cm}^2/\text{s}$  at LL injection ( $10^{15} \text{ cm}^{-3}$ ) down to  $D_{\text{amb}} \approx 8 \text{ cm}^2/\text{s}$  and approximately saturates above the exciton-Mott transition,  $\Delta n = (5–7) \times 10^{17} \text{ cm}^{-3}$  [5,6,13]. The main mechanism for this diffusion reduction is the dynamic narrowing of the bandgap [20]. Such bandgap narrowing will oppose the diffusive carrier flow and, thus, will lower the diffusivity. The quantum mechanical

diffusion calculations of this dependence can only reproduce about 50% of the experimental reduction in  $D_{amb}$ . On the other hand, e-e and h-h type energy randomisation may serve to reduce the lattice mobility, which is related to the ambipolar motion by the same amount as for the drift mobility. The simultaneous diffusion of excitons and excitonic scattering may be an important factor in explaining the experimentally observed total diffusion coefficient reduction at higher injected carrier densities [13,14].

Noreika et al [21] have measured at 300 K an increasing density dependence of ambipolar diffusivity beginning at  $10^{19} \text{ cm}^{-3}$  and reaching  $D_{amb} = 35 \text{ cm}^2/\text{s}$  at  $4 \times 10^{19} \text{ cm}^{-3}$ .

The influence of the electric field on the ambipolar diffusion coefficient has been experimentally investigated by Vaitkus et al [22]. They measured a decrease of  $D_{amb}$  when E is parallel to the diffusion and an increase of  $D_{amb}$  when E is transverse to the diffusion for  $E \leq 2 \text{ kV/cm}$  and an injection of about  $10^{17} \text{ cm}^{-3}$  at room temperature.

## **E EXCITON DIFFUSION**

Exciton diffusion has been measured in intrinsic Si below 20 K by two independent methods by Laurich et al [23] and by Tamor and Wolfe [24]. Both obtained the result

$$D_{ex} = 300 T^{-1/2} (\text{cm}^2/\text{s}) \quad (5)$$

The approximate value at room temperature  $D_{ex} \approx 2 (\text{cm}^2/\text{s})$ , was extracted in [13].

## **F CONCLUSION**

The basic equations for carrier mobility have been outlined. Lattice vibrations are the main scattering mechanism at low injection rates, although ionised/neutral impurity scattering becomes important at low temperatures. Typical mobilities and diffusivities for both holes and electrons are presented. Mobilities decrease at higher carrier densities, particularly at low temperatures, due to electron-hole scattering. The ambipolar diffusion coefficient decreases as the injection level increases, due to bandgap narrowing.

## **REFERENCES**

- [1] S.M. Ryvkin [ *Photoelectric Effects in Semiconductors* (Cons. Bureau, New York, USA, 1964) ]
- [2] K. Seeger [ *Semiconductor Physics* 6th Edn. *Springer Ser. Solid-State Sci. (Germany)* vol.40 (Springer, Berlin, 1997) ]
- [3] E. Velmre, A. Udal, T. Kocsis, F. Masszi [ *Phys. Scr. (Sweden)* vol.T54 (1994) p.263 ]
- [4] A. Schenk [ *J. Appl. Phys. (USA)* vol.79 (1996) p.814 ]
- [5] J. Linnros, V. Grivickas [ *Phys. Rev. B (USA)* vol.50 (1994) p.16943 ]
- [6] M. Rosling, H. Bleichner, P. Jonsson, E. Nordlander [ *J. Appl. Phys. (USA)* vol.76 (1994) p.2855 ]
- [7] K. Misiakos, D. Tsamakis [ *Appl. Phys. Lett. (USA)* vol.64 (1994) p.2007 ]
- [8] J. Krausse [ *Solid-State Electron. (UK)* vol.15 (1972) p.1377 ]; L. Dannähauser [ *Solid-State Electron. (UK)* vol.15 (1972) p.1371 ]
- [9] V. Grivickas, M. Willander, J. Vaitkus [ *Solid-State Electron. (UK)* vol.27 (1984) p.565 ]
- [10] B.J. Baliga [ *Modern Power Devices* (J. Wiley and Sons, New York, USA, 1987) ]
- [11] J.M. Dorkel, P. Leturcq [ *Solid-State Electron. (UK)* vol.24 (1981) p.821 ]

- [12] D.B.M. Klaassen [ *Solid-State Electron.* (UK) vol.35 (1992) p.953 and p.961 ]
- [13] V. Grivickas, J. Linnros, A. Galeckas, V. Bikbajevas [ *Proc. 23rd Int. Conf. on The Physics of Semiconductors* (World Scientific, Singapore, 1996) vol.1 p.91 ]
- [14] E. Velmre, A. Udal [ *Proc. 27th Euro. Solid-State Device Research Conf.* Stuttgart, Germany, 22-24 Sept. 1997 (Editions Frontieres, Paris, France, 1997) p.212-5 ]
- [15] S.K. Pang, A. Rohatgi [ *J. Appl. Phys.* (USA) vol.74 (1993) p.5554 ]
- [16] D.H. Auston, A.M. Johnson, P.R. Smith, J.C. Bean [ *Appl. Phys. Lett.* (USA) vol.37 (1980) p.371 ]
- [17] R.A. Smith [ *Semiconductors* (Cambridge Univ. Press, London, 1978) ]
- [18] D.E. Kane, R.M. Swanson [ *J. Appl. Phys.* (USA) vol.72 (1992) p.5294 ]
- [19] T.T. Mnatsakanov [ *IEEE Trans. Electron Devices* (USA) vol.42 (1995) p.2251 ]
- [20] J.F. Young, H.M. van Driel [ *Phys. Rev. B* (USA) vol.26 (1982) p.2147 ]
- [21] D. Noreika, V. Netiksis, M. Petrauskas, M. Lentzner [ *Solid State Phenom.* (Switzerland) vol.19&20 (1991) p.517 ]
- [22] J. Vaitkus, K. Jarasiunas, E. Gaugas, L. Jonikas, R. Pranaitis, L. Subacius [ *IEEE J. Quantum Electron.* (USA) vol.22 (1986) p.1298 ]
- [23] B. Laurich, H. Hillmer, A. Forchel [ *J. Appl. Phys.* (USA) vol.61 (1987) p.1480 ]
- [24] M.A. Tamor, P. Wolfe [ *Phys. Rev. Lett.* (USA) vol.44 (1980) p.1703 ]

## 13.8 Mobility and diffusion of photogenerated carriers in doped and treated c-Si

V. Grivickas and M. Willander

January 1998

### A INTRODUCTION

The most convenient method to describe the carrier transport in arbitrary situations (with respect to doping, injection, carrier gradient and various boundary conditions) is based on the generalised linear transport equations, for which the usual drift-diffusion approximations for the current densities are valid:

$$\vec{J}_e = en\mu_e \vec{E}_n + eD_e \frac{dn}{dx}, \quad \vec{J}_h = ep\mu_h \vec{E}_p - eD_h \frac{dp}{dx} \quad (1)$$

The first terms in EQN (1) represent carrier drift, and the second terms represent carrier diffusion flow. E is the actual electric field strength acting on the carriers. These expressions are the starting point of conventional device analysis, for example in p-i-n diodes. The effect of bandgap narrowing should also be included in the acting electric field [1]. Note that the ordinary procedure of using the Einstein relation between mobility and diffusivity cannot be applied to simplify these equations further, as it would lead to serious loss of generality for the electron–hole (e–h) scattering effects acting quite differently at LL-injection (drag situation) or in the situation when the current in a specific device volume is maintained equal to zero by an external electric field [2].

The general way of inserting the momentum exchange between electrons and holes due to e–h scattering is to write the transport equations using Kohler's variational method with a coupling between the electron and hole transport currents [2–4]. Taking for simplicity only the drift terms, for the isothermal case we may write:

$$\begin{aligned} \vec{J}_e &= -qn\mu_e \vec{\nabla} \Phi_n + qp\mu_{eh} \vec{\nabla} \Phi_p \\ \vec{J}_h &= qn\mu_{he} \vec{\nabla} \Phi_n - qp\mu_h \vec{\nabla} \Phi_p \end{aligned} \quad (2)$$

where  $\Phi_n$  and  $\Phi_p$  are the electron and hole quasi-Fermi levels. These equations are correct from considerations of irreversible thermodynamics. Then, the mobilities can be obtained in the following form [2]:

$$\mu_e = \mu_e^0 \left( \frac{1 + \frac{\mu_h^0}{\mu_{he}}}{1 + \frac{\mu_e^0}{\mu_{eh}} + \frac{\mu_h^0}{\mu_{he}}} \right)$$

$$\mu_h = \mu_h^0 \left( \frac{1 + \frac{\mu_e^0}{\mu_{eh}}}{1 + \frac{\mu_e^0}{\mu_{eh}} + \frac{\mu_h^0}{\mu_{he}}} \right) \quad (3)$$

$$\mu_{eh} = \mu_e^0 \left( \frac{1 + \frac{\mu_h^0}{\mu_{eh}}}{1 + \frac{\mu_e^0}{\mu_{eh}} + \frac{\mu_h^0}{\mu_{he}}} \right) = \mu_{he}$$

where  $\mu_{e,h}^0$  are mobilities calculated under the assumption of no e-h scattering and  $\mu_{eh}$  and  $\mu_{he}$  are e-h scattering mobilities. General equations with two diffusion terms are given by Mnatsakanov et al [3]. The Einstein relation (see EQN (5) in Datareview 13.1) between mobility and diffusivity of minority-carriers can be restored only in a matrix form. Minority-carrier mobilities cannot be assumed to be identical to majority-carrier mobilities in the material of the opposite type. In this connection, it is worth mentioning that various papers continue publishing data for minority carriers in Si with rather different inconsistencies between measured values, which are pointed out in these papers. For the background to the problem see [2–5] and references cited therein.

## B MAJORITY CARRIER MOBILITY IN DOPED Si

If the doping density is larger than  $N = 10^{15} \text{ cm}^{-3}$  then, at 300 K, the majority carrier mobility will begin to be dependent on N. This dependence is mainly caused by ionised impurity scattering. Due to the dependence of the scattering cross-section on the particle velocity, ionised impurity scattering tends to become dominant at low temperature where the electron energies are small and, moreover, lattice scattering freezes out (Datareview 13.7). Li and Thurber [6] have pointed out that the carrier energy randomisation due to e-e or h-h scattering must be considered in numerical simulations both for the lattice and the ionised impurity mobility, at doping densities exceeding  $N = 10^{17} \text{ cm}^{-3}$ . High-energy carriers which are not much scattered by ionised impurities, lose energy to low-energy carriers that have been scattered by these impurities, resulting in an overall decrease in the mobility.

At high doping densities,  $N \geq 3 \times 10^{18} \text{ cm}^{-3}$ , the shallow levels in the forbidden gap begin to merge with the free band edge and the doping atoms are always ionised. The screening radius decreases considerably. Mobility is influenced by a variety of additional effects, reviewed in [7], in the first instance by dispersive screening, but also by the real density-of-states in the band and multipotential scattering. In addition, Fischetti [8] showed the importance of the electron-plasmon interaction at these doping densities. Fischetti considered only plasmons that survive Landau damping long enough to decay mainly by momentum dissipation and randomisation, which affects the majority carrier mobility directly. For device simulation purposes a practical solution has to be found, because inclusion of additional effects leads to an increase in computation time, which would become unacceptable [7,9].

A theoretical model describing carrier scattering by divalent impurities in indirect semiconductors has been presented recently by Itoh et al [10]. Sasaki et al [11] reported on the Hall factor  $r_H$  doping dependencies in heavily doped Si. In general, this factor lies above unity in n-type Si and below unity in p-type Si.

## C MINORITY CARRIER TRANSPORT IN DOPED Si, DRAG EFFECT

Under low injection conditions minority carrier transport is an important parameter in many devices, such as n-p-n and heterojunction bipolar transistors. Frequent e-h collisions between minority and majority carriers would lead to a significant net momentum transfer to the minority carriers opposing their drift and resulting in a lowering of their mobility. This so called ‘drag’ effect, where minority carriers are swept along by the flow of counter-moving majority carriers, was first demonstrated by Morohashi et al [12] at low temperatures for minority electrons in p-Si of doping  $6 \times 10^{15} \text{ cm}^{-3}$  in an electric field up to 700 V/cm. At room temperature, this effect has been experimentally determined only in a few cases, i.e. by Tang et al [13] in p-Si with doping of  $4.5 \times 10^{16} \text{ cm}^{-3}$  and by Linnros and Grivickas [14] in p-Si with doping of  $3 \times 10^{17} \text{ cm}^{-3}$  and in n-Si with doping  $1.2 \times 10^{17} \text{ cm}^{-3}$ . The last measurements have been obtained by an absorptive transient grating technique which allows separate measurement of both mobility and diffusivity of minority carriers.

Theoretically, the strength of the drag effect is determined by two factors, namely, the number of scattering centres (majority carrier concentration) and the ratio of the effective masses [3,15]. The degree of the reduction depends on whether the majority carriers are nearly static, as in diffusion situations, or whether they are drifting opposite to minority carriers. Mnatsakanov et al [3] developed simplified relationships between minority-carrier diffusivity and mobility depending on the doping density. Based on these relationships they provided analysis of different experimental data for the doping range  $10^{17} - 5 \times 10^{18} \text{ cm}^{-3}$  obtained in recent years for silicon, such as the measurement of diffusion length. After necessary correction, it was shown that the mobility of minority-carriers is lower by a factor of approximately 1.5 for electrons and by a factor of 2 for holes with respect to the mobility obtained via the Einstein relation. This was a widespread error in the interpretation of experimental results on minority-carrier transport in several publications (see [3]). As a consequence of this error, it was frequently concluded that the minority-carrier mobility is greater than the majority-carrier values due to less effective scattering by ionised dopants, because the scattering is repulsive for minority-carriers but attractive for majority-carriers [16]. While, in principle, this statement cannot be rejected, in particular at very high doping, the effect has to be re-examined more accurately.

Recently, Deway and Osman [17] performed a Monte Carlo simulation of the minority electron transport in Si. They showed a sharp reduction in mobility with an increase of the electric field from zero value. At high electric field strengths, a smaller scattering cross-section results in saturation of the drag effect. These data agree with time-of-flight measurements performed by Tang et al [13]. However, at low electric field, the theoretical simulation by Deway and Osman must be stated to lead to disagreement with experimental results on mobility and diffusivity obtained in [14]. Clearly, more efforts are needed to resolve these questions.

## D AMBIPOLAR DIFFUSION IN DOPED Si

Grivickas et al [18] have measured the ambipolar diffusion coefficient in medium-heavily doped Si:Al, Si:In and Si:Sb MBE layers under constant pumping conditions to the density  $4 \times 10^{19} \text{ cm}^{-3}$  at 300 K.  $D_a$  was found to be almost constant at a value of  $8 \text{ cm}^2/\text{s}$  in the equilibrium carrier density range of  $10^{16} - 2 \times 10^{19} \text{ cm}^{-3}$  and was independent of the doping type. At higher density, evidence for a sharp increase in  $D_a$  was also observed. Relative insensitivity of  $D_a$  to the doping is explained by HL injection, the ‘tight screening’ regime which assures the screening of particular impurity ions.

Ambipolar diffusion of the order  $10^{-2} \text{ cm}^2/\text{s}$  was measured in microcrystalline Si by Komuro et al [19].

## E CARRIER TRANSPORT IN MODIFIED Si

Finally, carrier transport is influenced by various growth techniques and treatments used in Si technology.

Ono and Sumino [20] have shown that in plastically deformed Si at 750°C, with introduced dislocation densities ranging between  $10^4$  and  $10^8 \text{ cm}^{-3}$ , majority carrier mobility is considerably lower than that of as-grown material. This behaviour is observed to be more pronounced for electron mobility because it is thought that the introduced scattering complexes are more charged in n-type material.

Grivickas et al [21] have shown that  $\mu_e + \mu_h$  is reduced down to about  $150 \text{ cm}^2/\text{V s}$  close to the interface on silicon-on-sapphire (SOS) films, which was associated with carrier scattering by grown-in defects [22]. Furthermore, as demonstrated by Smith et al [23], drift mobilities in SOS can be reduced down to  $10 \text{ cm}^2/\text{V s}$  with the radiation damage caused by ion-implantation (with O doses varying from  $10^{11}$  to  $3 \times 10^{15} \text{ ions cm}^{-2}$ ), therefore still being at least an order of magnitude higher than those of the amorphous material. Improving the crystalline quality of silicon layers by a few annealing procedures usually increases carrier mobility to the level determined by the doping: see Sze [24].

Large enhancements in the electron mobility are reported for structures containing a pair of closely spaced  $\delta$ -doped layers in Si. As shown by Radamson et al [25] for the case of Si:Sb, the room temperature mobility can be enhanced by a factor of 2 compared to corresponding uniformly doped layers. Even higher mobilities ( $1200 \text{ cm}^2/\text{V s}$ ) were obtained by using a Schottky gate on top and applying a voltage to adjust the potential well. The high mobility is attributed to wave functions with nodes at the  $\delta$ -doped layers.

A highly efficient lateral transport has been observed by Leung et al [26] in annealed stable defect layers (SDL) produced by proton implantation in p-type Si. Photogenerated minority electrons have been collected at a Schottky junction several millimetres away from the generation site, i.e. at a distance more than 30 times the diffusion length in comparable bulk material. A model is proposed in which bending of the energy bands near the SDL expels majority holes leaving no recombination mechanism for minority carriers trapped in the layer.

## F CONCLUSION

Generalised linear transport equations are used to describe the mobilities and diffusion coefficients in arbitrary situations, and it is noted that minority carrier and majority carrier mobilities are not necessarily identical in material of opposite type. As doping density increases above  $\sim 10^{15} \text{ cm}^{-3}$ , at 300 K, the majority carrier mobility becomes dependent on the density. At high densities ( $> 3 \times 10^{18} \text{ cm}^{-3}$ ) other scattering mechanisms play a part. Under low injection conditions, electron hole collisions reduce minority carrier mobility, the so-called ‘drag’ effect. Introducing dislocations into silicon dramatically reduces majority carrier mobility, particularly for electrons. Mobilities can be increased using  $\delta$ -doping.

## REFERENCES

- [1] D.B. Klaassen, J.W. Slotboom, H.C. de Graaff [ *Solid-State Electron. (UK)* vol.35 (1992) p.125 ]

13.8 Mobility and diffusion of photogenerated carriers in doped and treated c-Si

- [2] D.E. Kane, R.M. Swanson [ *IEEE Trans. Electron Devices (USA)* vol.40 (1993) p.1496 ]
- [3] T.T. Mnatsakanov, B.N. Gresserov, L.I. Pomortseva [ *Solid-State Electron. (UK)* vol.28 (1995) p.225 ]
- [4] E. Velmre, A. Udal, T. Kocsis, F. Masszi [ *Phys. Scr. (Sweden)* vol.T54 (1994) p.263 ]
- [5] T.T. Mnatsakanov [ *IEEE Trans. Electron Devices (USA)* vol.42 (1995) p.2251 ]
- [6] S.S. Li, W.R. Thurber [ *Solid-State Electron. (UK)* vol.20 (1977) p.609 ]; S.S. Li [ *Solid-State Electron. (UK)* vol.21 (1978) p.1109 ]
- [7] A. Schenk [ *J. Appl. Phys. (USA)* vol.79 (1996) p.814 ]
- [8] M.V. Fischetti [ *Phys. Rev. B (USA)* vol.44 (1991) p.5527 ]
- [9] D.B.M. Klaassen [ *Solid-State Electron. (UK)* vol.35 (1992) p.953 and p.961 ]
- [10] K.M. Itoh et al [ *Phys. Rev. B (USA)* vol.56 (1997) p.1906 ]
- [11] Y. Sasaki, K. Itoh, E. Inoue, S. Kishi, T. Mitsuishi [ *Solid-State Electron. (UK)* vol.31 (1988) p.5 ]
- [12] M. Morohashi, N. Sawaki, I. Akasaki [ *Jpn. J. Appl. Phys. (Japan)* vol.24 (1985) p.732 ]
- [13] D.D. Tang, F.F. Fang, M. Scheuerman, T.C. Chen [ *Appl. Phys. Lett. (USA)* vol.49 (1986) p.1540 ]
- [14] J. Linnros, V. Grivickas [ *Proc. 22nd Conf. on The Physics of Semiconductors* (World Scientific, Singapore, 1995) vol.1 p.53 ]
- [15] I.M. Dykman, P.M. Tomchuk [ *Sov. Phys.-Solid State (USA)* vol.6 (1964) p.1085 ]
- [16] A.B. Sproul, M.A. Green [ *J. Appl. Phys. (USA)* vol.73 (1993) p.1214 ]
- [17] J. Deway, M.A. Osman [ *Appl. Phys. Lett. (USA)* vol.62 (1993) p.187 ]
- [18] V. Grivickas et al [ *J. Appl. Phys. (USA)* vol.48 (1990) p.617 ]
- [19] A. Komuro, Y. Aoyagi, Y. Segawa, S. Namba, A. Masuyama [ *J. Appl. Phys. (USA)* vol.56 (1984) p.1658 ]
- [20] H. Ono, K. Sumino [ *J. Appl. Phys. (USA)* vol.54 (1983) p.4426, *Jpn. J. Appl. Phys. (Japan)* vol.19 (1980) p.L629 ]
- [21] V. Grivickas, M. Willander, J.A. Tellefsen [ *J. Appl. Phys. (USA)* vol.55 (1984) p.3169 ]
- [22] S. Cristoloveanu [ *Rep. Prog. Phys. (UK)* vol.50 (1987) p.327 ]
- [23] P.R. Smith, D.H. Auston, A.M. Johnson, W.M. Augustyniak [ *Appl. Phys. Lett. (USA)* vol.38 (1981) p.47 ]
- [24] S.M. Sze [ *Semiconductor Devices* (Wiley, New York, 1985) ]
- [25] H.H. Radamson et al [ *Appl. Phys. Lett. (USA)* vol.64 (1994) p.1842 ]
- [26] D.C. Leung, P.R. Nelson, O.M. Stafsudd, J.B. Parkinson, G.E. Davis [ *Appl. Phys. Lett. (USA)* vol.67 (1995) p.88 ]

## CHAPTER 14

### IMPLANTATION/IRRADIATION OF SILICON *(Edited by R. Elliman)*

- 14.1 Ion implantation range theory
- 14.2 Ion implantation into c-Si: basic mechanisms and modelling
- 14.3 Electrical properties of ion implanted and electron irradiated c-Si
- 14.4 Structure of ion implantation induced defects in c-Si
- 14.5 Energy levels, structure and properties of point defects induced by ion implantation and electron irradiation of c-Si
- 14.6 Dopant ionization energies in c-Si

## 14.1 Ion implantation range theory

R.E. Brindos, P.H. Keys and K.S. Jones

November 1998

### A INTRODUCTION

The success of ion implantation depends on the ability to predict where the implanted ions will be located after implantation. During device design, simulations that produce the proper implant profiles for a specified dose and energy save both time and money. Theoretical models based on energy interaction mechanisms between the implanted ions and the target material are used to make accurate predictions of implanted profiles. FIGURE 1 is an outline of the models developed for predicting implantation profiles and the conditions under which these predictions are valid [1].

### B THEORY

As energetic ions penetrate a solid target material, they lose energy due to collisions with atomic nuclei and electrons in the target material and the ions eventually come to rest. The ions are stopped in a solid by two processes: nuclear and electronic stopping. The dominant stopping mechanism depends on the atomic weight and input energy of the implanted species. At lower energies ions are stopped by nuclear stopping (elastic), while at higher energies the ions are stopped by electronic stopping (inelastic) [2,3]. FIGURE 2 shows an illustration of energy loss versus implant energy for an implanted ion [4]. The stopping power of the target is the loss of energy per unit distance,  $-dE/ds$ , which is defined as

$$-\frac{dE}{ds} = N[S_e(E) + S_N(E)] \quad (1)$$

where  $E$  is the ion energy,  $s$  is the co-ordinate along the path whose direction changes as a result of binary nuclear collisions,  $N$  is the density of atoms in the target material,  $S_e$  is the electronic stopping power and  $S_N$  is the nuclear stopping power. The total distance that an ion travels in a solid is known as the range, and is defined as

$$R = \int ds = \frac{1}{N} \int_0^E \frac{dE}{S_e(E) + S_N(E)} \quad (2)$$

EQN (1) was reformulated by Lindhard, Scharff and Schoitt (LSS theory) for implantation into amorphous material in terms of the reduced parameters,  $\varepsilon$  and  $\rho$ , as

$$\rho = \frac{RN M_1 M_2 4\pi a^2}{M_1 + M_2} \quad (3)$$

and

$$\varepsilon = \frac{E_0 M_2 a}{Z_1 Z_2 q^2 (M_1 + M_2)} \quad (4)$$

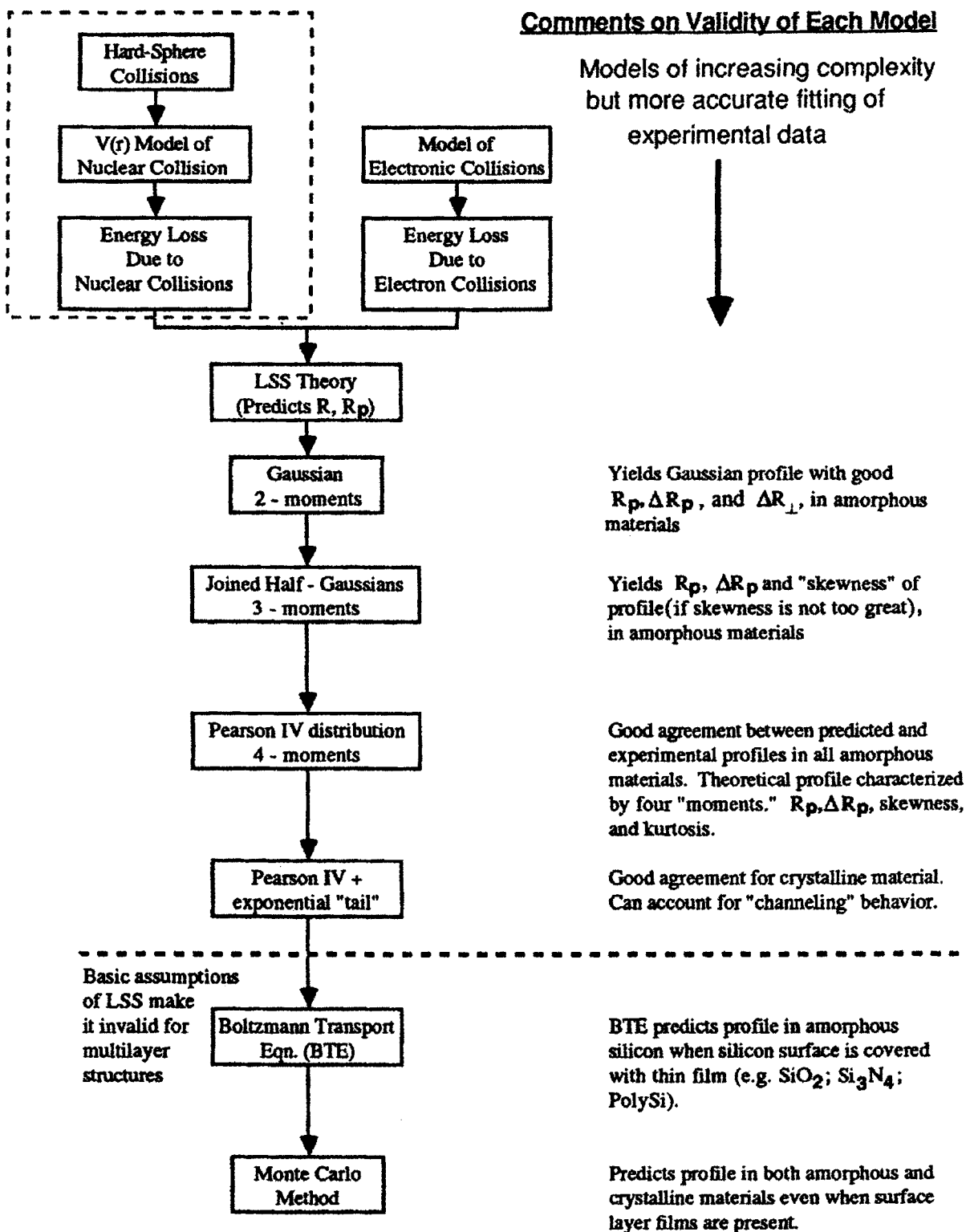


FIGURE 1 Mathematical models for simulation of ion implantation concentration profiles (from [1]).

#### 14.1 Ion implantation range theory

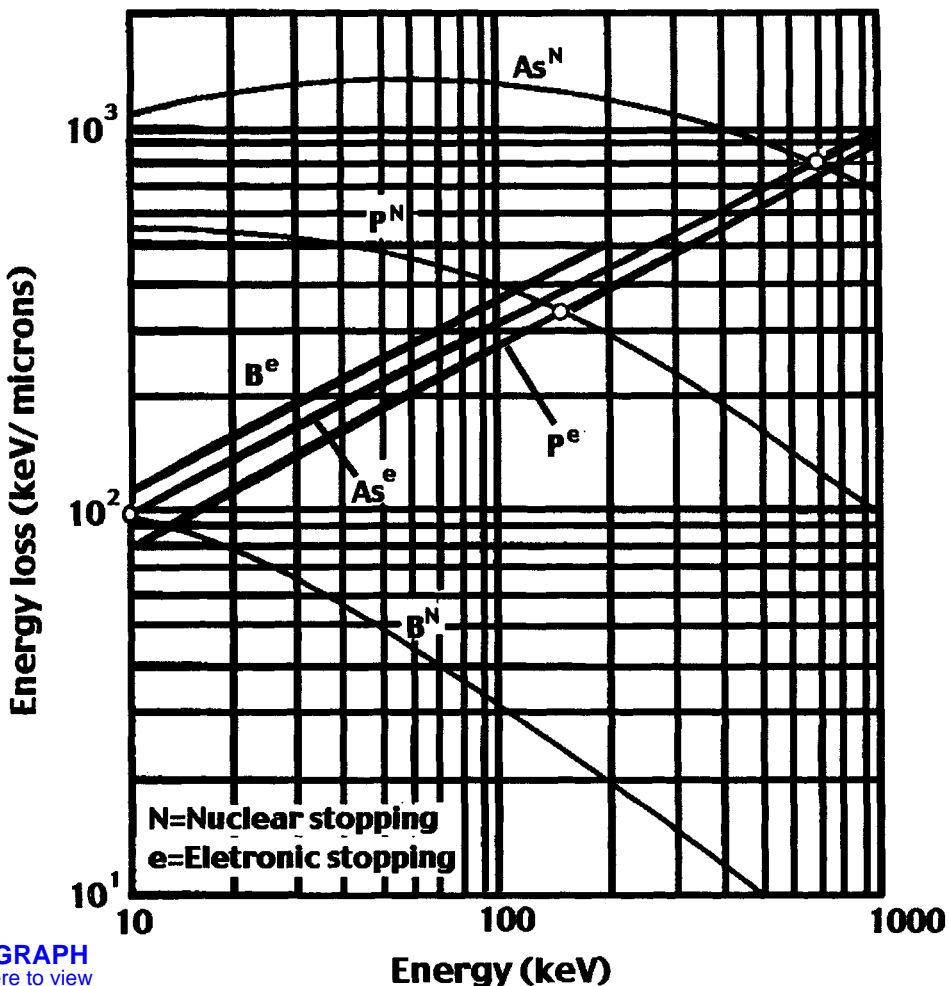


FIGURE 2 Energy loss versus implant energy for As, B, and P (from [1]).

where  $M_1$  and  $Z_1$  are the mass and atomic number of the incident ion, respectively,  $M_2$  and  $Z_2$  are the mass and atomic number of the target atoms, respectively,  $N$  is the number of atoms per unit volume and  $a$  is the screening length, equal to

$$a = \frac{0.88a_0}{(Z_1^{1/3} + Z_2^{2/3})^{1/2}} \quad (5)$$

where  $a_0$  is the Bohr radius. (Calculations for  $\epsilon$  and  $\rho$  can be found in the paper by Lindhard et al [5].) Using EQN (3) the value of  $\rho$  can be converted to the range,  $R$ , and then the projected range,  $R_p$ , which is the average depth below the surface an ion penetrates, can be obtained from the expression

$$R_p \approx \frac{R}{1 + \left(\frac{M_2}{3M_1}\right)} \quad (6)$$

#### 14.1 Ion implantation range theory

Assuming that the distribution of the implanted ions in amorphous materials could be described by a symmetrical Gaussian curve, then the ion concentration,  $n$ , as a function of depth,  $x$ , is given by

$$n(x) = \frac{\phi}{\sqrt{2\pi}\Delta R_p} \exp\left[\frac{-(x - R_p)^2}{2\Delta R_p^2}\right] \quad (7)$$

where  $\phi$  is the ion dose in  $\text{cm}^{-2}$ ,  $x$  is the junction depth,  $R_p$  is the projected range, and  $\Delta R_p$  is the projected straggle.  $\Delta R_p$  is the standard deviation of the Gaussian distribution and is given by

$$\Delta R_p = \frac{2R_p}{3} \left[ \frac{\sqrt{M_1 M_2}}{M_1 + M_2} \right] \quad (8)$$

The peak concentration is when  $x = R_p$  which leads to

$$n_{\max}(R_p) = \frac{\phi}{\sqrt{2\pi}\Delta R_p} = \frac{0.4\phi}{\Delta R_p} \quad (9)$$

FIGURE 3 is the projected range and projected straggle for boron, phosphorus, and arsenic in silicon and silicon dioxide ( $\text{SiO}_2$ ) for various implant energies [4]. Modified Gaussian profiles can be adopted by incorporating additional moments to account for deviations such as skewness [6]. A four-moment approach that gives a reasonably good approximation of range, straggle, skewness and kurtosis is described by the Pearson IV distribution function [4,7]. Channelling effects can also be accounted for by applying an exponential tail on the implant distribution. To avoid this tail, typical IC implants are done at a tilt angle of  $7^\circ$  and a twist of  $30^\circ$  [8].

In the LSS theory it was assumed that the target material was homogeneous and isotropic. Therefore, the LSS theory has been widely used as a first order approximation of the primary ion range and damage distributions in amorphous, semi-infinite substrates. However, in VLSI (very large scale integration) processing it is common to implant into a crystalline substrate covered by thin layers of different materials. Due to the basic assumptions of the LSS theory it cannot be applied to multilayered structures. A numerical solution of the Boltzmann transport equation (BTE) [9,10] or Monte Carlo (MC) [11–13] simulations give more accurate predictions of profiles into multilayered structures.

Use of the BTE on multilayered structures can account for the recoil distribution of target atoms. This method is useful when calculating damage distributions and stoichiometric disturbances in multicomponent target materials. However, for single crystal silicon this is not often a problem. For more in-depth coverage of this topic, the reader is referred to [14].

Simulation of implantation into amorphous and crystalline materials can be accomplished using a Monte Carlo simulation [15,16]. In the amorphous simulation, the target atom position follows a Poisson distribution. In the crystalline simulation, the atom position corresponds to the position that the atom would assume in the lattice. The Monte Carlo approach simulates ion implantation by tracking the history of an energetic ion through successive collisions with target atoms using the binary collision assumption. A large number of ion trajectories are calculated, and the depth at which each ion stops is determined. The predicted profile is generated by plotting histograms of the number of ions stopped within each depth interval.

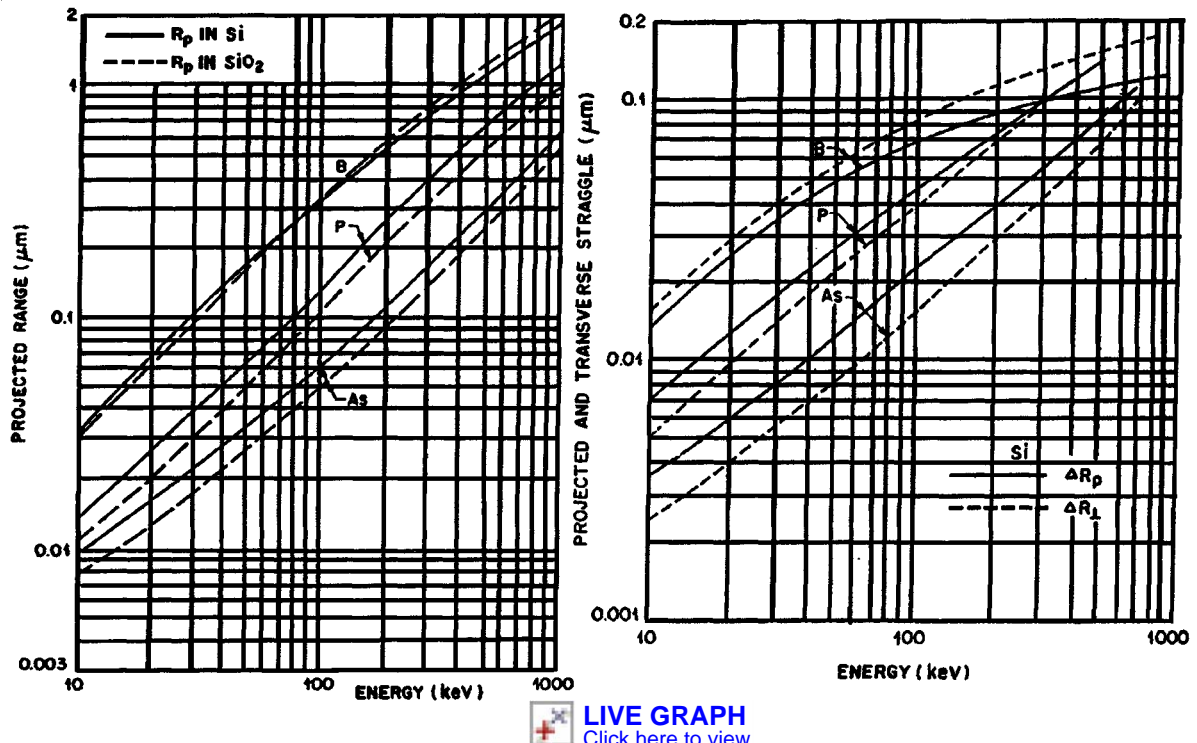


FIGURE 3 (Left) projected range,  $R_p$ , versus implant energy. (Right) projected straggle,  $\Delta R_p$ , versus implant energy. (From [4].)

Monte Carlo simulation offers three advantages over the BTE. First, it is intrinsically a three-dimensional technique. Secondly, due to the tracking of an ion in Monte Carlo there is no problem with ions being backscattered toward the surface, where BTE does not take into account backscattered ions. Thirdly, it permits simulation into crystalline materials. This allows for the calculation of a channelling tail, which will not be present in amorphous calculations (i.e. MARLOWE calculations are better for channelling tails versus TRIM calculations). However, BTE calculations are less computationally intense than Monte Carlo calculations.

## C CONCLUSION

Expressions have been presented to describe the stopping power of a target, the range of ions implanted within a material and the peak concentration. The early theory (LSS) can be used for implantation into amorphous, semi-infinite substrates. However, in crystalline silicon covered by multi-layer structures numerical solutions or Monte Carlo simulations are required.

## REFERENCES

- [1] S. Wolfe, R.N. Tauber [ *Silicon Processing for the VLSI Era, Vol. 1: Process Technology* (Lattice Press, California, 1986) ]
- [2] Y. Xia, C. Tan [ *Nucl. Instrum. Methods B (Netherlands)* vol.13 (1986) p.100 ]
- [3] G. Dearnaley, J.H. Freeman, R.S. Nelson, J. Stephen [ *Ion Implantation* (New Holland Amsterdam, 1973) ]
- [4] B. Smith [ *Ion Implantation Range Data for Silicon and Germanium Device Technologies, Research Studies* (Forest Grove, Oregon, 1977) ]

#### *14.1 Ion implantation range theory*

- [5] J. Lindhard, M. Scharff, H. Schoitt [ *Mat.-Fys. Medd. K. Dan. Vidensk. Selsk. (Denmark)* vol.33 (1963) p.1 ]
- [6] J.F. Gibbons, S. Mylroie [ *Appl. Phys. Lett. (USA)* vol.22 (1973) 568 ]
- [7] W.K. Hofker [ *Philips Res. Rep. Suppl. (Netherlands)* no.8 (1975) ]
- [8] N.L. Turner [ *Solid State Technol. (UK)* vol.28 (1985) p.163 ]
- [9] D.H. Smith, J.F. Gibbons [ in *Ion Implantation in Semiconductor 1976* Eds. F. Chernow et al (Plenum, New York, 1977) ]
- [10] L.A. Cristel, J.F. Gibbons [ *J. Appl. Phys. (USA)* vol.51 (1980) p.6176 ]
- [11] W. Fichtner [ in *VLSI Technology* Ed. S.M. Sze (McGraw-Hill, New York, 1983) ch.10 p.390 ]
- [12] J.P. Biersack, L.G. Haggmark [ *Nucl. Instrum. Methods (Netherlands)* vol.174 (1980) p.257 ]
- [13] A. DeSalvo, R. Rosa [ *Radiat. Eff. (UK)* vol.31 (1976) p.41 ]
- [14] J.S. Williams, J.M. Poate [ *Ion Implantation and Beam Processing* (Academic Press, New York, 1984) ]
- [15] W.P. Petersen, W. Fitchner, E.H. Grosse [ *IEEE Trans. Electron Devices (USA)* vol.30 (1983) p.1011 ]
- [16] J.P. Biersack, L.G. Haggmark [ *Nucl. Instrum. Methods (Netherlands)* vol.174 (1980) p.257 ]

## **14.2 Ion implantation into c-Si: basic mechanisms and modelling**

T. Diaz de la Rubia and M.-J. Caturla

January 1998

### **A INTRODUCTION**

Ion implantation is routinely used in silicon device manufacturing to dope the active regions of transistors. As the minimum feature size of integrated circuits has decreased over the years, the implant energies used by the semiconductor industry have changed. In present day CMOS technology, these energies range from a few keV for doping the source, drain and channel regions of the transistor, to tens of MeV for the formation of retrograde wells [1,2]. Boron implantation in the sub 1 keV regime is currently being explored as a way to manufacture ultra-shallow junctions for 0.1  $\mu\text{m}$  devices [3,4].

The depth distribution of the implanted ions after they come to rest, the damage created in the lattice by the ions and energetic recoils, and the relocation of dopant atoms by diffusion during high temperature annealing are all valuable quantities required in manufacturing. Moreover, predictive technology computer aided design (TCAD) for front end of line processing (FEOL) requires detailed and accurate information about these phenomena. Current TCAD tools are based on empirical models with parameters fitted to experimental data and are not predictive.

Critical issues to be resolved in order to improve modelling of ion implantation in semiconductors are: (1) accurate modelling of ion range distributions for a wide variety of implantation conditions such as beam angle of incidence and ion energy and mass; (2) quantification and identification of structural damage produced by individual ions; (3) defect diffusion and agglomeration as well as defect-dopant interactions occurring between collision cascades; (4) damage accumulation; and (5) dopant diffusion during thermal annealing at elevated temperatures. All these processes need to be understood in order to predict effects such as ion beam induced amorphisation or transient enhanced diffusion. The large number of parameters involved (ion mass, temperature and ion flux among others) make this a challenging problem for solid state modelling.

In the following Datareview, we briefly describe the models currently used to obtain depth and damage distribution profiles of dopants in silicon and discuss the most recent developments and improvements. We also describe recent calculations of kinetic properties of defects in silicon, such as point defect diffusivities and binding energies of defect and dopant clusters, and provide a summary of some of the values that can be found in the literature.

### **B MONTE CARLO MODELS BASED ON THE BINARY COLLISION APPROXIMATION**

Most computational treatments of ion ranges and damage in solids are based on the binary collision approximation and the modified Kinchin-Pease model [5,6]. In these models, energetic collisions between ions and target atoms and among secondary and higher order recoils are treated as a series of two body collisions in which one of the atoms is moving and the other is stationary. Some codes such as TRIM [7] assume the target to be amorphous, while others such as MARLOWE [5] and Crystal-TRIM [8] take the lattice structure of the target into account. The interaction potential among the atoms is a purely repulsive two-body function, and a collision is assumed to result in an atomic

displacement and the production of a Frenkel pair if more than a certain threshold energy is imparted from the moving to the stationary atom.

Inelastic collisions with target electrons also play a very significant role in determining the range of an ion in a solid. In particular, in the case of silicon implantation, where ion channelling can be a very important process, accurate models of the electronic stopping power are important. Several electronic stopping models [9,10] have been developed to account for the local inelastic interactions between the electron cloud of the ion and the core electrons of the target atoms, and, for the non-local electronic stopping, due to the interaction of the ion with the valence electrons. The former is based on Firsov's model of electronic stopping [11] while the latter is based on the Brandt-Kitagawa effective charge theory [12]. The result of these developments is a marked improvement in the prediction of range profiles for both channelling and non-channelling directions of the incident ions [13,14]. One significant development is the UT-MARLOWE code developed at the University of Texas by Tasch et al [14]. This code is based on the original program of Robinson and Torrens [6] and has been optimised by Tasch et al for silicon applications. UT-MARLOWE has been shown to give accurate range profiles for boron [15], BF<sub>2</sub> [16], arsenic [17], phosphorus and silicon implanted into silicon at room temperature for a wide variety of implant angles and energies between 5 and 200 keV. Examples of such profiles are shown in FIGURE 1.

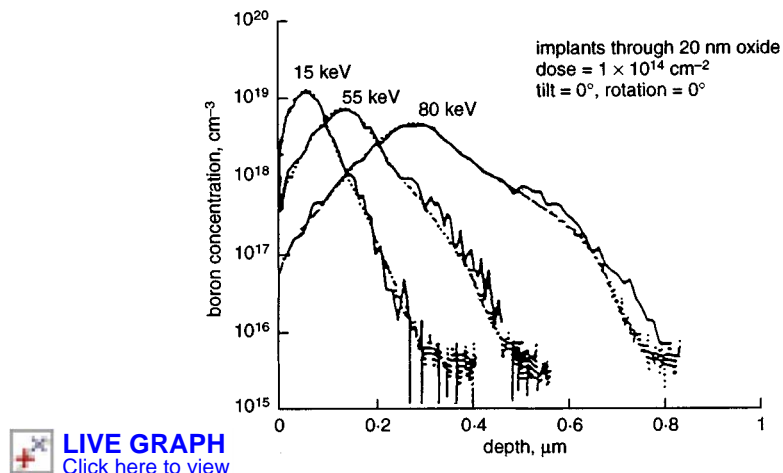


FIGURE 1 Results from UT-MARLOWE for boron implantation at 15, 35 and 80 keV on silicon. The calculated profiles (solid lines) are plotted with the experimental SIMS results (dashed lines). (Reproduced with permission from Professor A. Tasch, University of Texas at Austin.)

Advanced damage accumulation models [14,18] have also been implemented in Monte Carlo simulations in order to predict the differences in shape of the ion range profiles as the dose increases. These differences arise from dechannelling of the ions due to damage build-up. The dynamic change of the lattice structure as the dose increases is described by phenomenological models, and depends on the temperature of the lattice and on the mass and energy of the ion. These models include the production of point defects, amorphous pockets and the formation of amorphous layers when a critical defect density is achieved. However, due to the lack of a complete understanding of the underlying microscopic mechanisms of damage accumulation, at least two empirical parameters are necessary in these simulations. Nevertheless, experimental data on amorphous layer thickness for various implantation conditions can be used to determine these parameters and to provide accurate descriptions of damage build-up as a function of ion dose [14]. FIGURE 2 shows the result of a UT-MARLOWE calculation of the boron depth concentration profile in silicon at three different doses

using the Kinchin–Pease damage model implemented in version 4 of the program and the comparison with SIMS.

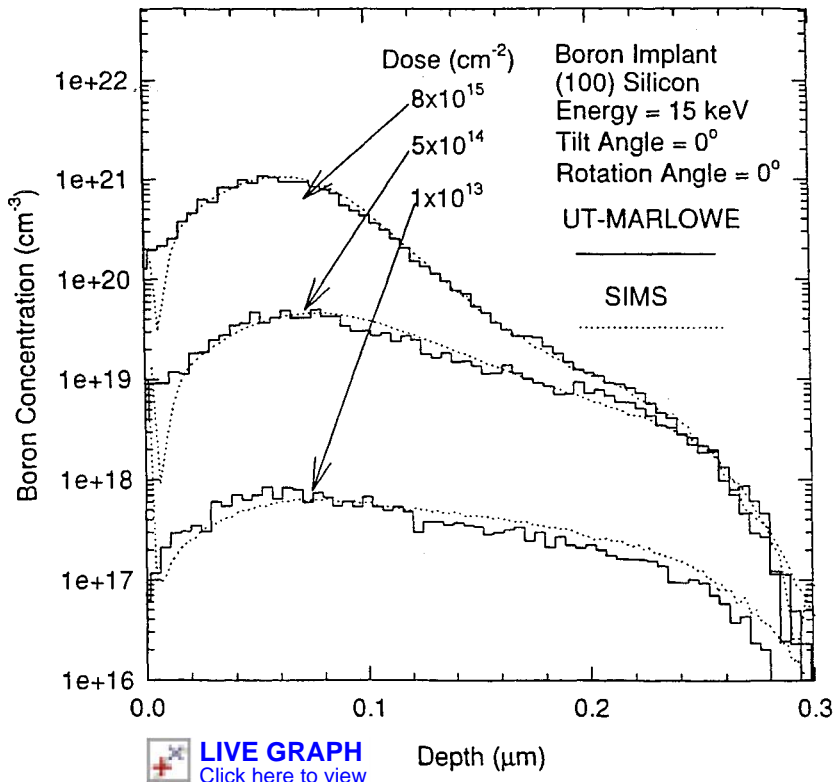


FIGURE 2 UT-MARLOWE calculation of boron implantation at three different doses using the Kinchin–Pease damage accumulation model. Observe the good agreement with the SIMS profiles.  
(Reproduced with permission from Professor A. Tasch, University of Texas at Austin.)

The computational efficiency of these Monte Carlo models has been improved significantly through the inclusion of rare event algorithms [8,14], which provide good statistics in a reasonable amount of CPU time. These algorithms consist of splitting those particles that reach a certain depth at the tail of the profile and that are, therefore, rare cases. These events will then be followed until the particles stop. The randomness of the simulation will provide different paths for these particles, therefore increasing the statistics of the calculation without substantially increasing the computational time.

## C MOLECULAR DYNAMICS MODELS

Binary collision models provide a good description of depth concentration and damage profiles. However, because of the simplifications introduced by the BCA, the microscopic mechanisms for damage deposition and production are lost in these simulations. In particular, collective many-body effects that can be important during the thermal spike phase of the displacement cascade are ignored. Molecular dynamics (MD) simulations integrate the phase space trajectories of an ensemble of atoms in a crystallite by solving the classical equations of motion. The atoms are assumed to interact via empirical interatomic potential functions that often take into account the many-body nature of atomic interactions in a solid. For example, in the case of silicon, three-body potentials such as those by Stillinger and Weber [19] and Tersoff [20] are often used. These potentials are designed to properly model interactions in covalently bonded semiconductors.

Despite the demanding computational time required for this type of simulation, making it difficult to obtain good statistical values and to model processes over long time scales ( $>10^{-11}$  s), MD has recently been used to calculate ion range distributions for low energy ions [21] and the results have been compared to binary collision simulations. These simulations show that the results for ion range distributions obtained from MD and binary collision models agree for energies as low as a few eV if a proper electronic stopping model is included.

MD is also a valuable tool for studying the complete evolution of the collision cascade, since this process lasts only a few picoseconds. Simulations of 5 keV Si cascades in Si [22] using the Stillinger–Weber interatomic potential show that during the collisional stage temperatures higher than the melting point of Si are reached in the core of the cascade. Then, during the cooling stage, the fast quench of the liquid produces an amorphous like region, leaving only a few isolated point defects. Recent MD simulations [23] found higher values for the number of defects produced by heavy ions than those obtained by the modified Kinchin–Pease model discussed above. In particular, for As the number of defects is twice the number predicted by this simple model, while for low mass ions the values are comparable. The formation of amorphous pockets during the bombardment with heavy ions accounts for this difference.

Direct accumulation of the damage produced by ions and electrons in silicon has been simulated using MD with the Stillinger–Weber interatomic potential [24]. These calculations show that for ion bombardment damage accumulates linearly at very low doses. As the dose increases, sublinear behaviour is observed due to recombination and clustering of defects. However, for low recoil energies (~50 eV), characteristic of electron irradiation, a saturation damage level is obtained due to a balance between damage production and recombination. This explains the failure to amorphise silicon using electron beam irradiation [25]. Amorphisation of the lattice by point defect accumulation has also been studied by sequentially inserting a fixed number of defects into a perfect lattice [26,27]. Further studies are needed in order to understand how the phenomenon of damage accumulation, and in particular the crystalline to amorphous transition, occurs.

## D MOLECULAR DYNAMICS AND AB INITIO CALCULATIONS OF DEFECT PROPERTIES IN SILICON

Understanding the microscopic defect structures that can develop during irradiation, as well as the possible diffusion mechanisms for dopants in silicon, requires the development of physical models that take into account defect and dopant diffusion and clustering. In turn, this requires a solid fundamental understanding of defect properties. Here, we present a summary of recent results of theoretical calculations of these properties. Naturally, much experimental data exists and the reader is referred to other recent reviews for summaries of that data [28]. Recently, Stillinger–Weber based MD simulations have been used to calculate defect diffusivities [29,30] and binding energies of point defect clusters of different sizes [29,31]. In addition, the continuous improvement in the capabilities of desktop workstations and parallel supercomputers has enabled calculations of these parameters using first principles models such as tight binding (TBMD) or Car–Parrinello (CPMD) molecular dynamics [32,33]. In TABLE 1 we present some of the calculated values that can be found in the literature. It is interesting to note that the TBMD results for vacancy and interstitial properties agree well with experimental data for self diffusion in silicon [32].

## 14.2 Ion implantation into c-Si: basic mechanisms and modelling

TABLE 1 Formation energies  $U^f$  and migration energies  $U^m$  for vacancies and self interstitials in silicon obtained by different simulation models.

Method	Self-interstitial $U_i^f$	Self-interstitial $U_i^m$	Vacancy $U_v^f$	Vacancy $U_v^m$	Ref
SW	3.65	0.9	2.64	0.43	[29]
CPMD	3.3	0.3	4.1	0.3	[34]
LDA/GGA	3.7	0.9	3.65	0.3	[35]
TBMD	3.8	1.43	3.69	0.1	[33]

Ab initio pseudopotential methods can also be used to calculate the interactions between impurity atoms and silicon defects. Diffusion mechanisms for different dopants in silicon have been studied, although further work on this topic is still necessary for a complete understanding. For the case of boron, these calculations have shown that boron diffuses through a kick out mechanism [34,35], where a boron atom is kicked out from the substitutional position by a Si self interstitial. The boron interstitial is capable of migrating long distances before falling back into a substitutional site. Values for the migration of the boron as well as the binding energies of B and silicon self interstitials have been calculated for both the neutral and the charged states [34]. For the case of As, diffusion appears to be mediated by both vacancies and interstitials [28]. The binding energy of an As-vacancy pair is approximately 1.2 eV [36,28] as obtained from both ab initio calculations and experiments. In TABLE 2 we present some results for the activation energy for Si, P, As, B and Sb.

TABLE 2 Activation energy,  $E_a$ , formation energy,  $E_f$ , migration energy,  $E_m$ , and binding energy,  $E_b$ , for different dopants in Si. Pi, Bi or Asi correspond to the interstitial position for the different dopants. AsV is an As-vacancy pair.

Species	$E_a$ (eV)	$E_f$ (eV)	$E_m$ (eV)	$E_b$ (eV)	Ref
Pi	3.8	3.0	0.8		[36]
PV	3.4	2.5	0.94	1.0	[36]
Asi	3.6	3.2	0.4		[37]
AsV	3.4	2.3	1.07	1.2	[36]
AsV	-	-	-	1.17	[38]
Sbi	4.9	4.7	0.2		[36]
SbV	3.6	2.3	1.28	1.2	[36]
Bi	-	3.5	0.3	1.0	[37]

## E KINETIC MONTE CARLO MODELS

The information obtained from binary collision models, molecular dynamics calculations and ab initio simulations can be combined into a kinetic Monte Carlo model [37,38] of defect and dopant diffusion. These models can span an extremely wide range of length and time scales, and therefore can provide a complete atomic-level picture of ion implantation and diffusion in silicon. This type of simulation can easily account for dose, dose rate and temperature effects.

In a kinetic Monte Carlo simulation the defects produced by the incoming ions are calculated using either binary collision models, such as UT-MARLOWE, or more accurate models such as MD. These defects are allowed to diffuse following the kinetics obtained by ab initio, tight binding or MD calculations such as those reported above. The cascades accumulate according to the dose rate considered until the final dose is achieved. This model has been used to simulate the damage produced by low energy boron ions as a function of dose and dose rate [39]. Significant annealing

between cascades is observed for these light ions and consequently a sublinear dependence of the damage with the ion dose. This effect increases as the dose rate decreases.

Kinetic Monte Carlo models have been used to study transient enhanced diffusion of buried boron spikes as well as boron implants, successfully reproducing the experimental profiles [40] for different annealing times and temperatures. These simulations constitute a bridge between atomic scale calculations and analytical models, providing physically based parameters for continuum models.

## F CONCLUSION

We have summarised the most recent advances in the area of computer simulation of ion implantation and annealing in silicon. We have described developments in the area of BCA simulations of ion ranges and damage distributions, and MD simulations of defect production and the primary damage state. In addition, we have discussed recent theoretical efforts aimed at calculating the properties of point defects and defect-dopant interactions. Finally, we have discussed very recent developments in the area of kinetic Monte Carlo simulations of defect and dopant diffusion. The combination of all these tools to construct an atomic-scale model of ion beam interactions with solids is a very promising area of research where much more effort is expected in the next few years.

## REFERENCES

- [1] [ *The National Technology Roadmap for Semiconductors* (Semiconductor Industry Association, San Jose, 1994) ]
- [2] J. Poate [ in *Ion Implantation and Beam Processing* (Academic Press, Orlando, 1984) ]
- [3] E.J.H. Collart, D.J. Gravesteijn, E.G.C. Lathouwesand, W. Kersten [ *Mater. Res. Soc. Symp. Proc. (USA)* vol.378 (1995) p.115 ]
- [4] M. Foad, J. England, S. Moffat, D. Armour [ *Ion Implantation Technology* Austin, Texas, June 1996 ]
- [5] M.T. Robinson, I.M. Torrens [ *Phys. Rev. B (USA)* vol.9 (1974) p.5008 ]
- [6] P. Sigmund [ *Appl. Phys. Lett. (USA)* vol.14 (1969) p.114 ]
- [7] J.F. Ziegler, J.P. Biersack, U. Littmark [ *The Stopping and Range of Ions in Solids* vol.1 of *The Stopping and Range of Ions in Matter* Ed. J.F. Ziegler (Pergamon, New York, 1985) p.25 ]
- [8] Q.K.K. Liu, J.P. Biersack, M. Posselt [ *Nucl. Instrum. Methods Phys. Res. B (Netherlands)* vol.102 (1995) p.3 ]
- [9] D. Cai, N. GronbechJensin, C.M. Snell, K.M. Beardmore [ *Phys. Rev. B (USA)* vol.54 (1996) p.17147 ]
- [10] R.J. Mathar, M. Posselt [ *Phys. Rev. B (USA)* vol.51 (1995) p.15798 ]
- [11] O.B. Firsov [ *Sov. Phys. JETP (USA)* vol.36 (1959) p.1076-80 ]
- [12] W. Brandt, M. Kitagawa [ *Phys. Rev. B (USA)* vol.25 (1982) p.5631 ]
- [13] M. Posselt [ *Nucl. Instrum. Methods Phys. Res. B (Netherlands)* vol.90 (1993) p.373 ]
- [14] S. Tian et al [ UT-MARLOWE, version 4.0, March 1997 ]
- [15] K.M. Klein, C. Park, A.F. Tasch [ *IEEE Trans. Electron Devices (USA)* vol.39 (1992) p.1614 ]
- [16] S.H. Yang, C.M. Snell, S.J. Morris, S. Tian [ *J. Electrochem. Soc. (USA)* vol.143 (1996) p.3784 ]
- [17] S.H. Yang, S.J. Morris, S.Y. Tian [ *IEEE Trans. Semicond. Manuf. (USA)* vol.9 (1996) p.49 ]
- [18] M. Posselt, B. Schmidt, C.S. Murthy, T. Feudel [ *Proc. 4th Int. Symp. Process Physics and Modelling in Semiconductor Technology* Eds. G.R. Srinivasan, C.S. Murthy, S.T. Dunham (The Electrochemical Society, 1996) p.452 ]
- [19] F.H. Stillinger, T.A. Weber [ *Phys. Rev. B (USA)* vol.31 (1985) p.5262 ]

## 14.2 Ion implantation into c-Si: basic mechanisms and modelling

- [20] J. Tersoff [ *Phys. Rev. B (USA)* vol.39 (1989) p.5566 ]
- [21] K. Nordlund [ *Comput. Mater. Sci. (Netherlands)* vol.3 (1995) p.448 ]
- [22] T. Diaz de la Rubia, G.H. Gilmer [ *Phys. Rev. Lett. (USA)* vol.74 (1995) p.2507 ]
- [23] M.J. Caturla, L.A. Marques, T. Diaz de la Rubia, G.H. Gilmer [ *Phys. Rev. B (USA)* vol.54 (1996) p.16683 ]
- [24] D.M. Stock, G.H. Gilmer, M. Jaraiz, T. Diaz de la Rubia [ *Nucl. Instrum. Methods Phys. Res. B (Netherlands)* vol.102 (1995) p.207 ]
- [25] D.N. Seidman, R.S. Averback, P.R. Okamoto, A.C. Baily [ *Phys. Rev. Lett. (USA)* vol.58 (1987) p.900 ]
- [26] L. Colombo, D. Maric [ *Europhys. Lett. (Switzerland)* vol.29 (1995) p.623 ]
- [27] D. Maroudas, M.E. Barone, B. Meng [ *Proc. 4th Int. Symp. Process Physics and Modelling in Semiconductor Technology* Eds. G.R. Srinivasan, C.S. Murthy, S.T. Dunham (The Electrochemical Society, 1996) p.387 ]
- [28] O.M. Fahey, P.B. Griffin, J.D. Plummer [ *Rev. Mod. Phys. (USA)* vol.61 (1989) p.289 ]
- [29] G.H. Gilmer, T. Diaz de la Rubia, D.M. Stock, M. Jaraiz [ *Nucl. Instrum. Methods Phys. Res. B (Netherlands)* vol.102 (1995) p.247 ]
- [30] D. Maroudas, S.T. Pantelides [ *Chem. Eng. Sci. (UK)* vol.49 (1994) p.3001 ]
- [31] N. Cuendet, T. Halicioglu, W.A. Tiller [ *Appl. Phys. Lett. (USA)* vol.69 (1996) p.4071 ]
- [32] M. Tang, L. Colombo, J. Zhu, T. Diaz de la Rubia [ *Phys. Rev. B (USA)* vol.55 (1997) p.14279 ]
- [33] P.E. Blöchl, E. Samargiassi, R. Car, D.B. Laks, W. Andreoni, S.T. Pantelides [ *Phys. Rev. Lett. (USA)* vol.70 (1993) p.2435 ]
- [34] J. Zhu, T. Diaz de la Rubia, L.H. Yang, C. Mailhiot, G.H. Gilmer [ *Phys. Rev. B (USA)* vol.54 (1996) p.4741 ]
- [35] C.S. Nichols, C.G. Van de Walle, S.T. Pantelides [ *Phys. Rev. B (USA)* vol.40 (1989) p.5458 ]
- [36] O. Pankratov, H. Huang, T. Diaz de la Rubia, C. Mailhiot [ *Phys. Rev. B (USA)* vol.56 (1997) p.13172-6 ]
- [37] H.L. Heinisch [ *Nucl. Instrum. Methods Phys. Res. B (Netherlands)* vol.102 (1995) p.47 ]
- [38] M. Jaraiz, G.H. Gilmer, J.M. Poate, T. Diaz de la Rubia [ *Appl. Phys. Lett. (USA)* vol.68 (1996) p.409 ]
- [39] M.-J. Caturla, T. Diaz de la Rubia [ *Mater. Res. Soc. Symp. Proc. (USA)* vol.438 (1996) p.89 ]
- [40] L. Pelaz et al [ *Appl. Phys. Lett. (USA)* vol.70 (1997) p.2285-7 ]

## **14.3 Electrical properties of ion implanted and electron irradiated c-Si**

**S. Coffa and F. Priolo**

March 1998

### **A INTRODUCTION**

The electronic properties of ion implanted and electron irradiated crystalline Si have been intensively studied in the last thirty years and are still the object of an intense research effort [1–20]. This interest is twofold. First of all, the electronic properties are extremely sensitive to perturbation of the crystalline structure and thus provide an excellent tool for the investigation of the damage structure of irradiated silicon and of its evolution upon annealing [21–26]. Secondly, both ion implantation and electron irradiation are intensively applied in semiconductor processing. In particular, ion implantation is by far the most widely used technique for dopant introduction in semiconductor devices and according to the Si Roadmap will maintain this leading role even in the next generation of deep submicron electronic devices [27]. The enormous potentiality offered by ion implantation in terms of the precise control of the amount of incorporated dopants as well as the tuning of their depth and lateral distributions, has allowed the development of dopant engineering strategies in which the planned dopant distribution can be achieved with a reduced overall thermal budget. These strategies, which include for example twin wells and large-angle-tilt implanted drain (LATID), are now fundamental pillars of the submicron CMOS technology [28]. There are, however, crucial issues that challenge the application of ion implantation in the future generation of submicron devices. In fact, the damage introduced by ion implantation and the incorporation of the extra ions are responsible for several phenomena such as transient enhanced diffusion, dopant clustering and secondary defect formation. These phenomena, caused by defect-defect and defect-dopant interactions, severely challenge our capability to develop reliable submicron devices and hamper the fabrication of the shallow junctions required by the next generation (e.g. 30 nm for the 0.07  $\mu\text{m}$  technology). In order to control, monitor and simulate these processes detailed information on damage evolution is crucial and analysis of the electrical properties provides a unique tool for this achievement.

The case of electron irradiation is rather different but equally important. Most of our information on the electrical and structural properties of intrinsic defects, defect complexes and defect-impurity pairs comes from the early studies of electron irradiated silicon [1–15]. Electron irradiation has found several applications in semiconductor processing albeit to a much lower extent than ion implantation. One of the most important applications of electron irradiation is carrier lifetime control in power silicon devices [14,15,29–31] which have a broad range of applications such as home appliances and automotive control. Furthermore, since irradiation produces large variations of the electrical properties of devices, electron irradiated devices, e.g. bipolar transistors, can be used as low price dosimeters in a large variety of applications such as the sterilisation of foods. The lifetime control is based on the fact that silicon irradiation by high energy electrons (1 – 10 MeV) results in the introduction of a uniform concentration of deep levels within the entire thickness of the wafer. In these applications, the damage evolution and recovery during subsequent low temperature (200 – 400°C) processes in device fabrication is again a crucial issue. Understanding damage evolution results in a precise tuning of the carrier lifetime.

Most recently, issues related to damage evolution in crystalline Si, such as the role of the impurity content of the substrate (O, C) [21,22,35], dopant clustering [32,33], damage recovery [20–22] and

defect clustering upon annealing [20–32], have all been significantly elucidated by monitoring of the electrical properties. In the following a more detailed description of the electrical properties of defects in Si and of the application of electrical measurements in the assessment of the defect properties of irradiated Si is given.

## B ROOM TEMPERATURE ELECTRICAL PROPERTIES OF DAMAGED Si

### B1 Shallow (Dopant Related) versus Deep (Defect Related) Levels

In defect-free intrinsic crystalline Si the room temperature (RT) concentration of free carriers is  $\sim 10^{10}/\text{cm}^2$  corresponding to a resistivity of  $\sim 10^5 \Omega \text{ cm}$ . The incorporation of shallow acceptors (e.g. B, Al) or donors (e.g. P, As) results in the introduction of free holes or free electrons, respectively, and in the possibility of modulating the resistivity in the range  $10^{-3} - 10^3 \Omega \text{ cm}$ . In fact electrons (holes) are weakly bound ( $\sim 0.045 \text{ eV}$ ) to the donor (acceptor) dopant atoms and are promoted to the conduction (valence) band at room temperature.

The introduction of damage produces dramatic perturbation of the electronic properties since most of the defects are electrically active and introduce deep levels in the Si bandgap. Several papers [1–22,35–37] have focused on the electrical properties of as-damaged (electron irradiated or ion implanted) Si and have established the kinetics and branching ratios in the interaction between simple point defects (self-interstitials, I, and vacancies, V) and impurities and dopants in the substrate. Both ion implantation and electron irradiation result in the generation of Frenkel pairs (I-V pairs). These defects are mobile at room temperature and undergo long range migration which is interrupted by: (a) recombination in the bulk or at the surface; (b) agglomeration into defect clusters such as V-V; or (c) interaction with impurity such as O, C and dopant atoms. The scenario proposed for I and V is schematically represented in FIGURE 1 where the different routes through which highly mobile simple point defects transform into more complex and room temperature stable defect complexes are identified. It is interesting to note, for example, that Si I will replace either B or C (depending on the relative concentration of these two species) through the Watkins replacement mechanism [7]: the resulting species (interstitial C,  $C_i$ , or interstitial B,  $B_i$ ) are mobile at room temperature and will eventually form defect complexes with other impurities (e.g. boron-boron, carbon-boron and carbon-oxygen pairs). On the other hand free vacancies cluster into divacancies or are trapped by either O or P atoms forming immobile, room temperature stable, impurity-defect pairs. The total concentration of room temperature stable defects is 4 – 10% of the total concentration of the Frenkel pairs generated by the irradiation demonstrating that most of the defects do not escape direct I-V recombination.

The deep level properties and annealing behaviour of these defect pairs have been extensively studied and the results are summarised in TABLE 1 for many I-type and V-type defects. It is interesting to note that these simple defect pairs anneal out at low temperatures (200 – 400°C). Thermal annealing at 400°C for 30 min produces a reduction of more than one order of magnitude in the concentration of defects. In addition second order defects (such as for example  $V_2O$ ) are generated (at much lower concentration) as a result of this annealing. The structure and thermal stability of these second order defects are critically dependent on the irradiation conditions such as, for ion implanted samples, ion fluence and ion mass. These defects dominate the electrical properties of the irradiated samples for annealing temperatures above 500°C and will be discussed in more detail in Section C.

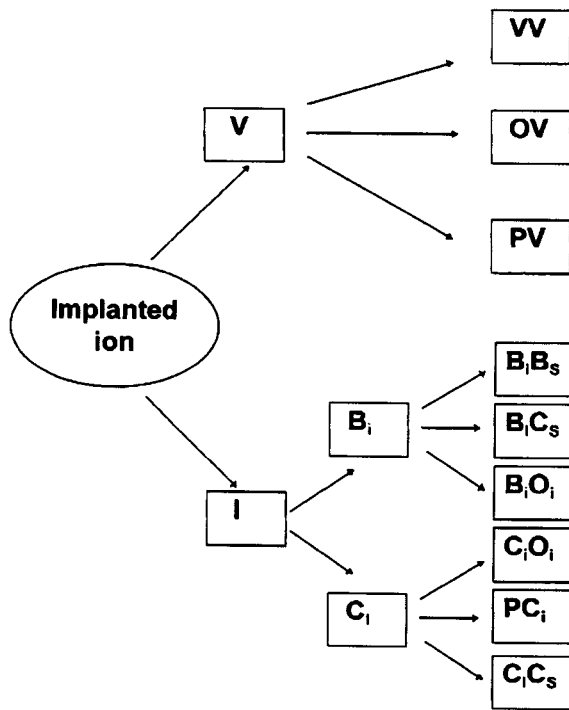


FIGURE 1 Schematic of room temperature defect evolution in crystalline Si.

TABLE 1 Energy levels and annealing temperature of several point-like defects in crystalline Si (from [1-13]). Energy levels indicated by E are measured from the bottom of the conduction band; energy levels indicated by H are measured from the top of the valence band. Some of the electronic configurations (indicated by ME or MH) are metastable.

Defect	Energy	Ann. temperature
<b>Vacancy type</b>		
VV	E (0.41) E (0.23) H (0.21)	250°C
O-V	E (0.17)	350°C
P-V	E (0.44)	150°C
V <sub>2</sub> O	E (0.30)	300°C
V <sub>3</sub> O	E (0.27)	450°C
<b>Interstitial type</b>		
C <sub>i</sub>	H (0.27)	30°C
C <sub>i</sub> O <sub>i</sub>	H (0.36)	400°C
C <sub>i</sub> P <sub>s</sub>	ME (0.30) ME (0.21) ME (0.23) ME (0.29)	~100°C
C <sub>i</sub> C <sub>s</sub>	E (0.17)	220°C
B <sub>i</sub>	E (0.13) E (0.45)	-30°C
B <sub>i</sub> -B <sub>s</sub>	H (0.30)	400°C
B <sub>i</sub> -C <sub>s</sub>	H (0.29)	400°C

## B2 Defect-Defect and Defect-Impurity Interaction: Consequences on the Electrical Properties

According to TABLE 1, defect-related deep levels most often act as effective traps for free carriers thus producing dopant compensation. In fact, deep levels in the upper part of the gap (which will dominate electrical properties of n-type Si) act as traps for electrons, while levels in the lower half of the gap (which will dominate electrical properties of p-type Si) act as hole traps. Therefore, in addition to deep level transient spectroscopy (by which energy location and concentration of the levels reported in TABLE 1 were determined), resistivity measurements are extremely sensitive tools for monitoring defect evolution. For example, the increase in resistivity produced by dopant compensation due to the presence of positively charged deep levels can be described by solving the charge neutrality equation:

$$n + N_A^- = p + N_D^+ + N_T^+ \quad (1)$$

$p$  and  $n$  being the concentration of free electrons and free holes respectively,  $N_A$  and  $N_D$  the concentration of electrically active acceptors and donors, and  $N_T$  the concentration of charged deep traps. The concentration of charged traps is given by:

$$N_T^+ = \frac{N_T}{1 + X_T e^{\left(\frac{E_T - E_F}{kT}\right)}} \quad (2)$$

where  $N_T$  is the total concentration of defects,  $E_T$  the energy level of the trap in the bandgap,  $E_F$  the Fermi level and  $X_T$  the entropy factor for the ionisation of the level. The resistivity of the damaged silicon will be given by:

$$\rho = \frac{1}{qn\mu_n + qp\mu_p} \quad (3)$$

$q$  being the electron charge and  $\mu_n$  ( $\mu_p$ ) the electron (hole) mobility. The resistivity will be therefore very sensitive to the reduction in free carrier concentration produced by the defects.

Solution of EQNS (1) and (2) allows calculation of the defect concentration from electrical measurements. Although this technique is not spectroscopic, it has been proven to be a very valuable tool in characterising electrical properties when the defect concentration exceeds the dopant concentration. Some examples of the application of resistivity measurements to defect studies can be found in [19,35–37,41,42].

## B3 Defect-Induced Dopant Deactivation

In addition to the compensation produced by deep levels, point defects can also produce dopant deactivation by a direct interaction with electrically active dopants. This dopant deactivation phenomenon leads to the formation of dopant-defect pairs in which the dopant atom has lost its electrical activity. Recent experiments [35] have used this phenomenon to explore room temperature migration of simple point defects injected by low energy ion implantation in the bulk of crystalline Si wafers. The dopant deactivation, resulting from the interaction with those point defects that escape direct recombination and clustering in the region directly modified by the ions (up to 0.4  $\mu\text{m}$  from the surface), has been observed up to depths as great as 3  $\mu\text{m}$  in highly pure epitaxial Si. The deactivation

is instead limited to the region directly modified by the ion when the impurity (C, O) content exceeds  $\sim 10^{16}/\text{cm}^3$ . In this last case in fact, free defect migration is rapidly interrupted by trapping at the impurities. From these measurements a lower limit of  $10^{-10} \text{ cm}^2/\text{s}$  has been established for the room temperature migration of Si self-interstitials. This value is of noticeable importance since most of the existing data on RT interstitial diffusion come from extrapolation of high temperature diffusion studies [38,39] or from analyses of electron irradiated samples [40]. This example shows nicely how electrical measurements can also be used to assess fundamental defect properties.

#### **B4 Evolution of Resistivity upon Ion-Implantation: from Dopant Concentration by Point-Like Defect Complexes to Amorphisation**

In-situ [41,42] and ex-situ resistivity measurements can be used to study the evolution in the electronic properties of ion implanted Si as a result of ion implantation. One example of in-situ resistivity measurements during ion implantation (400 keV Si at room temperature) is shown in FIGURE 2. Upon implantation conductivity decreases by several orders of magnitude for fluences up to  $1 \times 10^{13}/\text{cm}^2$ . At this fluence a resistivity close to that of intrinsic silicon is measured. This conductivity decrease has been attributed to dopant compensation by deep levels in the bandgap (according to EQNS (1), (2) and (3)). In particular, divacancy and oxygen-vacancy signals have been shown to dominate the deep level transient spectroscopy (DLTS) signal at low fluences. At fluences above  $10^{13}/\text{cm}^2$  the conductivity starts to increase and eventually saturates at fluences above  $5 \times 10^{14}/\text{cm}^2$ . Transmission electron microscopy (TEM) analyses in this regime show the formation of a discontinuous amorphous phase at the end of the range and eventually the formation of a buried amorphous layer at higher doses: it is the current flow through the buried amorphous layer that produces the conductivity increase observed in the dose range  $1 \times 10^{13} - 5 \times 10^{14}/\text{cm}^2$ . Finally, at fluences higher than  $5 \times 10^{14}/\text{cm}^2$  a continuous amorphous layer is formed and the conductivity value saturates at  $\sim 10^{-4} \Omega^{-1} \text{ cm}^{-1}$ , a value typical of ion implanted amorphous Si [43].

### **C DEFECT EVOLUTION UPON ANNEALING**

#### **C1 Thermal Stability of Residual Damage**

Electrical measurements have provided valuable information on the thermal stability of residual damage. Annealing of irradiated crystalline Si results in an evolution of the damage structure until at high temperature crystallinity is again fully restored. The temperature at which this occurs is strongly dependent on the irradiation conditions (substrate temperature, fluence, etc.) which determine the structure of the residual damage. Electron irradiation and low fluence implantation with light ions (such as for example He and Si) result in the introduction of the simple point-defect pairs described in FIGURE 1 and TABLE 1. These pairs typically anneal out at temperatures below 300 – 350°C with similar annealing kinetics in electron irradiated and ion implanted samples [22]. Most of the point defects (I and V) produced in the dissociation of these pairs recombine in the bulk. A small fraction of them will instead agglomerate into second order defects, such as for example V<sub>2</sub>O, which are stable at these temperatures. Damage evolution at temperatures above 350°C is quite different for ion implanted and electron irradiated samples. Indeed, in spite of the fact that identical defect structures are introduced by these two processes, they certainly present significant differences. First of all the energy density deposited by ions is several orders of magnitude higher than for electrons: this results in much denser collision cascades and, for heavy ions, in the formation of highly disordered (amorphous) zones as a direct consequence of the collision process. Furthermore, the introduction of an equal number of I and V through the formation of Frenkel pairs is, in the case of ion implantation, unbalanced by the extra implanted ion. Hence, an interstitial excess is left in ion implanted samples when most of the I and V introduced by the irradiation have recombined [21]. This interstitial excess

is responsible for phenomena such as transient enhanced diffusion (TED), formation of secondary defects and dopant clustering which challenge our ability to fabricate ultra shallow junctions using ion implantation [44,45]. It is interesting to note that the high implantation fluences (typically higher than  $10^{13}/\text{cm}^2$ ) used in device fabrication are outside the domain usually explored by electrical techniques such as DLTS. In this domain, damage evaluation is traditionally obtained with techniques such as Rutherford backscattering spectrometry (RBS) and TEM. Electrical measurements have been used to monitor electrical activation of the incorporated dopants and only a few attempts have been made to use electrical methods to analyse the defect structure [23]. Most recently it has been shown [21–23] that electrical measurements can be used to complement structural analyses and help elucidate defect evolution from simple defect pairs to extended defects.

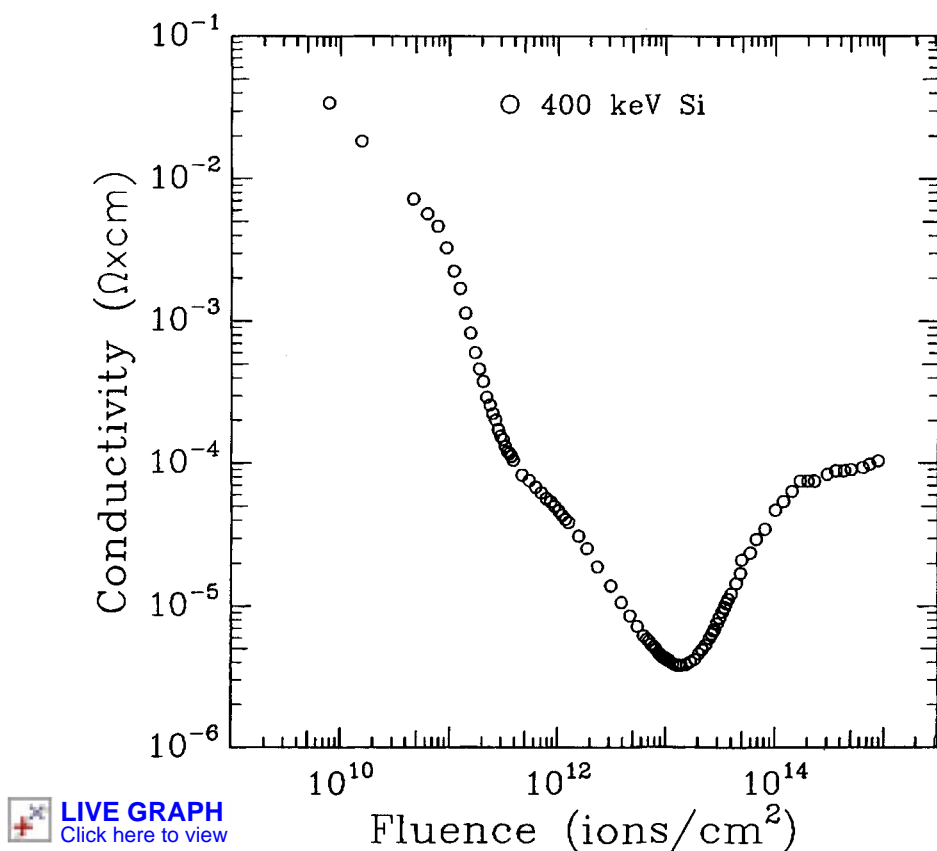


FIGURE 2 In-situ conductivity measurements on n-type Si samples implanted with 400 keV Si at room temperature.

## C2 Defect Clustering, Dopant Clustering, Dopant Activation

Until now, simulations rather than experimental evidence have provided the only quantitative description of damage evolution from Frenkel pair generation to extended defects [46]. Using a kinetic Monte Carlo method and semi-empirical fits to the experimentally observed extended defects {311}, simulations have successfully reproduced the phenomena of extended defect formation and dissolution. Several hints on the physical mechanisms involved in defect growth have been elucidated. In particular interstitial clusters have been clearly identified as the primary factor in determining damage evolution upon annealing and the extra implanted ions have been shown to be mainly

responsible for this interstitial excess. The interstitial clusters undergo an Ostwald ripening process since larger clusters are more stable than smaller ones. Hence upon annealing the cluster dimension increases and, when a critical cluster size is exceeded, extended defects are formed. The Si self-interstitial supersaturation maintained during defect evolution drives the phenomenon of TED through the formation of mobile defect-dopant pairs. As described in Section C3 electrical measurements can provide an important validation of the predictions of these simulations.

There is another phenomenon which is driven by the interstitial supersaturation. In B implanted samples the formation of an electrically inactive and immobile component during diffusion is often observed [26]. This phenomenon is caused by the formation of B clusters which occurs even at concentrations far below the B solubility limit. Recently new light has been shed on this phenomenon by a combination of first-principle calculations of the B-Si kinetics and thermodynamics [47] and kinetic Monte Carlo simulations [33,34]. According to this model, and in agreement with experimental observations, B clusters are formed in the presence of the high supersaturation of self-interstitials produced by the beam. These B clusters also store self-interstitials and hence their formation reduces the effect of TED on the remaining B atoms. However, the recovery of B electrical activity, necessary in order to achieve a low sheet resistance junction, results in the release of the stored interstitials and produces additional transient diffusion. Electrical measurements (and in particular spreading resistance) have been of fundamental importance in pointing out the strong relation between B deactivation and high interstitial supersaturation.

### C3 Structure versus Electrical Properties of Residual Damage: Point-Like Defect Complexes, Defect Clusters, Extended Defects

The transition from simple point defects to clusters and to extended defects is accompanied by severe changes in the electrical properties of the material. These changes can be monitored in order to achieve valuable information on the evolution process not only at low implanted fluences (as described in Section C1) but also in the high fluence regime. Recent experiments [23] have shown that when ion implanted samples are annealed at temperatures above 500°C the residual damage is dominated by the signature of interstitial-type defects. These defects store about one interstitial per implanted ion as a direct consequence of the extra implanted ion. Interstitial cluster signatures dominate the residual damage of silicon implanted at fluences in the range  $1 \times 10^{12} - 2 \times 10^{13}$  and annealed at temperatures above 550°C. Moreover, for Si implanted at high fluences ( $\geq 5 \times 10^{13}/\text{cm}^2$ ) and annealed at  $T \geq 680^\circ\text{C}$ , a new signal, exhibiting capture kinetics typical of an extended defect, has been observed and correlated (by comparison with TEM analyses) to the rodlike {311} defects which are known to store the interstitials responsible for transient enhanced diffusion. These data represent an important validation of the simulations described in Section C2.

## REFERENCES

- [1] G.D. Watkins [ in *Electronic Structure and Properties of Semiconductors* Ed. W. Schröter (VCH, Weinheim, 1991) ch.3 ]
- [2] L.C. Kimerling [ *Inst. Phys. Conf. Ser. (UK)* no.31 (1977) p.221 ]
- [3] G.D. Watkins [ in *Deep Centers in Semiconductors* Ed. S.T. Pantelides (Gordon and Breach, New York, 1986) ch.3 ]; G.D. Watkins [ *Mater. Res. Soc. Symp. Proc. (USA)* vol.469 (1997) p.139-50 ]
- [4] M.T. Asom, J.L. Benton, R. Sauer, L.C. Kimerling [ *Appl. Phys. Lett. (USA)* vol.51 (1987) p.256 ]
- [5] J.L. Benton, M.T. Asom, R. Sauer, L.C. Kimerling [ *Mater. Res. Soc. Symp. Proc. (USA)* vol.104 (1988) p.85 ]
- [6] G.D. Watkins, J.W. Corbett [ *Phys. Rev. (USA)* vol.121 (1961) p.1001 ]

- [7] G.D. Watkins [ *Phys. Rev. B (USA)* vol.12 (1975) p.5824 ]
- [8] P.J. Drevinsky, H.M. De Angelis [ *13th Int. Conf. on Defects in Semiconductors* Eds. L.C. Kimerling, J.M. Parsey (Warrendale, PA, 1984) p.307 ]
- [9] P.J. Drevinsky, C.E. Cafer, L.C. Kimerling, J.L. Benton [ *Proc. Int. Conf. on the Science and Technology of Defect Control in Semiconductors* Ed. K. Sumino (Elsevier Science, North Holland, Amsterdam, 1990) p.342 ]
- [10] P.M. Mooney, L.J. Cheng, M. Sull, J.D. Gerson, J.W. Corbett [ *Phys. Rev. B (USA)* vol.15 (1977) p.3836 ]
- [11] J.W. Corbett, G.D. Watkins [ *Phys. Rev. A (USA)* vol.138 (1965) p.555 ]
- [12] P.J. Drevinsky, C.E. Cafer, S.P. Tobin, J.C. Mikkelsen Jr., L.C. Kimerling [ *Mater. Res. Soc. Symp. Proc. (USA)* vol.104 (1988) p.167 ]
- [13] L.C. Kimerling [ *Inst. Phys. Conf. Ser. (UK)* no.31 (1977) ch.2 p.221 ]
- [14] S.D. Brotherton, P. Bradley [ *J. Appl. Phys. (USA)* vol.53 (1982) p.5720 ]
- [15] S.D. Brotherton, P. Bradley [ *J. Appl. Phys. (USA)* vol.52 (1982) p.119 ]
- [16] B.G. Svensson, C. Jagadish, A. Hallen, J. Lalita [ *Nucl. Instrum. Methods Phys. Res. B (Netherlands)* vol.106 (1995) p.183 ]
- [17] J. Lalita, C. Jagadish, B.G. Svensson [ *Nucl. Instrum. Methods Phys. Res. B (Netherlands)* vol.106 (1995) p.237 ]
- [18] B.G. Svensson, C. Jagadish, J.S. Williams [ *Phys. Rev. Lett. (USA)* vol.71 (1993) p.1860 ]
- [19] S. Coffa, V. Privitera, F. Priolo, S. Libertino, G. Mannino [ *J. Appl. Phys. (USA)* vol.81 (1997) p.1639 ]
- [20] J.L. Benton, S. Libertino, P. Kringshoi, D.C. Eaglesham, J.M. Poate, S. Coffa [ *J. Appl. Phys. (USA)* vol.82 (1997) p.120 ]
- [21] S. Libertino et al [ *Appl. Phys. Lett. (USA)* vol.71 (1997) p.389 ]
- [22] S. Libertino et al [ *Appl. Phys. Lett. (USA)* vol.70 (1997) p.3002 ]
- [23] J.R. Ayres, S.D. Brotherton [ *J. Appl. Phys. (USA)* vol.71 (1992) p.2702 ]
- [24] S.D. Brotherton, J.P. Gowers, N.D. Young, J.B. Clegg, J.R. Aures [ *J. Appl. Phys. (USA)* vol.60 (1986) p.3567 ]
- [25] A. Armigliato, D. Nobili, P. Ostoja, M. Servidori, S. Solmi [ in *Semiconductor Silicon* Eds. H.R. Hul, E. Sirtl (Electrochemical Society, Pennington, New Jersey, USA, 1977) p.638 ]
- [26] P.A. Stolk, H.-J. Goessmann, D.J. Eaglesham, D.C. Jacobson, J.M. Poate [ *Appl. Phys. Lett. (USA)* vol.66 (1995) p.568 ]
- [27] [ *National Technology Roadmap for Semiconductors* (Semiconductor Industry Association, San Jose, USA, 1995) ]
- [28] C.Y. Chang, S.M. Sze [ *ULSI Technology* (McGraw Hill International Editions, New York, USA, 1996) ]
- [29] B.J. Baliga, E. Sun [ *IEEE Trans. Electron Devices (USA)* vol.ED-24 (1977) p.685 ]
- [30] S.D. Brotherton, P. Bradley [ *Solid-State Electron. (UK)* vol.25 (1982) p.119 ]
- [31] S.C. Sun, J.D. Plummer [ *IEEE Trans. Electron Devices (USA)* vol.ED-27 (1980) p.356 ]
- [32] J.L. Benton, S. Libertino, S. Coffa, D.J. Eaglesham [ *Mater. Res. Soc. Symp. Proc. (USA)* (1997) in press ]
- [33] L. Pelaz et al [ *Appl. Phys. Lett. (USA)* (1998) in press ]
- [34] L. Pelaz et al [ *Mater. Res. Soc. Symp. Proc. (USA)* (1997) in press ]
- [35] K. Kyllesbech Larsen, V. Privitera, S. Coffa, F. Priolo, S.U. Campisano, A. Carnera [ *Phys. Rev. Lett. (USA)* vol.76 (1996) p.1493 ]
- [36] V. Privitera, S. Coffa, F. Priolo, K. Kyllesbech Larsen, S. Libertino, A. Carnera [ *Nucl. Instrum. Methods Phys. Res. B (Netherlands)* vol.120 (1996) p.9 ]
- [37] V. Privitera, S. Coffa, F. Priolo, K. Kyllesbech Larsen, G. Mannino [ *Appl. Phys. Lett. (USA)* vol.68 (1996) p.3422 ]
- [38] P.M. Fahey, P.B. Griffin, J.D. Plummer [ *Rev. Mod. Phys. (USA)* vol.61 (1989) p.289 ]
- [39] F.F. Morehead, R.F. Lever [ *Appl. Phys. Lett. (USA)* vol.48 (1986) p.151 ]

- [40] G.D. Watkins [ *Mater. Res. Soc. Symp. Proc. (USA)* vol.469 (1997) in press ]
- [41] A. Battaglia, S. Coffa, F. Priolo [ *Appl. Phys. Lett. (USA)* vol.65 (1994) p.306 ]
- [42] A. Battaglia, S. Coffa, F. Priolo, C. Spinella, S. Libertino [ *Nucl. Instrum. Methods Phys. Res. B (Netherlands)* vol.96 (1995) p.219 ]
- [43] S. Coffa, F. Priolo, A. Battaglia [ *Phys. Rev. Lett. (USA)* vol.70 (1993) p.3756 ]
- [44] N.E.B. Cowern, K.T.F. Jansses, H.F.F. Jos [ *J. Appl. Phys. (USA)* vol.68 (1990) p.6191 ]
- [45] K.S. Jones, S. Prussin, E.R. Weber [ *Appl. Phys. A (Germany)* vol.45 (1988) p.1 ]
- [46] M. Jaraiz, G.H. Gilmer, T. Diaz de la Rubia, J.M. Poate [ *Appl. Phys. Lett. (USA)* vol.68 (1996) p.409 ]
- [47] J. Zhu, T. Diaz de la Rubia, L.H. Yang, C. Mailhiot, G.H. Gilmer [ *Phys. Rev. B (USA)* vol.54 (1996) p.4741 ]

## CHAPTER 15

### GETTERING (*Edited by E.R. Weber*)

- 15.1 Gettering of transition metals in c-Si:  
gettering in silicon technology
  - 15.2 Gettering of transition metals in c-Si:  
gettering mechanisms
  - 15.3 Gettering of transition metals in c-Si:  
gettering techniques
  - 15.4 Gettering of transition metals in c-Si:  
summary of current state of understanding
  - 15.5 Gettering of transition metals in c-Si:  
future trends
- References for Chapter 15:  
Gettering of transition metals in c-Si

## **15.1 Gettering of transition metals in c-Si: gettering in silicon technology**

H. Hieslmair, S.A. McHugo, A.A. Istratov and E.R. Weber

June 1998

### **A METAL IMPURITY EFFECTS ON DEVICES**

It is well established that contamination of silicon wafers with transition metals can reduce device yield even if the concentration of metals is below  $10^{12} \text{ cm}^{-3}$ . When dissolved in silicon, transition metals can form deep levels [1] which increase p-n junction leakage currents by generation [2–4] of carriers in reverse biased depletion regions (or by recombination in small forward biases) [5–7]. Furthermore, metal impurities in p-n junctions can lower the reverse bias breakdown voltage [8]. Metal precipitates can also form bands of deep levels [9,10], which greatly increase leakage currents and can even directly short p-n junctions [11–13]. In bipolar junction transistors, dissolved metals generally increase the base currents, power consumption and heat production, and degrade the emitter efficiency and base transport factors [2]. MOS devices are sensitive to metal contamination [14] since many transition metals precipitate at the Si/SiO<sub>2</sub> interface or become trapped in the oxide layer [15,16]. The resulting reduction of the dielectric strength of the oxide layer leads to oxide breakdown device failures [5,17–27] and/or an increase in generation rates [28], often referred to as a decrease in gate oxide integrity (GOI). Furthermore, transition metals have been linked to poor retention times (high refresh rates) in DRAMs [29] and pixel failures [3,4,18] in CCD devices. CCD devices can be sensitive to iron concentrations as low as  $5.4 \times 10^8 \text{ Fe}/\text{cm}^3$  and to gold concentrations of  $3.6 \times 10^8 \text{ Au}/\text{cm}^3$  [3]. Solar cell conversion efficiency is also degraded by metal impurity related recombination centres [30–34]. These centres can be due to dissolved or precipitated metal impurities introduced during growth and/or processing. Finally, dissolved metals have also been shown to decrease the barrier of formation of oxidation-induced stacking faults (OSF) and dislocations [18]. For example, iron has been shown to enhance the nucleation and growth of oxygen precipitates [35]. These effects may help induce deleterious structural defects within active regions of the device, causing device failure [36,37].

### **B TRANSITION METAL DIFFUSIVITY AND SOLUBILITY**

Transition metals are generally fast diffusers with high solubilities [38] at high temperatures,  $> 800^\circ\text{C}$ . Metals can either be incorporated into the bulk of silicon ingots during crystal growth, or contaminate the wafer surface during polishing, chemical treatments, ion implantation, oxidation steps, or other processing steps, and then diffuse into the bulk during subsequent high temperature heat treatments. Some of the fastest diffusing metal impurities are Cu and Ni, which have diffusivities approaching liquid intermixing during the high temperature treatments, i.e.  $10^{-4} \text{ cm}^2/\text{s}$ . Other common impurities, such as Fe and Cr, are slower diffusers, with typically 1–2 orders of magnitude lower diffusivities than Cu or Ni, but can still diffuse tens to hundreds of microns during heat treatments. At these high temperatures, the solubility of metals is given by the familiar thermodynamic expression for solubility as

$$C_{\text{eq}} = e^{-\Delta G/kT} = e^{\Delta S/k} e^{-\Delta H/kT} = C_0 e^{-\Delta H/kT} \quad (1)$$

where H, S and G are the enthalpy, entropy and free energy of formation, respectively. The energy of formation G is actually the sum of a number of energy terms as

$$\Delta G = E_b - E_e + E_s \quad (2)$$

where  $E_b$  is the binding energy of the metal to the boundary phase,  $E_e$  is the electron interaction energy of the outer electron orbitals of the metal and the silicon matrix, and  $E_s$  is the elastic strain energy of the metal atom in the silicon lattice. Solubilities of transition metals in silicon are defined as the equilibrium dissolved metal concentration in silicon when bounded by a specific phase such as  $\text{FeSi}_2$  in the case of iron [38]. If the boundary phase were constrained to be  $\text{FeSi}$ , or pure Fe, a different solubility could be obtained.

The solubility of a metal can also be affected by a change in the silicon matrix due to strain, structural defects, or melting. Such changes will affect one or both of the interaction energies,  $E_e$  and  $E_s$ . Masuda-Jindo [39] attempted to calculate the interaction (segregation) energy between strained regions resulting from structural defects and metal impurities (i.e.  $E_e(\text{defect}) - E_e(\text{matrix})$ ), using linear combination of atomic orbitals (LCAO). His results indicated that V, Cr, Mn and Fe are attracted to tensile regions ( $E_{\text{segregation}} \approx 0.25$  eV for 5% tensile strain) while Cu is attracted to compressed regions. Certainly, these trends need to be experimentally verified, but the general conclusion is that structural changes most likely affect the equilibrium concentration (solubility) of metal impurities. One can, in fact, consider the defect structure, i.e. the dislocation core, as an entirely different phase with different impurity solubility.

## C GETTERING: REMOVAL OF METALS FROM DEVICES

It is a continuing challenge to reduce the deleterious effect of metals on devices without introducing costly processing steps. Although it is almost impossible to avoid metal contamination during integrated circuit (IC) manufacturing, numerous techniques were developed to keep unintentionally introduced metals away from the device regions. These techniques are generally referred to as gettering techniques. Gettering is the process whereby impurity concentrations are reduced in the device region of the wafer by localizing them in separate pre-defined regions of the wafer [40,41]. Despite the use of ultra-clean Si wafers, clean-room technology, and hyper-pure chemicals, gettering procedures are necessary in device manufacturing to maintain high yields, especially in the case of an accidental contamination and/or process variations. The current gettering techniques have been optimised primarily through yield studies and, while little is known of their quantitative aspects, the techniques appear adequate for current fabrication technologies. However, the tolerable limit of metal concentrations is continually decreasing as the IC industry is moving toward larger wafers, possibly with lower oxygen concentrations [42], novel structures (SOI, epitaxial layers, etc.), and smaller device dimensions with larger electric fields and current densities [43,44]. The American Semiconductor Industry Association (SIA) guidelines for maximum allowable dissolved iron concentrations have dropped to  $\approx 10^{10}$  at/cm<sup>2</sup> for 1998–2000 [42]. Costly efforts are made in contamination prevention techniques, yet yield is becoming ever more sensitive to the slightest perturbations of the manufacturing environment. Thus, it is imperative to quantitatively understand and optimise the mechanisms of gettering to maintain high yield and provide insurance against yield drop by unintentional contamination during device processing.

In general, gettering can be considered a three-step process [45]. The impurity must be (1) released from its original and undesirable state to then (2) diffuse through the crystal from the device region to the gettering sites, and be (3) captured at the gettering site. It is well established that for the slower diffusing transition metals, such as iron or gold, diffusion to the gettering site is typically the rate-limiting step [46–48]. Since the IC industry is progressing towards lower thermal budgets, it is highly desirable to bring the gettering region closer to the device region. Gettering techniques within 10 µm

## 15.1 Gettering of transition metals in c-Si: gettering in silicon technology

of the device region are known as proximity gettering techniques and hold promise to perform well even with the lower thermal budgets.

There are two general classes of gettering, defined by the capture mechanisms, segregation and relaxation. Some authors have proposed gettering assisted by self-interstitial injection as the third mechanism [49–51]. In this chapter, we will describe the injection assisted gettering within the segregation gettering section.

Gettering techniques are subdivided into internal and external gettering, depending on how the gettering sites were introduced in the wafer. Internal gettering does not require any external treatment (except for annealings) to achieve a gettering effect. External gettering typically requires an external treatment such as diffusion, mechanical damage or ion implantation to form a precipitation/segregation region in the wafer. Sometimes, gettering techniques are still classified as intrinsic and extrinsic, depending on whether the gettering region is located inside the wafer or at the wafer surfaces.

The next Datareview presents a synopsis of the relaxation and segregation gettering mechanisms, while the subsequent one gives a detailed discussion of each gettering technique. References to articles where the gettering efficiency of particular metals was studied with different gettering techniques are summarized in TABLE 1 and listed at the end of the chapter.

TABLE 1 Database of references on gettering of transition metals in silicon, classified according to the gettering techniques (columns) and gettered metals (rows).

Metal	Intrinsic gettering	Phosphorus-diffusion gettering	Substrate gettering (e.g. p/p <sup>++</sup> , n/n <sup>++</sup> )	Si surface and Si/SiO <sub>2</sub> gettering, including wafer bonding
Fe	[46, 67, 89–91, 93, 94, 96, 97, 100, 101, 105, 106, 207, 251, 319–325]	[125, 133, 138, 326]	[57, 278–283, 327, 328]	[145, 287, 292]
Cu	[17, 88, 97, 99, 102, 103, 196, 249, 320, 323, 329–336]	[56, 115, 120, 121, 133, 326]	[56]	[194, 285–287, 291, 296, 298, 329, 330, 337]
Ni	[17, 51, 93, 97, 102, 103, 106, 108, 320, 325, 332–334, 338]	[104, 125, 326]		[285, 287, 337]
Co	[97, 338]	[51, 124, 126–128, 339]	[57]	[124, 128, 285]
Au	[340]	[50, 51, 116, 117, 119–123, 129, 133, 134, 151, 155, 212, 254, 314, 318, 341–345]	[59, 60]	[228, 296, 297]
Cr	[94, 112, 346]	[347]		[145, 287]
Pt		[130, 149, 345, 348, 349]		[350]
Pd	[96, 97, 102, 103]			[285]
Ti		[138, 293, 347]		[293]
Ag	[351]			
Mn	[352]		[57]	
Mo		[138]	[281]	
V		[347]		
Device yield	[75, 79, 85, 114, 353–357]	[36, 70–72, 79, 115, 130, 133–145, 162, 354, 358–365]	[159, 160]	[222]

*15.1 Gettering of transition metals in c-Si: gettering in silicon technology*

TABLE 1 continued

Metal	Implantation gettering	Backside damage gettering	Chemical gettering	Al-backside gettering
Fe	[224, 226, 229, 230, 235–237, 242–244, 250, 251, 261, 262, 366–370]	[48, 93, 190, 191, 207, 283, 371]	[15, 16]	[174]
Cu	[224, 226, 230, 236, 239–243, 245–250, 259, 260, 262, 264, 366, 369, 372–376]	[187, 190, 194, 196]	[16, 223]	[69, 167]
Ni	[224, 241, 246, 366, 369, 377]	[93]		[69]
Co	[224, 250, 366, 367, 369, 378–381]			[52]
Au	[122, 151, 192, 212, 224, 227, 228, 238, 243, 252, 254, 255, 257, 258, 260, 337, 366, 376, 382–385]	[209, 213, 340]	[223]	[69, 167]
Cr	[239, 241]		[16]	
Pt	[247, 257, 386–389] [247]			
Pd				
Ti				
Ag	[389]			[167]
Mn				
V				
Device yield	[36, 222, 225, 234, 238, 253, 256, 266, 390–392]	[69, 93, 135, 185, 188, 189, 192, 193, 197, 198, 354]		[30, 68, 69, 72, 162, 168–177, 393, 394]

**REFERENCES**

See p. 796.

## 15.2 Gettering of transition metals in c-Si: gettering mechanisms

H. Hieslmair, S.A. McHugo, A.A. Istratov and E.R. Weber

June 1998

### A SYNOPSIS OF RELAXATION GETTERING

In any relaxation gettering technique, heterogeneous precipitation sites are intentionally formed in regions away from the device/surface region. The gettering process requires an impurity supersaturation, which typically occurs during a cool-down from high temperatures. Any mobile and supersaturated impurity will quickly precipitate in regions of the silicon wafer with high concentrations of precipitation sites. In these regions, the dissolved impurity concentration remains close to the thermodynamic equilibrium solubility. In neighbouring regions, such as the device/surface region with low nucleation site densities, supersaturated impurities will not precipitate quickly, and thus impurity concentrations may significantly exceed the thermodynamic equilibrium concentrations during a cool-down. This difference in precipitation rates creates a dissolved impurity concentration gradient. In this manner, supersaturated impurities diffuse away from the surface/device region and into the bulk during a cool-down. This process is often referred to as relaxation gettering since it requires the supersaturation of impurities to 'relax' to equilibrium concentrations during a cooling step.

The most widely used gettering technique in the IC industry is internal gettering, which utilises oxygen precipitates and the associated structural defects (punched out dislocation loops and stacking faults), which are inherent in CZ wafers, as heterogeneous nucleation sites for any supersaturated transition metals. Backside relaxation gettering techniques introduce gettering sites by damaging the backside of the wafer or by depositing a layer of polysilicon, which contains heterogeneous nucleation sites such as dislocations, and grain boundaries. Backside gettering techniques are effective for fast diffusing impurities such as copper and nickel. Proximity gettering techniques introduce heterogeneous nucleation sites in the vicinity of the device region. These techniques are beneficial for slow diffusing impurities and low temperature gettering cycles since they do not require impurity diffusion through the whole wafer.

### B SYNOPSIS OF SEGREGATION GETTERING

Segregation gettering is driven by a gradient or a discontinuity in the impurity solubility. The region of higher solubility acts as a sink for impurities from the lower solubility region. As with relaxation gettering techniques, the segregation gettering region is located outside the active device region; however, it has the advantage over relaxation gettering in that no supersaturation is required. Thus, in principle, low impurity concentrations in the device region could be quickly realised at elevated temperatures where the impurities diffuse quickly. A segregation coefficient,  $S$ , is defined as the ratio of the equilibrium impurity solubility in the gettering region,  $C_{\text{gett}}$ , to the solubility in the gettered region (i.e. the device region),  $C_{\text{dev}}$ :

$$S = \frac{C_{\text{gett}}}{C_{\text{dev}}} \quad (1)$$

The relative thickness of the device to the gettering regions affects the total amount of impurity that can be gettered. Assuming no additional impurities are introduced into the wafer during a heat

## 15.2 Gettering of transition metals in c-Si: gettering mechanisms

treatment, the final thermodynamically equilibrated concentration of the impurity in the device region  $N_{dev}$  is given by

$$N_{dev} = N_0 \times \left[ \frac{1}{1 + \left( S \frac{w_{gett}}{w_{non}} \right)} \right] \quad (2)$$

where  $N_0$  is the initial impurity concentration in the wafer, and  $w_{gett}$  and  $w_{non}$  are the thicknesses of the gettering and gettered regions, respectively. From EQN (2) we clearly see that a gettering region will not completely remove all impurities from the device region after a gettering heat treatment. Rather, only a fraction of the impurities is removed which depends on the initial contamination level, the segregation coefficient and the relative thickness of the device and the gettering regions.

The segregation effect can result from a) a difference in phase, e.g. between crystalline and liquid silicon during crystal growth, b) a difference in material, e.g. aluminium which has a greater solubility for metal impurities than silicon [52], c) the Fermi level effect on solubility of metals [45,53–58], e.g. Au in phosphorus doped silicon [56,57,59,60], d) ion pairs, e.g. Fe–B pairs [61–64], e) strain which may increase or decrease the solubility of metal impurities and has been demonstrated to either directly getter metals [65,66], or influence metal gettering at defects [67].

Generally, segregation coefficients increase at lower temperatures due to the rapid decrease in impurity solubility in silicon relative to the solubility in the gettering layer. However, metal diffusivities also become smaller at lower temperatures. Thus, the ideal temperature for segregation gettering is a balance between the segregation coefficient and diffusivity [45]. Additionally, the time duration of the gettering anneals [68] and the initial level of contamination must be taken into account. An optimal temperature has been reported by a number of researchers, e.g. [45,68–72], although the reported temperatures varied in the studies. These variations are most likely due to differences in gettering times, impurity type and contamination from outside sources.

Segregation gettering of impurities in a semiconductor can be accomplished by numerous techniques. For photovoltaic silicon substrates, the most common techniques are aluminium and phosphorus gettering. These techniques can be easily incorporated into solar cell production and getter impurities out of the entire active device region, i.e. the entire thickness of the material. In the IC industry, epitaxial films grown on highly doped/high quality substrates are becoming of great importance. One of the structures which is of particular interest is a p epitaxial layer grown on a p<sup>++</sup> substrate (p/p<sup>++</sup>). Aside from device design advantages, there exists the added advantage that Fermi level and pairing type segregation between the p layer and the p<sup>++</sup> substrate reduces transition metal contaminant concentration in the p layer. Furthermore, for IC devices, segregation to implant regions may be a viable alternative because of the proximity nature of the technique.

## REFERENCES

See p. 796.

## **15.3 Gettering of transition metals in c-Si: gettering techniques**

H. Hieslmair, S.A. McHugo, A.A. Istratov and E.R. Weber

June 1998

### **A INTERNAL GETTERING**

As early as 1957, Kaiser [73] and later Mets [74] established that oxygen precipitates are sinks for metal impurities. Tan et al [75] were the first to suggest a gettering model which uses oxygen precipitates as gettering sites. Oxygen is incorporated into the silicon crystal during Czochralski-type crystal growth primarily from the  $\text{SiO}_2$  crucible in concentrations of about  $10^{17}$  to  $10^{18} \text{ cm}^{-3}$ . This concentration exceeds the oxygen equilibrium solubility at temperatures used in device processing and results in precipitation of the supersaturated oxygen. Since formation of oxygen precipitates in the device region reduces device yield, much effort in the early days of the silicon era was concentrated on engineering of oxygen precipitation. It was shown that it is possible to create a layer free of oxygen precipitates near the surface/device region (denuded zone (DZ)) and to precipitate supersaturated oxygen in the bulk of the wafer. The DZ can be formed by heating the wafer to high temperatures in order to allow the oxygen in the near surface region to diffuse out of the wafer. After this out-diffusion, the resulting oxygen concentration in the surface region is significantly lower than the bulk concentration. Thus, during a subsequent lower temperature annealing, nucleation of oxygen only takes place in the bulk [75–78]. The nuclei then grow during subsequent high temperature anneals. Since this early work, numerous studies have been performed to optimise the oxygen precipitation procedure by variation in time and temperature [76,79–86,87], as well as manipulation of the near surface vacancy concentration [88]. Studies made by Gilles et al [46], Aoki et al [89,90] and Hieslmair et al [91] confirmed that iron precipitates at oxygen precipitate-related defects and proved that internal gettering is a relaxation-type gettering. This means that the internal gettering process requires a supersaturation of mobile metallic impurities, which typically occurs in device processing during cooling.

Although the internal gettering technique has been found to reduce the concentration of metallic impurities in the device-active region in Si device technology, some aspects of internal gettering are not yet completely understood. For example, the nature of the precipitation sites has been disputed for a long time. It is known that oxygen can precipitate in different morphologies depending on its initial concentration in the wafer and growth regime [78,92], which may affect the gettering efficiency. Furthermore, the oxygen precipitates produce structural defects such as punched-out dislocations and stacking faults during precipitate growth, which also could serve as precipitation sites. Only recently has it become clear that each metal has different precipitation behaviour and precipitates preferably at different defects [93–99]. There are indications that iron [46,91,100,101] and nickel [102–104] precipitate at oxygen precipitates themselves and possibly at stacking faults [105]. On the other hand, copper and palladium precipitate preferably at punched-out dislocations and stacking faults [99,106]. This behaviour has been related to the crystallographic structure of metal-silicides, where high silicon content silicides (such as  $\text{FeSi}_2$ ,  $\text{NiSi}_2$ ,  $\text{CoSi}_2$ : see [107–110]) relieve compressive strains [67,111] and thus would be favourable in regions of high compressive strain field such as near oxygen precipitates. Additionally, it has been reported that strain fields of oxygen precipitates stabilise the Fe precipitates [67]. Low silicon content silicides (such as  $\text{Pd}_2\text{Si}$ ,  $\text{Cu}_3\text{Si}$ : see [108–110,112]) require the emission of silicon interstitials and nucleation of such a precipitate would be inhibited near an oxygen precipitate. These metals precipitate at punched-out dislocations and stacking faults and, due to additional stresses, cause dislocations to move and multiply, creating additional nucleation sites [113]. Apparently, oxygen precipitates with long stacking faults and punched-out dislocation networks

would provide gettering sinks for both high silicon-content and low silicon-content metal precipitates. This was confirmed by device yield studies [85,114] and comparative analysis of gettering of different metals [102].

An advantage of internal gettering is that no special gettering step is needed since the gettering occurs during cooling from high temperatures during integrated circuit manufacturing. Internal gettering was shown to be effective for removal of all major metal impurities from the active device layer (see TABLE 1 in Datareview 15.1), which is explained by a variety of gettering sites introduced by oxygen precipitates, and by the proximity of the gettering region to the device-active layer. However, the relaxation mechanism of gettering, which requires impurities to be supersaturated at temperatures where they remain mobile, limits the applicability of the internal gettering for some slow diffusing metals. Furthermore, as the required contamination level of impurities decreases, lower temperatures, longer anneals and more reproducible morphology and density of oxygen precipitates in the bulk are required.

## B EXTERNAL GETTERING

### B1 Phosphorus Diffusion Gettering

The first indirect observation of gettering by phosphorus in-diffusion was made by Goetzberger and Shockley [115], who found that characteristics of diodes improved with deposition of either a phosphorus or boron glass followed by a heat treatment. Shortly thereafter, a direct measurement of the gettering effect was performed by Wilcox et al [116,117], who discovered that high concentrations of phosphorus both hindered gold diffusion and increased its solubility. In the same year Hall and Racette [56] measured an increased copper solubility in heavily phosphorus, arsenic and boron-doped wafers. Thereafter, a number of researchers directly confirmed the phosphorus gettering effect [50,51,55,59,60,104,118–130]. Observations from these studies include: 1) the impurity distribution follows the phosphorus in-diffused profile [60,119,129]; 2) dislocations form with extremely high phosphorus concentrations [119,131]; 3) little or no metal impurity gettering occurs in the glass layer used for phosphorus in-diffusion [121,123,124]; 4) a relationship exists between the carrier gas used for glass formation [121], the growth speed of the glass layer [127], and the amount of impurity gettered; 5) impurities precipitate in the phosphorus doped layer [104,121,125]; 6) SiP precipitates can form in the near surface region of the phosphorus doped region [104,125,127,132]; and 7) a high concentration of substitutional Co and Mn is observed in heavily phosphorus doped regions [57,126].

Phosphorus gettering has been used to improve the performance of both single crystal and polycrystalline silicon. Improvements in diode quality [79,115,133–135] and minority carrier diffusion length [130,136,137] have been realised with phosphorus gettering of silicon used for integrated circuits. Additionally, great gains in solar cell performance have been achieved with phosphorus gettering [70–72,138–145]. For polycrystalline silicon solar cells, the response of the material to the phosphorus gettering treatment depends on the concentration of structural defects [70,72,144] as well as oxygen and carbon concentrations [71,72,142]. As shown in TABLE 1 (Datareview 15.1), phosphorus diffusion has been successfully applied for gettering of almost all transition metals.

Phosphorus in-diffusion gettering can be accomplished using the carrier gas  $\text{POCl}_3$  while other gas carriers such as  $\text{PBr}_3$  [121,123] or  $\text{P}_2\text{O}_5$  [104,115,120,124], or a spin-on source [45,115] produce gettering as well. A phosphosilicate glass (PSG) can form on the silicon surface when an oxidising atmosphere is present. This glass then acts as the doping source for the phosphorus in-diffusion.

### *15.3 Gettering of transition metals in c-Si: gettering techniques*

A layer heavily doped with phosphorus provides a number of potential mechanisms for gettering: solubility enhancement by the Fermi level effect and ion pairing, gettering to dislocations, and silicon self-interstitial injection assisted gettering. The Fermi level effect and ion pairing are expected to be active during phosphorus in-diffusion because solubility enhancements have been observed for heavily P and As doped wafers [56,57,59,60] where dislocation formation and self-interstitial injection do not occur. The Fermi level effect [53,146–148] increases the solubility of positively or negatively charged impurities in p<sup>++</sup> or n<sup>++</sup> substrates, respectively, without changing the solubility of neutral impurities: thus the total impurity solubility (neutral plus charged) is increased. As the substrate doping level becomes larger than the intrinsic carrier concentration at the temperature of interest, the concentration of charged impurities increases linearly with p- or n-type dopant concentration. Ion pairing primarily occurs by Coulombic attraction between the impurity and a charged ion, usually a dopant atom. The exact solubility enhancement generated by ion pairing is difficult to estimate since few studies have been performed on metal impurity pairing with phosphorus atoms, with no studies performed at elevated temperatures. However, the results of Hall and Racette [56] strongly suggest some degree of ion pairing may be occurring in addition to the Fermi level effect. Calculation of the enhancement via ion pairing is possible with the use of a number of simplifications as outlined by Reiss et al [147]. Chou and Gibbons [55] have performed calculations for Au–P pairs where they note at most a factor of four enhancement via ion pairing.

While the Fermi level effect and ion pairing are active during phosphorus gettering, some phosphorus in-diffusion studies [55,121,129,149] have measured more gettered impurities than would be expected considering only the Fermi level effect and ion pairing. These studies suggest another gettering mechanism is active during phosphorus in-diffusion. Two possible mechanisms are gettering by dislocations, formed due to lattice mismatch, and gettering induced by silicon self-interstitial injection.

Dislocation formation can augment the gettering process via precipitation of the impurities (relaxation gettering) [119,121,131,150,151]. However, gettering by dislocations cannot fully explain the observed effect since the gettering enhancement has also been observed without dislocation formation [129,149] and, moreover, some studies have shown no precipitation of the impurities at the dislocations [55,119,121].

The second mechanism which may enhance phosphorus gettering is via silicon self-interstitial injection. Self-interstitial injection occurs during phosphorus in-diffusions as has been observed by extrinsic stacking fault growth [152], dislocation climb [153,154], epitaxial re-growth of silicon at the phosphosilicate/silicon interface [104,125,132], oxygen precipitate dissolution [155] and vacancy defect (D-defect) dissolution [156]. The injection of self-interstitials can enhance the diffusion of some metal impurity species, e.g. Au and Pt, via the kick-out mechanism [157], which accelerates the kinetics of the gettering process [51,129,130]. However, the accelerated diffusion does not explain the increase in the total amount of gettered impurities. In addition to this diffusion enhancement, researchers [50,51,104,125,127,128] have provided a theoretical model which suggests phosphorus in-diffusion produces a flux of self-interstitials towards the phosphosilicate glass (PSG)/silicon interface. This flux is speculated to enhance the concentration of interstitial metal impurities above their solubility, thus driving precipitation of the impurities. This precipitation increases the amount of impurities gettered to the phosphorus-doped layer. For a further comparison on the mechanism of phosphorus gettering see [158].

Comparison of phosphorus diffusion gettering to gettering in arsenic or boron in-diffused wafers [59,121], chemical gettering [159], backside polysilicon deposition [135], backside damage [79,135], implantation-induced gettering [36,122,159,160] and internal gettering [36,79,159,160] showed that phosphorus gettering, in most cases, performs as well as, and sometimes better than, these techniques.

Some further benefits are realised when phosphorus gettering is combined with another gettering technique. A combination of phosphorus and aluminium gettering has been shown to greatly improve material performance beyond the use of one gettering technique [71,136,143,161,162], suggesting a synergistic effect occurs with combined phosphorus and aluminium gettering [161]. Phosphorus gettering has also been successfully combined with HCl gettering. This is accomplished by adding trichloroacetic acid into the phosphorus annealing gas. Improvements have been realised for solar cells [144] and CMOS integrated circuit devices [159].

## B2 Aluminium Gettering

The aluminium gettering phenomenon was first suggested by researchers who noted a marked increase in solar cell performance when annealing an Al layer on the backside of a silicon substrate [163–166]. Thompson and Tu [167] were the first to directly observe Al gettering of metal impurities when they noted a significant accumulation of Cu in an Al layer on the backside of a silicon substrate following intentional contamination on the frontside of the substrate and subsequent heating. Thereafter, Al gettering has been shown to improve material properties in polycrystalline silicon used for solar cells in thick silicon substrates [30,69,72,168–171], and thin film silicon [172] as well as IC grade single crystal silicon [72,173–177]. Minority carrier diffusion lengths in these materials can be increased by 100–200  $\mu\text{m}$  while overall solar cell efficiencies have been shown to increase by as much as 0.5–1%.

Aluminium gettering is accomplished by deposition and subsequent heating of a thin Al or 2% Si-Al film on the backside of a silicon substrate. The primary mechanism for Al gettering is segregation of the impurities from the silicon to the Al-Si liquid layer. Most metal impurities, including Fe, Cu and Ni, have a solubility of 1 to 10 at % in Al over a wide temperature range [178,179], even with a moderate concentration of silicon in the Al. Metal impurity solubilities in silicon are significantly lower and decrease with decreasing temperature. Therefore, a segregation coefficient of  $10^3$  to  $10^9$  is expected, depending on the metal impurity and temperature. Essentially, this segregation coefficient depends on the difference in formation energy between the impurity in the silicon matrix and the impurity in the Al or Al-Si layer. Additionally, pitting or damage at the Si/Al-Si interface may act as precipitation sites for relaxation gettering of metal impurities [171] although this mechanism has not been directly proven. Furthermore, the annealing of Al forms a  $\text{p}^+$  layer, which can be used to reflect electrons and avoid recombination at the surface. This is effectively used on the back surface of silicon solar cells where carrier recombination is unwanted. The reflection process is known as the back surface field (BSF) effect [180,181]. Overall, Al gettering is extremely useful and practical in gettering impurities from solar cell silicon, since impurities must be removed from the entire thickness of the material and an Al layer is already used as a backside contact. However, Al gettering of impurities from IC device regions is less reasonable due to Al junction spiking and the relatively high vapour pressure of Al, which can evaporate from the back surface and contaminate the front surface.

Direct measurements of the Al segregation coefficient have been made by Apel et al [52] for Co in silicon and Hieslmair et al [174] for Fe in silicon. Apel et al [52] found  $10^3$  as a lower bound for the segregation coefficient of Co between silicon and an Al layer at 820°C. Hieslmair et al [174] found, as a lower bound, segregation coefficients of  $10^5$ – $10^6$  for Fe between silicon and an Al layer at temperatures from 750 to 950°C.

The efficiency at which Al gettering improves material quality is comparable to phosphorus diffusion gettering [143,162,182,183] as well as gettering to implantation induced cavities [177]. Material properties, such as minority carrier diffusion length, have been shown to greatly improve for co-gettering with P and Al [71,136,143,162,184]. A synergistic effect has been measured experimentally [71,162] and explained theoretically [161]. It was suggested that the synergistic effect originates from

the silicon self-interstitial injection by the phosphorus in-diffusion, which accelerates the gettering process by increasing both the dissolution of metal precipitates and the diffusivity of some impurities. Furthermore, the gettering ability of the Al layer is significantly more stable than that of the P layer, due to continued P in-diffusion and a decrease in the peak phosphorus concentration. Therefore, when both mechanisms are combined, the gettering action is enhanced.

### B3 Backside Damage (BSD) and Poly-Backside Seal (PBS) Gettering

Backside damage and polysilicon backside gettering utilises gettering sites introduced at the backside of the wafer by mechanical damage of silicon (sandblasting, lapping, etc.) [74,135,185–187], by laser damage [188,189], or by deposition of a polysilicon layer [48,190–192] or an Si<sub>3</sub>N<sub>4</sub> film [192,193]. Gettering by a layer of porous silicon [194], by deposition of germanium [47] or by defects created using impact sound stressing [195] have also been reported. TEM studies [192,196], X-ray topography [187,189,193] and selective etching of the samples [185,197,198] revealed that the damaged layer consists of complicated networks of dislocations, intrinsic stacking faults and regions with intensive lattice strain. Since the structure of the damaged layer was shown to depend significantly on the type and intensity of the damage [186,197] and could vary with high-temperature annealing [193,198], it is very difficult to characterise backside damage gettering mechanisms in general or compare different types of damage. Likewise, the physical model of backside damage gettering remains controversial. Currently, there are three models for backside gettering:

- a) Backside damage gettering is relaxation gettering since backside damage provides an abundance of heterogeneous nucleation sites for precipitation of supersaturated metal impurities [187,191,199–201].
- b) Backside gettering is segregation gettering, in which metals are trapped at defects by strain fields or enhanced solubility in the vicinity of structural defects (see, for example, discussion in Sumino [202]). This model suggests that metals become trapped at the extended defects at high temperatures without supersaturation [66,135,190,197,198,203–206].
- c) Backside treatments enhance internal gettering [48,192,207] via acceleration of oxygen precipitate growth by absorption of silicon self-interstitials in the damaged layer [208–211]. This last model is still under discussion since some authors argue that mechanically damaged layers inject self-interstitials [207,212].

The authors of this review believe the actual gettering mechanism combines all three models to varying extents. Since the number of segregation trapping sites in the gettering layer is limited [213], the segregation mechanism would dominate at low impurity concentrations, such as in device yield studies. At higher impurity concentrations, such as in studies with intentional contamination, the segregation gettering sites may become saturated and the relaxation gettering mechanism becomes dominant.

Backside mechanical damage gettering may no longer be a viable gettering technique since the damage introduces particulate contaminants further into the process line. To reduce particulate contamination levels, 300 mm and 400 mm wafers may have a polished backside surface to reduce particulate generation, entrapment and shedding [214]. However, other backside gettering techniques, such as gettering by polysilicon layers, may remain viable as gettering techniques in the future.

#### B4 Chemical Gettering

Chemical gettering consists of high-temperature oxidation anneal (usually between 1000°C and 1100°C) in dry oxygen with small amounts (usually less than 1%) of chlorine-bearing species (Cl<sub>2</sub>, HCl, C<sub>2</sub>HCl<sub>3</sub>, or trichlorethylene). The gettering effect is due to the chlorine in the oxidising atmosphere which prevents positive alkaline ions from being introduced into the growing oxide through the formation of volatile chloride compounds. Chlorine incorporated into the oxide also has a passivating effect against sodium drift [215–217]. It was suggested that the passivating species are Si-O-Cl complexes, and Na<sup>+</sup> ions are trapped in the oxide near the Si/SiO<sub>2</sub> interface [216, 217], where the concentration of chlorine atoms has a maximum [218]. Oxidation in the presence of chlorine species was shown to decrease the density of surface states at the Si/SiO<sub>2</sub> interface [219] and to improve breakdown characteristics of MOS capacitors [220]. However, the chemical gettering could only moderately decrease the bulk concentration of metals. Robinson and Heiman [221], Engel and Souza [222] and Jastrzebski et al [145] studied the influence of chemical gettering on minority carrier lifetime and found only small improvements. This was understood after experiments of Baginski and Monkowski [223], Ohsawa et al [16] and Honda et al [15], who studied effects of chemical gettering on intentionally contaminated wafers. They found that Cu could be easily gettered from the wafers by the addition of HCl to the oxidising ambient, whereas Au, Fe and Cr were not affected.

### C PROXIMITY GETTERING

#### C1 Implantation-Induced Gettering

Metal impurities in silicon can be gettered to regions of implantation, where either the implanted atoms or the implantation damage getters the impurities. A beneficial aspect of implantation gettering is the close proximity of the gettering layer to IC device regions, whereby gettering can occur with low thermal budgets. Additionally, the implant region provides a uniform gettering layer as compared to internal gettering where the gettering sites are widely dispersed.

Metal impurities are gettered to implanted regions by either a relaxation or segregation type mechanism. Relaxation occurs either at implantation-induced damage or at clusters/precipitates of the implanted species. Segregation can occur to a separate phase formed by a high dose implant, or via the Fermi level effect or metal ion pairing with the implant species, e.g. boron, arsenic or phosphorus implants, or via chemisorption to internal surfaces of cavities formed by implantation with helium or hydrogen.

Gettering has been observed for implantation with silicon [122,224–230], phosphorus [122,151], carbon [231–237], oxygen [225,236,238–245], helium [236,243,246–252], argon [222,225,238,253–257], neon [255,258], krypton [253], xenon [225,253], hydrogen [227,228,245,259,260], boron [226,237,253,261,262], germanium [263,264], chlorine [238], aluminium and chromium [265]. Implant energies range from 50 keV to 10 MeV with implant doses ranging from 10<sup>13</sup> to 10<sup>17</sup> atoms cm<sup>-2</sup>. The implant atoms usually are light elements in order to avoid amorphisation of the near surface region. Metal impurities, such as Cu, Fe, Au, Cr, Ni and Pt, have been successfully gettered to implant regions (see TABLE 1 in Datareview 15.1).

It should be noted that implantation of oxygen to high doses forms a buried oxide layer which has many benefits in terms of radiation hardness and reduction of device latch-up. This implantation process is known as separation by ion implantation of oxygen (SIMOX). Impurities such as copper, chromium and iron can be gettered either into the oxide layer [239], at the oxide/silicon interfaces [240], or at the implant damage located deeper than the oxide layer [241,242,245].

### 15.3 Gettering of transition metals in c-Si: gettering techniques

In general, implantation is an effective means to getter metal impurity. IC device characteristics have been shown to improve with various implantations [36,222,225,234,238,253,256,266]. Compared to other gettering techniques, implantation getters a comparable amount of impurity significantly faster than standard techniques such as internal gettering [249,251]. The true strength of implantation gettering is the close proximity of the gettering layer to the device region. This allows for rapid gettering of impurities away from the devices as has been directly observed for boron implantation [261], carbon implantation [235] and implantation-induced cavities [249,251].

Direct comparisons amongst various implant species have been performed in order to qualitatively determine the most effective implant for gettering. Amongst implant species which rely on relaxation mechanisms, Ar implantation seems most effective where Seidel et al [122] find more effective gettering with Ar implantation than with O or Si implantation. Furthermore, Beyer and Yeh [225] have demonstrated a greater improvement in MOS capacitor performance with Ar implantation than with Si, O or Xe implantation. Nassibian and Golja [238] found that IC device performance is improved to a greater extent with Ar implantation than with O or Cl implantation, although they speculate that Cl out-diffuses during post-implantation annealings, thus lessening the gettering capability of this implant species. Contrary to these works are studies by Geipel and Tice [253] who show that Ar, Kr and Xe implantation are equally effective in improving device performance.

Comparisons have been made between implant species that rely on segregation mechanisms and species that rely on relaxation mechanisms. Kuroi et al [226] found more Cu is gettered to boron implants than silicon implants. However, their I-V measurements indicate the silicon implants are more effective in reducing leakage currents with intentional Cu and Fe contamination. Benton et al [237] show that boron implants getter more Fe than silicon implants, and carbon implants fall in between boron and silicon in terms of Fe gettering effectiveness. The data of Benton et al [237] for carbon gettering is in agreement with Skorupa et al [235] in terms of residual dissolved Fe in the near surface region. Wong-Leung et al [227,228] compared Si implantation damage and H implantation-induced cavities where more Au is gettered to cavities than the Si implant region. This work is in agreement with Myers and Petersen [252], who measured a higher binding energy of Au to cavities than to the Au-Si phase. Moreover, Overwijk et al [236] presented results on implantation gettering of Fe and Cu where they show that carbon and oxygen implantation gettering is active at implant doses below  $6 \times 10^{15}$  atoms cm<sup>-2</sup> but He implantation is not. However, at doses greater than  $6 \times 10^{15}$  atoms cm<sup>-2</sup>, the He implantation getters significantly more Fe and Cu than carbon or oxygen. Skorupa et al [242] found that Cu getters to the cavities rather than to the SIMOX damage layer. Furthermore, Zhang et al [245] noted that more Cu getters to H implantation-induced cavities than to the damage layer created from SIMOX formation, in agreement with the work of Skorupa et al [242].

The above studies suggest that gettering by implantation by a segregation mechanism is more effective than by a relaxation mechanism. Although a large number of studies suggest this is true, studies by Geipel and Tice [253] show B implantation requires an order of magnitude higher dose than Ar, Kr or Xe in order to achieve effective gettering. Furthermore, studies by Seidel et al [122] have determined that gettering of Au varies with implant species with the effectiveness ranking as: Ar ≥ O > P > Si > As ≥ B. Additionally, Skorupa et al [242] observed more efficient gettering of Fe and Cu by carbon implantation than He implantation-induced cavities or SIMOX related damage structure. In fact, in Skorupa's work, Fe was observed to be gettered only by carbon implantation, in contradiction of work on Fe gettering to cavities [250,251].

In the above comparisons one must consider the annealing temperature which can affect gettering to the P, As, B implant regions and to the cavities due to the temperature dependence of segregation gettering. Furthermore, the cooling conditions or degree of supersaturation can drastically change the gettering effectiveness of non-dopant implant species, e.g. Ar, O and Si, which getter by a relaxation

mechanism, as has been demonstrated by Lecrosnier et al [254] and Grob et al [257] for Ar implantation.

Difficulties can arise from gettering by ion implantation, including an increase in native point defect concentrations, i.e. vacancies and self-interstitials, which can enhance dopant diffusion and hinder shallow junction formation [267]. This problem could possibly be alleviated with co-implantation of carbon, which has been shown to inhibit dynamic annealing of implant damage [268], suggesting the carbon implant captures self-interstitials as has been shown in electron irradiation work [269]. Another drawback to implantation gettering is the required high implant doses, which correspond to undesirably long implantation times. However, plasma immersion ion implantation allows for rapid implantation of many species, e.g. an implantation of  $2 \times 10^{17}$  H atoms  $\text{cm}^{-2}$  takes on the order of 2 minutes [243,270].

## C2 Gettering by Heavily Doped Substrates

Effective gettering of metal impurities can be achieved with heavily doped substrates. Epitaxial layers  $\approx 10 \mu\text{m}$  thick with low to moderate doping are deposited on the heavily doped substrates in order to provide an active region for IC devices. The substrates are typically doped with boron, phosphorus or arsenic depending on the device application. The heavy doping additionally acts as a sink for stray currents between IC devices, thus retarding latch-up problems [271]. The substrates possess a higher solubility for metal impurities than the epitaxial layers. The difference in solubility drives segregation of the impurities from the epi-layer into the substrate. Heavily doped substrates effectively getter even with low thermal budgets because the substrates are located in close proximity to the device region and the substrates act as a continuous sink for impurities.

Heavily doped substrates getter primarily by the Fermi level effect and ion pairing, which increase the solubility of the impurity in the substrate relative to the low or moderately doped epitaxial layer. The Fermi level effect [53,146–148] increases the solubility of positively or negatively charged impurities in p<sup>++</sup> or n<sup>++</sup> substrates, respectively, without changing the solubility of neutral impurities: thus the total impurity solubility is increased. As the substrate doping level becomes larger than the intrinsic carrier concentration at the temperature of interest, the concentration of charged impurities increases linearly with p- or n-type dopant concentration. Ion pairing occurs primarily by Coulombic attraction between the impurity and a charged ion, usually a dopant atom. As the substrate doping level becomes larger than the intrinsic carrier concentration, the concentration of pairs increases as the square of the p- or n-type dopant concentration. Dislocation formation at the epi/substrate interface [131,272–274] as well as accelerated oxygen precipitation in the substrate [275–277] may enhance the gettering effect even further. For further information on the mechanism of substrate gettering see [158].

Hall and Racette [56] were the first researchers to directly measure enhanced solubility of a metal impurity (Cu) in heavily doped silicon wafers. These enhancements increased with decreasing temperatures in the range 300–700°C. Cagnina [59] and O’Shaughnessy et al [60] measured enhanced Au concentrations in heavily phosphorus and arsenic doped wafers in the temperature range 1000–1200°C. Later work by Gilles et al [57] revealed increased solubilities of Fe, Mn and Co in heavily boron, phosphorus and arsenic doped wafers. Recently, McHugo et al [278] have determined that the solubility enhancement of Fe in silicon doped with  $10^{19}$  boron atoms  $\text{cm}^{-3}$  is significant only below 900°C, due to a shift in the Fe energy level towards the valence band at elevated temperatures. Overall, these results suggest that heavily doped substrates can provide an excellent means of proximity gettering, although some impurities may not be effectively gettered at elevated temperatures due to energy level shifts.

### 15.3 Gettering of transition metals in c-Si: gettering techniques

Studies of IC device performance by Gregor and Stinebaugh [159] and Cerofolini et al [160] have shown increased performance with the use of epi-heavily doped wafers. Since these earlier works, researchers have directly measured removal of impurities from epitaxial layers with the use of heavily boron doped substrates ( $p/p^{++}$  wafers) [279–282]. Additionally, Fe has been removed from lightly doped wafers with the use of heavily boron doped backside layers only 1  $\mu\text{m}$  thick [283]. However,  $p/p^{++}$  wafers were shown not to effectively remove Mo from the epitaxial layers [281].

In comparison to other gettering techniques, heavily doped substrates are one of the most effective means to getter impurities. IC device characteristics have been shown to be better for  $p/p^{++}$  or  $n/n^{++}$  wafers than for wafers with internal gettering sites [159,160]. Furthermore, Aoki et al [280] demonstrated that  $p/p^{++}$  wafers were more effective in removing Fe from the device region than internal gettering for moderate to low contamination levels. These results provide a clear example of the advantages of segregation gettering over relaxation gettering.

### C3 Gettering by the Silicon Surface, by Si/SiO<sub>2</sub> Interface and Wafer Bonding Interface

A wafer surface or Si/SiO<sub>2</sub> interface is an important sink for transition metals, and can attract impurities in the absence of competing gettering sites. Gettering by free silicon surface and Si/SiO<sub>2</sub> interface can be considered as an undesirable gettering effect which attracts impurities to the active layer of silicon devices rather than a useful gettering technique. However, it can be used for practical purposes if the interface is located in the depth of the wafer, which can be realised by wafer bonding. It is well-established that Cu, Ni, Co and Pd form precipitate colonies at the surface after high-temperature diffusion and slow cool of the wafers [98,284–286]. Shabani et al [287,288] observed out-diffusion of Cu, Ni and Cr to the wafer surfaces, whereas Fe remained homogeneously distributed in the bulk. Out-diffusion of Cu from the bulk of Si wafers to the surface was confirmed by McCarthy et al [289]. Correia et al [286] observed precipitates of platinum at the Si/SiO<sub>2</sub> interface. Similar observations were reported by Wendt et al [290] and Bai et al [291] for copper. On the contrary, iron [292] and titanium [293] did not aggregate at the surface in the absence of extended defects. Surface gettering effects were observed in the literature and were explained by a combination of the following factors: a) the surface acts as a strain free site for the growth of metal-silicides with large volume expansions, b) the surface is a sink for silicon self-interstitials, such that metals which need interstitials for diffusion via the kick-out mechanism (like gold or platinum) are trapped, c) near-surface defects (dislocations, oxidation-induced stacking faults, surface contamination by other elements) may serve as nucleation sites for metal precipitation, d) some metals may become trapped in silicon oxide as the oxide grows, e) segregation to the surface, i.e. surface chemisorption.

During the last few years, silicon wafer bonding has become more and more interesting as a basic technology for silicon-on-insulator (SOI) devices and power electronics (see [294,295] and references therein). Yang et al [296,297] have shown that the bonded interface of directly bonded FZ silicon wafers is an effective gettering site for gold and copper. They found that gold was distributed in a double U profile in the bonded wafer pair with a maximum at the bonded interface. Copper was found to precipitate at the bonded interface by forming single colonies or pyramidal-shaped interfaces. Kissinger et al [298] compared gettering efficiency of copper at a direct bonded interface with the gettering efficiency of bulk oxygen precipitate-related gettering sites in CZ silicon. They showed that in wafer pairs without intentionally grown internal gettering sites, copper precipitated primarily at the bonded interface. In wafers which received oxygen precipitate nucleation annealing, copper precipitated mainly in the bulk defect zone and only few precipitates were detected at the bonded interface. Thus, internal gettering is significantly more effective than that of the bonded interface. It was speculated [297] that the mechanism of gettering by the bonding interface is essentially the same as gettering by the free silicon surface. Yang et al [297] suggested using this gettering mechanism for

proximity gettering. However, one can expect that its efficiency will be rather low since the fabricated IC devices themselves will be competitive gettering sites for the impurities.

## **REFERENCES**

See p. 796.

## CHAPTER 16

### ETCHING (*Edited by K.R. Williams*)

- 16.1 Silicon wet isotropic etch rates
- 16.2 Silicon wet orientation-dependent (anisotropic) etch rates
- 16.3 Silicon preferential (defect delineation) etch rates
- 16.4 Silicon plasmaless gas-phase etch rates
- 16.5 Silicon sputtering and ion milling etch rates
- 16.6 Silicon chemical plasma and reactive ion (RIE) etch rates
- 16.7 Silicon reactive-ion-beam and ion-beam-assisted etch rates
- 16.8 Silicon laser-assisted etch rates

## **16.1 Silicon wet isotropic etch rates**

K.R. Williams

July 1998

### **A INTRODUCTION**

Our emphasis in the Datareviews in this chapter is on technologically important etches used in microelectronics fabrication, micromachining and materials characterization.

Wet single-crystal silicon etchants can be divided into isotropic etchants, which etch at nearly the same rate in all directions, and orientation-dependent etchants, which etch at rates that vary with the crystallographic direction. The latter will be discussed in the next Datareview.

### **B ISOTROPIC ETCHESES**

The most popular etchant for isotropic wet etching is the HF + HNO<sub>3</sub> + diluent system. In these solutions, etching proceeds in two steps: silicon is oxidised by HNO<sub>3</sub>, followed by etching of the oxidation product by HF. These two acids are usually diluted by either H<sub>2</sub>O or CH<sub>3</sub>COOH. The advantages of a CH<sub>3</sub>COOH diluent have alternatively been given as preventing dissociation of HNO<sub>3</sub> (undissociated HNO<sub>3</sub> is the primary oxidant) [1,2] and as producing better wetting and therefore smoother etched surfaces [3,4]. We refer to any combination of these reagents as 'HNA' for hydrofluoric-nitric-acetic.

At low HF concentrations, the etch rate is limited by the etching of the oxide, which is typically limited by diffusion of HF to the reaction site above room temperature (the transition point depends on the concentrations) [5]. This diffusion-limited process has a lower activation energy (around 0.18 eV) and therefore a weaker dependence on temperature. Because the etch is transport-limited, HF depletion in the nearby bulk solution tends to result in etching near the centre of a mask window proceeding more slowly than near the edges of the mask. Agitation improves isotropy, giving more rounded features [6]. At these low HF concentrations, the etch rate is approximately proportional to the HF concentration [7]. At low HF and high HNO<sub>3</sub> concentrations, the etch surface is smooth [7]. The etch rate drops with use as HF is consumed [8]. Below room temperature, the etch rate becomes limited by the reaction itself, with a higher activation energy.

For a range of HNA solutions (e.g. in a ratio of 1:3:8), the silicon etch rate is reduced by more than an order of magnitude for doping levels (whether n or p type) below 10<sup>17</sup> cm<sup>-3</sup> [2,9]. This is related to the charge-carrier concentration available for charge transfer as part of the reaction.

At low HNO<sub>3</sub> concentrations, the etch rate is limited by the oxidation step, with an activation energy in the 0.43 to 0.86 eV range [5]. Oxidation of silicon and thus the etch rate is a function of crystal orientation, defects and doping [7]. Etching tends to be difficult to initiate, but is aided by a catalyst such as NaNO<sub>3</sub> [1].

The etch rate in HNA peaks at over 200 µm/min at a concentration of about 1 part 70-weight-% HNO<sub>3</sub>: 2 parts 49-weight-% HF (no added diluent).

### *16.1 Silicon wet isotropic etch rates*

The HF in HNA solutions removes native oxide films, so an HF dip is not necessary as it is with some orientation-dependent silicon etchants. Low-HF-concentration etchants can be masked with photoresist [8]; silicon nitride and gold have also been used [2]. High-HF solutions, however, cannot be used with photoresist because it tends to lift off or with silicon nitride because it is etched by HF [8]. HNA etches are not used as much commercially as alkaline etches due to the difficulty of controlling the etch rate, but are useful in rounding sharp corners in microstructures to reduce stress concentration.

Aside from the HNA system, several HF-based solutions (e.g. concentrated HF, 5:1 buffered HF) have been found to etch silicon very slowly. Besides  $\text{HNO}_3$ ,  $\text{H}_2\text{O}_2$  has been used as the oxidizing agent [10].

## **C WET-ETCH-RATE VARIATION**

Published etch rates frequently do not agree, and indeed experience with many etchants and materials shows that it is difficult to reproduce etch rates perfectly [8]. Following are sources of wet etch-rate variation that apply to the wet etches in this and the next two Datareviews:

- (1) temperature variation, both with position in a bath and over time, which affects both surface-reaction rates and diffusion rates;
- (2) depletion of reactive species with use;
- (3) loss of volatile chemicals (e.g.  $\text{H}_2\text{O}$ , HF,  $\text{NH}_3$ ) to evaporation;
- (4) mixing, whether forced or due to natural convection, which improves the etchant-concentration uniformity across a surface and in deep features [2,6,8];
- (5) stratification of a solution with depth into denser and less dense regions [8];
- (6) reaction-product blocking of chemical flow (e.g. bubbles or a passivating film);
- (7) elapsed time from the start of an etch due to (a) wetting time, (b) initially high etch rate before reactants are consumed locally and a steady-state condition is reached, or (c) time to break through a slow-etching surface film (e.g. a native oxide);
- (8) variation in applied potential [2], which can be (a) due to power-supply variation, (b) due to changes in etch-bath resistance in electrochemical etching, or (c) caused by self-biasing due to materials with different work functions in contact with the solution [11];
- (9) illumination, which can (a) bias a p-n junction in silicon and then bias the solution [12] and can also (b) generate free carriers that may assist electrochemical reactions;
- (10) contamination of the solution, which may (a) consume reactive species, (b) form an etch product that blocks the flow of fresh chemicals, or (c) catalyse a reaction;
- (11) impurities in or on the material being etched;
- (12) variation in the microstructure (i.e. grain size, grain orientation, and dislocation and stacking-fault density) of the material being etched [13];
- (13) stress in the material being etched [14];
- (14) masking material, which may also consume the etchant;
- (15) variation in distribution and fraction of the surface area exposed due to loading effects; and
- (16) variation in structure geometry (e.g. deep trenches or mask-layer undercuts).

## **D ETCH-RATE DATA**

In the following etchant recipes, ratios of reagents are for practical reasons by volume, but the reagents themselves are supplied by weight as follows (unless otherwise noted): hydrofluoric acid is approximately 49% by weight, balance water; nitric acid is 70% by weight, balance water; acetic acid is 100% (glacial); and ammonium fluoride is 40% by weight, balance water.

### 16.1 Silicon wet isotropic etch rates

Etch-rate data for silicon in HNA etchants (including water replacing acetic acid) are given in TABLE 1 in  $\mu\text{m}/\text{min}$ . Silicon etch rates in other isotropic etchants are in TABLE 2 in  $\text{nm}/\text{min}$ . The etch rates of several other materials used in micromachining and microfabrication in HF-based etchants have been measured by Williams and Muller [8]. Many other isotropic etchants are discussed by Kern [15,16].

TABLE 1 Isotropic wet etch rates of silicon in HNA etchants.

Etchant	Temperature ( $^{\circ}\text{C}$ )	Etch rate ( $\mu\text{m}/\text{min}$ )	Remarks	Ref
7 $\text{HNO}_3$ (69.5%): 3 HF (49.25%)	25	127		[7]
21 $\text{HNO}_3$ : 4 HF	25	13.8 8.39 6.17	w/ large Si area w/ $\text{SiO}_2$ mask w/ AZ mask	[17]
25 $\text{HNO}_3$ : 1 HF: 25 $\text{H}_2\text{O}$	25	0.36 0.54 0.69	c-Si $n^+$ poly Si poly Si	[18]
75 $\text{HNO}_3$ : 8 HF: 17 $\text{CH}_3\text{COOH}$	25	5	'Planar etch'	[19]
5 $\text{HNO}_3$ : 3 HF: 3 $\text{CH}_3\text{COOH}$	25	50–75	'CP-4'	[5]
40 $\text{HNO}_3$ : 1 HF: 15 $\text{CH}_3\text{COOH}$	25	0.15 {111} 0.20 {100}	'B-etch'	[19]
3 $\text{HNO}_3$ : 1 HF: 10 $\text{CH}_3\text{COOH}$	25	3	sensitive to type and density of dopants	[19]
27 $\text{HNO}_3$ : 27 HF: 46 $\text{CH}_3\text{COOH}$	25	25		[17]
126 $\text{HNO}_3$ : 60 $\text{H}_2\text{O}$ : 5 $\text{NH}_4\text{F}$	20	0.15 0.31 0.10	c-Si (100) $n^+$ poly Si undoped poly Si 'Trilogy etch'	[8]

TABLE 2 Isotropic wet etch rates of silicon in other etchants.

Etchant	Temperature ( $^{\circ}\text{C}$ )	Etch rate ( $\text{nm}/\text{min}$ )	Remarks	Ref
HF (48%)	25	0.03 0.07	c-Si a-Si	[20]
1 HF (48%): 4 $\text{H}_2\text{O}$	25	0.047		[20]
7 $\text{NH}_4\text{F}$ (40%): 1 HF (48%)	25	0.04	7:1 buffered HF	[21]
5 $\text{NH}_4\text{F}$ : 1 HF	20	0.9 0.2	$n^+$ poly Si undoped poly Si	[8]
20 $\text{H}_2\text{O}$ : 1 $\text{H}_2\text{O}_2$ : 1 HF	20	1.2	$n^+$ poly Si	[8]

## E CONCLUSION

This Datareview has summarised the properties of the isotropic wet etching systems for crystalline silicon based on HF +  $\text{HNO}_3$  + diluent. The etches proceed in two steps with the  $\text{HNO}_3$  oxidising the silicon and the HF etching the oxide. The various sources of etch-rate variation are listed as are typical values of etch rates.

## REFERENCES

- [1] H. Robbins, B. Schwartz [ *J. Electrochem. Soc. (USA)* vol.107 (1960) p.108-11 ]
- [2] M.J. Madou [ *Fundamentals of Microfabrication* (CRC Press, 1977) ch.4 ]
- [3] M.W. Jenkins [ *J. Electrochem. Soc. (USA)* vol.124 (1977) p.948 ]

## 16.1 Silicon wet isotropic etch rates

- [4] W.R. Runyan, K.E. Bean [ *Semiconductor Integrated Circuit Processing Technology* (Addison Wesley, 1990) ch.6.2 ]
- [5] B. Schwartz, H. Robbins [ *J. Electrochem. Soc. (USA)* vol.108 (1961) p.365 ]
- [6] K.E. Petersen [ *Proc. IEEE (USA)* vol.70 (1982) p.420-57 ]
- [7] B. Schwartz, H. Robbins [ *J. Electrochem. Soc. (USA)* vol.123 (1976) p.1903 ]
- [8] K.R. Williams, R.S. Muller [ *J. Microelectromech. Syst. (USA)* vol.5 (1996) p.256-69 ]
- [9] H. Muraoka, T. Ohashi, T. Sumitomo [ *Proc. Semiconductor Silicon* Chicago, USA, 1973, p.327-38 ]
- [10] B. Tuck [ *J. Mater. Sci. (UK)* vol.10 (1975) p.321 ]
- [11] C.M.A. Ashruf, P.J. French, P.M. Sarro, M. Nagao, M. Esashi [ *Sens. Actuators A (Switzerland)* vol.66 (1998) p.284-91 ]
- [12] H. Nielsen, D. Hackleman [ *J. Electrochem. Soc. (USA)* vol.130 (1983) p.708-12 ]
- [13] D.A. Sechenov, V.N. Fomina, V.V. Bespyatov, A.P. Arushanov [ *Phys. Chem. Mater. Treat. (UK)* vol.17 (1983) p.492-6 ]
- [14] I. Stiharu, R. Bhat, M. Kahrizi, L. Landsberger [ *Proc. SPIE. – Int. Soc. Opt. Eng. (USA)* vol.2015 (1993) p.243-62 ]
- [15] W. Kern [ *RCA Rev. (USA)* vol.39 (1978) p.278 ]
- [16] W. Kern, C.A. Deckert [ in *Thin Film Processes* Eds J.L. Vossen, W. Kern (Academic Press, New York, 1978) ch.V-1 ]
- [17] G. Kaminsky [ *J. Vac. Sci. Technol. B (USA)* vol.3 (1985) p.1015-24 ]
- [18] S.B. Felch, J.S. Sonico [ *Solid State Technol. (USA)* vol.29 (1986) p.70 ]
- [19] K.E. Bean [ *IEEE Trans. Electron Devices (USA)* vol.ED-25 (1978) p.1185 ]
- [20] S.M. Hu, D.R. Kerr [ *J. Electrochem. Soc. (USA)* vol.114 (1967) p.414 ]
- [21] W. Hoffmeister [ *J. Appl. Radiat. Isotopes* vol.2 (1969) p.139 ]

## 16.2 Silicon wet orientation-dependent (anisotropic) etch rates

K.R. Williams

January 1999

### A PROPERTIES OF ORIENTATION-DEPENDENT (ANISOTROPIC) ETCHEs

Wet orientation-dependent etches (ODEs) are aqueous alkaline solutions that anisotropically etch silicon at rates that vary with crystallographic direction. ODEs etch rapidly in <110>, <100>, and some higher-order crystal directions, effectively terminating at {111} planes as the etch rate drops by over an order of magnitude. Several authors have attributed the low {111} etch rate to high atomic packing density [1], but this theory has not adequately been extended to explain the differences in etch rates of other planes.

In the most common application of orientation-dependent etching, a (100) silicon surface is etched through a rectangular mask window whose sides are parallel to <110> directions. The etch proceeds downward until {111} planes are reached, forming a V-shaped pit. The angle of the sidewalls with the removed surface can be calculated from vector mathematics to be 54.74°, but with silicon wafers this will vary slightly as the alignment of the surface and wafer flat with the crystal directions is rarely perfect. Alternatively, trenches with vertical sidewalls can be formed in a (110) surface using a parallelogram-shaped mask window with sides parallel to <111> directions.

When {111} planes meet at concave corners of a mask, etching effectively halts. At convex corners, however, undercutting of the mask occurs [2], with the fastest-undercutting planes being {411} [3,4]. Mask misalignment with respect to the crystal also results in mask undercutting until {111} planes are reached. Shaping the undercutting of masks by adding mask structures to convex corners (known as corner compensation) is sufficiently important that several papers and simulation programs have been written addressing the subject [3,5–8].

The order of directional etch rates varies considerably with conditions and even etchant. A representative order based on several sources, from fastest to slowest-etching planes, is {411}, {110}, {311}, {441}, {211}, {100}, {331}, {221}, {111} [4,9,10]. Etch-rate ratios for the primary directions <110>:<100>:<111> range from 20:12:1 up to 400:200:1 [11–13].

In addition to dependence on orientation, ODEs also slow or stop etching at heavily boron-doped (p-type) regions. As explained by Seidel [14] and by Raley [15], at intermediate steps in the electrochemical reaction, four free electrons are generated that reside in the silicon near the etch surface before being exchanged. p-Type doping reduces this surface supply of electrons. The etch rate in ethylenediamine and weaker potassium hydroxide solutions (described below) decreases with the fourth power of the concentration beyond degeneracy, which occurs at about  $2 \times 10^{19} \text{ cm}^{-3}$  of active boron atoms. The drop in etch rate varies with etchant.

While p<sup>+</sup> silicon is used as an etch stop without the application of an external bias, KOH can be made to etch through a p-type layer and stop on n-type silicon with the use of an electrochemical etch stop by protecting the n-type silicon from the solution and reverse-biasing the p-n diode that is formed [16,17]. Methods of protecting one side of a wafer (applicable to both unbiased and biased etching) include coating the surface with silicon nitride or a thick wax, mechanically sealing the surface with an etch-resistant device such as a Teflon gasket, and placing wafers back to back in the etchant.

## 16.2 Silicon wet orientation-dependent (anisotropic) etch rates

Electrodeless electrochemical etching can also be performed by generating a potential from gold contacting both the n-type silicon and the etchant [18].

The rate of orientation-dependent etching is limited under most conditions by the surface reaction rate rather than mass transport, resulting in more uniform etching than with HNA isotropic etchants. Slower etching is observed, however, in the centres of larger exposed areas and deep grooves in <110> silicon. Stratification of etchant concentration has been observed in some unstirred solutions, resulting in etch-rate variation with depth in a solution [19].

ODEs also etch polycrystalline silicon, but isotropically, at rates generally faster than single-crystal silicon [19].

## B ORIENTATION-DEPENDENT ETCHANTS

### B1 Alkali Hydroxides/KOH

Alkali hydroxides such as KOH, NaOH and LiOH in water etch silicon at about the same rate for the same molarity, independent of the cation [11]. KOH is the most popular ODE, having been in industrial use for decades. It can produce a fast etch rate of several micrometres per minute at 100°C. KOH is supplied both as solid pellets (which can contain 10–15% H<sub>2</sub>O [20]) and as a pre-mixed aqueous solution.

Different chemical reactions are given in the literature for hydroxide etching of silicon [11,21]. They involve both OH<sup>-</sup> and H<sub>2</sub>O, which explains the initial increase in etch rate with KOH concentration (up to 18% by weight at 80°C), followed by a decrease at higher KOH (and therefore lower H<sub>2</sub>O) concentration [11]. Etch-surface smoothness, however, tends to improve as the concentration is increased [17], especially above 30% KOH [11]. The concentration of maximum etch rate is therefore usually not used because of the rough surfaces and because of the formation of insoluble residues below 15% KOH [11]. A concentration of 30% KOH by weight at 80°C is a representative etch. Higher temperatures give a faster etch, with an activation energy E<sub>A</sub> of 0.595 eV used in the curve-fit equation

$$\{100\} \text{ etch rate of Si in KOH} = k_0 [\text{H}_2\text{O}]^4 [\text{KOH}]^{1/4} \exp(-E_A/kT) \quad (1)$$

where the concentrations are in mol/litre and  $k_0 = 413 \mu\text{m}/\text{min} \cdot (\text{mol/litre})^{-4.25}$  [11]. (The density and molecular weight of KOH are 2.055 g/cm<sup>3</sup> and 56.11 g/mol, respectively, and 1.00 g/cm<sup>3</sup> and 18.02 g/mol for water [22].)

KOH etching has several disadvantages. Hydrogen gas bubbles are evolved during etching, which can locally block the transport of reactants to the surface, increasing roughness, and can also damage delicate microstructures. All of the alkali hydroxides, of course, contain alkali ions, which are not compatible with MOS circuitry (and therefore not allowed in many IC-fabrication facilities) that may be integrated on the same silicon chip as microstructures to produce integrated sensors. Also of concern for on-chip circuitry, KOH etches aluminium.

Adding isopropyl alcohol (IPA) to KOH solutions reduces convex-corner undercutting [12] and also improves uniformity [11], but slows etching by about 20% and lowers the {100}:{111} etch-rate ratio [12].

Boron doping can be used as an etch stop for KOH etching, but, except at KOH concentrations below about 10%, it is not as effective as in EDP etching [14]. KOH can be masked by silicon nitride or gold

## 16.2 Silicon wet orientation-dependent (anisotropic) etch rates

[2] and by silicon dioxide for short etches due to a non-negligible oxide etch rate (1–8 nm/min [14,19]). Photoresist is rapidly removed.

### B2 EDP

Ethylenediamine ( $\text{NH}_2(\text{CH}_2)_2\text{NH}_2$ ) + pyrocatechol ( $\text{C}_6\text{H}_4(\text{OH})_2$ ) + water (EDP or EDPW), sometimes with the addition of pyrazine ( $\text{C}_4\text{H}_4\text{N}_2$ ), is a classic ODE that exhibits etch rates roughly half those of KOH. Ethylenediamine and water are the primary etchants, with a maximum etch rate when mixed in a molar ratio of 2:1 [11]. Adding pyrocatechol up to 4 mol % raises the etch rate up to a factor of 3. Pyrazine has the same effect at up to 3 g/l.

EDP has the preferable properties over KOH of halting etching at boron etch stops more effectively [14], leaving generally smooth surfaces, having a much better selectivity over silicon dioxide [11], and not containing alkali ions. Because the etch rate of silicon dioxide is so low, native oxide should be removed (e.g. with a 30 s 10:1 HF dip) before EDP etching. EDP is not used as much as KOH, however, because it is considered to be too toxic, forms insoluble residues (which can be controlled somewhat by using a formulation appropriate for the temperature [23]), and ages quickly with oxygen exposure, giving a faster etch rate and turning the solution opaque [17,23].

### B3 Quaternary Ammonium Hydroxides/TMAH

Several quaternary ammonium hydroxides, tetramethylammonium hydroxide (TMAH), tetraethylammonium hydroxide (TMEH), and choline (each in water), came into use for orientation-dependent etching in the early 1990s [13]. TMAH has the advantages over KOH of etching silicon dioxide very slowly, not containing alkali ions, and not attacking aluminium when properly ‘doped’, all of which make TMAH compatible with MOS circuitry already present on the same chip on which microstructures are to be formed. It also has the advantage over EDP of not being considered as toxic. TMAH solutions, however, have a lower etch-rate ratio of {100} to {111} planes of 12–50:1 [13,24], etch silicon at about half the rate of KOH at the same concentration and temperature [11,13], and tend to yield rougher surfaces [25]. The maximum {100} etch rate is at 2% by weight for TMAH [24] and 20% for TEAH [13] over the temperature range of 60–90°C. Smooth surfaces are obtained above 22% TMAH [13]. The {100}:{111} etch-rate ratio rises continuously as the TMAH concentration is reduced [24].

By adding 1–2 mol/l of  $\text{NH}_4\text{HPO}_4$  (an acid) and/or dissolving over 2–4 mol/l of silicon in a 22% TMAH solution at 90°C, the pH can be raised sufficiently to reduce the etch rate of aluminium by several orders of magnitude [26]. This, however, decreases the silicon etch rate and makes the surfaces rougher.

TMAH with several per cent surfactant (30 wt % polyoxyethylene alkyl phenyl ether) added has the unusual property of etching in <100> directions faster than in <110> directions, leaving {110} planes exposed after short etches [38].

$\text{NH}_4\text{OH}$  has also been used experimentally, but was slower than KOH and resulted in rough surfaces [27]. The addition of  $\text{H}_2\text{O}_2$  gave smoother surfaces and faster etch rates.

### B4 Other ODEs

Hydrazine + water [28] is an ODE that has only been used to a limited degree. Because it is toxic and hydrazine by itself is explosive, it is not commonly used. It is clear that it has maximum practical etch

## 16.2 Silicon wet orientation-dependent (anisotropic) etch rates

rates similar to KOH (several  $\mu\text{m}/\text{min}$ ), stops etching on oxide and heavy p-type doping, and can be masked by most metals (but not Al), but has a lower  $\{100\}:\{111\}$  selectivity than KOH.

Linde and Austin [29] studied combinations of several amines and complexing agents in water. Gallic acid + ethanolamine + pyrazine + water was found to be the most useful. It has etch rates similar to KOH, stops on heavily boron-doped regions better than EDP, etches silicon dioxide slowly, does not contain alkali ions, and does not present the toxicity problems of EDP and hydrazine.

### C ETCH-RATE DATA

Etch rates of the above etchants under a variety of concentrations and temperatures are found in TABLES 1–4. Concentrations are by weight unless otherwise noted.

TABLE 1 Silicon orientation-dependent etch rates in KOH.

Etchant	Temperature (°C)	Direction (plane)	Etch rate ( $\mu\text{m}/\text{min}$ )	Remarks	Ref	
20% KOH: 80% $\text{H}_2\text{O}$	20	(100)	0.025	Near peak etch rate at this conc. across temperature	[11]	
	40	(100)	0.118			
	60	(100)	0.45			
	80	(100)	1.4			
	100	(100)	4.1			
30% KOH: 70% $\text{H}_2\text{O}$	20	(100)	0.024	Smoothen surfaces than at lower conc.	[11]	
	40	(100)	0.108			
	60	(100)	0.41			
	80	(100)	1.3			
	100	(100)	3.8			
	20	(110)	0.035	Faster etch rate for (110) than for (100)		
	40	(110)	0.16			
	60	(110)	0.62			
	80	(110)	2.0			
	100	(110)	5.8			
40% KOH: 60% $\text{H}_2\text{O}$	20	(100)	0.020		[11]	
	40	(100)	0.088			
	60	(100)	0.33			
	80	(100)	1.1			
	100	(100)	3.1			
20% KOH: 80% (4 $\text{H}_2\text{O}$ : 1 IPA)	20	(100)	0.015	Lower etch rate Smoothen Less undercutting Lower (100):(111) etch-rate ratio	[11]	
	40	(100)	0.071			
	60	(100)	0.28			
	80	(100)	0.96			
	100	(100)	2.9			
44 % KOH: 56% $\text{H}_2\text{O}$	120	(100)	5.8	High temperature	[30]	
		(110)	11.7			
		(111)	0.02			
23.4% KOH: 63.3% $\text{H}_2\text{O}$ : 13.3% IPA	80	(100)	1.0	Sensitive to boron conc.	[31]	
		(111)	0.06			

## 16.2 Silicon wet orientation-dependent (anisotropic) etch rates

TABLE 2 Silicon orientation-dependent etch rates in EDP solutions.

Etchant	Temperature (°C)	Direction (plane)	Etch rate (μm/min)	Remarks	Ref
500 ml $\text{NH}_2(\text{CH}_2)_2\text{NH}_2$ : 88 g $\text{C}_6\text{H}_4(\text{OH})_2$ : 234 ml $\text{H}_2\text{O}$	110	(100) (110) (111)	0.47 0.28 0.028	EDP 'T' etch Oldest EDP formula ER rises to > 0.83 μm/min after exposure to oxygen	[32]
500 ml $\text{NH}_2(\text{CH}_2)_2\text{NH}_2$ : 160 g $\text{C}_6\text{H}_4(\text{OH})_2$ : 160 ml $\text{H}_2\text{O}$	115	(100)	0.45	EDP 'F' etch Fast etch rate Must be used at high T to avoid residue	[23]
F etch above w/1.0 g $\text{C}_4\text{H}_4\text{N}_2$	115	(100)	1.13	Faster w/ pyrazine Less sens. to oxygen Smoothen	[23]
F etch above w/3.0 g $\text{C}_4\text{H}_4\text{N}_2$	115	(100)	1.35		[23]
500 ml $\text{NH}_2(\text{CH}_2)_2\text{NH}_2$ : 80 g $\text{C}_6\text{H}_4(\text{OH})_2$ : 3.6 g $\text{C}_4\text{H}_4\text{N}_2$ : 66 ml $\text{H}_2\text{O}$	50 75 95 105 110	(100) (100) (100) (100) (100)	0.075 0.22 0.43 0.57 0.75	EDP 'S' etch Slower etch rate Suitable for lower temperature use without residue	[23]
46.4 mol% $\text{NH}_2(\text{CH}_2)_2\text{NH}_2$ : 4 mol% $\text{C}_6\text{H}_4(\text{OH})_2$ : 49.4 mol% $\text{H}_2\text{O}$	118	(100) (110) (111)	0.83 0.50 0.017	Stops on p <sup>++</sup>	[33]
250 ml $\text{NH}_2(\text{CH}_2)_2\text{NH}_2$ : 45 g $\text{C}_6\text{H}_4(\text{OH})_2$ : 120 ml $\text{H}_2\text{O}$	110	(100) (111)	1.1 negl.		[34]

TABLE 3 Silicon orientation-dependent etch rates in ammonium hydroxide and TMAH.

Etchant	Temperature (°C)	Direction (plane)	Etch rate (μm/min)	Remarks	Ref
2.64 M $\text{NH}_4\text{OH}$ in $\text{H}_2\text{O}$	80	(100)	0.50		[27]
2.64 M $\text{NH}_4\text{OH}$ : 0.0065– 0.0184 M $\text{H}_2\text{O}_2$ in $\text{H}_2\text{O}$	80	(100)	1.25 2.0	p Si n <sup>++</sup> Si	[27]
5% TMAH: 95% $\text{H}_2\text{O}$	60 70 80 90 60 70 80 90 60 90	(100)  (110)  (111)	0.33 0.48 0.87 1.4 0.64 0.74 1.4 1.8 0.026 0.034		[13]
10% TMAH: 90% $\text{H}_2\text{O}$	60 70 80 90	(100)	0.28 0.41 0.72 1.2		[13]
2% TMAH: 98% $\text{H}_2\text{O}$	80	(100) (111)	0.65 0.41		[24]
5% TMAH: 95% $\text{H}_2\text{O}$	80	(100) (111)	0.63 0.013		[24]
10% TMAH: 90% $\text{H}_2\text{O}$	80	(100) (111)	0.57 0.014		[24]

## 16.2 Silicon wet orientation-dependent (anisotropic) etch rates

Etchant	Temperature (°C)	Direction (plane)	Etch rate (μm/min)	Remarks	Ref
22% TMAH in H <sub>2</sub> O	90	(100) (110) (111)	0.9 1.8 0.018	(110) is fastest without surfactant	[38]
22% TMAH in H <sub>2</sub> O + 0.5% surfactant	90	(100) (110) (111)	0.6 0.12 0.01	(100) is fastest with surfactant	[38]
22% TMAH in H <sub>2</sub> O + 1% surfactant	90	(100) (110) (111)	0.6 0.1 0.009	Surfactant effect saturates	[38]

TABLE 4 Silicon orientation-dependent etch rates in other ODEs.

Etchant	Temperature (°C)	Direction (plane)	Etch rate (μm/min)	Remarks	Ref
50% N <sub>2</sub> H <sub>4</sub> : 50% H <sub>2</sub> O	100	(100) (111)	2.0 negl.	Sensitive to temp. and dopant conc.	[35,36]
50% N <sub>2</sub> H <sub>4</sub> : 50% H <sub>2</sub> O	70 100	(100)	1.5 3.3		[28]
1 mol/l Cu(NO <sub>3</sub> ) <sub>2</sub> : 4 mol/l NH <sub>4</sub> F	22	(100) (110) (111)	0.185 0.117 0.012		[37]
100 g gallic acid: 305 ml ethanolamine: 140 ml water: 1.3 g pyrazine: 0.26 ml 10% FC-129 surfactant	118 108 97	(100) (111) (100) (100)	1.7 0.017–0.034 0.10 0.05		[29]

## D CONCLUSION

This Datareview has summarised the properties of the anisotropic wet etching systems for crystalline silicon based on aqueous alkaline solutions, both inorganic and organic in origin. These etches effectively stop at {111} and on heavy p-type doping planes. Typical values of etch rates are tabulated.

## REFERENCES

- [1] K.E. Bean [ *IEEE Trans. Electron Devices (USA)* vol.ED-25 (1978) p.1185-93 ]
- [2] K.E. Petersen [ *Proc. IEEE (USA)* vol.70 (1982) p.420-57 ]
- [3] G.K. Mayer, H.L. Offereins, H. Sandmeier, K. Kuhl [ *J. Electrochem. Soc. (USA)* vol.137 (1990) p.3947-51 ]
- [4] R.P. van Kampen [ *Bulk-Micromachined Capacitive Servo-Accelerometer* (Delft University Press, 1995) p.166-77 ]
- [5] H. Sandmaier, H.L. Offereins, K. Kuhl, W. Lang [ *Proc. 1991 Int. Conf. Solid-State Sensors and Actuators (Transducers '89)* San Francisco, USA, 1991, p.456-9 ]
- [6] Y. He, J. Marchetti, S. Akkaraju [ *SPIE Int. Symp. on Micromachining and Microfabrication* Santa Clara, USA, Sept. 1998 ]
- [7] K. Nishidate, M. Baba, R.J. Gaylord [ *Comput. Phys. (USA)* vol.12 (1998) p.88-93 ]
- [8] O. Than, S. Buttgenbach [ *Sens. Actuators A (Switzerland)* vol.45 (1994) p.85-9 ]
- [9] E. Herr, H. Baltes [ *Proc. 6th Int. Conf. Solid-State Sensors and Actuators (Transducers '91)* San Francisco, USA, 1991 (IEEE, New York, NY, 1991) p.807-10 ]
- [10] P. Barth [ *Proc. Micro-electrochemical Devices-Photonics, Materials, Sensors, and Technology* 1984 ]

## 16.2 Silicon wet orientation-dependent (anisotropic) etch rates

- [11] H. Seidel, L. Cseperege, A. Heuberger, H. Baumgarel [ *J. Electrochem. Soc. (USA)* vol. 137 (1990) p.3626-32 ]
- [12] D.L. Kendall [ *J. Vac. Sci. Technol. A (USA)* vol.5 (1990) p.3598-605 ]
- [13] O. Tabata, R. Asahi, H. Funabashi, K. Shimaoka, S. Sugiyama [ *Sens. Actuators A (Switzerland)* vol.34 (1992) p.51-7 ]
- [14] H. Seidel, L. Cseperege, A. Heuberger, H. Baumgarel [ *J. Electrochem. Soc. (USA)* vol. 137 (1990) p.3612-26 ]
- [15] N.F. Raley, Y. Sugiyama, T. Van Duzer [ *J. Electrochem. Soc. (USA)* vol.131 (1984) p. 161-71 ]
- [16] B. Kloeck, S.D. Collins, N.F. de Rooij, R.L. Smith [ *IEEE Trans. Electron Devices (USA)* vol.36 (1989) p.663-9 ]
- [17] M.J. Madou [ *Fundamentals of Microfabrication* (CRC Press, 1977) p.168-98 ]
- [18] C.M.A. Ashruf, P.J. French, P.M. Sarro, M. Nagao, M. Esashi [ *Sens. Actuators A (Switzerland)* vol.66 (1998) p.284-91 ]
- [19] K.R. Williams, R.S. Muller [ *J. Microelectromech. Syst. (USA)* vol.5 (1996) p.256-69 ]
- [20] Fisher Chemical/Fisher Scientific [ *Bottle label of potassium hydroxide, solid* Fisher Chemical, Fair Lawn, New Jersey, USA, 1996 ]
- [21] W.R. Runyan, K.E. Bean [ *Semiconductor Integrated Circuit Processing Technology* (Addison Wesley, 1990) ch.6.2 ]
- [22] R.C. Weast (Ed.) [ *CRC Handbook of Chemistry and Physics, 65th edn.* (CRC Press, Boca Raton, Florida, USA, 1984) p.B-100 and p.B-128 ]
- [23] A. Reisman, M. Berkenbilt, S.A. Chan, F.B. Kaufman, D.C. Green [ *J. Electrochem. Soc. (USA)* vol.126 (1979) p.1406-14 ]
- [24] U. Schnakenberg, W. Benecke, P. Lange [ *Proc. 1991 Int. Conf. Solid-State Sensors and Actuators (Transducers '91)* San Francisco, USA, 1991 (IEEE, New York, NY, 1991) p.815-8 ]
- [25] G.T.A. Kovacs [ *Micromachined Transducers Sourcebook* (WCB McGraw-Hill, 1998) ch.5.1 ]
- [26] O. Tabata [ *Sens. Actuators A (Switzerland)* vol.53 (1996) p.337-9 ]
- [27] U. Schnakenberg, W. Benecke, B. Lochel, S. Ullerich, P. Lange [ *Sens. Actuators A (Switzerland)* vol.25-27 (1991) p.1-7 ]
- [28] M. Mehregany, S.D. Senturia [ *Sens. Actuators (Switzerland)* vol.13 (1988) p.375-90 ]
- [29] H. Linde, L. Austin [ *J. Electrochem. Soc. (USA)* vol.139 (1992) p.1170-4 ]
- [30] D.L. Kendall [ *Annu. Rev. Mater. Sci. (USA)* vol.9 (1979) p.373 ]
- [31] J.B. Price [ *Semiconductor Silicon-1973* Eds. H.R. Huff, R.R. Burgess (Electrochem. Soc., Pennington, 1973) p.339 ]
- [32] R.M. Finne, D.L. Klein [ *J. Electrochem. Soc. (USA)* vol.114 (1967) p.965-70 ]
- [33] E. Bassous [ *IEEE Trans. Electron Devices (USA)* vol.ED-25 (1978) p.1178 ]
- [34] G. Kaminsky [ *J. Vac. Sci. Technol. B (USA)* vol.3 (1985) p.1015-24 ]
- [35] D.B. Lee [ *J. Appl. Phys. (USA)* vol.40 (1969) p.4569 ]
- [36] M.J. DeClercq, L. Gerzberg, J.D. Meindl [ *J. Electrochem. Soc. (USA)* vol.122 (1975) p.545 ]
- [37] W.K. Zwicker, S.K. Kurtz [ *Semiconductor Silicon-1973* Eds. H.R. Huff, R.R. Burgess (Electrochem. Soc., Pennington, 1973) p.315 ]
- [38] M. Sekimura [ *Proc. 12<sup>th</sup> IEEE Int. Micro-Electro Mechanical Systems Conf. (MEMS 1999)*, Orlando, Florida, USA, p.650-5 ]

## **16.3 Silicon preferential (defect delineation) etch rates**

K.R. Williams

July 1998

### **A INTRODUCTION**

Preferential etches are used to delineate crystal defects such as dislocations, stacking faults and twins by removing material faster where the defects meet the surface. The etch-rate enhancement is due to a higher local reaction rate, rather than being transport-limited [1]. Sechenov et al [2] give a theoretical basis for the higher etch rate of defects in silicon. Etching is sensitive to crystallographic orientation, doping level, temperature and agitation.

### **B ETCH-RATE DATA**

All of the silicon preferential etches given in the literature use a two-step etch process similar to the HNA etchants (discussed in Datareview 16.1): silicon is first oxidised, then the resulting oxidised material is etched by HF. A few preferential etches use  $\text{HNO}_3$  as an oxidising agent, but most researchers have achieved better results by adding or instead using the  $\text{Cr}_2\text{O}_7^{2-}$  ion, which can come from  $\text{K}_2\text{Cr}_2\text{O}_7$  (which has a low solubility in water [3]) or be formed from  $\text{CrO}_3$  in water [4].

The oldest of the preferential etches, the Dash etch [5,6], reveals defects in both (100) and (111) silicon surfaces, but is very slow, taking several hours to form sufficient pits [4]. The Sirtl etch [7] works faster on (111) surfaces. The Secco etch delineates low-angle grain boundaries and slip lines in (100) silicon well [8], but gives elliptically shaped dislocation pits [4] and may generate anomalous defect etch pits due to cavitation during ultrasonic agitation [9]. These three etchants seem to have been superseded by newer etches.

The Schimmel etch [9] targets (100) silicon surfaces of both p- and n-type with lower doping (resistivities of 0.6–15  $\Omega \text{ cm}$ ), while the modified Schimmel etch is geared toward more heavily doped silicon. It takes about half as long as the Secco etch to produce etch pits of equivalent size, but the pits are circular [3]. It does not require ultrasonic agitation.

The Wright etch [4] gives clear orientation-dependence of defects on (100) and (111) surfaces, has enhanced etching of defects due to the inclusion of an oxidising agent from  $\text{Cu}(\text{NO}_3)_2$ , works over a wide resistivity range (0.02–20  $\Omega \text{ cm}$ ), and is very stable at room-temperature storage for several weeks, but may be insensitive to dislocations generated during crystal growth [3]. It produces a smooth surface surrounding defects, possibly due to the wetting action of the  $\text{CH}_3\text{COOH}$  [4]. Agitation is not needed with wafers oriented vertically, but is needed with horizontal wafers to prevent surface deposits. The solution is saturated when it becomes discoloured and leaves artifacts.

Yang [3] has studied the effects of varying the ratio of  $\text{CrO}_3$  to HF in preferential etches. The resulting Yang etch is better at revealing dislocations generated by crystal growth than the Wright etch [3]. Preferential etching for this etchant occurs more easily on (111) than (100) surfaces, and also works on (110) surfaces. Each surface orientation gives a unique dislocation etch-pit shape. Care must be taken to avoid artifacts such as mounds formed by  $\text{CrF}_3$  precipitates, but their rate of formation is slower than in Wright and Schimmel etches. No agitation is required.

### 16.3 Silicon preferential (defect delineation) etch rates

The Sopori etch is optimised for revealing defects in polycrystalline silicon.

Preferential etch compositions and notes on their use are given in TABLE 1 in historical order. Mixture ratios are by volume, while reagent concentrations are by weight or molarity as noted. Etch rates are for the smooth, defect-free regions of the silicon surface.

TABLE 1 Preferential etch rates.

Etchant	Temperature (°C)	Target surface	Etch rate (μm/min)	Name/remarks	Ref
1 HF (49%): 3 HNO <sub>3</sub> (70%): 10 CH <sub>3</sub> COOH (100%)	20	(100) (111)	0.13 0.005	Dash etch Slow etch requires long etch time (esp. (111)) Slows at low doping	[5,6]
1 HF (49%): 1 CrO <sub>3</sub> (5 M)	20	(111)	3.0	Sirtl etch Not as good for (100)	[7]
1 HF (49%): 1 K <sub>2</sub> Cr <sub>2</sub> O <sub>7</sub> (0.15 M)	20	(100)	1.5	Secco etch Agitation speeds etch Good for linear defects	[8]
60 ml HF (49%): 30 ml HNO <sub>3</sub> (69%): 30 ml CrO <sub>3</sub> (5 M (1 g CrO <sub>3</sub> :2 ml H <sub>2</sub> O)): 2 g Cu(NO <sub>3</sub> ) <sub>2</sub> ·3 H <sub>2</sub> O: 60 ml CH <sub>3</sub> COOH (100%): 60 ml H <sub>2</sub> O	20	(100) (111)	1.0 not spec.	Wright etch Add Cu(NO <sub>3</sub> ) <sub>2</sub> to H <sub>2</sub> O first Good for OSF, swirl, striations	[4]
2 HF (49%): 1 CrO <sub>3</sub> (5 M)	20	(100)	~1.8	Schimmel etch For resistivity range 0.6–15 Ω cm	[9]
2 HF (49%): 1 CrO <sub>3</sub> (1 M): 1.5 H <sub>2</sub> O	20	(100)	~1.8	Modified Schimmel etch For resistivities below 0.6 Ω cm	[9]
1 HF (49%): 1 CrO <sub>3</sub> (1.5 M)	20	(100) (111) (110)	~1.5 ~1.5 not spec.	Yang etch No agitation needed	[3]
36 HF (49%): 1–2 HNO <sub>3</sub> (70%): 20 CH <sub>3</sub> COOH (100%)	20	Polysilicon	5–20	Sopori etch For defects in polysilicon	[10]

## C CONCLUSION

This Datareview has summarised the properties of preferential wet etching systems for crystalline silicon based on various solutions. These etches reveal crystal defects such as dislocations, stacking faults and twins. Typical values of etch rates are tabulated.

## REFERENCES

- [1] B. Tuck [ *J. Mater. Sci. (UK)* vol.10 (1975) p.321-39 ]

- [2] D.A. Sechenov, V.N. Fomina, V.V. Bespyatov, A.P. Arushanov [ *Phys. Chem. Mater. Treat.* (UK) vol.17 (1983) p.492-6 ]
- [3] K.H. Yang [ *J. Electrochem. Soc. (USA)* vol.131 (1984) p.1140 ]
- [4] M.W. Jenkins [ *J. Electrochem. Soc. (USA)* vol.124 (1977) p.757-62 ]
- [5] K.E. Bean [ *IEEE Trans. Electron Devices (USA)* vol.ED-25 (1978) p.1185 ]
- [6] W.C. Dash [ *J. Appl. Phys. (USA)* vol.27 (1956) p.1193 ]
- [7] E. Sirtl, A. Adler [ *Z. Met.kd. (Germany)* vol.52 (1961) p.529 ]
- [8] F. Secco d'Aragona [ *J. Electrochem. Soc. (USA)* vol.119 (1972) p.948 ]
- [9] D.G. Schimmel [ *J. Electrochem. Soc. (USA)* vol.126 (1979) p.479 ]
- [10] B.L. Sopori [ *J. Electrochem. Soc. (USA)* vol.131 (1984) p.667 ]

## CHAPTER 17

### METAL-SILICON CONTACTS *(Edited by L. Schowalter)*

- 17.1 Recent advances in silicide technologies
- 17.2 Epitaxial silicide contacts

# 17.1 Recent advances in silicide technologies

K. Maex

January 1998

## A INTRODUCTION

Silicide formation is a key process step in current integrated circuit (IC) fabrication. The silicides are introduced to lower sheet resistance of poly-runners and to shunt the highly doped source/drain regions. In this Datareview, an overview will be given of the various materials aspects of silicidation of Co and Ti and their implementation in a full IC fabrication process.

## B THERMAL PROCESS WINDOW EVOLUTION OF $\text{TiSi}_2$ AND $\text{CoSi}_2$

The technological implementation of a material in a full IC process is built on a detailed knowledge about the material and its formation [1,2]. This is particularly so for silicidation, since the reaction is very sensitive to many factors that change its kinetics. From a thermodynamic point of view, a system consisting of a thin metal film on a Si substrate is far from equilibrium. When kinetic constraints are removed, e.g. by heating and allowing elements to diffuse, the system will evolve in order to lower its free energy by the formation of intermetallic compounds. For Co on Si, a Co-rich phase,  $\text{Co}_2\text{Si}$ , forms prior to the monosilicide,  $\text{CoSi}$ . These reactions are diffusion controlled. The final phase of the reaction is  $\text{CoSi}_2$  and its formation is nucleation controlled. The specific resistivity of  $\text{CoSi}$  and  $\text{CoSi}_2$  are  $180 \mu\Omega \text{ cm}$  and  $18 \mu\Omega \text{ cm}$ , respectively.

In the case of Ti on Si, the  $\text{TiSi}_2$  phase forms immediately. There are, however, two allotropic  $\text{TiSi}_2$  phases i.e. one with the (highly defective) C49 structure and one with the C54 structure. The transformation is nucleation controlled and only the C54 phase has the desired low resistivity. The nucleation of the C54 phase from the C49 phase becomes more difficult for thinner layers and narrower areas. This cumbersome transformation is inherently a problem for the scaling of  $\text{TiSi}_2$ . The C49  $\text{TiSi}_2$  has a specific resistivity of about  $60 \mu\Omega \text{ cm}$ , whereas C54  $\text{TiSi}_2$  has one equal to  $15 \mu\Omega \text{ cm}$ .

For both Ti and Co systems, the silicide phase which is in thermal equilibrium with Si, the disilicide, also has the lowest electrical resistivity among their competing compounds. A counter example to that is the Ni/Si system for which  $\text{NiSi}_2$  is the most stable compound but  $\text{NiSi}$  has the lowest specific resistivity. Moreover the solid solubility of Ti and of Co in Si is extremely low ( $10^{16} \text{ Co/cm}^3$  and  $10^{14} \text{ Ti/cm}^3$  at  $1200^\circ\text{C}$ ), such that Ti and Co impurities remain at a level where they do not interfere with the almost ideal semiconducting properties of Si.

In a self-aligned silicidation process, the silicidation of the metal occurs selectively on the exposed Si areas (see FIGURE 1). In order to avoid lateral diffusion of Si in the overlaying metal, commonly two steps are used to complete the reaction. In a first temperature step, denoted as RTP1, the reaction is started and the silicide growth is strictly confined to the Si areas. No interactions should occur between the metal and Si-oxide or -nitride layers. After washing away the unreacted metal, the silicidation reaction is completed in a second temperature step, denoted as RTP2, allowing for a higher temperature for the final phase formation. Since Ti reacts with the  $\text{N}_2$  ambient, a competing Ti-N reaction will take place and the chemical etch will remove the TiN formed on top of the silicided areas and on top of the dielectrics. In the case of  $\text{CoSi}_2$ , in general, all the Co on Si has reacted and the chemical removal of Co is limited to the isolation areas.

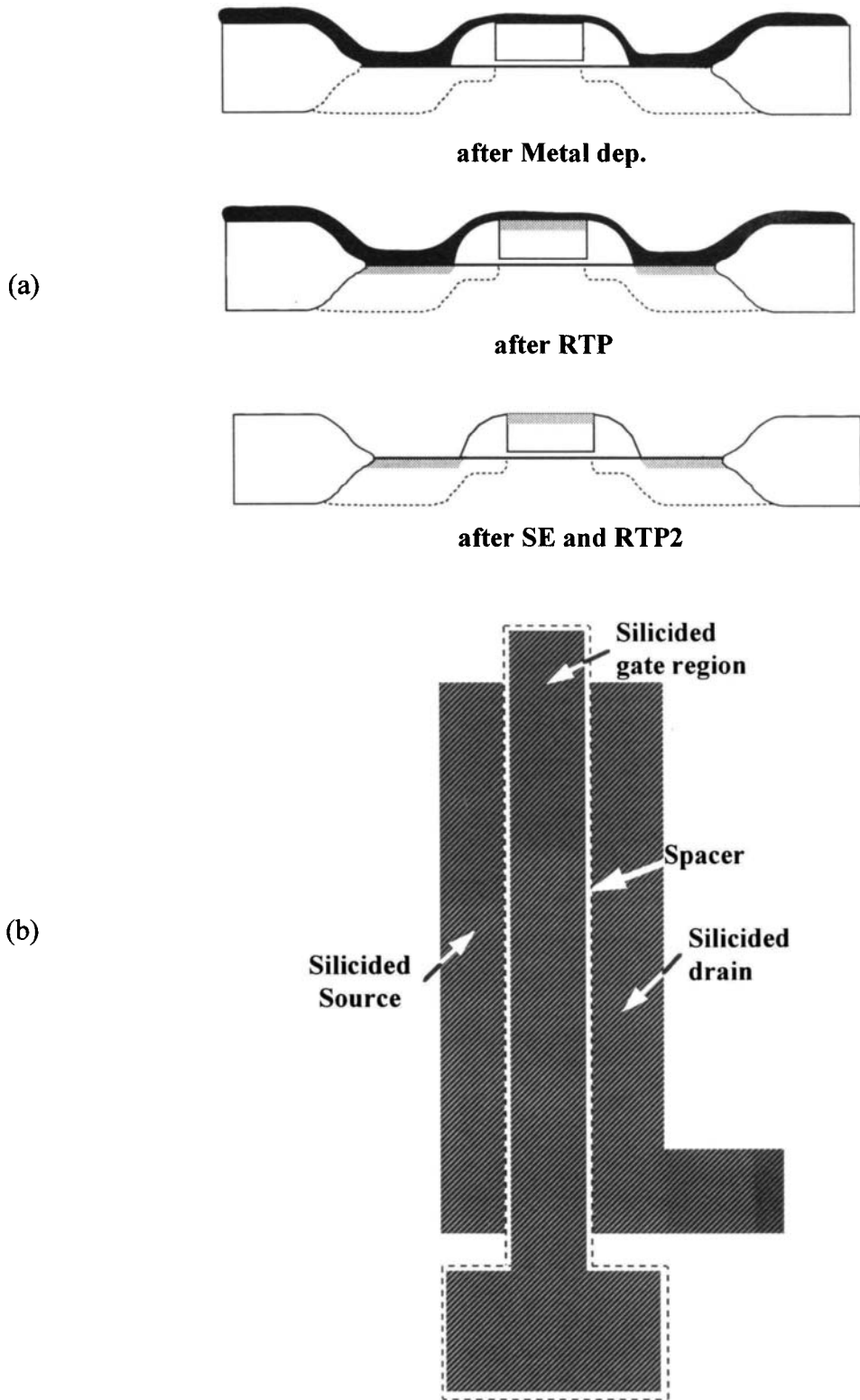


FIGURE 1 Cross-section and plan view drawing of a transistor.

In a self-aligned silicidation process, the temperature windows of both RTP1 and RTP2 are important. RTP1 defines the thickness of the silicide, since the remainder of the metal will be removed in the selective etch. It also determines the process latitude for lateral growth. The distance between

## 17.1 Recent advances in silicide technologies

source/drain and gate is determined by the spacer and is therefore very small. Any lateral formation of silicide over the spacer would be detrimental for the yield of the process. The process window for RTP2 is defined by a minimal lower temperature, that is required to achieve the formation of the low resistive phase, and a maximal temperature, that is defined by the thermal disintegration of the silicide.

In the case of Co/Si, the process window for RTP1 is critical. Indeed, one aims at the situation where all the Co is converted to CoSi, without lateral growth of the silicide. The most important parameters to improve the process window are cleaning prior to metal deposition and the use of a capping layer. The dependence of the silicidation on doping level, doping type and crystallinity of the substrate is fairly small. The nucleation of the  $\text{CoSi}_2$  phase from the CoSi is triggered by the removal of the remaining Co [3]. Therefore, the  $\text{CoSi}_2$  formation temperature decreases as film thickness shrinks. Both CoSi formation during RTP1 and  $\text{CoSi}_2$  formation during RTP2 are linewidth independent. In FIGURE 2 sheet resistance data are reported for  $\text{CoSi}_2$  down to 0.08  $\mu\text{m}$  linewidth. A sheet resistance of less than 5  $\Omega/\text{sq}$  can be achieved for all lines down to 0.12  $\mu\text{m}$  [4]. Only the narrowest lines have a yield loss of about 50%. This confirms the independent nature of linewidth of the Co-silicidation process. A more detailed discussion on the scalability of the various processes follows in Section D.

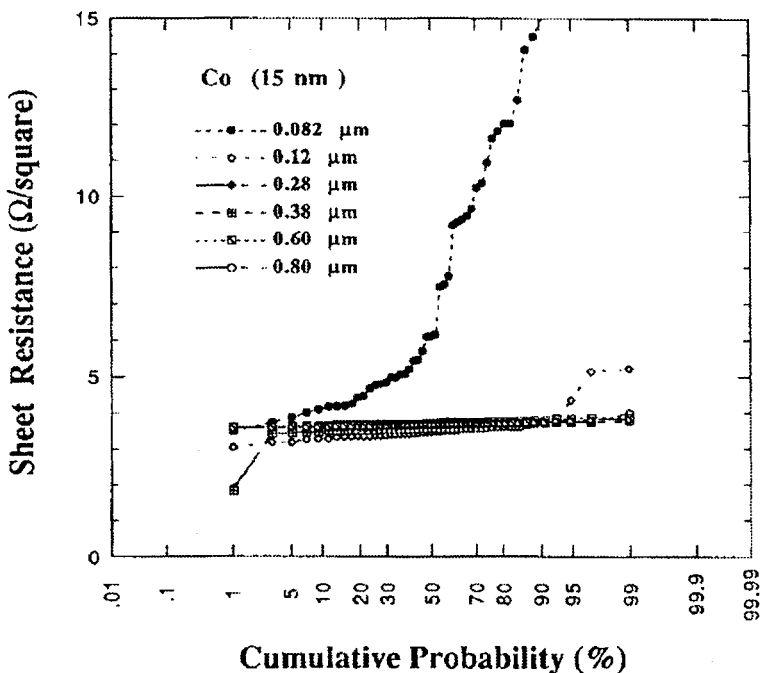


FIGURE 2 Cumulative plot of the sheet resistance of silicided poly-Si runners for various linewidths. The silicide grown was  $\text{CoSi}_2$  from a 15 nm Co film.

For  $\text{TiSi}_2$ , the process window of RTP2 is critical. The lower temperature is the one required for the formation of the low resistivity phase. This is, for example, the temperature where the transition of the C49 into the C54 phase is completed. The higher temperature is related to the allowable thermal budget during or after silicide formation in the back end process, before film disintegration occurs. It is important to realise that, in some cases, a direct silicidation of  $\text{SiO}_2$  can take place for Ti. If so, this puts a more stringent upper limit to the process window for RTP1. When the  $\text{TiSi}_2$  thickness or the linewidth are reduced, the lower end of the process window shifts to higher temperatures because of a retardation effect on the C49–C54 transition [5–7], which is attributed to a lack of C54 nucleation

## 17.1 Recent advances in silicide technologies

sites and a reduction for 2-dimensional (in large areas) to 1-dimensional growth (in narrow areas). The retardation of the C49-C54 transformation has been characterised *in situ* by Clevenger and co-workers [8,9] using synchrotron diffraction. Since the nucleation is, in essence, statistical, a minimal linewidth exists which allows for a large enough process window to achieve Ti-silicided lines with a sufficiently high yield. This is illustrated in FIGURE 3, showing sheet resistance versus linewidth for  $\text{TiSi}_2$  down to 0.3  $\mu\text{m}$  poly-Si lines. Whereas for the 0.5  $\mu\text{m}$  lines an RTP2 temperature of 825°C might have been sufficient, the 0.35  $\mu\text{m}$  lines require a temperature of 850°C for RTP2. The most critical case is the 0.3  $\mu\text{m}$  line, for which the C49–C54 transition is only completed at 875°C. The effect of the higher temperature is observed through the narrower distribution of the sheet resistance, as well as through the decreased number of outliers. Recently, a study [10] using the micro-Raman technique has revealed that indeed within a single narrow line the C49 and C54 phases occur next to each other (FIGURE 4).

For both silicides, the higher limit for the process window is dictated by film integrity. The highest allowable temperature is decreasing for both silicides upon scaling, since the thermal stability of a thin film decreases with layer thickness. It is also linewidth dependent since the formation of silicide agglomerates is more destructive for a narrow line than for a wide line. The linewidth dependency of the thermal stability of silicide lines has been extensively reported [11–13].

The effect of dopants has been studied by *in situ* resistance measurement [14]. It has been shown that the dopants retard the C49–C54 transition. The C54 formation temperature is lowest for undoped Si and increases from low to high in the order B, As and P. For  $\text{CoSi}_2$ , the effect of dopants is much less pronounced than for  $\text{TiSi}_2$ , since neither the reaction nor the thermal stability is affected greatly by dopant elements. The effect of As doping on the Co-Si reaction was monitored *in situ* by emissivity measurements [15] indicating only a very limited retardation of the reaction.

The crystallinity of the Si also plays an important role. In the case of amorphous Si, the reaction is faster and starts at lower temperatures due to the heat of crystallisation of a-Si which is on the order of 15 kJ/mol [16].

It is evident that the temperature control during silicidation is a key issue since the process windows, as discussed above, become very narrow. Although furnaces outperform rapid thermal processors on temperature control, the dynamic character of the RTP seems to be essential to maintain process controllability. Slightly higher temperatures for shorter times widen the process window for  $\text{TiSi}_2$  since the reaction is basically in the nucleation controlled regime [17]. Over the last few years major improvements in temperature control have been achieved. However, a good temperature measurement at the low temperatures of silicidation is not obvious, since the optical constants of wafers vary significantly with temperature and with layers covering the wafer back side [18].

## C CRITICAL PROCESS ISSUES DUE TO CHEMICAL REACTIVITY OF METAL AND SILICIDE

Whereas in the previous section the boundaries of the process window have been discussed in terms of thermal processes, this section will deal with the controllability of the silicidation module in a full process for current and future technologies in terms of chemical reactions.

## 17.1 Recent advances in silicide technologies

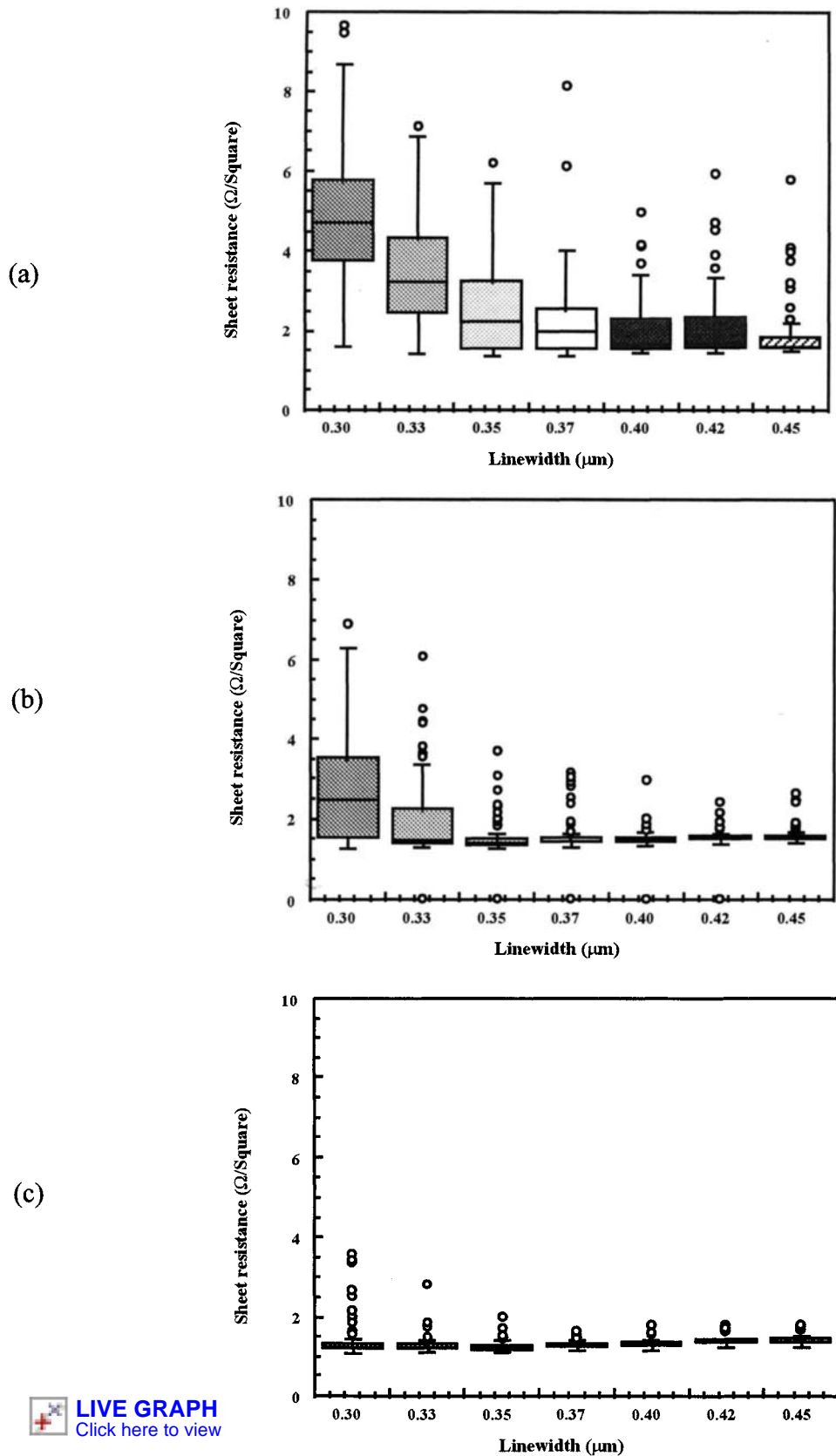
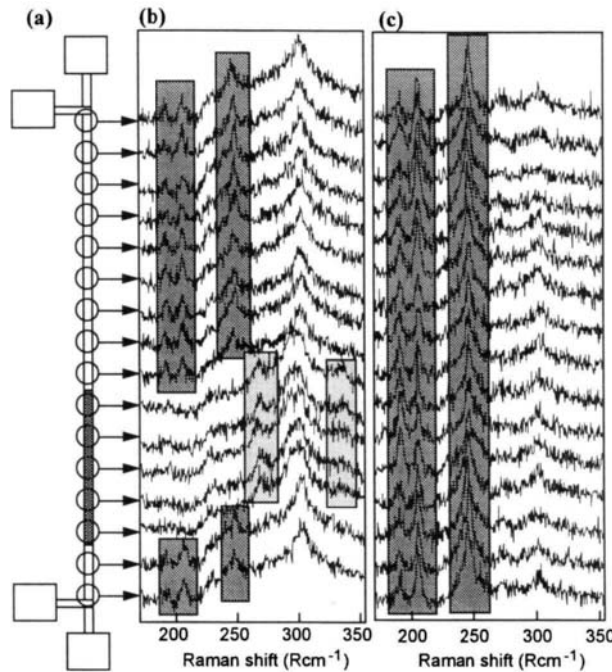


FIGURE 3 Sheet resistance versus linewidth plots for the TiSi<sub>2</sub> process, consisting of an RTP1 temperature at 730°C, a selective etch and an RTP2 temperature of (a) 825°C, (b) 850°C and (c) 875°C.



**FIGURE 4** Micro-Raman measurements of the C54 and C49 phases of TiSi<sub>2</sub> in 0.25 μm wide, silicided lines: (a) schematic of the line, indicating the 16 measurement points, (b) measurement of a narrow line with a sheet resistance of 4 Ω/square, (c) same for a narrow line with a sheet resistance of 2 Ω/square.

## C1 Cleaning Prior to Metal Deposition

Cleaning of the Si before metal deposition is a key factor in silicide technology. Whereas Ti reduces SiO<sub>2</sub> and therefore reacts with Si even through a thin native oxide, Co is thermodynamically stable on SiO<sub>2</sub>. A thin oxide between Si and Co blocks the reaction or limits it to local spurts of silicidation at weak spots. Besides native oxide, remnants of dry etching processes (usually C-F polymers) for spacer formation also need to be removed carefully. Sacrificial oxidation steps and/or surface Si etching are also part of the cleaning process. The selectivity of the clean with respect to oxide etching is an important factor, since the design of the spacer is a technological parameter which directly influences the device behaviour. HF-last cleans are attractive since they result in a passivated Si surface with low metallic contamination. In particular Ca, which has a very stable oxide which cannot be reduced by Co or Ti, must be removed in HF-last cleans [19]. Typical problems related to HF-last cleaning are the formation of drying spots, which can lead to defects in the silicided areas [20].

There are special issues related to HF-last cleans of highly doped regions, as discussed in [21].

## C2 Ambient Control During RTP

The ambient control during the thermal treatments is very important. Slight traces of moisture or oxygen can have a large effect on the silicide reaction at the wafer surface. In-situ measurements in the RTP system have indicated that the moisture level varies during steady state processing due to desorption from the chamber walls and even from the wafer [22]. The effect of ambient processing conditions is directly reflected in the yield of the silicide process. Keeping in mind the high reactivity

of Ti, it can be understood that any ambient contaminant has an effect on the reaction. In the case of Co this is less evident.

Although the underlying mechanism is still under investigation, the effect of ambient on the silicide yield is more pronounced for small dimensions than for wider silicided feature sizes [23]. Minor amounts of impurities seem to have a large impact on the silicidation reaction, especially on narrow lines. It was demonstrated that the wafer itself is an important contributor to ambient contamination in RTP. Indeed the desorption from the wafer interferes with the silicide formation [24–26].

### C3 Interaction Metal Oxide/Nitride

As important as the reaction of the metal with Si is the interaction with  $\text{SiO}_2$ . Whereas Co has no significant interaction with  $\text{SiO}_2$ , Ti reduces  $\text{SiO}_2$  because of its high reactivity with oxygen. The possibility to reduce native oxide remnants on the Si surface makes the Ti reaction less dependent on surface cleaning procedures before metal deposition.

In order to understand the reaction of Ti or Co with  $\text{SiO}_2$  and  $\text{Si}_3\text{N}_4$  it is important to consult the M-Si-O and M-Si-N ternary diagrams [1, 2]. Ti reduces both  $\text{SiO}_2$  and  $\text{Si}_3\text{N}_4$ , allowing the formation of silicide compounds on top of these dielectrics. Co is in principle stable to these materials, although reactions can occur when other species, like ambient  $\text{O}_2$  or moisture, are available during the reaction [27,28].

### C4 Dry Etch of Contact Holes

The selectivity of the dry etching of  $\text{SiO}_2$  towards an exposed silicide has become an important issue. This is a consequence of the planarisation schemes at the pre-metal dielectric. Since the dielectric is planarised, it will be thicker on the lower areas, such as an active area, and thinner on the poly-Si areas on top of the field. The contact etch will therefore reach the silicide on the higher areas first and the silicide remains exposed until the deep contact holes to the diffusion regions have been opened (FIGURE 5).

When silicide is exposed to an etching plasma, two mechanisms have basically to be considered in order to understand the etch selectivity, i.e. the chemical reaction of the silicide with the plasma and the protective polymer film formation. Recently, many experiments have been carried out to understand the underlying mechanisms of fluorination, etching and cleaning after dry etch on silicides [29–31].

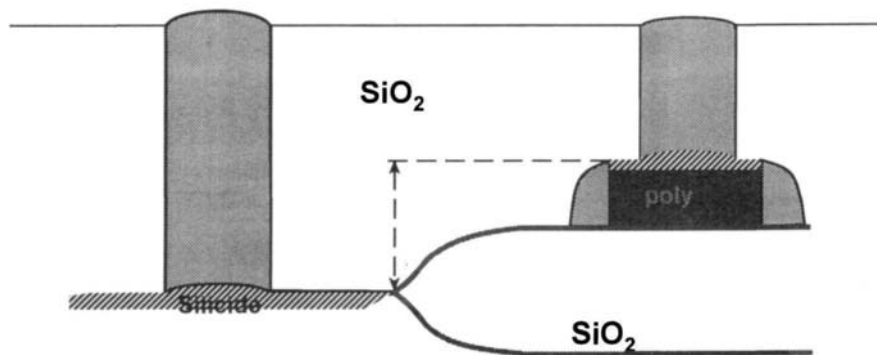


FIGURE 5 Schematic cross-section of the contact areas of a transistor, indicating the difference in aspect ratio for contacts to the active area (low level) and the poly-Si (high level).

## D ALTERNATIVE PROCESSES

All kinds of alternative processes have been proposed and investigated in order to widen the process windows. In the case of  $\text{TiSi}_2$  it is predominantly the temperature process window that one tries to enlarge as well as to make the silicide thickness less dependent on dopant type and level. In the case of  $\text{CoSi}_2$ , it is mainly the reproducibility on narrow areas and, related to that, the thermal stability that is under investigation, as well as the critical dependence on cleaning conditions.

### D1 $\text{TiSi}_2$

#### D1.1 Ti/TiN

The Ti silicide process with a sputtered TiN cap has been proposed. The main purpose of the TiN cap is to reduce the interaction of the Ti layer with the  $\text{N}_2$  ambient [32]. In this way the difference in silicide thickness on the areas with various doping types and levels can be reduced. It has been shown that the TiN cap can reduce some of the process related non-uniformities of the  $\text{TiSi}_2$ . The Ti/TiN process tends to fail, however, on the narrowest lines, limiting its further scalability. A characteristic of the failures is that they do not exhibit a higher sheet resistance, indicative of an incomplete C49–C54 transition, but a complete break up of the electrical line, indicative of a silicide rupture. It is not clear whether the stress induced by the capping layer causes these failures.

#### D1.2 Pre-amorphisation

An implant pre-amorphisation of the Si prior to Ti deposition has been demonstrated to be very successful in order to enhance the completion of the C49–C54 transition [33]. The additional energy involved in the reaction due to the recrystallisation of the Si opens the process window especially of RTP2 both by reducing the C49–C54 completion temperature and by increasing the thermal stability of the silicide. A typical result on sheet resistance for narrow lines is presented in FIGURE 6. In this case, an amorphising implant of  $3 \times 10^{14}$  As/cm<sup>2</sup> was used. The spread on the silicide resistance is remarkably good. However, the pre-amorphising implant also affects the contact resistance and the junction performance of the diodes. A very detailed optimisation of the full process is required in order to introduce this technology in a full fabrication process.

#### D1.3 Introduction of metal impurities

The introduction of small amounts of metals like Mo, W, and also Nb, has been shown to have a large effect on the Ti silicidation reaction. Implantation of these impurities at doses on the order of  $5 \times 10^{13}$  at/cm<sup>2</sup> into the Si prior to Ti deposition has an effect on the C49–C54 transition [34,35]. Indeed the temperature of transition can be reduced by 100–150°C in the case of Mo. This opens up the process window of RTP2.

Similarly, an interposed Mo layer (<2 nm thick) between the Ti and the Si enhances the formation of the C54 phase of  $\text{TiSi}_2$  by first forming an Mo-bearing silicide phase [36]. The traditional route of C49 and C54 phase formation is altered in this case.

Based on these techniques the scalability of the  $\text{TiSi}_2$  process (also in combination with the pre-amorphisation process) has been claimed down to 0.06  $\mu\text{m}$  gate lengths [37,38].

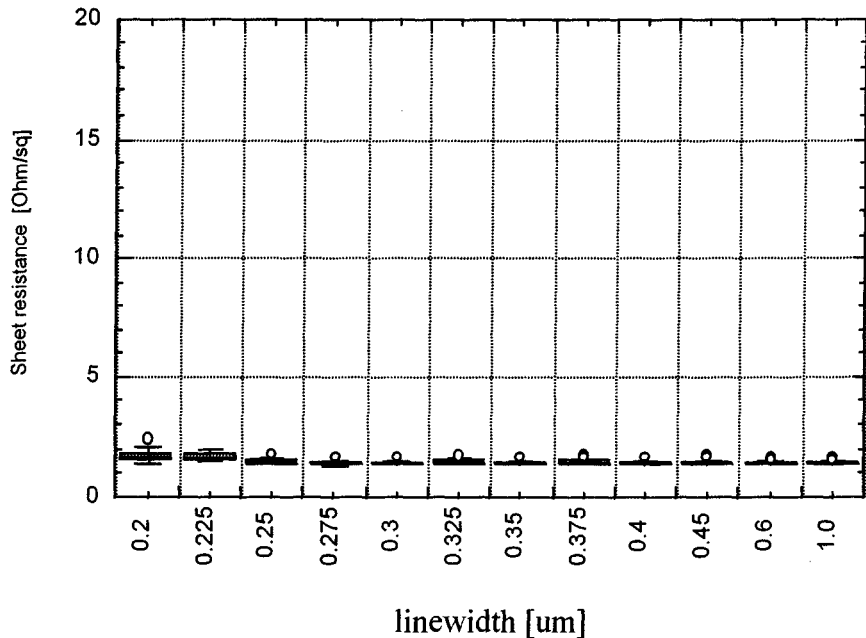


FIGURE 6 Boxplot showing the distribution of the sheet resistance on Ti-silicided poly lines versus linewidth. The silicide process used a  $3 \times 10^{14}$  As pre-amorphising implant, 50 nm of Ti and an RTP1 at 710°C and RTP2 at 850°C.

## D2 CoSi<sub>2</sub>

CoSi<sub>2</sub>, formed by the reaction of Co on Si, exhibits a thinning of the silicide at the edges. Despite the fact that this thinning effect puts a possible boundary to scaling of the linewidth that can be silicided, it also puts a limitation to the thermal budget. The bowing effect can be drastically reduced by engineering the poly-Si sidewall spacers [39,40]. Another drawback of the Co/Si process is its poor reproducibility. Both the Ti/Co process, using Ti as an interfacial layer, and the Co/Ti process, using Ti as a capping layer, aim to alleviate the edge thinning problem and therefore improve the thermal stability of the silicide on narrow lines. It is not clear whether the presence of the Ti has an additional contribution to the improved thermal stability besides this geometrical effect of film morphology.

### D2.1 Ti/Co (Ti at interface)

The Ti/Co process, where a Ti layer is deposited in between the Co and the Si, is very attractive, since it results in growth of epitaxial CoSi<sub>2</sub> in a way which is completely compatible with current integrated processes [41]. The thickness of the Ti layer has been under discussion as well as its relation to the phase formation sequence [42–44]. An enlightening view on the epitaxial CoSi<sub>2</sub> formation process has been given by Tung [45] who has looked into similar CoSi<sub>2</sub> growth using the oxide mediated epitaxial growth (OME). A drawback of epitaxial silicides is, however, that they induce a lot of stress in the surrounding Si, which might lead to voids and diode failures [46].

### D2.2 Co/Ti (Ti cap)

In an attempt to combine some of the advantages of the Ti/Co (Ti at interface) process with those of the conventional Co process, silicidation based on Co/Ti bilayers, with Ti as a capping layer, was investigated [4]. In contrast to the previous process, the Ti capping layer does not delay the initial

reaction to higher temperatures. The Ti capping layer process does not yield epitaxial  $\text{CoSi}_2$  as in the case of the process with Ti as an interfacial layer. A preferential orientation in the (220) direction has been observed from XRD.

The role of the Ti cap layer in the Co-silicidation process and the comparison with a TiN cap layer [47,48] have been studied by monitoring the ambient during RTP1. The main species of interest are the evolution of the  $\text{O}_2$  content in the ambient, the  $\text{H}_2\text{O}$  content and the  $\text{CO}_2$  content. It is important to notice that the wafer itself plays an active role by adsorbing and desorbing these species during processing [49].

This process has been implemented in a technology with feature sizes of  $0.1 \mu\text{m}$ . Its robustness for  $0.25 \mu\text{m}$  processes has been demonstrated. FIGURE 7 shows cumulative probability curves of the Co/Ti process on narrow poly-Si runners with a width varying from  $0.8$  down to  $0.08 \mu\text{m}$ . Very good and uniform sheet resistances are obtained even on the narrowest lines, without any yield loss.

## E CONCLUSION

This Datareview has summarised the important process of silicide formation in IC manufacture. Emphasis has been placed on Co and Ti silicidation. The importance of phase identification and establishing a thermal process window has been stressed. Self-aligned silicidation occurred selectively on exposed Si areas. Cleaning, prior to metal deposition, and the use of capping layers are both crucial steps and are discussed in detail in this Datareview.

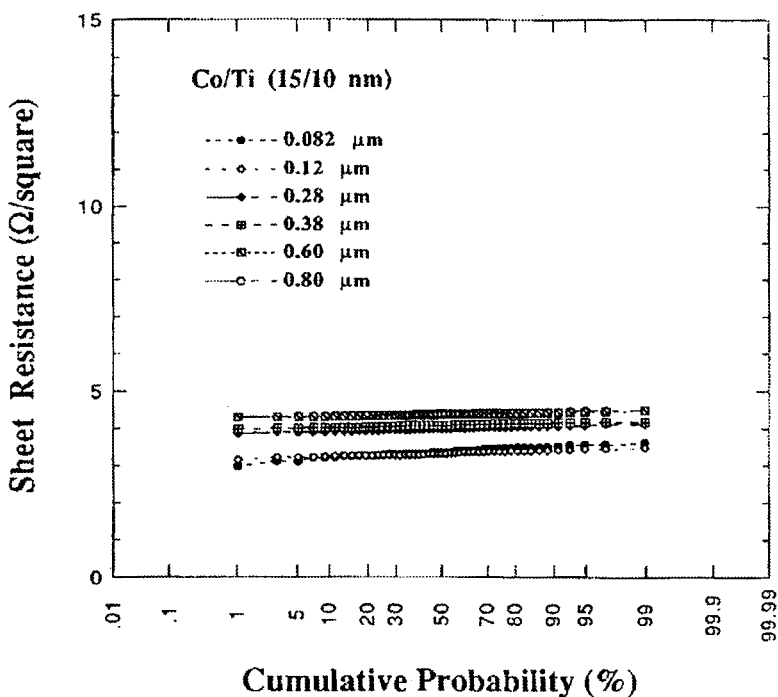


FIGURE 7 Cumulative plot of the sheet resistance of silicided poly-Si runners for various linewidths. The silicide grown was  $\text{CoSi}_2$  from a  $15 \text{ nm}$  Co film, with a cap layer of  $10 \text{ nm}$  Ti.

## REFERENCES

- [1] For an overview on materials data see K. Maex, M. Van Rossum (Eds.) [ *Properties of Metal Silicides* EMIS Datareviews Series No. 14 (INSPEC, IEE, London, UK, 1995) ]
- [2] K. Maex [ *Mater. Sci. Eng. R (Switzerland)* vol.11 (1993) p.53-153 ]
- [3] U. Gösele, K.N. Tu [ *J. Appl. Phys. (USA)* vol.53 (1982) p.3252 ]
- [4] Q.F. Wang et al [ *Symp. VLSI Technol.* Kyoto, Japan, 6-8 June 1995 (Japan Soc. Appl. Phys., Tokyo, Japan, 1995) p.17-8 ]
- [5] H.J.W. van Houtum, I.J.M.M. Raaijmakers, T.J.M. Menting [ *J. Appl. Phys. (USA)* vol.61 (1987) p.3116 ]
- [6] H. Jeon, C.A. Sukow, J.W. Honeycut, G.A. Rozgonyi, R.J. Nemanich [ *J. Appl. Phys. (USA)* vol.71 (1992) p.4269 ]
- [7] J.B. Lasky, J.S. Nakos, O.J. Cain, P.J. Geiss [ *IEEE Trans. Electron Devices (USA)* vol.28 (1991) p.262 ]
- [8] L.A. Clevenger et al [ *J. Mater. Res. (USA)* vol.10 (1995) p.2355 ]
- [9] L.A. Clevenger et al [ *Mater. Res. Soc. Symp. Proc. (USA)* vol.402 (1996) p.257 ]
- [10] I. De Wolf, D.J. Howard, A. Lauwers, K. Maex, H.E. Maes [ *Appl. Phys. Lett. (USA)* vol.70 (1997) p.2262 ]
- [11] H. Norström, K. Maex, P. Vandenabeele [ *J. Vac. Sci. Technol. B (USA)* vol.8 (1990) p.1223 ]
- [12] H. Norström, K. Maex, P. Vandenabeele [ *Thin Solid Films (Switzerland)* vol.198 (1991) p.53 ]
- [13] E.G. Colgan, J.P. Gambino, Q.Z. Hong [ *Mater. Sci. Eng. R (Switzerland)* vol.16 (1996) p.43-96 ]
- [14] L.A. Clevenger, R.W. Mann, R.A. Roy, K.L. Saenger, C. Cabral Jr., J. Piccirillo [ *J. Appl. Phys. (USA)* vol.76 (1994) p.7874 ]
- [15] K. Maex, R. Schreutelkamp [ *Mater. Res. Soc. Symp. Proc. (USA)* vol.260 (1992) p.133 ]
- [16] F.M. d'Heurle, C.S. Petersson [ *Thin Solid Films (Switzerland)* vol.128 (1995) p.283 ]
- [17] B. Davari et al [ *IEEE Trans. Electron Devices (USA)* vol.39 (1992) p.967 ]
- [18] K. Maex [ in *Advances in Rapid Thermal and Integrated Processing* Ed. F. Roozeboom (Kluwer Academic Publishers, 1996) p.333-74 ]
- [19] M.M. Heyns K. Maex, R. Schild [ *Semiconductor Fabtech (UK)* No. 3 (1996) p.213 ]
- [20] G. Zou, F. Jonckx, R. Donaton, K. Maex, M. Meuris, M. Heyns [ *Proc. UCPSS*, Bruges, Belgium, 19-21 Sept. 1994 (Acco, Leuven, Belgium, 1994) ]
- [21] E. Kondoh, M.R. Baklanov, F. Jonckx, K. Maex [ *Mater. Sci. Semicond. Processing (UK)* vol.1 (1998) p.107-17 ]
- [22] M. Filleul, P. Carr [ *Eur. Semicond. (UK)* February/April (1993) ]
- [23] Q.F. Wang, A. Lawers, F. Jonckx, M. de Potter, C-C. Hen, K. Maex [ *Mater. Res. Soc. Symp. Proc. (USA)* vol.402 (1996) p.221 ]
- [24] E. Kondoh, G. Vereecke, M.M. Heyns, K. Maex, T. Gutt, Z. Nenyei [ *Mater. Res. Soc. Symp. Proc. (USA)* vol.525 (1998) ]
- [25] K. Maex et al [ *Mater. Res. Soc. Symp. Proc. (USA)* vol.514 (1998) ]
- [26] P. Besser et al [ *Mater. Res. Soc. Symp. Proc. (USA)* vol.514 (1998) p.375 ]
- [27] T. Nguyen, H.L. Ho, D.E. Kotecki, T.D. Nguyen [ *J. Appl. Phys. (USA)* vol.79 (1996) p.1123 ]
- [28] E. Kondoh, R.A. Donaton, S. Jin, H. Bender, W. Vandervorst, K. Maex [ *Appl. Surf. Sci. (Netherlands)* vol.136 (1998) p.87 ]
- [29] M. Baklanov, S. Vanhaelemeersch, W. Storm, Y.-B. Kim, W. Vandervorst, K. Maex [ *J. Vac. Sci. Technol. A (USA)* vol.15 (1997) p.3005 ]
- [30] M. Baklanov, S. Vanhaelemeersch, K. Maex [ in *Advanced Metallization, Interconnect Systems for ULSI applications: 1996* (Materials Research Society, 1997) p.199 ]

- [31] M.R. Baklanov, S. Vanhaelemeersch, W. Storm, W. Vandervors, K. Maex [ *J. Vac. Sci. Technol. B (USA)* vol.16 (1998) p.164 ]
- [32] P. Apte, A. Paranjpe, G. Pollack [ *IEEE Electron Device Lett. (USA)* vol.17 (1996) p.506 ]
- [33] K. Fujii, K. Kikuta, T. Kikkawa [ *1995 Symp. on VLSI Technol.* Kyoto, Japan, 6-8 June 1995 (Japan Soc. Appl. Phys., Tokyo, Japan, 1995) p.57-8 ]
- [34] L.A. Clevenger et al [ *VMIC Santa Clara*, June 1995, p.626 ]
- [35] R.W. Mann et al [ *Appl. Phys Lett. (USA)* vol.67 (1995) p.3729 ]
- [36] A. Mouroux, S.-L. Zhang, W. Kaplan, S. Nygren, M. Östling, C.S. Petersson [ *Appl. Phys. Lett. (USA)* vol.69 (1996) p.975 ]
- [37] J.A. Kittl et al [ *1997 Symp. VLSI Tech. Dig. (USA)* (1997) p. 103 ]
- [38] J.A. Kittl, Q.Z. Hong, M. Rodder, T. Breedijk [ *IEEE Electron Device Lett. (USA)* vol.19 no.5 (1998) p.151-3 ]
- [39] H. Norström, K. Maex, A. Romano-Rodriguez, J. Vanhellemont, L. Van den Hove [ *Microelectron. Eng. (Netherlands)* vol.14 (1991) p.327 ]
- [40] Q. Wang, A. Lauwers, B. Deweerdt, R. Verbeeck, F. Loosen, K. Maex [ *IEEE Trans. Semicond. Manuf. (USA)* (1995) p.449 ]
- [41] M.L.A. Dass, D.B. Fraser, C.-S. Wei [ *Appl. Phys. Lett. (USA)* vol.58 (1991) p.1308 ]
- [42] S.L. Shia, T.Y. Tan, P. Smith, G.E. McGuire [ *J. Appl. Phys. (USA)* vol.70 (1991) p.7579 ]
- [43] C. Cabral Jr., L.A. Clevenger, G.B. Stephenson, S. Brauer, G. Morales, K.F. Ludwig Jr. [ *Mater. Res. Soc. Symp. Proc. (USA)* vol.375 (1995) p.253 ]
- [44] T.I. Selinder et al [ *J. Appl. Phys. (USA)* vol.77 (1995) p.6730 ]
- [45] R.T. Tung [ *Appl. Phys. Lett. (USA)* vol.68 (1996) p.3461 ]
- [46] K. Maex, I. De Wolf, D. Howard, A. Steegen, A. Lauwers [ *4th Int. Workshop on Stress Induced Phenomena in Metallization 1997* Tokyo, Japan 4-6 June 1997 (AIP, USA, 1998) p.72 ]
- [47] A.C. Berti, V. Bolkhovsky [ *VMIC Conf.* Santa Clara, June 1992, p.267 ]
- [48] K. Goto et al [ *1994 Symp. VLSI Technol.* Honolulu, HI, USA, 7-9 June 1994 (IEEE, New York, NY, 1994) p.119-20 ]
- [49] A. Lauwers et al [ *Int. Interconnect Technology Conf. (IITC)* San Francisco, USA, June 1998 ]

## CHAPTER 18

### SILICON ON INSULATOR TECHNOLOGY *(Edited by S.S. Iyer)*

- 18.1 Overview of SOI
- 18.2 Silicon on sapphire
- 18.3 Physics and chemistry of silicon wafer bonding
- 18.4 Bond, grindback and polish SOI
- 18.5 Bond and etchback SOI
- 18.6 Hydrogen-induced exfoliation of c-Si
- 18.7 Diffusion in SOI material
- 18.8 Bond and etchback SOI using an epitaxial layer over porous silicon
- 18.9 Technology and properties of SIMOX
- 18.10 Comparison of properties of available SOI materials

## 18.1 Overview of SOI

S.S. Iyer

June 1998

Silicon-on-insulator (SOI) refers specifically to a single crystal film of silicon on a dielectric film, usually silicon oxide. Thus, for the purposes of this chapter we specifically exclude the treatment of polycrystalline Si films grown on dielectrics. These are treated elsewhere in this volume. We also exclude epitaxial overgrowth techniques. From a materials perspective, SOI presents an interesting situation where we have a relatively perfect crystalline film in intimate contact with an amorphous film—raising serious questions about heteroepitaxy in a situation of extreme lattice mismatch. The nature of the film and especially the interface is certainly intriguing and depends on the nature of the fabrication method. This unfortunately means that the properties of the superficial crystalline Si film depend to a large extent on the defect structure of the film and the extent to which these have been annealed out. Also, in most applications the films are thin, increasing the importance of the properties of the interface. For this reason, the method of fabrication of the SOI film plays a crucial role. FIGURE 1 identifies the key parts of an SOI wafer.

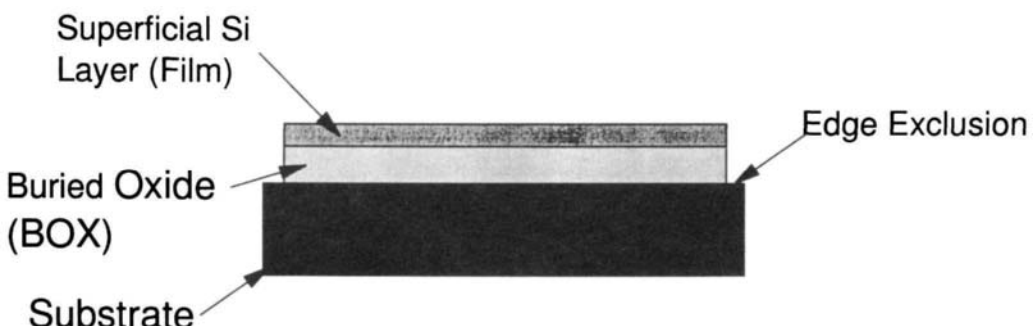


FIGURE 1 SOI wafer schematic.

There are essentially two distinct methods of fabricating SOI. In the wafer bonding method, generally, two oxidised silicon surfaces are brought into intimate contact and through a thermally assisted chemical reaction, the oxides are fused. Thus, to a first order, the interfaces are the classic Si–SiO<sub>2</sub> interfaces and the films, in principle, retain their bulk-like quality. Unfortunately, one of the layers of Si needs to be thinned, and this can introduce a variety of damage and contamination mechanisms on which the film properties depend. Datareviews 18.3–18.6 and Datareview 18.8 deal with different bonding and thinning methods of fabrication of SOI. Bonding allows for dissimilar substrate and film properties (composition, orientation, etc.). The second method widely used to fabricate SOI is by a variant of mesoepitaxy called Simox (separation by implantation of oxygen). Here, high-energy oxygen ions are implanted deep into a Si substrate amorphising a buried layer and saturating it with oxygen. The structure is then annealed and the oxygen and Si react, forming a SiO<sub>2</sub> buried layer that grows by Ostwald ripening while, simultaneously, the damaged Si surface layer is annealed. The interfaces in this case are more complex as is the film defect structure. Datareview 18.9 describes the Simox fabrication process. Datareview 18.10 deals with the general properties of SOI films and is an outgrowth of a critical evaluation of SOI films undertaken by Sematech. Datareview 18.7 deals with the all important issue of diffusion in SOI films. Diffusion is critical in that all dopant profiles and metal reactions are diffusion controlled. The analysis is rendered complex because of the film defect

### *18.1 Overview of SOI*

structure and the unique properties of the interface, which can greatly accelerate diffusion on the one hand and also getter impurities in large quantities. Datareview 18.2 deals with silicon on sapphire (SOS)—a specific type of SOI where silicon is deposited on a sapphire substrate. This is the classic mismatch heteroepitaxy, with a high defect density, although more recent regrowth techniques, where the layer near the mismatched interface is amorphised and regrown from the top down, where the relatively less defective surface layer is used as the seed, have been developed.

The use of SOI in silicon microelectronics is proliferating. Briefly, there are two general applications. In the first, the SOI is used structurally, for example to fabricate membranes for gas and pressure sensors, micromachined gyroscopes, accelerometers, etc. The key property used in these applications is the dissimilar properties of the relatively thick buried oxide, which is usually etched off to fashion a cavity or a Si microbeam or cantilever. These applications tend to employ thick layers and are invariably fabricated by wafer bonding. The second class of applications makes use of the isolating properties of the buried oxide layer. This buried oxide (or in the case of SOS, the entire substrate) effectively isolates the active layer (in which the circuits are fabricated) from the substrate. This means the capacitance of the device layers with the substrate is greatly reduced. The reduction of the parasitic capacitance to the substrate can enhance the circuit speed by about 25%. This enhancement is comparable to that achieved by scaling a generation and thus SOI offers a very attractive and potentially economic enhancement to performance improvement without further scaling. This improvement can be sustained by scaling and can be obtained for both bipolar and CMOS circuits. Another improvement in device speed can result because of the so-called floating body effect. This causes a parasitic lateral bipolar transistor to augment the surface channel. Unfortunately, this effect is somewhat unpredictable and most designs tend to suppress the effect either by tying the body down to a fixed potential or by going to a very thin SOI layer which is fully depleted. Furthermore, optimised SOI designs allow for the use of lower threshold voltages, and permit the lowering of operating voltage beyond conventional scaling permits. This in turn affords the possibility of lower power application. Additionally, the complete DC isolation of the substrate from the active layer improves the radiation resistance of the active layer.

The market for SOI is still nascent and is only a small fraction (<1%) of the total Si market, but it can grow dramatically if the mainstream CMOS applications are successful. It is very likely that wafer cost will dominate the reasons for the choice of a particular SOI fabrication method. The fabrication techniques, though practised for several years, are still evolving, so the film properties are still being improved. The status of SOI discussed in the following Datareviews represents our best estimate of where things are at present and will no doubt improve as the wafer fabrication and processing techniques evolve.

## **18.2 Silicon on sapphire**

I. Lagnado and P.R. de la Houssaye

February 1999

### **A INTRODUCTION**

The major requirement for computer processors and interface devices (mixed signal and analogue) is ever increasing computation power at lower cost [1]. One of the most important ways to accomplish this objective is to increase the speed and bandwidth of the computer processor chips, but increased speed also implies increased power dissipation. Although power dissipation has not so far been a serious issue, it will become an increasingly critical problem within the next few years.

Silicon-on-insulator (SOI) technology and its founding member, silicon-on-sapphire (SOS), have the potential to alleviate the critical speed/power problem. Although there are a number of demonstrated advantages for SOI over bulk silicon for fabrication of CMOS circuitry, the two main features are greatly reduced parasitic junction capacitances and better device isolation, hence freedom from latch-up. These features translate to both higher speed and packing density at lower power density [2]. As device and materials problems are solved and their respective characteristics improved, the higher packing density, smaller active device area, and simpler processing of SOS/SOI CMOS will also lead to a cost-competitive technology, despite the present, low volume higher cost of the starting material (\$700 for SOI/SOS in quantities smaller than 1000 today for 200-mm diameter sapphire substrates to \$395 for both SOI/SOS in larger volumes of 20 000 versus \$200 for bulk silicon).

The following sections review chronologically the results achieved on previous and current research in SOS materials (which has led to very thin silicon films on sapphire, 30 nm to 100 nm thick commensurate with 100 nm and smaller design rules), appropriately applicable to high performance devices ( $f_t$  in excess of 100 GHz) and high density CMOS circuitry for RF/microwave, analogue, and mixed signal system-on-a-chip applications.

### **B MATERIAL PROPERTIES**

Silicon-on-sapphire (SOS) has all the advantages of other SOI technologies as well as many others relevant to microwave circuits. These include reduced self-heating effects (due to higher thermal conductivity, 0.46 W/cm K, of sapphire as compared to SiO<sub>2</sub>, 0.014 W/cm K), reduced device parasitic capacitances, radiation hardness, reduction of latch-up in CMOS structures, higher packing density, and improved isolation. SOS also has lower minority carrier lifetimes (~1 ns), that result in higher source-drain breakdown voltage and reduced parasitic bipolar gain. Another SOS characteristic to note is that the silicon film is under compressive stress. This stress splits the light and heavy hole valence bands leading to increased hole mobilities over that of bulk silicon. At the same time, this stress also causes lower electron mobilities as compared to bulk. This is similar to the effects seen in SiGe on Si. In SOS, PMOS and NMOS devices are more closely matched than in other CMOS variants.

Sapphire, and more generally poly-crystalline sapphire (alumina), has been known for many decades to have excellent dielectric properties. The dielectric constant, dielectric loss tangent, and resistivity of sapphire are  $\epsilon_t = 9.39$ ,  $\tan \delta < 0.0001$  at 3 GHz,  $\rho = 10^{14} \Omega \text{ cm}$ . Hence, in addition to the desirable

## 18.2 Silicon on sapphire

traits of other SOI technologies, the sapphire wafers make an excellent microwave substrate for passive elements such as transmission lines and inductors.

The development of SOS started with the description by Manasevit and Simpton [3] of a technology to achieve single-crystal silicon on a sapphire substrate in 1964. Since then, as evidenced from several well documented reviews [4,5], the technological advances achieved for SOS can be traced, in parallel with the evolutionary establishment of the silicon VLSI industrial infrastructure from PMOS to NMOS to NMOS E/D and to the current workhorse CMOS. In the late 1970s, Lau et al [6] demonstrated that the crystalline quality of SOS films could be improved by utilizing a silicon implant to create a buried amorphous layer followed by a thermal anneal which caused regrowth of an improved film from the surface downward. This process is labelled ‘solid phase epitaxy’ (SPE).

The application of the technique suddenly renewed the interest in SOS technology for its use in high-speed, low power CMOS circuitry implemented with sub-micrometre minimum device feature size. Almost concurrently, two research teams [7–9] applied the SPE (or double SPE, DSPE) process to achieve device-crystal-quality to 200 nm thin film silicon on sapphire. Garcia and Reedy [10,11] extended their work to 20 nm thin films, commensurate with an 80–100 nm minimum device feature size, characterized by (a) the absence of aluminium outdiffusion from the substrate as shown from SIMS profiling (FIGURE 1) [9], (b) higher carrier mobility ( $\mu_e = 500$  and  $\mu_p = 200 \text{ cm}^2/\text{V s}$  for electrons and holes, respectively) and (c) the drastic reduction (almost elimination) of deep traps ( $<1 \times 10^{11} \text{ cm}^{-2}$ ) associated with the Si/sapphire interfacial region. Garcia and Reedy established the DSPE-improved 300 nm thick SOS wafers by the method previously described [9]. The essential steps were deep amorphization by a 170 keV  $^{28}\text{Si}$  implant at  $1 \times 10^{15} \text{ cm}^{-2}$  followed by a thermal anneal of 550°C for 2 hr, then 1050°C for 1 hr in flowing nitrogen. The top surface of the Si film was then amorphized by a 100 keV Si implant to  $1 \times 10^{15} \text{ cm}^{-2}$  followed by the same anneal cycle. Thinning the film was accomplished by growth of an oxide at 875°C in steam. Film thicknesses are measured by interferometry and by spreading resistance.

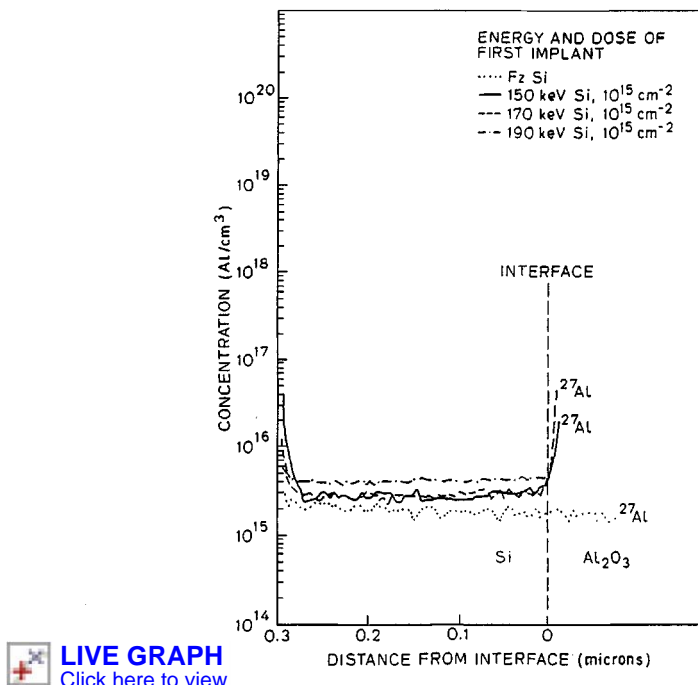


FIGURE 1 SIMS profile showing absence of Al in Si layer.

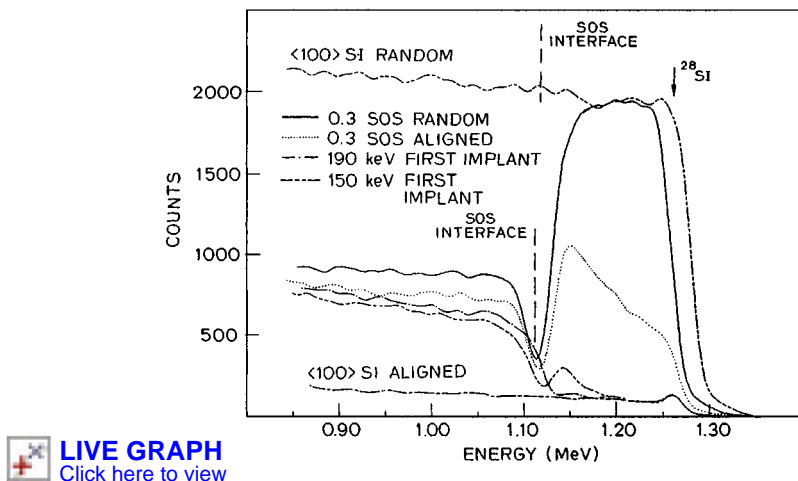


FIGURE 2 Channelled RBS data of as-received and DSPE improved SOS samples. Two different improvement energies (150 and 190 keV) are included.

The 2.2 MeV  ${}^4\text{He}^+$  channelled RBS data (FIGURE 2) and the high resolution TEMs (FIGURE 3) of both ‘as-received’ (non-implanted) SOS and DSPE-improved SOS samples show (a) the virtual elimination of ‘twin’ defects throughout the film, and (b) the dechannelling in the DSPE-improved SOS wafers coming very close to that obtained for the bulk silicon. Furthermore, the SIMS data give a uniform background concentration for  ${}^{27}\text{Al}$  of approximately  $1\text{--}3 \times 10^{15} \text{ cm}^{-3}$  which is within the error of minimum detectability for both the bulk silicon and the DSPE-improved SOS samples [2].

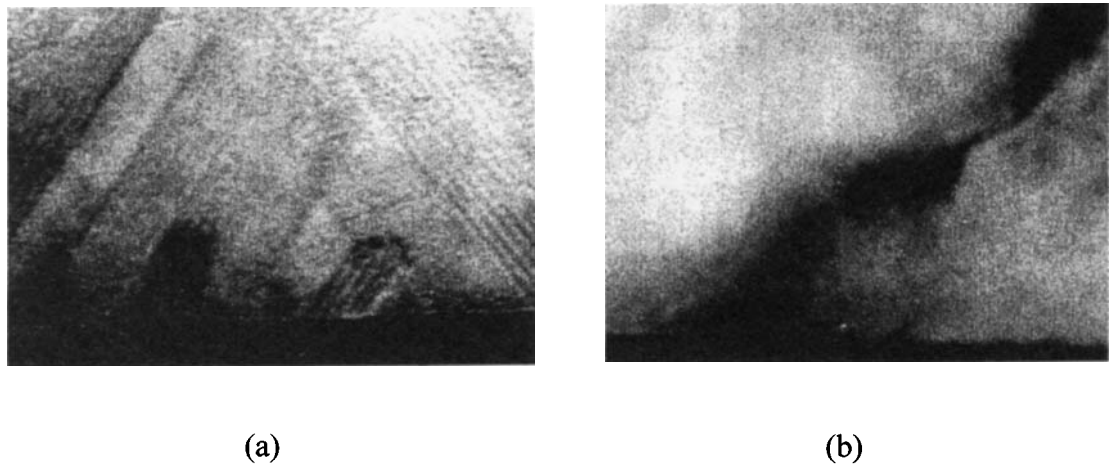


FIGURE 3 TEM images of a silicon layer, before (a) and after (b) improvement.

## C ELECTRICAL PROPERTIES

### C1 Static Characteristics

The solid-phase epitaxial (SPE) regrowth techniques optimized to improve the crystallinity of the silicon/sapphire interfacial region have been used to fabricate defect-free SOS films as thin as 30–40 nm. By confining the active semiconductor region to a thin surface layer on an insulating substrate,

the shallow source/drain regions, necessary for proper device behaviour as gate dimensions are reduced down to 100 nm, are automatically achieved. Before the advent of DSPE, the crystalline microstructure of the silicon, within 100 nm of the sapphire interface, was too defective to support high-performance CMOS device behaviour in this region [12]. With the optimized DSPE, near bulk Si crystallinity and electrical characteristics are observed: n- and p-channel mobilities of  $500 \text{ cm}^2/\text{V s}$  and  $200 \text{ cm}^2/\text{V s}$ , respectively, have been measured and deep trap levels associated with the silicon/sapphire interface have been reduced from  $2\text{--}3 \times 10^{12} \text{ cm}^{-2}$  in as-grown material, to less than  $1 \times 10^{11} \text{ cm}^{-2}$  [10,11]. This result is significant because it permits the tight control of threshold voltages required for high performance fully-depleted (FD) CMOS VLSI circuitry.

The DSPE improvement process has enhanced by a factor 5:1 the peak electron mobility and a factor 2:1 the peak hole mobility versus the as-grown material [10]. The relative larger mobility improvement for electrons compared to holes can be attributed to a decreased compressive stress [13], in addition to reduced defect densities. The decreased compressive stress in DSPE improved crystallinity raised the electron mobility [14] and lowered the hole mobility [15].

Concomitant with enhanced mobility, the threshold voltages for n- and p-channel devices, in 100 nm thick DSPE-improved SOS films, are significantly smaller [11] than in those identical devices fabricated in as-grown material. Sasaki and Togei [16] attributed the shift in threshold voltages in the thinner films towards smaller values as the films were DSPE improved to the considerably smaller concentration of deep donor and acceptor levels associated with the crystal defects concentrated near the silicon/sapphire interface. Using the two-level model of Sasaki and Togei [16] combined with the threshold voltage data [11], the trap densities in 100 nm thick as-grown and DSPE-improved SOS were evaluated and found to have been reduced by a factor of 25 respectively from  $2.5 \times 10^{12} \text{ cm}^{-2}$  to  $1 \times 10^{11} \text{ cm}^{-2}$  [11].

## C2 Radiation Hardness

Silicon on sapphire technology has been used for more than twenty years in radiation hard applications. Early SOS technology used silicon films from 3000 to 5000 Å thick in which to fabricate CMOS integrated circuits with the lower part of the film containing a high number of defects. This same technology is used today to fabricate radiation hard parts with gate lengths of 2 µm or more. A Title III program to produce SOS for radiation hard applications was pursued with the objective of improving the radiation hardness by creating even more defects near the silicon/sapphire interface. The thick film with defective interface is not suitable for short channel device technologies needed for higher density circuits since the defects degrade the quality of the diode junctions and result in higher leakage currents. Recently, processes have been developed for both materials which heavily dope the interface region to keep the channel depletion zone from entering the defective areas. This process supports 0.8 µm gate lengths.

In order to support the shortest channel devices, good crystal quality is necessary throughout the film. This has been achieved in SOS through the DSPE-improved regrowth process. With the good crystal structure throughout the film, the thicker silicon layer is no longer required as functional devices are implemented in the recrystallized film which is thinned to 100 nm or less, resulting in thin film SOS (TFSOS). In fact, the physical structure at this point is very similar to other thin film SOI material, such as SIMOX or BESOI.

Individual transistors on TFSOS have been radiation tested over several years with results varying with the process used to fabricate them. There are two conclusions drawn from this body of testing. First, the back channel hardness of TFSOS can be extremely good. It appears to be best in devices which include a lightly doped drain-type structure. Back channel hardness appears to degrade as the

## 18.2 Silicon on sapphire

drain doping next to the gate increases. This trend seems to imply that the LDD structure affects positive charge accumulation in the insulators such as the gate oxide and sapphire substrate by reducing the peak electric fields in those regions. This hypothesis has been difficult to verify due to uncontrolled process variations which affect the reproducibility of the LDD structure. Recent improvements in the gate etch allowing repeatable sidewall formation should result in reproducible radiation hardness levels. The second conclusion is that the current mesa isolation process requires a halo or edge implant to raise the threshold voltage of the island edge under the gate. The implanted island edge will turn on at a higher gate voltage than the main transistor channel and will not contribute to the OFF state leakage current. The set of figures (FIGURES 4–7) show the after radiation data of n- and p-type TFSOS, n-FET SIMOX and n-FET bulk Si which were measured at Northrup-Grumman (previously Westinghouse Advanced Technology Laboratories).

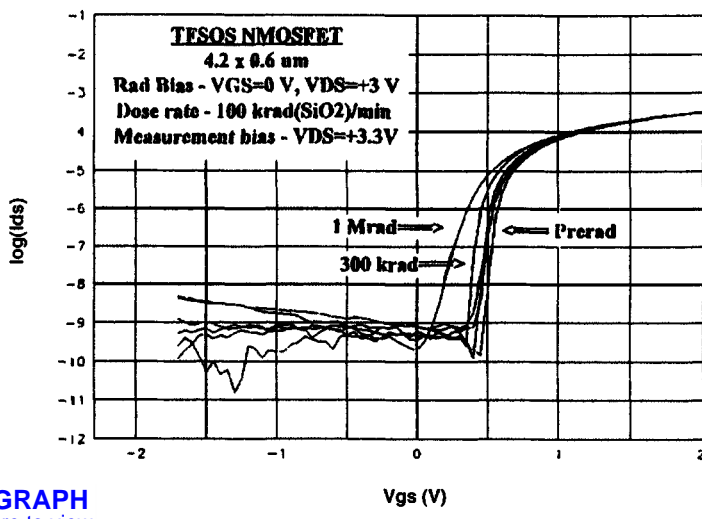


FIGURE 4 Radiation data for TFSOS NMOSFET.

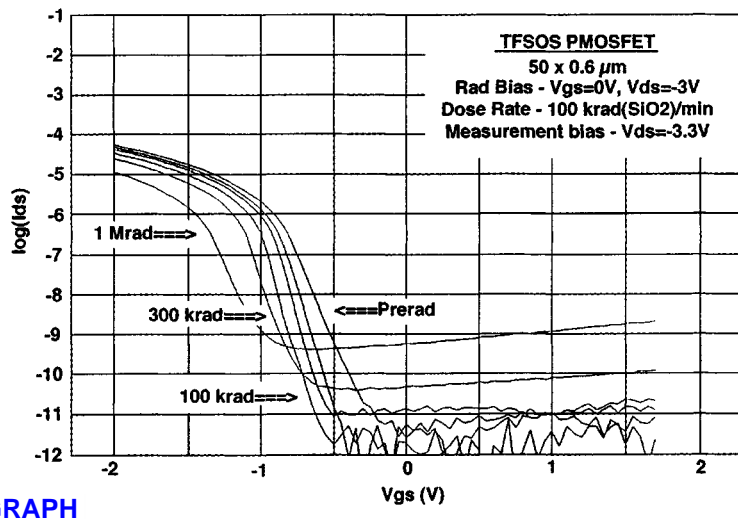


FIGURE 5 Radiation data for TFSOS PMOSFET.

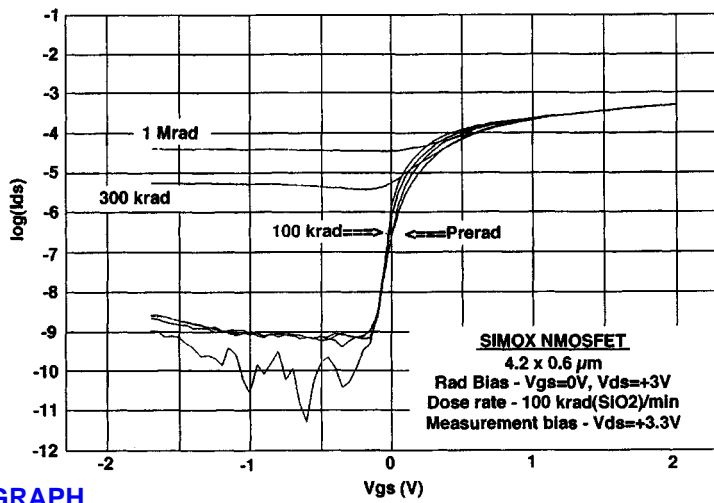


FIGURE 6 Radiation data for SIMOX NMOSFET.

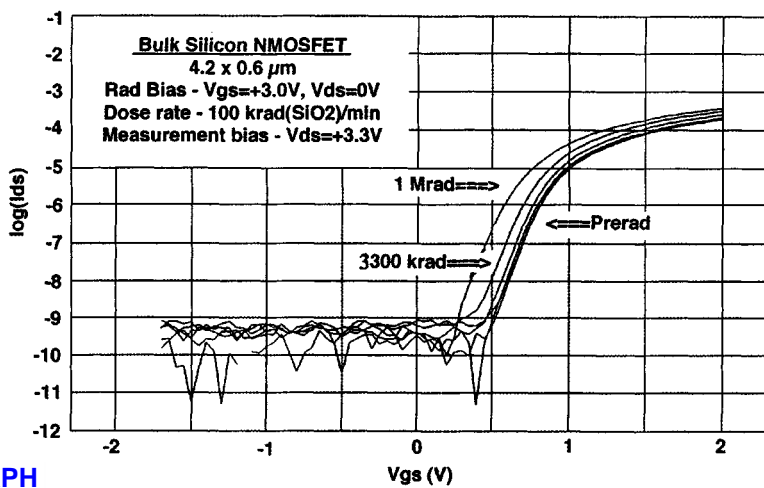


FIGURE 7 Radiation data for bulk Si NMOSFET.

Additional radiation testing at the Brookhaven National Laboratories of a 1-K SRAM circuit (FIGURE 8) (without an edge implant, controlled LDD process or any special design tricks) yielded the following results:

- dose rate hardness greater than  $2 \times 10^{11}$  rad/s (maximum on LINAC);
- SEU hardness using heavy ions—no upsets—LET threshold greater than 240 MeV cm<sup>2</sup>/g (highest available LET);
- SEU hardness using 148 MeV protons—no upsets.

### C3 Dynamic Characteristics

The DSPE-improved SOS material has led to an exhaustive set of experiments on devices [17–21] and various circuit functions [22,23] for (a) demonstration of record performance achievements and, more

## 18.2 Silicon on sapphire

importantly, reproducibility and (b) illustration of its potential at radio frequencies (RF) extending into microwave K-band, combined with low noise characteristics [21]. Concomitantly, extremely high quality inductors [24] have been demonstrated on the same sapphire substrate suitable for inclusion in silicon RF circuits. In contrast, other SOI materials are also being explored for RF applications; however, the non-linear effects caused by self-heating in these materials and attendant losses in transmission lines could preclude the use of the more lossy  $\text{SiO}_2$  dielectric, the preponderant insulator in SOI substrates.

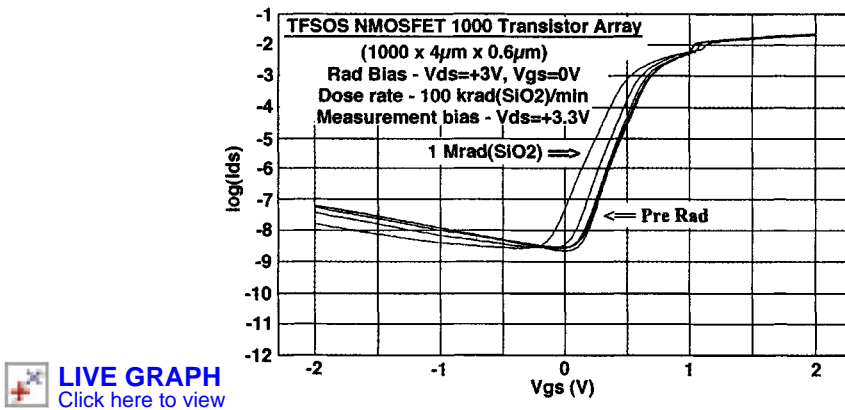


FIGURE 8 Radiation data for TFSOS NMOSFET 1000 transistor array.

To achieve ‘microwave’ performance, one is required to examine the equations for the maximum frequency of oscillation  $f_{\max}$  [25] and Fukui’s noise figure,  $Nf_{\min}$  [26], for a microwave transistor ( $Nf_{\min} = 1 + k L_g f (g_m (R_g + R_s))^{1/2}$ ) and observe the absolute requirement for the minimization, primarily, of  $R_g$ , the gate resistance which is a crucial parameter to be lowered to 1 ohm/sq versus the 100 ohm/sq obtained in polysilicon gates. Therefore, applying the well-known configuration of the T-gate, commonly used for high frequency analogue circuits in GaAs and other III-Vs, the gate resistance is dramatically reduced, resulting in achieving a very high  $f_{\max}$ , a much lower noise figure  $Nf_{\min}$ , and highest associated gain. The principal ingredients are therefore present to design optimally a transistor for microwave applications (highest power gain, expressed through  $f_{\max}$ ), in contrast to those required for digital applications where the high speed requirement is expressed as  $f_t$  which is governed by the gate length and gate capacitance.

The addition of the T-gate (metal-gate strap) configuration is incorporated into a CMOS fabrication process, in a manner similar to that used by Schmitz et al [27]. Chang et al [19], de la Houssaye et al [20,28] and Johnson et al [21,29] have described in a chronological sequence a ‘device’ design activity which has culminated with the addition of the metal-gate strap (T-gate) configuration, in a manner similar to that used by Schmitz et al [27], which has been incorporated efficiently into a CMOS fabrication process minimally altered, and has achieved minimum noise figure  $Nf_{\min}$  of 0.9 dB at 2 GHz, and  $f_{\max}$  values in excess of 66 GHz (41 GHz) for nMOS (pMOS) transistors (TABLE 1). A comparison of noise figures for different technologies is given in TABLE 2.

TABLE 1  $f_t$  and  $f_{\max}$  for nMOS and pMOS transistors on SOS.

Device	$L_g$ ( $\mu\text{m}$ )	$f_t$ (GHz)	$f_{\max}$ (GHz)
nMOS	0.5	25	66
nMOS	0.7	17	54
pMOS	0.5	14	41
pMOS	0.7	9	31

TABLE 2 Comparison of noise figures for different technologies.

	Tech.	$L_g$ ( $\mu\text{m}$ )	$f = 2 \text{ GHz}$		$f = 8 \text{ GHz}$		$f = 12 \text{ GHz}$		Ref
			$F_{\min}$ (dB)	$G_a$ (dB)	$F_{\min}$ (dB)	$G_a$ (dB)	$F_{\min}$ (dB)	$G_a$ (dB)	
nMOS	TF SOS	0.5	0.9	21	1.4	11	1.8	8.5	
pMOS	TF SOS	0.5	0.9	13	1.3	4.7	-	-	
nMOS	MICROX	0.25	1.5	18	3.25	8.5	-	-	[30]
pMOS	MICROX	0.25	2.7	15	-	-	-	-	
nMOS	MICROX	0.6	0.8	17	1.6	9.8	2.2	6.8	[31]
nMOS	BESOI	1.0	5.0	6.4	-	-	-	-	[32]
HBT	SiGe	$2 \times 0.6 \times 8$	0.5	12	0.8	-	1.0	-	[33]
HBT	InP/InGaAs	$3.5 \times 3.5$	0.46	11.6	1.4	-	2.0	-	[34]
pHEMT	GaP/InGaAs	0.15	0.2	-	0.33	-	0.41	13	[35]
JFET	GaAs	0.5	0.4	-	1.6	-	-	-	[36]
MESFET	GaAs	0.25	0.4	-	1.7	-	-	-	[37]

As can be seen from the IV characteristics [28] (FIGURE 9), the devices have high breakdown voltages and low output conductances without suffering from the ‘kink’ or self-heating effects—this property is observed down to 70 nm gate length. The latter is one additional major difference to the higher breakdown voltages for SOS than for other SOI configurations for similar gate lengths. Given that linearity and speed requirements for analogue circuits necessitate the largest operating voltage swing possible, the higher breakdown voltage is a major advantage for DSPE-improved very thin material film SOS.

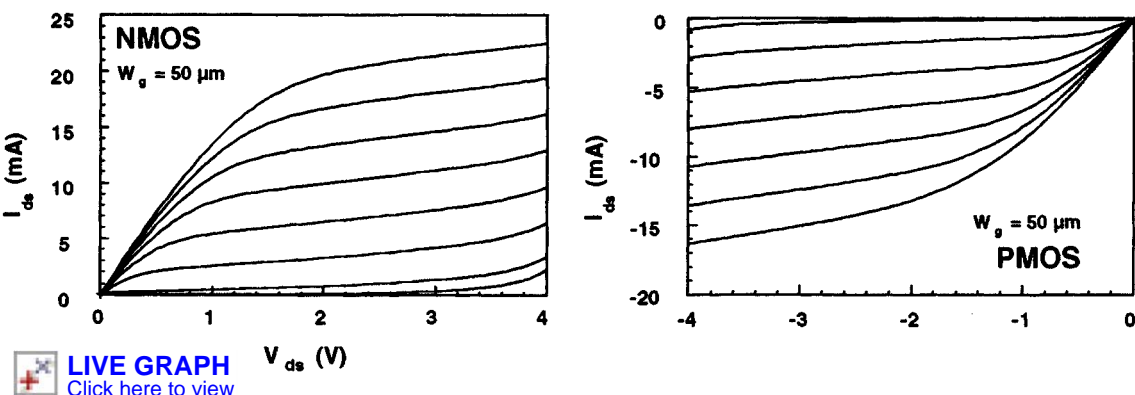


FIGURE 9 I–V characteristics of SOS devices.

Another important physical characteristic of SOS is its property of being under compressive stress (0.3%), as a result of the difference in thermal expansion coefficients. This stress is practically the same after DSPE-improvement and also after device/CMOS circuit fabrication. High resolution TEM studies of the Si-sapphire system report an inhomogeneous interface with no evidence of misfit dislocations [38], although others report some evidence of misfits [39]. The amount of compressive strain in the film is approximately that of  $\text{Si}_{0.9}\text{Ge}_{0.1}$  and a similar increase in hole mobility of 10–20% is seen due to the strain [40]. The effect is more pronounced at low temperature. Peak hole mobilities as high as  $250 \text{ cm}^2/\text{V s}$  at 300 K,  $1700 \text{ cm}^2/\text{V s}$  at 77 K, and over  $2500 \text{ cm}^2/\text{V s}$  at 15 K have been measured in p-channel MOSFETs [41]. This is consistent with the work of Ipri and Zemel [42] who first showed a crossover behaviour in compressively stressed Si films, where Hall hole mobilities

become equal to and eventually surpass those of the electrons as the temperature is reduced. This stress in the film has a number of important advantages for circuit applications.

There are a number of compelling reasons why a higher performance p-channel device is desired for circuits. In bulk material and in other non-stressed SOI, the p-channel device has lower performance than the n-channel device due to the lower hole mobility. p-Channel devices therefore consume more area in a CMOS configuration to optimize the noise margin. To optimize both the noise margin and speed, equal mobilities (and equal thresholds) are desired. For high speed analogue circuits, the speed is limited by approximately  $f/3$  for stable broad-band circuits and  $f_{max}$  for narrow band circuits. In circuits where a p-channel is desired for low power, the system bandwidth is limited by the speed of the p-channel device. Additionally, p-channel devices do not suffer as much from avalanche noise at low frequency, so it is advantageous to use one as a front end when input noise is of concern.

#### C4 System-on-a-Chip Applications

The exploitation of the combination of high performance MOSFETs (described in the previous paragraphs) and passive components (e.g. inductors) operating in the microwave regime was explored through the design, simulation, fabrication, and characterization of basic building blocks of a 2.4 GHz transmitter-receiver (transceiver). The demonstrated performances, unachievable in bulk silicon technologies, of (a) transmit/receive switch [22], (b) mixer [9], and (c) low noise amplifier [23] make possible the integration of an RF front-end and VLSI digital circuits on the same substrate. The resulting system-on-a-chip implementation can reduce cost and increase overall performance for functions targeted at wireless/satellite communication, radar, image processing and others in the military/industrial/scientific/commercial sectors.

The function of the transmit/receive (TR) switch (FIGURE 10(a)) is needed to connect the antenna to the receiver chain (receive mode) or the transmitter chain (transmit mode). A specific requirement for the switch is the importance of very low insertion loss, in order not to degrade the signal-to-noise ratio prior to the low noise amplifier on the receive side, or reduce the efficiency on the transmit side. In addition, non-linearity must be good to accommodate large output power and isolation from one side to the other must be high. The measured data demonstrates the excellent suitability to this combination of requirements of the switch implemented in DSPE-improved SOS. FIGURE 10(b) illustrates the insertion loss around 1.7 dB and an isolation greater than 30 dB at 2.4 GHz. At 5 GHz, the insertion loss dropped to only 2.0 dB and the isolation remained greater than 25 dB; while the isolation is the same, the insertion loss for SOS is three times lower than for SIMOX. The switch also displays excellent linearity and power handling capability. The two-tone measurements ( $f_1 = 2.4$  GHz,  $f_2 = 2.425$  GHz) show an input-referred third order intercept point (IIP3) of 18 dBm.

The mixer, used in up- and/or down-conversion of the carrier frequency (RF) (2.4 GHz) to the intermediate frequency (IF) (250 MHz) has good local oscillator (LO) (2.15 GHz, 0.7 dBm power) and RF isolation, as well as high IP3 (5 dBm) and low noise figure. As opposed to the ‘Gilbert cell’ mixer which is characterized with high gain and usually poor IP3, the selected SOS design (FIGURE 11(a) and FIGURE 11(b)) targets high IP3 (18 dBm) with little gain (the SOS mixer has 5 dB conversion loss). It is easier to increase the gain in the receiver chain than to increase IP3. TABLE 3 summarizes the SOS CMOS mixer with other CMOS mixer implementations; the SOS option compares favourably, particularly with respect to its high IIP3 to DC (8.4 mW) ratio and high frequency of operation.

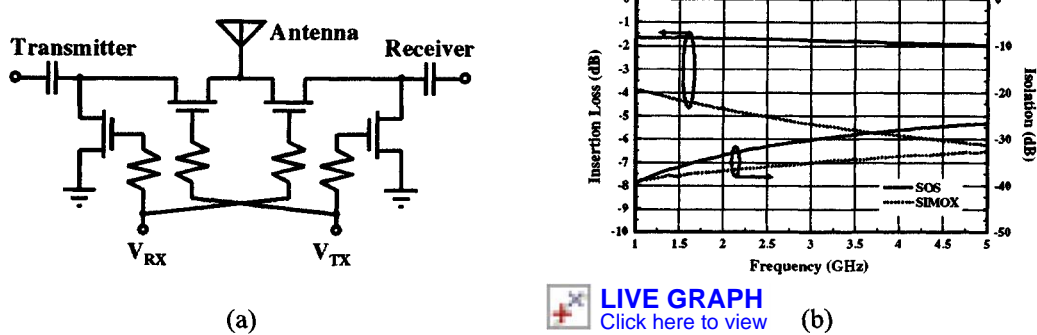


FIGURE 10 (a) Schematic and (b) insertion loss as a function of frequency of transmit/receive switch.

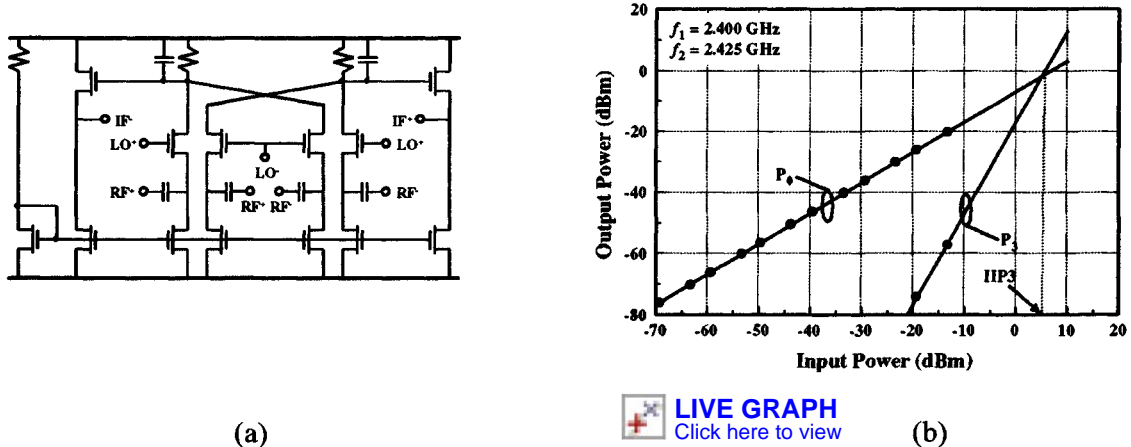


FIGURE 11 Mixer (a) schematic and (b) power characteristics.

TABLE 3 Summary of recent CMOS mixer results.

Technology	Type	RF freq. (GHz)	IF freq. (MHz)	NF (dB)	Gain (dB)	IIP3 (dBm)	$P_{DC}$ (mW)	LO power (dBm)
This work	Modified Gilbert	2.4	250	-	-5	5	8.5	0.7
2 $\mu\text{m}$ CMOS	Gilbert	0.86	100	8	10.5	-4	25	-
0.8 $\mu\text{m}$ CMOS	Folded Gilbert	0.9	100	6.7	8.8	-6	-	0
0.8 $\mu\text{m}$ CMOS	Gilbert	1.9	250	10	0.5	-6	8.5	-8

The low noise amplifier (LNA), a critical element of the receive path, has very low noise as well as high gain and output IP3 (OIP3). FIGURE 12(a) shows the circuit schematic of the LNA. Spiral inductors and MIM capacitors were used to match the FETs to the minimum noise figure at  $\Gamma_{\text{opt}}$ . Circuit parameters were:  $L_g = 0.5 \mu\text{m}$ ,  $W_g = 400 \mu\text{m}$ ,  $L_{g1} = 4.4 \text{ nH}$ ,  $L_{g2} = 14.8 \text{ nH}$ ,  $L_s = 0.3 \text{ nH}$ ,  $L_d = 2.6 \text{ nH}$ ,  $C_1 = 40 \text{ pF}$ ,  $C_d = 12 \text{ pF}$  and  $C_2 = 60 \text{ pF}$ .

## 18.2 Silicon on sapphire

The LNA was operated at  $V_{ds} = 1.5$ ,  $V_{gs} = 0.7$  V. The DC current consumption at low input power levels is 8.8 mA (while it rises to 9.9 mA for an input power corresponding to the 1-dB compression point). This corresponds to an average power dissipation of 14 mW. Using the spiral inductors, the LNA is well matched for gain (10 dB) and noise figure (2.8 dB) at 2.4 GHz. Two-tone ( $f_1 = 2.4$  GHz,  $f_2 = 2.425$  GHz) linearity measurements of the LNA were performed and are shown in FIGURE 12(b). The output referred 1 dB compression point and third-order intercept (OIP3) are 4 dBm and 14 dBm respectively.

These results represent the highest frequency CMOS low noise amplifier reported to date. TABLE 4 summarizes recently reported CMOS LNA results. The noise characteristics of this LNA are of the order of those required for numerous wireless systems and on the same order as obtained with silicon bipolar circuits. On the basis of simulation, we believe that even lower noise figure would be possible if the metal thickness used to realize the on-chip inductors was greater. The excellent linearity observed may be attributed to the good turn-off and low output conductance of the SOS FETs, together with the absence of the body effect. The combination of low noise figure, high OIP3 and low power consumption is particularly desirable for wireless receiver circuits.

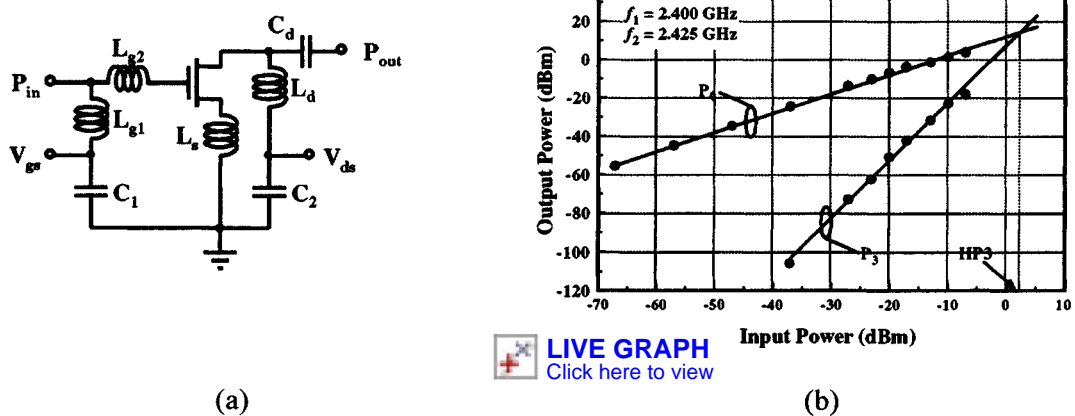


FIGURE 12 Low noise amplifier, (a) schematic and (b) power characteristics.

TABLE 4 Summary of recent CMOS LNA results.

Author	Lg (μm)	Freq. (GHz)	Gain (dB)	NF (dB)	OIP3 (dBm)	-1 dB (dBm)	Power (mW)
This work	0.5	2.4	10	2.8	14	4	14
Karanicolas [43]	0.5	0.9	15.6	2.2	12.4	-	20
Chang et al [44]	2	0.75	14	6.0	-	-	7
Sheng et al [45]	1	0.9	11	7.5	-	-	36
Rofougaran et al [46]	1	0.9	22	3.5	-	-	27
Shaefner and Lee [47]	0.6	1.5	22	3.5	12.7	0	30

## C5 Future Prospects

### C5.1 DSPE-improved SOS/CMOS with cryoelectronics

One of the most interesting aspects of SOS technology is the ease with which the sapphire substrate lends itself to monolithic integration with other technologies. One example is that of high temperature superconducting (HTS) devices and circuits.

HTS and SOS-CMOS are a perfect example of the synergistic combination of two technologies. Superconducting quantum interference devices (SQUIDs) and bolometers are the most sensitive magnetic and radiation detectors, yet have such low impedance that driving the signals off-chip is very difficult. Dense memories in SQUID technology are nearly impossible, as magnetic cross-talk and yield become major issues. CMOS circuits can easily drive signals (digital and analogue) off-chip. Circuits that have large memory and processing functions can be easily fabricated in the mature Si technology. Due to difficulties in growing films directly on silicon, copper and oxygen contamination (even into the silicon substrate) and the high temperature environments during growth of  $\text{Y}_1\text{Ba}_2\text{Cu}_3\text{O}_{7-\delta}$  (YBCO) films, YBCO has not been fully integrated with semiconductor based technology. Several attempts have been made to fabricate HTS circuits or devices directly on Si or other semiconductor surfaces [48,49]; these layers were of low quality and were stress limited, and no devices were fabricated in the layers. The  $\{1102\}$  sapphire plane usually used for SOS fabrication is, however, one of the preferred substrates for growth of the YBCO layers necessary for HTS devices. For the DSPE improved SOS/CMOS circuits and HTS functions, the devices functioned as expected at 77 K, including step-edge SQUIDs with a modulation voltage at 77 K of  $40 \mu\text{V}/\text{F}_0$  [50]. Monolithically combining SQUIDs and bolometers with SOS CMOS memories, latches, low noise amplifiers, silicon based sensors, and driving electronics was shown to be possible.

It should be noted that the success of this effort makes it clear that, in a similar manner, SOS CMOS can be combined with microelectromechanical systems (MEMS) which may involve the deposition of materials or require passivation against materials incompatible with silicon. Ferroelectric materials can be similarly integrated with SOS [51]. Also, device isolation allows for easier fabrication of high voltage circuits [52]. In addition, as silicon based optoelectronics begins to take hold, the transparent nature of the sapphire may be of use, allowing light to be detected from the back side of the circuit [53].

### C5.2 SiGe on DSPE-improved SOS

As previously discussed, one of the primary driving factors in SOS technology is the ability to increase the performance of the p-channel FET through higher hole mobility. In a similar fashion, work has been done to increase p-channel mobility in CMOS circuitry by use of a SiGe heterostructure MODFET [54–56]. By confining the holes to an undoped channel away from the Si/SiO<sub>2</sub> interface in a strained layer where the hole mobility is enhanced, a significant improvement in hole transport can be realized. Effective hole-mobility enhancements of 50% at 300 K and more than 100% at 90 K over bulk Si control devices have recently been reported [57]. More recently, 3–4× increases in both hole mobility and electron mobility using SiGe films with high levels of germanium (70%) have been reported [58]. Performance of both polarity devices can be enhanced in the same set of layers using tensilely strained Si on relaxed SiGe for the n-channel devices and compressively strained high germanium content SiGe layers for the p-channel devices. This requires, however, thick layers of SiGe graded buffer layers to bury the misfit dislocations beneath, which is incompatible with ultrathin silicon on insulator technology.

A promising approach for increasing the performance of the p-channel device even further for high speed microwave circuits while retaining the advantages of SOS is to combine SiGe technology with SOS. By including SiGe films grown on top of the improved Si layer, the individual devices can be optimized for high speed performance. A 40% increase in p-channel mobility is reported with a commensurate 40% increase in peak  $f_t$  in unoptimized devices using UHVCVD deposited SiGe with modest levels of Ge concentration films on SOS [59]. Typical increases in  $f_t$  for 1 micron drawn gates are from 5.0 GHz in pure SOS to 7.8 GHz for  $\text{Si}_{0.8}\text{Ge}_{0.2}$  channels on SOS. Work to increase these values as well as optimize n-channel performance is ongoing.

Another exciting development for SiGe and sapphire technology is the direct deposition of SiGe on sapphire (SGS). Recent reports have demonstrated the feasibility of epitaxial deposition of single crystal SiGe alloys using MBE [60] and RTCVD [61]. FIGURE 13 shows the results of the RTCVD deposition. As can be seen from the TEM and the selected area diffraction pattern, the twinning defects characteristic of as-deposited SOS are present in the SGS; SPE processing of the films should eventually yield similar quality films to the present SOS.

### C5.3 100 nm devices and CMOS circuitry in DSPE-improved SOS

Fully-depleted (FD) devices with 100 nm gate-length defined with X-ray lithography on 30–40 nm thin DSPE-improved SOS were characterized and were compared to similar devices implemented on SOI and bulk Si substrates. The 100 GHz  $f_t$  data for SOS are shown in FIGURE 14; heating effect in SIMOX devices is responsible for lower  $f_t$  values.

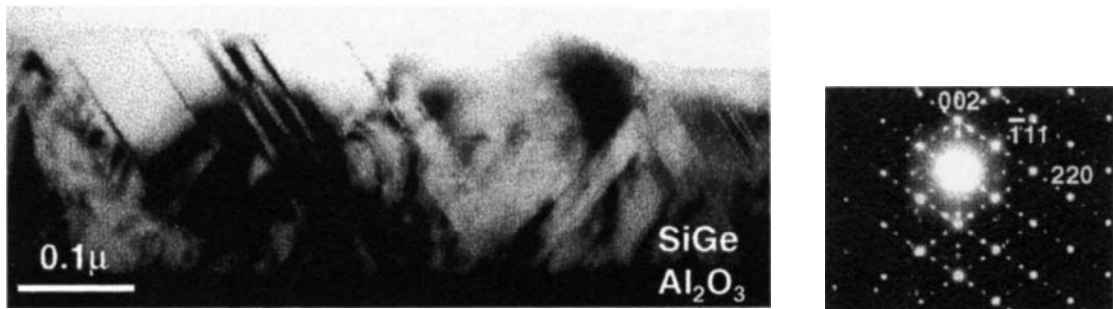


FIGURE 13 Cross-sectional transmission electron micrograph and selected area diffraction (SAD) pattern from SiGe on sapphire. Twinning defects evident in the film are responsible for the extra spots in the SAD. Rutherford backscattering (RBS) showed a uniform 5% concentration of germanium.

Very fast unloaded CMOS switching speeds have been observed (sub-ten-picosecond delay was measured). For three-way NAND ring oscillators, SOS devices are faster than SIMOX because of the higher hole mobility and lower threshold voltage (FIGURE 15).

## D CONCLUSION

DSPE-improved silicon-on-sapphire CMOS technology, based on optical lithography, in combination with T-gates can yield very low noise figures and high  $f_{\max}$ . Combined with the low loss dielectric substrate and the low cost and mature nature of the Si-based manufacturing infrastructure, thin film SOS has the potential to address the present and future need for microwave products, with increased circuit performance, unachievable in bulk silicon technologies, at reduced cost. With further scaling

## 18.2 Silicon on sapphire

of device geometries, to 100 nm gate-length, SOS has the potential to achieve RF circuits at K-band (20–40 GHz) regime.

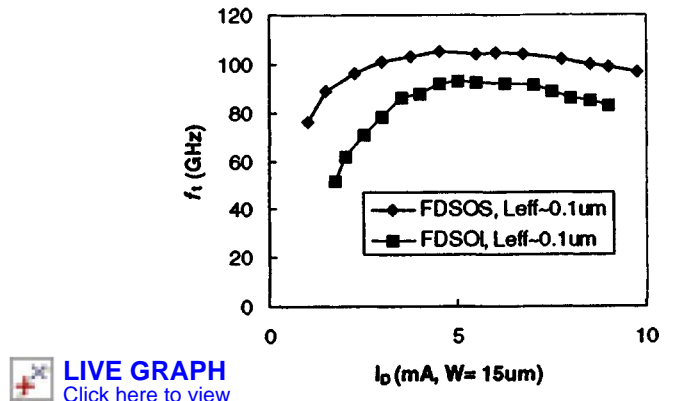


FIGURE 14  $f_t$  versus  $I_d$  for FDSOS and FDSOI with  $L_{eff} \sim 0.1 \mu m$ .

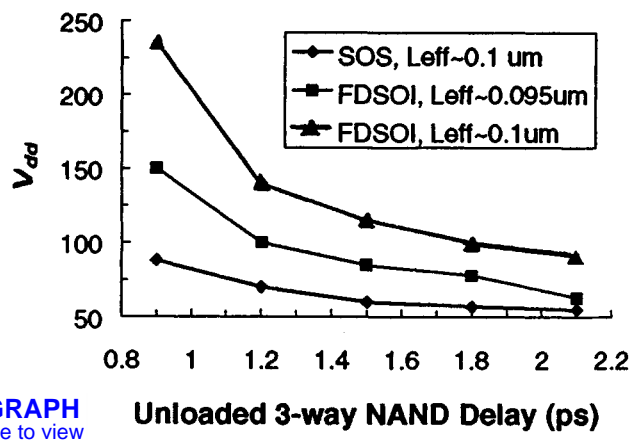


FIGURE 15 Unloaded 3-way NAND delay (ps) for SOS and FDSOI.

## REFERENCES

- [1] [ National Technology Roadmap for Semiconductors (Semiconductor Industry Association) ]
- [2] R.E. Reedy, G.A. Garcia [ Mater. Res. Soc. Symp. Proc. (USA) vol.107 (1988) p.365-76 ]
- [3] H.M. Manasevit, W.S. Simpton [ J. Appl. Phys. (USA) vol.35 (1964) p.1349 ]
- [4] G.W. Cullen, C.C. Wang (Eds.) [ Heteroepitaxial Semiconductors for Electronic Devices (Springer-Verlag, Berlin, Germany, 1978) ]
- [5] S. Cristoloveanu [ Rep. Prog. Phys. (UK) vol.50 (1987) p.327-71 ]
- [6] S.S. Lau et al [ Appl. Phys. Lett. (USA) vol.34 (1979) p.76-8 ]
- [7] T. Inone, T. Yoshii [ Appl. Phys. Lett. (USA) vol.36 (1980) p.64-6 ]
- [8] T. Yoshii, S. Taguchi, T. Inoue, H. Tango [ Jpn. J. Appl. Phys. 1, Regul. Pap. Short Notes (Japan) vol.21 (1982) p.175-9 ]
- [9] R.E. Reedy, T.W. Sigmon, L.A. Christel [ Appl. Phys. Lett. (USA) vol.42 (1983) p.707-9 ]
- [10] G.A. Garcia, R.E. Reedy [ Electron. Lett. (UK) vol.22 (1986) p.537-8 ]
- [11] G.A. Garcia, R.E. Reedy, M.L. Burgener [ IEEE Electron Device Lett. (USA) vol.9 (1988) p.32-4 ]
- [12] M.S. Abrahams, C.J. Buiocchi [ Appl. Phys. Lett. (USA) vol.27 (1975) p. 325-7 ]

- [13] Y. Ohmura, T. Inoue, T. Yoshii [ *Solid State Commun. (USA)* vol.37 (1981) p.583-5 ]
- [14] J. Hynecek [ *J. Appl. Phys. (USA)* vol.45 (1974) p.2631-5 ]
- [15] A.J. Hughes [ *J. Appl. Phys. (USA)* vol.46 (1975) p.2849-63 ]
- [16] N. Sasaki, R. Togei [ *Solid-State Electron. (UK)* vol.22 (1979 p.417-21 ][17] M. Roser, S.R. Clayton, P.R. de la Houssaye, G.A. Garcia [ paper presented at the 50th Device Research Conf., Boston, MA, June 22-24, 1992 ]
- [18] R.A. Johnson, S.D. Kasa, P.R. de la Houssaye, G.A. Garcia, I. Lagnado, P.M. Asbeck [ *Proc. 1997 IEEE Int. SOI Conf.* Fish Camp, CA, Oct. 6-9, 1997 ][19] C.E. Chang, P.M. Asbeck, P.R. de la Houssaye, G. Imthurn, G.A. Garcia, I. Lagnado [ *Proc MTT-S Int. Microwave Symp.* San Diego, CA, May 23-27, 1994 ]
- [20] P.R. de la Houssaye et al [ *IEEE Electron Device Lett. (USA)* vol.16 (1995) p.289 ]
- [21] R. Johnson, C.E. Chang, P.R. de la Houssaye, G.A. Garcia, I. Lagnado, P.M. Asbeck [ paper presented at the 1995 IEEE Int. SOI Conf. Tucson, AZ, 3-5 October 1995 ]
- [22] R.A. Johnson et al [ *Electron. Lett. (UK)* vol.33 (1997) p.1324-6 ]
- [23] R.A. Johnson, C.E. Chang, P.R. de la Houssaye, G.A. Garcia, P.M. Asbeck, I. Lagnado [ *IEEE Microw. Guid. Wave Lett. (USA)* vol.7 (1997) p.350-2 ]
- [24] R.A. Johnson, C.E. Chang, P.M. Asbeck, M.E. Wood, G.A. Garcia, I. Lagnado [ *IEEE Microw. Guid. Wave Lett. (USA)* vol.6 ( 1996) p.322-5 ]
- [25] S.M. Sze [ *Physics of Semiconductor Devices* (Wiley, New York, 1981) p.343 ]
- [26] H. Fukui [ *IEEE Trans. Electron Devices (USA)* vol.26 (1979) p.1032 ]
- [27] A.E. Schmitz et al [ *IEEE Electron Device Lett. (USA)* vol.12 (1991) p.16-8 ]
- [28] P.R. de la Houssaye et al [ submitted to *IEEE Trans. Electron Devices (USA)* ]
- [29] R. Johnson et al [ submitted to *IEEE Trans. Electron Devices (USA)* ]
- [30] M.H. Hanes et al [ *IEEE Electron Device Lett. (USA)* vol.14 (1993) p.219-21 ]
- [31] A.K. Agarwal et al [ *MTT-S Workshop*, May 1995 ]
- [32] A.L. Caviglia, R.C. Potter, L.J. West [ *IEEE Electron Device Lett. (USA)* vol.12 (1991) p. 26-7 ]
- [33] H. Schumacher, U. Erben, A. Gruhle [ *Proc. IEEE/MTT-S Int. Microwave Symp. - MTT '94* San Diego, CA, USA, 23-27 May 1994, Eds. H.J. Kuno, C.P. Wen, vol.2 p.1167-70 ]
- [34] Y.K. Chen, R.N. Nottenburg, M.B. Panish, R.A. Hamm, D.A. Humphrey [ *IEEE Electron Device Lett. (USA)* vol.10 (1989) p.470-2 ]
- [35] M. Takikawa, K. Joshi [ *IEEE Electron Device Lett. (USA)* vol.14 (1993) p.406-8 ]
- [36] D. Scherrer et al [ *IEEE Electron Device Lett. (USA)* vol.14 (1993) p.428-30 ]
- [37] P.J. Apostolakis, J.R. Middleton, D. Scherrer, M. Feng, A.N. Lepore [ *IEEE Electron Device Lett. (USA)* vol.15 (1994) p.239-41 ]
- [38] F.A. Ponce [ *Appl. Phys. Lett. (USA)* vol.41 (1982) p.371-3 ]
- [39] M Aindow [ PhD Thesis, University of Liverpool, 1989 ]
- [40] W.B. Dubbelday et al [ *Proc. 7<sup>th</sup> Int. Symp. on Silicon-on-Insulator Technology and Devices* Los Angeles, CA, USA, 5-10 May 1996 (Electrochem. Soc., Pennington, NJ, USA) p.237-47 ]
- [41] M. Roser, S.R. Clayton, P.R. de la Houssaye, G.A. Garcia [ 50th Device Research Conf. Boston, MA, June 22-24, 1992 ]
- [42] A.C. Ipri, J.N. Zemel [ *J. Appl. Phys. (USA)* vol.44 (1973) p.744 ]
- [43] A.N. Karanicolas [ *1996 IEEE Int. Solid-State Circuits Conf. Digest* (1996) p.50-1 ]
- [44] J.Y.-C. Chang, A.A. Abidi, M. Gaitan, [ *IEEE Electron Device Lett. (USA)* vol.14 (1993) p.246 ]
- [45] S. Sheng, L. Lynn, J. Peroulas, K. Stone, I. O'Donnell, R. Brodersen [ *ISSCC Dig. Tech. Papers (USA)* vol.39 (1996) p.346-7, 471 ]
- [46] A. Rofougaran, J.Y.-C. Chang, M. Rofougaran,, A.A. Abidi [ *IEEE J. Solid-State Circuits (USA)* vol.31 (1996) p.880-9 ]
- [47] D.K. Shaefner, T.H. Lee [ *IEEE J. Solid-State Circuits (USA)* vol.32 (1997) p.745-59 ]
- [48] D.K. Fork et al [ *Appl. Phys. Lett. (USA)* vol.57 (1990) p.1161-3 ]

- [49] D.K. Fork, K. Nashimoto, T.H. Geballe [ *Appl. Phys. Lett. (USA)* vol.60 (1992) p.1621-3 ]
- [50] M.J. Burns et al [ *Appl. Phys. Lett. (USA)* vol.63 (1993) p.1282-4 ]
- [51] W. Braun et al [ *Appl. Phys. Lett. (USA)* vol.63 (1993) p.467-9 ]
- [52] W.B. Dubbelday, L.D. Flesner, G.P. Imthurn [ US Patent 5,330,918, July 19, 1994 ]
- [53] R.L. Shimabukuro et al [ *Proc. SPIE (USA)* vol.2174 (1994) p.82-90 ]
- [54] S. Verdonckt-Venderbroek et al [ *IEEE Electron Device Lett. (USA)* vol.EDL-12 (1991) p.447-9 ]
- [55] T.P. Pearsall, J.C. Bean [ *IEEE Electron Device Lett. (USA)* vol.EDL-7 (1986) p.308-10 ]
- [56] D. Nayak, J.C.S. Woo, J.S. Park, K.L. Wang, K.P. MacWilliams [ *IEEE Electron Device Lett. (USA)* vol.EDL-12 (1991) p.154-9 ]
- [57] P.M. Garone, V. Venkataraman,, J.C. Sturm [ *IEEE Electron Device Lett. (USA)* vol.EDL-13 (1992) p.56-8 ]
- [58] A. Sadek, K. Ismail [ *Solid-State Electron. (UK)* vol.38 (1995) p.1731-4 ]
- [59] S.J. Mathes et al [ *Device Research Conference* Fort Worth, CO, June 1997 ]
- [60] H. Wado, K. Ohtani, M. Ishida [ *J. Cryst. Growth (Netherlands)* vol.169 (1996) p.457-62 ]
- [61] W.B. Dubbelday et al [ *MRS Conf.* San Francisco, 1 April 1997 ]

# Index

<u>Index terms</u>	<u>Links</u>
<b>A</b>	
<b>A centre</b>	494    501    705    706    715
ab initio modeling techniques	330
acceptors, double	670
Al gettering	780    786    787
alkali impurities in c-Si	593
diffusion	594
solubility	594    595
allotaxy	870
ambipolar diffusivity	722    728
doping effects	728
amorphisation	750    755    759
anisotropic wet etching	815
anisotropy factor	101
anisotropy ratio	101
antiphase defects	109    373
formation energy	111
migration energy	111
asymptotic lifetime	718
atmospheric pressure CVD	73    86
atomic weight	157
Auger coefficients	441    449
Auger de-excitation coefficient	
Er in c-Si	586
Auger lifetime	709    710    715    716
Auger recombination coefficient	715
<b>B</b>	
<b>B-interstitial clustering</b>	617
continuum model	617
dissociation barriers	618
kinetic Monte Carlo model	617    618
reaction tree	617    618
backside damage gettering	780    787

<u>Index terms</u>	<u>Links</u>
band structure	381 402
modeling	253 254 257 264 383
spin-orbit splitting	390
strain effects	402
symmetry points	381 382 385
band structure calculation	383
empirical pseudopotential method	384 385
empirical tight-binding method	383 384
Green's function methods	387
local density approximation methods	386 387
quantum Monte Carlo methods	388
bandgap	288 387 391 399
direct	399 400
doping effects	394
indirect	391 399 400
lattice constant dependence	399 400
pressure dependence	399
strain effects	402
temperature dependence	391
baroclinic instability	9 12
base wafer	923
binary collision approximation	739
bipolar junction transistor	777
bond and etchback SOI	938 960 962 971 976
diffusion	960 962 971
double etchstop	939
epitaxial layer over porous Si	976 977
single etchstop	938 939
total thickness variation	938
bond, grindback and polish SOI	923
annealing	925
bonding	923
carrier concentration	935 937
crystal defects	934 936
grinding	928
polishing	930
thickness uniformity	926 930
thinning	926
wafer size availability	933
warpage	933

<u>Index terms</u>	<u>Links</u>
bond wafer	923
bonded SOI wafers	923 960 962 971 976 977 992
bow	994 995
BOX breakdown field	999
contamination	996
cost	992
crystalline defects	994 995
defect density	992
edge exclusion	994 995
fixed charge density	999
flatness	994 995
generation lifetime	999
HF defect density	997
interface trap density	999
recombination lifetime	999
site total indicator reading	994 995
surface roughness	993 994
thickness uniformity	993 994
total thickness variation	994 995
warp	994 995
bonding energy	253
modeling	253
Born-Oppenheimer approximation	330 331
brittle-ductile transition	122 144
impurity effects	145 146
load-controlled	147
pre-deformation effects	145
bulk modulus	93 100 101
pressure dependence	100 101
Burgers vector	108 120 138 357 358 360 755 757
buried oxide defects	987 988 997 998
buried oxides	923 925 926 933 942 979

**C**

<b>C-H complexes</b>	532
C in c-Si	503 504 506
diffusion	506
IR absorption	503 504

<u>Index terms</u>	<u>Links</u>
C in c-S ( <i>Continued</i> )	
segregation coefficient	503
solubility	504
capture cross sections	561    764
transition metal impurities	563
Car-Parrinello molecular dynamics	348    349
carrier concentrations	414
doping dependence	414
temperature dependence	416    417
carrier continuity equations	457    458
carrier generation models	467
Grant's model	468
impact ionization models	467
Selberherr model	468    469
carrier ionization coefficients	450
electric field dependence	452
electron	450
hole	450
orientation dependence	452
temperature dependence	450
carrier recombination models	469    470
Shockley-Read-Hall recombination	469    470
carrier saturation velocity	460    465
cathodoplastic effect	141    142
CCD devices	777
chalcogen impurities in c-Si	573
binding energy	575
degree of localization	576
electronic states	573
charge transport models	458
chemical etchstop technology	938
double etchstop	939    940
single etchstop	938    939
chemical gettering	780    788
chemical plasma etching	832
chemical vapour deposition	
atmospheric pressure	73    86
low pressure	86
rapid thermal	86
ultra high vacuum	77
very low pressure	84

<u>Index terms</u>	<u>Links</u>
Clausius-Clapeyron equation	156 157
CMOS applications	888 892 895 988
Co silicidation	851
Cochran flow	12
cohesive energy	352
complex point defects	627 631
compliances	99 100 403 424
compressibility	100
compression	139 140
conduction band minima	381 405
strain effects	405
corona oxide semiconductor method	208 209
CoSi <sub>2</sub>	
crystal structure	864
lattice mismatch	864
lattice parameters	864
sheet resistance	853
specific resistivity	851 864
crack arrest toughness	146
crack tips	144
creep curve	122
critical points	406 407
strain effects	406 407
crystal originated particles	39 45
crystal structure	91 104
silicides	863 864
current density	459
cyclic cluster model	245 253
Czochralski growth	20 23 39
critical pull rate	39 41
growth rate	20
oxygen transportation	23
C(3) centre	767
<b>D</b>	
<b>dangling bonds</b>	109 175 183 288 291
	292 295 364 645
Debye temperature	151
deep levels	561 575 589 763
chalcogen impurities	575

**Index terms****Links**

deep levels ( <i>Continued</i> )					
electron irradiation induced defects	763				
Er-doped Si	589				
ion implantation induced defects	763				
transition metal impurities	561				
deep reactive ion etching	833	838			
defect clustering	751	752			
defect delineation	822	823			
defect energy levels	643	647	653	659	665
	666	670	702	703	705
	706	747	748		
deformation potentials	403	404	406	407	
dehydrogenation	215				
density	95	156	157		
doping effects	95				
molten Si	156	157			
temperature dependence	95	156			
density functional theory	245	246	257	332	386
	387				
generalized gradient approximations	336				
gradient expansion approximation	336				
Hohenberg-Kohn theorem	332	333			
Kohn-Sham equations	333	334	343		
local density approximation	334	336			
local spin-density approximation	335				
parametrisation	335	336			
reliability	336	337			
density of states effective mass	408	409	439		
pressure dependence	439				
depletion layer width	207	208			
device modeling	457				
device wafer	923				
devices, metal impurity effects	777				
diamond, cohesive energy	352				
dichroism	481				
dielectric function	679	683			
doping effects	681				
sapphire	889				
temperature effects	681				
differential overlap	247				
modified methods	250				

<u>Index terms</u>	<u>Links</u>
differential overlap ( <i>Continued</i> )	
neglect of differential overlap	248
partial retention of diatomic differential overlap	247
zero differential overlap	247    248
diffusion coefficient	699
diffusion coefficients of dopants in c-Si	
Al	599    600
As	610
Ga	601
In	604
P	607
Sb	613
Tl	605
diffusion coefficients of dopants in SiO <sub>2</sub>	973
As	973
B	973
P	973
diffusion coefficients of impurities in c-Si	
C	506
enhanced	481
Er	586
H	278    279    511    517
K	594
Li	594
N	539
Na	594
O	269    479
temperature dependence	480    507    508    511    512
transition metals	539    549    556    594
transition metals	547    777    778
diffusion current	699
diffusion in SOI material	957
dopant segregation	972    973
implantation damage enhanced	963
oxidation enhanced	957
vacancy mediated enhanced	971
diffusion length	699
diffusion modeling	607
dihydrogen defects	528
dimer-adatom-stacking fault model	178    179    195    290    291

<u>Index terms</u>	<u>Links</u>
dimer buckling	175 291 293 294 297
dimer bond length	176 177 291 294
dimer tilt angle	176 177 291
dimerisation	175 290
dimers	
binding energy	269
O	269 270 480 481 497
dislocation climb	120 133
dislocation core defects	369
kinks	370 371
solitons	369 370
dislocation core structure	364
reconstruction	365 366 375
30° partial	365 366
60° partial	367
90° partial	366 367
dislocation cross-slip	120 132 133
dislocation dissociation	360
dislocation dissociation width	140
dislocation glide	144 306 373
dislocation half-loop	109 110 139
dislocation immobilization	118 119
doping effects	118
release stress	118
temperature dependence	118
dislocation-impurity interactions	654 655
dislocation loops	758 759
dislocation mobility	109 113 130 373
partial dislocations	140
dislocation modeling	362
boundary conditions	362 363
cluster method	362
interatomic potentials	363 364
unit cell method	363
dislocation motion	373
dislocation pinning	541
dislocation shuffle	306
dislocation velocity	113 119 120 141 142 373
doping effects	114 141

<u>Index terms</u>	<u>Links</u>
dislocation velocity ( <i>Continued</i> )	
electron irradiation effects	119 141 142
laser illumination effects	119 141 142
recombination enhanced	119 142
stress dependence	113 114 116 141
temperature dependence	113 117 141
dislocations	108 357 653
edge	357 358 375
electrical properties	653
glide set	109 359 360
glissile	108
luminescence	655 656
minority	375
modeling	357
partial	108
perfect	357 360
screw	109 113 120 358 360 375
shuffle set	109 359 360
SIMOX	981
60°	109 113 359 360
displacement current	459
distribution coefficients of impurities in c-Si	622 623
Al	621 622
Ga	621 623
In	621 624 625
Sb	633
Tl	626 627
divacancies	316 645 706 715 765 766
charge states	316
energy levels	706
ionization level	316
structure	316 644 645
symmetry	316
donor levels	
Er in c-Si	586 588 589
donors	
chalcogen-related	575
double	669
electronic states	573

<u>Index terms</u>	<u>Links</u>
donors ( <i>Continued</i> )	
thermal	270    480    481    492    496
500	659
thermal double	663    670
dopant activation	751    752
dopant activation energy	743
dopant clustering	751    752
dopant deactivation	749    750
dopant diffusion	599
acceptors	599
donors	607
dopant-H complexes	525
dissociation energy	526
structure	525
dopant ionization energy	773
dopant segregation	62    63    65    66    972
973	
dopant sticking probability	62
temperature dependence	62
doping range	63    64
double acceptors	670
double donors	669
energy-level transitions	669
ionization energy	669    670
thermal	663    670
double solid phase epitaxy	890
DRAM applications	989
drift-diffusion model	458
drift mobility	699
dynamical recovery	129
doping effects	131    132
first stage	129
second stage	132    133
<b>E</b>	
<b>E centre</b>	706    768
effective density of states	415
effective distribution coefficient	19    20
effective mass approximation	574    575    578

<u>Index terms</u>	<u>Links</u>
elastic constants	98      99      102      402
doping dependence	102
second order	98      99
temperature dependence	98      99
third order	99
elastoresistance coefficients	422
electrical activation	
Er in c-Si	586      588      589
electrical characterization of Si surfaces	202
electrical conductivity	
liquid Si	696
electroluminescence	590
electroluminescence excitation cross section	
Er in c-Si	586
electrolytic in-process dressing grinding method	928
electron diffusion coefficient	434
electron diffusion length	440
doping dependence	440
minority carrier	440
electron drift velocity	434
electric field dependence	435      437
modeling	435
temperature dependence	437
electron effective mass	408
doping dependence	408
longitudinal	408
temperature dependence	408
transverse	408
electron ionization coefficients	450
electron-irradiated Si	705      706      746
annealing effects	750
defect energy levels	747      748
dopant deactivation	749      750
photoconductivity spectra	705      706
resistivity	749
electron irradiation effects	705      706      714      715      746
temperature dependence	706
electron irradiation induced defects	763
electron lifetime	440      441
doping dependence	441

<u>Index terms</u>	<u>Links</u>
electron lifetime ( <i>Continued</i> )	
minority carrier	440    441
temperature dependence	441
electron mobility	203    430    460    461
electric field dependence	433
epitaxial Si	438
impurity effects	431    432
minority carrier	439
pressure dependence	439
silicon on sapphire	430
SIMOX	981    986
strain effects	430
temperature dependence	430    431
electron transport modeling	435
scattering processes	436    437
elemental partial pressures	55    56
ELTRAN™	976    977
energy balance transport model	470
current flux density	471
density of states	471
energy balance equations	470    471
energy-dependent impact ionization	474    475
energy-dependent mobility	474
energy flux density	471
energy relaxation times	473    474
epitaxial silicide contacts	863
epoxide formation	215
equilibrium distribution coefficient	16    499
Er in c-Si	585
Auger de-excitation coefficient	586
diffusivity	586
donor levels	586    588    589
electrical activation	586    588    589
electroluminescence excitation cross section	586
incorporation methods	586    587
luminescence intensity	589    590
minority carrier lifetime	586    589
reactivity	588
segregation coefficient	586    587
site structure	588
solubility	586

LinksIndex terms

etch rates				
chemical plasma etching	832			
doping dependence	811	815	834	
ion-beam-assisted etching	842			
ion milling	829	830		
isotropic wet etching	811			
laser-assisted etching	845			
orientation-dependent wet etching	815			
plasmaless gas-phase etching	825			
preferential etching	822	823		
reactive-ion-beam etching	842	843		
reactive ion etching	832	837	838	
sputtering	828	829		
etchstop technology	938			
eutectic temperature				
Si-As	630			
Si-B	620			
Si-P	627			
Si-Sb	632			
Si-transition metals	543	544	546	547
evaporation rate of impurities from Si melt	21	22		
doping effects	29	30		
O	24	29	30	
exciton binding energy	392			
exciton diffusion	724			
exfoliation by H implantation	942			
blistering	943	950	955	
bonding effects	953			
flaking	943	950	951	
surface roughness	945	946		
thermal evolution of defects	947			
extended defects	751	752	755	
external gettering	784			
extinction coefficient	679	681	683	
liquid Si	696			
<b>F</b>				
<b>facet bars</b>	878			
Fischler rule	499	503		
floating zone growth	39			

<u><b>Index terms</b></u>	<u><b>Links</b></u>
fracture toughness	144
polycrystalline Si	146     147
Frank-Turnbull mechanism	551
Frenkel pairs	650     747     750     758
fully-depleted devices	901     902
 <b>G</b>	
<b>GaAs</b>	
lattice constant	337
phonon frequencies	337
gamma irradiation effects	714     715
gas-source molecular beam epitaxy	69
doping	72
GeSi	70     71     73
growth kinetics	70
growth rate	70
layer quality	73     74
selective growth	73
surface hydrogen	72     73
systems	69     70
transition abruptness	72     73
gauge factor	422
<b>Ge</b>	
lattice constant	337
phonon frequencies	337
UHV/CVD	82
generalized gradient approximations	336
generation lifetime	699     713
SOI materials	999
<b>GeSi</b>	
gas-source MBE	70     71     73
low pressure CVD	86
UHV/CVD	82
<b>GeSiC</b>	
UHV/CVD	82
gettering of transition metals	777
Al-backside	780     786     787
backside damage	780     787
chemical	780     788
external	784
implantation	780     788

LinksIndex termsgettering of transition metals (*Continued*)

in Si technology	111
internal	783    784
intrinsic	779
P-diffusion	779    784
poly-backside seal	787
proximity	788
relaxation	781
segregation	781    782
Si surface and Si/SiO <sub>2</sub>	779
simulation	794
substrate	779    790    791
trends	794    795
gradient expansion approximation	336
grain boundaries	299
atomistic modeling	299
nanocrystalline Si	302    303
quantum mechanical calculations	304    305
tilt	300
twist	300    301    303
Grashof number	8
grinding	928
electrolytic in-process dressing	928
grown-in defects	39
pull rate effects	39    40
simulation	41
growth kinetics	70
growth rate	
gas-source MBE	70
MBE	56    58
surface migration	59
temperature dependence	58    70    81
UHV/CVD	80
Gruneisen relation	153

**H****H-containing point defects**

522

C-H complexes	532
charge states	523    524
configurations	523    524
dihydrogen complexes	528

**Index terms****Links**

H-containing point defects ( <i>Continued</i> )				
dopant-H complexes	525			
H-decorated lattice defects	527	528		
O-H complexes	532			
total energies	522			
transition-metal-H complexes	531	532		
H decorated lattice defects	527	528		
H-implantation induced defects	947			
thermal evolution	947			
H in c-Si				
diffusion	511	517		
point defects	522			
profiles	517			
solubility	516	517		
H-O complexes	532			
H passivation of dopants	280	525	526	
acceptors	280	525	526	
donors	280	525	526	
Hall coefficients	422			
Hall factor	438	446		
Hall mobility	43	8		
handle wafer	923			
hardness	136			
temperature dependence	136	137		
Hartree-Fock theory	245	331	332	
Hartree-Fock-Roothaan equation	246	247		
heat of fusion	157	171		
HF etching	211	212	811	
HF vapour cleaning	226			
condensed phase regime	228	229		
enhanced adsorption regime	229	230		
gas phase regime	230			
kinetics	230	231		
oxide removal	226			
selectivity	231			
surface contaminants	231	232		
systems	227	228		
high pressure phases	104			
high temperature sputtering	872	873		
high temperature superconducting devices	900			

<u>Index terms</u>		<u>Links</u>
Hohenberg-Kohn theorem	332	333
hole diffusion length	447	448
doping dependence	447	448
minority carrier	447	448
hole effective mass	409	
heavy hole	409	
light hole	409	
hole ionization coefficients	450	
hole lifetime	448	449
doping dependence	448	449
minority carrier	448	449
temperature dependence	449	
hole mobility	443	460 461
epitaxial Si	446	
impurity effects	443	
minority carrier	447	
SIMOX	981	986
temperature dependence	443	444
<b>I</b>		
<b>IC manufacture</b>	851	979 985
ideality factor	73	74
implantation-induced gettering	780	788
impurities in Si		
diffusion coefficient	20	
effective distribution coefficient	19	20
equilibrium distribution coefficient	16	
evaporation rate from melt	21	22
solubility	16	
tetrahedral covalent radii	16	
impurity-dislocation interactions	372	373
impurity energy levels	561	573 583 584 588
	589	
chalcogen-related donors	573	
Er	588	589
rare-earth ions	583	584
3d transition metals	563	
4d transition elements	566	567
5d transition elements	568	
impurity modeling	277	
alkali metals	284	

<u>Index terms</u>		<u>Links</u>
impurity modeling ( <i>Continued</i> )		
C	281	282
Ge	282	
H	277	
N	282	
transition metals	283	284
impurity segregation	16	304 305
macroscopic	21	
inelastic neutron scattering	160	
infrared absorption		
C	503	504
calibration	496	497 540
N	540	541
O-related	492	500 501
infrared absorption coefficient		
C	503	
calibration factor	501	503
O	501	
infrared absorption spectra	160	213
interface structure		
CoSi <sub>2</sub> /Si	877	879 880
NiSi <sub>2</sub> /Si	876	
internal gettering	783	784
internal thermal oxidation	980	984 985 987 993
interstitial diffusion mechanism	547	
interstitial O	492	500 501
interstitial-related defects	648	
annealing	648	
interstitial sites	277	278
interstitial supersaturation	609	612 615 752 958
interstitials	33	319 646
C	281	766 767
diffusivity	35	
equilibrium concentration	35	
formation energy	322	
H	277	278
isolated	648	
mobility	646	
O	267	268
self-interstitials	319	

LinksIndex termsinterstitials (*Continued*)

Si	646
trapped	646
ion beam assisted sputtering	587
ion implantation induced defects	755 763
clamshell	756 760
defect density	755 757
end of range	756 758 759
point defects	763
precipitation related	756 760
regrowth related	756 759 760
subthreshold	756
ion implantation into c-Si	587 636 733 739
As	735 737
atomic profile	636 638
B	636 637 735 737 740 741
Er	587
ion channeling effects	636 637
models	637 638 733 739
P	638 735 737
range theory	733
ion implantation modeling	637 638 733 739
binary collision approximation	739
concentration profile	733 740 742
kinetic Monte Carlo models	743 744
molecular dynamics models	741 742
Monte Carlo models	736 737 739
ion implantation range theory	733
Boltzmann transport equation	736
Monte Carlo simulation	736 737
stopping power	733
straggle	736 737
ion-implanted Si	418 702 703 746
amorphisation	750
annealing effects	750
defect energy levels	747 748
dopant deactivation	749 750
photoconductivity spectra	702 703
resistivity	749
sheet resistance	418

<u><b>Index terms</b></u>	<u><b>Links</b></u>				
ion milling	829	830			
ionization threshold	253				
modeling	253				
isotropic wet etching	811				
 <b>K</b>					
<b>kick-out mechanism</b>	551	553	672	743	791
kinetic Monte Carlo models	743	744			
kinks	109	120	370	371	373
formation energy	374				
migration energy	111	370			
Knudsen cell	111				
Knudsen relationship	57	61	62		
Kohn-Sham equations	55				
basis set	258	260	262	333	334
boundary conditions	343	345			
Brillouin zone sampling	343				
Car-Parrinello molecular dynamics	345				
diagonalisation	348	349			
direct minimization	346	347			
	349				
 <b>L</b>					
<b>L-pits</b>	344	345			
laser-assisted etching	344				
photoablation	845	846			
photon assisted chemical etching	845	846			
photon enhanced plasma etching	845	847			
lattice expansion coefficient	488				
lattice mismatch					
$\text{Er}_3\text{Si}_5/\text{Si}$	488				
silicide/Si	864				
lattice parameter	91	105	106	253	337
high pressure phases	91				
impurity effects	105	106			
modeling	93				
pressure dependence	253				
silicides	93				
temperature dependence	864				
lattice parameter measurement	93				

LinksIndex terms

lattice vacancies	643			
leakage currents	777			
light emitting diodes	590			
limited reaction processing	86			
linear combination of atomic orbitals	258			
linear scaling methodologies	349			
charge density matrix method	350	351		
divide and conquer methods	350			
grid based methods	351	352		
localization of orbitals	350			
liquid Si				
density	3	156	157	
electrical conductivity	696			
extinction coefficient	696			
molar volume	157			
optical absorption coefficient	696			
refractive index	696			
specific heat	152			
surface tension	4	170		
thermal conductivity	166			
viscosity	5			
local density approximation	334	336	386	387
low noise amplifier	898	899		
low pressure CVD	86			
lower yield stress	122	126	139	
doping effects	127			
strain-rate dependence	124	127		
temperature dependence	126	128	139	

**M**

<b>Marangoni drying</b>	222	223		
Marangoni flow	3	5	25	
melt convection	8			
crucible rotation effects	9			
crystal rotation effects	12	13		
flow modes	8	9		
gravity effect	8			
magnetic field effects	10			
thermo-capillary effect	9			
thermo-solutal effect	9			

<u>Index terms</u>	<u>Links</u>
melt density	3
doping effects	3     5
temperature dependence	3
melt flow modes	8     9
laminar	8     9
oscillatory	8     13
turbulent	8     9
melt growth	
grown-in defects	39
impurity segregation	16
oxygen transportation	23
self-interstitials	33
simulation of defect formation	41
vacancies	33
melting point	122    151    153    155
pressure dependence	156    157
mesotaxy	870    871
metastable phases	105
microelectromechanical systems	427    900
micromachining	833
microwave-photoconductivity decay method	209
migration enthalpy	548    549
migration of H	278    279
minority carrier diffusion length	206    440    447    448
minority carrier lifetime	203    209    440    441    448
mixer	449    586    589
mobile ionic charge	897    898
mobility modeling	593
field-dependent	459
inversion layer models	465
Klaassen's model	465
Tasch model	461
molar volume	465
liquid Si	157
molecular beam epitaxy	157
apparatus	55
co-evaporated dopants	56
co-ion-implanted dopants	61
growth rate	63

<u><b>Index terms</b></u>	<u><b>Links</b></u>
molecular beam epitaxy ( <i>Continued</i> )	
silicides	865
sources	57      58
molecular cluster model	245      252      255
molecular dynamics	741
monolayer solid phase epitaxy	868      870
MOS devices	777      788      789      969
MOS transistors	895      896
MOSFET	893      967      999
threshold voltage	968
multiple internal transmission infrared spectra	912      919      920
muonium centres	523      524
anomalous	523      524
normal	523      524
Murnaghan equation of state	400
 <b>N</b>	
<b>N-defect interactions</b>	541
N in c-Si	
diffusion	539
IR absorption	540      541
segregation coefficient	538
solubility	538
N-O complexes	541
nanocrystalline Si grain boundaries	302      303
negative-effective-U levels	309      315      317      375      515
	524      644      645      647      665
	666      768
neutron irradiation effects	714      715
noise figures	896
normal freezing	21
normal freezing law	484
nuclear radiation detectors	595
 <b>O</b>	
<b>O concentration in c-Si</b>	31      267
O in c-Si	
diffusion	479
IR absorption	492      500      501
precipitation	500

<u><b>Index terms</b></u>	<u><b>Links</b></u>		
O in c-Si ( <i>Continued</i> )			
segregation coefficient	484    499    500		
solubility	488		
O point defects	267		
diffusion barrier	267    268		
dimers	269    270		
interstitial	267    268		
thermal donors	270		
O-related defects	494    495		
complexes	494    495		
irradiation defects	494    495		
O-related precipitates	495    496		
O solubility in Si melt	27		
doping dependence	29    30		
temperature dependence	27    28		
O transportation during CZ growth	23		
diffusion layers	31		
dissolution rate	23    24    26		
doping effects	29    30		
evaporation rate	24    25    29		
temperature dependence	23		
O-vacancy defect	494    501    764    765		
optical absorption coefficient	681    683		
liquid Si	696		
orientation-dependent wet etching	815		
alkali hydroxides/KOH	816		
EDP	817    819		
quaternary ammonium hydroxides/TMAH	817    819    820		
oxidation enhanced diffusion	957		
oxidation induced stacking fault ring	39    45    46    48		
oxidation induced stacking faults	39    45    46    48    960		
oxide mediated epitaxy	874		
 <b>P</b>			
<b>P-diffusion gettering</b>	779    784		
parametrised pseudopotential methodology	264		
passivation	211    280    525    526    654 719		
Peierls mechanism	124    127    306		
Perdew-Zunger parametrisation	335		

<u><b>Index terms</b></u>	<u><b>Links</b></u>			
phase diagrams				
Si-impurity	16	17		
phase transformation sequences	104	105		
phenomenological oxygen segregation coefficient		31		
phonon frequencies	159	160	337	
acoustic	159	160	337	
optical	159	160	337	
phonon spectrum	159			
bulk c-Si	161			
heterostructures	162			
surface effects	161	162		
photoablation	845	846		
photoconductivity		699		
injection level	700	701		
measurement	700			
photoconductivity spectra	702	703	705	706
electron irradiated Si	705	706		
ion-implanted Si	702	703		
temperature dependence	706			
photogenerated carrier diffusion	722	726		
doping effects	728			
drag effect	728			
exciton	724			
injection dependence	723	724		
modified Si	729			
photogenerated carrier lifetime	708	712		
Auger lifetime	709	710	715	716
degradation factor	714	715		
doped and treated Si	712			
ion implantation effects	715			
irradiation effects	714	715		
radiative lifetime	709			
radiative recombination coefficient	709			
recombination centres	714			
Shockley-Read-Hall lifetime	708	709	712	713
temperature treatment effects	714			
photogenerated carrier mobility	722	723	726	
doping effects	727	728		
drag effect	728			
injection dependence	723			
modified Si	729			

<u>Index terms</u>	<u>Links</u>			
photoluminescence	655	656	673	
dislocation-related	655	656		
temperature dependence	656			
photoluminescence intensity				
Er-doped Si	589	590		
photon assisted chemical etching	845	846		
photon enhanced plasma etching	845	847		
photoplastic effect	141	142		
pi-bonded chain model	177	178	199	200
	289			288
piezo-Hall effect	422			
piezoresistance	421			
models	427			
piezoresistive sensors	427	428		
piezoresistivity coefficients	421			
impurity dependence	425			
linear	422			
polycrystalline Si	426	427		
second order	422	426		
size effects	427			
SOI	427			
temperature dependence	425	426		
third order	422	426		
plasma assisted chemical etching	932	933		
plasma cleaning	236			
mechanisms	237			
plasma etching	832			
plasmaless gas-phase etching	825			
high temperature	825			
room temperature	825	826		
plastic deformation	122	138		
dynamical recovery	129			
yield point	123			
platelet defects	518	529		
point defect charge states	33			
point defect diffusivity	35			
temperature dependence	35			
point defect equilibrium concentration	33			
Fermi level effect	34	35		
lattice stress effect	34	35		
temperature dependence	35			

LinksIndex terms

point defect modeling	267				
vacancies	309				
point defects	763				
capture cross sections	764				
deep levels	763				
electron irradiation induced	763				
ion implantation induced	763				
Poisson's equation	457				
Poisson's ratio	101	102	424	425	
Reuss average	101	102			
Voigt average	101	102			
polishing	930	938	940	941	
polycrystalline Si					
etch rates	816	823			
fracture	146	147			
gauge factor	426				
piezoresistivity	426	427			
polysilicon backside gettering	787				
porous Si	976	977			
precipitation of O in c-Si	500				
preferential etching	822	823			
proton irradiation effects	714	715			
proximity gettering	788				
pseudopotentials	337	384	385		
approximations	339	340			
ionic	338	339			
norm conservation	340				
soft	342				
pulsed laser melting	872	873			

**Q**

<b>quantum chemical modeling methods</b>	245				
differential overlap	247				
parametrisation	249				
quantum mechanical modeling methods	257				
parametrised pseudopotential methodology	264				
tight-binding methodology	257				
quantum Monte-Carlo methods	352	353	388		
diffusion	352	353			
variational	352	388			

<u><b>Index terms</b></u>	<u><b>Links</b></u>
quantum wells	74
GSMBE-grown	74
MBE-grown	74
quasi-Fermi levels	458
 <b>R</b>	
<b>radiation hardness</b>	892
radiative lifetime	709
radiative recombination coefficient	709
Raleigh number	8
Raleigh-Benard instability	9
Raman frequency	253
modeling	253
Raman spectra	160    161
pressure effects	161
rapid thermal CVD	86
rare-earth-doped c-Si	583
energy levels	583    584
Rayleigh mode	289    293    296
RCA clean	215    219
reactive ion etching	832    837    838
deep RIE	833    838
recombination centres	714
capture cross sections	714
recombination lifetime	699    708    713
Auger	708
radiative	708
Shockley-Read-Hall	708
SOI materials	999
refractive index	679    681    683
liquid Si	696
relaxation gettering	781
resistivity	413    414    426
doping dependence	413    414
electron irradiation effects	749
ion-implanted Si	749
n-type Si	413    414
p-type Si	413    414
sapphire	889
silicides	851    864
temperature dependence	426

Links**S**

<b>sapphire</b>	889			
dielectric constant	889			
dielectric loss tangent	889			
resistivity	889			
thermal conductivity	889			
Schottky barrier heights				
CoSi <sub>2</sub> /Si	879	880		
inhomogeneity	880			
NiSi <sub>2</sub> /Si	876			
secondary defect formation	33	751		
Seebeck coefficient	161			
segregation coefficient				
As in Si/SiO <sub>2</sub>	973			
B in Si/SiO <sub>2</sub>	973			
C in c-Si	503			
Er in c-Si	586	587		
Nine-Si	538			
O in c-Si	484	499	500	
P in Si/SiO <sub>2</sub>	973			
transition metals in c-Si	781	782	786	
segregation enthalpy	73			
segregation gettering	781	782		
segregation coefficient	781	782		
self-diffusion coefficient	327	328		
activation enthalpy	327			
self-interstitial aggregates	39			
simulation	41			
self-interstitial migration	326	750		
electron irradiation effects	326			
self-interstitials	319	646	743	
charged	324	325		
clusters	326			
formation energy	322	743		
migration	326	743		
neutral	322			
structure	320			
sessile drop method	26	27		
shallow thermal donors	274	659		
energy levels	659			
ionization energy	274	659	660	

<u>Index terms</u>	<u>Links</u>
shear modulus	101 102 122
Reuss average	101 102
Voigt average	101 102
sheet resistance	418
annealing effects	418
ion-implanted Si	418
silicides	853
SOI films	972
temperature coefficients	419
Shockley partial dislocations	108 360
Shockley-Read-Hall lifetime	708 709 712 713
injection dependence	712 713
Si surface and Si/SiO <sub>2</sub> gettering	779 791
SiGe on sapphire	901
SiGe on SOS	900 901
silicidation	851
ambient control	856 857
capping layers	858
chemical reactivity	854 856 857
cleaning	856
CoSi <sub>2</sub>	851
thermal process window evolution	851
TiSi <sub>2</sub>	851
silicide epitaxial growth	865
allotaxy	870
high temperature sputtering	872 873
MBE	865
mesotaxy	870 871
monolayer solid phase epitaxy	868 870
oxide mediated epitaxy	874
pulsed laser melting	872 873
solid phase epitaxy	865 866
template growth	866 868 870
Ti-interlayer mediated epitaxy	873 874
silicided poly-Si runners	853 860
silicides	
crystal structure	863 864
lattice mismatch	864
lattice parameters	864
resistivity	864

<u>Index terms</u>	<u>Links</u>
silicon on insulator	
bond and etchback	938
bond, grindback and polish	923
bonded wafers	992
costs	992
diffusion	957
H-induced exfoliation	942
material properties	992
overview	887
piezoresistance	427
porous Si	976
sheet resistance	972
silicon on sapphire	889
SIMOX	979
wafer bonding	905
silicon on sapphire	889
compressive stress	896
deep traps	892
electron mobility	430
hole mobility	890
material properties	889
minority carrier lifetime	889
radiation hardness	892
thin film	892
silicon on silicon dioxide	957
SIMOX	788
	992
bow	994
BOX breakdown field	999
BOX defects	987
contamination	996
costs	979
crystalline defects	994
defect density	995
diffusion	992
dislocation density	960
edge exclusion	981
electron mobility	994
fixed charge density	989
flatness	999
generation lifetime	995
	999

<u>Index terms</u>	<u>Links</u>
SIMOX ( <i>Continued</i> )	
HF defect density	981 985 996 997
hole mobility	981 986
interface state density	981
interface trap density	999
low dose	980 997 999
medium dose	981 988
microstructure	981
oxide charge	981
process	979 988 989
radiation hardness	894
recombination lifetime	999
short density	981 986 987
site total indicator reading	994 995
stacking fault tetrahedra	981
standard dose	979 985 997 999
surface roughness	981 985 993 994
thickness	981
thickness uniformity	993 994
total thickness variation	994 995
transconductance	981
warp	994 995
simulation of defect formation	41
excess point defect concentration	41
O precipitation	45 46 48 49 51
OSF ring formation	45 46 48
point defect aggregation	43
SiO vapour pressure	500
SiO <sub>2</sub> , thermal conductivity	889
slip geometry	138
SmartCutTM process	942 947 955
solar cells	777 782 784 786
solid phase epitaxy	865 866 890
solitons	369 370 373
formation energy	370 375
solubility of B in SiO <sub>2</sub>	973
solubility of impurities in c-Si	16
Al	621 622
As	630
B	620 621
C	504

LinksIndex terms

solubility of impurities in c-Si ( <i>Continued</i> )						
Co	851					
doping effects	790					
Er	586					
Ga	623	624				
H	516	517				
In	624	625				
in liquid Si	488	489	504	538		
Li	594					
N	538					
Na	595					
O	27	28	488			
P	627					
Sb	632					
temperature dependence	489	490	504	516	517	
	556	594	620	629	633	
	634	790				
Ti	851					
Tl	626	627				
transition metals	543	555	777	778	786	
solution enthalpy	543	544				
solution entropy	543	544				
SOS devices	894					
frequency	895	896				
I-V characteristics	896					
noise figure	895	896				
space group	104					
specific heat	151					
molten Si	152					
temperature dependence	151	152				
spin-orbit coupling constant	403	404				
spin-orbit splitting	390					
sputter cleaning	236					
sputtering	828	829				
sputter yield	828	829				
SQUID	900					
stacking fault energy	108	305	359	360		
stacking faults	108	305	306			
extrinsic	108	305	306			
intrinsic	108	305	306			
modeling	305	306				

<u>Index terms</u>	<u>Links</u>			
steady-state creep	132	133		
sticking coefficients	71	72	80	
temperature dependence	72			
stiffness	98	99	424	426
temperature coefficients	426			
stress-strain curves	122	139		
temperature dependence	122	123	126	
structural modeling				
ab initio techniques	330			
dislocations	357			
grain boundaries	299			
minor impurities	277			
O point defects	267			
quantum chemical methods	245			
quantum mechanical methods	257			
self-interstitials	319			
stacking faults	305			
surfaces	288			
vacancies	309			
substrate gettering	779	790	791	
surface Brillouin zones	190	196	289	293
surface charge density	206	292	295	
surface charge imaging	206			
surface charge profiling	207	208		
surface cleaning				
HF vapour	226			
in situ thermal annealing	235	236		
plasma	236			
sputter	236			
wet chemical	215	219		
surface dimers	175			
surface electrical characterization	203			
contact methods	203			
corona oxide semiconductor method	208	209		
microwave-photoconductivity decay method	209			
non-contact methods	205			
surface charge imaging	206			
surface charge profiling	207	208		
surface photovoltaic method	205	206		
surface electrical properties	202			
electric charge density	202			

**Index terms****Links**

surface electrical properties ( <i>Continued</i> )					
minority carrier lifetime	202				
minority carrier velocity	202				
mobility	202				
surface electron states	291	292	294		
surface electronic structure	189				
back-bond surface states	192				
dangling-bond surface states	190				
dimer bond state	194	195			
Si(100)	189				
Si(111)	195				
surface state dispersions	190	198			
surface free energy	175				
surface generation velocity	719				
surface hydrogenation	211				
surface oxidation	212				
water-induced	213				
wet chemical oxides	215	216			
surface passivation	719				
surface phonons	161	162	288	290	293
	296				
surface photovoltage method	205	206			
surface potential	202	205			
surface recombination lifetime	207	208			
surface recombination velocity	209	718	962		
damaged surfaces	718	719			
doping effects	720				
passivated surfaces	719				
SOI materials	962				
surface reconstruction	175	183	189	288	
cleavage surface	177	178			
dimer buckling	175	291	293		
dimerisation	175	290			
Si(001)	175	291			
Si(110)	179	180			
Si(111)	177	288			
Si(113)	295	296			
surface roughness	202				
SIMOX	981	985	993	994	
SOI materials	962	977	993	994	
surface state density	202	205			

<u>Index terms</u>	<u>Links</u>			
surface structure	183	288		
surface tension	4	170		
O effects	4	5		
temperature dependence	4	170		
system-on-a-chip applications	897			
 <b>T</b>				
<b>temperature scales</b>	155			
template growth	868	870		
tetrahedral covalent radii	16	94	95	
thermal cleaning	235	236		
thermal conductivity	165			
doping effects	166			
liquid Si	166			
sapphire	889			
SiO <sub>2</sub>	889			
temperature dependence	165	166		
thermal diffusivity	168	169		
doping effects	169			
temperature dependence	168	169		
thermal donors	270	480	481	492
	500	659	663	496
bistability	270	273	665	666
double	663	670		
ionization energy	270			
local vibrational modes	496			
models	270			
thermal double donors	663	670		
binding energy	664			
bistability	665	666		
energy-level transitions	664			
symmetry	666			
thermal expansion coefficient	93	153		
linear	93			
temperature dependence	153			
thermal velocity effective mass	408	409		
thermo-capillary forces	9			
thermo-solutal forces	9			
thin film silicon on sapphire	892			
radiation hardness	893			
three-dimensional integration	989			

<u>Index terms</u>	<u>Links</u>
thyristors	715
Ti-interlayer mediated epitaxy	873    874
Ti silicidation	851
tight binding approximation	257    383    384
ab initio multicentre	263
density-functional based	263
Hartree-Fock based	263    264
parameter-free	262    263
parametrisation	259
TiSi <sub>2</sub>	
phase transition	853    854    856
sheet resistance	854    855
specific resistivity	851
transient enhanced diffusion	319    617    744    751    752 757    759    763    768    957 963
in SOI materials	963
temperature dependence	963    964
transistors	777    852    857    893    967 999
transition-metal-H complexes	531    532
transition metal impurities in c-Si	
deep levels	561
diffusion	547
interstitially dissolved	543    549
solubility	543    555
substitutionally dissolved	546    547    551
transmit/receive switch	897    898
twins	138    139
<b>U</b>	
<b>ULSI devices</b>	863    880    992
ultra high vacuum chemical vapour deposition	77
Ge	82
GeSi	82
GeSiC	82
growth initiation	78    79
growth mechanism	79    80
growth rate	80
material quality	85
multi-wafer	77    78

**Index terms****Links**

ultra high vacuum chemical vapour deposition ( <i>Continued</i> )					
reactants	79				
single-wafer	78				
transition abruptness	85				
ultra-shallow thermal donors	661				
UniBondTM	993				
upper yield stress	122	126	127		
doping effects	127				
<b>V</b>					
<b>vacancies</b>	33	309	643	743	
diffusivity	35	316	644	645	
equilibrium concentration	35				
formation energy	311	317	743		
formation entropy	315	316			
lattice	643				
migration energy	644	645	743		
modeling	309				
vacancy aggregates	39				
simulation	41				
vacancy clusters	317				
vacancy concentration	93				
vacancy-defect interactions	645	646			
annealing	646				
vacancy diffusivity	316	644	645		
vacancy-dislocation interactions	371	372			
vacancy mediated enhanced diffusion	971				
vacancy structure	309	643	644		
charge states	309	643			
charged	313				
clusters	317				
computational schemes	310	311			
divacancies	316				
ionic relaxation	311	317			
ionization level	315	317			
neutral	311				
point symmetry	312	317			
supercell approximation	310				
vacancy supersaturation	46	609	612	615	971
vacuum mean free path	55				

<u><b>Index terms</b></u>	<u><b>Links</b></u>			
valence band maxima	381	403	404	
strain effects	403	404		
vapour pressure of SiO	500			
Vegard's law	93	94		
very low pressure CVD	84			
vicinal surface structure	183			
facets	187			
miscut angle	184			
Si(001)	183			
Si(111)	185			
step energy	183	184		
step structure	183			
viscosity	5			
temperature dependence	6	7		
void density	40			
Vosko-Wilk-Nusair parametrisation	335			
 <b>W</b>				
<b>wafer bonding</b>	905	923		
hydrophilic	906			
hydrophobic	907	909	910	918
interfacial energy	907			
interfacial voids	906	907		
wafer bonding interface gettering	791	792		
wet chemical cleaning	215	219		
drying	222			
HF etch	220	221		
Pirhana etch	215	219		
RCA clean	215	219		
reduced chemical consumption	223	224		
reduced water consumption	223	224		
rinsing	222			
wet etching	211	212	811	815
	823			
work hardening	122	129	132	138
 <b>Y</b>				
<b>yield point</b>	122			
doping effects	125	127	128	
lower yield stress	122	126	139	
predeformation effects	128			

<u>Index terms</u>	<u>Links</u>
yield point ( <i>Continued</i> )	
surface effects	128
temperature dependence	125
upper yield stress	122    126    127
Young's modulus	101    102    424    425
Reuss average	101    102
Voigt average	101    102

**Z**

<b>zipper defects</b>	760
-----------------------	-----